Symmetry Properties in Transmission Lines Loaded with Electrically Small Resonators

Circuit Modeling and Application to Common-Mode Suppressed Differential Lines, Microwave Sensors, and Spectral Signature Barcodes

Ph.D. Thesis

Author:
Jordi Naqui

Supervisor:
Prof. Ferran Martín

Programa de Doctorat en Enginyeria Electrònica
Universitat Autònoma de Barcelona
Escola d'Enginyeria
Departament d'Enginyeria Electrònica

Bellaterra (Cerdanyola del Vallès), September 5, 2014

The undersigned, Ferran Martín Antolín, Professor of the Electronics Engineering Department (Engineering School) of the Universitat Autònoma de Barcelona,

CERTIFIES:
that the thesis entitled "Symmetry Properties in Transmission Lines Loaded with Electrically Small Resonators: Circuit Modeling and Application to Common-Mode Suppressed Differential Lines, Microwave Sensors, and Spectral Signature Barcodes,"has been written by Jordi Naqui Garolera under his supervision.

And hereby to acknowledge the above, sign the present.

Jordi Naqui Garolera Ferran Martín Antolín

Programa de Doctorat en Enginyeria Electrònica
Universitat Autònoma de Barcelona
Escola d'Enginyeria
Departament d'Enginyeria Electrònica

Bellaterra (Cerdanyola del Vallès), September 5, 2014

Contents

Acknowledgments

I would like to express my most sincere gratitude to those who have contributed to the present thesis. First of all, many thanks to my supervisor Prof. Ferran Martín because he gave me the opportunity to begin the Ph.D degree. His motivation, knowledge, and continuous help during these last years have played a key role to this thesis. I would also like to thank the people of the research group CIMITEC, the Department of Electronics Engineering, and the Engineering School. Specially, I am very grateful to Gerard Sisó and Javier Hellín. Although they are not formally coauthors of the publications included in this thesis, they are of course part of them. Almost all experimental results in this thesis are merit of their outstanding and patient work.

I am also very grateful to my colleagues from national and international universities with whom I have collaborated. Many thanks to Francisco Medina, Francisco Mesa, and Armando Fernández from University of Seville for our continuous collaboration. Many thanks to Rolf Jakoby and Christian Damm to let me carry out a great stay in Darmstadt University of Technology.

Finally, I would also like to express my gratitude to my friends, specially to Marín and Novo, as well as my family. Thanks to Dana, my Boxer dog, for receiving me with so much enthusiasm every weekday! A special gratitude to those who have really suffered my difficult and stressful moments: my wife Amalia and my little daughter Martina, my mother Mercè, my grandmother Mercè who died last July 3, and my parents-in-law Antonio and Amalia. Thank you for your patience!

Jordi

Summary

This thesis focuses on the analysis, circuit modeling, and applications of transmission lines loaded with electrically small resonators (e.g. split ring resonators −SRRs− or stepped impedance resonators −SIRs−) subjected to symmetry considerations. The results obtained in this thesis expand the state-of-the-art in the frame of metamaterial-based and resonator-loaded transmission lines. For this reason, we first review the fundamental theory of metamaterials and electrically small resonators.

Next, we present some advances in the lumped-element equivalent circuit models of transmission lines loaded with electrically small resonators: (*a*) we model magnetoelectric coupling between the transmission line and the resonators, since it must be considered depending on the relative line-to-resonator orientation, particularly when the structure is symmetric at the midplane; (*b*) by applying the theory of infinite periodic structures using four-port transmission matrices, we show that inter-resonator coupling in resonator-loaded transmission lines enhances the stopband bandwidth due to the appearance of complex modes; and (*c*) we infer the limits on the range of implementable values of inductance and capacitance of shunt-connected series resonators by means of stepped-impedance shunt-stubs.

Afterwards, we analyze and model the behavior of resonator-loaded transmission lines on the basis of symmetry properties. We show that stopband characteristics (frequency, bandwidth, and/or magnitude) can be controlled in terms of symmetry at the midplane of the structures. The results indicate that the orientation of the resonators with regard to the line determines the line-to-resonator coupling strength and nature (electric and/or magnetic), which in turn modulates the attenuation characteristics. The most interesting orientation is the one where resonance condition is inhibited, and accordingly the corresponding loaded-transmission line exhibits an all-pass response.

Finally, we demonstrate the applicability of the theory derived from symmetry considerations for filtering, sensing, and encoding purposes: (*a*) we synthesize differential microstrip lines with common-mode rejection, where wideband suppression is obtained for the common mode while the differential mode is practically unaffected; (*b*) we propose spatial sensors for alignment, displacement, position, and velocity measurements; (*c*) we

also present a differential sensor and comparator for permittivity measurements. The main advantage of the reported symmetry-based sensors is their inherent robustness against variable environmental factors; and (*d*) we propose an alternative encoding mechanism for the design of spectral signature-based chipless radio-frequency identification (RFID) tags, where the relative orientation of the resonators determines the binary values of the code.

Proof-of-concept prototypes (in microstrip or coplanar waveguide technologies) support the validity and potentiality of the proposed symmetry-based approach. Throughout this thesis, the circuit simulations, the electromagnetic simulations, and the experimental results are in good agreement.

Chapter 1

Introduction

Wireless communications and sensing systems are increasingly demanding for low-cost solutions, miniaturization, high performance, reconfigurability, as well as new functionalities. In recent years, novel and potential ideas have emerged in the microwave community inspired by metamaterial concepts for the design of RF/microwave components, circuits, and systems. Typically, metamaterial-based devices are composed of transmission lines loaded with reactive elements (inductors, capacitors, and/or both of them in the form of resonators). These structures have been extensively shown to exhibit high controllability in their transmission characteristics. Since the characteristic impedance and the electrical length of these structures are controllable (obviously, to some extent), such a design is referred to as dispersion and impedance engineering.

The aim of the present Ph.D thesis is to go beyond the state-of-the-art in the analysis, circuit modeling, and applications of transmission lines loaded with electrically small resonators (i.e. without individual inductors and capacitors). In contrast to the dispersion and impedance engineering, the controllability in this thesis is focused on stopband characteristics provided by the resonant elements. Specifically, this thesis deals with these planar structures subjected to symmetry considerations. We gain insight into the behavior of resonator-loaded transmission lines in terms of symmetry properties with an eye to designing innovative RF/microwave devices. Particularly, the theory behind such symmetry properties has been applied to common-mode suppressed differential lines, microwave sensors for spatial variables, microwave sensors for differential permittivity measurements, and chipless radio-frequency identification (RFID) barcodes.

This Ph.D thesis has been written as a *compendium of articles*. Therefore, most of the research on the concerning topic has been already published in international journals and conference proceedings. The articles included in this thesis can be found in **Articles in the Ph.D Thesis**. All

the author's publications and contributions to conferences are listed in **Publications by the Author**. Some publications have been coauthored with the Microwaves Group of the University of Seville by virtue of a national collaboration. An international collaboration has also been carried out; as a result of a stay at the Institute for Microwave Engineering and Photonics in Darmstadt University of Technology, this thesis applies for the *International Mention*. The outline of the thesis is as follows:

- **Chapter 1** is the present introduction to the thesis which is aimed at the motivations, the projects and grants funding this thesis, and the organization.

- **Chapter 2** is addressed to the fundamental theory of metamaterials and electrically small resonators. The background necessary to understand this thesis is reviewed.

- **Chapter 3** presents advances in the lumped-element equivalent circuit models of transmission lines loaded with electrically small resonators. We model mixed magnetoelectric coupling effects in the line-to-resonator coupling, we investigate the effects of inter-resonator coupling applying the theory of infinite periodic structures, and we infer the limits on the synthesis of quasi-lumped shunt-connected series resonators.

- **Chapter 4** analyzes and models the behavior of resonator-loaded transmission lines on the basis of symmetry properties. Controllability of the transmission attenuation (frequency, bandwidth, and/or level) is achieved in terms of the symmetry/asymmetry of the structures.

- **Chapter 5** is devoted to the synthesis of common-mode suppressed differential microstrip lines, where balanced (symmetric) structures are required.

- **Chapter 6** presents novel sensors based on symmetry properties where the principle of operation is based on symmetry disruption. Most of the proposed devices are spatial sensors involving the measurement of a physical spatial variable, such as displacements and velocities. The exception is a differential sensor for permittivity measurements.

- **Chapter 7** proposes an alternative binary encoding mechanism based on symmetric/asymmetric configurations for the design of spectral signature-based chipless RFID tags. In comparison to the standard encoding strategy, the proposed approach has a new degree of freedom that brings more flexibility in the encoding.

- **Chapter 8** summarizes the most relevant results and contributions reported in this thesis. Some future work is proposed by virtue of the research lines that have been emerged from this thesis.

The work conducted during the realization of this thesis was carried out within the group GEMMA (Grup d´Enginyeria de Microones, Metamaterials i Antenes)/CIMITEC (Centre d´Investigació en Metamaterials per a la Innovació en Tecnologies Electrònica i de Comunicacions), which is part of the Electronics Engineering Department of the Universitat Autònoma de Barcelona. GEMMA/CIMITEC has been part of the European Network of Excellence NoE 500252-2 METAMORPHOSE (Metamaterials organized for radio, millimeter wave and photonic super lattice engineering), the main objective of which was to research, study and promote artificial electromagnetic materials and metamaterials within the European Union. It has recently given rise to the Virtual Institute for Artificial Electromagnetic Materials and Metamaterials (METAMORPHOSE VI AISBL). Furthermore, CIMITEC is one of the centers of the Technological Innovation Network of TECNIO (ACC1Ó) of the Catalan Government, created with the objective of promoting the transference of technology to industry in the field of Information and Communication Technology and has been recognized as a Consolidated Group by the Catalan Government (AGAUR).

Among the projects with the different institutions and companies that have given support to the developed research activities or that have emerged from them, we would like to highlight:

- Project RTC-2014-2550-7 RETOS DE COLABORACIÓN 2014 by the Spanish Government granted to a consortium composed of Scytel Secure Electronic Voting, Instituto de Microelectrónica de Barcelona-CNM (CSIC), and UAB-CIMITEC. Title: *Desarrollo tecnológico de tags chipless RFID mediante tecnologías de impresión sobre substratos de bajo coste para su integración en sistemas de modernización electoral (Chipless RFID).*

- Project TEC2013-40600-R by the Spanish Government. Title: *Diseño y síntesis de componentes de RF/microondas basados en conceptos avanzados y su aplicación a circuitos de comunicaciones, sensores y RFID.*

- Project A00016166 Innovation Triangle Initiative (ITI) by the European Space Agency (ESA) granted to EMXYS Embedded Instruments & Systems, UAB-CIMITEC, and Universitat Politècnica de Valencia (UPV). Title: *Coplanar Symmetry-based Contactless Rotation sensor.*

- Project TEC2011-13615-E EXPLORA by the Spanish Government. Title: *Nuevos sensores y detectores basados en las propiedades de simetría de resonadores de anillos abiertos.*

- Project TEC2010-17512 METATRANSFER by the Spanish Government. Title: *Nuevas estrategias de diseño y síntesis de componentes de microondas basados en conceptos de METAmateriales con orientación a la TRANSFERrencia tecnológica.*

- Project CSD2008-00066 CONSOLIDER INGENIO 2010 granted to a consortium composed of eight research groups from different Spanish Universities and funded by the Spanish Government. Title: *Ingeniería de Metamateriales (EMET).*

This Ph.D thesis has also been supported by a national predoctoral fellowship (grant AP2010-0431) from the Training of University Staff Program (FPU) of the Spanish Ministry of Education, Culture, and Sports (MECD).

Chapter 2

Fundamentals of Metamaterials and Subwavelength Resonators

Electromagnetic metamaterials have been a subject of huge research worldwide in the electromagnetic and microwave communities since the first so-called left-handed structure was experimentally conceived in 2000. These efforts have been primarily motivated by the exotic (unusual) electromagnetic properties that these artificial media may feature, such as backward wave propagation. Meanwhile, electrically small resonators based on split rings, which are typical key building blocks to the synthesis of metamaterials, have also attracted much attention. The research activity on these resonant particles has not only been focused on the implementation of metamaterials but also on the design of RF/microwave circuits and components. Thus, novel ideas have emerged in the microwave community to envisage devices inspired by metamaterial concepts with high performance, small size and/or new functionalities. In this regard, in the present thesis these metamaterial-based particles are not used to construct metamaterial structures, but to design innovative RF/microwave devices. Nonetheless, a brief introduction to metamaterials is due for a historical standpoint and to make the Thesis complete, although reporting the current state-of-the-art is beyond the scope of this chapter.

This chapter is devoted to metamaterials and electrically small split-ring resonators, mainly from a circuit approach perspective. It is worth mentioning that a significant part of the intensive work in such topics has been published (or will be published shortly) in textbooks by several pioneering research groups in the last decade [1–6]. Section 2.1 provides a brief description of the fundamental properties of metamaterials as well as a historical overview. In Section 2.2, the different approaches of transmission-line metamaterials are introduced, which are of particular

interest to the microwave community. Specifically, the main focus is aimed at the so-called resonant-type approach in planar technology where subwavelength resonators are used for its synthesis. Inside this category, structures with stopband characteristics will received the most attention. Next, Section 2.3 describes the subwavelength resonators that are used throughout this thesis, with special emphasis on the properties derived from symmetry assumptions. Finally, Section 2.4 is addressed to waves induced in chains of coupled resonators, namely electro-inductive and magneto-inductive waves.

2.1 Electromagnetic Metamaterials

Electromagnetic metamaterials may be broadly defined as *artificial* (man-made) *effectively homogeneous structures* (usually made up of an arrangement of metals and dielectrics) *with unusual properties not readily available in nature* [1].[1] Certainly, the prefix *meta* means *beyond* or *after* in Greek, suggesting that the medium possesses properties that transcend those available in natural materials, this being the most relevant characteristic of metamaterials[2].

A medium is regarded to be effectively (on average) homogeneous (uniform) if its unit-cell dimension is much smaller than the guided wavelength. This homogenization (averaging) procedure plays a key role in considering the structure electromagnetically homogeneous along the direction of propagation. Consequently, a metamaterial behaves as a real material in the sense that the macroscopic (in a piece of matter) response to an electromagnetic field can be characterized by effective macroscopic constitutive parameters, namely, the permittivity ϵ and the permeability μ [1, 2]. Indeed, this approach is a direct translation of the characterization of natural media, which are made by atoms and molecules with dimensions many orders of magnitude smaller than the wavelength; the original objective in defining a permittivity and a permeability was to present an homogeneous view of the electromagnetic properties of a discrete natural medium. Analogously, metamaterials are usually synthesized by embedding a periodic[3] array of artificial small inclusions (man-made atoms and molecules) at a sufficiently electrically small mutual distance in a specified host medium [2]. Therefore, the design parameters in the synthesis process

[1] Since the international scientific community has not achieved a consensus in the definition of electromagnetic metamaterials [6], other artificial inhomogeneous structures with controllable electromagnetic properties (e.g., electromagnetic bandgaps which are based on the Bragg regime) are also sometimes regarded as metamaterials [2].

[2] The subject has been known for a long time as artificial dielectrics, composite materials, or microstructured materials. The aim has always been to reproduce physical responses of known materials or to obtain some desirable responses not readily available in nature.

[3] Periodicity is not fundamental, but eases the design.

of a metamaterial (such as the shape, arrangement or alignment of the inclusions) provides a large collection of independent parameters (or freedom degrees) in order to engineer an artificial material with a specific controllable electromagnetic response different to that obtained by its constitutive materials [2]. In summary, the macroscopic view of metamaterials consists of replacing an artificial structurally inhomogeneous structure by an effectively homogeneous medium characterized by effective constitutive parameters.

2.1.1 Material Classification

Since the response of a medium to an electromagnetic field is determined by its properties (ϵ and μ)[4], this allows for the classification of a medium depending on the sign of the constitutive parameters, as illustrated in Figure 2.1 [1, 2]. Media with both permittivity and permeability greater than zero are known as *double-positive* (DPS) media. A medium with either permittivity or permeability less than zero is designated as *epsilon-negative* (ENG) medium or *mu-negative* (MNG) medium, respectively, or alternatively *single-negative* (SNG) medium in both scenarios. More interestingly, media with negative permittivity and permeability are called *double-negative* (DNG) media, following the preceding nomenclature. However, several other terminologies have been suggested, such as *left-handed* (LH), *backward-wave* (BW), and *negative-refractive index* (NRI) media [1, 2].[5] While natural DPS and SNG media are known to exist (see Figure 2.1), a DNG medium has not yet been found in nature to date [1, 2], and for this reason the most popular metamaterials in the considered classification belong to this category [1]. As will be explained in Subsection 2.1.2, DNG media may be artificially synthesized by pairs of elements, in which an array of one of the elements produces a negative effective permittivity and an array of the other element induces a negative effective permeability.

As is well known, the propagation of electromagnetic waves through a medium at the macroscopic level is governed by Maxwell's equations, and such a propagation depends on the constitutive parameters as follows. When either permittivity or permeability is negative, the medium supports only non-propagating evanescent modes (the medium is opaque to signal transmission). Consequently, there cannot be energy transfer through the medium because the incident electromagnetic waves suffer reactive attenuation (reflection, but not dissipation[6]) and decay exponentially in amplitude away from the source [4, 7]. By contrast, when permittivity and

[4] If losses are absent, as is assumed throughout this chapter, ϵ and μ are real numbers.
[5] The term NRI describes the particularity that the index of refraction in these media is negative, while the terminologies LH and BW will be addressed shortly.
[6] Recall that losses are precluded in the whole chapter.

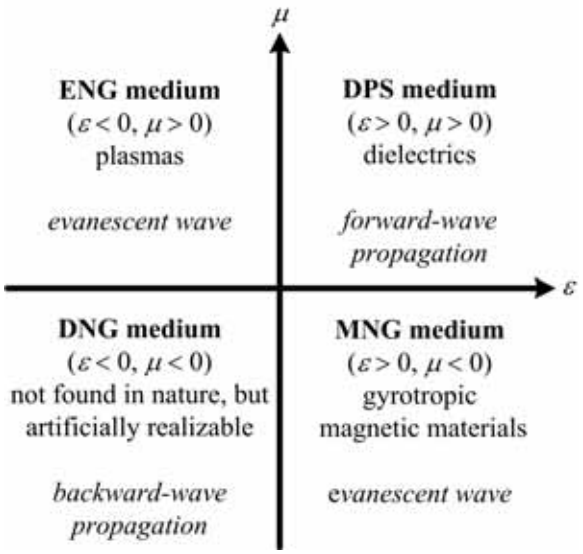

FIGURE 2.1: Material type according to the sign of permittivity-permeability.

permeability are both either positive or negative, wave propagation is possible into a medium (the medium is said to be transparent).

2.1.2 Left-Handed Media

Left-handedness expresses the fact that the propagation of plane waves is described by the electric field **E**, the magnetic field **H**, and the propagation constant **k** building a left-handed triplet, in contrast to conventional materials (with positive constitutive parameters) where this triplet is right-handed (see Figure 2.2). However, **E**, **H**, and the Poynting vector **S** maintain a right-handed relationship. As a consequence, the phase velocity (parallel to the direction of phase propagation or propagation constant) given by[7]

$$v_p = \frac{\omega}{\beta}, \tag{2.1}$$

and the group velocity (parallel to the direction of power flow or Poynting vector) defined as

$$v_g = \frac{d\omega}{d\beta}, \tag{2.2}$$

travel in opposite directions, a physical phenomenon that is called *backward-wave* propagation. Therefore, LH media are characterized by the propagation of waves exhibiting anti-parallel[8] phase and group velocities,

[7] In the literature the propagation constant is represented by k or β [8]. Hereafter the symbol β will be used since it is the usual convention in microwave engineering.

[8] Anti-parallel vectors are collinear vectors (lying in the same line) with opposite directions.

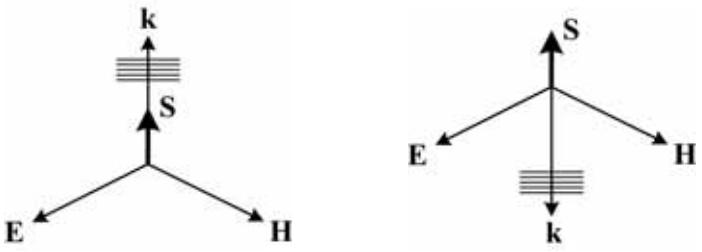

FIGURE 2.2: Orientation of electric field **E**, magnetic field **H**, propagation constant **k**, and Poynting vector **S** for a transverse electromagnetic (TEM) plane wave in a orthogonal system of vectors, as prescribed by Maxwell's equations. (a) Right-handed medium. (b) Left-handed medium.

contrary to the case of wave propagation in conventional media that is known to be *forward*[9] [1–4]. As a result, it follows that, since energy transfer is always outward from the source, the direction of propagation of the wavefronts in a LH medium is inward to the source. In consequence, the phase of a backward wave increases in the direction of group velocity (phase advance), in contrast to conventional materials which incur a negative phase (phase lag). It is also worth mentioning that backward-wave propagation has implications in well known physical effects related to electromagnetic wave propagation, such as the reversal of Snell's law, Doppler effect, and Cherenkov radiation [1, 3].

The history of metamaterials may be considered to start in 1967 with the seminal work by Veselago [11], who examined the feasibility of media characterized by simultaneously negative permittivity and permeability. He concluded that such media are allowed by Maxwell's equations, establishing their fundamental properties and predicting some unusual electromagnetic phenomena, such as backward-wave propagation and left-handedness. Accordingly, he labeled conventional materials as RH media, and media with negative constitutive parameters as LH media.

Although Veselago may be considered the father of left-handed media [1], more than 3 decades elapsed until the first LH material was conceived and experimentally demonstrated by Smith *et al.* in 2000 [12].

This metamaterial was a composite structure of conducting wires and split-ring resonators (SRRs) [13], as shown in Figure 2.3(a). On one hand,

[9] Backward-wave propagation has been known for decades. For instance, periodic structures support an infinite number of positive (forward) and negative (backward) space harmonics in addition to the fundamental space harmonic [7, 9]. The novelty of LH materials is that they are effectively homogeneous structures operating in a backward-wave fundamental space harmonic [1, 2]. Forward/backward waves should not be confused with forward-/backward-traveling waves which are simply forward waves traveling in the positive/negative direction of propagation [10].

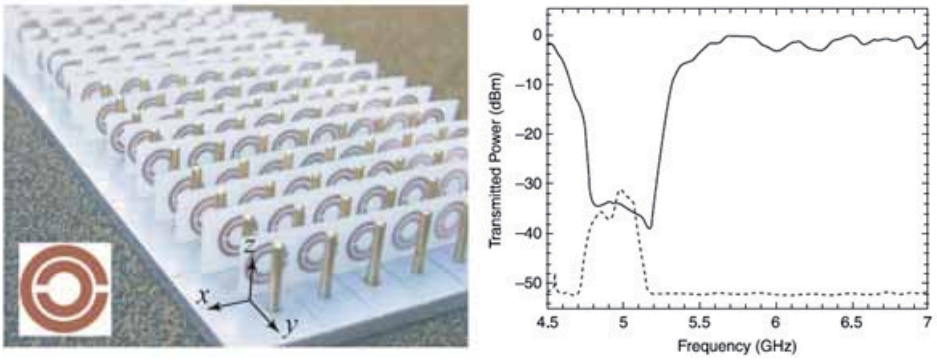

(a) **(b)**

FIGURE 2.3: First artificially synthesized LH structure. (a) Photograph of the structure from [1]. (b) Transmitted power when only SRRs are considered (solid line) and when wires and SRRs are present (dashed line) from [12]. The incident electric field is parallel to the wires (z-axis orientation), while the incident magnetic field is polarized along the axis of the rings (y-axis orientation).

the effective permeability of an array of SRRs becomes negative in a narrow band above their resonance frequency, and a stopband response arises in the vicinity of that frequency. On the other hand, an array of parallel thin metallic wires produces an effectively negative permittivity below a cutoff frequency[10], exhibiting a high-pass behavior. Thereby, by properly combining the SRRs with wires (i.e. achieving a frequency region with simultaneously negative constitutive parameters), the stopband near the resonance of the SRRs switches to a passband with a LH signature [see Figure 2.3(b)]. Although this metamaterial is a bulk construction, since left-handed behavior occurs for a specific polarization and direction of propagation of the incident electromagnetic field, this structure can be viewed as a one-dimensional metamaterial. It should be noted that a LH medium made of a combination of natural media may also be possible. Unfortunately, the negative value of the constitutive parameters occurs at different frequency bands, preventing simultaneously negative permittivity and permeability [3].

[10] This cutoff frequency is usually called plasma frequency in analogy to the permittivity function of a plasma.

2.2 Transmission-Line Metamaterials

Transmission-line metamaterials (or *metamaterial transmission lines*)[11] are a kind of *artificial transmission lines* [6] that consist of a host (conventional) transmission line[12] loaded with reactive elements, the latter providing higher design flexibility in comparison to conventional lines [3, 4, 6]. Specifically, one-dimensional transmission-line metamaterials are effectively homogeneous structures whose electromagnetic characteristics can be controlled or engineered to some extent through a specific direction of propagation.

2.2.1 Application of the Transmission-Line Theory to Metamaterials

Soon after the first experimental demonstration of left-handedness, several pioneering groups focused their research efforts on developing a transmission-line approach (non-resonant) of metamaterials exhibiting backward-wave propagation [14–16].

The reported approach originates from the fact that Maxwell's equations with plane-wave propagation in homogeneous and isotropic media have an identical form as the equations describing TEM propagation on a transmission line derived using circuit theory, known as the telegrapher equations. Hence, such an analogy allows the series and shunt elements of the well-known ladder circuit model of a transmission line to be related to the constitutive parameters of a medium (exhibiting the same propagation characteristics) by mapping the telegrapher equations to Maxwell's equations. The resulting relationships are [1–4]

$$Z'_s = Z_s/l = j\omega\mu, \tag{2.3a}$$

$$Y'_p = Y_p/l = j\omega\epsilon, \tag{2.3b}$$

where Z'_s and Y'_p are the (distributed) per-unit-length series impedance (Ω/m) and shunt admittance (S/m), respectively, Z_s and Y_p are the per-unit-cell series impedance (Ω) and shunt admittance (S), respectively, and l is the unit cell length (the period).

Accordingly, in conventional RH media, the mapping yields

$$\mu = L' = L/l, \tag{2.4a}$$

$$\epsilon = C' = C/l, \tag{2.4b}$$

[11] In this thesis *transmission-line metamaterials* and *metamaterial transmission lines* are synonyms because we are focused on one-dimensional structures (transmission lines). When the same concept is extended to two and three dimensions, the structures are referred to transmission-line metamaterials (i.e. metamaterial transmission lines only apply to one-dimensional structures) [6].

[12] Note that host transmission lines are commonly implemented on a ordinary dielectric substrate whose permittivity is different to the effective permittivity of the metamaterial.

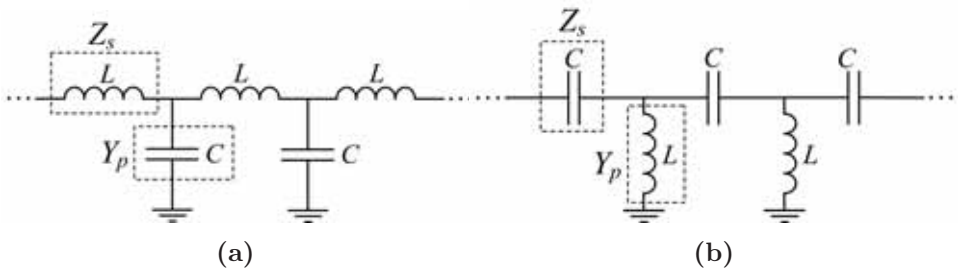

FIGURE 2.4: Equivalent circuit model of a transmission line. (a) Conventional RH transmission line. (b) Dual LH transmission line.

where L' and C' are the per-unit-length series inductance (H/m) and shunt capacitance (F/m), respectively, while L and C represents the per-unit-cell series inductance (H) and shunt capacitance (F), respectively. The resulting well-known equivalent circuit is shown schematically in Figure 2.4(a), whose propagation is forward with a propagation constant and a characteristic impedance given by

$$\beta_R = \omega\sqrt{L'C'}, \tag{2.5a}$$

$$Z_{cR} = \sqrt{\frac{L'}{C'}}, \tag{2.5b}$$

respectively. In the transmission line approach of metamaterials this well established analogy has been extended to the other (exotic) combinations of the constitutive parameters depending on their sign. Thus, for a LH medium, the series inductance and the shunt capacitance should become negative according to (2.4). Since from an impedance perspective a negative inductance/capacitance may be interpreted as a positive capacitance/inductance [2], a ladder network as the one depicted in Figure 2.4(b) with alternately series-connected capacitors and shunt-connected inductors supports the propagation of backward waves. Such a network is called the *dual*[13] of the equivalent circuit of a RH transmission line. The mapping in this dual network is given by

$$\mu = -\frac{1}{\omega^2 C'} = -\frac{1}{\omega^2 Cl}, \tag{2.6a}$$

$$\epsilon = -\frac{1}{\omega^2 L'} = -\frac{1}{\omega^2 Ll}, \tag{2.6b}$$

where C' and L' are now the time-unit-length[14] series capacitance (F·m) and shunt inductance (H·m), respectively, while C and L stands for the per-

[13] Duality here is defined in terms of complementary response (e.g., the dual of a low-pass filter is a high-pass filter) so that the series/shunt impedance of a network is proportional to the series/shunt admittance of the other network.
[14] This ensures properly defined units in Z_s' (Ω/m) and Y_p' (S/m).

unit-cell series capacitance (F) and shunt inductance (H), respectively. The corresponding propagation constant and characteristic impedance yield

$$\beta_L = -1/\omega\sqrt{L'C'}, \tag{2.7a}$$

$$Z_{cL} = \sqrt{\frac{L'}{C'}}, \tag{2.7b}$$

respectively. Note that a LH transmission line is intrinsically dispersive by nature because its propagation constant is not a linear function of frequency, in contrast to a dispersionless RH line. It should be also emphasized that the mapping given in (2.3) is valid only in the long wavelength regime, where the period is much smaller than the guided wavelength

$$\lambda_g = \frac{2\pi}{|\beta|}, \tag{2.8}$$

which is defined only in the passbands [1]. Only under this circumstance the definition of effective constitutive parameters is fully feasible and a ladder circuit describes properly either a RH or a LH transmission line, by (2.5) or (2.7), respectively.

Figure 2.5 summarizes the generalization [2] of the aforementioned transmission-line approach of metamaterials by means of unit-cell equivalent T-circuit models. Besides the RH (or DPS) and LH (or DNG) transmission lines, the equivalent circuits of SNG transmission lines are also indicated. It should be noted that waves cannot propagate in neither ENG nor MNG transmission lines because their models are exclusively made of inductors or capacitors. To sum up, the transmission-line theory in metamaterials links field to circuit quantities, offering an alternative interesting physical interpretation leading to the same functional results.

2.2.2 Composite Right-/Left-Handed (CRLH) Transmission Lines

From a practical point of view, a purely left-handed (PLH) transmission line as that depicted in Figure 2.4(b) cannot be implemented. A necessary host transmission line introduces inevitably parasitic elements, as illustrated in Figure 2.6 [1–4]. Since these elements cannot be neglected in general and induce wave propagation of forward nature, practical realizations of left-handed transmission lines exhibit left- or right-handed propagation, depending on the frequency interval. For this reason, such lines are termed as composite right-/left-handed (CRLH) transmission lines [17], and they constitute the most general transmission-line metamaterial [1]. Indeed, as will be shown shortly, a CRLH line is able to behave as a DPS, DNG, or ENG/MNG transmission line within a particular frequency range.

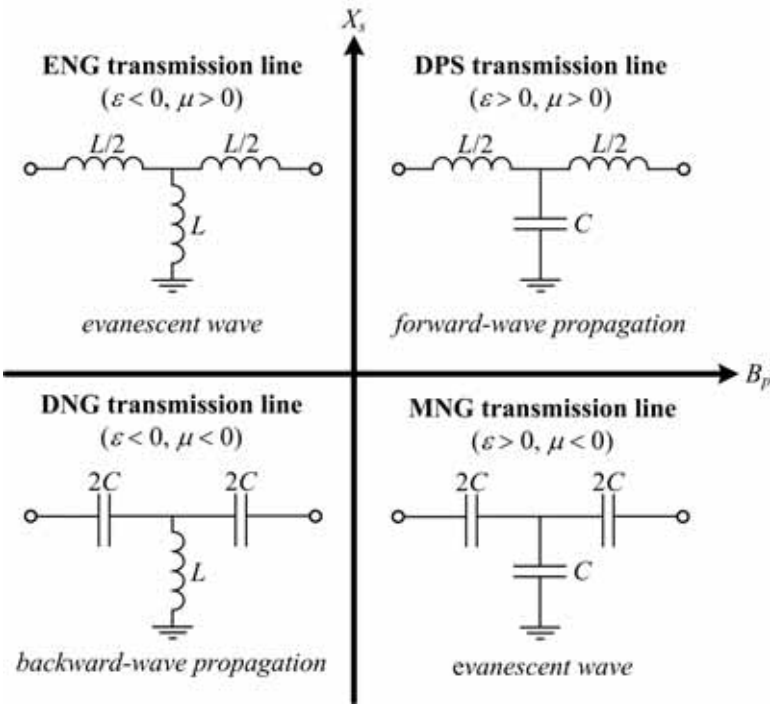

FIGURE 2.5: Unit-cell equivalent T-circuit models of transmission lines according to the sign of the series reactance, X_s ($Z_s = jX_s$), and shunt susceptance, B_p, ($Y_p = jB_p$). The validity of these models is restricted to the long wavelength regime. Wavelength, however, cannot be defined if propagation is forbidden as occurs in SNG transmission lines.

Rather than describing the transmission characteristics of CRLH lines obtaining their effective constitutive parameters by (2.3), Figure 2.7 shows the typical dispersion diagram[15] of a CRLH line, which indicates (for a unit cell) the variation of the propagation constant with frequency. Hence, the dispersion diagram reveals the passbands/stopbands as well as the nature (RH or LH) of the passbands since the phase and group velocities can be easily inferred from (2.1) and (2.2)[16], respectively. As can be seen, if $\omega < \min(\omega_s, \omega_p)$, $v_p < 0$ and $v_g > 0$ have opposite signs, meaning that propagation is backward. Conversely, when $\omega > \max(\omega_s, \omega_p)$, $v_p > 0$ and $v_g > 0$ exhibit the same sign, indicating that wave propagation is of forward nature.[17] The frequency at the transition from a passband to a

[15] The calculation procedure of the dispersion relation of a periodic structure composed of a cascade of two-port unit-cell circuits is well-known [10].

[16] The phase velocity is the slope of the line segment from the origin of the dispersion curve $\omega(\beta)$ to a point in the curve, whereas the group velocity is the slope of the tangent to the dispersion curve at a point.

[17] Alternatively, when $|\beta|$ increases with frequency, v_p and v_g are parallel and the propagation is forward. Otherwise the propagation is backward.

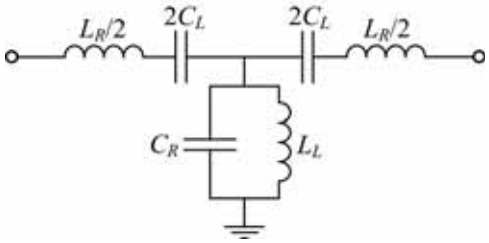

FIGURE 2.6: Unit-cell equivalent T-circuit of a composite right-/left-handed (CRLH) transmission line; the subscripts L and R stands for the corresponding LH and RH elements, respectively.

stopband ($\beta l = 0$ or $\pm\pi$) is often called cutoff frequency [10], being the group velocity equal to zero. There are some stopbands (or bandgaps) in the CRLH line, characterized by evanescent waves caused by reflections. On one hand, when $\omega \to 0$ there is a stopband due to the highpass nature of the LH elements, whereas when $\omega \to \infty$, a stopband arises because of the lowpass behavior of the RH components. It is thus apparent that the transmission characteristics of a CRLH line at low and high frequencies tend to behave as purely LH and RH transmission lines, respectively (this is due to periodicity, since a RH transmission line exhibits an all-pass response at all frequencies). On the other hand, in the general case when the series resonance, $\omega_s = 1/\sqrt{L_R C_L}$, does not coincide with the shunt resonance, $\omega_p = 1/\sqrt{L_L C_R}$, a stopband appears between these frequencies, and the line is known to be *unbalanced*. By contrast, in the case that $\omega_s = \omega_p = \omega_0$, there is a continuous transition between the left- and right-handed bands[18], and the CRLH line is said to be *balanced* [1–3][19].

The guided wavelength[20], given by (2.8), can also be readily derived from the dispersion curve. As mentioned in Section 2.1, an effectively homogeneous structure is defined as that whose unit cell size l is much smaller than λ_g. The effective-homogeneity condition is usually $l < \lambda_g/4$ [1], which in terms of the electrical length becomes $|\beta l| < \pi/2$. Since in the unbalanced configuration the structure is effectively homogeneous at the edges of the bandgap that ranges from ω_s to ω_p, in terms of the constitutive parameters, this stopband is due to either $\epsilon < 0$ (if $\omega_s < \omega_p$) or $\mu < 0$ ($\omega_s > \omega_p$) [1]. By contrast, the stopbands at low and high frequencies are not within the long wavelength regime. Therefore, at these frequencies, effective constitutive parameters cannot be rigorously defined and the circuit model of Figure 2.6 is no longer valid to represent an effectively homogeneous CRLH transmission-line metamaterial. In order to model correctly RH/LH (or CRLH) transmission lines at higher/lower

[18] Wave propagation is allowed at ω_0 with infinite v_p but (non-zero) finite v_g.
[19] The term *balanced* does not mean *differential* in this context.
[20] The guided wavelength is different to that guided in the host line since $\beta \neq \beta_R$.

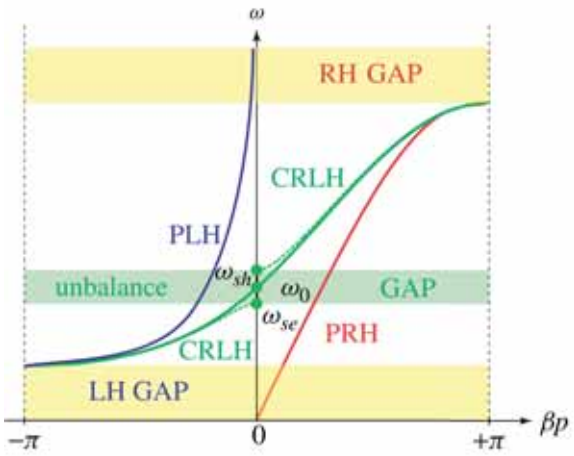

FIGURE 2.7: Typical dispersion diagram for a unbalanced/balanced CRLH transmission line from [2]. The period is indicated as $p = l$, while the series and shunt resonances are indicated as $\omega_{se} = \omega_s$ and $\omega_{sh} = \omega_p$, respectively. The case with $\omega_s < \omega_p$ is illustrated, although $\omega_s > \omega_p$ is also possible. The curves for a purely RH (PRH) line ($L_L = C_L \to \infty$) and for a purely LH (PLH) line ($L_R = C_R = 0$) described by (2.5a) and (2.7a), respectively, are also shown.

frequencies, we need to reduce the period, and accordingly to reduce/increase the per-section inductance and capacitance as given in (2.4) and (2.6), so that operation in the long wavelength regime holds. In other words, the circuit models of RH/LH/CRLH transmission lines mimics transmission lines only in their passbands where homogeneity is satisfied. Note that the circuit model of a CRLH transmission line is the same as that of a bandpass filter, and the circuits of RH and LH lines are lowpass and highpass filters, respectively. Classical filters, however, are characterized at all frequencies (from $\omega = 0$ to $\omega \to \infty$). Therefore, as a fundamental property, filters exhibit both passband and stopband characteristics according to the filter type.

2.2.3 *CL*-loaded and Resonant-type Approaches

Because CRLH transmission lines are not readily available in nature, these structures have to be implemented by means of a host transmission line loaded with reactive elements (inductors, capacitors, and/or both of them in the form of resonators). Experimental CRLH lines were reported for the first time by Caloz *et al.* in microstrip technology [16], and by the Group of Eleftheriades in coplanar waveguide implementation [18]. The reactive elements responsible for backward propagation in both configurations were

synthesized by semi-lumped[21] components, such as series capacitive gaps and shunt metallic inductive strips (discrete commercial chip components can also be used instead [1]). This direct implementation is referred to as *LC network implementation* [1] or *CL-loaded approach* [3, 6]. Alternatively, transmission-line metamaterials featuring a CRLH behavior can also be built up by the so-called *resonant-type approach* [3, 6]. This realization consists of loading a host transmission line with subwavelength resonators[22] in combination with other reactive elements (inductors or capacitors), the typical resonant particles being split-ring resonators (SRRs) or other related topologies as those described in Section 2.3.[23] The first reported structure concerning this approach was proposed by Martín *et al.* [20], and it was conceptually based on and equivalent to the preceding Smith's LH structure shown in Figure 2.3. Specifically, a coplanar waveguide (CPW) was periodically loaded with pairs of SRRs and signal-to-ground inductive strips (see Figure 2.8). The SRRs were etched on the back side of the substrate, and underneath the slots of the CPW in order to enhance line-to-resonator magnetic coupling (this is the main coupling mechanism of SRRs as will be reviewed in Subsection 2.3.1 [21]). Another possibility to implement a CRLH response based on the resonant-type approach is by means of series capacitive gaps, and the complementary version (see Subsection 2.3.5) of the SRR, that is, the so-called (complementary split-ring resonator) (CSRR). A chain of complementary split-ring resonators (CSRR) provides a negative effective ϵ, while a negative effective μ is achieved through the gaps. Such a kind of line is illustrated in Figure 2.9, where the CSRRs are etched in the ground plane of a microstrip line, beneath the signal strip, as strong line-to-resonator electric coupling (the dominant excitation field of CSRRs [21]) is achieved.

Since the resonant-type approach employs subwavelength resonators, the individual unit cells can be modeled by lumped-element equivalent circuit models. However, the frequency response of a CRLH transmission line obtained by the resonant-type approach does not obey exactly the

[21] Semi-lumped components are planar elements whose physical dimensions are usually restricted to be smaller than a quarter of wavelength. The components may also be termed as lumped elements when the dimensions are smaller than one-eighth wavelength. These terminologies are in contrast to distributed (transmission line) elements in which the physical size is comparable to or larger than the wavelength [10, 19]. The advantage of electrically small planar (i.e. semi-lumped or lumped) elements is that their behavior may be approximate by ideal (sizeless) lumped components using circuit theory.

[22] Subwavelength resonators are those whose physical size is a small portion of the wavelength, and accordingly they may be referred to as semi-lumped or lumped resonators when composed of semi-lumped or lumped inductors and capacitors, respectively [19].

[23] Note that CRLH lines based on the *CL*-loaded approach are also resonant by nature despite self-resonant elements are not used.

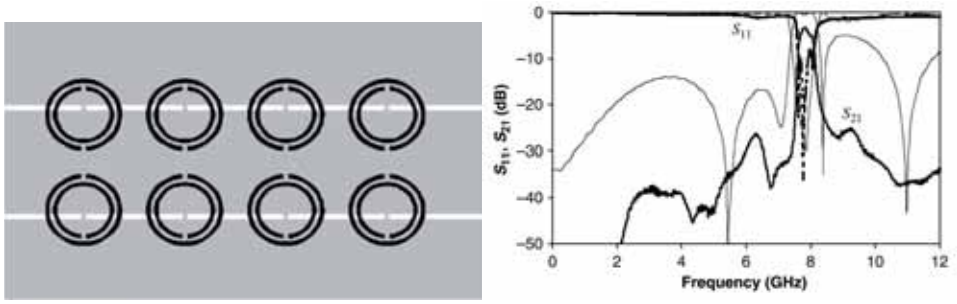

(a) **(b)**

FIGURE 2.8: CRLH transmission line based on SRRs and shunt inductive strips in coplanar waveguide technology. (a) Layout. (b) Simulated (thin line) and measured (thick line) frequency response. The passband is LH, since the CRLH is not balanced and the RH passband is beyond the shown frequency range. Figures extracted from [20].

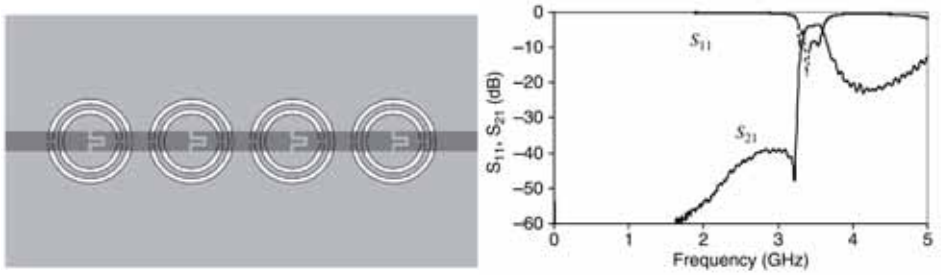

(a) **(b)**

FIGURE 2.9: CRLH transmission line based on CSRRs and series capacitive gaps in microstrip technology. (a) Layout from [21]. (b) Measured frequency response from [3]. The RH passband is outside the measured frequency range.

same behavior as the canonical[24] circuit of Figure 2.6. Nevertheless, the corresponding models are qualitatively quite similar to the canonical one. The meaningful difference is the presence of a transmission zero on the left-hand side of the backward wave band [3], which naturally is very useful in filtering applications. The first equivalent circuit models of SRR- and CSRR-based CRLH transmission lines were reported by Martín *et al.* [20] and Baena *et al.* [21], respectively, and these models were later revised and improved by Aznar *et al.* [22] and Bonache *et al.* [23], respectively. The main improvement is relative to the fact that by adding shunt strips (in SRR-loaded CPWs) and series gaps (in CSRR-loaded microstrip lines), the transmission zero is displaced, and this fact was not predicted by the initial models. These circuits models are not shown here,

[24] Canonical refers to the simplest or standard form.

but they are very similar to those of SNG transmission lines that will be presented in Subsection 2.2.4.

2.2.4 Resonant-type Single-Negative Transmission Lines

A CRLH structure is intended to be used as a transmission line in the sense that only the passband is directly useful, the stopbands being usually parasitic effects [1]. Instead, structures exhibiting equivalent single negative (SNG) constitutive parameters are preferred to implement stopband responses. In fact, SNG-based structures are of paramount importance in this thesis because it is focused on them. One-dimensional resonant-type μ-negative (MNG) and ϵ-negative (ENG) structures can be artificially synthesized by merely loading a host line with SRRs and CSRRs, respectively. Signal propagation in these structures is inhibited in a narrow band in the vicinity of the resonance frequency of the resonators, whereas wave propagation is forward outside the forbidden band. Such a narrowband response is of course due to the self-resonant behavior of the loading particles and, consequently, these structures behave qualitatively as the canonical circuit models describing SNG transmission lines depicted in Figures 2.5 only within a certain frequency range.

This section is focused on SRR-loaded CPWs and CSRR-loaded microstrip lines. In these configurations, a significant component of the dominant excitation field (namely, magnetic field in SRRs and electric field in CSRRs) results parallel to the resonator axis[25]. However, it is important to highlight that the corresponding circuit models and parameter extraction procedures are *general*. This means the models may be valid regardless of the resonator topology (Section 2.3) and the host line technology (e.g., CPW or microstrip) as long as the resonator is electrically small and coupled either magnetically (as the SRR) or electrically (as the CSRR) to the line. With regard to the extraction methodology, in spite of the fact that it requires the electromagnetic simulation of the structure, it is versatile in the sense that there is no restriction in the internal structures involved, in contrast to what usually occurs in analytical models. Therefore, the transmission and reflection characteristics of SRR- and CSRR-loaded lines are indeed somewhat general and may be extrapolated to other related structures.

2.2.4.1 SRR-loaded μ-Negative Coplanar Waveguides

Figure 2.10(a) shows the first proposed SRR-based μ-negative transmission line. It is the same structure as the CRLH line in Figure 2.8(a) with the exception that the metallic strips are not introduced. Clearly the most relevant feature is that, by removing such strips, the backward passband in

[25] The field distribution of CPWs and microstrip lines will be analyzed in Chapter 3.

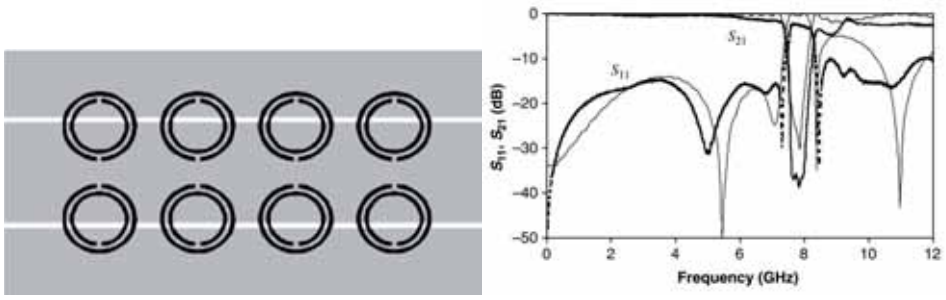

(a) **(b)**

FIGURE 2.10: MNG transmission line based on SRRs in coplanar waveguide implementation. (a) Layout. (b) Simulated (thin line) and measured (thick line) frequency response. Figures extracted from [24].

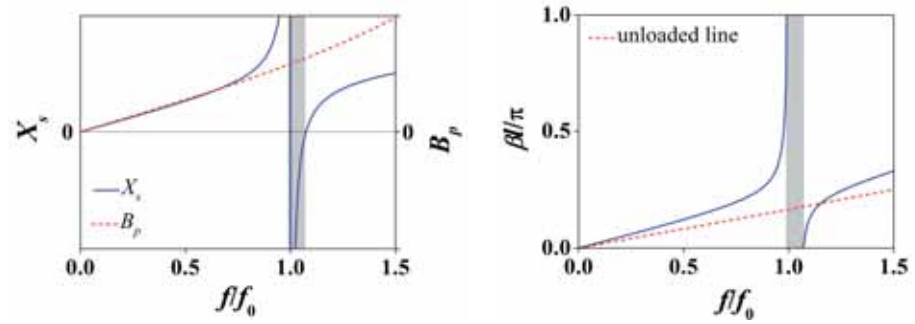

(a) **(b)**

FIGURE 2.11: Typical behavior of a unit-cell SRR-loaded transmission line. (a) Series reactance, X_s, and shunt susceptance, B_p, of an equivalent π-network extracted from electromagnetic simulation. (b) Dispersion diagram assuming an infinite periodic structure; the dispersion of the unloaded transmission line section is also shown. The stopband is highlighted in gray.

the vicinity of the SRR resonance frequency switches to a stopband response, as shown in Figure 2.10(b) [20, 24].

In order to gain more insight into the transmission and reflection properties of SRR-loaded lines, the equivalent series reactance and shunt susceptance of a typical unit cell are depicted in Figure 2.11(a). The dispersion relation corresponding to an infinite structure obtained by cascading identical unit cells is shown in Figure 2.11(b). As can be observed, there is a stopband in the vicinity of the resonance frequency, f_0, which occurs when the length of the unloaded line is a small fraction of the guided wavelength (the dispersion for the considered transmission line section without the SRR is also shown). An analysis in terms of the impedances is as follows. Beyond f_0, the series impedance is capacitive in a narrow band, and signal propagation is inhibited because the shunt

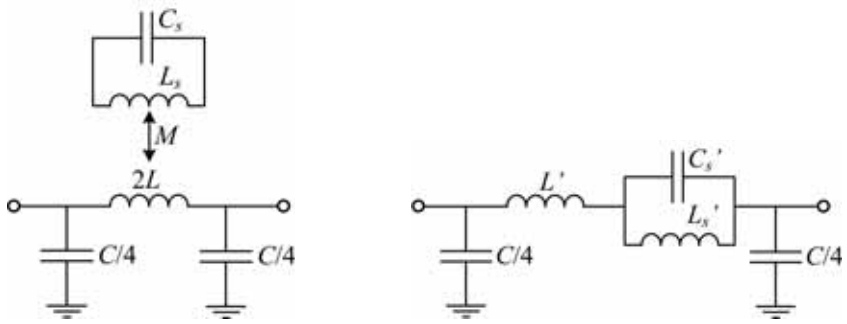

FIGURE 2.12: Unit-cell equivalent circuit model of an SRR-loaded CPW. (a) Model corresponding to a half structure since a *magnetic wall* (or an open circuit) has been applied along the midplane by virtue of the symmetrical topology and excitation mode (an even mode). (b) Equivalent transformed model using (2.9).

impedance is also capacitive. However, the stopband region extends also below f_0, in spite of the fact that the series and shunt impedances behave inductively and capacitively, respectively; the reason lies in the fact that the series impedance attains highly inductive values.[26] In relation to the constitutive parameters, the stopband has been associated to a negative μ in a narrow region above f_0. Within this frequency band the structure behaves as the canonical MNG transmission line shown in Figure 2.5, since the structure is effectively homogeneous near this frequency band ($\beta l = 0$ at the lower edge of the second propagating band). It is on occasions said that this stopband is also due to an extremely high positive μ in a narrow frequency range below f_0. However, this statement is somewhat misleading in a strict sense, since as the series impedance becomes more and more inductive the operation regime goes away from the homogeneity condition ($\beta l \to \pi$).

Due to the small electrical dimensions of the SRRs at resonance, the behavior of SRR-loaded lines can be explained by the unit-cell equivalent circuit model depicted in Figure 2.12(a). This circuit model was initially proposed by Martín *et al.* [20, 24], and later revised by Aznar *et al.* [22]. The per-section inductance and capacitance of the line are modeled by L and C, respectively, and the SRR is described by the resonant tank $L_s - C_s$ (see Subsection 2.3.1) that is magnetically coupled to the line through the

[26] Simultaneously positive or negative values of ϵ and μ is a necessary and sufficient condition for wave propagation, as was illustrated in Figure 2.1 (operation in the long wavelength regime is of course implicitly fulfilled). By contrast, the same sign of X_s and B_p (or different sign of X_s and $X_p = -1/B_p$) cannot guarantee wave propagation, unless the operation band is explicitly restricted to the long wavelength regime, as indicated in Figure 2.5. Although it may be impedance mismatching with feeding sources at the port terminals in practical situations resulting in reflections, such a reflection phenomenon is not considered in the aforementioned assertions.

mutual inductance M. This circuit can be simplified to the equivalent one depicted in Figure 2.12(b), provided that [3, 22]

$$L' = 2L - L'_s, \tag{2.9a}$$

$$L'_s = \omega_0^2 M^2 C_s, \tag{2.9b}$$

$$C'_s = \frac{L_s}{\omega_0^2 M^2}, \tag{2.9c}$$

where

$$\omega_0 = \frac{1}{\sqrt{L_s C_s}} = \frac{1}{\sqrt{L'_s C'_s}} = 2\pi f_0, \tag{2.10}$$

is the angular resonance frequency of the SRR. Note that a zero in the transmission coefficient ($S_{21} = 0$) arises at this frequency, since the series branch is open-circuited. Therefore, the transformed circuit model clearly explains that the excitation of the SRR is responsible for returning the injected power to the source. Moreover, the lumped-element values of this transformed circuit can be easily extracted systematically [25] (this procedure is used throughout this thesis). Finally, it should be noted that the circuit model converges to that of MNG transmission lines within a narrow bandwidth above resonance. Conversely, in the light of Figure 2.11(a), the proposed circuit model is able to mimic the behavior of SRR-loaded lines up to beyond f_0 (the region of interest), that is, not limited to the long wavelength region.[27]

2.2.4.2 CSRR-loaded ϵ-Negative Microstrip Lines

The first reported CSRR-loaded microstrip line is shown in Figure 2.13(a), which is the same as the one shown in Figure 2.9(a) but with a uniform conductor strip (i.e. without the gaps). As can be seen in Figure 2.13(b), by removing the series gaps, signal propagation is inhibited in a narrow frequency band in the vicinity of the CSRR resonance frequency.

In order to inquire about the propagation characteristics of CSRR-based transmission lines, the typical series reactance, shunt susceptance, and dispersion relation are plotted in Figure 2.14. As can be observed, the stopband in the vicinity of the transmission zero frequency, f_z, is due to a shunt susceptance with negative ($f > f_z$) and extremely positive ($f < f_z$) values. Regarding the constitutive parameters, a CSRR-loaded line has been interpreted to behave (in the long wavelength regime) as a one-dimensional ϵ-negative metamaterial (where the structure may be viewed as the canonical ENG transmission line schematically depicted in Figure 2.5).

[27] The range of validity of circuit models are carried out throughout the thesis by comparing circuit simulations with full-wave electromagnetic simulations and measurements.

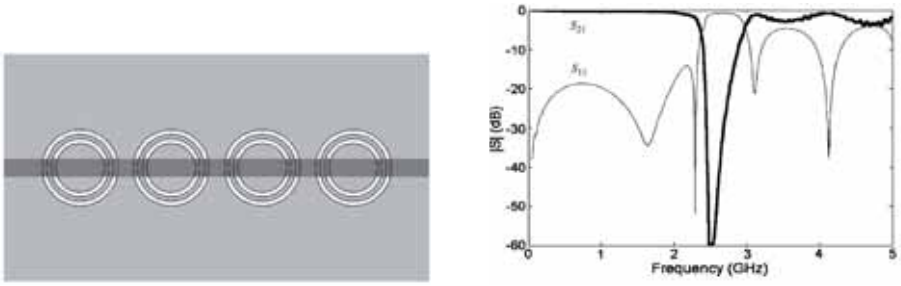

(a) (b)

FIGURE 2.13: ENG transmission line based on a CSRR-loaded microstrip line. (a) Layout and (b) measured frequency response from [26].

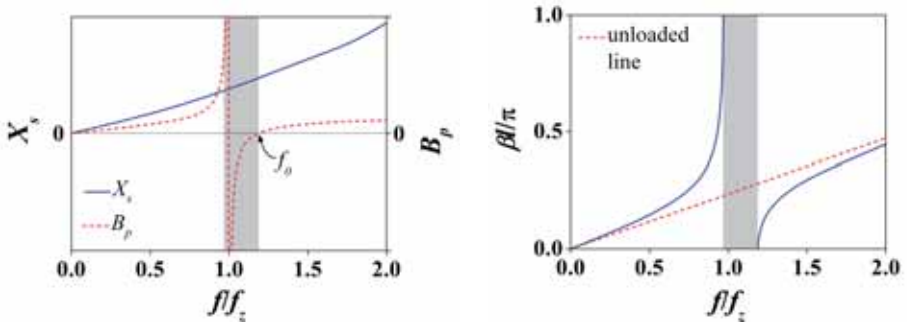

(a) (b)

FIGURE 2.14: Typical behavior of a unit-cell CSRR-loaded transmission line. (a) Series reactance, X_s, and shunt susceptance, B_p, of an equivalent T-network extracted from electromagnetic simulation. (b) Dispersion diagram for an infinite periodic structure; the dispersion of the unloaded transmission line section is also shown. The stopband is highlighted in gray.

As long as the CSRRs are electrically small at their fundamental resonance, CSRR-loaded lines can be modeled by the unit-cell lumped-element circuit shown in Figure 2.15 [21]. The CSRR is represented by the resonant tank $L_c - C_c$ (Subsection 2.3.5), and the per-section line inductance and capacitance are modeled by L and C, respectively. More specifically, C in reality accounts for the line-to-resonator electric coupling as this coupling can be modeled by connecting in series the line capacitance to the CSRR. The extraction of the values of the circuit parameters for a particular CSRR-loaded line is straightforward [27]. Inspection of this circuit model reveals that there is a transmission zero at a frequency

$$\omega_z = \frac{1}{\sqrt{L_c(C + C_c)}} = 2\pi f_z, \tag{2.11}$$

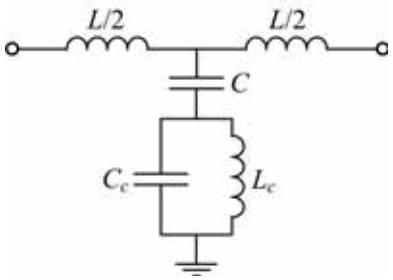

FIGURE 2.15: Unit-cell equivalent circuit of a CSRR-loaded microstrip line.

at which the shunt branch is short-circuited. Interestingly, the resonance frequency of the CSRR, given by

$$\omega_0 = \frac{1}{\sqrt{L_c C_c}} = 2\pi f_0, \tag{2.12}$$

occurs at a higher frequency than the transmission zero (i.e. $f_0 > f_z$).

To end this section, it is interesting to realize that the circuit models of SRR- and CSRR-loaded lines (Figures 2.12 and 2.15) are formally dual circuits, that is, the series/shunt impedance of one of these models is proportional to the shunt/series admittance of the other circuit[28] [see Figures 2.11(a) and 2.14(a)]. Hence, although SRR- and CSRR-loaded lines are not structurally complementary[29], their corresponding behavior manifests the duality property because the complementary resonators are illuminated by dual fields (this means that the equivalent circuits are independent of the technology of the host transmission line). Thus, the dispersion relation of SRR- and CSRR-loaded lines is the same (at least qualitatively), a property derived from dual circuits [Figures 2.11(b) and 2.14(b)]. When formally dual circuits are also numerically exact dual, their dispersion relation is exactly the same.

2.2.5 Discussion about Homogeneity and Periodicity

Homogenization in metamaterials means that the homogeneity condition is achieved in the vicinity of the operating frequency. As has been shown, the transmission-line approach of metamaterials characterizes the electromagnetic properties of homogeneous transmission-line metamaterials by either effective constitutive parameters or immittances[30]. However, this description is limited to the long wavelength regime, and

[28] Two networks are said to be (formally and numerically) dual if $Z_{ii} = Y_{ii}$ and $Z_{ij} = -Y_{ij} (i \neq j)$, where Z_{ij} are the impedance matrix parameters of one network and Y_{ij} are the admittance matrix parameters of its dual one [19].

[29] Besides the fact that complementary structures are defined in terms of a single plane, coplanar strips (CPS) are the complementary counterpart of a CPW.

[30] Immittances are either impedances or admittances [19].

cannot be extended to frequencies where the wavelength becomes comparable to the period. Obviously, such a restriction may mask and forbid useful functionalities, since some interesting phenomena occur outside the long wavelength regime. Contrarily, the propagation constant as well as the characteristic impedance of periodic structures (including transmission-line metamaterials) can be defined rigorously at all frequencies by using the powerful classical theory of periodic structures established by Brillouin about half a century ago [28], without invoking the theory of effective-medium approximation. Therefore, from an engineering standpoint, periodic metamaterial structures are usually characterized by their propagation constant and characteristic impedance rather than by their effective permittivity and permeability [1, 3, 4].

In general, the synthesis of LH (or CRLH) devices is usually referred to as *dispersion and impedance engineering* [3, 4, 6] since the relevant parameters are the electrical length and the characteristic impedance. Indeed, for the design of circuits and components, homogeneity is irrelevant to tailor the electrical length and the impedance. Furthermore, these devices are commonly composed of a single unit cell[31] towards miniaturization, leading to indisputably inhomogeneous structures. With respect to stopband structures, by sacrificing homogeneity, significant signal rejection may be achieved within a determined forbidden band by a few periods, making unnecessary a large structure made of many cells. To sum up, the design of devices in the RF/microwave community are not usually focused on the implementation of effectively homogeneous transmission lines, but take advantage of their high controllability in the response, and/or their small electrical size. When the effective-homogeneity condition is not satisfied and there are not many cells, these devices cannot be strictly considered as metamaterials. However, as suggested by Martn *et al.* [6] and Aznar et. al [29] and in contrast to the definition given at the beginning of Section 2.2, the definition of metamaterial transmission lines is not usually restricted to those exhibiting homogeneity and periodicity (or quasi-periodicity). Consequently, terms as *transmission-line metamaterials*, *metamaterial transmission lines*, *metamaterial-inspired lines*, or even *metalines*, are often used in a broad sense to describe artificial transmission lines based on metamaterial concepts, ignoring whether effective homogeneity and periodicity are accomplished or not.

[31] The propagation constant and the characteristic impedance obtained from the theory of periodic structures is still valid for a single unit cell.

2.3 Metamaterial-based Resonators

This section analyzes several resonator topologies in the form of split rings[32] employed for the synthesis of metamaterials, transmission-line metamaterials, or RF/microwave devices inspired by metamaterials. These resonators are often known as *metamaterial-based resonators* or simply *metamaterial resonators*. Indeed, negative permeability/permittivity structures may be implemented by topologies different to that of the original split-ring resonator (SRR[33]/CSRR). The considered elements are *strip* (made of an arrangement of metals) as well as *slot* (engineered apertures in a metallic plane) resonators. Many electrically small planar resonators have been reported in the literature [3, 5, 6], and they can be classified according to several criteria. The list here is limited to those split ring type resonators that are used throughout this thesis[34]. All of them have in common the following features: (a) subwavelength, and accordingly they may be referred to as semi-lumped or lumped resonators; (b) closed, in the sense that external electromagnetic fields induce resonant currents[35]; (c) *planar*, being fully compatible with planar technology; (d) and symmetric, so that when the topology is bisected, one-half is the mirror image of the other half (a plane of symmetry acts as a mirror). Additionally, in the presence of two symmetry planes, the resonators are said to be also bisymmetric.

However, all the topologies exhibit different peculiarities that make them useful or more appropriate in some circumstances. The main purpose of this section is to gain insight into the electromagnetic characteristics of the resonators derived from symmetry properties and on the equivalent circuit models as well, rather than to discuss different alternatives to synthesizing metamaterial structures. With a view to doing so, the SRR topology still holds special attention because of its relevance.

The most basic assumption in effective media theory (Section 2.1) is that homogenization (averaging) makes sense only if the variation of the average field is small at the scale of the period of the structure [3, 13]. The validity of homogenization is usually expressed in terms of the size of the elements forming the discrete medium, so that they must be small as compared with the wavelength. Therefore, it is assumed here that the size of the resonators is on a scale much shorter than the wavelength, such that an average value for the fields may be sensibly defined. Thus, the resonators are supposed to be illuminated by external uniform (i.e. spatially constant

[32] *Split rings* are also sometimes called *open rings*.
[33] *SRR* is here exclusively used to designate the original split-ring resonator topology [13].
[34] Exceptionally, stepped-impedance shunt-stubs (SISSs) will also be utilized in this thesis.
[35] On the contrary, *open* split-ring resonators have well defined port terminals, e.g., the open split-ring resonator (OSRR) [30] or the open complementary split-ring resonator (OCSRR) [31].

in magnitude and phase) time-varying electric or magnetic fields with the customary sinusoidal, or harmonic, time dependence $e^{j\omega t}$.

2.3.1 Split-Ring Resonator (SRR)

The split-ring resonator (SRR) consists of two metallic concentric and coupled split rings with slits on opposite sides, as depicted in Figure 2.16(a). Although there are some precedents in the scientific literature related to split-ring resonators [5, 32], this specific topology was proposed by Pendry *et al.* [13] to build up for the first time a negative permeability medium [12]. When the rings are excited by an external time-varying magnetic field directed along the axial direction (z-oriented), an electromotive force around the rings is generated that in turn induces currents in the rings. The slit (or gap) in each ring prevent current from flowing around the individual rings, so that the slits force the electric current to flow from one ring to the other through the inter-ring slot, taking the form of a displacement current [see Figure 2.16(b)].

As is apparent from Figures 2.16(b) and 2.17, the symmetry plane (xz-oriented) behaves as a virtual *electric wall*. The current loops induce a magnetic dipole moment along the resonator axis (z-orientation).[36] Additionally, an electric dipole moment is also generated in the plane of the particle, orthogonally oriented to the plane of symmetry (y-direction).[37] For symmetry, the charges in the upper half of the SRR are the images of the charges in its lower half, and two parallel electric dipoles are generated on each half. This means that a time-varying electric field is also able to excite the SRR, inducing a charge density in the form of an electric dipole that causes currents to flow. When there is present an/a electric/magnetic dipole in a metamaterial resonator, the particle is said to be electrically/magnetically polarized.[38] Since both an electric dipole and a magnetic dipole are induced, the SRR suffers cross-polarization effects, so that it may become electrically polarized as a response to an applied magnetic field, and vice versa [5, 34]. This property may also be derived from the fact that the SRR is not invariant by inversion, since any resonator without inversion symmetry with regard to

[36] The SRR may induce strong magnetic dipole moments with negative values (i.e. with opposite direction to the field that induce them). This is the key to attaining a negative effective permeability in arrays of SRRs, since a strong overall magnetic response may be achieved.

[37] The radiation of split-ring resonators can be quantified by the induced dipole moments through an equivalent radiation resistance. However, since the dimensions of the dipoles are small relative to the wavelength, in general radiation may be neglected [5, 33].

[38] Polarization is referred to the generation of local (microscopic) dipole moments in the presence of external fields (like medium electric and magnetic polarizations accounted for by ϵ and μ, respectively, at the macroscopic level), and not to wave polarization.

its center must exhibit some degree of cross-polarizability [3].[39] However, although the SRR shows simultaneously magnetoelectric response at resonance, the magnetic field has been found to be the dominant excitation mechanism [21, 35, 36].

As long as the perimeter of the SRR is electrically small with regard to a half-wavelength[40], a quasistatic analysis is plausible which eases the analysis of the resonator. Under the quasistatic approximation, the behavior of the SRR can be modeled as a self-resonant closed LC circuit as that shown in Figure 2.18 that may couple to external electromagnetic fields [34]. The inductance L represents the self-inductance of the SRR and the capacitance C stands for the distributed capacitance between the rings. Analytical expressions for L and C have been reported in the literature [3, 34]. In this quasistatic model, the capacitance associated to the slits of the rings is neglected, since most of the electrostatic energy is located between the rings [13]. It is worth mentioning that a more detailed circuit model with distributed elements and taking into account the gap capacitance was later reported [37, 38]. The two gap capacitances, produced by the accumulation of electric charges, can be regarded as being added in parallel to the inter-ring capacitance. It was shown that such a distributed model converges to the quasistatic model when the gap capacitances are neglected and the electrical length of the SRR is small.

Figures 2.19 shows the quasistatic distribution of voltage and current. On each ring, currents vanish at the slits because the gap capacitance is disregarded, whereas currents attain maximum values at the center of the rings (namely, $\phi = 0$ for the outer ring and $\phi = \pi$ for the inner ring). Given that the SRR is electrically small, currents on each ring are supposed to vary linearly midway between these extreme values (this results in a triangular current distribution). However, the total current on the SRR taken as the sum of the individual currents is uniform around its perimeter. Hence, the whole SRR behaves as a small closed loop of uniform current whose self-inductance can be calculated as the average inductance of the two rings, i.e. as the inductance of a single closed loop with identical width to that of the individual rings (c) and identical mean radius (r_0) [34]. With respect to the voltage distribution, it also exhibits a linear variation in each ring. However, the voltage difference across the slots is constant in each half of the SRR, and the slot between the rings may be modeled by two series capacitances (associated to each half) that stores the same amount of charge (but of opposite sign) at both sides of the slot. As expected, the voltage distribution is anti-symmetric with regard to the symmetry axis ($\phi = 0$

[39] A bidimensional object possesses inversion symmetry when is invariant by rotating 180° taking its center as the rotation axis.

[40] The overall size of the SRR is about one-tenth of the wavelength [3].

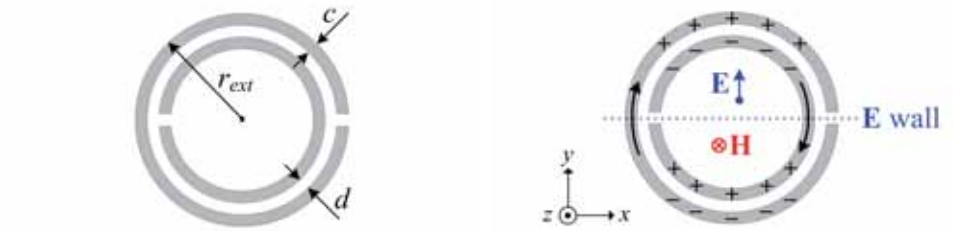

(a) **(b)**

FIGURE 2.16: Symmetric split-ring resonator (SRR). (a) Circular-shaped topology. (b) Fundamental resonance: orientation of the polarization fields, sketch of the charge distribution and currents, and boundary condition at the symmetry plane.

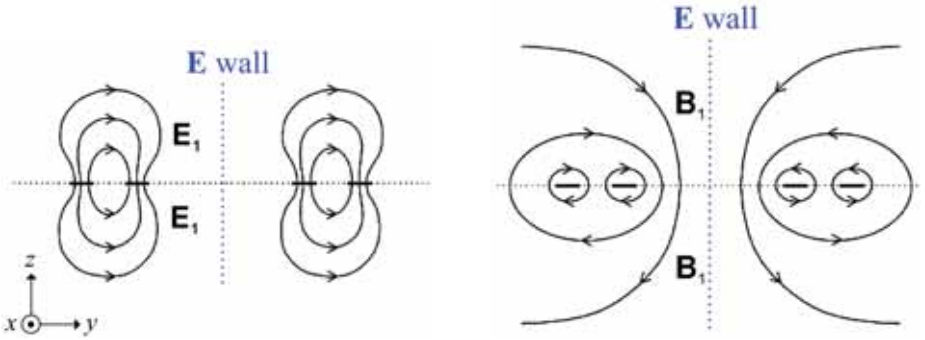

(a) **(b)**

FIGURE 2.17: Sketch of the electric (a) and magnetic (b) field distributions in the SRR at the fundamental resonance frequency. Field distributions from [21].

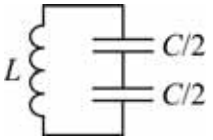

FIGURE 2.18: Equivalent circuit model of a split-ring resonator (SRR). The total capacitance across the slot between the rings is C, which is divided into two series components corresponding to the two identical halves of the resonator ($C = 2\pi r_0 C'$, where C' is the per-unit-length capacitance along the slot and $r_0 = r_{ext} - c - d/2$ is the mean radius). The SRR behaves as an externally driven LC resonator.

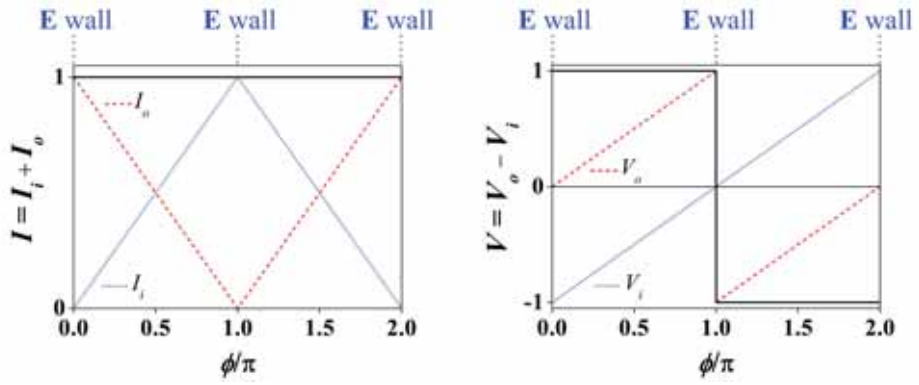

FIGURE 2.19: Angular dependence of the quasistatic current and voltage in the SRR; the inner ring is cut at $\phi = 0$. (a) Normalized current distribution in the inner ring (subscript i), in the outer ring (subscript o), and in both rings as a summation. (b) Normalized voltage distribution. The total current in both rings and the voltage across the two rings in each half are constant.

and π). Therefore, the voltage is zero at the symmetry plane since a virtual short circuit (an electric wall) appears along this plane.

It is also interesting to analyze the SRR fundamental resonance from the theory of coupled resonators [19]. When the mean circumference of a closed ring resonator is equal to an integral multiple of the wavelength, resonance is established. By cutting the ring by a split, the resulting resonator is essentially a distributed open-circuited half-wavelength resonator with a (weak) loading capacitance at the open end. Since the inner and outer rings in the SRR are not identical, their self-resonances are different to each other. By coupling these half-wavelength rings, the lower resonance frequency (associated to the outer ring) shifts downwards, giving rise to quasistatic conditions as a first-order approximation (see Figure 2.20). The first, or lowest, resonance frequency ($\omega_0 = 1/\sqrt{LC}$) is referred to as the fundamental or the quasistatic resonance frequency due to the above-mentioned reasons. Obviously, SRRs (and all the other considered resonators) exhibit higher-order resonances that can be excited at higher frequencies (Figure 2.20). These higher-order resonant modes (out of the scope) are referred to as *dynamic* resonances, since non-uniform total currents are induced and the particle is thus no longer electrically small [3, 39].

2.3.2 Double-Slit Split-Ring Resonator (DS-SRR)

The double-slit split-ring resonator (DS-SRR) is derived from the original topology of the SRR by introducing an additional cut in each ring and by

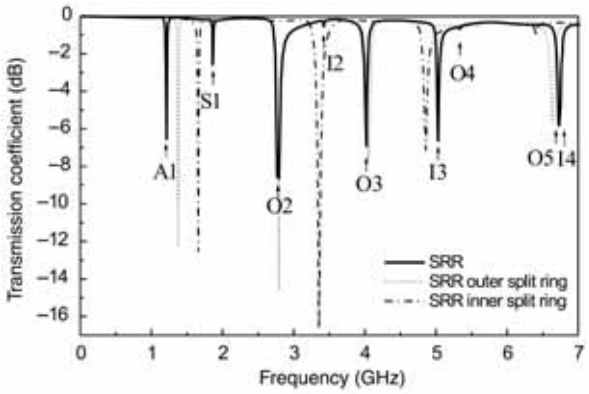

FIGURE 2.20: Quasistatic (identified as A1) and dynamic resonance frequencies of an SRR from [39]. The resonances corresponds to transmission zeros in the transmission coefficient of an SRR-loaded microstrip line.

rotating one of the rings 90°, as shown in Figure 2.21(a) [40]. This particle is bisymmetric, which means that it possesses two orthogonal symmetry planes, resulting invariant by inversion. As Figure 2.21(b) depicts, the two symmetry axis behave as electric walls at resonance and, because of their orthogonality, the appearance of a net electric dipole is prevented. As a result, the fundamental resonance of the DS-SRR cannot be electrically excited. Contrarily, an axial (z-direction) time-harmonic magnetic field can establish resonance inducing a magnetic dipole moment. Therefore, this particle does not exhibit cross polarization.

In comparison to the original SRR, by applying a quasistatic analysis, the DS-SRR has almost the same inductance but four times smaller capacitance (provided that the overall dimensions of the resonators are the same). The reduction in the total capacitance arises from the series connection of the four capacitances, each of them corresponding to each quadrant (see Figure 2.22). As a consequence, the resonance frequency of the DS-SRR is twice that of the SRR, and the electrical size as well (in fact this is likely to be expected because the length of the individual split rings has been decreased by a factor of two). Accordingly, despite the equivalent circuit model of the DS-SRR is effectively the same as that of the SRR, the description of the electrical behavior of the particle is less accurate in the DS-SRR.

2.3.3 Folded Stepped-Impedance Resonator (SIR)

Stepped-impedance resonators (SIRs) are common planar building blocks in microwave engineering [41]. SIRs are essentially open-ended resonators where the width of the strip is varied abruptly. It is well known that a tri-section SIR can be made electrically small (as compared to a uniform

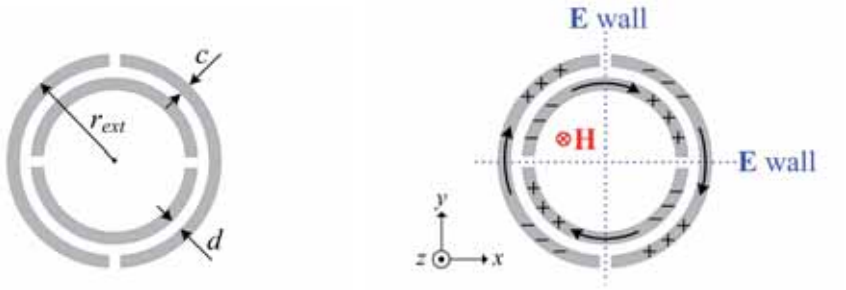

FIGURE 2.21: Bisymmetric double-slit split-ring resonator (DS-SRR). (a) Circular-shaped topology. (b) Fundamental resonance: orientation of the polarization fields, sketch of the charge distribution and currents, and boundary conditions at the symmetry planes.

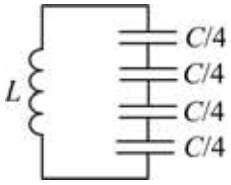

FIGURE 2.22: Equivalent circuit model of a double-slit split-ring resonator (DS-SRR). The total capacitance, $C = 2\pi r_0 C'$, is divided into the four quadrants.

half-wavelength resonator) by narrowing the central section and widening the external ones. Further miniaturization can be achieved by folding the SIR, as depicted in Figure 2.23(a). The fundamental resonance frequency of the folded SIR can be excited by time-harmonic electric (y-direction) and/or magnetic (z-orientation) fields. Hence, cross-polarization effects are present, and both an electric dipole and a magnetic dipole are induced. At the plane of symmetry, an electric wall boundary condition is established. Figure 2.23(b) illustrates all the above-cited properties at resonance.

In terms of electric circuit parameters, basically, the inductive component of the particle is directly related to the inductance of the narrow strip (w_2), while its capacitance is provided by the wide sections (w_1) and the gap (s). Thus, a folded SIR may be regarded as a planar implementation of a capacitively-loaded loop. As a consequence, the equivalent circuit model of a folded SIR (see Figure 2.24) is qualitatively the same as that of an SRR.

2.3.4 Electric Inductive-Capacitive (ELC) Resonator

The so-called electric inductive-capacitive (ELC) resonator (or electric-coupled LC resonator) was proposed by Schurig *et al.* [42] as an alternative to metallic wires for the implementation of negative permittivity (ENG) media. As illustrated in Figure 2.25(a), the ELC

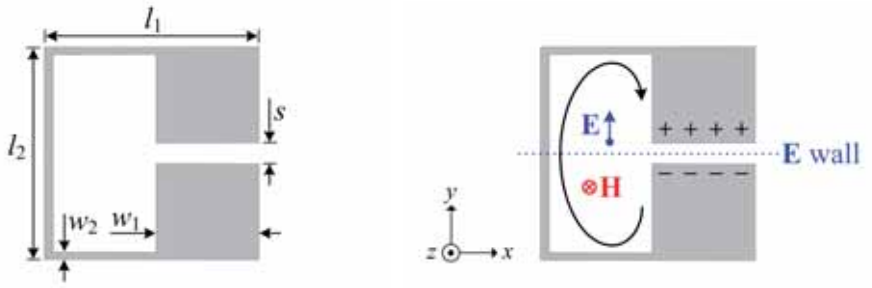

FIGURE 2.23: Symmetric stepped-impedance resonator (SIR). (a) Square-shaped topology. (b) Orientation of the polarization fields, sketch of the charge distribution and currents, and boundary condition at the symmetry plane at the fundamental resonance.

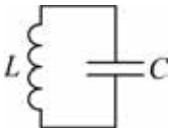

FIGURE 2.24: Equivalent circuit model of a folded stepped-impedance resonator (SIR).

resonator is a bisymmetric planar structure consisting of a pair of capacitively-loaded metallic loops in contact. Clearly, this particle can be viewed as two combined (merged) folded SIRs.

As indicated in Figure 2.25(b), besides an electric wall, the ELC resonator exhibits a *magnetic wall* in an orthogonal plane at the fundamental resonance. At this resonance, the current flows through the central branch so that the (instantaneous) current is clockwise in one loop and counterclockwise in the other one, giving rise to a net displacement current in the gap. In consequence, the opposite magnetic moments originated by the two current loops cancel out and prevent the presence of a net axial magnetic dipole moment (z-direction). For such reason this resonator cannot be driven by means of a uniform axial time-varying magnetic field.[41] However, an electric dipole moment is still present in the plane of the particle directed along the gap (y-oriented), which means that this resonator can be excited through a uniform time-harmonic electric field applied to that direction. As a result, cross-polarization does not affect the ELC resonator, a property that can also be inferred because of its inversion symmetry inherent to its bisymmetry.

[41] Nevertheless, the particle can be magnetically excited if the applied magnetic field in the individual loops is uniform but in opposite directions to each other.

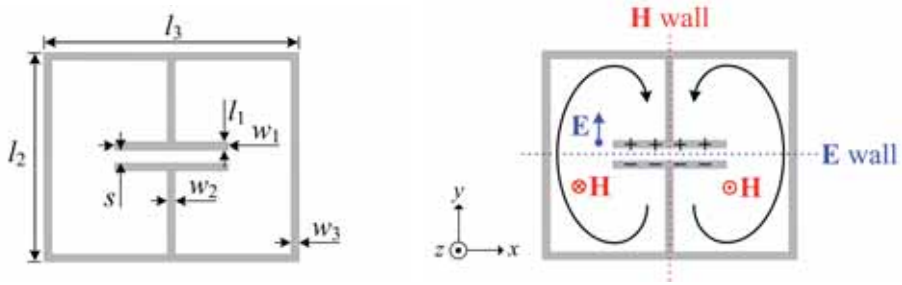

(a) (b)

FIGURE 2.25: Bisymmetric electric inductive-capacitive (ELC) resonator. (a) Rectangular-shaped topology. (b) Polarization fields, sketch of the charge distribution and currents, and boundary conditions at the two orthogonal symmetry planes at the fundamental resonance.

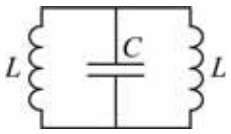

FIGURE 2.26: Equivalent circuit model of an electric inductive-capacitive (ELC) resonator. Mesh currents must flow in the same direction through the capacitor for establishing resonance.

The equivalent circuit model of an electrically small ELC resonator is schematically depicted in Figure 2.26 [42]. As in the folded SIR, the narrow section of each loop (w_2 and w_3) is associated to an inductance, while the wide section (w_1) and the gap (s) is modeled by a capacitance. Therefore, the ELC resonator is in essence an electrically-coupled LC resonator under uniform fields, as its terminology suggests.

2.3.5 Complementary Resonators

The complementary counterparts of the resonators analyzed in the preceding subsections are presented here. As is well known, two complementary structures are defined as those where one is obtained from the other by exchanging the apertures (slots) for the solid (metallic) parts of a plane [43]. Therefore, when complementary structures are combined, they form a single infinite solid screen with no overlaps. As suggested in the literature [44], to avoid ambiguity, we refer to a resonator made of electrically conducting strips as a *strip resonator*, whereas a resonator obtained by cutting slots in a metallic surface as a *slot resonator*.

With a view to analyzing the behavior of resonators in the form of slots, the concepts of duality and complementarity are invoked as often [43, 44]. Electromagnetic duality (often referred to as Babinet's

(a) **(b)**

FIGURE 2.27: Complementary resonators. (a) SRR and (b) CSRR.

Principle) means that Maxwell's equations possess duality in electric and magnetic quantities; the mathematical solution for an electromagnetic field is identical to that for its dual one obtained by a suitable interchange of electric and magnetic quantities. The dual of a strip resonator can be mathematically obtained by the definition of fictitious magnetic conductors. In practice, a physical dual is implemented by a slot resonator. Thus, strip and slot resonators are the physical implementation of dual problems. It follows that, except for a constant, the electromagnetic fields of complementary structures are identical with the exception that the electric and magnetic fields are interchanged. Therefore, the electric/magnetic field distribution of a planar slot structure is the same as the magnetic/electric field distribution of a planar strip structure (the sign of the dual field, however, must change on each side of the slot structure in order to satisfy the boundary conditions in the plane of the particle). It is well known that the impedance and the admittance of complementary structures are also proportional, and accordingly their resonance frequencies are identical. Another interesting property derived from duality is that complementary periodic structures have exactly the same dispersion curve [9]. A case study on this matter will be addressed in Section 2.4.

It should be pointed out that duality in complementary structures strictly apply to infinite, planar, zero thickness, and perfectly conducting electric screens [43]. Although in practice such ideal conditions cannot be fulfilled, for very thin good conductors and metallic planes substantially larger than the wavelength and the slot region, Babinet's Principle predicts the actual behavior to a high degree [33]. One of the most relevant discrepancies due to deviation from ideal conditions is a shift in the resonance frequency.

Let us consider as an illustration the complementary screen of the SRR, i.e. the complementary split-ring resonator (CSRR) [26], as shown in Figure 2.27.[42] The electromagnetic field distribution at the fundamental

[42] Despite the nomenclature, the SRR is the complementary of the CSRR as well.

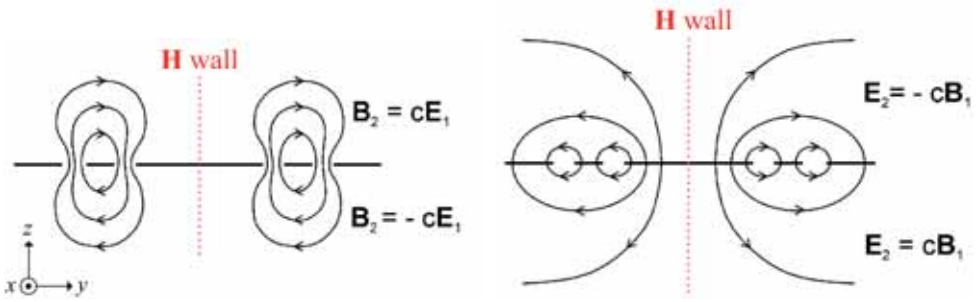

FIGURE 2.28: Sketch of the magnetic (a) and electric (b) field distributions in the CSRR at the fundamental resonance frequency. The field distributions of the CSRR and the SRR are dual, c being the velocity of light. Field distributions from [21].

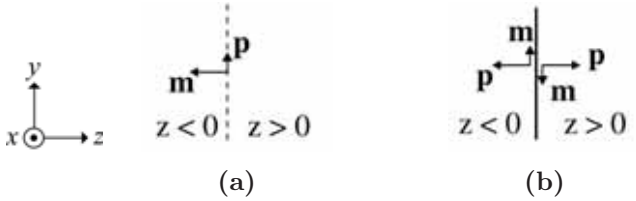

FIGURE 2.29: Induced electric (p) and magnetic (m) dipoles in the (a) SRR and (b) CSRR from [45]. The resonators are in the plane $z = 0$. No net dipoles are induced in the CSRR seen from both sides.

resonance of the CSRR is sketched in Figure 2.28. It is apparent that the electric and magnetic fields in the vicinity of the CSRR are the dual fields to those of the SRR (see Figure 2.17), since the roles of the electric and magnetic fields are interchanged. Thus, at the symmetry axis of the CSRR, a magnetic wall arises. The induced electric and magnetic dipoles are also dual, as illustrated in Figure 2.29 [45]. While the SRR behaves as an axial magnetic dipole and an electric dipole in the plane of the rings, the CSRR (when is seen from one side) exhibits an axial electric dipole and a magnetic dipole in its plane. Note that the sign of the dipoles points in opposite directions on the two sides ($z < 0$ and $z > 0$) of the CSRR. Therefore, the net electric and magnetic dipoles in the CSRR become zero. This ensures that both the total magnetic polarization parallel to the screen (y-axis) and the total electric polarization perpendicular to the screen (z-axis) vanish, as it must be for a metallic plane (electric currents confined in a plane can produce only net tangential electric moments and normal magnetic moments) [3]. As a consequence, when referring to slot resonators, uniform and temporally varying fields are applied only on one side. The CSRR can thus be excited by an axial electric field and/or a

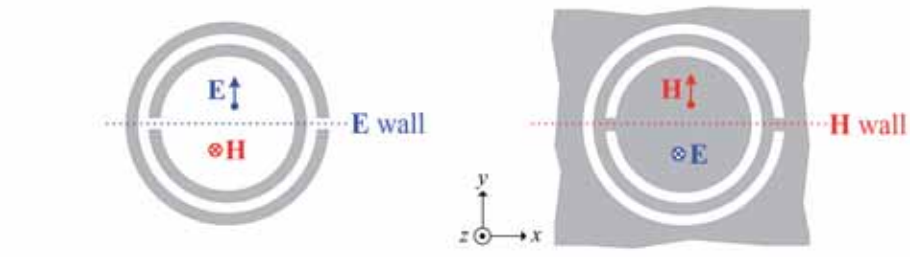

(a) SRR and CSRR.

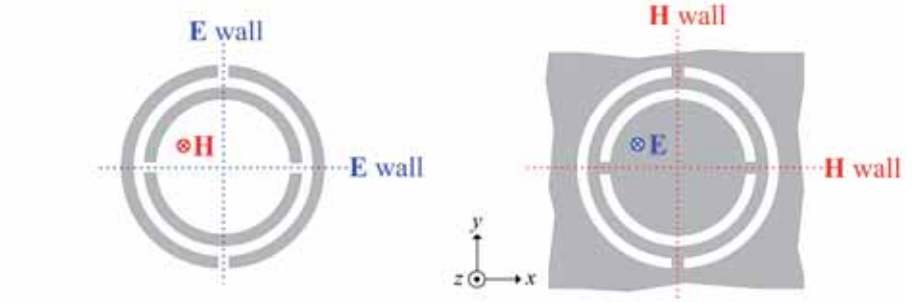

(b) DS-SRR and DS-CSRR.

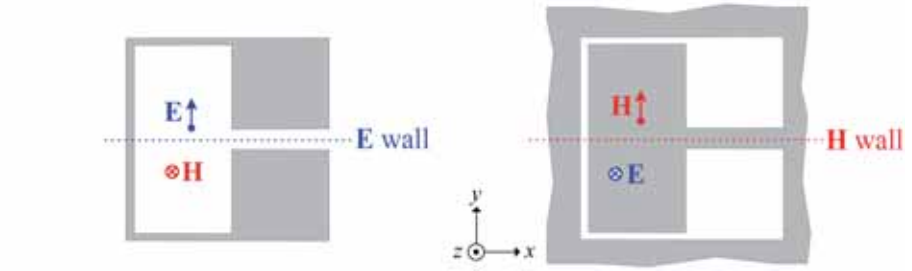

(c) Folded SIR and folded dumbbell DGS.

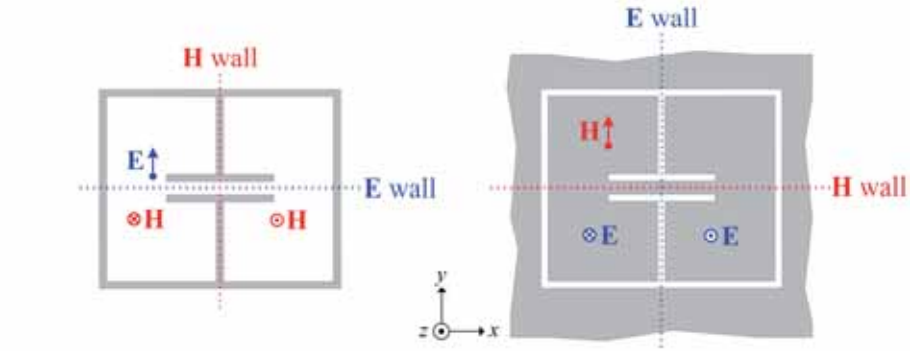

(d) ELC and MLC resonators.

FIGURE 2.30: Polarization fields and boundary conditions at the symmetry planes at the fundamental resonance in complementary split-ring resonators by applying duality.

magnetic field polarized in the direction orthogonal to the symmetry plane, as depicted in Figure 2.30(a). Hence, cross-polarization effects are also present in the CSRR, the electric field being the main driving mechanism [21].

Figure 2.30 shows the results after applying duality to all of our considered resonators. The complementary of the DS-SRR is called double-slit complementary split-ring resonator (DS-CSRR) [40]. Like the SIR, its complementary counterpart [46] has been extensively used in the last decade in the microwave community, and here is referred to dumbbell-shaped defected ground structure (DGS)[43], as is often called in the literature. Neither the unfolded nor the folded dumbbell DGS is used in the present thesis, but it is included here for completeness. The physical dual of the ELC resonator has been called magnetic-LC (MLC) resonator for coherence, since uniform fields are able to excite its fundamental resonance only if the magnetic field is properly polarized.

Finally, it may be shown that electromagnetic duality implies circuit theory duality. Consequently, any planar structure and its complementary screen are dual in circuit theory as well [47]. Thus, the equivalent circuit models of slot resonators may be inferred by the dual circuits of the models corresponding to the strip resonators. By applying circuit duality, inductances are replaced by capacitances, and series-connected elements become parallel-connected circuit elements. The equivalent circuit models for the CSRR and the DS-CSRR are represented in Figure 2.31 [21]. The capacitance of the CSRR may be calculated as the capacitance of a disk of radius $r_0 - c/2$ ($r_0 = r_{ext} - c - d/2$) surrounded by a metal plane at a distance c of its edge (analytical expressions have been derived [21]). The CSRR inductance is given by the parallel combination of the two inductances connecting the inner disk to the outer metallic region of the CSRR. Such inductances may be calculated as the inductance of a CPWs with a strip width d and slot width c. A circuit model of the MLC resonator is developed in **article IJAP13**, while the circuit of the dumbbell-shaped DGS can be readily derived from it.

2.4 Magneto- and Electro-Inductive Waves

This section is devoted to propagating structures based on inter-resonator coupling. Indeed, metamaterial resonators not only may be excited, for instance, by a transmission line, but also by coupling them. Without loss of generality, imagine the periodic chains shown in Figure 2.32 made of either split-ring resonators (SRRs) or complementary split-ring resonators (CSRRs). Since these two arrays complement each other to form a solid

[43] In fact, *slot* resonators are sometimes referred to as *defected ground structures* (DGS) or *patterned ground structures* (PGS).

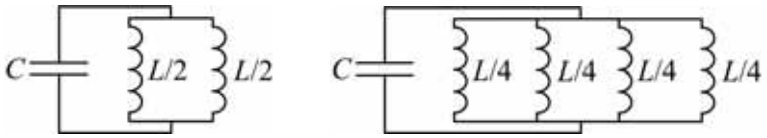

(a) (b)

FIGURE 2.31: Equivalent circuit model of a (a) CSRR and a (b) DS-CSRR. The total inductance, $L = 2\pi r_0 L'$, is divided into equal parallel contributions, where L' is the per-unit-length inductance.

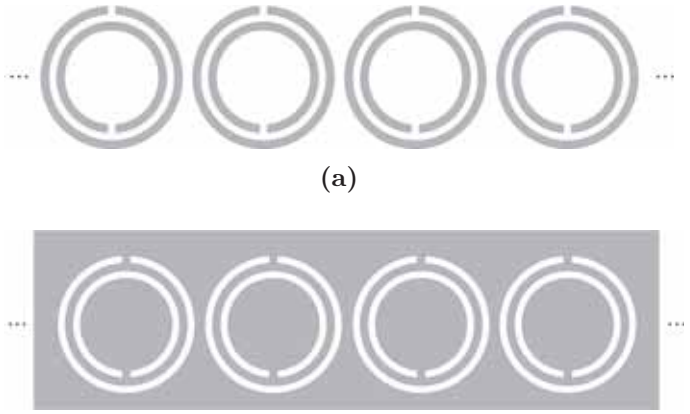

(a)

(b)

FIGURE 2.32: Periodic array of coupled (a) SRRs and (b) CSRRs through which dual magneto- and electro-inductive waves may arise, respectively.

screen, both structures exhibit exactly numerically the same dispersion relation, as mentioned in Subsection 2.3.5. However, it is apparent from duality that the nature of the propagation in the two arrays must somehow interchange dual variables. As will be argued, planar arrays of SRRs and CSRRs are able to guide backward *magneto-inductive waves* and *electro-inductive waves*, respectively.

2.4.1 Magneto-Inductive Waves in Arrays of Magnetically-Coupled Resonators

Magneto-inductive waves (MIWs) were first reported and studied in the frame of metamaterial science by Shamonina *et al.* [48, 49], and many subsequent works have been published by the same research group [5]. MIWs are a form of guided waves that propagate through an array of magnetically-coupled resonators that acts as a waveguide. A lumped-element circuit representation of a periodic magneto-inductive waveguide is illustrated in Figure 2.33(a). Each resonator is modeled by an

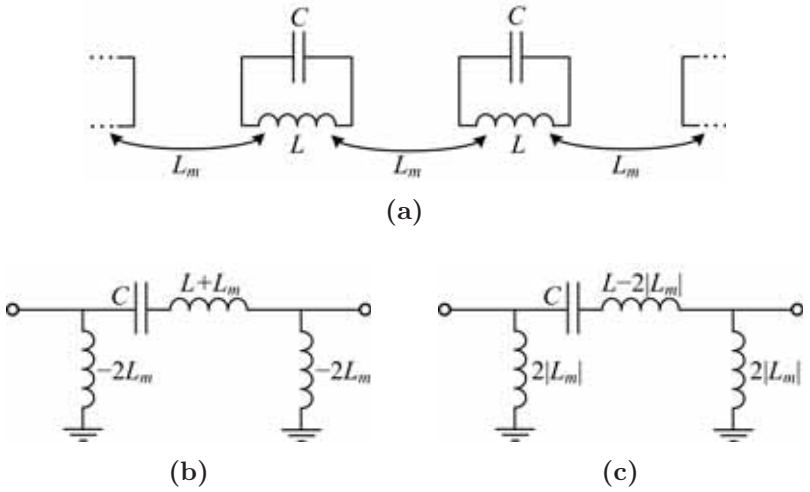

FIGURE 2.33: Equivalent circuit of a periodic magneto-inductive waveguide assuming magnetic interaction only between adjacent resonators. (a) Circuit with mutual inductance. Unit-cell transformed circuit [19] assuming (b) positive and (c) negative mutual inductance supporting forward and backward waves, respectively.

inductance L and a capacitance C, and is coupled to its nearest neighbor[44] by a mutual inductance L_m. Thus, the term *magneto-inductive wave* originates from the fact that such waves arise due to voltages induced by magnetic coupling between the resonant elements [50]. The propagation of MIWs occurs within a narrow passband around the resonance frequency of the isolated elements, i.e. $\omega_0 = 1/\sqrt{LC}$, and the associated bandwidth is dependent on how strongly the resonators are coupled to each other. The stronger the interaction between the elements, the wider the passband of the MIWs [50]. Both forward and backward MIWs may exist, depending on the sign of the mutual inductance between resonators [see Figures 2.33(b) and (c)]. While mutual inductance is positive in an axial configuration, it is negative when the resonators are arranged in a coplanar configuration since the magnetic field originating in one resonator crosses another one in the opposite direction [49].

MIWs are expected to be present in whatever chain of resonant elements that can be described by LC resonant tanks as long as the coupling between them is magnetic [49, 51], or dominantly magnetic in the presence of negligible cross-polarization effects [3]. The first magneto-inductive waveguide was in the form of a theoretical periodic array of magnetically-coupled capacitively-loaded loops, as can be seen in Figure 2.34(a) for coplanar arrangement [49]. The corresponding dispersion

[44] The first neighbor approximation assumes that the field strength declines so rapidly away from a resonator that it is too small beyond the nearest neighbor. The accuracy of this first-order coupling is dependent on the resonant elements [3, 5].

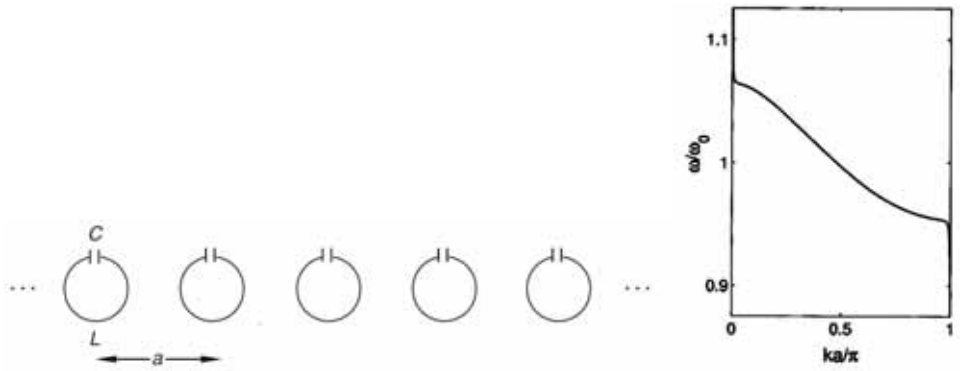

(a) (b)

FIGURE 2.34: Backward magneto-inductive waves in an array of coplanar capacitively-loaded loops. (a) Theoretical layout from [52]. (b) Dispersion relation with nearest neighbor coupling from [49].

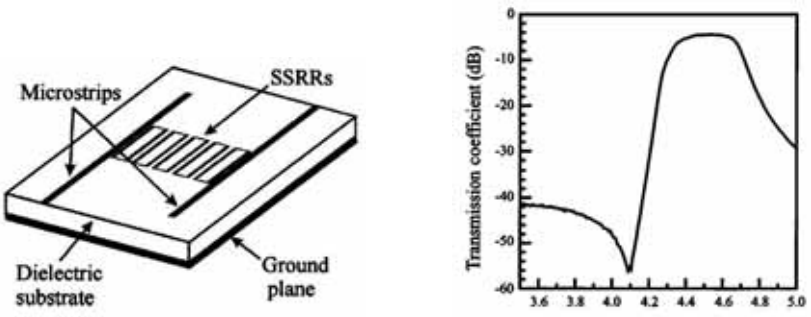

(a) (b)

FIGURE 2.35: Backward magneto-inductive waves in an array of split-ring resonators in planar configuration in microstrip technology. (a) Layout; input/output SSRRs are coupled to input/output microstrip lines. (b) Measured transmission coefficient from [51].

diagram assuming that coupling is restricted to nearest neighbors is shown in Figure 2.34(b), where the backward wave nature is clearly visible. Soon after, MIWs were also excited in a periodic arrangement of split squared ring resonators (SSRRs), as shown in Figure 2.35 [51] (this type of split-ring resonator, which is not symmetric and was not described in Section 2.3, does not suffer cross-polarization effects).

It is also worth mentioning that MIWs belong to the category of slow waves, since its phase velocity may be orders of magnitude smaller than the velocity of an electromagnetic wave propagating in the same medium [3, 6][45]. Since slow-wave structures are of interest in device miniaturization, and

[45] Slow-wave effect is usually accounted for by the resulting phase velocity reduction factor (or slow-wave factor).

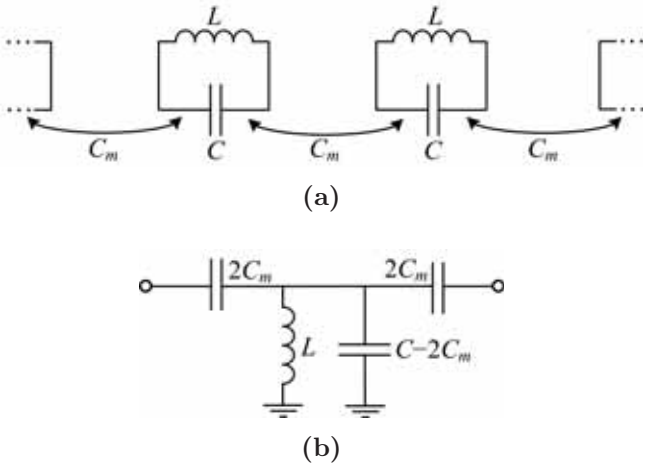

FIGURE 2.36: Equivalent circuit of a periodic electro-inductive waveguide with electric interaction only between adjacent resonators. (a) Circuit with mutual capacitance. (b) Unit-cell transformed circuit model [19] where wave propagation is backward.

bandpass characteristics are useful in signal filtering, MIWs have found many diverse applications. Some examples are power dividers [49], delay lines [51], passive chipless tags for radiofrequency identification (RFID) [53], and phase shifters [54].

2.4.2 Electro-Inductive Waves in Arrays of Electrically-Coupled Resonators

Electro-inductive waves (EIWs) can be considered as the dual counterpart of magneto-inductive waves [55].[46] Therefore, EIWs propagate through a waveguide whose guiding mechanism is based on electric interaction between neighboring resonant elements, in parallelism (or duality) to MIWs. The lumped-element equivalent circuit modeling a periodic electro-inductive waveguide in the first neighbor approximation is depicted in Figure 2.36(a), where the mutual capacitance C_m accounts for the inter-resonator electric coupling. The resulting equivalent circuit model for a planar arrangement of electrically-coupled resonators is also included. As can be seen, the circuits of electro-inductive waveguides are dual to the circuits modeling magneto-inductive waveguides (Figure 2.33). In fact, this is not surprising since as was asserted in Subsection 2.3.5, electromagnetic duality involves circuit duality. Therefore, the dispersion relation inferred from the equivalent circuit models of magneto- and electro-inductive waveguides exhibit exactly the same dispersion relation if they are exactly

[46] However, propagation through electrically-coupled metallic rods have been known for a long time [56].

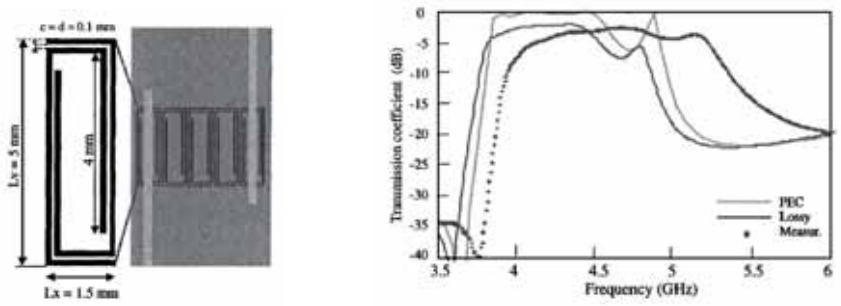

(a) **(b)**

FIGURE 2.37: Electro-inductive waves in an array of complementary split-ring resonators in planar configuration in microstrip implementation. (a) Layout and (b) simulated and measured transmission coefficient from [55].

numerically dual. The meaningful difference lie in the nature (MIW- or EIW-related) of the propagating band.

Electro-inductive waveguides have been implemented, e.g., in microstrip technology using the complementary split squared ring resonator (CSSRR), that is, the complementary version of the SSRR [55]. Figure 2.37 shows the layout of the structure as well as the transmission coefficient. As expected, this waveguide behaves in a similar way as compared with its dual counterpart[47] [51] (Figure 2.35).

References

[1] C. Caloz and T. Itoh, *Electromagnetic Metamaterials: Transmission Line Theory and Microwave Applications.* John Wiley & Sons, 2005.

[2] N. Engheta and R. W. Ziolkowski, *Metamaterials: Physics and Engineering Explorations.* John Wiley & Sons, 2006.

[3] R. Marqués, F. Martín, and M. Sorolla, *Metamaterials with Negative Parameters: Theory, Design and Microwave Applications.* John Wiley & Sons, 2008.

[4] G. V. Eleftheriades and K. G. Balmain, *Negative-Refraction Metamaterials: Fundamental Principles and Applications.* John Wiley & Sons, 2005.

[5] L. Solymar and E. Shamonina, *Waves in Metamaterials.* Oxford University Press, 2009.

[47] In a strict sense, however, multilayer structures cannot be dual.

[6] F. Martín, *Artificial Transmission Lines for RF and Microwave Applications*. John Wiley & Sons, to be published.

[7] S. Ramo, J. R. Whinnery, and T. Van Duzer, *Fields and Waves in Communication Electronics*. John Wiley & Sons, 1965.

[8] C. A. Balanis, *Advanced Engineering Electromagnetics*. John Wiley & Sons, 1989.

[9] R. E. Collin, *Foundations for Microwave Engineering*, 2nd ed. McGraw-Hill, 1992.

[10] D. M. Pozar, *Microwave Engineering*, 4th ed. John Wiley & Sons, 2012.

[11] V. G. Veselago, "The electrodynamics of substances with simultaneously negative values of ϵ and μ," *Physics-Uspekhi*, vol. 10, no. 4, pp. 509–514, Jan. 1968.

[12] D. R. Smith, W. J. Padilla, D. C. Vier, S. C. Nemat-Nasser, and S. Schultz, "Composite medium with simultaneously negative permeability and permittivity," *Phys. Rev. Lett.*, vol. 84, no. 18, pp. 4184–4187, May 2000.

[13] J. B. Pendry, A. J. Holden, D. J. Robbins, and W. J. Stewart, "Magnetism from conductors and enhanced nonlinear phenomena," *IEEE Trans. Microw. Theory Tech.*, vol. 47, no. 11, pp. 2075–2084, Nov. 1999.

[14] A. K. Iyer and G. V. Eleftheriades, "Negative refractive index metamaterials supporting 2-D waves," in *IEEE MTT-S Int. Microw. Symp. Dig.*, vol. 2, Seattle, WA, USA, Jun. 2002, pp. 1067–1070.

[15] A. A. Oliner, "A periodic-structure negative-refractive-index medium without resonant elements," in *IEEE-APS/URSI Int. Symp. Dig.*, vol. 41, San Antonio, TX, USA, Jun. 2002.

[16] C. Caloz and T. Itoh, "Application of the transmission line theory of left-handed (LH) materials to the realization of a microstrip "LH line"," in *IEEE-AP-S USNC/URSI National Radio Science Meeting*, vol. 2, Sant Antonio, TX, USA, Jun. 2002, pp. 412–415.

[17] ——, "Novel microwave devices and structures based on the transmission line approach of meta-materials," in *IEEE MTT-S Int. Microw. Symp. Dig.*, vol. 1, Philadelphia, PA, USA, Jun. 2003, pp. 195–198.

[18] A. Grbic and G. V. Eleftheriades, "Experimental verification of backward-wave radiation from a negative refractive index metamaterial," *J. App. Phy.*, vol. 92, no. 10, pp. 5930–5935, Nov. 2002.

[19] J.-S. Hong and M. J. Lancaster, *Microstrip Filters for RF/Microwave Applications*. John Wiley & Sons, 2001.

[20] F. Martín, J. Bonache, F. Falcone, M. Sorolla, and R. Marqués, "Split ring resonator-based left-handed coplanar waveguide," *App. Phys. Lett.*, vol. 83, no. 22, pp. 4652–4654, Dec. 2003.

[21] J. D. Baena, J. Bonache, F. Martín, R. M. Sillero, F. Falcone, T. Lopetegi, M. A. G. Laso, J. García-García, I. Gil, M. F. Portillo, and M. Sorolla, "Equivalent-circuit models for split-ring resonators and complementary split-ring resonators coupled to planar transmission lines," *IEEE Trans. Microw. Theory Tech.*, vol. 53, no. 4, pp. 1451–1461, Apr. 2005.

[22] F. Aznar, J. Bonache, and F. Martín, "Improved circuit model for left-handed lines loaded with split ring resonators," *App. Phys. Lett.*, vol. 92, no. 043512, Feb. 2008.

[23] J. Bonache, M. Gil, O. García-Abad, and F. Martín, "Parametric analysis of microstrip lines loaded with complementary split ring resonators," *Microw. Opt. Technol. Lett.*, vol. 50, no. 8, pp. 2093–2096, Aug. 2008.

[24] F. Martín, F. Falcone, J. Bonache, R. Marqués, and M. Sorolla, "Miniaturized coplanar waveguide stop band filters based on multiple tuned split ring resonators," *IEEE Microw. Wireless Compon. Lett.*, vol. 13, no. 12, pp. 511–513, Dec. 2003.

[25] F. Aznar, M. Gil, J. Bonache, L. Jelinek, J. D. Baena, R. Marqués, and F. Martín, "Characterization of miniaturized metamaterial resonators coupled to planar transmission lines through parameter extraction," *J. App. Phys.*, vol. 104, no. 114501, Dec. 2008.

[26] F. Falcone, T. Lopetegi, J. D. Baena, R. Marqués, F. Martín, and M. Sorolla, "Effective negative-ϵ; stopband microstrip lines based on complementary split ring resonators," *IEEE Microw. Wireless Compon. Lett.*, vol. 14, no. 6, pp. 280–282, Jun. 2004.

[27] J. Bonache, M. Gil, I. Gil, J. García-García, and F. Martín, "On the electrical characteristics of complementary metamaterial resonators," *IEEE Microw. Wireless Compon. Lett.*, vol. 16, no. 10, pp. 543–545, Oct. 2006.

[28] L. Brillouin, *Wave Propagation in Periodic Structures: Electric Filters and Crystal Lattices*. McGraw-Hill, 1946.

[29] F. Aznar, M. Gil, J. Bonache, and F. Martín, "Modelling metamaterial transmission lines: a review and recent developments," *Opto-Electron. Rev.*, vol. 16, no. 3, pp. 226–236, Sep. 2008.

[30] J. Martel, R. Marqués, F. Falcone, J. Baena, F. Medina, F. Martín, and M. Sorolla, "A new LC series element for compact bandpass filter design," *IEEE Microw. Wireless Compon. Lett.*, vol. 14, no. 5, pp. 210–212, May 2004.

[31] A. Vélez, F. Aznar, J. Bonache, M. Velázquez-Ahumada, J. Martel, and F. Martín, "Open complementary split ring resonators (OCSRRs) and their application to wideband CPW band pass filters," *IEEE Microw. Wireless Compon. Lett.*, vol. 19, no. 4, pp. 197–199, Apr. 2009.

[32] W. N. Hardy and L. A. Whitehead, "Split-ring resonator for use in magnetic resonance from 200-2000 MHz," *Rev. Sci. Instrum.*, vol. 52, no. 2, pp. 213–216, Feb. 1981.

[33] C. A. Balanis, *Antenna Theory: Analysis and Design*, 2nd ed. John Wiley & Sons, 1997.

[34] R. Marqués, F. Medina, and R. Rafii-El-Idrissi, "Role of bianisotropy in negative permeability and left-handed metamaterials," *Phys. Rev. B*, vol. 65, no. 144440, Apr. 2002.

[35] P. Gay-Balmaz and O. J. F. Martin, "Electromagnetic resonances in individual and coupled split-ring resonators," *J. App. Phys.*, vol. 92, no. 5, pp. 2929–2936, Sep. 2002.

[36] N. Katsarakis, T. Koschny, M. Kafesaki, E. Economou, and C. Soukoulis, "Electric coupling to the magnetic resonance of split ring resonators," *App. Phys. Lett.*, vol. 84, no. 15, pp. 2943–2945, Apr. 2004.

[37] M. Shamonin, E. Shamonina, V. Kalinin, and L. Solymar, "Properties of a metamaterial element: Analytical solutions and numerical simulations for a singly split double ring," *J. App. Phys.*, vol. 95, no. 7, pp. 3778–3784, Apr. 2004.

[38] ——, "Resonant frequencies of a split-ring resonator: Analytical solutions and numerical simulations," *Microw. Opt. Technol. Lett.*, vol. 44, no. 2, pp. 133–136, Dec. 2005.

[39] J. García-García, F. Martín, J. D. Baena, R. Marqués, and L. Jelinek, "On the resonances and polarizabilities of split ring resonators," *J. App. Phys.*, vol. 98, no. 033103, Aug. 2005.

[40] R. Marqués, J. Baena, J. Martel, F. Medina, F. Falcone, M. Sorolla, and F. Martín, "Novel small resonant electromagnetic particles for metamaterial and filter design," in *Proc. Int. Conf. Electromagnetics Advanced Application (ICEAA '03)*, Torino, Italy, Sep. 2003, pp. 439–442.

[41] M. Makimoto and S. Yamashita, "Compact bandpass filters using stepped impedance resonators," *Proc. IEEE*, vol. 67, no. 1, pp. 16–19, Jan. 1979.

[42] D. Schurig, J. Mock, and D. Smith, "Electric-field-coupled resonators for negative permittivity metamaterials," *App. Phys. Lett.*, vol. 88, no. 041109, Jan. 2006.

[43] H. Booker, "Slot aerials and their relation to complementary wire aerials (Babinet's principle)," *J. IEE Part IIIA*, vol. 93, no. 4, pp. 620–626, May 1946.

[44] R. King and G. H. Owyang, "Complementarity in the study of transmission lines," *IEEE Trans. Microw. Theory Tech.*, vol. 8, no. 2, pp. 172–181, Mar. 1960.

[45] F. Falcone, T. Lopetegi, M. Laso, J. Baena, J. Bonache, M. Beruete, R. Marqués, F. Martín, and M. Sorolla, "Babinet principle applied to the design of metasurfaces and metamaterials," *Phy. Rev. Lett.*, vol. 93, no. 197401, Nov. 2004.

[46] C.-S. Kim, J.-S. Park, D. Ahn, and J.-B. Lim, "A novel 1-D periodic defected ground structure for planar circuits," *IEEE Microw. Guided Wave Lett.*, vol. 10, no. 4, pp. 131–133, Apr. 2000.

[47] W. Getsinger, "Circuit duals on planar transmission media," in *IEEE MTT-S Int. Microwave Symp. Dig.*, Boston, MA, USA, May 1983, pp. 154–156.

[48] E. Shamonina, V. A. Kalinin, K. H. Ringhofer, and L. Solymar, "Magneto-inductive waveguide," *Electron. Lett.*, vol. 38, no. 8, pp. 371–373, Apr. 2002.

[49] ——, "Magnetoinductive waves in one, two, and three dimensions," *J. App. Phys.*, vol. 92, no. 10, pp. 6252–6261, Nov. 2002.

[50] R. R. A. Syms, E. Shamonina, and L. Solymar, "Positive and negative refraction of magnetoinductive waves in two dimensions," *Eur. Phys. J. B*, vol. 46, no. 2, pp. 301–308, Aug. 2005.

[51] M. J. Freire, R. Marqués, F. Medina, M. A. G. Laso, and F. Martín, "Planar magnetoinductive wave transducers: Theory and applications," *App. Phys. Lett.*, vol. 85, no. 19, pp. 4439–4441, Nov. 2004.

[52] R. R. A. Syms, E. Shamonina, and L. Solymar, "Magneto-inductive waveguide devices," *IEE Proc. Microw. Antennas Propag.*, vol. 153, no. 2, pp. 111–121, Apr. 2006.

[53] F. J. Herraiz-Martínez, F. Paredes, G. Zamora González, F. Martín, and J. Bonache, "Printed magnetoinductive-wave (MIW) delay lines for chipless RFID applications," *IEEE Trans. Antennas Propag.*, vol. 60, no. 11, pp. 5075–5082, Nov. 2012.

[54] I. S. Nefedov and S. A. Tretyakov, "On potential applications of metamaterials for the design of broadband phase shifters," *Microw. Opt. Technol. Lett.*, vol. 45, no. 2, pp. 98–102, Apr. 2005.

[55] M. Beruete, F. Falcone, M. J. Freire, R. Marqués, and J. D. Baena, "Electroinductive waves in chains of complementary metamaterial elements," *App. Phys. Lett.*, vol. 88, no. 083503, Feb. 2006.

[56] J. Shefer, "Periodic cylinder arrays as transmission lines," *IEEE Trans. Microw. Theory Tech.*, vol. 11, no. 1, pp. 55–61, Jan. 1963.

Chapter 3

Advances in Equivalent Circuit Models of Resonator-loaded Transmission Lines

The present chapter focuses on advances relative to equivalent circuit models of transmission lines loaded with electrically small resonators. An accurate circuit model should include all the elements (a transmission line and an array of resonators in our case) as well as all the inter-element couplings involved. Note that neither mixed magnetoelectric coupling nor inter-resonator coupling was considered in the previous chapter (Subsection 2.2.4). The mixed coupling between the line and the resonators is usually neglected because only the dominant coupling is the one modeled, but it may become important under some resonator orientations. Regarding the coupling between resonators, it may be ignored when the resonators are not closely spaced. By contrast, if the resonators are close to each other, inter-resonator interaction must be taken into account since it influences the frequency response to a considerably extent. In this chapter we analyze mixed coupling in the line-to-resonator coupling as well as inter-resonator coupling, providing unit-cell equivalent circuit models. Additionally, we also investigate the limits on the synthesis of stepped-impedance shunt-stubs (SISSs). While the *analysis* is aimed at getting useful electromagnetic information about a particular structure, the inverse process is called *synthesis*. The latter is of paramount importance for design and optimization purposes.

This chapter is divided into three sections. Section 3.1 deals with mixed coupling between the transmission line and the resonators. In Section 3.2 we analyze resonator-to-resonator coupling effects on the frequency response as well as on the dispersion relation. Finally, Section 3.3 reports a

methodology for obtaining the physically implementable values of inductance and capacitance using electrically small SISSs.

3.1 Line-to-Resonator Magnetoelectric Coupling

As was explained in Subsection 2.3.1, resonators that do not possess inversion symmetry may suffer from cross-polarization effects [1]. This means the resonators may become electrically polarized as a response to an applied magnetic field, and vice versa [2, 3], and that they may be magnetically and/or electrically excited if the resonators are properly oriented [4, 5]. In general, mixed coupling is usually ignored because the dominant coupling is the only modeled coupling mechanism [6]. However, under some resonator orientations, mixed coupling effects may become relevant. The important aspect for us is to model the line-to-resonator coupling, rather than the polarizabilities. Therefore, depending on the resonator orientation in regard to the transmission line, mixed magnetoelectric coupling arise.

In this section, we characterize the relative orientation of metamaterial-inspired resonators when they are loading elements in transmission lines, where the illuminating fields to the resonators are not uniform. As will be shown in Chapters 4−7, the resonator orientation plays a key role in the presented symmetry-based devices. The focus in the present section is on modeling only classical coplanar waveguides (CPWs) loaded with split-ring resonators (SRRs) and complementary split-ring resonators (CSRRs) loading microstrip lines loaded (**article AWPL13**) since this suffices to illustrate the modeling of magnetoelectric coupling. However, mixed-coupling effects are also modeled in CPWs loaded with CSRRs or per-unit-cell single SRRs (Subsection 4.2.3, **article APA12**), and in ELC- and MLC-loaded differential microstrip lines (Subsection 4.2.2, **article APA13**).

3.1.1 SRR-loaded Coplanar Waveguides and CSRR-loaded Microstrip Lines

As seen in Subsection 2.2.4, equivalent circuit models of SRR-loaded CPWs and CSRR-loaded microstrip lines were proposed by Martín *et al.* [7, 8] and Baena *et al.* [6], respectively (the former was revised by Aznar *et al.* [9]). In these models, mixed coupling is not considered. Since these circuit models are symmetric with regard to the ports, the SRR- and CSRR-loaded lines should also be symmetric when looking into the ports. Certainly, in the literature the slits of the SRRs/CSRRs are usually (but not always!) oriented orthogonally to the line axis. Under these circumstances, these resonator-loaded lines are symmetric with regard to ports. Indeed, it has been demonstrated through

circuit parameter extraction that these models describe the frequency response of the corresponding structures to a very good approximation [10, 11]. However, as indicated in **article AWPL13**, if the symmetry of the loaded lines (in regard to the ports) is disrupted by rotating the SRRs/CSRRs, the models as well as the parameter extraction procedures may fail. For the particular case where the slits are oriented in parallel to the line axis (where the structures are symmetric with regard to their midplane, but not to the ports), the asymmetry leads to substantially different phases of the two reflection coefficients. As will be seen in Chapters 4−7, symmetry at the midplane is important in the applications considered in this thesis.

Article AWPL13 investigates the effects of rotating SRRs and CSRRs in the frequency response of SRR-loaded CPWs and CSRR-loaded microstrip lines. If the SRRs/CSRRs slits are aligned orthogonally to the line axis, the SRR/CSRR cannot be excited through electric/magnetic coupling. However, if the particles are rotated, a nonnegligible component of the electric/magnetic field orthogonal to the symmetry plane of the SRRs/CSRRs appears, and both magnetic and electric coupling must be considered. Obviously, the optimum case to favor mixed coupling is the one where the slits are oriented in parallel to the line axis. Hence, the dependence of the frequency response of SRR- and CSRR-loaded lines on particle orientation is attributed to mixed coupling effects. To support this hypothesis, we also perform the rotation analysis considering a non-bianisotropic SRR (NB-SRR) [12] and a non-bianisotropic CSRR (NB-CSRR). These particles do not exhibit cross-polarization since they have inversion symmetry with regard to their center. The results show that the frequency response does not change appreciably by rotating the NB-SRR/NB-CSRR. Therefore, unless the resonator slits are aligned along the orthogonal direction to the line axis, mixed magnetoelectric coupling between the host line and the resonators must be considered to accurately describe the lines with arbitrarily oriented SRRs or CSRRs. To this end, we update the equivalent circuit models of SRR-loaded CPWs [Figure 2.12(a)] and CSRR-loaded microstrip lines (Figure 2.15) including mixed coupling effects. We introduce a capacitance and a mutual inductance in the SRR- and CSRR-based circuits to model the line-to-resonator capacitive (electric) and inductive (magnetic) coupling, respectively. Like the models without mixed coupling, the resulting equivalent circuit models satisfy the duality property (Subsection 2.2.4). It is also observed that the magnetic coupling provides the necessary asymmetry in the circuit models to explain the lack of symmetry with regard to the ports. We validate the proposed equivalent circuits by comparing circuit simulations with electromagnetic simulations and measurements, where good agreement is obtained.

Finally, it should be highlighted that the proposed equivalent circuits are considerably complex, and essentially such circuits allow for the modeling of the phase response of the reflection coefficients. Therefore, rather than being useful for design purposes (unless accurate phase response modeling is required), the presented circuits (a) allow for the understanding of the associated line-to-resonator coupling phenomenology, (b) point out the relevance of particle orientation on its excitation, and (c) indicate that the parameter extraction procedures may fail when the symmetry plane of the resonators is not orthogonally aligned with the line.

3.2 Inter-Resonator Coupling

The previous section was devoted to the line-to-resonator coupling. However, in an array of resonator-loaded transmission lines, the inter-resonator coupling can also be meaningful. Likewise, the coupling between two resonant elements depends on their relative orientation, and may be electric, magnetic, or mixed [13–15]. The aim of this section is to consider inter-resonator coupling between resonators of adjacent unit cells.[1] As in Section 2.4, we assume the coupling to be restricted to the first-neighbor[2] and to the dominant coupling mechanism (i.e. mixed-coupling is not considered). As will be shown, inter-resonator coupling enhances the stopband bandwidth, and this is useful for the design of bandstop filters. In Subsection 5.3.1 (**article TMTT12**), inter-resonator coupling helps to broaden the stopband of the common mode in CSRR-loaded differential lines.

3.2.1 SRR-loaded Coplanar Waveguides and CSRR-loaded Microstrip Lines

Transmission lines periodically loaded with SRRs or CSRRs inhibit wave propagation in the vicinity of the resonator fundamental resonance, and support forward waves outside this forbidden band (Subsection 2.2.4). It is also known that chains of coupled SRRs (and other magnetic resonators) or CSRRs (and other electric resonators) arranged in the same plane support backward waves, and such waves have been called magneto-inductive (MIWs) and electro-inductive waves (EIWs), respectively (Section 2.4). Interestingly, coupling manifestations between

[1] When the unit cell of periodic resonator-loaded transmission lines is composed of more than one resonator, inter-resonator coupling within the unit cell may also exist (this will be analyzed in Subsections 4.4.1 and 4.4.2).

[2] Coupling between each resonator and a number of neighbors may be significant. The decay of the coupling coefficient, that varies with inter-resonator separation, should determine the number of couplings to take into account. However, if many couplings are involved, it is difficult to model and design structures.

MIWs/EIWs and electromagnetic waves (propagating through an array of SRRs/CSRRs and a transmission line, respectively) may arise. First, the dispersion characteristics of transmission lines loaded with SRRs (considering coupled and decoupled SRRs) and metallic rods was analyzed by Syms *et al.* [16]. It was shown that MIWs and electromagnetic waves may interact leading to a stopband. Some years later, Syms and Solymar carried out a theoretical analysis of SRR-loaded lines with coupled resonators (i.e. without the rods), and they found that the stopband is due to the presence of *complex modes* [17].[3] Complex modes have been known for a long time in the literature, and have been found in several structures [18–22]. Despite the assumption of the absence of losses, complex modes have conjugate complex propagation constants ($\gamma = \alpha \pm j\beta$, where α is the attenuation constant and β is the phase constant) and appear as conjugate pairs in reciprocal structures. Since the power contributions of the modes are in opposite direction to each other, complex modes do not generally carry net power.[4]

In **article JAP14** and **article AWPL12** we study SRR- and CSRR-loaded lines with coupled resonators, respectively. The topology of the considered SRR-loaded lines (unit cell) consists of a CPW loaded with pairs of SRRs etched on the back side of the substrate. The considered CSRR-loaded line is a microstrip line loaded with an array of CSRRs etched in the ground plane. To achieve significant inter-resonator coupling, we assume nearby and rectangular-shaped resonators (the long side being oriented along the transversal direction of propagation). It is important to highlight that the symmetry plane of the resonators (along the slits) is orthogonally oriented to the line axis. This orientation guarantees that the line is capable of exciting the SRR/CSRR fundamental resonance through only the magnetic/electric coupling. With different orientations, mixed coupling is required for an accurate description of the structure, as discussed in Subsection 3.1.1 (obviously, mixed coupling between the line and the resonators makes the present analysis much more cumbersome).

In the equivalent circuit models of Figures 2.12(a) and 2.15, we include inter-resonator coupling with the nearest-neighbor interaction approximation.[5] According to the orientation of the resonators, the inter-resonator coupling is supposed to be dominantly magnetic and electric in SRRs and CSRRs, respectively, and this is the only coupling modeled (the magnetic coupling between SRRs of adjacent cells being negative). Losses are neglected in the circuit models, and this is an

[3] According to Syms and Solymar, in an SRR-loaded line with coupled resonators, the region of complex modes leads to a complex effective permeability (under lossless conditions).

[4] Under some circumstances, the individual complex modes may be selectively excited [23].

[5] Although inter-resonator coupling beyond the first neighbor may be significant using rectangular-shaped resonators, this approximation suffices for our purpose.

important assumption when we derive the dispersion relation as will be shown shortly. The resulting lumped-element equivalent circuit models of the corresponding unit cells are four-port circuits. Qualitatively, the four-port unit cell circuit of SRR-loaded lines with coupled resonators is composed of a conventional two-port transmission line-type circuit magnetically coupled to a secondary propagating circuit that supports the propagation of MIWs. Analogously, the unit cell of CSRR-loaded lines when the resonators are coupled consists of a transmission-line circuit electrically coupled to a circuit that is able to support EIWs. As multiconductor theory predicts, both unit cells can support two modes [24]. While a conventional transmission line supports the propagation of forward waves (Subsection 2.2.1), an array of coupled resonators in coplanar arrangement supports either MIWs or EIWs of backward nature (Subsections 2.4.1 and 2.4.2, respectively). In consequence, forward and backward waves are expected to coexist at some frequency band.

With a view to validating the circuit models, we compare the transmission and reflection coefficients corresponding to the circuit and electromagnetic simulations. It is important to realize that, in a truncated periodic structure, the resonators of the input/output cells are not externally fed. Only the transmission line is driven by port terminals, and MIWs/EIWs are excited from the electromagnetic waves generated by the line that illuminate the resonators. Therefore, when the periodic structure is truncated the ports modeling the inter-resonator coupling are open-ended, and we compute the frequency response of two-port circuits. For one-cell and two-cell (where there is nearest-neighbor interaction only) structures, the accordance of the circuit responses with those inferred from electromagnetic simulations is remarkable. For higher-order structures, where the nearest-neighbor approximation plays an active role, the accuracy of the circuit model drops to some extent. Nevertheless, the first-neighbor approximation is still valid for the purpose of the study. It is also important to point out that inter-resonator coupling splits the fundamental resonance frequency, so that the number of transmission zeros equals the number of resonators (without coupling there would be a single resonance frequency). As is well known, the stronger the coupling, the stronger the frequency splitting [13]. Accordingly, the stopband bandwidth broadens with inter-resonator coupling, this enhancement being limited.

Next, the dispersion characteristics of these resonator-loaded lines are obtained from Bloch mode theory applied to the four-port networks. The currents and voltages at both sides of the networks are linked through an order-4 transmission ($ABCD$) matrix, as is typically performed in two-port networks [25]. To derive the dispersion relation, we assume a complex propagation constant, $\gamma = \alpha + j\beta$. For reciprocal, lossless, and symmetric

networks, the two[6] modal solutions for the complex propagation constant can be easily found [26]. The results show that in the first allowed band, there is a region with bi-valued propagation constant (i.e. with multimode propagation): one forward (where the propagation constant is purely imaginary and positive) corresponding to transmission-line type propagation and the other backward (the propagation constant being purely imaginary and negative) related to MIWs (in SRR-based lines) or EIWs (in CSRR-based lines). Then, a region with a pair of complex modes appears ($\gamma = \alpha \pm j\beta$)[7], followed by a region of evanescent waves (where the propagation constants are purely real). Finally, a forward wave transmission band emerges again. The results obtained from Bloch mode theory are therefore in good agreement with those reported by Syms and Solymar [17]. Since complex modes do not carry net power, the frequency band supporting such modes is a rejection band. Therefore, complex modes contribute to stopband broadening in SRR- and CSRR-loaded lines with coupled resonators.[8] It is apparent that the stopband characteristics in the complex wave region can be interpreted as a result of the destructive interference of antiparallel forward transmission line propagation and backward MIWs or EIWs. Note that the behavior of SRR- and CSRR-loaded lines with coupled resonators is very similar to each other. The meaningful difference is the nature of the backward waves, which belong to MIWs or EIWs in SRR- and CSRR-loaded lines, respectively.

We also obtain the modal solutions (only the phase constant) of an infinite periodic structure composed of a cascade connection of the two corresponding SRR- and CSRR-based unit cells by means of the full-wave eigenmode solver of *CST Microwave Studio*. There is good agreement with the theoretical analytical dispersion curves predicted by the circuit models. For comparison purposes, we also consider a structure with higher inter-resonator distance providing a much weaker coupling. The dispersion diagram reveals that the resulting stopband bandwidth is significantly narrower. It is thus noticed that most of the stopband in the considered structures is related to the presence of complex, rather than evanescent,

[6] There are actually four mathematical solutions corresponding to the complete set of forward- and backward-traveling waves. For convention, we assume the solutions associated to positive group velocity, which represent power flow in the reference direction.

[7] The dispersion relation of a circuit that is formally the same as that corresponding to CSRR-loaded lines is obtained from a four-port impedance matrix by Tsai and Wu [27], but the appearance of complex modes is not reported.

[8] Analogously, in **article AWPL12** we also conclude that in composite right/left handed (CRLH) structures based on transmission lines loaded with CSRRs and series gaps (Subsection 2.2.3), the left-handed passband broadens as inter-resonator coupling increases. The reason is a constructive interference between EIWs and the backward wave propagation of the CRLH structure. Prior circuit modeling of these structures without applying Bloch mode theory was presented by Gil *et al.* [28].

modes. Therefore, as long as inter-resonator coupling is significant, complex modes may be the dominant mechanism of signal rejection.

Finally, to experimentally confirm the effects of inter-resonator coupling on bandwidth enhancement, we measure the frequency response of two order-9 structures; one with nearby resonators (providing a strong coupling), and another one with distant resonators (achieving a weak coupling). For the SRR-loaded CPWs, the measured fractional stopband bandwidth at -20 dB is 5.2% and 2.4% for close and distant resonators, respectively. For the CSRR-loaded microstrip lines, these values are 9.4% and 6.2%. The measured stopbands are also in accordance with those obtained from the dispersion relation.

3.3 Limits on the Synthesis of Electrically Small Resonators

In microwave engineering, the *synthesis* of resonators concerns the design of a particular physical topology providing a certain inductance and capacitance, usually prescribed by design specifications (e.g. to widen the rejection bandwidth of a bandstop filter). Frequently, practical limitations exist when synthesizing resonators, that is, for a particular resonance frequency, it is not possible to achieve any arbitrary combination of inductance and capacitance. Analytical models can be derived in order to find the inductance and capacitance of a given resonator topology. For example, analytical values of the inductance and capacitance of SRRs and CSRRs have been reported in the literature [1, 2, 6]. However, these analytical expressions do not give information about the electrical length of the resonators, and this is indeed of paramount importance for modeling the resonant elements as lumped LC circuits.

Particularly, this section analyzes the limits on the implementable values of stepped-impedance shunt-stubs (SISSs). Since these resonators are implemented through microstrip lines, and there are available well-established expressions for microstrip technology, the electrical size of the resonator may be determined. This analysis highlights the well-known practical limitations when synthesizing resonators, and is useful for the design of microwave components based on SISSs. For instance, the reported results have been used for the automatic synthesis of SISSs through aggressive space mapping (ASM) [29, 30] ([30] corresponds to **conference C5**). In this thesis, SISS-loaded lines will be further analyzed in Subsections 4.4.1 and 6.7.1 (**conference article IMS14**).

3.3.1 Microstrip Lines loaded with shunt-connected SIRs (SISSs)

There are many different topologies and feedings of stepped-impedance resonators (SIRs), originally proposed by Makimoto and Yamashita [31]. In Subsection 2.3.3 we introduced the folded SIR which can be excited electrically and/or magnetically. In this section, by contrast, the focus is on shunt-connected SIRs. Such SIRs can be viewed as stubs exhibiting a high-impedance section in contact with the host line, cascaded to an open-ended low-impedance section (port terminals are utilized to excite these SIRs). For this reason, these shunt-connected resonators are also referred to as stepped-impedance shunt-stubs (SISS) [32, 33].

Article MAP11 studies the implementation of shunt-connected series LC resonators by means of SISSs in microstrip technology. The aim of the work is to propose a procedure to determine the implementable inductance and capacitance values of a lumped LC resonator by means of an SISS, so that the response of the SISS accurately describe the response of the ideal LC resonator up to a given frequency (obviously beyond resonance). The implementable values, which depend on the substrate characteristics and technological constraints, are plotted in an LC plane for smart visualization.

An important parameter of an SISS is its impedance ratio (or contrast), which defines the relation between the low and high characteristic impedances of the resonator sections. From a distributed (transmission line) model, we conclude that: the higher the impedance contrast, the smaller the total electrical length of the SISS. The reduction of the resonator size is important for miniaturization, and also to be able to model it by means of a lumped element model (a series LC resonator). Therefore, if the impedance contrast is high enough, the electrical lengths of the resonator sections may attain small sizes at resonance. Accordingly, the SISS may be referred to as a semi-lumped resonator.

The allowable LC values are dictated by the limits on the minimum and maximum implementable characteristic impedances. Since it is convenient to deal with extreme characteristic impedances, we need to determine the maximum and minimum value of the characteristic impedance that can be achieved with the considered substrate and fabrication technology. The maximum achievable impedance is that corresponding to the narrowest possible line, which is subjected to the fabrication process. On the other hand, the lowest impedance limit is not given by any technological constraint, but a maximum width must be considered to avoid transverse resonances [34]. To guarantee that the SISS can be described by a lumped resonator, we impose the electrical lengths of the SISS sections to be smaller than $\pi/4$[9] up to a particular frequency

[9] A line is typically considered to be electrically short if its electrical length is smaller than $\pi/4$, but we can specify whatever arbitrary maximum permissible electrical length.

beyond the resonance frequency. Provided that the two sections of the SISS are electrically small, its distributed behavior may be approximated to that of a shunt-connected series LC resonator to a high degree. We provide accurate and simple closed-form expressions of the inductance and capacitance. Furthermore, as is well known, as a first-order approximation the inductance/capacitance of the SISS is mainly determined by the inductance/capacitance of the high/low impedance section [13].

The implementable values are hence given as a function of the frequency range of interest, the accuracy, the substrate parameters, and the fabrication technology. The higher the frequency range and the higher the accuracy, the smaller the implementable values. The study considers several commercial microwave substrates (with different thicknesses and dielectric constants) and determines the corresponding achievable lumped values. For a set of particular specifications, as the resonance frequency increases, the allowable interval of inductance and capacitance decreases dramatically, and finally collapses (there is a fundamental limit on the maximum resonance frequency, but structure scaling down is possible if necessary). The width of the capacitive line section, which must decrease to avoid the transverse resonance mode, is the responsible for this frequency limitation. Finally, the procedure is validated by some fabricated SISS-loaded microstrip lines with LC values lying inside and outside the allowable range. The transmission and reflection coefficients (in amplitude and phase) of these SISS-loaded microstrip lines are compared to those obtained by the same line loaded with the corresponding lumped resonators. As expected, highly accurate modeling is obtained when the inductance and capacitance belong to the physically implementable values. The transverse resonance mode in the SISS-based structures is clearly visible beyond the frequency range of interest.

References

[1] R. Marqués, F. Martín, and M. Sorolla, *Metamaterials with Negative Parameters: Theory, Design and Microwave Applications.* John Wiley & Sons, 2008.

[2] R. Marqués, F. Medina, and R. Rafii-El-Idrissi, "Role of bianisotropy in negative permeability and left-handed metamaterials," *Phys. Rev. B*, vol. 65, no. 144440, Apr. 2002.

[3] L. Solymar and E. Shamonina, *Waves in Metamaterials.* Oxford University Press, 2009.

[4] P. Gay-Balmaz and O. J. F. Martin, "Electromagnetic resonances in individual and coupled split-ring resonators," *J. App. Phys.*, vol. 92, no. 5, pp. 2929–2936, Sep. 2002.

[5] N. Katsarakis, T. Koschny, M. Kafesaki, E. Economou, and C. Soukoulis, "Electric coupling to the magnetic resonance of split ring resonators," *App. Phys. Lett.*, vol. 84, no. 15, pp. 2943–2945, Apr. 2004.

[6] J. D. Baena, J. Bonache, F. Martín, R. M. Sillero, F. Falcone, T. Lopetegi, M. A. G. Laso, J. García-García, I. Gil, M. F. Portillo, and M. Sorolla, "Equivalent-circuit models for split-ring resonators and complementary split-ring resonators coupled to planar transmission lines," *IEEE Trans. Microw. Theory Tech.*, vol. 53, no. 4, pp. 1451–1461, Apr. 2005.

[7] F. Martín, J. Bonache, F. Falcone, M. Sorolla, and R. Marqués, "Split ring resonator-based left-handed coplanar waveguide," *App. Phys. Lett.*, vol. 83, no. 22, pp. 4652–4654, Dec. 2003.

[8] F. Martín, F. Falcone, J. Bonache, R. Marqués, and M. Sorolla, "Miniaturized coplanar waveguide stop band filters based on multiple tuned split ring resonators," *IEEE Microw. Wireless Compon. Lett.*, vol. 13, no. 12, pp. 511–513, Dec. 2003.

[9] F. Aznar, J. Bonache, and F. Martín, "Improved circuit model for left-handed lines loaded with split ring resonators," *App. Phys. Lett.*, vol. 92, no. 043512, Feb. 2008.

[10] F. Aznar, M. Gil, J. Bonache, L. Jelinek, J. D. Baena, R. Marqués, and F. Martín, "Characterization of miniaturized metamaterial resonators coupled to planar transmission lines through parameter extraction," *J. App. Phys.*, vol. 104, no. 114501, Dec. 2008.

[11] J. Bonache, M. Gil, I. Gil, J. García-García, and F. Martín, "On the electrical characteristics of complementary metamaterial resonators," *IEEE Microw. Wireless Compon. Lett.*, vol. 16, no. 10, pp. 543–545, Oct. 2006.

[12] R. Marqués, J. Baena, J. Martel, F. Medina, F. Falcone, M. Sorolla, and F. Martín, "Novel small resonant electromagnetic particles for metamaterial and filter design," in *Proc. Int. Conf. Electromagnetics Advanced Application (ICEAA '03)*, Torino, Italy, Sep. 2003, pp. 439–442.

[13] J.-S. Hong and M. J. Lancaster, *Microstrip Filters for RF/Microwave Applications*. John Wiley & Sons, 2001.

[14] F. Hesmer, E. Tatartschuk, O. Zhuromskyy, A. A. Radkovskaya, M. Shamonin, T. Hao, C. J. Stevens, G. Faulkner, D. J. Edwards, and E. Shamonina, "Coupling mechanisms for split ring resonators: Theory and experiment," *Phys. Status Solidi B*, vol. 244, no. 4, pp. 1170–1175, Mar. 2007.

[15] E. Tatartschuk, N. Gneiding, F. Hesmer, A. Radkovskaya, and E. Shamonina, "Mapping inter-element coupling in metamaterials: Scaling down to infrared," *J. App. Phys.*, vol. 111, no. 094904, May 2012.

[16] R. R. Syms, E. Shamonina, V. Kalinin, and L. Solymar, "A theory of metamaterials based on periodically loaded transmission lines: Interaction between magnetoinductive and electromagnetic waves," *J. App. Phys.*, vol. 97, no. 064909, Mar. 2005.

[17] R. R. A. Syms and L. Solymar, "Effective permeability of a metamaterial: Against conventional wisdom," *App. Phys. Lett.*, vol. 100, no. 124103, Mar. 2012.

[18] M. Mrozowski and J. Mazur, "Matrix theory approach to complex waves [in shielded lossless guides]," *IEEE Trans. Microw. Theory Tech.*, vol. 40, no. 4, pp. 781–785, Apr. 1992.

[19] T. Tamir and A. Oliner, "Guided complex waves," *Proc. Inst. Elect. Eng.*, vol. 110, no. 2, pp. 310–334, Feb. 1963.

[20] W.-X. Huang and T. Itoh, "Complex modes in lossless shielded microstrip lines," *IEEE Trans. Microw. Theory Tech.*, vol. 36, no. 1, pp. 163–165, Jan 1988.

[21] M. J. Freire, F. Mesa, and M. Horno, "Excitation of complex and backward mode on shielded lossless printed lines," *IEEE Trans. Microw. Theory Tech.*, vol. 47, no. 7, pp. 1098–1105, Jul. 1999.

[22] F. Elek and G. Eleftheriades, "Dispersion analysis of the shielded sievenpiper structure using multiconductor transmission-line theory," *IEEE Microw. Wireless Compon. Lett.*, vol. 14, no. 9, pp. 434–436, Sep. 2004.

[23] R. Islam and G. Eleftheriades, "On the independence of the excitation of complex modes in isotropic structures," *IEEE Trans. Antennas Propag.*, vol. 58, no. 5, pp. 1567–1578, May 2010.

[24] R. K. Mongia, J. Hong, P. Bhartia, and I. J. Bahl, *RF and Microwave Coupled-Line Circuits*. Artech House, 1999.

[25] D. M. Pozar, *Microwave Engineering*, 4th ed. John Wiley & Sons, 2012.

[26] R. Islam, M. Zedler, and G. Eleftheriades, "Modal analysis and wave propagation in finite 2D transmission-line metamaterials," *IEEE Trans. Antennas Propag.*, vol. 59, no. 5, pp. 1562–1570, May 2011.

[27] C.-H. Tsai and T.-L. Wu, "A broadband and miniaturized common-mode filter for gigahertz differential signals based on negative-permittivity metamaterials," *IEEE Trans. Microw. Theory Tech.*, vol. 58, no. 1, pp. 195–202, Jan. 2010.

[28] I. Gil, J. Bonache, M. Gil, J. García-García, F. Martín, and R. Marqués, "Accurate circuit analysis of resonant-type left handed transmission lines with inter-resonator coupling," *J. App. Phys.*, no. 074908, Oct. 2006.

[29] J. Selga, "Synthesis of microwave circuits based on metamaterials using aggressive space mapping algorithms," Ph.D. dissertation, Universitat Autònoma de Barcelona, Oct. 2013.

[30] J. Selga, J. Naqui, M. Durán-Sindreu, F. Martín, A. Rodríguez, and V. Boria, "Application of aggressive space mapping (ASM) to the efficient synthesis of stepped impedance resonators (SIRs)," in *Europ. Microw. Conf. (EuMC)*, Nuremberg, Germany, Oct. 2013, pp. 636–639.

[31] M. Makimoto and S. Yamashita, "Compact bandpass filters using stepped impedance resonators," *Proc. IEEE*, vol. 67, no. 1, pp. 16–19, Jan. 1979.

[32] J.-K. Lee, D.-H. Lee, and Y.-S. Kim, "A compact low-pass filter with double-step impedance shunt stub and defected ground structure for wideband rejection," *Microw. Opt. Technol. Lett.*, vol. 52, no. 1, pp. 132–134, Nov. 2010.

[33] J. Park, J.-P. Kim, and S. Nam, "Design of a novel harmonic-suppressed microstrip low-pass filter," *IEEE Microw. Wireless Compon. Lett.*, vol. 17, no. 6, pp. 424–426, Jun. 2007.

[34] T. C. Edwards and M. B. Steer, *Foundations of Interconnect and Microstrip Design*. John Wiley & Sons, 2000.

Chapter 4

On the Symmetry Properties of Resonator-loaded Transmission Lines

This chapter is focused on the symmetry properties of transmission lines loaded with electrically small resonators. The transmission characteristics of these structures are derived from theoretical concepts in terms of symmetry. By breaking symmetry, controllability in the signal transmission is obtained. Two different approaches are considered which achieve different transmission controllability, depending on whether the line is loaded with single or pairs of resonators (per-unit-cell). In the former, symmetric transmission lines are loaded with single symmetric resonators. Since no other reactive elements (neither inductances nor capacitances) are loaded to the line, one should expect to obtain stopband responses (Subsection 2.2.4). However, it may be obtained not only stopband responses, but also all-pass responses. As will be shown, this can be achieved by inhibiting resonance. In the latter, symmetric transmission lines are loaded with pairs of identical resonators. In these structures resonance always occurs, but controllability in the frequency of the resonances is performed.

The organization of this chapter is as follows. Section 4.1 describes some typical transmission lines used throughout this thesis, with special emphasis on the symmetry properties of the fundamental propagation modes. Specifically, microstrip lines, coupled microstrip lines, and coplanar waveguides are considered. Electrically small resonators are beyond the scope of this chapter because they were already introduced in Section 2.3. Sections 4.2 and 4.3 are devoted to the particular case of alignment and misalignment of symmetry planes in the former approach, respectively. Finally, Section 4.4 generalizes the behavior of the two considered approaches as a function of symmetry properties.

4.1 On the Symmetry Properties of Transmission Lines

Figure 4.1 shows the three symmetric transmission lines that are utilized throughout this thesis: microstrip lines, pairs of coupled microstrip lines, and coplanar waveguides (CPWs). Microstrip lines are two-conductor transmission lines that support a single fundamental mode of propagation, whereas coupled microstrip lines and CPWs are three-conductor transmission lines allowing for the propagation of two fundamental modes, namely, the *even mode* and the *odd mode*. Since part of the electromagnetic fields extends into the air beyond the substrate, the considered transmission lines are inhomogeneous propagating structures. However, the propagation modes supported by these lines are of quasi-TEM (transverse electromagnetic) nature, and are characterized by their characteristic impedance and propagation constant. Therefore, the electric and magnetic fields are transverse to the direction of propagation (to a considerably extent), the distribution of fields being sketched in Figure 4.1. As can be seen, in a microstrip line, there is a virtual magnetic wall at its symmetry plane. In coupled microstrip lines and CPWs, the symmetry plane behaves as a virtual electric or magnetic wall for the odd- and even-mode, respectively (in an/a electric/magnetic wall, the electric/magnetic field lines are normal to the corresponding plane since the tangential components vanish [1]).

When a network is symmetric, it is convenient to bisect it into two identical halves with respect to its symmetry plane, because the analysis of N-port networks is reduced to that of $N/2$-port networks using the *even/odd-mode analysis* [1–3]. Even and odd excitations apply in-phase and anti-phase signals, respectively. When an odd excitation is applied to a network, the symmetry plane is short-circuited, and the two halves become the same two-port network, namely, the odd-mode network. In a similar fashion, under an even excitation, the symmetry plane is open-circuited and the two halves become the two-port even-mode network. Therefore, in symmetric structures based on coupled microstrip lines and CPWs, we can restrict the analysis to a half of the structure. Thereby equivalent circuit models for the even and odd-mode can be derived.

In CPWs, the even- and odd-mode are also referred to as the *CPW mode* and the *slot* (or *slotline*) *mode*, respectively. Typically, the even mode of the CPW is excited by feeding the central strip and grounding the lateral planes, whereas the odd mode is a parasitic mode.[1] In symmetric CPWs, the propagation of the even- and odd-mode is independent (any arbitrary excitation can be treated as a superposition of the even- and

[1] Coupled microstrip lines, coplanar strips (CPS), or slotlines are preferred to be fed by odd-mode sources [4, 5].

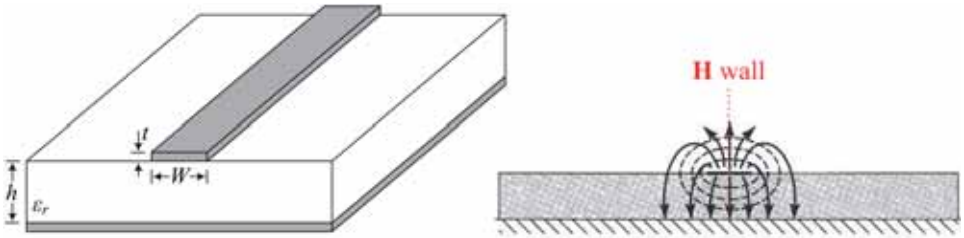

(a) Microstrip line. The field distribution is extracted from [1].

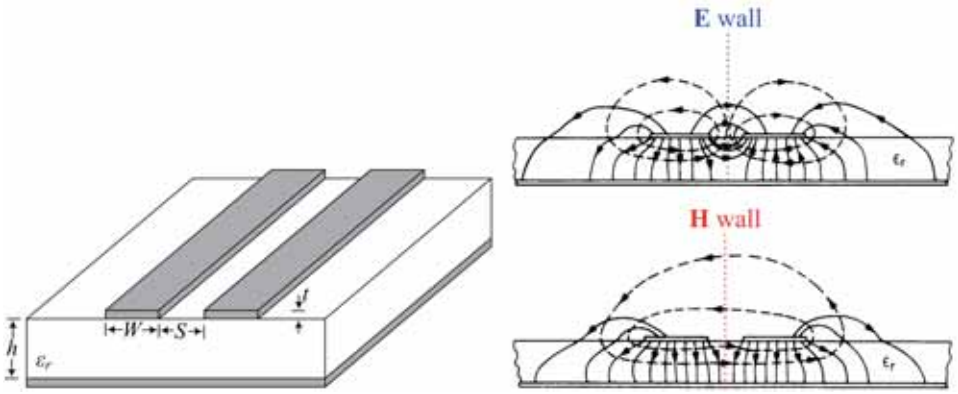

(b) Coupled microstrip lines. The field distributions of the odd- (top) and even-mode (bottom) are extracted from [3].

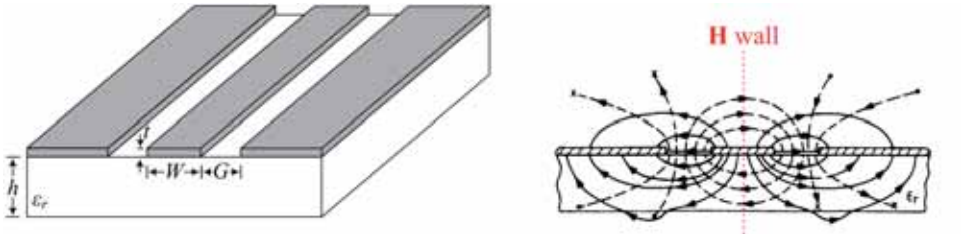

(c) Coplanar waveguide. The even-mode field distribution is extracted from [4]. The field distribution of the parasitic odd-mode is not shown.

FIGURE 4.1: Geometry, and electric (solid lines) and magnetic (dashed lines) field distributions in planar transmission lines. The boundary condition (electric or magnetic wall) at the symmetry plane is indicated.

odd-mode [6]), and power conversion from one mode to another does not arise. Therefore, an even-mode excitation cannot generate an odd-mode signal along the structure (and vice versa). However, when a CPW-based structure is asymmetric, the two fundamental modes are coupled to each other, and energy is continuously exchanged between the coupled modes (i.e. there is *mode conversion*) [4]. From an even-mode source applied to a

CPW, the parasitic slot mode may be excited by coupling power from the desired CPW mode. A common procedure to suppress the slot mode in CPWs consists of introducing air bridges to short circuit the ground planes in a transversal plane [7]. In printed circuit board (PCB) technology, via-holes in the substrate and strips etched on the back substrate side are usually used to connect the ground planes. Analogously, in a symmetric pair of coupled microstrip lines, the even- and odd-mode are also independent to each other. Conversely, when the pair of coupled lines is asymmetric, the mode conversion phenomenon may occur. Coupled microstrip lines are useful for the design of differential microstrip lines. In contrast to CPWs, in differential circuits based on coupled microstrip lines, the undesired mode is the even mode. In this context, the odd- and even-mode are often referred to as the *differential-* and *common-mode* (Chapter 5).

Finally, it is also worth discussing about the main advantages of the considered transmission lines [4, 7, 8]. The advantage of microstrip technology over CPWs is the presence of the ground plane in the back side of the substrate, which effectively isolates the structure preventing from possible interferences.[2] An advantage of single microstrip lines is that conversion between fundamental modes is not possible. With regard to the advantages of CPWs against microstrip lines, CPWs need only a single metallic layer and their characteristic impedance does not univocally determine the transverse dimensions (W and G) providing design flexibility.

4.2 On the Alignment of Symmetry Planes

Let us consider a symmetric transmission line loaded with a single symmetric resonator. Typically, when a transmission line is loaded with a resonator coupled to it, the transmission coefficient exhibits a stopband (a transmission zero or notch) at the fundamental resonance frequency. Suppression of the signal transmission occurs because the injected power is reflected back to the source. However, it is possible to prevent resonance and the appearance of the associated notch in the transmission coefficient. The principle of operation behind the absence or presence of resonance[3] is based on the alignment of the symmetry planes of the line and the resonator as follows. *Assume that the symmetry plane of the resonator* (Section 2.3) *is perfectly aligned with the symmetry plane of the*

[2] CPWs with backside metalization are known as conductor-backed CPWs (CB-CPWs), but the inclusion of the metalization may give rise to parasitic modes [4].

[3] Although the fundamental resonance as well as higher-order resonances may be prevented, this thesis is focused on the fundamental resonance only.

transmission line (Section 4.1), *so that the structure is perfectly symmetric with regard to its midplane.*

(*a*) *If the two symmetry planes are of the same sort* (both exhibiting electric or magnetic walls), *the resonator is excited as often. The structure is resonant and signal transmission is suppressed in the vicinity of the resonance frequency, resulting in a stopband response* ($S_{21} \approx 0$). *The resonator may be electrically, magnetically, or magnetoelectrically coupled to the line.*

(*b*) *If the two symmetry planes are of different sort* (one being a magnetic wall and the other one an electric wall), *the resonator cannot be excited. Because of perfect symmetry, the net electric and magnetic field components illuminating the resonator exactly cancel (the electric and magnetic fluxes in the resonator area are zero). Therefore, the resonance condition is inhibited because it cannot be established by neither electric nor magnetic coupling. Accordingly, the whole structure behaves like a transmission line exhibiting an all-pass response* ($S_{21} \approx 1$).[4]

It should be pointed out that the above-mentioned behavior holds regardless of the physical topologies of the transmission line and the resonator, and the line-to-resonator coupling mechanism (electric and/or magnetic). To clarify the previous assertions related to the resonance prevention, consider as an illustrative example a microstrip line (see Figure 4.2). Such a transmission line exhibits a propagation mode with a magnetic wall at the symmetry plane. If we align with such a line a resonator that exhibits a magnetic wall at resonance, the resonator will be excited. On the contrary, in the case where there is an electric wall at the symmetry plane of the resonator, it will not resonate.

Now assume bimodal symmetric transmission lines such as differential microstrip lines and coplanar waveguides. These lines support the propagation of the even- and odd-mode which exhibit walls of different nature (magnetic and electric walls, respectively). In the presence of a resonator symmetrically loaded to these lines, the electric and magnetic walls at the symmetry plane of the transmission lines are preserved for their corresponding modes. It follows that we can *selectively suppress either the even- or odd-mode while preserving the other mode unaltered (or almost unaltered) by aligning a resonator with a magnetic wall or an*

[4] Obviously, the resonator may change the electrical parameters (i.e. the characteristic impedance and the phase constant) of the resulting propagative transmission line-type structure. In other words, the resonator may actually influence the transmission line parameters due to line-to-resonator coupling. However, since the resonance is effectively prevented, line-to-resonator coupling is sometimes said to be canceled throughout this thesis.

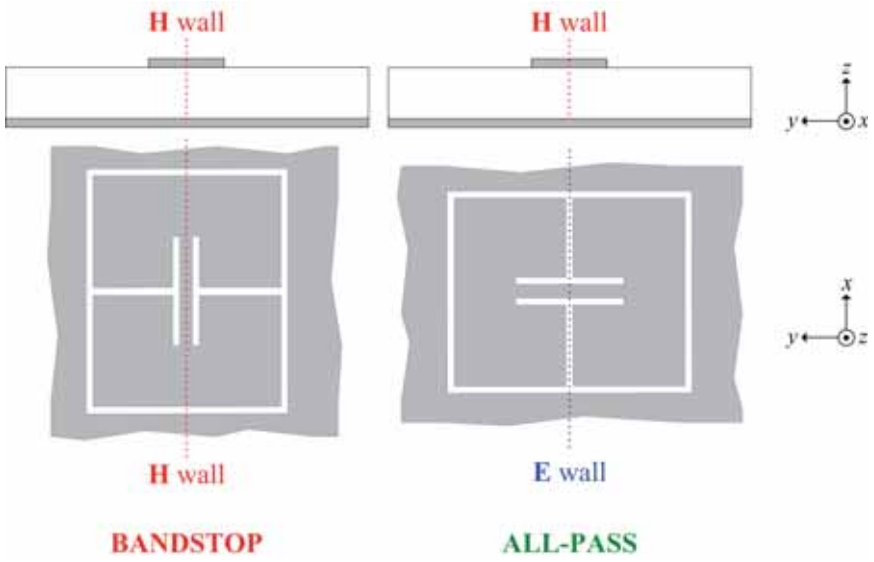

FIGURE 4.2: Illustration of how resonance can be prevented. A microstrip line loaded with a magnetic inductive-capacitive (MLC) resonator in the ground plane is considered.

electric wall, respectively. This selective mode suppression is illustrated in Figure 4.3. To the author's knowledge, the alignment of the symmetry plane of a resonator to that of a transmission line was applied for the first time in the frame of differential lines with common mode suppression [9]. Indeed, in this thesis the alignment of symmetry planes is mainly exploited to designing common-mode suppressed differential microstrip lines (Chapter 5). However, we have also validated the selective mode suppression in coplanar waveguides. Next subsections are devoted to the considered implementations for achieving a selective mode suppression. Interestingly, since the structures are symmetric, the even/odd-mode analysis can be applied, and equivalent circuit models for even- and odd-mode excitations can be obtained.

4.2.1 SRR- and CSRR-loaded Differential Microstrip Lines

Either the odd- or even-mode in differential microstrip lines can be selectively rejected using split-ring resonators (SRRs) or complementary split-ring resonators (CSRRs), respectively. The resonators are symmetrically loaded BY etching the SRRs between the pair of microstrip lines and the CSRRs in the ground plane. The possibility of rejecting the common mode while preserving the differential mode is of general interest in differential lines and circuits. The selective mode suppression in CSRR-loaded differential microstrip lines is analyzed for the first time in **conference article IMS11**. Subsequently, a comprehensive analysis was

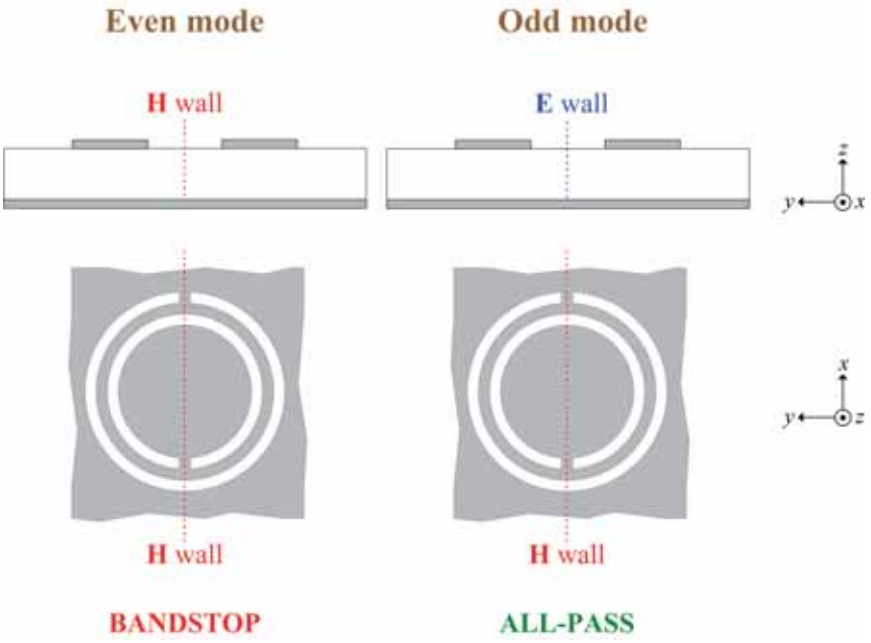

FIGURE 4.3: Illustration of a selective mode suppression. A differential microstrip line loaded with a complementary split-ring resonator (CSRR) in the ground plane is considered.

carried out in an extended work presented in **article TMTT12**.[5] Therein, the double-slit complementary split-ring resonator (DS-CSRR) particle is also considered as an alternative to the CSRR to enhance the rejection bandwidth. An equivalent circuit model for the whole structure is proposed, and the circuits derived from even- and odd-mode excitations are also obtained. The resulting circuit for the odd mode is that of a conventional transmission line (with an all-pass response), while the circuit for the even mode is equivalent to that of a CSRR-loaded microstrip line (with a stopband response). In spite of the fact that for the considered symmetric CSRR-loaded differential lines there is line-to-resonator magnetoelectric coupling, mixed coupling is neglected (the DS-CSRR does not suffer from cross-polarization effects). This simplification eases the design of common-mode suppressed differential lines (Chapter 5).

4.2.2 ELC- and MLC-loaded Differential Microstrip Lines

The selective mode suppression in differential lines has also been validated by means of ELC (electric inductive-capacitive) and MLC (magnetic inductive-capacitive) resonators, the results being reported in

[5] In **conference C14**, the selective mode suppression using CSRRs as well as SRRs is demonstrated.

article APA13. As in SRR- and CSRR-loaded differential lines, the ELC and MLC resonators are symmetrically placed between the microstrip lines and in the ground plane, respectively. These resonators are bisymmetric and exhibit orthogonally oriented magnetic and electric walls. Therefore, the odd- and even-mode can be selectively suppressed by loading the lines with either ELC or MLC resonators (four different topological combinations are possible, two with even-mode suppression and the other two with odd-mode rejection). It is shown that by rotating the resonators 90° we can selectively choose the suppressed mode in the vicinity of the fundamental resonance frequency. The circuit models of ELC- and MLC-loaded differential lines with even- and odd-mode suppression are formally the same as SRR-loaded coplanar waveguides and CSRR-loaded microstrip lines without mixed coupling (Subsection 2.2.4), respectively. Note that the considered particles are designated as electric- or magnetic-coupled LC resonators, in reference to the fact that they can be excited only by either electric or magnetic fields when the fields are uniform (Section 2.3). However, in the considered structures, the ELC and MLC resonators are excited by non-uniform magnetic and electric fields, respectively. By contrast, MLC- and ELC-loaded differential lines for even- and odd-mode suppression suffer from magnetoelectric coupling, which is taken into account in the equivalent circuits. It should be highlighted that due to the bisymmetry of the resonators, all the four configurations and their corresponding circuits are also symmetric with regard to the ports (i.e. the reflection coefficients are identical) .[6] Theory is experimentally validated by means of a balanced bandstop filter composed of three cascaded MLCs (as mentioned before, the reported equivalent circuit model of an MLC-loaded differential microstrip line for the odd mode is formally equivalent to that of a CSRR-loaded microstrip line).

4.2.3 SRR- and CSRR-loaded Coplanar Waveguides

Coplanar waveguides symmetrically loaded with SRRs or CSRRs are analyzed in **article APA12**. The SRRs are loaded on the back side of the substrate, whereas the CSRRs are etched in the CPW central strip. Symmetric loading is merely achieved by aligning the cuts of the rings with the line axis. It is demonstrated that CPWs loaded with single (per-unit-cell) symmetrically loaded SRRs are transparent to signal propagation for the even mode, whereas they inhibit the odd mode in the vicinity of resonance (equivalently to classical CPWs loaded with pairs of

[6] Symmetry with regard to both the midplane and the ports cannot be satisfied with resonators with a single symmetry plane.

SRRs).[7] By contrast, CSRR-loaded CPWs are transparent for the slot mode, and opaque for the CPW mode in the vicinity of CSRR resonance (similar to CSRR-loaded microstrip lines). Due to the line-to-resonator orientation, mixed magnetoelectric coupling is present for the modes that are able to excite the resonators. We provide and validate equivalent circuit models with magnetoelectric coupling of SRR- and CSRR-loaded CPWs, including the resulting equivalent circuits for even- and odd-mode excitations. The selective suppression of either the CPW (even) or the slot (odd) mode in CPWs using CSRRs and SRRs, respectively, is also supported by experimental results.

It is worth mentioning that a potential application of the selective mode suppression in CPWs might be the rejection of the parasitic slot mode that appears in certain applications (namely, where a CPW-based structure is non-symmetric). In this thesis the potentiality of the slot-mode suppression by means of symmetric resonators has not been deeply investigated. However, it seems difficult to improve the performance of air bridges, the standard solution to cancel the slot mode. Air bridges are very efficient structures for broadband slot-mode suppression, the CPW mode being practically unaltered. For this reason, air bridges are used throughout this thesis to cancel the slot mode where asymmetric CPW-based structures are designed.

4.3 On the Misalignment of Symmetry Planes

This section extends the analysis of the resonator excitation explained in Section 4.2 to any resonator orientation. Therefore, it is also considered that the resonator can be misaligned with the line. *Assume that a symmetric transmission line is loaded with a symmetric resonator* (see Figure 4.4).

(a) *If the two symmetry planes are aligned, there are two complementary situations* (as explained in Section 4.2):

  (i) *if the symmetry planes are of the same nature, resonance is established, and there is signal suppression in the vicinity of the resonance frequency* ($S_{21} \approx 0$).

  (ii) *if the symmetry planes are of distinct nature, resonance is inhibited, and there is not signal suppression* ($S_{21} \approx 1$).

(b) *If the symmetry planes are not aligned, resonance occurs regardless of the nature of the symmetry planes, and signal transmission*

[7] Typical CPWs loaded with pairs of SRRs inhibit the CPW (even) mode in the vicinity of the resonance frequency of the SRRs (Subsection 2.2.4). Unlike such typical SRR-loaded CPWs where the SRRs are etched below the slots, the considered SRR-loaded CPWs are loaded with single SRRs below the CPW central strip.

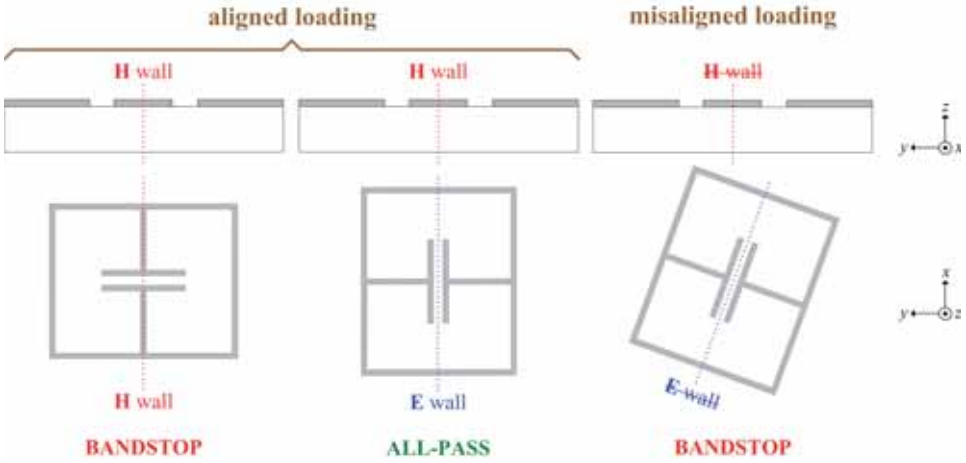

FIGURE 4.4: Illustration of the suppression modulation by alignment/misalignment of the symmetry planes. A CPW loaded with an ELC resonator and excited by an even mode is considered. The stopband characteristics may be modulated by rotating the resonator. For misaligned loadings, the magnetic wall at the symmetry plane of the line is altered.

> *suppression in the form of a notch arises. The reason is that there cannot be a perfect cancellation of the electromagnetic field components illuminating the resonator, which can be excited electrically and/or magnetically.* Interestingly, *the stopband characteristics (frequency, bandwidth, and/or magnitude) are modulated by the line-to-resonator coupling strength, which in turn is determined by the degree of misalignment* $(0 < S_{21} < 1)$.

Therefore, the transmission characteristics of transmission lines loaded with symmetric resonators can be controlled by the orientation of the resonator with regard to the line. In order to model different orientations, equivalent circuit models with variable parameters depending on the resonator position are required. Consequently, any change in the resonator position should be modeled by adjusting the appropriate circuit parameters. Obviously, when the symmetry planes are misaligned there is neither an electric wall nor a magnetic wall at the line axis, and the even/odd-mode analysis cannot be applied. It is also important to mention that to model the notch magnitude, lossy equivalent circuit models are necessary. Otherwise, $S_{21} = 0$ in the absence of losses. In this thesis, losses in an equivalent circuit model are evaluated in **article TMTT13**.

Any misalignment can be straightforwardly accounted for by relative linear (through a straight line) and/or angular (rotation) displacements between the line and the resonator. The misalignment of symmetry planes was proposed as a novel sensing mechanism (of alignment and displacements) for the first time in **article S11**. In this thesis, the

misalignment of symmetry planes has not only been used as a sensing mechanism, but also as an encoding mechanism. The design of microwave sensors and radio-frequency (RF) barcodes by that means is addressed in Chapters 6 and 7, respectively. Next subsections present the results for the considered resonator-loaded transmission lines where the resonator is both aligned and misaligned with the line. As will be shown, the modulation (controllability) of the suppression in terms of alignment/misalignment is validated by variable electric or magnetic line-to-resonator coupling.

4.3.1 SRR- and Folded SIR-loaded Coplanar Waveguides

Article S11 reports for the first time the validation of the suppression modulation by means of misalignments. An SRR is etched on the back side of the substrate in a CPW and different resonator orientations are considered by laterally displacing or rotating the resonator from the aligned configuration. As expected, the more displacement, the stronger the notch (obviously, up to a certain displacement). Because of the resonator orientation, magnetoelectric line-to-resonator coupling is present. In this seminal work, however, an equivalent circuit model is not presented. It is important to highlight that thin substrates are considered to enhance line-to-resonator coupling. Thereby smaller misalignments can be detected. As a result, the coupling between the two split rings forming the SRR is seen to be limited at the expense of an increase in the coupling between the rings and the CPW (the substrate thickness is smaller than the inter-ring separation). In consequence, the SRR fundamental resonance frequency is identical to the one obtained with the larger ring in the absence of the smaller one. Therefore, the SRR structure does not behave as a pair of coupled ring resonators (Subsection 2.3.1), and we cannot take advantage of its supposedly electrically small size. For such a reason, we can indistinguishably use single split-ring resonators, as demonstrated in **article S12**.

As an alternative proposal to the SRR and the single split-ring resonator, **conference article IMS12** investigates in depth CPWs loaded with folded stepped-impedance resonators (SIRs) in terms of alignment/misalignment. Like in SRR-based CPWs, there are mixed coupling effects. However, since the considered substrate is thin, by designing the open-ended sections of the SIRs with a wide width, high line-to-resonator electric coupling may be obtained. An equivalent circuit model neglecting the magnetic coupling is presented. As is demonstrated, this simplified model suffices to accurately describe the transmission coefficient magnitude (with the exception of the notch depth, since the circuit model is assumed to be lossless). In such an equivalent circuit, the electric coupling is modeled by capacitances that depend on the relative position of the resonator. The results agree with the theory behind the alignment/misalignment of symmetry planes.

It is worth pointing out that in **conference article IMS12** we also compare CPWs loaded with either SRRs or SIRs (with the same area). The results indicate that lower notch frequencies are obtained using SIRs. As mentioned before, the inter-ring coupling in SRRs is limited to a considerably extent, preventing from their quasi-static resonance. By contrast, very low resonance frequencies may be obtained utilizing SIRs due to the high achievable electric coupling. Accordingly, for thin substrates, SIR-loaded CPWs are electrically smaller than those based on SRRs. Moreover, using SIRs not only smaller notch frequencies are obtained, but also wider notches. This is also attributed to the strong electric coupling in SIR-based CPWs.

4.3.2 ELC-loaded Coplanar Waveguides

In **conference article IMS13** a CPW is loaded with an ELC resonator whose axis is aligned with the line axis, and a dynamic loading with resonator rotation is considered. It is shown that the transmission coefficient of the structure depends on the angular orientation of the resonator. Since an ELC resonator exhibits two symmetry planes, one being an electric wall and the other one a magnetic wall, the resonator can symmetrically load a CPW by aligning the line axis with either its electric or magnetic wall. For the fundamental CPW mode, an ELC resonator cannot be excited if its electric wall is aligned with the line axis, and the loaded line is transparent. Conversely, the resonator is driven if its magnetic wall is aligned with that axis, and a transmission zero in the transmission coefficient appears. For intermediate (asymmetric) orientations, the resonator is also excited and the attenuation strength (notch bandwidth and depth) is dependent on the resonator orientation. Obviously, owing to the orthogonal electric and magnetic walls of the resonator, the angular orientation range is limited to 90°. The optimum orientation for the strongest attenuation is the one corresponding to perfect alignment between the ELC magnetic wall and the symmetry plane of the line. Therefore, by spatially rotating the resonator the frequency response switches from an all-pass to a stopband behavior, the latter being dependent on the angular orientation.

Article TMTT13 is an expanded work of the **conference article IMS13**. An equivalent circuit model valid for any arbitrary loading angle and very useful for design purposes is proposed. Note that despite the nomenclature to designate the resonator, in these ELC-loaded CPWs the resonator is excited by the non-uniform fields generated by the transmission line. Interestingly, the resulting line-to-resonator coupling is not electric, but magnetic. The magnetic field lines penetrating the individual loops of the resonator are in opposite directions to each other, and this makes the resonance establishment possible. The circuit model

indicates that the line-to-resonator magnetic coupling depends on the resonator angular orientation. The effect of losses on the notch that appears in the transmission coefficient is evaluated through the circuit model including losses (it is assumed that power loss is dominated by the resonator losses). While the notch magnitude of a lossless notch filter is infinite, in real circuits losses always prevent the attenuation from going to infinity. As reported, the proposed lossy equivalent circuit model explains that the notch magnitude depends not only on losses, but also on the line-to-resonator magnetic coupling that in turn depends on the rotation angle of the resonator (the notch bandwidth broadens with the magnetic coupling strength, enhancing the notch depth). Experimental data show good agreement with the theoretical concepts.

4.3.3 MLC-loaded Microstrip Lines

As compared to other slot resonators, apart from a magnetic wall, the MLC resonator exhibits an electric wall (Subsection 2.3.5). In **article IJAP13** a microstrip line is loaded with an MLC resonator etched in the ground plane. An equivalent circuit model for an isolated MLC resonator is presented. It is shown that if the electric wall of the MLC is aligned with the symmetry plane of the microstrip line, there is an all-pass response. By contrast, when the MLC is laterally displaced, a notch arises. The higher the displacement, the stronger the notch. An equivalent circuit model that explains such behavior is proposed and validated, where the MLC is electrically coupled to the line as a function of its position. The measurements are also consistent with such a theory.

4.3.4 SIR-loaded Microstrip Lines

Article IJAP14 analyses a microstrip line loaded with a SIR. Note that it is not possible to somehow symmetrically load a conventional microstrip line with a strip resonator, since three metal layers are required. It is assumed that the SIR is etched in an additional layer located above the microstrip line. The unfolded configuration of the SIR is used to avoid mixed coupling[8], although folded topologies can also be used instead. As a result, the SIR is seen to be electrically coupled to the microstrip line. Since the symmetry plane of the SIR behaves like an electric wall[9], if the SIR is aligned with the line, the structure is transparent to signal propagation. On the contrary, by rupturing symmetry through a displacement of the resonator (along the transversal direction), a notch appears. The higher the displacement, the wider and deeper the notch, and the lower the resonance frequency. The

[8] An unfolded SIR is bisymmetric and does not suffer cross-polarization effects.

[9] Although the unfolded SIR is bisymmetric, we consider only the symmetry plane with an electric wall that bisects the resonator like in the folded configuration.

reported equivalent circuit model accounts for the displacement through a variable capacitance modeling the coupling between the signal strip and the resonator, and the resonator-to-ground coupling as well. Experimental results are provided supporting the principle of operation.

4.4 On the Generalization of Symmetry Rupture

In this section we generalize the symmetry properties in transmission lines loaded with resonators, regardless of the number of (per-unit-cell) resonators and the symmetry disruption mechanism. In the previous section, we ruptured the symmetry of a transmission line loaded with a resonator by misaligning the symmetry planes of the two elements. Accordingly, the structure is symmetric or asymmetric depending on whether the resonator is aligned or not with the line, respectively. However, the lack of symmetry can be caused by other mechanisms different to the relative orientation between the line and the resonator. For instance: (a) the resonator symmetry may be topologically destroyed; (b) other elements can be included (e.g. dielectric loads); or (c) the surrounding medium can be subjected to inhomogeneities. In those cases where the symmetry rupture is not based on geometrical misalignments, the propagative characteristics of the structure should be defined in a general sense in terms of symmetry/asymmetry rather than on alignment/misalignment. *Provided that a transmission line is loaded with a resonator, and that the line may also be loaded with other inclusions* (see Figure 4.5):

(a) *if the whole structure is symmetric (for which the line and the resonator are necessarily symmetric), if the symmetry planes of the line and the resonator are of:*

  (i) *distinct nature, resonance is inhibited* ($S_{21} \approx 1$).

  (ii) *the same nature, resonance is established* ($S_{21} \approx 0$).

(b) *if the whole structure is asymmetric, resonance is allowed, the stopband characteristics being dependent on the asymmetry* ($0 < S_{21} < 1$).

Therefore, the stopband characteristics may be modulated by symmetry properties as a whole. The previous statements are valid regardless of the symmetry disruption mechanism.

Thus far, we have analyzed the symmetry properties of transmission lines loaded with a single (per-unit-cell) resonator. However, symmetry properties in transmission lines loaded with any number of resonators (in the same transversal plane to the line) can also be derived. In this thesis we consider the particular case with pairs of resonators. The generalization

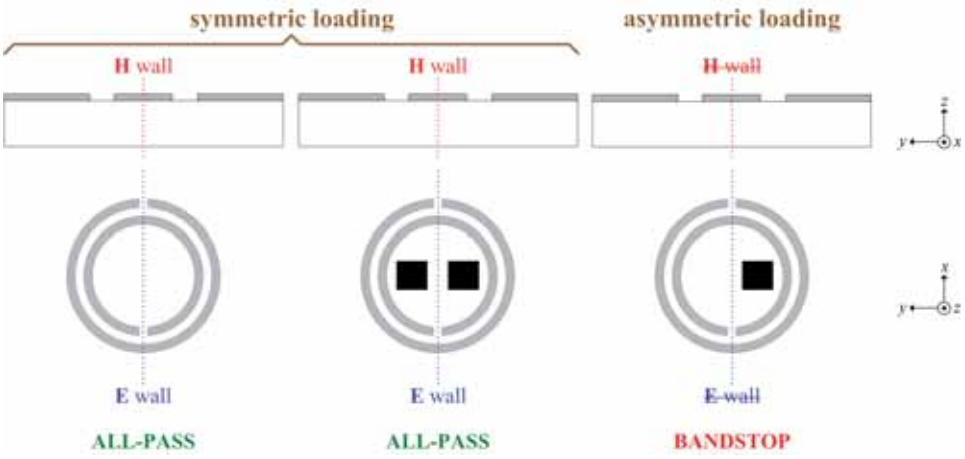

FIGURE 4.5: Illustration of symmetry rupture by square-shaped inclusions in the approach based on a single resonator. A CPW is loaded with an SRR on the back side of the substrate. For asymmetric loadings, the magnetic wall at the symmetry plane of the line is altered.

on the symmetry rupture for pairs of resonators is subjected to using identical resonators (symmetric resonators are not necessary) in order to exhibit a plane of symmetry (at the midway between the resonators).[10] Thereby the loaded line can be symmetric by aligning the plane of symmetry of the two resonators with the line. However, there is a fundamental difference as compared to using a single resonator: the two resonators cannot be simultaneously aligned with the line (we can align only one resonator). Therefore, resonance frequency cannot be inhibited in transmission lines loaded with pairs of resonators (and in the general case with more than a single resonator). In terms of absolute symmetry, *provided that a transmission line is loaded with a pair of resonators, and that the line may also be loaded with other inclusions:*

(*a*) *if the whole structure is symmetric (where the line must be symmetric and the pair of resonators must be identical and equally oriented to the line axis) there is only one transmission zero because the resonance frequencies of the two resonators degenerate to the same* ($S_{21} \approx 0$ @ f_0).

(*b*) *if the whole structure is asymmetric, there are in general*[11] *two transmission zeros because two different resonances arises* ($S_{21} \approx 0$ @ f_1, f_2).

[10] Note that this is the case for classical CPWs loaded with pairs of SRRs.

[11] An asymmetric structure based on pairs of resonators may exhibit a single transmission zero (e.g. when two resonators with the same resonance frequency are different and not coupled to each other), but this case is expected to be less convenient for practical applications.

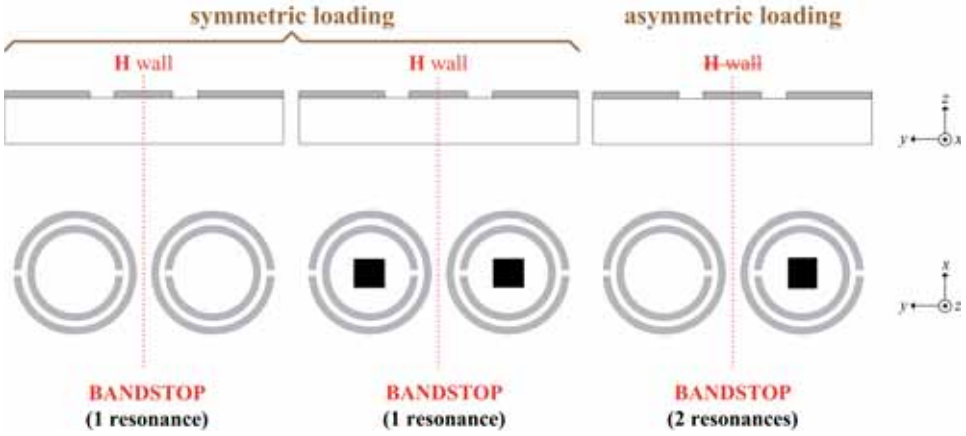

FIGURE 4.6: Illustration of symmetry rupture by square-shaped inclusions in the approach based on pairs of resonators. A CPW is loaded with a pair of SRRs on the back side of the substrate. Note that if symmetric SRRs are considered, their symmetry planes are not required to be aligned along the longitudinal x-direction. For asymmetric loadings, the magnetic wall at the symmetry plane of the line is not preserved.

Consequently, in this approach based on pairs of resonators, a high controllability in regard to the number and frequency of resonances as a function of symmetry may be achieved (the bandwidth and the depth of the notches, however, may also depend on symmetry). Figure 4.6 illustrates the above-mentioned assertions where symmetry is disrupted by inclusions. As can be seen, an interesting aspect of this approach is that, if the resonators are symmetric, they are not needed to be longitudinally aligned (this is interesting to cancel mixed coupling effects in certain topologies).

Symmetry rupture by adding inclusions to the structure may be useful for the implementation of differential sensors and comparators. With single resonators, we have only broken symmetry by misalignments (Section 4.3). Using pairs of resonators, we have explored symmetry disruption by changing the topology of the resonators or by introducing external inclusions. The corresponding results for the considered implementations are summed up in the next subsections. To the author's best knowledge, the first reported structure disrupting symmetry by means of different dimensions of a pair of resonators was used as a sensing device for displacements by Horestani *et al.* [10] (**journal J1**). On the other hand, the first transmission line loaded with pairs of resonators whose symmetry was broken by means of inclusions was proposed as a differential sensor and comparator for dielectric measurements in **conference article IMS14** (Chapter 6). In both sensors, sensing is based on the shift of resonance frequencies.

4.4.1 Transmission Lines loaded with Pairs of SISSs

In **conference article IMS14** we investigate the behavior of a microstrip line loaded with a pair of stepped-impedance shunt-stubs (SISSs). As compared to SIRs, SISSs can be loaded to a conventional microstrip line and are excited by port terminals (directly connected to the line) rather than by electromagnetic coupling[12]. Because the two SISSs are loaded at the same junction, the resonators are close to each other, and they are seen to be magnetically coupled. Since the resonators are loaded on opposite sides to the microstrip line, the magnetic coupling is negative.

In this conference paper, firstly, symmetry is broken by changing the dimensions of the resonators. When the structure is symmetric (identical resonators), there is a single transmission zero. On the contrary, when symmetry is disrupted (different resonators), two transmission zeros appear. Interestingly, due to the inter-resonator coupling, the well-known resonance frequency shifting occurs [2]. As a result, the two resonance frequencies in the asymmetric case depend on the dimensions of the resonators as well as on the resonator-to-resonator coupling. An equivalent circuit model is proposed and validated. Measurements are also consistent with the previous theory. Secondly, a proof-of-concept demonstrator based on a symmetric pair of SISSs on conductor-backed coplanar waveguide (CB-CPW) technology is fabricated (the technology is dictated by the available experimental set-up). In this structure, symmetry is disrupted by loading a dielectric sample (a piece of glass) in one of the resonators, giving rise to the appearance of two transmission notches.

4.4.2 Coplanar Waveguides loaded with Pairs of SRRs

Conference C3 (not attached to this thesis) analyses CPWs loaded with pairs of SRRs assuming both equal and different resonators. In order to avoid mixed coupling in the line-to-resonator interaction, the slits of the SRRs are oriented along the transversal direction. Furthermore, the slits of the larger ring forming the SRRs are located on opposite sides to ensure that the dominant inter-resonator coupling is magnetic (obviously as the distance between the SRRs decreases, the inter-resonator magnetic coupling strengthens). Indeed, inter-resonator coupling is expected in CPWs loaded with pairs of SRRs, in spite of the fact that it is not usually modeled in the literature. An equivalent circuit model is presented, whose transmission zero frequencies are given by the same expressions as those obtained in microstrip lines loaded with pairs of SISSs (previous subsection). In these two quite different structures, the phenomenology associated to the effects of inter-resonator coupling is almost exactly the same. One exception is the sign of

[12] Consequently, the resonance frequency cannot be prevented in transmission lines loaded with single SISSs.

the magnetic coupling (negative in microstrip lines loaded with pairs of SISSs and positive in CPW loaded with pairs of SRRs). Another difference is the case of distinct resonators but exhibiting the same resonance frequency. In both cases, two resonance frequencies appear. However, for SRR-loaded lines there is an exceptional balance condition that nulls one of these frequencies, this being not possible in SISS-loaded lines.

References

[1] D. M. Pozar, *Microwave Engineering*, 4th ed. John Wiley & Sons, 2012.

[2] J.-S. Hong and M. J. Lancaster, *Microstrip Filters for RF/Microwave Applications*. John Wiley & Sons, 2001.

[3] R. K. Mongia, J. Hong, P. Bhartia, and I. J. Bahl, *RF and Microwave Coupled-Line Circuits*. Artech House, 1999.

[4] K. C. Gupta, R. Garg, I. J. Bahl, and P. Bhartia, *Microstrip Lines and Slotlines*. Artech house, 1996.

[5] T. C. Edwards and M. B. Steer, *Foundations of Interconnect and Microstrip Design*. John Wiley & Sons, 2000.

[6] G. D. Vendelin, A. M. Pavio, and U. L. Rohde, *Microwave Circuit Design Using Linear and Nonlinear Techniques*. John Wiley & Sons, 2005.

[7] R. N. Simons, *Coplanar Waveguide Circuits, Components, and Systems*. John Wiley & Sons, 2001.

[8] F. Martín, *Artificial Transmission Lines for RF and Microwave Applications*. John Wiley & Sons, to be published.

[9] W.-T. Liu, C.-H. Tsai, T.-W. Han, and T.-L. Wu, "An embedded common-mode suppression filter for GHz differential signals using periodic defected ground plane," *IEEE Microw. Wireless Compon. Lett.*, vol. 18, no. 4, pp. 248–250, Apr. 2008.

[10] A. K. Horestani, J. Naqui, Z. Shaterian, D. Abbott, C. Fumeaux, and F. Martín, "Two-dimensional alignment and displacement sensor based on movable broadside-coupled split ring resonators," *Sensor Actuat. A Phys.*, vol. 210, pp. 18 – 24, Apr. 2014.

Chapter 5

Application to Common-Mode Suppressed Differential Transmission Lines

The selective mode suppression inspired by the alignment of symmetry planes described in Section 4.2 can be useful for the design of microwave differential circuits and components. Specifically, differential structures with common-mode suppression can be implemented. In the present chapter, we focus on common-mode suppressed differential lines in microstrip technology. As is typically required, the proposed structures efficiently suppress the common-mode propagation, whereas the differential-mode signals are nearly unaffected by the presence of the resonators. The key aspect to suppressing the common mode whilst keeping the differential mode almost unaltered is the perfect alignment between the line and the resonator.

Section 5.1 introduces the state-of-the-art of common-mode suppressed filters. Section 5.1 briefly explains the principle of selective even/odd mode filtering. To end this chapter, in Section 5.3 we report an approach and corresponding prototypes of common-mode suppressed differential microstrip lines.

5.1 Introduction

Differential or balanced[1] circuits have been important in communication systems for more than 50 years. They have historically been used in low frequency applications, rather than in radio frequency (RF) and microwave

[1] *Balanced* line is the microwave term for *differential* [1].

systems. However, in last years, the demand for differential RF/microwave circuits has increased at a huge rate. The reason for such a trend is that differential-mode signals offer high noise immunity and low electromagnetic interference (EMI), excellent benefits for modern high-speed digital circuits and communication transceivers. Nevertheless, balanced systems commonly face the presence of the well-known common-mode noise, which can degrade the differential signal quality and produce unwanted radiated emissions as well.

For the characterization of differential circuits, the definition of the differential- and common-mode is more convenient than that of the odd- and even-mode (Section 4.1). For this reason, in microwave engineering, differential structures are usually characterized by mixed-mode scattering (S) parameters, rather than on standard S-parameters (there is a simple linear relationship between the mixed-mode and the standard single-ended S-parameters [2]). Thereby, the transmission and reflection coefficients for the differential and common modes can be obtained.

The common-mode choke is one of the most typical methods to suppress the common mode. Unfortunately, the choke works properly only at the MHz frequency range, and it does not fit today's small area requirement [3]. In this context, the design of differential lines in the GHz range able to suppress the common-mode noise while keeping the integrity of the differential signals is of great importance. The filters have the advantages of wideband suppression and low cost. For such filters, there are several specifications, typically high rejection level and broadband suppression for the common-mode noise, and low insertion loss and phase distortion for differential signals [4]. For GHz differential signals, common-mode filters based on negative permittivity structures [3] or multilayer LTCC (low temperature co-fired ceramic) [5] have been reported. These structures are compact and provide efficient common-mode rejection over wide frequency bands, but are technologically complex. There have been also presented several approaches for the design of differential lines with common-mode suppression based on defected ground structures (DGSs). Dumbbell-shaped periodic patterns etched symmetrically in the ground plane, underneath the differential lines, have been used to suppress the common mode [6]. Using U-shaped and H-shaped coupled resonators symmetrically etched in the ground plane have been also used to achieve a wide stop band for the common mode [7]. Recently, a comprehensive review of strategies for common-mode suppression has been published [10]. Apart from common-mode suppressed differential lines, balanced bandpass filters with common-mode rejection have also attracted much attention [4, 11–14] ([13] and [14] correspond to **journal J10** and **conference C9**, respectively).

5.2 Symmetry-based Selective Mode Suppression Mechanism

Bimodal symmetric transmission lines support even- and odd-mode propagation (Section 4.1). As explained in Section 4.2, we can selectively suppress either the even- or odd-mode while keeping the other mode almost unaltered by symmetrically loading these lines with a resonator that exhibits a magnetic wall or an electric wall, respectively. The rejection of the parasitic slot mode while remaining the coplanar waveguide (CPW) mode unaltered is of interest in CPW-based structures with asymmetric topologies. As was mentioned in Section 4.1, slot-mode rejection is usually and effectively achieved using air bridges to short-circuit this mode [15]. Unlike slot-mode (or odd-mode) suppression in CPWs, common-mode (or even-mode) suppression in differential microstrip lines is not so straightforward. This is the reason why this chapter is focused on the latter. For the purpose of suppressing the even mode while keeping the integrity of the odd mode, the transmission line must be aligned with a resonator that exhibits a magnetic wall at its symmetry plane. Next sections are devoted to the considered resonators for achieving common-mode suppression, while maintaining the differential mode unaffected. It is interesting to mention that the selective mode suppression by aligning resonant elements was first proposed by Liu *et al.* [6] also for common-mode suppression in differential microstrip lines

5.3 Common-mode Suppressed Differential Microstrip Lines

5.3.1 CSRR- and DS-CSRR-loaded Differential Microstrip Lines

A differential microstrip transmission line with common-mode suppression based on CSRRs is proposed and experimentally validated in **conference article IMS11**. The structure consists of a pair of parallel microstrip lines with an array of periodically etched complementary split-ring resonators (CSRRs) in the ground plane. The symmetry plane of the CSRRs, which behaves like a magnetic wall (Subsection 2.3.5), is aligned with the symmetry plane of the differential line that exhibits either a magnetic or an electric wall for the even and odd mode, respectively (Section 4.1). The behavior of the structure can be explained in terms of symmetry considerations as follows (Section 4.2). Since for the common mode there is a strong density of electric field lines in the same direction below the microstrip lines, a net axial electric field excites the CSRR producing a stopband. For the differential mode, the direction of the electric field lines

is opposite in the strips of the differential line. Since the structure is symmetric, the opposite electric field vectors in both lines exactly cancel, there is not a net axial electric field illuminating the CSRR, and resonance is prevented. Analogously, a net magnetic field results along the orthogonal direction to the CSRR symmetry plane for the common mode, but there is not a net magnetic field in that direction for the differential mode. Therefore, the CSRR cannot be excited by electric nor magnetic coupling in the differential mode, whereas there is mixed magnetoelectric effects in the line-to-resonator coupling for the common mode. Note that we cannot avoid mixed coupling due to the CSRR orientation for symmetry requirements, which is fundamental to the selective mode suppression. However, the line-to-resonator magnetic coupling is neglected for the sake of simplicity, and hence we consider only the dominant electric coupling.[2] We present an equivalent circuit model which explains that differential signals are insensitive to the presence of the CSRRs, while these resonators prevent the transmission of the common-mode in the vicinity of CSRR resonance frequency. For the odd mode, the resonator is short-circuited to ground, and the resulting model is the one of a conventional transmission line (all-pass response). For the even mode, we obtain formally the same circuit as that of a CSRR-loaded microstrip line (stopband response).

There are three main strategies to enhance the common-mode rejection bandwidth in CSRR-based structures: (a) to tune the resonance frequency of several resonators in order to cover a wide band; (b) to couple the resonators as much as possible; and (c) to enhance the bandwidth of the individual resonators (and, obviously, a combination of the previous approaches). Since the multiple tuned resonators approach is efficient but many particles are needed if narrowband resonators are used, we focus on the other two approaches (i.e. considering identical and closely spaced wideband resonators). According to the equivalent circuit model, to widen the rejection bandwidth of an individual CSRR, it is necessary to increase the line-to-resonator coupling capacitance, and to reduce the CSRR inductance and capacitance. In order to achieve a strong electric coupling between the pair of lines and the resonator, the lines must be fitted face-to-face with the CSRR inner region, and must be as wide as possible. Accordingly, weakly coupled lines are considered, since the width of the lines necessary to achieve a 50-Ω odd-mode impedance is wider. To reduce the inductance and capacitance of the CSRR, it is necessary to increase the witdh and the separation of the rings. Obviously, this results in an electrically larger CSRR (for a given transmission zero frequency) and the equivalent circuit model is no longer valid within a wide band, but the achievable rejection bandwidth is wider. As a final step, to enhance inter-resonator coupling, square-shaped CSRRs are designed. A fabricated

[2] Mixed coupling can be ignored because it is not significant for attenuation purposes.

prototype device is presented that exhibits a bandwidth for the common mode of 37% with more than 20-dB rejection. The dimensions of the slotted region of the structure are $0.43\lambda_e$ x $0.14\lambda_e$ (where λ_e is the guided wavelength at the central frequency for the even mode).

Further analysis and experimental results are reported in **article TMTT12** as an expanded work. In this article, the circuit model of the unit cell includes the electric coupling between adjacent resonators, resulting in a six-port network (such a coupling was neglected in the model presented previously in the conference article). For the even mode, we obtain the circuit of a conventional CSRR-loaded microstrip line with inter-resonator coupling. Hence, a four-port network (the same as in Subsection 3.2.1) is obtained. We analyze the dispersion relation to gain insight into the rejection bandwidth for the common mode. As was discussed in Subsection 3.2.1, the inter-resonator electric coupling widens the stopband due to the presence of complex modes. Therefore, inter-resonator coupling helps to broaden the stopband of the common mode in CSRR-loaded differential lines, but bandwidth enhancement based on CSRR-to-CSRR coupling is limited. This makes apparent the convenience of implementing common-mode rejection filters with broadband resonators, and for this reason the double-slit complementary split-ring resonator (DS-CSRR) is utilized. The DS-CSRR is bisymmetric, do not suffer from cross-polarization, and exhibits two orthogonal magnetic walls at the fundamental resonance (Subsection 2.3.5) which makes it appropriate for the selective mode suppression. We particularly align the slits of the inner rings of the DS-CSRR to the line axis. Thereby, the inter-resonator coupling is expected to be dominated by the electric field. As a result, the equivalent circuit model of differential lines loaded with DS-CSRR is the same as that using CSRRs. Since the DS-CSRR is larger than the CSRR (for a given transmission zero), the line-to-resonator coupling capacitance can also be larger and, by virtue of a smaller inductance (Subsections 2.3.2 and 2.3.5), a wider bandwidth can be obtained. An evaluation of the rejection bandwidth and size to compare the usefulness of CSRRs and DS-CSRRs is performed by electromagnetic simulations. Despite the fact that a DS-CSRR is larger than a CSRR, if we compare CSRR- and DS-CSRR-loaded lines with the same area, we conclude that the rejection bandwidth is wider for the latter.

On the basis of the even-mode equivalent circuit model, we also provide a design methodology to determine the common-mode filter dimensions for a required central filter frequency. We also predict the maximum achievable rejection bandwidth (obtained by an infinite number of cells) through the dispersion relation inferred from the circuit model (as performed in Section 3.1). It is shown that six resonators are sufficient to nearly achieve the maximum rejection bandwidth. The estimation of the maximum rejection bandwidth allows us to infer whether a specified rejection

bandwidth and central frequency can be roughly fulfilled or not. If the required bandwidth is wider, we are forced to consider electrically larger resonators and/or multiple tuned resonators. In these cases, however, filter design and maximum bandwidth estimation are not so straightforward. The advantage of using DS-CSRRs is that the bandwidth can be enhanced while preserving the description of the particle through an LC resonant tank (this is important for the proposed systematic synthesis procedure).

In order to illustrate the design methodology and the prediction of the maximum bandwidth, we consider a DS-CSRR with small ring width and separation (obviously, DS-CSRRs with wide and distant rings can also be considered to further enhance the common-mode rejection bandwidth, but in this case the circuit model cannot be used for predicting the stopband). A similar filter to that reported in the conference article is designed using tightly coupled DS-CSRRs. The differential signal is almost unaltered whilst the common mode is rejected more than 20 dB within a 41% fractional bandwidth (i.e. comparable to that achieved using CSRRs with wide and widely spaced rings). The DS-CSRR-based structure is a bit larger ($0.64\lambda_e$ x $0.14\lambda_e$) than that utilizing CSRRs, but the design is carried out following the reported systematic procedure. We also measure the eye diagrams of the differential line with and without DS-CSRRs, from which we draw that the DS-CSRRs do not significantly degrade the differential mode. Additonally, we experimentally validate the approach enhancing the common-mode suppressed band in a balanced passband filter. Even though the filter by itself rejects the common mode due to its symmetry, the common-mode rejection level in the region of interest (the passband) depends on the passband filter specifications. By merely cascading two identical DS-CSRRs to the proposed balanced filter, the common-mode rejection is roughly increased from 20 dB to 50 dB in the region of interest. The filter response (differential mode) is practically unaffected by the presence of the DS-CSRRs.

Finally, our CSRR- and DS-CSRR-based differential lines with common-mode suppression are compared with other structures reported in the literature. The combination of size, rejection bandwidth, and rejection level is competitive. The proposed common-mode suppression strategy is technologically simple and low cost, and the systematic design procedure is simple.

5.3.2 ELC- and MLC-loaded Differential Microstrip Lines

Subsection 4.2.2 was addressed to analyze the effect of electric and magnetic inductive-capacitive (ELC and MLC) resonators when they load symmetrically a differential microstrip line. The advantage of the ELC (against the CSRR and the MLC) to suppress the common mode is that the ground plane is kept unaltered (frequently, this is a requirement in

some applications). However, in the corresponding publication, **article APA13**, the results show that the even mode is not suppressed in a wide band using neither ELC nor MLC resonators. Since the rejection is not as efficiently as by means of CSRRs we have not designed any common-mode suppressed differential line employing neither ELC nor MLC resonators.

References

[1] T. C. Edwards and M. B. Steer, *Foundations of Interconnect and Microstrip Design.* John Wiley & Sons, 2000.

[2] D. Bockelman and W. Eisenstadt, "Combined differential and common-mode scattering parameters: theory and simulation," *IEEE Trans. Microw. Theory Tech.*, vol. 43, no. 7, pp. 1530–1539, Jul. 1995.

[3] C.-H. Tsai and T.-L. Wu, "A broadband and miniaturized common-mode filter for gigahertz differential signals based on negative-permittivity metamaterials," *IEEE Trans. Microw. Theory Tech.*, vol. 58, no. 1, pp. 195–202, Jan. 2010.

[4] C.-H. Wu, C.-H. Wang, and C. H. Chen, "Novel balanced coupled-line bandpass filters with common-mode noise suppression," *IEEE Trans. Microw. Theory Tech.*, vol. 55, no. 2, pp. 287–295, Feb. 2007.

[5] B.-C. Tseng and L.-K. Wu, "Design of miniaturized common-mode filter by multilayer low-temperature co-fired ceramic," *IEEE Trans. Electromagn. Compat.*, vol. 46, no. 4, pp. 571–579, Nov. 2004.

[6] W.-T. Liu, C.-H. Tsai, T.-W. Han, and T.-L. Wu, "An embedded common-mode suppression filter for GHz differential signals using periodic defected ground plane," *IEEE Microw. Wireless Compon. Lett.*, vol. 18, no. 4, pp. 248–250, Apr. 2008.

[7] T.-L. Wu, C.-H. Tsai, T.-L. Wu, and T. Itoh, "A novel wideband common-mode suppression filter for gigahertz differential signals using coupled patterned ground structure," *IEEE Trans. Microw. Theory Tech.*, vol. 57, no. 4, pp. 848–855, Apr. 2009.

[8] T.-W. Weng, C.-H. Tsai, C.-H. Chen, D.-H. Han, and T.-L. Wu, "Synthesis model and design of a common-mode bandstop filter (CM-BSF) with an all-pass characteristic for high-speed differential signals," *IEEE Trans. Microw. Theory Tech.*, vol. PP, no. 99, pp. 1–10, 2014.

[9] J. Choi, P. Hon, and T. Itoh, "Dispersion analysis and design of planar electromagnetic bandgap ground plane for broadband common-mode suppression," pp. 1–1, 2014.

[10] T.-L. Wu, F. Buesink, and F. Canavero, "Overview of signal integrity and EMC design technologies on PCB: Fundamentals and latest progress," *IEEE Trans. Electromagn. Compat.*, vol. 55, no. 4, pp. 624–638, Aug. 2013.

[11] J. Shi and Q. Xue, "Dual-band and wide-stopband single-band balanced bandpass filters with high selectivity and common-mode suppression," *IEEE Trans. Microw. Theory Tech.*, vol. 58, no. 8, pp. 2204–2212, Aug. 2010.

[12] J. Zhou, Y.-C. Chiang, and W. Che, "Compact wideband balanced bandpass filter with high common-mode suppression based on cascade parallel coupled lines," *IET Microw. Antennas Propag.*, vol. 8, no. 8, pp. 564–570, Jun. 2014.

[13] A. Fernández-Prieto, J. Martel, F. Medina, F. Mesa, S. Qian, J.-S. Hong, J. Naqui, and F. Martín, "Dual-band differential filter using broadband common-mode rejection artificial transmission line," *Progress In Electromagnetics Research*, vol. 139, pp. 779–797, 2013.

[14] P. Vélez, J. Naqui, A. Fernández-Prieto, M. Durán-Sindreu, J. Bonache, J. Martel, F. Medina, and F. Martín, "Differential bandpass filters with common-mode suppression based on stepped impedance resonators (SIRs)," in *IEEE MTT-S Int. Microw. Symp.*, Seattle, WA, USA, Jun. 2013, pp. 1–4.

[15] R. N. Simons, *Coplanar Waveguide Circuits, Components, and Systems.* John Wiley & Sons, 2001.

Chapter 6

Application to Microwave Sensors

The present chapter is devoted to the application of the symmetry properties in resonator-loaded transmission lines described in Chapter 4 to microwave sensors. Specifically, symmetry rupture in transmission lines loaded with either single or pairs of resonators is exploited as a sensing mechanism. The novel proposed sensors may be classified into two categories in terms of the nature of the measurable physical quantity. Most of the presented sensors (all except one) are spatial sensors that involve the measurement of spatial variables (e.g. displacement or velocity). The other sensor that we propose is a permittivity (an electromagnetic variable) sensor for differential measurements of the dielectric constant of materials. The former sensors are implemented using a transmission line loaded with a single resonator, whereas the latter sensor uses a transmission line loaded with a pair of resonators.

Section 6.1 introduces microwave sensors (mainly resonator-based microwave sensors), and some fundamental sensor parameters. In Section 6.2, the two reported sensing mechanisms are described depending on whether the line is loaded with either a single or a pair of resonators. Next sections are organized according to the measurand. Spatial sensors are addressed in Sections 6.3−6.6, while the permittivity sensor is presented in Section 6.7.

6.1 Introduction

A *sensor* is a device that measures a physical quantity (called *measurand*) and converts it into a signal that can be read by an observer or an

instrument.[1] *Microwave sensors* (and particularly *metamaterial-inspired microwave sensors* [2]) are attracting growing interest because they feature properties (e.g. miniaturization or cost) that cannot be provided by sensors working at lower frequencies or by other sensing principles. Microwave sensors are based on electromagnetic sensing principles, namely, a physical variable is measured from the variations of the characteristics of an RF/microwave signal.

Resonator-based microwave sensors are common devices where sensing is typically achieved through the variations experienced by the resonance frequency, phase, and/or quality factor of the resonant structures. In particular, split-ring resonators (SRRs) and other related particles have been exhaustively used for sensing purposes due to their small electrical size and high-Q factor at the fundamental resonance. Different resonator-based sensors have been proposed in the literature, such as displacement sensors [3–7], sensors for organic tissue analysis [8–10], or sensors for microfluidic dielectric characterization [11–14].

A full description of sensor parameters may be found in many text books [1, 15], so that in this section we briefly summarize the relevant parameters of the presented sensors in this thesis: (a) the relationship between an input physical variable and an output electrical variable is given by the so-called *transfer function*; (b) the *input dynamic range* is the range of values of the measurand that can be measured; (c) the *output dynamic range* corresponds to the values of the electrical variable; (d) the *resolution* is the smallest increment of the input variable which can be sensed; (e) the *sensitivity* is the slope of the transfer function and should be, in general, as high as and as constant as possible (ideal sensors are designed to be sensitive to the measurand, linearly or linearly to some simple mathematical function, e.g. logarithmic or exponential); the (f) *cross-sensitivity* defines the sensitivity to other physical variables, as generally occurs, degrading the sensor performance; (g) the *linearity* indicates the deviation of the transfer function from an ideal straight line (a linear transfer function is characterized by a constant sensitivity); (h) the *precision* of the measurement defines the error (sometimes referred to as noise) produced by random error sources (systematic errors are assumed to be removed from the measurement to define the precision).

Particularly, cross-sensitivity to environmental conditions (e.g. temperature, moisture, or pressure) are very common. Accordingly, environmental factors may and usually do affect the performance of sensors. In the case of microwave sensors based on the frequency shift of resonant elements, their transfer function can be altered by drifts caused

[1] The term *sensor* should be distinguished from *transducer*. The latter is a converter of one type of energy into another, whereas the former converts any type of energy into electrical [1].

by environmental changes. For example, environmental factors may degrade the performance of displacement and alignment sensors based on lines loaded with split-ring resonators where the operation principle is based on the shift of the resonance frequency [3]. Since the resonance frequency in resonator-based sensors changes as the permittivity of the host medium changes in response to variations in environmental parameters, sensing of environmental conditions is even possible [16]. Stability against variations of these conditions is often a very important requirement [1]. As will be shown in the next section, the proposed sensors in this thesis intend to face with cross-sensitivity due to environmental conditions.

To end this section, we briefly discuss on the measurement system. Typically, in resonator-based sensors, the sensing structure is merely a passive loaded transmission line whose cost is really insignificant. However, the physical variable is sensed by monitoring the transmission or reflection coefficient. Prototypes are usually characterized by measurements carried out by a vector network analyzer (VNA), which is a multifunctional, but heavy and expensive equipment. In a practical sensor, however, the measurement circuitry attached to the passive sensing structure should be implemented by low-cost electronic circuits and components. Otherwise, the proposed sensing solutions cannot be regarded as low-cost sensor systems at all.

6.2 Symmetry-based Sensing Mechanisms

In this thesis we have introduced two novel microwave sensor concepts inspired by symmetry properties of transmission lines loaded with resonant elements. The sensing proposals uses single or pairs of resonators. The former sensing strategy is exploited for the design of spatial sensors, whereas the latter for the implementation of permittivity sensors.[2] Most of the contributions of this thesis to microwave sensors is based on the former.

6.2.1 Transmission Lines loaded with Single Resonators

One of the sensing proposals is based on transmission lines loaded with a single resonator. Employing these structures, this thesis deals with the measurement of spatial variables (e.g. alignment, displacement, or velocity). In these spatial sensors, the resonator must be attached to a substrate (or object) different to that of the transmission line in order to

[2] Permittivity sensors based on a single resonator are also possible. Spatial sensors based on pairs of resonators can also be designed and, in fact, have been already reported in the literature [17] (**journal J1**). These kind of sensors, however, are not considered in this thesis.

allow for a relative motion between the resonator and the line[3]. The theory behind these sensors relies on the misalignment properties described in Section 4.3. If the resonator is properly aligned with the transmission line, line-to-resonator coupling is prevented, and the structure exhibits total transmission. By contrast, by breaking symmetry through the effects of a spatial variable, a transmission zero emerges, and the spatial variable can be inferred. The notched response is modulated by the degree of line-to-resonator coupling, which in turn is sensitive to the position of the resonator. Hence, the relative position between the two elements is measured through the transmission coefficient.

Most of the presented spatial sensors are characterized only by the notch depth, in logarithmic scale as usual to quantify attenuation. The key advantage of the proposed sensing solution is its robustness against variable environmental conditions because:

(a) the principle of operation relies on geometrical alignment/misalignment which cannot be altered by environmental factors. The proposed approach is therefore especially suitable for alignment purposes.

(b) the measurand is sensed by amplitude levels which have been seen to exhibit better cross-sensitivity than other variables (e.g. frequency) to variations on the substrate that may be produced by changing ambient factors.[4]

However, the disadvantage of sensing the amplitude is its susceptibility to electromagnetic interference or noise that may seriously affect the performance of the sensors. Nevertheless, in the case that interfering signals are present, the frequency of operation can be easily shifted (e.g. by tailoring the resonator dimensions). Another way of reducing unwanted interference may consider the appropriate shielding of the sensor.

The afore-mentioned sensing mechanism was proposed for the first time in **article S11** (Section 6.3) applying displacements to the resonator. Soon after, other sensor designs were reported in the literature [18–20] ([20] corresponds to **journal J3**).[5] Sections 6.3−6.6 are devoted to the reported spatial sensors for different spatial variables. Due to the available in-house

[3] Note that the resonator must be coupled to the line, but not connected to it like the stepped-impedance shunt-stub (SISS).

[4] The notch depth has also been observed to exhibit less cross-sensitivity to fabrication tolerances in the substrate as well as in the nominal values of the dimensions. By contrast, the resonance frequency of resonators is usually very sensitive to fabrication tolerances.

[5] In these designs, the main motivation is to obtain a frequency-independent notch that enables the proposed sensors to operate at a single fixed frequency. Otherwise, a frequency sweeping is necessary (for notch frequency tracking) when the transmission zero frequency is sensitive to the displacement, which increases the complexity of the measurement system.

facilities to fabricate (a drilling machine and a photo mask/etching process with a minimum strip and slot width of 200 µm) and measure the devices, the proposed spatial sensors are designed within the range 1−4 GHz (i.e. in the low regime of microwaves). However, frequency scaling is possible if necessary using an appropriate fabrication technology.

6.2.2 Transmission Lines loaded with Pairs of Resonators

The other proposed sensing concept relies on transmission lines loaded with pairs of resonators whose principle of operation was described in Section 4.4. As mentioned therein, dielectric loading may be a strategy to rupture symmetry. One possibility is to add a material or substance in a specific test region in the vicinity of the resonators. As long as the inclusion exhibits a symmetric distribution of the permittivity, there is a single transmission zero. However, if the dielectric loading is not symmetric, this can be detected by the appearance of two notches in the transmission coefficient. Another interesting possibility, which is the one considered, is to load each resonator with a dielectric load. In this case, no difference exists between the two dielectric samples if a single transmission zero is monitored. By contrast, the appearance of two transmission zeros in the frequency response indicates that different dielectric loads are introduced. By that means we can design differential sensors and comparators to perform real-time differential permittivity measurements. A *differential sensor* should deliver the difference between two permittivity values. Conversely, a *comparator* (differential by definition) simply compares two permittivities indicating whether these values are the same or not. A differential permittivity sensor may be useful for the analysis or characterization of the permittivity of materials and substances. A permittivity comparator may be interesting for the detection of defects or alterations in material samples by comparison to a well-known reference. Therefore, the proposed approach can be an alternative to sensors for analysis of organic tissues and dielectric monitoring of microfluidic channels that have been recently proposed [8–14].

It should be highlighted that even though the measurand is sensed by inspection of resonance frequencies, the proposed sensing approach performs a differential measurement. The advantage of differential measurements is their ability to reject the random errors introduced in the measurement due to frequency shifts caused by changing ambient factors. In differential measurements, the cross-sensitivities to ambient factors exhibit some degree of immunity. In fact, differential techniques are widely used to improve the performance of sensors [1]. Section 6.7 presents the proposed differential sensor and comparator for permittivity measurements. To the best knowledge of the author, this is the first structure consisting of transmission lines loaded with pairs of resonators

whose symmetry is broken by means of inclusions. The first reported transmission line loaded with pairs of resonators, whose symmetry was disrupted for sensing purposes, was used as a displacement sensor by Horestani *et al.* [17] (**journal J1**).

6.3 Linear Alignment and Displacement

In this section we show how one-dimensional (1D) linear (along a straight line) alignment and displacement sensors can be designed on the basis of the symmetry properties described in Section 4.3. The displacement is sensed only in terms of magnitude (the sensing of the direction for linear displacements is addressed in Section 6.4).

6.3.1 SRR- and Folded SIR-loaded Coplanar Waveguides

In Subsection 4.3.1 we analyzed the response of a coplanar waveguide (CPW) loaded with a split-ring resonator (SRR), a folded using folded stepped-impedance resonator (SIR), or a single split-ring resonator (**article S11**, **conference article IMS12**, and **article S12**, respectively). As concluded, if these resonators are symmetrically etched on the back side of the line, both the magnetic and electric field components inside the resonators exactly cancel, and the particles are not driven at the fundamental resonance. This situation does not hold if the symmetry is broken, and therefore, a possible lack of alignment and a relative linear displacement between the line and the resonator can be detected and measured, respectively, from the transmission coefficient.

Article S11 presents the first proof-of-concept sensor based on the above-mentioned symmetry properties. The sensing is produced by inspection of the notch magnitude of the transmission coefficient. Therefore, the sensitivity is defined as the variation of the notch magnitude with the displacement. Obviously, it is important to obtain a high sensitivity of the notch magnitude with the variable that destroys the symmetry of the structure, in this case a linear lateral (along the transversal direction) displacement. The key point in this article is to validate the proof-of-concept for this novel sensing principle. Thus, an SRR is etched on the back side of the substrate rather than considering a sensing device with a movable SRR, which is technologically more complex. As a result, the sensitivity is dependent on the line and the resonator geometries, but also on the substrate thickness. In order to achieve a high sensitivity, it is necessary to use very thin substrates to enhance the line-to-resonator coupling (in a practical sensor this means that the resonator and the line should be as close as possible). Thereby stronger notches are obtained for a particular displacement. A commercial substrate of 127-µm thickness is used. With regard to the geometry, the

transversal dimension of the resonators should not excessively extend beyond the slot regions of the CPW. Thus, a rectangular-shaped SRR is etched just below the central strip of the CPW (the resonance frequency may be adjusted with the longitudinal length).

Several fixed SRR-loaded CPWs with different lateral displacements are fabricated. The input dynamic range is limited to the distance between the two slots of the CPW. Concerning our specific structure, the resulting dynamic range is about 0.6 mm ($\pm$0.6 mm if the two possible directions are considered), the longest transversal dimension of the sensor (taken as the distance between the CPW ground planes) being 1.87 mm. Within the dynamic range, the larger the lateral shift, the deeper the notch in the transmission coefficient, and the resulting linearity is reasonable. For a displacement of 0.3 mm, the measured notch magnitude is -21.1 dB.

It is important to stress that by decreasing the overall dimensions of the SRR-loaded CPW by a particular factor, the sensitivity enhances almost proportionally to the scaling factor. If we scale down the structure, the frequency response experiences a shift upwards roughly maintaining the same notch magnitude (as the scaling factor increases, the notch depth is degraded by losses). Nevertheless, the limits on the scaling are dictated by the available fabrication technology.

As an alternative, in **conference article IMS12** a proof-of-concept demonstrator based on a CPW loaded with a folded SIR is presented. The same substrate and dimensions as in the previous SRR-based sensor are considered for comparison purposes. Again, a symmetric structure and additional structures with the SIR laterally displaced are characterized. For a displacement of 0.3 mm, the measured notch magnitude is -15.3 dB. Better linearity within the dynamic range is obtained as compared to the SRR-based sensor.

6.3.2 SIR-loaded Microstrip Lines

Subsection 4.3.4 reported the behavior of a microstrip line loaded with a SIR in an additional third layer (**article IJAP14**). According to the proposed equivalent circuit model, the electric coupling between the line and the resonator plays a key role to strengthen the notch (depth and bandwidth) and to tune the notch frequency as well. **Article IJAP14** presents a displacement sensor based on SIR-loaded microstrip lines.

With a view to designing alignment and displacement sensors by inspection of the notch depth and frequency, the line-to-resonator electric coupling should be as high as possible. In order to boost this coupling it is important to enhance the patch capacitance of the SIR to the line (as well as to the ground). For this reason the microstrip line width is widened. Since this reduces the line characteristic impedance, in order to match the line to 50-Ω ports, a slot window in the ground plane below the signal strip

is etched. This enhances the line inductance and drops the line capacitance simultaneously, compensating the reduction of the characteristic impedance by widening the strip. We have designed the slot so that good impedance matching is obtained in the symmetrically loaded structure.

A sensor prototype is designed consisting of a microstrip line structure stacked on bottom of another substrate where the SIR is etched on the top face (it is assumed that there is not an in-between air layer to enhance the line-to-resonator electric coupling, but the lack of air prevents relative motion of the SIR in regard to the line). This prototype is characterized by several lateral displacements. The results show that both the notch depth and the notch frequency are very sensitive to the displacements, which is indicative of a significant increase in the line-to-SIR-to-ground capacitive coupling with the displacement. The input dynamic range is 2 mm (the longest transversal dimension of the sensor is that of the SIR which is 6 mm). The output dynamic range is 38.2 dB in amplitude and about 860 MHz in frequency (from 2.10 GHz to 2.97 GHz). The resulting sensitivity is particularly very high in notch magnitude for small displacements, and this makes the sensor very suitable for alignment purposes. Specifically, the average sensitivity in notch frequency is 43 MHz/100 µm in the full dynamic range. The average sensitivity in notch magnitude is 5.4 dB/100 µm in the range up to 400 µm.

The previous proof-of-concept demonstrator was fabricated and measured in an experimental setup that enables three-dimensional (3D) calibrations through manual positioners (for each relative displacement, the top substrate is separated from the bottom substrate, it is displaced, and it is stacked again onto the bottom substrate). It should be highlighted that it was not possible to perfectly align the SIR with the line due to the fact that the sensor features a very high sensitivity for small shifts, and this points out its remarkable resolution for alignment capabilities. Another observed deviation in the experimental data is that a considerable upward frequency shift is obtained, and it is attributed to a very thin but not negligible air layer between the substrates. Nevertheless, the sensing concept is experimentally validated.

6.4 Linear Position

The sensors to detect the lack of linear alignment and to measure linear displacements presented in Section 6.3 apply to a one-dimensional (1D) space. Furthermore, those sensors are capable of sensing only the displacement magnitude, but not the direction of motion. In this section we show that the sensing capability can be easily extended to a two-dimensional (2D) space, and the direction of displacement is also

measurable. Therefore, a 2D alignment and position sensor for linear displacements is presented.

6.4.1 Coplanar Waveguides loaded with Folded Split Rings

Article S12 may be regarded as an expanded work of **article S11**, where we extend the sensing capability to a 2D space and the direction of displacement is also detected. With a view to extending the sensing capability to a 2D space, a folded CPW (with a right angle bend) loaded with two SRRs (one in each orthogonal direction) are used. These SRRs must be tuned at different frequencies to discriminate the two spatial dimensions in the frequency response. In order to provide the direction of motion, two additional resonators (also resonating at different frequencies) are used, one for each spatial dimension. However, for the aligned configuration, these resonators are etched beneath one of the CPW ground planes, near a CPW slot. Thereby, if the displacement direction drives such additional resonators towards the slot of the CPW, this is detected by a notch at the resonance frequency of these resonators. Conversely, by shifting the SRRs to the opposite direction such notches do not appear. This is the principle for sensing the direction of linear displacements.

The substrate and the CPW (strip and slot widths) parameters are the same as in **article S11**. However, in this 2D sensor, split-ring resonators composed of only one ring are considered. This is due to two reasons; (*a*) because for thin substrates (as is considered) the coupling between the inner and the outer ring of the SRRs is negligible (Subsection 4.3.1); and (*b*) because the second resonance frequency of a single split ring is located beyond the one of SRRs with two rings. The latter feature is important to avoid (or reduce) interference between the four transmission notches corresponding to the four different resonators.

The proposed sensing structure is validated by considering several proof-of-concept prototypes with different displacements, where the resonators are etched on the back side of the substrate (vias and backside strips are used to prevent the parasitic slot mode). Obviously, in a real sensor, the SRRs must be etched on a different substrate in order to achieve relative motion between the sensing SRRs and the bended CPW, but this complicates the measurement from a mechanical viewpoint. Nevertheless, the prototype device suffices to illustrate the potential of the approach. The input dynamic range is ± 0.3 mm. The dependence of the notch magnitude is similar and roughly linear in the two orthogonal directions, with a measured value of approximately -19 dB for a displacement of ± 0.3 mm. It is worth mentioning that inter-notch

interference limits the performance (e.g. the input dynamic range) of the proof-of-concept sensor.[6]

6.5 Angular Alignment and Displacement

This section presents sensors to detect the lack of angular alignment and to measure the angular displacement (e.g. rotation) between two objects. To this end, the resonator axis is perpendicular to the line axis intersecting it, and different angular orientations of the resonator are considered. The proposed sensors are able to measure the displacement magnitude, but not the direction.

6.5.1 SRR- and Folded SIR-loaded Coplanar Waveguides

As demonstrated in Subsection 6.3.1, SRR- or folded SIR-loaded CPWs can be useful for the implementation of linear alignment and displacement sensors. Additionally, these structures can also be designed to operate as angular alignment and displacement sensors. In **article S11** and **conference article IMS12**, the same SRR- and folded SIR-loaded CPWs that are characterized with linear displacements, are also evaluated by applying small rotations (up to 6°). Several SRR- and folded SIR-loaded CPWs with different angular displacements are fabricated to validate the approach (the resonators are etched on the back side of the substrate). Since the dynamic range of angular displacements is very small (about 6°), the proposed sensors may be especially suitable for angular alignments. For a rotation of 6°, the measured notch magnitude is −12.7 dB (SRR-based sensor) and −9.6 dB (SIR-based sensor).

6.5.2 ELC-loaded Coplanar Waveguides

As explained in Subsection 4.3.2, the transmission coefficient of an ELC-loaded CPW depends on the angular orientation of the resonator. Specifically, due to the electric and magnetic walls of the ELC resonator, CPWs loaded with this resonator exhibit total transmission or a notched response by rotating the resonators 90°. These transmission characteristics are interesting to implement angular alignment and displacement sensors by measuring the notch depth in the transmission coefficient. The sensing principle is based on the fact that the line-to-resonator magnetic coupling strength is sensitive to the angular displacement.

In **conference article IMS13** an angular alignment and displacement sensor based on ELC-loaded CPWs is presented. In the first place, the sensing principle is validated with different resonator orientations by some

[6] Better performance is expected using folded SIRs since further increase in the ratio between the second and first resonances can be achieved.

conventional fixed structures (where the resonator is etched on the back side of the substrate). However, for sensing purposes, the resonator must be attached to another substrate in order to allow for a relative motion between the resonator and the CPW. Then, in the second place, a more sophisticated prototype is developed where the CPW and the resonator are etched on different substrates in parallel planes with an in-between air layer. The resonator substrate is suspended by another substrate attached to the top of the CPW substrate, and is manually moved. Finally, in the third place, in **article TMTT13**, which is an expanded work of **conference article IMS13**, the sensor is tested using a more realistic experimental setup. Therein a prototype sensor is characterized with the resonant element being attached to a cylinder that is rotated by a step motor. Such a motor allows for an accurate control of the angular position. A 3D spatial calibration between the CPW and the resonator by means of manual positioners is carried out.

In the previous sensor prototypes a circular ELC resonator loading an also circular-shaped CPW is designed to improve the linearity of the notch magnitude with the rotation angle. In **article TMTT13** we demonstrate analytically and by circuit parameter extraction that the line-to-resonator mutual inductance varies quasi-linearly with the rotation as a consequence of the circular shape. As a result, good linearity in the notch magnitude with the rotation angle is obtained, so that the sensitivity is approximately constant. The resulting measured linearity and sensitivity are 5.1% and 0.26 dB/° in average, respectively. The input dynamic range of measurable rotations is of course limited to 90°, while the output dynamic range is 23.7 dB. It should also be pointed out that the resonance frequency as well as the notch magnitude experiences an increase when an in-between air layer is considered, as it must be in a real sensor system. Vias and backside strips are used at both sides of the resonator to prevent the slot mode since the CPW-based structure is asymmetric for most of the rotation angles.

6.5.3 ELC-loaded Microstrip Lines

In Subsection 4.2.2 (**article APA13**) the behavior of a pair of microstip lines symmetrically loaded with an ELC resonator was analyzed. As explained therein, when the line pair is fed by an even-mode signal, the structure exhibit either total transmission or a transmission zero by means of 90° particle rotation. Accordingly, rotations within a 90° dynamic range can be measured from the common-mode transmission coefficient, being the notched response related to the line-to-resonator magnetic coupling. Indeed, the behavior of this structure is basically the same as that of the ELC-loaded CPWs used in the previous subsection.

An angular displacement sensor inspired by an ELC-loaded parallel microstrip line pair operating in common mode is designed in

article JS13. However, rather than using a common-mode source, a T-junction power divider cascaded to another one acting as a combiner are used. By that means the structure is excited like a conventional microstrip line: by feeding the structure with a single-ended signal, the divider acts as a single-ended to common-mode signal transition. Conversely, the combiner converts the common-mode signal into a single-ended signal. Despite the fact that undesired common-to-differential mode conversion may arise for asymmetric angular loadings, the differential mode is indeed short circuited at the junctions of the dividers (i.e. at both sides of the resonator). The resonator is the same circular one as in Subsection 6.5.2 (**conference article IMS13** and **article TMTT13**), and the two dividers are accordingly circular-shaped designed to improve linearity. The measurement setup is also the same as in that subsection with the exception that the resonator is closer to the line to boost their coupling. The decrease in the line-to-resonator distance is due to the fact that the notch depth in this microstrip implementation is seen to be poorer than in the CPW implementation for a particular distance. The measured output dynamic range is 23.3 dB, and the measured linearity and sensitivity are 9.7% and 0.26 dB/° (in average), respectively. As compared to angular displacement sensors based on ELC-loaded CPWs, this microstrip implementation does not require air bridges, and the ground plane provides backside isolation.

6.6 Angular Velocity

The basic idea behind many velocity or acceleration sensors is a measurement of the displacement of an object with respect to some reference object. Therefore, displacement sensors are integral parts in many of them [1]. In this section we show that the angular velocity of a rotating object can be measured in a simple manner using the angular displacement sensors based on measuring amplitude levels of Section 6.5 as building blocks. A novel and high precision angular velocity sensor concept based on symmetry properties is proposed.

6.6.1 ELC-loaded Coplanar Waveguides and Microstrip Lines

Assume the angular displacements sensors of Section 6.5 where the resonator is rotating at a particular velocity. The angular velocity is the change of the angular position with time. Therefore, the angular position varies with time, and the notch magnitude as well (the signal at the output of the displacement sensor is amplitude modulated). Due to the displacement sensor symmetry, the transfer function is periodic every 180% varying between a maximum and a minimum. As a result, by feeding the

line with a harmonic signal tuned in the vicinity of the fundamental resonance frequency[7], the time distance between consecutive transmission peaks corresponds to half a period of rotation.

The proposed concept for angular velocity sensing is characterized and validated for the first time in **article TMTT13**. To experimentally measure the angular velocity in time domain we cascade a circulator (to avoid unwanted reflections) and an envelope detector (to obtain the envelope of the amplitude modulated signal) at the output port of the angular displacement sensors of Section 6.5. The waveform of the envelope is directly related to the transfer function (ideally they should be identical). The step motor is configured with a uniform angular velocity of $\omega_r = 2\pi f_r$, where $f_r = 1$ Hz and 50 Hz (60 and 3000 rpm, respectively, the latter being the maximum angular velocity of the motor). At the detector output, the envelope signal in the time domain is visualized by an oscilloscope. The measured linear velocities are $f_r = 0.998$ Hz and 49.751 Hz in coplanar waveguide implementation (**article TMTT13**), and $f_r = 0.998$ Hz and 50.251 Hz in microstrip technology (**article SJ13**). The measured values are very close to the velocities specified in the step motor (the error is 0.2% and 0.5% for 1 Hz and 50 Hz, respectively), validating the sensing approach.

It is important to highlight certain features of the sensing proposal:

(*a*) The sensor is able to measure the speed (i.e. the magnitude) of the angular motion, but not the direction.

(*b*) As long as the harmonic signal frequency is much higher than the linear frequency of rotation (in practice this condition should be always satisfied), the measurable range of velocities is theoretically unlimited.

(*c*) To enhance precision, the velocity measurement can be done between very distant nonconsecutive peaks (or by averaging the time between adjacent peaks), although in this case the velocity should be constant.

(*d*) The circulator, the detector, and the oscilloscope could be replaced by a post-processing stage with low-cost electronic circuits and components.

(*e*) Any structure capable of producing a periodically time-varying transmission coefficient with angular motion may be used. However, the advantage of our solution is that since we use an angular displacement sensor as a building block, an all-in-one sensor able to measure the displacement and the velocity may be possible through a suitable calibration and post-processing stage.

[7] Although the resonance frequency is sensitive to the displacement, a single fixed frequency can also attain a reasonable transfer function of the notch magnitude with the displacement for velocity sensing purposes.

(f) The resonator axis is required to be aligned with the axis of rotation (the resonator must be etched in a plane parallel to the planar transmission line, e.g. at the top or bottom face of a cylinder).

Finally, it is worth mentioning that the proposed experimental sensor system resembles an amplitude modulation (AM) system, in which a carrier signal is amplitude modulated by an information signal of lower frequency that is subsequently recovered through the envelope of the modulated signal.

6.7 Differential Permittivity

This section proposes a differential sensor and comparator for permittivity measurements whose principle of operation relies on the symmetry properties of transmission lines loaded with pairs of resonators (Section 4.4).

6.7.1 Transmission Lines loaded with Pairs of SISSs

The proposed symmetry-based differential permittivity sensor is reported in **conference article IMS14**. It consists of a microstrip line loaded with a pair of identical stepped-impedance shunt-stubs (SISSs) at the same junction.[8] The behavior of this structure was already explained in Subsection 4.4.1, and in the present subsection we focus on its capabilities for sensing differential permittivities.

An equivalent circuit model where each of the resonators is capacitively-perturbed (e.g. by a dielectric load) is derived. For differential sensing purposes, the differential input is the difference in the two capacitances (or dielectric constants of the loads), while the differential output is the difference between the two resonance frequencies (which may degenerate to the same one). The differential sensitivity is defined as the variation in the difference between the resonance frequencies due to the variation in the difference between the capacitances. From the equivalent circuit, we gain insight into the theoretical resonance frequencies and sensitivity as a function of the input differential capacitance. As expected, for balanced perturbations, the frequency response exhibits a single transmission zero. By contrast, when the capacitive perturbations are different to each other, two resonance frequencies arise, each of them being dependent on both capacitive perturbations. This means that the two resonance frequencies are not independent to each other (because of the resonator-to-resonator coupling), and a wide bandwidth is required since coupling separates the resonance frequencies. As the inter-resonator

[8] Note that any dielectric perturbation loaded to a SISS may be sensed by monitoring the change in the resonance frequency. However, real-time differential measurements of two dielectric loads cannot be performed by loading a transmission line with a single SISS.

coupling increases, the difference in the two resonance frequencies strengthens degrading the sensitivity. Indeed, the maximum sensitivity corresponds to the hypothetical case of uncoupled SISSs. It is important to highlight that a significant drop in the sensitivity occurs for small perturbations. Accordingly, the considered topology of parallel-connected SISSs seem to be not much suitable to operate as a sensor due to the inevitably presence of inter-resonator coupling. On the other hand, the resonance frequency separation caused by coupling may be interesting to designing a comparator. However, the smaller the difference in the perturbations, the narrower the lower notch (the bandwidth of the lower notch is narrow by nature). Therefore, the resolution for small differential inputs, which is of special interest for designing comparators, is expected to be degraded by losses. It is also worth mentioning that since the transfer function is not linear, the sensitivity is not constant. Moreover, the sensitivity is not a symmetric function in the sense that its magnitude increases or decreases as the input capacitance is increasingly negative or positive, respectively.

Although in the equivalent circuit model the perturbations are modeled by generalized capacitances, in a permittivity sensor the perturbations must be due to changes in the dielectric constant of dielectric loads (samples of the materials under test). The optimum position of the dielectric loads to enhance sensitivity is where the electric energy is concentrated, namely, in the vicinity of the low impedance section of the SISSs (Subsection 3.3.1). An on-wafer in-house proof-of-concept prototype operating around 60 GHz is fabricated (in the facilities of Darmstadt University of Technology) to experimentally validate the sensing principle. Because of the available measurement set-up, the structure is based on a symmetric pair of parallel SISSs implemented on conductor-backed coplanar waveguide (CB-CPW) technology. Microwave CPW probes are used to measure the structure (a) without external inclusions and (b) with a piece of a dielectric glass on top of one of the SISSs. As expected, there is a single transmission zero when the structure is not loaded (the structure remains symmetric), whereas two transmission zeros arise when the structure is broken by the dielectric sample.

Finally, it is worth mentioning that an alternative topology will be proposed after this Ph.D dissertation in an extended work of **conference article IMS14**. The topology is aimed at preventing inter-resonator coupling, and is intended to face with the drawbacks that parallel SISSs exhibit. Specifically, the structure consists of a cascade connection of two identical SISSs, spaced by a transmission line section (the resonators are sufficiently separated so that their coupling is negligible). Thereby, the two resonators can be tuned independently because the coupling between the resonance frequencies is prevented, even for asymmetric perturbations. Preliminary results (not included in this thesis) show that a cascade

connection of SISSs is a good solution to avoid coupling between them, achieving in turn significant advantages: the resonances are independent to each other, their bandwidth is not narrow by nature, and narrower frequency bandwidth of operation is required since the resonance frequencies are not separated by coupling. Work is in progress to characterize the two topologies (parallel SISSs and cascaded SISSs) for the design of differential permittivity sensors and comparators.

References

[1] J. Fraden, *Handbook of Modern Sensors: Physics, Designs, and Applications*, 3rd ed. Springer, 2004.

[2] M. Schüßler, C. Mandel, M. Puentes, and R. Jakoby, "Metamaterial inspired microwave sensors," *IEEE Microw. Mag.*, vol. 13, no. 2, pp. 57–68, Mar. 2012.

[3] C. Mandel, B. Kubina, M. Schüßler, and R. Jakoby, "Passive chipless wireless sensor for two-dimensional displacement measurement," in *Europ. Microw. Conf. (EuMC)*, Manchester, UK, Oct. 2011, pp. 79–82.

[4] ——, "Metamaterial-inspired passive chipless radio-frequency identification and wireless sensing," *annals of telecommunications-annales des télécommunications*, vol. 68, no. 7-8, pp. 385–399, Aug. 2013.

[5] X. Liu, C. Xue, S. Yan, J. Xiong, and W. Zhang, "Integrated high sensitivity displacement sensor based on micro ring resonator," in *4th IEEE Int. Conf. Nano/Micro Engineered and Molecular Systems (NEMS)*, Shenzhen, China, Jan. 2009.

[6] Z. Shaterian, A. K. Horestani, and C. Fumeaux, "Metamaterial-inspired displacement sensor with high dynamic range," in *4th Int. Conf. on Metamaterials, Photonic Crystals and Plasmonics (META)*, Sharjah, UAE, Mar. 2013.

[7] A. Ebrahimi, W. Withayachumnankul, S. Al-Sarawi, and D. Abbott, "Metamaterial-inspired rotation sensor with wide dynamic range," *IEEE Sensors J.*, vol. 14, no. 8, pp. 2609–2614, Aug. 2014.

[8] M. Puentes, C. Weiss, M. Schüßler, and R. Jakoby, "Sensor array based on split ring resonators for analysis of organic tissues," in *IEEE MTT-S Int. Microw. Symp. Dig.*, Baltimore, MD, USA, Jun. 2011, pp. 1–4.

[9] M. Puentes, M. Maasch, M. Schüßler, and R. Jakoby, "Frequency multiplexed 2-dimensional sensor array based on split-ring resonators for organic tissue analysis," *IEEE Trans. Microw. Theory Tech.*, vol. 60, no. 6, pp. 1720–1727, Jun. 2012.

[10] M. Puentes, *Planar Metamaterial Based Microwave Sensor Arrays for Biomedical Analysis and Treatment*. Springer Thesis, 2014.

[11] A. Abduljabar, D. Rowe, A. Porch, and D. Barrow, "Novel microwave microfluidic sensor using a microstrip split-ring resonator," *IEEE Trans. Microw. Theory Tech.*, vol. 62, no. 3, pp. 679–688, Mar. 2014.

[12] A. Ebrahimi, W. Withayachumnankul, S. Al-Sarawi, and D. Abbott, "High-sensitivity metamaterial-inspired sensor for microfluidic dielectric characterization," *IEEE Sensors J.*, vol. 14, no. 5, pp. 1345–1351, May 2014.

[13] W. Withayachumnankul, K. Jaruwongrungsee, A. Tuantranont, C. Fumeaux, and D. Abbott, "Metamaterial-based microfluidic sensor for dielectric characterization," *Sensor Actuat. A Phys.*, vol. 189, pp. 233–237, Jan. 2013.

[14] T. Chretiennot, D. Dubuc, and K. Grenier, "Optimized electromagnetic interaction microwave resonator/microfluidic channel for enhanced liquid bio-sensor," in *Europ. Microw. Conf. (EuMC)*, Nuremberg, Germany, Oct. 2013, pp. 464–467.

[15] J. G. Webster, *The Measurement, Instrumentation and Sensors Handbook*. CRC Press, 1999.

[16] E. Ekmekci and G. Turhan-Sayan, "Multi-functional metamaterial sensor based on a broad-side coupled SRR topology with a multi-layer substrate," *App. Phys. A*, vol. 110, no. 1, pp. 189–197, May 2013.

[17] A. K. Horestani, J. Naqui, Z. Shaterian, D. Abbott, C. Fumeaux, and F. Martín, "Two-dimensional alignment and displacement sensor based on movable broadside-coupled split ring resonators," *Sensor Actuat. A Phys.*, vol. 210, pp. 18 – 24, Apr. 2014.

[18] A. K. Horestani, C. Fumeaux, S. Al-Sarawi, and D. Abbott, "Displacement sensor based on diamond-shaped tapered split ring resonator," *IEEE Sensors J.*, vol. 13, no. 4, pp. 1153–1160, Apr. 2013.

[19] A. K. Horestani, D. Abbott, and C. Fumeaux, "Rotation sensor based on horn-shaped split ring resonator," *IEEE Sensors J.*, vol. 13, no. 8, pp. 3014–3015, Aug. 2013.

[20] A. K. Horestani, J. Naqui, D. Abbott, C. Fumeaux, and F. Martín, "Two-dimensional displacement and alignment sensor based on reflection coefficients of open microstrip lines loaded with split ring resonators," *IET Electron Lett.*, vol. 50, no. 8, pp. 620–622, Apr. 2014.

Chapter 7

Application to Spectral Signature Barcodes

The symmetry properties of transmission lines loaded with single symmetric resonators described in Chapter 4 may be used not only as a sensing mechanism (Chapter 6), but also as an encoding mechanism. In this chapter, we show preliminary results applying such symmetry properties for the implementation of chipless tags for radio-frequency identification (RFID). In particular, symmetry-based structures may be interesting for RF barcodes based on multiresonator structures that are encoded in the frequency domain. A binary encoding is merely done by switching from an all-pass response to a stopband response, depending on whether resonance frequency is prevented or not, respectively. We discuss some implementations, and their advantages and limitations are highlighted.

Section 7.1 presents a brief overview of RFID and multiresonator-based chipless tags. Section 7.2 is devoted to the encoding mechanism based on symmetry properties, which is the main contribution of this thesis to multiresonator-based chipless tags. Finally, Sections 7.3 and 7.4 are addressed to the presented proof-of-concept (3-bit) barcodes in coplanar waveguide and microstrip technologies, respectively, that validate the proposed approach for encoding.

7.1 Introduction

Radio-frequency identification (RFID) is a wireless data capturing technique that utilizes radio frequency (RF) waves for automatic identification of objects. RFID systems consist of three major components: a reader or interrogator, a tag or transponder, and middleware software. The reader sends interrogation signals to the tag that is required to be identified, and the software decodes the identification data. In recent years

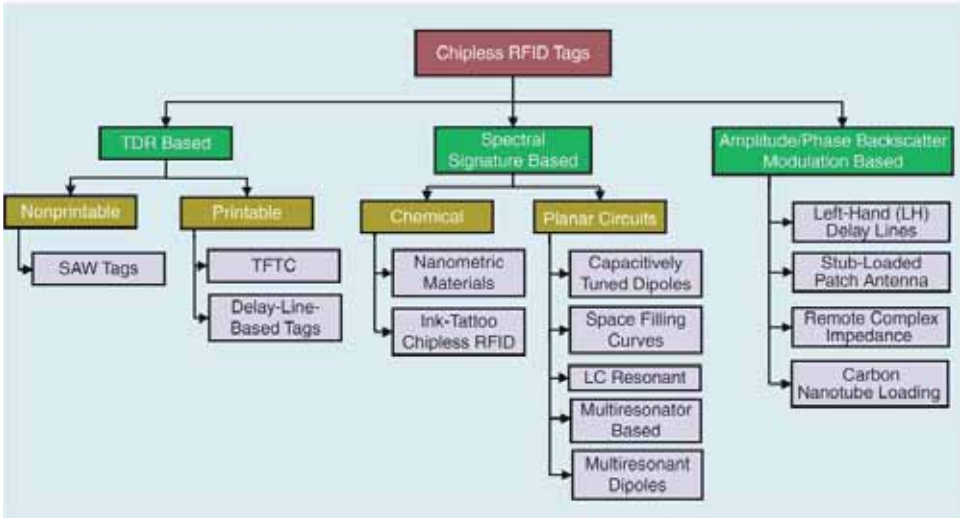

FIGURE 7.1: Classification of chipless RFID tags. In this thesis we have developed some proof-of-concept multiresonator-based spectral signature tags based on symmetry properties. Figure extracted from [1].

the tendency is to replace conventional *optical barcodes* with RFID tags. This trend is due to the fact that RFID offers several advantages over conventional barcodes, such as unique identification code for individual items, longer reading ranges, reading in the presence of obstacles, and automatic identification [1]. The only reason why RFID tags have not replaced the traditional optical barcode is the price of the tag, which is higher when compared to the price of the optical barcode. *Passive tags* are those that do not have any on-board power supply. In addition, the tags are regarded as *chipless tags* if the passive tags do not contain any integrated circuit (IC) [1]. Chipless tags are aimed at reducing the tag price as much as possible, obviously at the expense of performance (such as a poorer data storage capability or a shorter reading range). Although chipless RFID tags are relatively recent, a number of approaches have already been developed as shown in Figure 7.1. A comprehensive review of chipless RFID is out of the scope of this chapter, but it is available in the literature by Preradovic and Karmakar [1].

In this thesis we are focused on multiresonator-based chipless RFID tags. This sort of chipless tags was designed by Preradovic *et al.* at Monash University [2], and it was patented in 2008 [3]. Soon after, a Ph.D dissertation devoted to multiresonator-based chipless RFID systems was presented by Preradovic in 2009 [4]. In fact, most of the contributions about these chipless RFID systems have been published by the same authors. In these RF barcodes the information is stored in the so-called spectral signature of the tag (frequency-domain encoding). As is illustrated

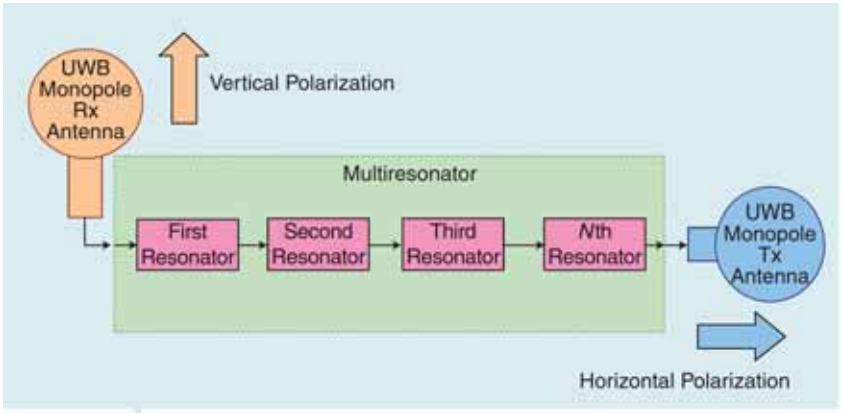

FIGURE 7.2: Block diagram of multiresonator-based chipless tags for spectral signature encoding. Figure extracted from [1].

in Figure 7.2, the chipless tag is composed of a multiresonating structure, and receiving and transmitting antennas. The spectral signature is obtained by loading a transmission line with an array of resonators, each one resonating at a different frequency. Thereby we can set a binary code, where each resonator corresponds to a bit value (logic '1' or '0') that is controlled by the presence or absence of the resonance frequency corresponding to that bit. The encoding is typically in amplitude, which is characterized by notches in the spectral signature, although phase encoding is also possible. By interrogating the chipless tag by a multi-frequency signal, it is possible to detect the variations in the magnitude and phase of the received signal from the tag and decode the identification [4, 5]. In the literature, tags implemented in microstrip technology as well as in coplanar waveguide technology have been reported [1, 4]. Figure 7.3 shows a barcode reported by Preradovic *et al* that may be regarded as a reference one [6].

As compared to other chipless tags, the advantages of the multiresonator-based approach are [1]: fully printable, low cost, and robust. Therefore, these tags can be implemented in flexible substrates by means of printed techniques for low-cost item tracking [7–9]. Conversely, this approach requires a large spectrum, a wideband reader, and an appropriate tag orientation (cross-polarized transmitting and receiving antennas are used) [1, 10, 11]. A key aspect in RFID is that the most appropriate technology depends on the application requirements. The multiresonator-based chipless tags may be suitable for applications that do not require to store too much information and do not need a high level of security (e.g. for document identification or electoral processes with small voting members). It is worth mentioning that there is an increasingly trend to develop microwave wireless sensors integrated with RFID [12–15].

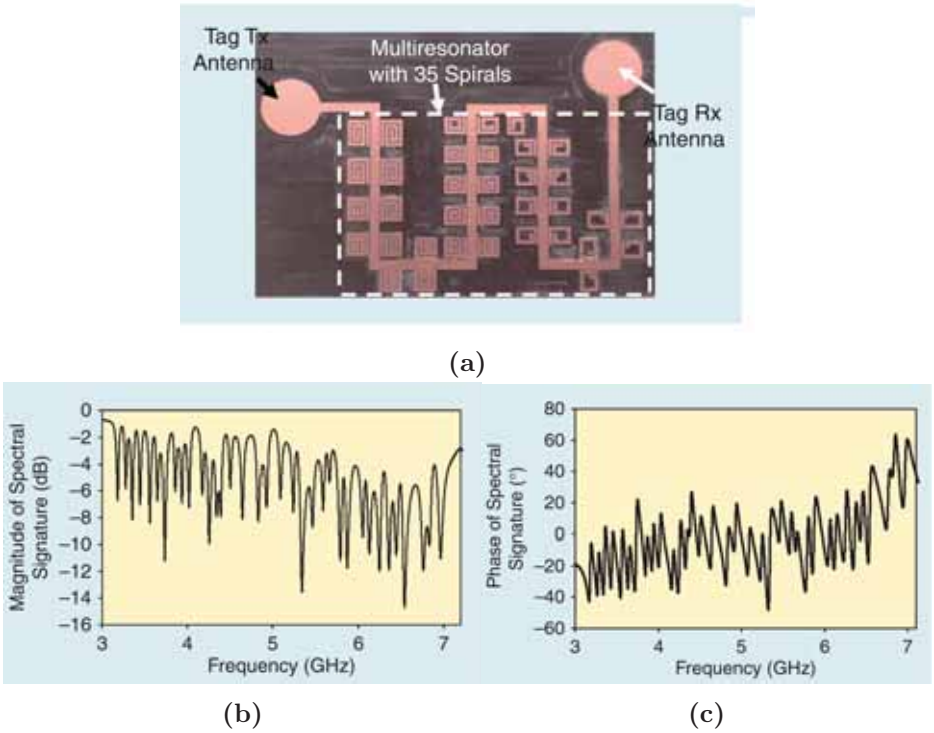

FIGURE 7.3: 35-bit chipless tag based on a microstrip line loaded with spiral resonators. (a) Photograph. (b) Magnitude and (c) phase of the spectral signature. Figures extracted from [1].

There are several considerations to bear in mind in the design of multiresonator-based tags. The data storage capacity is related to the spectral band efficiency. In order to accommodate the maximum number of resonators (resonance frequencies) in a predefined frequency spectrum, relatively narrow notches are required (typically weak line-to-resonator coupling is required). Even though the resulting notch level (intimately related to the bandwidth) is not very deep, this is not a critical drawback in binary codes. Another requirement is that inter-resonator coupling must be avoided at all costs to prevent resonance frequency shifting. Instead, the resonances should be independent to each other (each resonance should be tuned by its corresponding resonator).

7.2 Symmetry-based Encoding Mechanism

In the conventional approach [1, 2, 4], resonance is established (logic level '1' in our convention) by loading a transmission line with a resonator. On the contrary, the resonance is prevented (logic '0') by removing or short-circuiting the resonator (this shifts the resonance frequency upwards

and outside the frequency band of interest). In this thesis we propose an alternative to this standard approach, whose encoding mechanism is based on exploiting the symmetry properties of transmission lines loaded with symmetric resonators explained in Chapter 4. More specifically, it suffices to align properly a resonator to a transmission line in order to prevent resonance; the necessary and sufficient condition is that the symmetry planes of the line and the resonator must be of different electromagnetic nature (one a magnetic wall and the other one an electric wall).

Therefore, using symmetric resonators, the main advantage of the proposed approach is that it is not necessary to remove or short-circuit the resonators to set a logic '0'. The binary values can be simply modified to '1' by displacing or rotating the resonators, or by any other means of symmetry rupture of the bit cells (e.g. by adding adhesives with metallic or dielectric loads). Interestingly, with this strategy, reconfigurable (programmable) barcodes are potentially possible as long as the resonators can be somehow shifted independently. The constraining challenge, however, concerns to how mechanically reconfigure the resonators. On the other hand, it can be readily observed that one limitation of the proposed encoding mechanism is that a transmission line can be loaded just with one (per-unit-cell) resonator. Accordingly, for a particular number of resonators, the tag cannot be as compact as using, for example, pairs of resonators (see the tag of Figure 7.3).[1]

In this thesis we have focused only on the multiresonator structure which is characterized by its transmission coefficient (a full tag with antennas has not been designed yet). Next sections are devoted to the reported proof-of-concept multiresonating structures implemented with different transmission lines and resonators. Each multiresonating structure consists of a transmission line loaded with three resonators with different dimensions to provide three different resonance frequencies, so that each resonator stands for a 1-bit information. The 3-bit spectral signature is encoded in the frequency range 2−3 GHz, and the inter-notch frequency distance is about 100 MHz. The encoding has been achieved by the alignment/misalignment of symmetric (or bisymmetric) resonators to a transmission line, as explained in Section 4.3.

[1] Note that since the notched response in the symmetry-based approach depends on the level of asymmetry, it may be considered to provide more than 1-bit information per resonator. In amplitude encoding, the higher the dynamic range in the notch depth, the higher the number of logic levels. A tradeoff arises in the spectral band efficiency, however, because the bandwidth of the notch increases with the notch depth. This approach (not explored in this thesis) may be regarded as the digitalization of the sensors based on symmetry rupture.

7.3 Coplanar Waveguide Implementations

A drawback of devices implemented in coplanar waveguides (CPWs) is that they may suffer problematic mode conversion (from the CPW to the slot mode) if the structures are not symmetric. In these cases, air bridges are required to suppress the slot mode, which increases the fabrication complexity and cost as well.

7.3.1 SRR- and Folded SIR-loaded Coplanar Waveguides

Barcodes of 3-bit capacity consisting of a CPW loaded with split-ring resonators (SRRs) or folded stepped-impedance resonators (SIRs) are reported in **article APA12** and **conference article IMS12**, respectively. The behavior of these topologies was explained in Subsection 4.3.1. The resonators are etched on the back side of the substrate, and are aligned or laterally misaligned to set the corresponding binary values. Adjacent resonators are laterally displaced in opposite directions in order to get a negligible inter-resonator coupling. It is apparent that the barcodes based on these topologies are in general asymmetric structures (the only symmetric structure is that corresponding to the code with all the resonators aligned with the line). For the purpose of preventing the presence of the slot mode, via-holes in the substrate and strips on the bottom side of the substrate (in the same layer as the resonators) are used at the inter-resonator interfaces.

7.3.2 ELC-loaded Coplanar Waveguides

The electric inductive-capacitive (ELC) resonator is an interesting particle to implement barcodes in CPW technology. The reason lies on its bisymmetry, and to the application of a rotation instead of a linear displacement. As explained in Subsection 4.3.2, the structure is transparent if the electric wall of the resonator is aligned with the symmetry plane of the line (state '0'). Then, by rotating the resonator 90°, symmetry is preserved (and thus the slot mode cannot emerge) while strong magnetic coupling between the line and the resonator arises, and the transmission coefficient exhibits a notch with maximum attenuation for this angle. It is apparent that the advantage of exhibiting symmetry at the two binary values is at the expense of a larger size as compared to SRR- or SIR-based CPW barcodes. A 3-bit proof-of-concept barcode based on this topology is presented in **conference C6** (not attached to this thesis).

7.4 Microstrip Line Implementations

An important advantage of microstrip barcodes is that no parasitic modes are generated when the resonators are not aligned with the transmission line. In contrast, as stressed earlier, air bridges are generally necessary in CPW barcodes to suppress the parasitic slot mode. Another advantage of microstrip implementation is that, as long as the ground plane is kept unaltered, the ground provides backside isolation so that objects made up of conductive materials can be labeled. To avoid ground plane etching, however, three metal layers (ground, signal strip, and resonator) are required.

7.4.1 Folded SIR-loaded Microstrip Lines

In **article IJAP14** we deal with microtrip lines loaded with SIRs on the basis of mechanical reconfigurability (Subsection 4.3.4). A 3-bit barcode based on symmetry properties is implemented by loading folded SIRs in a third metallic layer situated above the signal strip, where lateral displacements are applied to the resonators. This implementation provides backside isolation by means of the ground plane, but the resonator must be etched in an additional metallic layers.

7.4.2 MLC-loaded Microstrip Lines

Article IJAP13 is devoted to the analysis of microstrip lines loaded with magnetic inductive-capacitive (MLC) resonators (Subsection 4.3.3). As a possible application, this article presents a 3-bit barcode with the electric wall of the MLC aligned or misaligned with the line, depending on the bit value to be implemented. Since the array of resonators are etched on the same metallic plane, long inter-resonator distances are required to avoid inter-resonator coupling. As compared to SIR-loaded microstrip lines, this approach utilizes two metal layers but does not provide backside isolation since the ground plane is etched.

References

[1] S. Preradovic and N. Karmakar, "Chipless RFID: Bar code of the future," *IEEE Microw. Mag.*, vol. 11, no. 7, pp. 87–97, Dec. 2010.

[2] S. Preradovic, I. Balbin, N. Karmakar, and G. Swiegers, "A novel chipless RFID system based on planar multiresonators for barcode replacement," in *IEEE Int. Conf. RFID*, Las Vegas, NV, USA, Apr. 2008, pp. 289–296.

[3] S. Preradovic, I. Balbin, S. Roy, N. Karmakar, and G. Sweigers, "Radio frequency transponder," in *Australian Provisional Patent Application (Ref: P30228AUP1)*, Apr. 2008, pp. 79–82.

[4] S. Preradovic, "Chipless RFID system for barcode replacement," Ph.D. dissertation, Monash University, Dec. 2009.

[5] R. Koswatta and N. Karmakar, "A novel reader architecture based on UWB chirp signal interrogation for multiresonator-based chipless RFID tag reading," *IEEE Trans. Microw. Theory Tech.*, vol. 60, no. 9, pp. 2925–2933, Sep. 2012.

[6] S. Preradovic, I. Balbin, N. Karmakar, and G. Swiegers, "Multiresonator-based chipless RFID system for low-cost item tracking," *IEEE Trans. Microw. Theory Tech.*, vol. 57, no. 5, pp. 1411–1419, May 2009.

[7] L. Yang, A. Rida, R. Vyas, and M. Tentzeris, "RFID tag and RF structures on a paper substrate using inkjet-printing technology," *IEEE Trans. Microw. Theory Tech.*, vol. 55, no. 12, pp. 2894–2901, Dec. 2007.

[8] L. Zheng, S. Rodríguez, L. Zhang, B. Shao, and L.-R. Zheng, "Design and implementation of a fully reconfigurable chipless RFID tag using inkjet printing technology," in *IEEE Int. Symp. Circuits Syst. (ISCAS)*, Seattle, WA, USA, May 2008, pp. 1524–1527.

[9] S. Preradovic and N. Karmakar, "Design of chipless RFID tag for operation on flexible laminates," *IEEE Antennas Wireless Propag. Lett.*, vol. 9, pp. 207–210, Mar. 2010.

[10] B. Nikfal and C. Caloz, "Hybrid time-frequency RFID system," in *IEEE MTT-S Int. Microw. Symp. Dig.*, Montreal, Canada, Jun. 2012, pp. 1–3.

[11] N. C. Karmakar, R. Koswatta, P. Kalansuriya, E. Rubayet *et al.*, *Chipless RFID Reader Architecture.* Artech House, 2013.

[12] C. Mandel, B. Kubina, M. Schüßler, and R. Jakoby, "Metamaterial-inspired passive chipless radio-frequency identification and wireless sensing," *annals of telecommunications-annales des télécommunications*, vol. 68, no. 7-8, pp. 385–399, Aug. 2013.

[13] D. Girbau, A. Lázaro, and R. Villarino, "Passive wireless permittivity sensor based on frequency-coded chipless RFID tags," in *IEEE MTT-S Int. Microwave Symp. Dig.*, Montreal, Canada, Jun. 2012, pp. 1–3.

[14] E. M. Amin and N. Karmakar, "Development of a chipless RFID temperature sensor using cascaded spiral resonators," in *IEEE Sensors*, Limerick, Ireland, Oct. 2011, pp. 554–557.

[15] S. Preradovic, N. Kamakar, and E. M. Amin, "Chipless RFID tag with integrated resistive and capacitive sensors," in *Asia-Pacific Microw. Conf. Proc. (APMC)*, Dec. 2011, pp. 1354–1357.

Chapter 8

Conclusions and Future Work

Conclusions

In this thesis, we have analyzed, modeled, and synthesized transmission lines loaded with electrically small resonators based on symmetry considerations. It has been shown that signal stopband characteristics (frequency, bandwidth, and/or amplitude) can be controlled as a function of symmetry properties. We have exploited such symmetry properties for the implementation of common-mode suppressed differential lines, microwave sensors, and radio frequency (RF) barcodes. The structures have been implemented in planar technology using either microstrip or coplanar waveguide transmission lines, and some different topologies of planar resonators have been considered (most of them may be regarded as metamaterial resonators). The synthesis of the resonator-loaded structures concerns the choice of the most appropriate transmission line and resonator, and the optimization of the geometrical topology as well. The following paragraphs are devoted to summarize the most relevant conclusions.

Throughout the development of this thesis (Chapters 3−7), **lumped-element equivalent circuit models of all the considered electromagnetic structures** haven been proposed. For a given structure, the **extraction of circuit parameters have been performed using available methodologies in the literature or proposing new procedures**. As is well known, there are numerous motivations to model electromagnetic structures with reliable equivalent circuit models. For instance, they provide an intuitive abstraction of the behavior of physical structures, they facilitate design and optimization stages, and their response can be obtained practically instantaneously using circuit simulators. The circuit model validity is restricted up to beyond the

fundamental resonance frequency of the resonators (i.e. the region of interest). However, the accuracy of the models depends strongly on the electrical size of the unit cells (the dimensions of the cells are needed to be small relative to the wavelength). Therefore, verification is always required, and to this end modern full-wave electromagnetic simulators are very useful. Despite of being time consuming and computationally intensive, these simulators are highly accurate and are excellent for verification purposes. Thus, throughout this thesis, **circuit simulations have been validated by electromagnetic simulations as well as experimental data**. However, it is worth mentioning that good agreement in the validations is always required, but it does not guarantee that the equivalent circuit models are certainly valid.

Mixed magnetoelectric coupling in the line-to-resonator interaction as a function of the relative orientation of the resonant elements (Chapter 3) has been modeled. Traditionally, mixed coupling is neglected, and only the dominant electric or magnetic coupling is considered. However, depending on the arbitrary relative orientation between the transmission line and the resonators, mixed coupling must be considered to accurately model these structures. Particularly, mixed coupling may be necessary when the structure is symmetric along the midplane. The most relevant conclusion is that the circuit parameter extraction procedures that have been used for many years may fail in the presence of mixed coupling, since these methods are based on the mapping of the scattering parameters obtained by electromagnetic simulation. In the particular case where the resonators exhibit a single symmetry plane, mixed coupling is shown to essentially change the phase of the reflection coefficients.

It is well known that periodic transmission lines loaded with (uncoupled) resonators exhibit a region of evanescent modes. With the assumption that the resonators are closely spaced apart, **inter-resonator coupling in resonator-loaded transmission lines** (Chapter 3) has been modeled by a four-port circuit network. Two ports are those corresponding to the transmission line ports, while the other two additional ports account for the inter-resonator coupling. Considering an infinite periodic structure, we have applied **Bloch mode theory to the four-port network using the transmission (*ABCD*) matrix method**. It has been shown that the considered structures may support bimodal propagation. Evanescent, forward, backward, and complex modes are found to exist. The appearance of complex modes enhances the stopband bandwidth (at the lower edge of the region of evanescent modes), and they are interpreted as the destructive interaction between forward and backward waves. Since electro- or magneto-inductive backward waves are supported by chains of electrically or magnetically coupled resonators, respectively, inter-resonator coupling is absolutely mandatory for complex

modes to emerge. The analytical modal solutions inferred from the equivalent circuit models have been corroborated by obtaining the modal solutions through a full-wave eigenmode solver of the corresponding electromagnetic structures. Experimental evidence of rejection bandwidth enhancement due to inter-resonator coupling is also provided.

In contrast to the analysis of electromagnetic structures obtaining the circuit elements of equivalent circuit models, it has also been important to synthesize physical topologies to optimize as much as possible the required specifications dictated by the corresponding application. Particularly, the **limits on the synthesis of shunt-connected series resonators by means of stepped-impedance shunt-stubs** (Chapter 3) have been analyzed comprehensively. We have provided the range of physically implementable values of inductance and capacitance, which is clearly finite in practice using semi-lumped resonators.

We have analyzed the fundamental resonance frequency of electrically small resonators (Chapter 2) and the fundamental propagation modes of transmission lines (Chapter 3) under symmetry considerations. We have characterized them in terms of electric or magnetic wall boundary conditions at their symmetry planes. By that means, regardless of the line-to-resonator coupling mechanism (electric and/or magnetic), we have established a necessary **condition to prevent the excitation of the resonance frequency**. If the symmetry planes of the line and the resonator are aligned and they are of distinct electromagnetic nature (one being an electric wall and the other one a magnetic wall), then electromagnetic coupling capable of exciting the resonator does not arise. The structure may be viewed as a transmission line with an all-pass response. By contrast, resonance is established if the symmetry planes of the line and the resonator are misaligned, if they are aligned but are of the same electromagnetic nature (either an electric or a magnetic wall), or if deviation from ideal symmetry is produced (e.g. by loading asymmetrically the structure with additional inclusions). Under these circumstances the structure exhibits a variable stopband (or notched) response in the vicinity of resonance that depends on the geometrical symmetry/asymmetry. Therefore, it has been demonstrated that the **transmission characteristics (stopband or all-pass) of transmission lines loaded with symmetric resonators depends strongly on the orientation of the resonator with regard to the line, which in turn determines the line-to-resonator coupling nature and strength**. It should be highlighted that when a transmission line is loaded with more than one resonator (per-unit-cell), the prevention of resonance is not possible becasue the two resonators cannot be aligned with the line simultaneously. However, transmission lines loaded with pairs of resonators have also been characterized in terms of symmetry, and have been shown to be useful by monitoring the resonance frequencies of the structure. We

have applied the properties derived from the previous analysis to filtering, sensing, and encoding purposes.

In coplanar waveguides and pairs of microstrip lines (three-conductor transmission lines), we have **selectively suppressed (stopband) either the even- or odd-mode while preserving (all-pass) the other mode almost unaltered by properly aligning resonators with the line** (Chapter 3). The **even/odd-mode analysis** has been applied to simplify the equivalent circuits, and the resulting even- and odd-mode networks have supported the theory relative to the selective mode suppression. As a practical application, we have proposed **differential microstrip lines with common-mode rejection** (Chapter 5). We have reported a simple and systematic design procedure. In order to enhance the common-mode rejection bandwidth, two strategies have been considered: (*a*) the design of unit cells exhibiting wideband common-mode rejection; and (*b*) coupling resonators as much as possible, so that squared-shaped resonators and very small inter-resonator distances have been considered. It has been assumed periodic structures to allow for their characterization using Bloch mode theory applied to the four-port equivalent circuit for the even mode (or common mode). Thereby, the limits on the maximum rejection bandwidth obtained by periodicity may be easily inferred. Two prototypes have been characterized and compared to other approaches. The reported solution is technologically simple, low cost, compact, provide wide common-mode stopbands with high rejection, and the differential-mode signal integrity is kept almost unaltered. If necessary, further bandwidth enhancement is expected to be obtained tuning the resonators at different frequencies.

We have introduced novel microwave sensor concepts based on symmetry disruption (Chapter 6). Proof-of-concepts of **spatial sensors for alignment, displacement, position, and velocity measurements** have been reported. These sensors consist of a transmission line and a resonator that must be etched on different substrates (or objects), and the relative position between them is estimated from the transmission coefficient (notch amplitude and/or frequency). The sensing principle has been experimentally demonstrated by a step motor that allows for an automatic relative spatial motion between the transmission line and the resonator. On the other hand, an approach for the design of **differential sensors and comparators for permittivity measurements** has also been proposed. These devices are composed of a transmission line loaded with pairs of identical resonators. A differential measurement is performed by loading the two resonators with dielectric samples. The difference in the dielectric constant of the two samples is expected to be found by measuring the resonance frequencies of the structure. Preliminary experimental results have supported the sensing principle. The proposed spatial and permittivity sensors are simple (from the design viewpoint),

compact in size, low cost (provided that the measurement system is implemented by simple electronic circuits and components), highly integrable, and robust against variable environmental conditions since they are based on symmetry properties.

Proof-of-concept **spectral signature barcodes for radio-frequency identification (RFID) chipless tags** inspired by symmetry properties (Chapter 7) have also been presented. Spectral signature-based barcodes have been known for a long time. A multiresonating structure is utilized to encode in the frequency domain. Specifically, a host transmission line is loaded with multiple resonators tuned at different frequencies, each one contributing with one bit to the binary code; the presence or absence of a certain resonance gives the logic binary value (logic '1' or '0'). In the conventional approach, the resonators are removed or short-circuited to avoid their corresponding resonance frequency. By contrast, in the reported strategy, the logic states are simply set by aligning or misaligning the resonators with the line (other symmetry disruption mechanisms can be alternatively used). We have discussed some implementations, highlighting their advantages and limitations.

Future Work

Some further work may be carried out in the research lines emerged from this thesis. Among them, we would like to highlight:

- Investigate the potentiality of designing a balanced filter with common-mode suppression based on the resonant-type approach of metamaterial transmission lines (i.e. employing a combination of split-ring resonators and inductors/capacitors).
- Design of an angular velocity sensor suitable for space applications, in particular for inertial wheels of satellites (Project A00016166 Innovation Triangle Initiative −ITI−).
- Integrate a simple measurement system to the proposed sensing resonator-loaded transmission lines (Project A00016166 Innovation Triangle Initiative −ITI−).
- Development of a full chipless RFID tag (with transmitting and receiving antennas) based on symmetry-inspired multiresonator structures with a competitive storage capacity (Project RTC-2014-2550-7 RETOS DE COLABORACIÓN 2014).
- Design and characterization of differential permittivity sensors and comparators based on pairs of stepped-impedance shunt-stubs.
- Development of microwave wireless sensors integrated with RFID.

Articles in the Ph.D Thesis

* Conference articles included in this thesis for completeness but that cannot be oficially part of the compendium of articles of the Ph.D thesis.

AWPL12: J. Naqui, M. Durán-Sindreu, A. Fernández-Prieto, F. Mesa, F. Medina, and F. Martín, "Multimode propagation and complex waves in CSRR-based transmission line metamaterials," *IEEE Antenn. Wireless Propag. Lett.*, vol. 11, pp. 1024–1027, Aug. 2012.

JAP14: J. Naqui, A. Fernández-Prieto, F. Mesa, F. Medina, and F. Martín, "Effects of inter-resonator coupling in split ring resonator loaded metamaterial transmission lines," *J. App. Phys.*, vol. 115, no. 194903, May 2014.

MAP11: J. Naqui, M. Durán-Sindreu, J. Bonache and F. Martín, "Implementation of shunt connected series resonators through stepped-impedance shunt stubs: analysis and limitations," *IET Microw. Antennas Propag.*, vol. 5, no. 11, pp. 1336–1342, Aug. 2011.

AWPL13: J. Naqui, M. Durán-Sindreu, and F. Martín, "Modeling split ring resonator (SRR) and complementary split ring resonator (CSRR) loaded transmission lines exhibiting cross polarization effects," *IEEE Antenn. Wireless Propag. Lett.*, vol. 12, pp. 178–181, Feb. 2013.

APA12: J. Naqui, M. Durán-Sindreu, and F. Martín, "Selective mode suppression in coplanar waveguides using metamaterial resonators," *Appl. Phys. A: Mater. Sci. Process.*, vol. 109, no. 4, pp. 1053–1058, Dec. 2012. Published online in Nov. 2012.

APA13: J. Naqui, M. Durán-Sindreu, F. Martín, "Selective mode suppression in microstrip differential lines by means of electric-LC (ELC) and magnetic-LC (MLC) resonators," *Appl. Phys. A: Mater. Sci. Process.*, vol. 115, no. 2, pp. 637–643, May 2014. Published online in Oct. 2013.

IMS11*: J. Naqui, A. Fernández-Prieto, M. Durán-Sindreu, J. Selga, F. Medina, F. Mesa, and F. Martín, "Split rings-based differential transmission lines with common-mode suppression," *IEEE MTT-S Int. Microw. Symp.*, Baltimore, MD, USA, Jun. 2011.

TMTT12: J. Naqui, A. Fernández-Prieto, M. Durán-Sindreu, F. Mesa, J. Martel, F. Medina, and F. Martín, "Common mode suppression in microstrip differential lines by means of complementary split ring resonators: theory and applications," *IEEE Trans. Microw. Theory Techn.*, vol. 60, no. 10, pp. 3023–3034, Oct. 2012. Published online in Aug. 2012.

S11: J. Naqui, M. Durán-Sindreu and F. Martín, "Novel sensors based on the symmetry properties of split ring resonators (SRRs)," *Sensors: Special Issue Metamaterials for Sensing*, vol. 11, no. 8, pp. 7545–7553, Jul. 2011.

S12: J. Naqui, M. Durán-Sindreu, and F. Martín, "Alignment and position sensors based on split ring resonators," *Sensors: Special Issue Ultra-Small Sensor Systems and Components*, vol. 12, no. 9, pp. 11790–11797, Aug. 2012.

IMS12*: J. Naqui, M. Durán-Sindreu, and F. Martín, "On the symmetry properties of coplanar waveguides loaded with symmetric resonators: analysis and potential applications," *IEEE MTT-S Int. Microw. Symp.*, Montreal, Canada, Jun. 2012.

IMS13*: J. Naqui, M. Durán-Sindreu, F. Martín, "Transmission lines loaded with bisymmetric resonators and applications," *IEEE MTT-S Int. Microw. Symp.*, Seattle, WA, USA, Jun. 2013.

TMTT13: J. Naqui, and F. Martín, "Transmission lines loaded with bisymmetric resonators and their application to angular displacement and velocity sensors," *IEEE Trans. Microw. Theory Techn.*, vol. 61, no. 12, pp. 4700–4713, Dec. 2013. Published online in Oct. 2013.

SJ13: J. Naqui and F. Martín, "Angular displacement and velocity sensors based on Electric-LC (ELC) loaded microstrip lines," *IEEE Sens. J.*, vol. 14, no. 4, pp. 939–940, Apr. 2014. Published online in Dec. 2013.

IJAP13: J. Naqui, M. Durán-Sindreu, and F. Martín, "Differential and single-ended microstrip lines loaded with slotted magnetic-LC resonators," *Int. J. Antennas Propag.*, vol. 2013, ID 640514, 8 pages, May 2013.

IJAP14: J. Naqui and F. Martín, "Mechanically reconfigurable microstrip lines loaded with stepped impedance resonators and potential applications," *Int. J. Antennas Propag.*, vol. 2014, ID 346838, 8 pages, Feb. 2014.

IMS14*: J. Naqui, C. Damm, A. Wiens, R. Jakoby, L. Su, and F. Martín, "Transmission lines loaded with pairs of magnetically coupled stepped impedance resonators (SIRs): modeling and application to microwave sensors," *IEEE MTT-S Int. Microw. Symp.*, Tampa, FL, USA, Jun. 2014.

Article AWPL12

Multimode Propagation and Complex Waves in CSRR-Based Transmission Line Metamaterials

J. Naqui, M. Durán-Sindreu, A. Fernández-Prieto, F. Mesa, F. Medina, and F. Martín

Multimode Propagation and Complex Waves in CSRR-Based Transmission-Line Metamaterials

Jordi Naqui, *Student Member, IEEE*, Miguel Durán-Sindreu, *Member, IEEE*, Armando Fernández-Prieto, *Student Member, IEEE*, Francisco Mesa, *Senior Member, IEEE*, Francisco Medina, *Fellow, IEEE*, and Ferran Martín, *Fellow, IEEE*

***Abstract*—Transmission-line metamaterials based on complementary split-ring resonators (CSRRs) are shown to support forward, backward, electroinductive, and complex waves. Two CSRR-based lines are considered: 1) stopband microstrip lines simply loaded with CSRRs, and 2) passband microstrip lines loaded with CSRRs and series gaps. The effects of interresonator coupling on bandwidth enhancement are analyzed on the basis of Bloch mode theory by considering the lumped-element equivalent 4-port circuit model of the unit cell. All the propagation modes are captured by the proposed multiterminal Bloch mode theory, from an eigenmode analysis. The results are validated through a commercial eigenmode solver and supported by experimental data.**

***Index Terms*—Complementary split-ring resonators (CSRRs), complex waves, electroinductive waves, metamaterials.**

I. Introduction

IT IS well known that transmission-line metamaterials based on complementary split-ring resonators (CSRRs) [1] can support forward or backward waves [2]. It has been reported that microstrip lines loaded with CSRRs etched in the ground plane (underneath the conductor strip) behave as effective media with negative permittivity in the vicinity of CSRR resonance. Wave propagation is inhibited in this region, and the line supports forward waves outside this forbidden band. By adding series capacitive gaps in the conductor strip, above the CSRRs, the stopband switches to a passband, with backward wave propagation, as a consequence of the negative value of the effective permeability introduced by the gaps [i.e., the structure is a double negative (DNG) medium in the vicinity of resonance] [2].

It has also been reported that chains of coupled CSRRs etched in the same metallic layer can support backward waves, and such waves have been called electroinductive waves (EIWs) [3] (in parallel to the magnetoinductive waves that can be induced in chains of split-ring resonators [4], [5]). However, neither the forward and backward multimode propagation nor the presence of complex waves in CSRR-based lines has been reported so far. Complex waves are modes that may appear in lossless structures that have complex propagation constants (in spite of the absence of losses) [6]. These modes appear as conjugate pairs in reciprocal lossless structures, and they carry power in opposite directions so that if the two modes are excited with the same amplitude, they do not carry net power [7]. Complex waves have been found in several structures, such as dielectrically loaded waveguides [8], finlines [9], shielded microstrip structures [10], and, more recently, in shielded mushroom-type Sievenpiper structures [11], among others. The main purpose of this letter is to provide a whBloch mode theory formulation of CSRR-loaded lines to catch the rich phenomenology of wave propagation in these structures, where forward, backward, electroinductive, and complex waves may be induced and coexist. It is also our aim to analyze to what extent the complex modes contribute to stopband broadening in CSRR-loaded lines, useful as stopband filters.

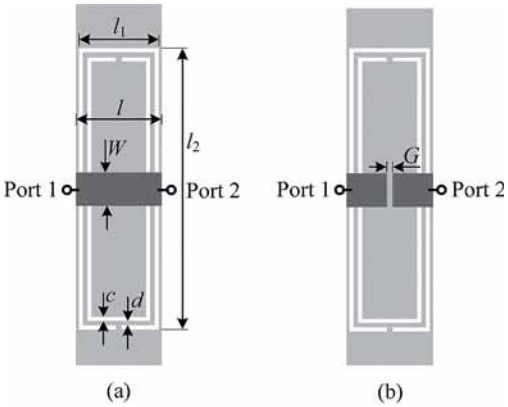

Fig. 1. Unit-cell topologies of the structures under study. (a) Microstrip line with a CSRR etched in the ground plane. (b) Microstrip line with a CSRR etched in the ground plane and with a series gap in the conductor strip. The ground plane is depicted in light gray. Dimensions are the following: $W = 1.17$ mm, $l = 3$ mm, $c = d = 0.15$ mm, $l_1 = 2.8$ mm, $l_2 = 9.8$ mm, and $G = 0.2$ mm. The considered substrate is the Rogers *RO3010* with thickness $h = 1.27$ mm, dielectric constant $\varepsilon_r = 10.2$, and loss tangent $\tan\delta = 0.0023$.

II. CSRR-Based Transmission-Line Metamaterials: Topologies and Circuit Models

The unit cells of the CSRR-loaded microstrip lines under consideration are shown in Fig. 1. The lumped-element circuit models of these structures, including the capacitive coupling between adjacent resonators (ports R2 and L2), are depicted in

Manuscript received May 24, 2012; revised July 27, 2012; accepted August 18, 2012. Date of publication August 23, 2012; date of current version September 07, 2012. This work was supported by MICIIN-Spain under Contracts TEC2010-17512, TEC2010-16948, CSD2008-00066, and TEC2011-13615-E and the Generalitat de Catalunya under Project 2009SGR-421.

J. Naqui, M. Durán-Sindreu, and F. Martín are with GEMMA/CIMITEC, Departament d'Enginyeria Electrònica, Universitat Autònoma de Barcelona, 08193 Bellaterra, Spain (e-mail: Jordi.Naqui@uab.cat; Ferran.Martin@uab.es).

A. Fernández-Prieto, F. Mesa, and F. Medina are with the Grupo de Microondas, Universidad de Sevilla, 41012 Sevilla, Spain (e-mail: Medina@us.es).

Color versions of one or more of the figures in this letter are available online at http://ieeexplore.ieee.org.

Digital Object Identifier 10.1109/LAWP.2012.2215000

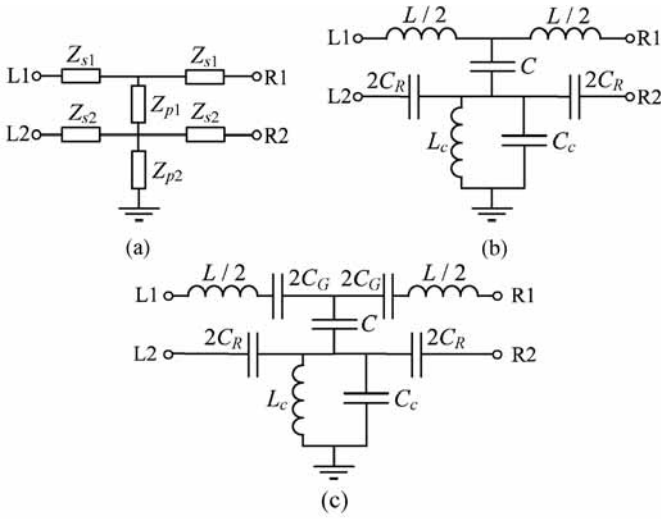

Fig. 2. Equivalent circuit models of the structures of Fig. 1, including interresonator coupling. (a) Generalized impedance model. (b) CSRR-loaded microstrip line model. (c) CSRR- and gap-loaded microstrip line model.

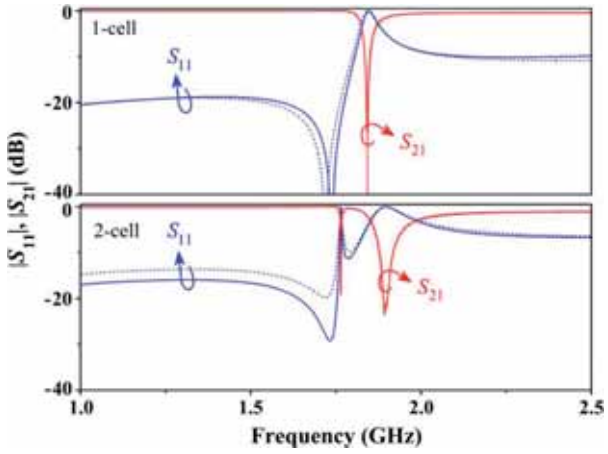

Fig. 3. Lossless transmission (S_{21}) and reflection (S_{11}) coefficients for a unit cell and for two cascaded unit cells of the structure of Fig. 1(a) and of its circuit of Fig. 2(b). The extracted circuit parameters for the unit-cell structure are the following: $L = 3.05$ nH, $C = 0.55$ pF, $L_c = 2.03$ nH, and $C_c = 3.12$ pF; for the two-cell structure, $C_R = 0.21$ pF, and C_c has been adjusted to account for interresonator coupling, i.e., $C_c = 2.98$ pF. Both the electromagnetic (solid line) and circuit (dashed line) simulations have been obtained by means of the Agilent ADS commercial software [which incorporates the full-wave electromagnetic (EM) simulator Momentum].

Fig. 2 (the first neighbor approximation for interresonator coupling is considered, and losses are neglected).

The validity of the models is restricted to those frequencies where the resonators are electrically small; this extends up to frequencies beyond the CSRR resonance, the region of interest. In the equivalent networks, L models the inductance of the microstrip section, C accounts for the electric coupling between the line and the CSRR, modeled by L_c and C_c, C_G is related to the series gap [11], and C_R describes the coupling between adjacent resonators (any CSRR-loaded line is thus described by simply cascading the 4-port networks of Fig. 2).

Fig. 3 shows the comparison between the transmission and reflection coefficients provided by the electromagnetic and circuit simulations for the unit cells of Figs. 1(a) and 2(b), respectively. CSRR dimensions are $l_1 = 0.05\lambda_g$ and $l_2 = 0.16\lambda_g$, where λ_g is the guided wavelength at the maximum reflection frequency for the single CSRR-loaded structure (i.e., 1.84 GHz). The circuit parameters are those given in the caption and have been extracted from the unit-cell structure according to the method reported in [13] (obviously C_R has been omitted). For the two-order structure, the value of C_R and the new value of C_c (the CSRR capacitance is reduced by the presence of neighboring CSRRs) have been inferred by direct fitting to the electromagnetic simulation. Notice that the transmission and reflection coefficients have been obtained by considering two-port structures, i.e., the external ports L2 (first cell) and R2 (last cell) of the model have been left opened since the CSRRs of the input and output cells are not externally fed.

III. Dispersion Relation

In order to analyze the dispersion characteristics of these CSRR-loaded lines, we can apply the Bloch mode theory to the circuits of Fig. 2. These circuits are multiport networks, and thus we can appeal to multiconductor line theory [14] in order to obtain the eigenmodes of the structure, and hence the propagation constants. Let us denote V_{L1}, V_{L2}, I_{L1}, and I_{L2} as the voltages and currents at the ports (1 and 2) of the left-hand side (subscript L) of the unit cell, and V_{R1}, V_{R2}, I_{R1}, and I_{R2} the variables at the right-hand-side ports. The variables at both sides of the network are linked through a generalized order-4 transfer matrix, according to

$$\begin{pmatrix} \boldsymbol{V}_{\mathbf{L}} \\ \boldsymbol{I}_{\mathbf{L}} \end{pmatrix} = \begin{pmatrix} \boldsymbol{A} & \boldsymbol{B} \\ \boldsymbol{C} & \boldsymbol{D} \end{pmatrix} \begin{pmatrix} \boldsymbol{V}_{\mathbf{R}} \\ \boldsymbol{I}_{\mathbf{R}} \end{pmatrix} \tag{1}$$

where $\boldsymbol{V}_{\mathbf{L}}, \boldsymbol{I}_{\mathbf{L}}, \boldsymbol{V}_{\mathbf{R}}$, and $\boldsymbol{I}_{\mathbf{R}}$ are column vectors composed of the pair of port variables, and $\boldsymbol{A}$, $\boldsymbol{B}$, $\boldsymbol{C}$, and $\boldsymbol{D}$ are order-2 matrices. The dispersion relation is obtained from the eigenmodes of the system (1), that is

$$\det \begin{pmatrix} \boldsymbol{A} - e^{\gamma l} \cdot \boldsymbol{I} & \boldsymbol{B} \\ \boldsymbol{C} & \boldsymbol{D} - e^{\gamma l} \cdot \boldsymbol{I} \end{pmatrix} = 0 \tag{2}$$

where $\boldsymbol{I}$ is the identity matrix, the propagation factor $\mathrm{e}^{\gamma l}$ is the eigenvalue, $\gamma = \alpha + \mathrm{j}\beta$ is the complex propagation constant, and l is the unit-cell length. For reciprocal, lossless, and symmetric networks, the eigenvalues can be simplified to the solutions of [15], [16]

$$\det\left(\boldsymbol{A} - \cosh(\gamma l) \cdot \boldsymbol{I}\right) = 0 \tag{3}$$

which gives

$$\cosh(\gamma l) = \frac{1}{2}\left(A_{11} + A_{22} \pm \sqrt{(A_{11} - A_{22})^2 + 4A_{12}A_{21}}\right) \tag{4}$$

where the elements of the $\boldsymbol{A}$ matrix [inferred from the network of Fig. 2(a)] are

$$\boldsymbol{A} = \boldsymbol{D}^t = \begin{pmatrix} 1 + \frac{Z_{s1}}{Z_{p1}} & -\frac{Z_{s1}}{Z_{p1}} \\ -\frac{Z_{s2}}{Z_{p1}} & 1 + \frac{Z_{s2}}{Z_{p1}} + \frac{Z_{s2}}{Z_{p2}} \end{pmatrix}. \tag{5}$$

Since it is assumed a lossless network, the elements of $\boldsymbol{A}$ (A_{ij}) are real numbers. Hence, if the radicand of the square root in (4) is positive, the propagation constant is either purely real ($\alpha \neq 0$, $\beta = 0$) or purely imaginary ($\alpha = 0$, $\beta \neq 0$), corresponding to evanescent or propagating modes, respectively. However, if the

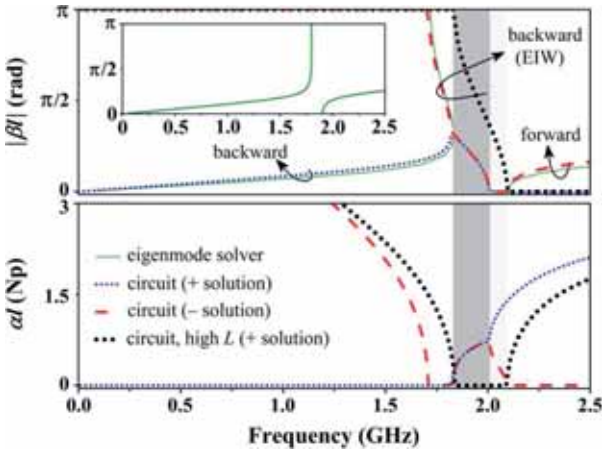

Fig. 4. Dispersion relation for the structure of Fig. 1(a) and for its equivalent circuit model of Fig. 2(b). The circuit parameters are those indicated in the caption of Fig. 3, except $C_{\rm c} = 2.84$ pF (readjusted to account for two first-neighbor adjacent couplings). The dispersion relation for the structure of Fig. 1(a) with $l = 4.8$ mm is depicted in the inset. Notice that the eigenmode solver is not able to provide neither the evanescent modes (light gray) nor the complex modes (dark gray region).

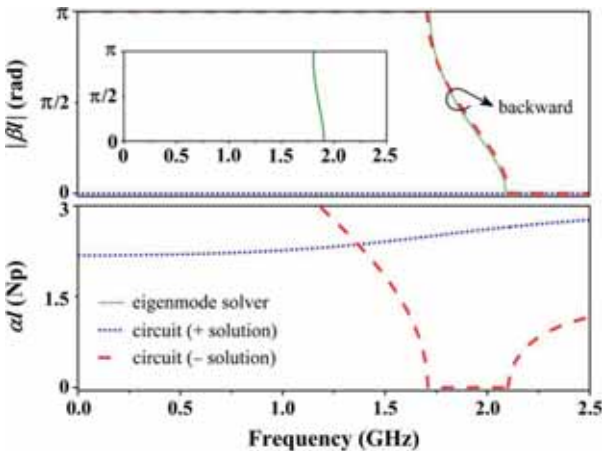

Fig. 5. Dispersion relation for the structure of Fig. 1(b) and for its circuit model of Fig. 2(c). The circuit parameters are the following: $L = 3.05$ nH, $C = 1.4$ pF, $L_{\rm c} = 2.02$ nH, $C_{\rm c} = 2.83$ pF, $C_{\rm G} = 0.2$ pF, $C_{\rm R} = 0.23$ pF. The dispersion relation for the structure of Fig. 1(b) with $l = 4.8$ mm is depicted in the inset.

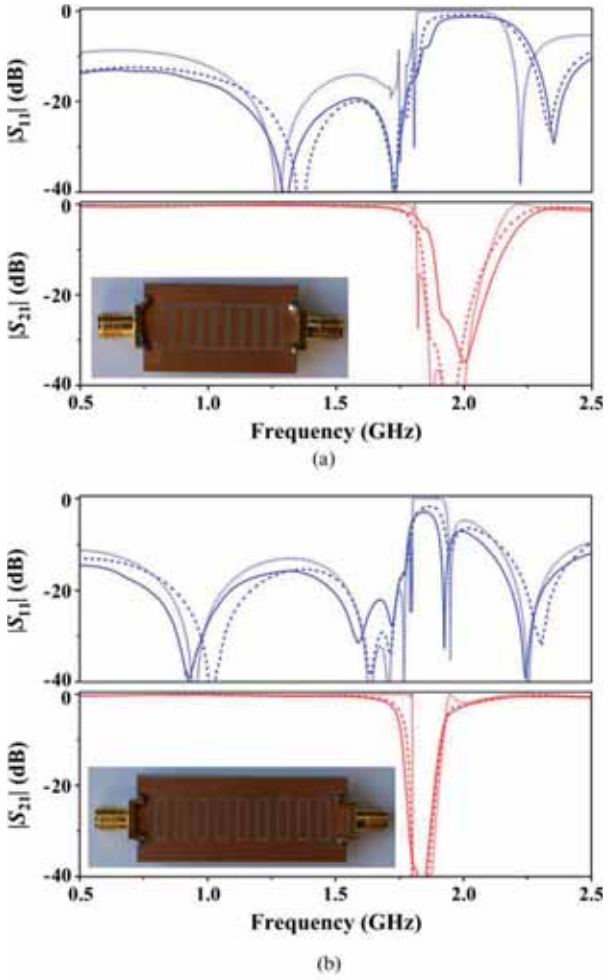

Fig. 6. Measurement (solid line), lossy electromagnetic simulation (dashed line), and circuit simulation (dotted line) of the transmission and reflection coefficients of the inset structures (only the bottom face is shown) relative to the structure of Fig. 1(a). (a) $l = 3$ mm, the circuit parameters being those indicated in Fig. 4. (b) $l = 4.8$ mm, the circuit parameters being those indicated in Fig. 4, except $C_{\rm R} = 0.017$ pF and $C_{\rm c} = 3.2$ pF. To better fit the measurement in (b), a transmission-line section of length 1.8 mm has been cascaded between consecutive $Z_{\rm s1}$ in the circuit model.

radicand in (4) is negative, the two solutions are of the form $\gamma = \alpha \pm {\rm j}\beta$, corresponding to complex modes. In order to obtain the frequency band that supports complex modes, we have forced the radicand in (4) to be negative, i.e.,

$$\left(\frac{Z_{\rm s1} - Z_{\rm s2}}{Z_{\rm p1}} - \frac{Z_{\rm s2}}{Z_{\rm p2}}\right)^2 + 4\frac{Z_{\rm s1}Z_{\rm s2}}{Z_{\rm p1}^2} < 0. \qquad (6)$$

According to (6) a necessary (although not sufficient) condition to have complex modes is an opposite sign for the reactances of $Z_{\rm s1}$ and $Z_{\rm s2}$. The expression (4), which was obtained for lossless structures, can also be used for lossy structures if low-loss dielectric and good conductors are used.

Let us first evaluate the dispersion relation of the CSRR-loaded line of Fig. 1(a), for which the pair of modal propagation constants given by expression (4) is depicted in Fig. 4. In the first allowed band, there is a region with bivalued propagation constant: one (forward) corresponding to transmission-line type propagation, and the other (backward) related to electroinductive waves. Then, a region with conjugate modes (complex modes) appears, followed by a region with $\beta = 0$ and $\alpha \neq 0$ for both modes (evanescent waves). Finally, a forward-wave transmission band emerges again. It is apparent that the stopband characteristics in the complex wave region can be interpreted as a result of the antiparallelism between the transmission line type (forward) and the electroinductive (backward) modes. To demonstrate the electroinductive nature of one of the modes in the upper region of the first allowed band, we have considered a large value of series inductance ($L \to \infty$, corresponding to an extremely narrow line), and the corresponding dispersion relation has been inferred and depicted in Fig. 4. According to this result, the backward-wave nature of the above-mentioned electroinductive waves is clear (the frequency shift is simply due to the fact that for the high-L case, the electroinductive waves propagate entirely through the interresonator capacitances).

The dispersion relation of a periodic structure composed of the unit cell of Fig. 1(a) in cascade has also been obtained by

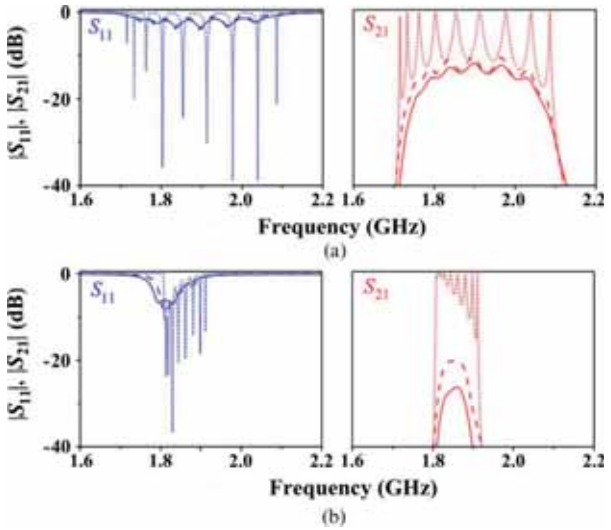

Fig. 7. Measurement (solid line), lossy electromagnetic simulation (dashed line), and circuit simulation (dotted line) of the transmission and reflection coefficients of an order-9 structure based on the topology of Fig. 1(b), whose bottom face is as in Fig. 6. (a) $l = 3$ mm, where the circuit parameters are those indicated in Fig. 5. (b) $l = 4.8$ mm, where the circuit parameters are those indicated in Fig. 5, except $C_{\rm R} = 0.02$ pF and $C_{\rm c} = 3.2$ pF. In (b), a transmission line of length 1.8 mm has been added between consecutive $Z_{\rm s1}$.

means of the eigenmode solver of CST Microwave Studio and is also plotted in Fig. 4. Good agreement with the dispersion relation inferred from the circuit model is obtained. We have also used the eigenmode solver to obtain the dispersion relation that results after increasing the unit-cell size to $l = 4.8$ mm (which corresponds to an increase in interresonator distance from 0.2 to 2 mm). For this interresonator distance (see the inset of Fig. 4), the electroinductive and complex modes are not present, and the fractional bandwidth of the stopband is reduced from 13.3% to 5.5%. These results indicate that, by reducing the distance between adjacent resonators, the forbidden band is enhanced due to the presence of complex modes; the power contribution of the individual modes cancel each other, and this expands the stopband beyond the evanescent modes region (however, under some circumstances, the individual complex modes may be selectively excited [7]).

The dispersion diagram for the structure of Fig. 1(b) is depicted in Fig. 5. As expected, a backward-wave transmission band is obtained. Bandwidth broadens as interresonator coupling increases since electroinductive waves aid backward wave propagation.

IV. Experimental Results

To experimentally validate the effects of interresonator coupling on bandwidth enhancement, four order-9 structures have been fabricated: two of them with the unit cells of Fig. 1; the other two by considering $l = 4.8$ mm. The measured transmission and reflection coefficients are in good agreement with those given by the electromagnetic and circuit simulation (Figs. 6 and 7). For the stopband structure, the measured fractional stopband bandwidth (computed at -20 dB) is 9.4% and 6.2% for the structure of Fig. 6(a) and (b), respectively. There is also good agreement between the measured stopbands and passbands and those inferred from the dispersion relation. Hence, the dispersion relation inferred from the multiterminal circuit model is a powerful tool to gain insight into the passbands and stopbands in CSRR-loaded lines.

V. Conclusion

It has been shown that transmission lines loaded with tightly coupled CSRRs exhibit forward, backward (electroinductive-related), and complex modes. If series gaps are etched in the conductor strip, the lines exhibit backward wave propagation, with a bandwidth enhanced by the presence of electroinductive waves. The structures have been analyzed from multiport Bloch mode theory applied to their equivalent circuit models, and the dispersion characteristics have been validated by means of an eigenmode solver. Finally, the effects of interresonator coupling on bandwidth enhancement have been experimentally validated. According to the present study, the destructive or constructive interference of modes supported by the lines plays a significant role in widening the stopband or the backward-wave passband in CSRR-loaded lines.

References

[1] F. Falcone, T. Lopetegi, J. D. Baena, R. Marqués, F. Martín, and M. Sorolla, "Effective negative-ε stopband microstrip lines based on complementary split ring resonators," *IEEE Microw. Wireless Comp. Lett.*, vol. 14, no. 6, pp. 280–282, Jun. 2004.

[2] F. Falcone, T. Lopetegi, M. A. G. Laso, J. D. Baena, J. Bonache, R. Marqués, F. Martín, and M. Sorolla, "Babinet principle applied to the design of metasurfaces and metamaterials," *Phys. Rev. Lett.*, vol. 93, p. 197401, Nov. 2004.

[3] M. Beruete, F. Falcone, M. J. Freire, R. Marqués, and J. D. Baena, "Electroinductive waves in chains of complementary metamaterial elements," *Appl. Phys. Lett.*, vol. 88, p. 083503, Feb. 2006.

[4] R. R. A. Syms, E. Shamonina, V. Kalinin, and L. Solymar, "A theory of metamaterials based on periodically loaded transmission lines: Interaction between magnetoinductive and electromagnetic waves," *J. Appl. Phys.*, vol. 97, p. 064909, Mar. 2005.

[5] M. J. Freire, R. Marqués, F. Medina, M. A. G. Laso, and F. Martín, "Planar magneto-inductive wave transducers: Theory and applications," *Appl. Phys. Lett.*, vol. 85, pp. 4439–4441, Nov. 2004.

[6] T. Tamir and A. A. Oliner, "Guided complex waves," *Proc. Inst. Elect. Eng.*, vol. 110, pp. 310–334, 1963.

[7] R. Islam and G. V. Eleftheriades, "On the independence of the excitation of complex modes in isotropic structures," *IEEE Trans. Antennas Prop.*, vol. 58, no. 5, pp. 1567–1578, May 2010.

[8] P. J. B. Clarricoats and K. R. Slinn, "Complex modes of propagation in dielectric loaded circular waveguide," *Electron. Lett.*, vol. 1, pp. 145–146, 1965.

[9] A. S. Omar and K. F. Schünemann, "The effect of complex modes at finline discontinuities," *IEEE Trans. Microw. Theory Tech.*, vol. MTT-34, no. 12, pp. 1508–1514, Dec. 1986.

[10] W. Huang and T. Itoh, "Complex modes in lossless shielded microstrip lines," *IEEE Trans. Microw. Theory Tech.*, vol. 36, no. 1, pp. 163–164, Jan. 1988.

[11] F. Elek and G. V. Eleftheriades, "Dispersion analysis of the shielded Sievenpiper structure using multiconductor transmission line theory," *IEEE Microw. Wireless Compon. Lett.*, vol. 14, no. 9, pp. 434–436, Sep. 2004.

[12] J. Bonache, M. Gil, O. García-Abad, and F. Martín, "Parametric analysis of microstrip lines loaded with complementary split ring resonators," *Microw. Opt. Technol. Lett.*, vol. 50, pp. 2093–2096, Aug. 2008.

[13] J. Bonache, M. Gil, I. Gil, J. Garcia-García, and F. Martín, "On the electrical characteristics of complementary metamaterial resonators," *IEEE Microw. Wireless Compon. Lett.*, vol. 16, no. 10, pp. 543–545, Oct. 2006.

[14] R. Mongia, I. Bahl, and P. Barthia, *RF and Microwave Coupled Line Circuits*. Norwood, MA: Artech House, 1999.

[15] J. Shekel, "Matrix analysis of multi-terminal transducers," *Proc. IRE*, vol. 42, no. 5, pp. 840–847, May 1954.

[16] R. Islam, M. Zedler, and G. V. Eleftheriades, "Modal analysis and wave propagation in finite 2D transmission-line metamaterials," *IEEE Trans. Antennas Propag.*, vol. 59, no. 5, pp. 1562–1570, May 2011.

Article JAP14

Effects of inter-resonator coupling in split ring resonator loaded metamaterial transmission lines

J. Naqui, A. Fernández-Prieto, F. Mesa, F. Medina, and F. Martín

JOURNAL OF APPLIED PHYSICS **115**, 194903 (2014)

Effects of inter-resonator coupling in split ring resonator loaded metamaterial transmission lines

J. Naqui,[1] A. Fernández-Prieto,[2] F. Mesa,[2] F. Medina,[2] and F. Martín[1]
[1]*GEMMA/CIMITEC, Departament d'Enginyeria Electrònica, Universitat Autònoma de Barcelona, 08193 Bellaterra, Barcelona, Spain*
[2]*Grupo de Microondas, Universidad de Sevilla, 41012 Sevilla, Spain*

(Received 9 January 2014; accepted 17 March 2014; published online 20 May 2014)

This paper investigates the effects of inter-resonator coupling in metamaterial transmission lines loaded with split ring resonators (SRRs). The study is performed from Bloch mode theory applied to the multiport equivalent circuit model of the unit cell of such artificial lines. From this analysis, it follows that the stopband bandwidth, inherent to SRR-loaded lines, is enhanced as inter-resonator coupling strengthens, and this enhancement is attributed to the presence of complex modes. The theoretical results are corroborated through calculation of the dispersion relation using a full-wave eigenmode solver, and also by measuring the frequency response of SRR-loaded lines with different inter-resonator distance and, hence, coupling. © *2014 AIP Publishing LLC*. [http://dx.doi.org/10.1063/1.4876444]

I. INTRODUCTION

Transmission lines periodically loaded with split ring resonators (SRRs)[1] inhibit wave propagation in the vicinity of the SRR fundamental resonance.[2,3] As long as the SRRs and their spacing are electrically small, these SRR-loaded lines can be considered to be one-dimensional effective media exhibiting a negative effective permeability in a narrow band above SRR resonance (the effective permeability of these structures is described by the Lorenz model[4,5]). Actually, the stopband of these lines includes not only the region where the effective permeability is negative but also a narrow band below the resonance frequency of the SRRs where the effective permeability may be interpreted to be highly positive. Additionally, according to Ref. 6, in the event that SRRs are coupled to each other, the effective permeability becomes complex (under lossless conditions) within a region that emerges in the transition from positive to negative values of its real part. Nevertheless, in the present work the interpretation of the stopband is based on the analysis of Bloch mode theory, rather than on the effective permeability.

SRR-loaded lines have been applied to the implementation of stopband filters, where bandwidth has been controlled by slightly varying the dimensions of the SRR array.[7] The resulting structures can be viewed as quasi-periodic transmission lines where the effective permeability varies along the line. With this strategy, it is clear that the resonance frequency of the different SRRs can be slightly tuned along the desired frequency range, with the result of a broadened stopband. Alternatively, bandwidth can be enhanced by using tightly coupled SRRs. This approach was recently considered in transmission lines periodically loaded with complementary split ring resonators (CSRRs),[8] formerly proposed in Ref. 9. Subsequently, this approach was applied in Ref. 10 to widen the common mode suppressed band of differential microstrip lines.

In order to achieve significant inter-resonator coupling, the CSRRs in Ref. 8 were chosen to be rectangular-shaped (the long side being oriented along the transversal direction of propagation) and separated by very small distances. As found therein, the relevant feature is that rejection bandwidth enhancement in CSRR-loaded lines with tightly coupled resonators can be related to the presence of complex modes supported by the corresponding periodic infinite structure. These modes, in spite of the absence of losses, have complex propagation constants and appear as conjugate pairs in reciprocal structures. Since the power contribution of the individual modes is in opposite direction to each other, complex modes do not generally carry net power.[11–17] The existence of these modes in CSRR-loaded lines was demonstrated through Bloch mode theory, by analyzing the equivalent four-port circuit model of the unit cell, and by obtaining the modal solutions through a full-wave eigenmode solver.[8] Analogously, the theoretical analysis of SRR-loaded lines with coupled resonators carried out in Ref. 6 also leads to a pair of complex propagation constants in the region where a complex effective permeability is exhibited.

In this paper, we study the effects of coupling in transmission lines loaded with pairs of SRRs magnetically coupled to the nearest neighboring pairs of resonators. The magnetic coupling between resonators of adjacent cells is thus accounted for in the model. Therefore, the resulting lumped element equivalent circuit model of the unit cell is a four-port circuit, in parallel to the four-port circuit that describes the unit cell of a CSRR-loaded line with inter-resonator coupling. The dispersion relation of SRR-loaded lines, inferred from Bloch mode analysis applied to the circuit model, was already derived in a previous publication by the authors.[18] In this paper, further details on the derivation of such relation are given. Moreover, the modal solutions obtained theoretically are validated by obtaining the dispersion relation by means of a numerical eigenmode solver. Finally, we report the characterization of two fabricated structures with different level of coupling between SRRs, in order to experimentally confirm the effects of coupling on bandwidth enhancement.

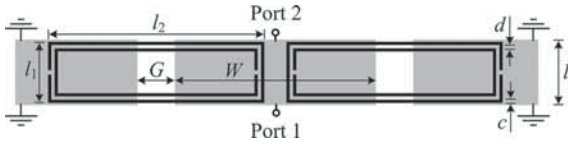

FIG. 1. Typical unit cell of a CPW transmission line loaded with a pair of SRRs designed to enhance coupling between resonators of neighboring cells. Dimensions are: $W = 9.1\,\text{mm}$, $G = 1.7\,\text{mm}$, $l = 3\,\text{mm}$, $c = d = 0.15\,\text{mm}$, $l_1 = 2.8\,\text{mm}$, and $l_2 = 9.8\,\text{mm}$. The considered substrate is *Rogers RO3010* with thickness $h = 1.27\,\text{mm}$ and dielectric constant $\varepsilon_r = 11.2$. The Bloch wave propagates from port 1 to port 2.

II. TOPOLOGY AND CIRCUIT MODEL OF THE SRR-LOADED LINES

The topology of the considered SRR-loaded lines (unit cell) is depicted in Fig. 1. It consists of a coplanar waveguide (CPW) transmission line loaded with pairs of rectangular SRRs etched on the back side of the substrate. It is important to highlight that the symmetry plane of the SRRs (crossing the gaps) is orthogonally oriented to the line axis. This orientation is necessary to guarantee that the line is only capable of exciting the SRR fundamental resonance through the magnetic coupling. With different orientations, mixed coupling is required for an accurate description of the structure, as discussed and reported in Ref. 19. Obviously, mixed coupling between the line and resonators makes the analysis of SRR-loaded lines with inter-resonator coupling much more cumbersome, and, for this reason, we have considered such SRR orientation in the present study. Thus, with this SRR orientation, the lumped-element equivalent circuit model of these structures, including the magnetic coupling between SRRs of neighboring cells, is depicted in Fig. 2(a) (the nearest-neighbor interaction approximation is considered, and losses are neglected).

The validity of the model is restricted to those frequencies where the resonators are electrically small enough; this extends up to frequencies beyond the SRR fundamental resonance, the region of interest. In the model, L and C are the per-section line inductance and capacitance, respectively; the SRR is described by the capacitance C_s and the inductance L_s; M is the mutual inductance between the line and the SRRs; finally, inter-resonator coupling is accounted for through the mutual inductance M_R. Note that the magnetic coupling between coplanar SRRs of adjacent cells is negative, and the proper modeling of the magnetic coupling sign is mandatory, i.e., the sign cannot be disregarded. Otherwise, the frequency response predicted by the circuit will not be able to describe correctly the behavior of the SRR-loaded lines. It is also important to highlight that when the SRRs of the same unit cell are close together, there can be positive magnetic coupling between them. However, this coupling is neglected here because its only effect is to decrease the resonance frequency.

In order to simplify the analysis of the circuit model, it is convenient to combine the parallel connection of the SRRs belonging to the same unit cell and to transform each pair of inductances coupled by the mutual inductance M_R to its equivalent T-circuit.[20] This leads us to the circuit of Fig. 2(b), from which it is possible to identify the four-port unit cell of Fig. 2(c). Qualitatively, this unit cell is composed of a conventional transmission line-type circuit magnetically coupled to a secondary propagating structure. This latter structure supports a kind of backward waves that have been studied in depth in Refs. 21–26 and have been called magnetoinductive waves (MIWs). MIWs propagate within a narrow frequency band in the vicinity of SRR resonance, and the associated bandwidth is dependent on how strongly the resonators are coupled to each other. The stronger is the

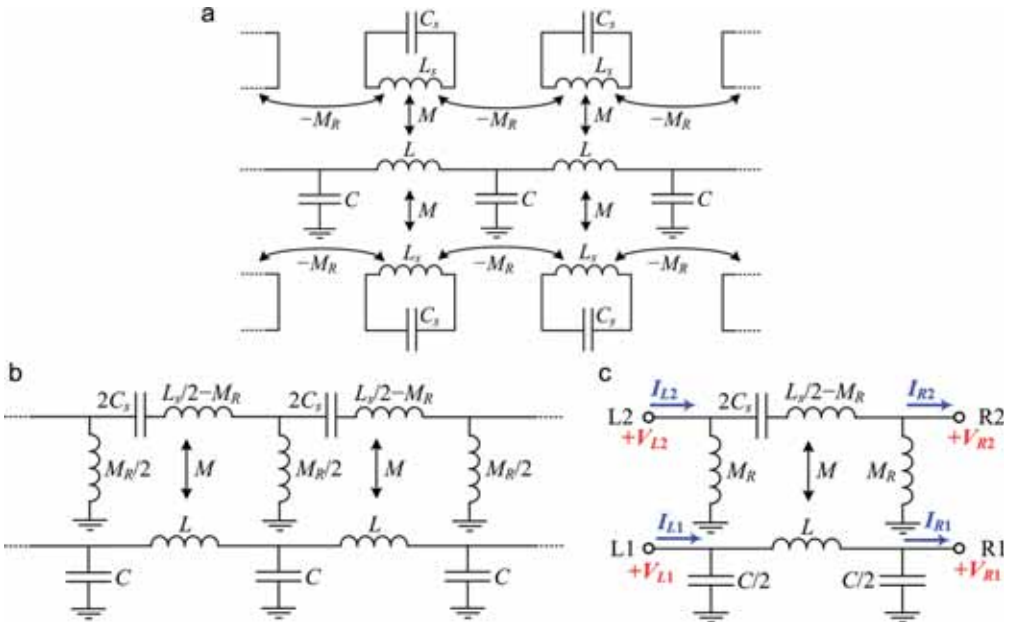

FIG. 2. Lumped-element equivalent circuit model of a periodic structure composed of an array of unit cells as the ones shown in Fig. 1, including magnetic coupling between resonators of adjacent cells; (a) model with mutual inductance between resonators, (b) transformed model, and (c) four-port unit cell model indicating the port voltages and currents relative to the calculation of the transfer *ABCD* matrix. (a) and (b) are reprinted with permission from Naqui *et al.*, *International Conference on Electromagnetics Advanced Applications (ICEAA)*, Copyright 2013 by IEEE.[18]

interaction between the resonant elements, the wider is the passband of the MIWs.[26] As multiconductor theory predicts that the resulting unit cell can propagate two modes,[27] forward and backward waves are expected to coexist at some frequency band.

III. BLOCH MODE ANALYSIS AND DISPERSION RELATION

The dispersion characteristics of these SRR-loaded lines can be obtained from Bloch mode theory applied to the four-port network of Fig. 2(c). Let us denote V_{Li} and I_{Li} as the voltages and currents at the ports ($i = 1, 2$) of the left hand-side of the unit cell, and V_{Ri} and I_{Ri} as the variables at the right hand-side ports. The variables at both sides of the network are linked through a generalized order-4 transfer matrix, according to

$$\begin{pmatrix} \boldsymbol{V_L} \\ \boldsymbol{I_L} \end{pmatrix} = \begin{pmatrix} \boldsymbol{A} & \boldsymbol{B} \\ \boldsymbol{C} & \boldsymbol{D} \end{pmatrix} \begin{pmatrix} \boldsymbol{V_R} \\ \boldsymbol{I_R} \end{pmatrix}, \tag{1}$$

where $\boldsymbol{V_L}$, $\boldsymbol{I_L}$, $\boldsymbol{V_R}$, and $\boldsymbol{I_R}$ are column vectors composed of the pair of port variables, and $\boldsymbol{A}$, $\boldsymbol{B}$, $\boldsymbol{C}$, and $\boldsymbol{D}$ are order-2 matrices.

The dispersion relation is obtained from the eigenmodes of the system (1)

$$\det\begin{pmatrix} \boldsymbol{A} - e^{\gamma l} \cdot \boldsymbol{I} & \boldsymbol{B} \\ \boldsymbol{C} & \boldsymbol{D} - e^{\gamma l} \cdot \boldsymbol{I} \end{pmatrix} = 0, \tag{2}$$

where $\boldsymbol{I}$ is the identity matrix, the propagation factor $e^{\gamma l}$ is the eigenvalue, $\gamma = \alpha + j\beta$ is the complex propagation constant, and l is the unit cell length. For reciprocal, lossless, and symmetric networks, the eigenvalues can be simplified to the solutions of[28,29]

$$\det(\boldsymbol{A} - \cosh(\gamma l) \cdot \boldsymbol{I}) = 0, \tag{3}$$

which gives

$$\cosh(\gamma l) = \frac{1}{2}\left(A_{11} + A_{22} \pm \sqrt{(A_{11} - A_{22})^2 + 4A_{12}A_{21}}\right), \tag{4}$$

where the elements of the $\boldsymbol{A}$ matrix (inferred from the network of Fig. 2(c) as detailed in Appendix A) are

$$\boldsymbol{A} = \boldsymbol{D}^t = \begin{pmatrix} 1 - \dfrac{LC}{2}\omega^2 & \dfrac{M}{M_R} \\ -\dfrac{MC}{2}\omega^2 & \dfrac{1}{2M_R}\left(L_s - \dfrac{1}{C_s\omega^2}\right) \end{pmatrix}. \tag{5}$$

Since the network of Fig. 2(c) is lossless, the elements of $\boldsymbol{A}$ (A_{ij}) are real numbers. Hence, if the expression under the square-root in (4) is positive, the propagation constant is either purely real ($\alpha \neq 0$, $\beta = 0$) or purely imaginary ($\alpha = 0$, $\beta \neq 0$), corresponding to evanescent or propagating modes, respectively. However, if that expression is negative, the two solutions are of the form $\gamma = \alpha \pm j\beta$, corresponding to complex modes. The frequency band that supports complex modes is thus obtained by forcing the expression under the square-root in (4) to be negative. Since complex modes do not carry net power, the frequency band supporting such modes is a rejection band, despite of being of different nature than that associated to evanescent modes (where $\alpha \neq 0$, $\beta = 0$).

Inspection of (4) and (5) reveals that a necessary condition for the presence of complex modes is that M is different from zero (this is always the case, unless the substrate of the considered CPW is extremely thick). Notice that $M = 0$ means that the host line and the SRR array are decoupled. Under this situation, the second term of the expression under the square-root in (4) is null, and hence, the square root is a real number, preventing the appearance of complex modes. Indeed, the two modal solutions for $M = 0$ are

$$\cosh(\gamma l) = A_{11} = 1 - \frac{LC}{2}\omega^2, \tag{6}$$

corresponding to the dispersion relation of a lossless transmission line described by the well-known LC ladder network, and

$$\cosh(\gamma l) = A_{22} = \frac{1}{2M_R}\left(L_s - \frac{1}{C_s\omega^2}\right), \tag{7}$$

that is, the dispersion of an array of inductively (edge) coupled SRRs, where MIWs are supported in a narrow frequency band in the vicinity of SRR resonance. Note that MIWs can exist as long as the reactance of the series resonator (between the ports L2 and R2) is capacitive and, obviously, this is another condition for supporting complex modes.

The dispersion relation (4) in the limit $M_R \to 0$, corresponding to negligible inter-resonator coupling, is also interesting to obtain. Under these conditions, the following result arises (see Appendix B):

$$\cosh(\gamma l) = 1 - \frac{LC}{2}\omega^2 + \frac{M^2C\omega^2}{\left(L_s - \frac{1}{C_s\omega^2}\right)}. \tag{8}$$

This is the dispersion relation of an SRR-loaded line without coupling between SRRs, which can be inferred from the bi-port model reported in Ref. 30 [and depicted in Fig. 3(b)] by applying Bloch mode analysis (see also Appendix B).

Although low-loss microwave substrates and very low-resistivity conductors are used, some losses are always present in real SRR-loaded lines. However, the dispersion relation given by (4) can still be considered as a reasonable approximation to the actual dispersion of the structure. Indeed, the analysis excluding losses suffices for the purposes of this

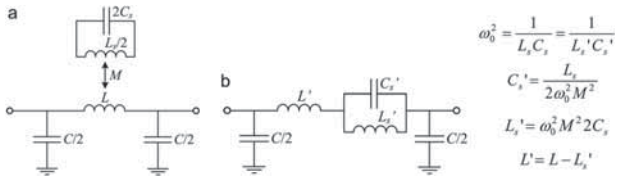

FIG. 3. Lumped element equivalent circuit model (unit cell) of the structure in Fig. 1 without inter-resonator coupling (a), and the corresponding transformed model (b). Reprinted with permission from Naqui *et al.*, *International Conference on Electromagnetics Advanced Applications (ICEAA)*, Copyright 2013 by IEEE.[18]

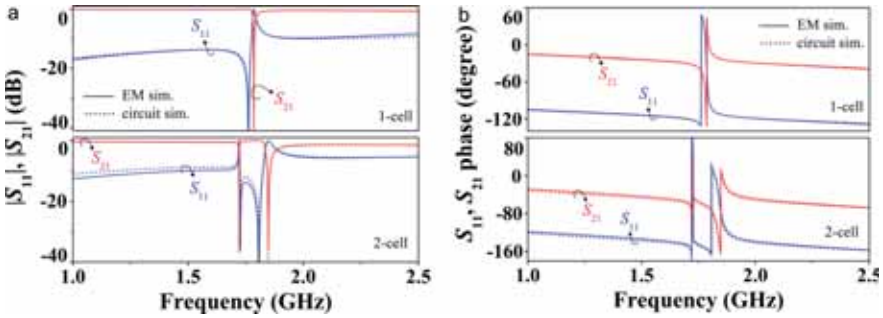

FIG. 4. Magnitude (a) and phase (b) of the lossless transmission (S_{21}) and reflection (S_{11}) coefficients for a unit cell and for two cascaded unit cells of the structure in Fig. 1. The extracted circuit parameters are: $L = 1.01$ nH, $C = 1.40$ pF, $L_s = 17.66$ nH, $C_s = 0.45$ pF, $M = 0.72$ nH, and $M_R = 1.17$ nH. (a) is reprinted with permission from Naqui *et al.*, *International Conference on Electromagnetics Advanced Applications (ICEAA)*, Copyright 2013 by IEEE.[18]

paper, i.e., the investigation of the effects of inter-resonator coupling on the dispersion characteristics and frequency response. In any case, the effects of losses may be easily evaluated by merely including resistors in the circuit model.

It is also worth mentioning that the dispersion characteristics of transmission lines loaded with SRRs (considering coupled and decoupled SRRs) and metallic rods was analyzed in Ref. 23. It was proven that interaction between MIWs propagating through an array of SRRs and incident electromagnetic waves (modeled by the equivalent circuit of a transmission line) may exist leading to the appearance of a stopband. Subsequently, an extended analysis was reported in Ref. 6 without the rods (i.e., by considering the same structure as in this work), and that stopband was found to be due to the presence of complex modes. In comparison to Refs. 6 and 23, in this paper, we obtain the dispersion relation from the multiport equivalent circuit providing the details of the calculation of the transfer matrix, and we consider a real device based on planar transmission lines and rings, instead of assuming a theoretical generic system. Moreover, we provide numerical results inferred from an eigenmode solver and experimental evidence of stopband bandwidth enhancement caused by inter-resonator coupling.

A. Parameter extraction and equivalent circuit model validation

We have extracted the circuit parameters of the structure of Fig. 1. To this end, the electromagnetic simulation of an isolated unit cell was performed (by the *Agilent Momentum* commercial software). The circuit model of a decoupled unit cell is depicted in Fig. 3(a). We have extracted the circuit elements of the transformed model of Fig. 3(b) following the procedure reported in Ref. 30. Then, L_s has been estimated as the self-inductance of an isolated (without the CPW structure) single split ring with the same average radius and ring width as the considered SRRs (in a quasi-static approximation, the total current flowing on the pair of SRR rings is independent of the position on the SRR[5]). Thus, the equivalent inductance seen between the end terminals of the single split ring has been extracted from the electromagnetic simulation. By using the estimated L_s (17.66 nH), the circuit elements of Fig. 3(a) have been obtained from the indicated transformation equations. Finally, we have inferred the mutual inductance M_R of the circuits of Fig. 2 by curve fitting the circuit simulation to the electromagnetic simulation of a 2-cell structure. It is important to realize that since the SRRs of the input/output cells are not externally fed, the ports L2 (input cell) and R2 (output cell) have been left opened. Therefore, the transmission and reflection coefficients are referred to a two-port circuit (L1 and R1) rather than to the four-port circuit of the proposed model.

The extracted parameters are listed in the caption of Fig. 4. The comparison between the electromagnetic and circuit simulations of a unit cell and of two cascaded unit cells is depicted in Fig. 4, where good agreement is observed in the transmission and reflection coefficients. Concerning the modeling of higher order structures, Fig. 5(a) shows the frequency response for nine cascaded unit cells. As can be seen,

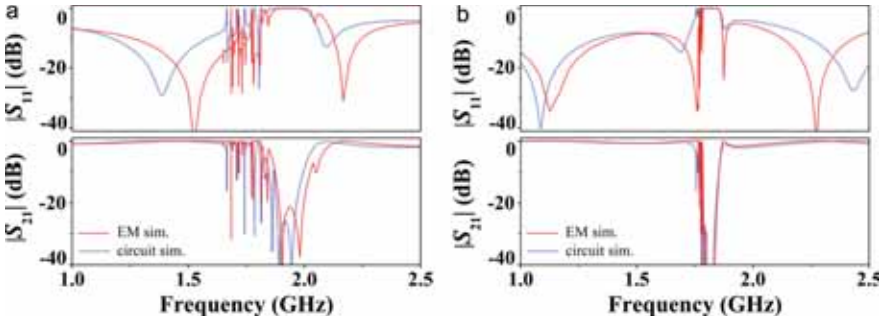

FIG. 5. Lossless electromagnetic and circuit simulations of the transmission and reflection coefficients (magnitude) for nine cascaded cells of the structure in Fig. 1 for (a) $l = 3$ mm and (b) $l = 4.8$ mm (the inter-resonator separation has been increased from 0.2 mm to 2 mm). The circuit parameters are those indicated in the caption of Fig. 4, with the exception of $M_R = 0.22$ nH in (b). Furthermore, in (b), a CPW section of 1.8 mm length has been cascaded between the port R1 and the port L1 of the contiguous cell in the circuit model.

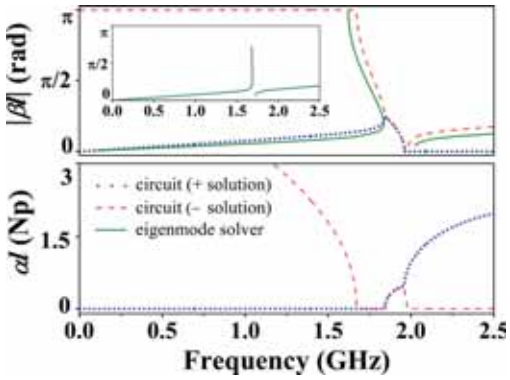

FIG. 6. Dispersion diagram for the structure of Fig. 1 inferred from an eigenmode solver and from its equivalent circuit model of Fig. 2(c). The circuit parameters are those indicated in the caption of Fig. 4. The dispersion diagram for the structure of Fig. 1 with $l = 4.8$ mm is depicted in the inset. The attenuation constant α is not provided by the eigenmode solver.

the central frequency of the stopband shifts upwards as the number of cells increases, being this effect produced by the negative inter-resonator coupling. It can also be observed that the stopband inferred from the electromagnetic simulation is even slightly more shifted than the one predicted by the circuit simulation. It has been found (by including additional couplings between non-adjacent cells) that this discrepancy is due to the assumption of first neighbor approximation. In this regard, as Fig. 5(b) confirms, an increase in the inter-resonator distance reduces the impact on the frequency response shift caused by such approximation. In any case, the first neighbor approximation suffices for the purpose of the present work.

It is also important to point out that inter-resonator coupling splits the SRR resonance frequencies, so that the number of transmission zeros equals the number of resonators. Moreover, the stronger the coupling, the stronger will be the the splitting.[20] As a result, the stopband bandwidth broadens with inter-resonator coupling, although this enhancement is limited since it saturates with relatively few cells. For instance, the stopband bandwidth (computed at -20 dB) obtained from the circuit simulation for an order-9 structure [Fig. 5(a)] ranges from 1.879 GHz to 1.966 GHz. This corresponds to a bandwidth similar to the maximum achievable bandwidth that will be given by the dispersion relation for an infinite structure in subsection III B.

B. Dispersion relation validation

Once the circuit parameters have been extracted, we can obtain the pair of modal propagation constants given by expression (4). The results are depicted in Fig. 6. As in Ref. 8, in the first allowed band, there is a region with bi-valued propagation constant: one (forward) corresponding to transmission-line type propagation and the other (backward) related to magnetoinductive waves. Then, a region with a pair of conjugate complex propagation constants (complex modes) appears where forward and backward waves interfere with each other, followed by a region of evanescent waves. Finally, a forward wave transmission band emerges again. Hence, the enhancement of the stopband due to inter-resonator coupling is explained by the appearance of complex modes in the low frequency region of that stopband (the complex modes exist from 1.843 GHz to 1.961 GHz, and the evanescent modes extends up to 1.977 GHz). However, the magnetic coupling between SRRs of adjacent cells is limited and so it is bandwidth broadening.

We have also obtained the dispersion relation of a periodic structure composed of a cascade of the unit cell in Fig. 1 by means of the full-wave eigenmode solver of *CST Microwave Studio*. The results, also depicted in Fig. 6, reveal that there is good agreement with the analytical dispersion curve predicted by the circuit model (the bi-valued region is perfectly predicted by the eigenmode solver). However, since there is no electromagnetic field pattern with net current transfer in the stopband, the tool is not able to provide the dispersion curves in that region.

For comparison purposes, we have also considered a structure with higher inter-resonator distance providing much weaker coupling. The dispersion diagram, depicted in the inset of Fig. 6, reveals that the stopband bandwidth is significantly narrower. Therefore, these dispersion diagrams indicate that most of the stopband in the structure of Fig. 1 is related to the presence of complex, rather than evanescent, modes. In other words, as long as inter-resonator coupling is significant, complex modes may be the dominant mechanism of signal rejection (in the vicinity of SRR fundamental resonance) of these SRR-loaded structures.

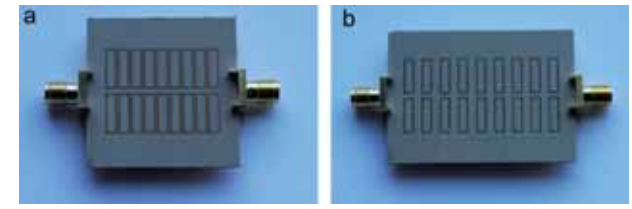

FIG. 7. Photograph of the bottom face of the fabricated order-9 structures composed of the unit cell in Fig. 1 with (a) $l = 3$ mm and (b) $l = 4.8$ mm.

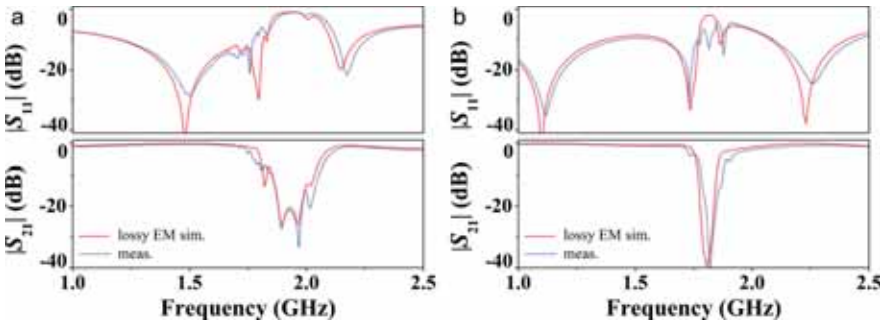

FIG. 8. Measurement and lossy electromagnetic simulation of the transmission and reflection coefficients (magnitude) of the structures in Fig. 7; (a) $l = 3$ mm and (b) $l = 4.8$ mm. The loss tangent in *Rogers RO3010* is $\tan\delta = 0.0023$.

IV. EXPERIMENTAL RESULTS

To experimentally validate the effects of inter-resonator coupling on bandwidth enhancement, two order-9 structures have been fabricated (Fig. 7): One of them with the unit cell of Fig. 1; the other by considering $l = 4.8$ mm. The measured transmission and reflection coefficients are in good agreement with those given by the lossy electromagnetic simulation (see Fig. 8). The measured fractional stopband bandwidth (computed at -20 dB) is 5.2% and 2.4% for the structures of Figs. 7(a) and 7(b), respectively. The measured stopbands are also in accordance with those obtained from the dispersion relation. Hence, the dispersion relation inferred from the multi-terminal circuit model is a powerful tool to gain insight into the stopband and the effects of inter-resonator coupling in SRR-loaded lines.

V. CONCLUSIONS

It has been demonstrated that SRR-loaded lines with tightly coupled resonators exhibit forward (transmission line-type), backward (magnetoinductive-related), and complex modes. The structures have been analyzed using multi-port Bloch mode theory applied to the lumped element equivalent circuit model, and the dispersion characteristics have been obtained. It has been found that complex modes are responsible for bandwidth enhancement of the stopband. These complex modes have been interpreted as the destructive interference between forward and backward waves. Since backward waves are supported by the chain of SRRs, inter-resonator coupling is absolutely mandatory for complex modes to emerge. Indeed, the behavior of SRR-loaded lines with strongly coupled resonators is very similar to that of CSRR-loaded lines.[8] The main difference is the nature of the propagating waves in the frequency region that supports backward waves (bi-valued region with multimode forward and backward propagation). In CSRR-loaded lines, the backward waves are electroinductive-like waves, whereas in SRR-loaded lines, backward transmission is due to magnetoinductive waves. The theoretical results have been validated by means of a numerical eigenmode solver, able to provide the dispersion relation, and also by measuring the transmission and reflection characteristics of two fabricated SRR-loaded lines (one with weak inter-SRR coupling, and the other one with significant coupling).

ACKNOWLEDGMENTS

This work has been supported by MICIIN-Spain (Contract No. TEC2010-17512, TEC2010-16948, CSD2008-00066, and TEC2011-13615-E), and by Generalitat de Catalunya (Project No. 2009SGR-421). Jordi Naqui has been awarded with a FPU Grant by MECD-Spain (Reference AP2010-0431).

APPENDIX A: CALCULATION OF THE *A* MATRIX ELEMENTS

The $\boldsymbol{A}$ matrix is an order-2 matrix that links the voltages of the pair of ports at both sides of the network of Fig. 2(c) under the condition $I_{R1} = I_{R2} = 0$, that is,

$$\begin{pmatrix} V_{L1} \\ V_{L2} \end{pmatrix} = \begin{pmatrix} A_{11} & A_{12} \\ A_{21} & A_{22} \end{pmatrix} \begin{pmatrix} V_{R1} \\ V_{R2} \end{pmatrix} \Bigg|_{I_{R1}=I_{R2}=0}. \tag{A1}$$

From (A1), it follows that

$$A_{11} = \frac{V_{L1}}{V_{R1}} \Bigg|_{V_{R2}=0}, \tag{A2}$$

$$A_{22} = \frac{V_{L2}}{V_{R2}} \Bigg|_{V_{R1}=0}, \tag{A3}$$

$$A_{12} = \frac{V_{L1}}{V_{R2}} \Bigg|_{V_{R1}=0}, \tag{A4}$$

$$A_{21} = \frac{V_{L2}}{V_{R1}} \Bigg|_{V_{R2}=0}. \tag{A5}$$

The derivation of A_{11} is straightforward since conditions $I_{R1} = I_{R2} = 0$ and $V_{R2} = 0$ means that there is not current flow across the inductance $L_s/2 - M_R$ in the circuit of Fig. 2(c). Therefore, we can write the voltage Kirchhoff's law between ports L1 and R1 (in the frequency domain) as

$$V_{L1} = j\omega L \cdot V_{R1} \cdot j\omega \frac{C}{2} + V_{R1}. \tag{A6}$$

From (A6), using (A2), the expression for A_{11} given in (5) is obtained.

Similarly, A_{22} is inferred from (A3) and

$$V_{L2} = \left(j\omega \left(\frac{L_s}{2} - M_R \right) + \frac{1}{j\omega 2C_s} \right) \cdot V_{R2} \cdot \frac{1}{j\omega M_R} + V_{R2}, \tag{A7}$$

which is simply the voltage Kirchhoff's law between ports L2 and R2 when $I_{R1} = I_{R2} = 0$ and $V_{R1} = 0$.

To calculate A_{12}, the boundary conditions in the circuit of Fig. 2(c) are set to $I_{R1} = I_{R2} = 0$ and $V_{R1} = 0$. Under these conditions, the voltage at port L1 can be expressed as

$$V_{L1} = j\omega M \cdot \frac{V_{R2}}{j\omega M_R}. \tag{A8}$$

From (A8) and (A4), the result for A_{12} shown in (5) is obtained.

Finally, to determine A_{21}, the circuit of Fig. 2(c) is subjected to $I_{R1} = I_{R2} = 0$ and $V_{R2} = 0$. The voltage at port L2 is then found to be

$$V_{L2} = j\omega M \cdot V_{R1} \cdot j\omega \frac{C}{2}, \tag{A9}$$

and A_{21} is deduced from (A9) and (A5).

APPENDIX B: DISPERSION OF AN SRR-LOADED LINE IN THE LIMIT $M_R \to 0$

By introducing the elements of (5) in (4), we obtain

$$2\cosh(\gamma l) = 1 - \frac{LC}{2}\omega^2 + \frac{1}{2M_R}\left(L_s - \frac{1}{C_s\omega^2}\right) \pm \sqrt{\left[1 - \frac{LC}{2}\omega^2 - \frac{1}{2M_R}\left(L_s - \frac{1}{C_s\omega^2}\right)\right]^2 - \frac{2M^2C\omega^2}{M_R}}. \tag{B1}$$

After some simple (but tedious) algebra, (B1) can be expressed as

$$2\cosh(\gamma l) = 1 - \frac{LC}{2}\omega^2 + \frac{1}{2M_R}\left(L_s - \frac{1}{C_s\omega^2}\right) \pm \frac{1}{2M_R}\left(L_s - \frac{1}{C_s\omega^2}\right) \times \sqrt{1 + \frac{4M_R^2\left(1 - \frac{LC}{2}\omega^2\right)^2}{\left(L_s - \frac{1}{C_s\omega^2}\right)^2} - \frac{4M_R\left(1 - \frac{LC}{2}\omega^2\right)}{\left(L_s - \frac{1}{C_s\omega^2}\right)} - \frac{8M^2M_RC\omega^2}{\left(L_s - \frac{1}{C_s\omega^2}\right)^2}}. \tag{B2}$$

Then, using the following Taylor series expansion up to the first order:

$$\sqrt{1-x} = 1 - \frac{1}{2}x + \frac{1}{4}x^2 - \cdots, \tag{B3}$$

expression (B2) can be approximated by

$$2\cosh(\gamma l) = 1 - \frac{LC}{2}\omega^2 + \frac{1}{2M_R}\left(L_s - \frac{1}{C_s\omega^2}\right) \pm \frac{1}{2M_R}\left(L_s - \frac{1}{C_s\omega^2}\right) \times \left\{1 - \frac{2M_R^2\left(1 - \frac{LC}{2}\omega^2\right)^2}{\left(L_s - \frac{1}{C_s\omega^2}\right)^2} - \frac{2M_R\left(1 - \frac{LC}{2}\omega^2\right)}{\left(L_s - \frac{1}{C_s\omega^2}\right)} - \frac{4M^2M_RC\omega^2}{\left(L_s - \frac{1}{C_s\omega^2}\right)^2}\right\}, \tag{B4}$$

and by choosing the "−" sign (i.e., the solution with physical meaning) in the last term, we obtain expression (8).

To demonstrate that (8) is the dispersion relation corresponding to the two-port that models the unit cell of an SRR-loaded line without inter-resonator coupling, we apply Bloch mode analysis to the model of Fig. 3(b), i.e.,

$$\cosh(\gamma l) = A = 1 + \frac{Z_s}{Z_p}, \tag{B5}$$

where A is the first element of the transfer matrix of the two-port, and Z_s and Z_p are the impedances of the series and shunt branches of the network of Fig. 3(b). Calculation of (B5) for the circuit of Fig. 3(b) gives

$$\cosh(\gamma l) = 1 - \frac{1}{2}L'C\omega^2\left(1 - \frac{1}{L'C_s'\omega^2\left(1 - \frac{\omega_o^2}{\omega^2}\right)}\right), \tag{B6}$$

where $\omega_o = (L_sC_s)^{-1/2}$. Using the element transformations of Fig. 3, expression (B6) can be rewritten as

$$\cosh(\gamma l) = 1 - \frac{1}{2}LC\omega^2 + M^2CC_s\omega_o^2\omega^2 + \frac{M^2C\omega_o^2}{L_s\left(1 - \frac{\omega_o^2}{\omega^2}\right)}, \tag{B7}$$

which, in turn, can be simplified to the dispersion relation shown in (8). Thus, it is clearly demonstrated that the general dispersion relation given in (4) for the four-port network of Fig. 2(c) is also able to account for the case of SRR-loaded lines with negligible inter-resonator coupling (i.e., $M_R \to 0$).

[1] J. B. Pendry, A. J. Holden, D. J. Robbins, and W. J. Stewart, IEEE Trans. Microwave Theor. Tech. **47**, 2075 (1999).
[2] F. Martín, F. Falcone, J. Bonache, R. Marqués, and M. Sorolla, Appl. Phys. Lett. **83**, 4652 (2003).
[3] F. Falcone, F. Martin, J. Bonache, R. Marqués, and M. Sorolla, Microwave Opt. Technol. Lett. **40**, 3 (2004).
[4] D. R. Smith, W. J. Padilla, D. C. Vier, S. C. Nemat-Nasser, and S. Schultz, Phys. Rev. Lett. **84**, 4184 (2000).
[5] R. Marqués, F. Martín, and M. Sorolla, *Metamaterials with Negative Parameters: Theory, Design and Microwave Applications* (John Wiley & Sons, 2008).
[6] R. R. A. Syms and L. Solymar, Appl. Phys. Lett. **100**, 124103 (2012).
[7] F. Martín, F. Falcone, J. Bonache, T. Lopetegi, R. Marqués, and M. Sorolla, IEEE Microwave Wireless Compon. Lett. **13**, 511 (2003).
[8] J. Naqui, M. Durán-Sindreu, A. Fernández-Prieto, F. Mesa, F. Medina, and F. Martín, IEEE Antennas Wireless Propag. Lett. **11**, 1024 (2012).
[9] F. Falcone, T. Lopetegi, J. D. Baena, R. Marqués, F. Martín, and M. Sorolla, IEEE Microwave Wireless Compon. Lett. **14**, 280 (2004).
[10] J. Naqui, A. Fernández-Prieto, M. Durán-Sindreu, F. Mesa, J. Martel, F. Medina, and F. Martín, IEEE Trans. Microwave Theor. Tech. **60**, 3023 (2012).
[11] T. Tamir and A. A. Oliner, Proc. IEEE **110**, 310 (1963).
[12] P. J. B. Clarricoats and K. R. Slinn, Electron. Lett. **1**, 145 (1965).
[13] A. S. Omar and K. F. Schünemann, IEEE Trans. Microwave Theor. Tech. **34**, 1508 (1986).

[14]W. Huang and T. Itoh, IEEE Trans. Microwave Theor. Tech. **36**, 163 (1988).
[15]M. J. Freire, F. Mesa, and M. Horno, IEEE Trans. Microwave Theor. Tech. **47**, 1098 (1999).
[16]F. Elek and G. V. Eleftheriades, IEEE Microwave Wireless Compon. Lett. **14**, 434 (2004).
[17]R. Islam and G. V. Eleftheriades, IEEE Trans. Antennas Propag. **58**, 1567 (2010).
[18]J. Naqui, M. Durán-Sindreu, F. Martín, A. Fernández-Prieto, F. Mesa, and F. Medina, *International Conference on Electromagnetics Advanced Applications (ICEAA)* (IEEE, 2013), p. 863.
[19]J. Naqui, M. Durán-Sindreu, and F. Martín, IEEE Antennas Wireless Propag. Lett. **12**, 178 (2013).
[20]J.-S. Hong and M. J. Lancaster, *Microstrip Filters for RF/Microwave Applications* (John Wiley & Sons, 2001).
[21]E. Shamonina, V. A. Kalinin, K. H. Ringhofer, and L. Solymar, Electron. Lett. **38**, 371 (2002).
[22]E. Shamonina, V. A. Kalinin, K. H. Ringhofer, and L. Solymar, J. Appl. Phys. **92**, 6252 (2002).
[23]R. R. A. Syms, E. Shamonina, V. Kalinin, and L. Solymar, J. Appl. Phys. **97**, 064909 (2005).
[24]M. J. Freire, R. Marqués, F. Medina, M. A. G. Laso, and F. Martín, Appl. Phys. Lett. **85**, 4439 (2004).
[25]L. Solymar and E. Shamonina, *Waves in Metamaterials* (Oxford University Press, 2009).
[26]R. R. A. Syms, E. Shamonina, and L. Solymar, Eur. Phys. J. B **46**, 301 (2005).
[27]R. Mongia, I. Bahl, and P. Barthia, *RF and Microwave Coupled Line Circuits* (Artech House, 1999).
[28]J. Shekel, Proc. IRE **42**, 840 (1954).
[29]R. Islam, M. Zedler, and G. V. Eleftheriades, IEEE Trans. Antennas Propag. **59**, 1562 (2011).
[30]F. Aznar, M. Gil, J. Bonache, L. Jelinek, J. D. Baena, R. Marqués, and F. Martín, J. Appl. Phys. **104**, 114501 (2008).

Article MAP11

Implementation of shunt connected series resonators through stepped-impedance shunt stubs: analysis and limitations

J. Naqui, M. Durán-Sindreu, J. Bonache and F. Martín

www.ietdl.org

Published in IET Microwaves, Antennas & Propagation
Received on 26th July 2010
Revised on 3rd March 2011
doi: 10.1049/iet-map.2010.0612

ISSN 1751-8725

Implementation of shunt-connected series resonators through stepped-impedance shunt stubs: analysis and limitations

J. Naqui M. Durán-Sindreu J. Bonache F. Martín

GEMMA/CIMITEC-Departament d'Enginyeria Electrònica, Universitat Autònoma de Barcelona, BELLATERRA (Barcelona) 08193, Spain
E-mail: Jordi.Naqui@uab.cat

Abstract: In this study, the implementation of shunt-connected series resonators in microstrip technology by means of stepped impedance shunt stubs (SISS) is analysed. The main aim of the work was to determine the achievable values of resonator's inductance and capacitance, under the restriction that the agreement between the frequency response of the SISS and that of the ideal shunt-connected LC resonator must be good in a wide band (far beyond the resonance frequency). The study is completed by considering different substrate types (with different thickness and dielectric constant) and determining the limitations of the achievable element values, by providing the allowable regions in the LC plane. Finally, the analysis is validated through the design and characterisation of different SISS structures.

1 Introduction

Stepped impedance transmission lines have been widely used as building blocks for the design of semi-lumped low-pass filters in both microstrip and coplanar waveguide (CPW) technologies [1, 2]. The shunt capacitances and series inductances of the circuit model of the low-pass filter are provided by the low characteristic impedance and high characteristic impedance transmission line sections, respectively, where a small electrical length (typically smaller than $\pi/4$ at the cut-off frequency) for each section is necessary to accurately describe the ideal filter response. Following this concept, stepped impedance resonators (SIR) were proposed as high-Q resonators useful for the design of compact band pass filters [3, 4] and low-pass filters with finite transmission zeros [5]. Subsequently, SIRs have found many applications, including the design of band pass filters with improved stop-band rejection [6].

There are many different configurations and variations of the SIR topology and feeding. In this work, the focus is on shunt-connected microstrip SIRs (Fig. 1). Such SIRs can be viewed as open stubs exhibiting a high-impedance (Z_2) section (in contact with the host line), and a low-impedance (Z_1) section in the extreme. For this reason, these shunt-connected resonators are called stepped impedance shunt stubs (SISS) in this paper (this terminology has been used before [7, 8]). Our aim is to study the SISS to be able to determine the implementable values of inductance and capacitance as a function of the substrate characteristics (thickness and dielectric constant) and technological constraints (minimum strip width). The main novelty and originality of the paper is thus the proposal of a procedure to determine the regions in the LC plane where the SISS describes properly the ideal LC resonator in a predetermined frequency range. Since such regions depend on the substrate characteristics, the procedure is applied to several commercial microwave substrates, and examples that validate the procedure are provided. This analysis is useful for the design of microwave components based on SISSs, such as elliptic low-pass filters and dual-composite right/left-handed lines, among others.

2 Analysis of the SISS

The topology of a typical SISS, the relevant dimensions (lengths and widths of the transmission line sections) and the electrical parameters (characteristic impedances and electrical lengths) are all depicted in Fig. 1. The admittance of the SISS (seen from the host line) is given by

$$Y_{\mathrm{SISS}} = -j\frac{\tan\Phi_1 + K\tan\Phi_2}{Z_2\tan\Phi_1\cdot\tan\Phi_2 - Z_1} \tag{1}$$

where Φ_1 and Φ_2 are the electrical lengths of the low- and high-impedance line sections, respectively, and

$$K = \frac{Z_1}{Z_2} \tag{2}$$

is the impedance ratio of the SISS [3]. At resonance, the denominator in (1) vanishes, and the following condition

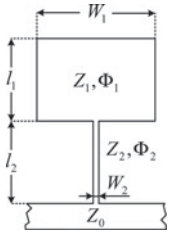

Fig. 1 *Topology of the SISS in microstrip technology and relevant dimensions ($Z_2 \gg Z_1$)*

results

$$K = \tan\Phi_1 \cdot \tan\Phi_2 \tag{3}$$

It is obvious from (1) that to minimise the total electrical length ($\Phi_T = \Phi_1 + \Phi_2$) of the resonator, the impedance ratio must be $K < 1$. Also, the higher the impedance contrast ($K \ll 1$), the smaller the electrical length of the SISS [3]. The reduction of Φ_T is important for two reasons: (i) to reduce the size of the SISS, and (ii) to be able to describe the SISS by means of a lumped element model (series LC resonator). Under the assumption that the two transmission line sections of the SISS are electrically small, we can linearise the tangents in (1), and the admittance of the SISS is found to be

$$Y_{\text{SISS}} = -\text{j}\frac{\Phi_1 + K\Phi_2}{Z_2\Phi_1\Phi_2 - Z_1} \tag{4}$$

This admittance is identical to that of an LC series resonant tank, given by

$$Y_{\text{LC}} = -\text{j}\frac{\omega C}{LC\omega^2 - 1} \tag{5}$$

(ω being the angular frequency), provided the following mapping is satisfied

$$C = \frac{l_1}{v_{p1}Z_1} + \frac{l_2}{v_{p2}Z_2} = C_1 + C_2 \tag{6}$$

$$L = \frac{Z_2 l_2}{v_{p2}}\frac{\{l_1/(v_{p1}Z_1)\}}{\{l_1/(v_{p1}Z_1)\} + \{l_2/(v_{p2}Z_2)\}} = L_2\frac{C_1}{C_1 + C_2} \tag{7}$$

where v_{p1} and v_{p2} are the phase velocities of the low- and high-impedance transmission line sections, respectively, C_1 and C_2 are the line capacitances, namely

$$C_1 = \frac{l_1}{v_{p1}Z_1} = C_{\text{pul1}} \cdot l_1 \tag{8}$$

$$C_2 = \frac{l_2}{v_{p2}Z_2} = C_{\text{pul2}} \cdot l_2 \tag{9}$$

C_{puli} ($i = 1, 2$) being the per unit length capacitances of the lines, and L_2 is the inductance of the high-impedance transmission line section, that is

$$L_2 = L_{\text{pul2}} \cdot l_2 \tag{10}$$

Notice that although C is dominated by the capacitance of the low-impedance transmission line section, C_1, the contribution of C_2 on C may be non-negligible if either K or l_2 are not very small. It is also interesting to note that L is somehow affected by the capacitive line section, such inductance being smaller than the inductance of the high-impedance transmission line section, L_2. Obviously, in a second-level approximation, $C \simeq C_1$ and $L \simeq L_2$, but this approximation sacrifices accuracy and it is not actually necessary for our purposes.

Our aim is to determine the implementable values of the inductance L and capacitance C of a shunt-connected resonator by means of an SISS, so that the response of the ideal resonator is accurately described by the SISS up to a given frequency (obviously beyond resonance). Since it is convenient to deal with extreme characteristic impedances, the first step is to determine the maximum and minimum value of the characteristic impedance of the high- and low-impedance transmission line sections, respectively, that can be achieved with the considered substrate and fabrication technology. For which concern the high-impedance section, the maximum achievable impedance is that corresponding to the narrowest possible line. Typically, for printed circuit boards, the strip width cannot be narrower than 100 μm. However, this may be a very optimistic value, and typically the considered line widths are not narrower than 150 μm. We have calculated (by means of the transmission line calculator of Agilent ADS) the characteristic impedance of 100, 150 and 200 μm width microstrip lines for different commercially available substrates. The values are indicated in Table 1. As expected, the highest characteristic impedance is that of the thickest substrate with the smallest dielectric constant (smaller line capacitance). However, choosing a thick substrate with a small dielectric constant goes against achieving low characteristic impedance for the capacitive line section. For the low-impedance transmission line section, the wider the line, the lower the characteristic impedance. In this case, the lowest impedance limit is not given by any technology constraint, but a maximum width must be considered to avoid transverse resonances.

Once the maximum and minimum values of Z_2 and Z_1, respectively, are determined, the next step for the determination of the allowable (implementable) L and C values is to express Φ_1 and Φ_2 as a function of L and C. The following results are obtained

$$\Phi_1 = \frac{C\omega Z_1}{2}\left(1 + \sqrt{1 - \frac{4L}{CZ_2^2}}\right) \tag{11}$$

Table 1 Characteristic impedance (in Ω) for different substrates (with the indicated dielectric constant, ε_r, and thickness, h) and line widths

	$W_2 = 100$ μm	$W_2 = 150$ μm	$W_2 = 200$ μm
(a) Rogers RO4003C, $\varepsilon_r = 3.55$, $h = 0.203$ mm	103.2	88.1	77.6
(b) Rogers RO4003C, $\varepsilon_r = 3.55$, $h = 1.524$ mm	182.7	167.3	156.2
(c) Rogers RO3010, $\varepsilon_r = 10.2$, $h = 0.254$ mm	70.2	60.5	53.6
(d) Rogers RO3010, $\varepsilon_r = 10.2$, $h = 1.27$ mm	110.8	100.9	93.8

$$\Phi_2 = \frac{C\omega Z_2}{2}\left(1 - \sqrt{1 - \frac{4L}{CZ_2^2}}\right) \tag{12}$$

These electrical lengths must be smaller than a certain predetermined value at a certain frequency. Typically, a line is considered to be electrically short if its electrical length is smaller than $\pi/4$. Therefore for an accurate description of the behaviour of the SISS by means of a simple LC series resonator in shunt connection, it seems reasonable to limit the electrical lengths of the high- and low-impedance line sections to be smaller than $\pi/4$ up to a frequency beyond the resonance frequency, $\omega_o = (\mathrm{LC})^{-1/2}$ (this guarantees that the SISS can be described by means of an LC resonator in the region of interest). Thus, we can choose $\omega = n\omega_o$ in (11) and (12), with $n > 1$. This leads to

$$\Phi_1 = \frac{nZ_1}{2Z_{\mathrm{eq}}}\left(1 + \sqrt{1 - 4\left(\frac{Z_{\mathrm{eq}}}{Z_2}\right)^2}\right) \tag{13}$$

$$\Phi_2 = \frac{nZ_2}{2Z_{\mathrm{eq}}}\left(1 - \sqrt{1 - 4\left(\frac{Z_{\mathrm{eq}}}{Z_2}\right)^2}\right) \tag{14}$$

where

$$Z_{\mathrm{eq}} = \sqrt{\frac{L}{C}} \tag{15}$$

is an equivalent impedance. Notice that expressions (13) and (14) depend on L and C through Z_{eq}, that is, they do not depend on the specific values of L and C, but on its ratio. By forcing (13) and (14) to be smaller than $\pi/4$, we obtain the implementable values of Z_{eq}. However, this must be done with some caution since the impedance of the low-impedance line, Z_1, is frequency dependent. Thus, for any combination of L and C, the first step is to determine the resonance frequency ω_o. The width of the low-impedance transmission line section (the capacitive line) is the maximum width that avoids the appearance of transverse-resonant modes at $n\omega_o$, namely [9]

$$W_{1\,\max} = \frac{c\pi}{n\omega_o\sqrt{\varepsilon_r}} - 0.4h \tag{16}$$

where c is the speed of light in vacuum, h the substrate thickness and ε_r the dielectric constant. From this, we can determine $Z_1(\omega_o)$. The next step is to represent the allowable values of Z_{eq} as a function of the resonance frequency, as Fig. 2 illustrates. In such figure, we have considered four commercially available substrates. For each substrate, we have calculated Z_2 (by forcing the width of the inductive line to 150 μm) and the dependence of Z_1 with frequency. In such figure, we have considered $n = 1.5$ and $n = 2$. As the resonance frequency increases, the allowable interval of Z_{eq} decreases, the upper limit being constant (the reason is that the upper limit is determined by Φ_2, which is not frequency dependent). We then translate the information given by Fig. 2 to the LC plane. That is, each resonance frequency corresponds to a certain curve in the LC plane. From the range of values of Z_{eq}

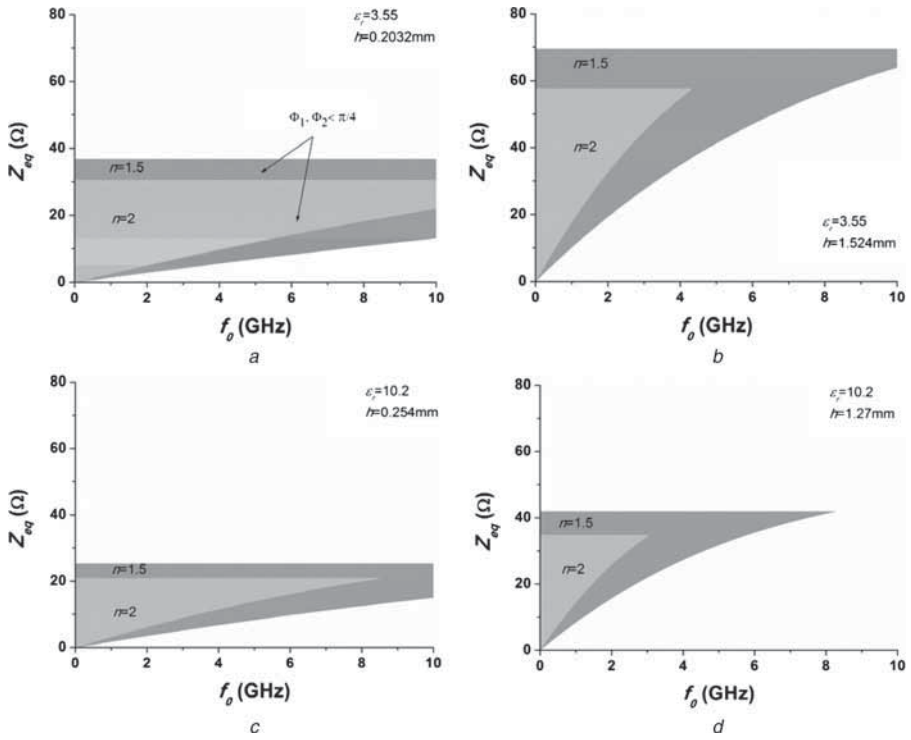

Fig. 2 *Allowable values of Z_{eq} as a function of the resonance frequency for four different (commercially available) microwave substrates for $n = 2$ and $n = 1.5$*

Substrate thickness h and dielectric constant ε_r are:
a $h = 0.203$ mm, $\varepsilon_r = 3.55$
b $h = 1.524$ mm, $\varepsilon_r = 3.55$
c $h = 0.254$ mm, $\varepsilon_r = 10.2$
d $h = 1.27$ mm, $\varepsilon_r = 10.2$

doi: 10.1049/iet-map.2010.0612

corresponding to such resonance frequency, the allowable values of L and C in each curve can be obtained.

The allowable values of L and C for the considered substrates are depicted in Fig. 3. According to Fig. 3, to implement resonators with large capacitive values and low inductive values, the strategy is to use thin substrates. Obviously, $n = 1.5$ is less restrictive, and the ranges of implementable values of L and C increase substantially.

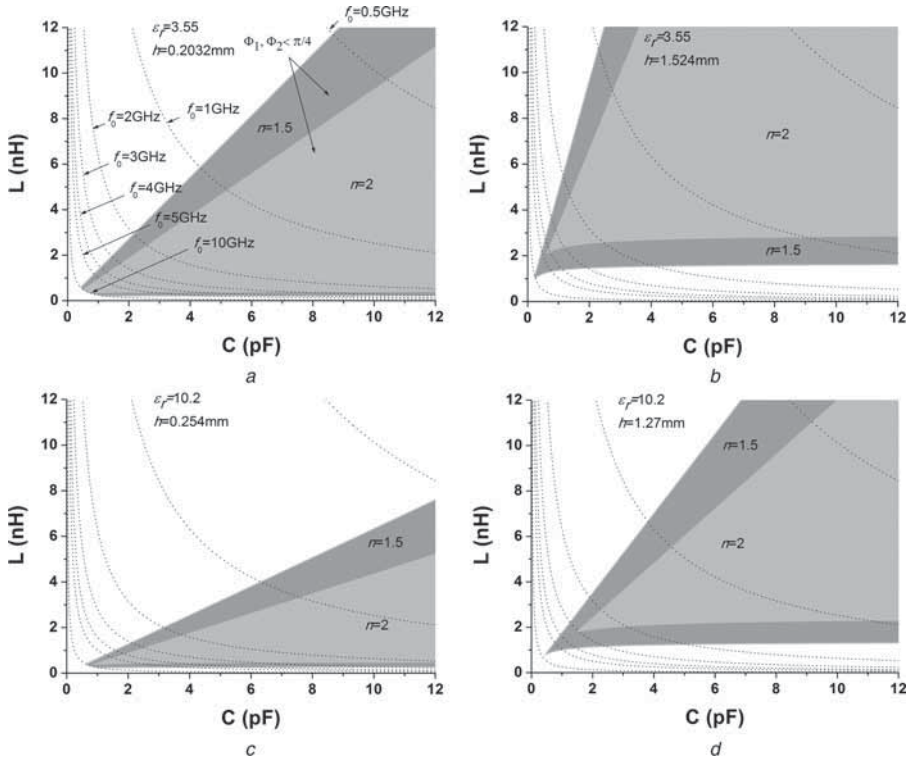

Fig. 3 *Allowable values of L and C for n = 2 and n = 1.5 and the considered substrates:*

a $h = 0.203$ mm, $\varepsilon_r = 3.55$
b $h = 1.524$ mm, $\varepsilon_r = 3.55$
c $h = 0.254$ mm, $\varepsilon_r = 10.2$
d $h = 1.27$ mm, $\varepsilon_r = 10.2$

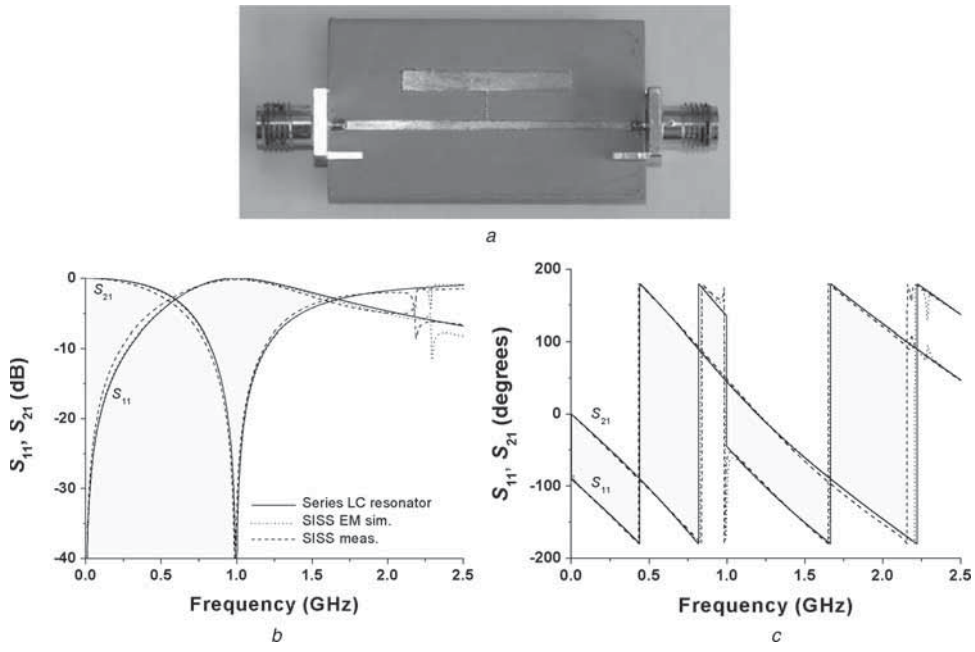

Fig. 4 *SISS-loaded microstrip line corresponding to case A*

a Illustration of structure
b Insertion and return losses
c Phase response

Indeed, Fig. 3 is limited to capacitances of 12 pF and inductances of 12 nH since higher values give too large SISS dimensions for being practical. However, from a theoretical point of view, very small values of ω_o with implementable values of L and C can be obtained. In contrast, as the resonance frequency increases, the range of L and C values providing such resonance decreases dramatically, and finally collapses. The reason is that as ω_o increases, the width of the capacitive line section must decrease. Under these circumstances, the capacitance is limited to small values to avoid electrically large capacitive lines.

3 Validation

To validate the previous analysis, we have synthesised four different SISS. Firstly, we have designed and fabricated three SISS in the commercial substrate Rogers RO3010 with dielectric constant $\varepsilon_r = 10.2$ and thickness $h = 1.27$ mm. In one case (case A), the considered inductance and capacitance are $L = 3.7$ nH and $C = 6.9$ pF, respectively, providing a resonance frequency of $f_o = \omega_o/2\pi = 0.996$ GHz. These reactive values lie within the allowable region in the LC plane for that substrate and $n = 2$, as can be seen in Fig. 3. Thus, we expect a very good agreement between the frequency response of the SISS synthesised according to the proposed procedure and that derived from the circuit simulation of the LC resonator at least up to $2f_o$. In the second case (case B), we have set $L = 7.2$ nH and $C = 3.5$ pF (roughly providing the same resonance frequency, that is, $f_o = \omega_o/2\pi = 1.003$ GHz), that is, a combination that does not belong to the allowable region in the LC plane for $n = 2$. The impedance of the inductive line is that corresponding to a line width of 150 μm, namely, $Z_2 = 100.9\ \Omega$. For the low-impedance transmission line section, the width (23 mm) has been determined from expression (16). This gives a characteristic impedance of $Z_1 = 5.8\ \Omega$. In the third case (case C), we have considered the same L and C values as in case A, but without applying the synthesis procedure of the previous section. Namely, we have set the low- and high-impedance values to $Z_1 = 29.6\ \Omega$ and $Z_2 = 40.2\ \Omega$, respectively, corresponding to line widths of 3 and 1.8 mm. In all three cases, the host microstrip line has a width of 1.18 mm (corresponding to a characteristic impedance of $Z_o = 50\ \Omega$) and a length of 43 mm.

For case A, the lengths of the lines, $l_1 = 2.8$ mm and $l_2 = 4$ mm, have been determined from (6) and (7) [actually some optimisation has been required owing to the effects of line discontinuities, not accounted for by the model, and the mapping given by expressions (6) and (7), which results from the Taylor approximation of expression (4)]. These line lengths correspond to electrical lengths of $\Phi_1 = 20.7^\circ$ and $\Phi_2 = 23.8^\circ$ at $2f_o$, that is, smaller than $\pi/4$ as expected. The electromagnetic simulation (obtained by means of the Agilent Momentum commercial software) and the measured frequency response of a 50 Ω line loaded with such an SISS is depicted in Fig. 4 (the photograph of the structure is also shown in the figure). We have also included in the figure the circuit simulation of the same line loaded with a shunt-connected LC resonator with the reactive values given above, for comparison purposes. The agreement is excellent up to $2f_o$, this confirming our expectations.

For case B, the design procedure applied before can be no longer used, and we have determined the line lengths ($l_1 = 0.65$ mm and $l_2 = 8.8$ mm) by curve fitting the reactance slope. The resulting structure is shown in Fig. 5, where the electromagnetic and circuit simulation of the structure, as well as the measured frequency response are depicted. In contrast to case A, the SISS does not properly describe the behaviour of the shunt-connected LC series resonator up to $2f_o$. At this frequency, the discrepancy between the circuit and electromagnetic simulation in S_{11} is clearly visible, and the phases of S_{11} and S_{21} differ in approximately $2-3^\circ$ (whereas for case A, the phase differences are smaller than 1°). Note that we provide the comparison between the circuit and electromagnetic simulation, since the experimental data can experience some deviations owing to fabrication-related tolerances and inaccuracies in the substrate parameters. The length of the high-impedance line for case B ($l_2 = 8.8$ mm) gives an electrical length (at $2f_o$) of $\Phi_2 = 52.4^\circ$, and hence this line section cannot be considered electrically small (on the contrary, the small capacitance gives a very short length for the capacitive line, i.e. $\Phi_1 = 4.8^\circ$).

For case C, the line lengths are $l_1 = 19$ mm and $l_2 = 7$ mm. The structure and its frequency response are depicted in Fig. 6. In this case the disagreement between the circuit

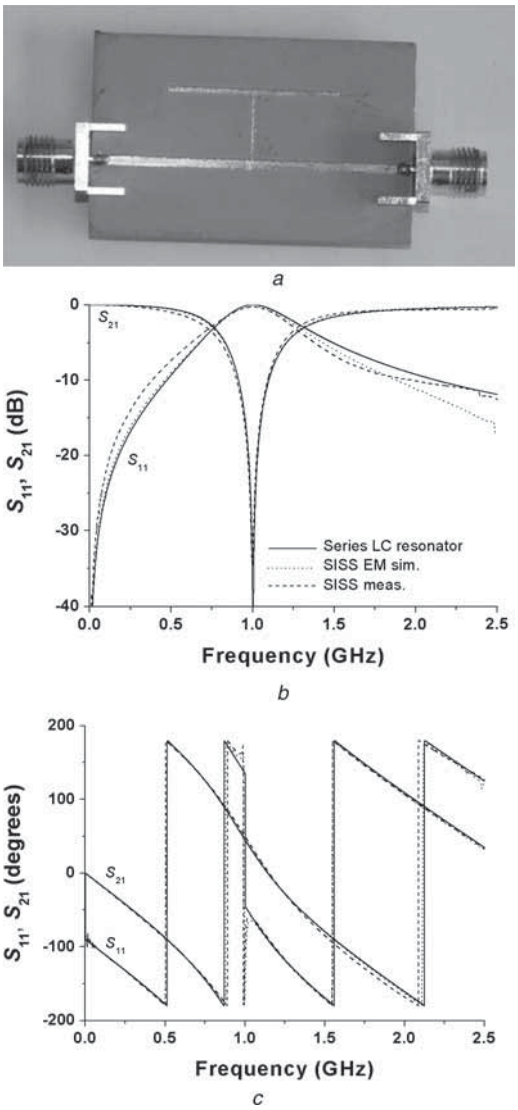

Fig. 5 *SISS-loaded microstrip line corresponding to case B*

a Illustration of structure
b Insertion and return losses
c Phase response

doi: 10.1049/iet-map.2010.0612

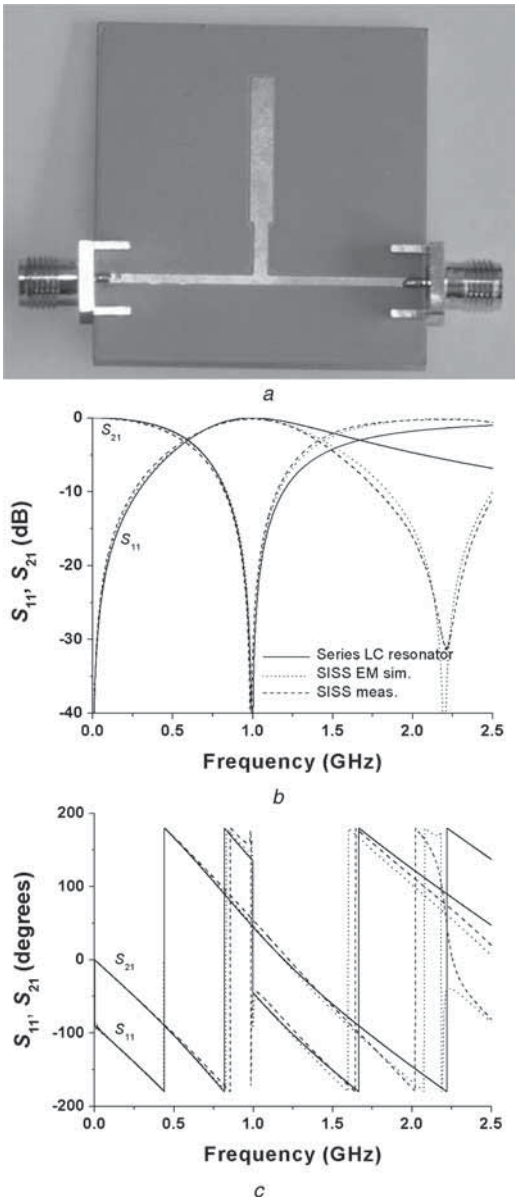

Fig. 6 *SISS-loaded microstrip line corresponding to case C*

a Illustration of structure
b Insertion and return losses
c Phase response

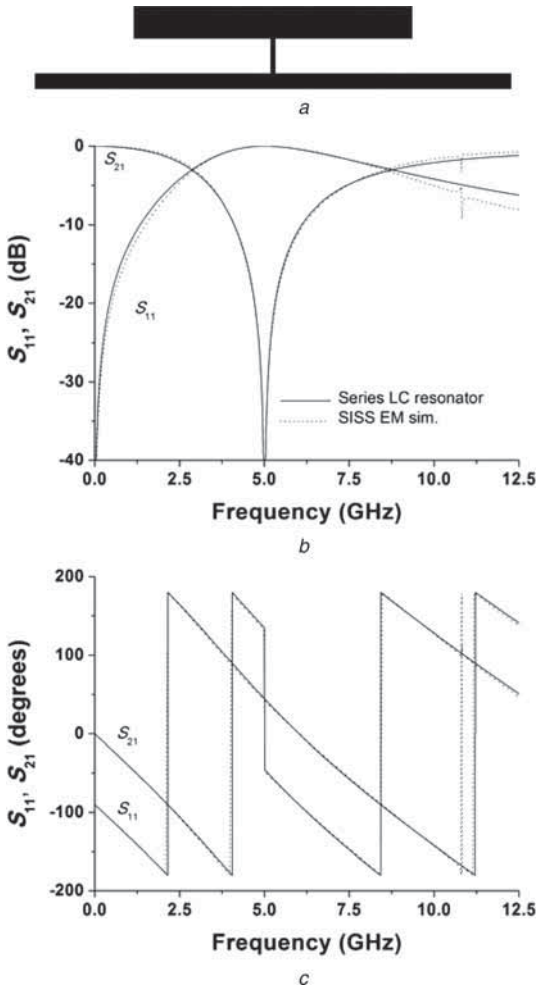

Fig. 7 *SISS-loaded microstrip line corresponding to case D*

a Layout of structure
b Insertion and return losses
c Phase response

simulation and electromagnetic simulation (or experimental data) is much larger, as expected since the line impedances of the SISS have not been optimised.

Finally, to validate that the presented method is also accurate at higher frequencies, we have designed an SISS whose fundamental resonance frequency is $f_0 = 5$ GHz (case D). Assuming $n = 2$ and that the desired inductance and capacitance values to be synthesised are $L = 0.68$ nH and $C = 1.5$ pF, according to Fig. 3, the more suitable substrate is (a) $\varepsilon_r = 3.55$ and $h = 0.2032$ mm (since the LC values lie on the allowable range only for this substrate). The minimum width is supposed to be 150 μm (as in case A and B), whereas the maximum width is found to be 7.88 mm according to expression (16). The resulting layout is shown in Fig. 7, for which the electrical lengths of the SISS lines (with no discontinuities) are $\Phi_1 = 20^\circ$ (being $l_1 = 0.99$ mm) and $\Phi_2 = 19^\circ$ ($l_2 = 0.9$ mm) at the maximum operating frequency $n{\cdot}f_0 = 10$ GHz. Host line length and width are 13.5 and 0.45 mm, respectively. In Fig. 7, we can see that the frequency response of a line loaded with the SISS obtained by electromagnetic simulation is in very good agreement with that of the same host line loaded with a lumped L and C elements, as expected.

The previous results clearly demonstrate that a given resonance frequency by itself cannot guarantee that the LC resonator can be properly described by means of an SISS; the necessary and sufficient requirement for that is that the low- and high-impedance lines must be electrically short, being the length of the low-impedance line the main limitation at high frequencies. With these structures and frequency responses, it is proved that the analysis carried out in this work (valid at any frequency) is very useful for the synthesis of shunt-connected LC series resonators by means of SISSs.

4 Conclusions

In conclusion, an exhaustive analysis of SISS structures has been carried out in this paper. It has been shown that under certain conditions the structure can be described by an LC series resonator far beyond the resonance frequency, and we have provided the procedure to determine the implementable L and C values as a function of substrate characteristics and required frequency range. The analysis of the work has been validated by designing an SISS-loaded transmission line with L and C values lying within the allowable range, an SISS

structure with L and C values in the forbidden region and an SISS with L and C values within the allowable region but improperly designed (i.e. by considering an impedance ratio close to 1). The results of this paper are useful for the design of any planar microwave component based on SISS structures.

5 Acknowledgments

This work has been supported by MICINN-Spain (contract TEC2010-17512 METATRANSFER), Generalitat de Catalunya (project 2009SGR-421) and MCI-Spain (project CONSOLIDER EMET CSD2008-00066).

6 References

1 Pozar, D.M.: 'Microwave engineering' (Addison Wesley, 1990)
2 Bahl, I., Barthia, P.: 'Microwave solid state circuit design' (John Wiley, 1988)
3 Makimoto, M., Yamashita, S.: 'Compact bandpass filters using stepped impedance resonators', *Proc. IEEE*, 1979, **67**, (1), pp. 16–19
4 Makimoto, M., Yamashita, S.: 'Bandpass filters using parallel-coupled stripline stepped impedance resonators', *IEEE Trans. Microw. Theory Tech.*, 1980, **MTT-28**, pp. 1413–1417
5 Matthaei, G., Young, L., Jones, E.M.T.: 'Microwave filters, impedance matching networks, and coupling structures' (Artech House, Norwood, MA, 1980)
6 Kuo, J.-T., Shih, E.: 'Microstrip stepped impedance resonator bandpass filter with an extended optimal rejection bandwidth', *IEEE Trans. Microw. Theory Tech*, 2003, **51**, (5), pp. 1554–1559
7 Lee, J.-K., Lee, D.-H., Kim, Y.-S.: 'A compact low-pass filter with double-step impedance shunt stub and defected ground structure for wideband rejection', *Microw. Opt. Technol. Lett.*, 2010, **52**, (1), pp. 132–134
8 Park, J., Kim, J.-P., Nam, S.: 'Design of a novel harmonic-suppressed microstrip low-pass filter', *IEEE Microw. Wirel. Compon. Lett.*, 2007, **17**, (6), pp. 424–426
9 Edwards, T.C., Steer, M.B.: 'Foundations of interconnect and microstrip design' (John Wiley, 2000, 3rd edn.)

doi: 10.1049/iet-map.2010.0612

Article AWPL13

Modeling Split Ring Resonator (SRR) and Complementary Split Ring Resonator (CSRR) Loaded Transmission Lines Exhibiting Cross Polarization Effects

J. Naqui, M. Durán-Sindreu, and F. Martín

Modeling Split-Ring Resonator (SRR) and Complementary Split-Ring Resonator (CSRR) Loaded Transmission Lines Exhibiting Cross-Polarization Effects

Jordi Naqui, *Student Member, IEEE*, Miguel Durán-Sindreu, *Member, IEEE*, and Ferran Martín, *Fellow, IEEE*

***Abstract*—The purpose of this letter is to understand and model the electromagnetic properties of transmission lines loaded with split-ring resonators (SRRs) and complementary split-ring resonators (CSRRs) arbitrarily oriented. It is shown that if the slits of these resonators are aligned in a nonorthogonal direction to the line axis, cross-polarization effects arise. Namely, the particles (SRRs or CSRRs) are excited through both magnetic and electric coupling. It is pointed out that the previously reported lumped element equivalent circuit models of SRR- and CSRR-loaded lines (where cross polarization is not considered) are valid as long as the slits are orthogonally oriented to the line axis, and new models that include cross polarization are presented and discussed. The validity and accuracy of the models is demonstrated through parameter extraction and comparison to full-wave electromagnetic simulations and measurements.**

***Index Terms*—Complementary split-ring resonator (CSRR), coplanar waveguide (CPW), metamaterials, microstrip, split-ring resonator (SRR).**

I. Introduction

METAMATERIAL-BASED transmission lines have been a subject of interest in the last decade [1]–[3]. Such artificial lines are implemented by loading a host transmission line [typically a microstrip or a coplanar waveguide (CPW)] with reactive elements. Thanks to the presence of the reactive elements, the dispersion and characteristic impedance of these lines can be engineered, and microwave devices with improved performance or with novel functionalities can be designed. Most metamaterial transmission lines have been implemented by loading the host lines with shunt inductances and series capacitances (lumped or semi-lumped) [4]–[6]. However, artificial lines loaded with electrically small resonators, such as split-ring resonators (SRRs) [7] or complementary split-ring resonators (CSRRs) [8], [9] have also been reported and applied to the design of novel microwave circuits (such as compact filters, enhanced bandwidth, multiband components, etc.) and antennas [3].

This letter is focused on microstrip lines loaded with CSRRs and CPWs loaded with SRRs. Such structures can be applied to the design of stopband filters [10], [11], common-mode rejection filters in differential lines [12], displacement and alignment sensors [13], and radio frequency bar codes [14], among others. For design purposes and for accurately predicting the electromagnetic behavior of SRR- and CSRR-loaded lines, reliable circuit models are necessary. This is the main motivation of the present letter. The relative orientation of SRRs or CSRRs is considered for the first time in this letter since this is relevant in certain applications [12]–[14]. It is demonstrated that for an accurate modeling of these artificial lines, with arbitrarily oriented SRRs or CSRRs, it is necessary to consider electric and magnetic coupling between the host line and the resonators.

Manuscript received December 20, 2012; accepted January 29, 2013. Date of publication February 05, 2013; date of current version March 12, 2013. This work was supported by Spain-MICIIN under project Contracts TEC2010-17512 METATRANSFER, CONSOLIDER CSD2008-00066 EMET, and EXPLORA TEC2011-13615-E and AGAUR (Catalan Government) under Project 2009SGR-421.

The authors are with GEMMA/CIMITEC (Departament d'Enginyeria Electrònica), Universitat Autònoma de Barcelona, 08193 Bellaterra, Spain (e-mail: Ferran.Martin@uab.es).

Color versions of one or more of the figures in this letter are available online at http://ieeexplore.ieee.org.

Digital Object Identifier 10.1109/LAWP.2013.2245095

II. Modeling SRR- and CSRR-Loaded Lines Including Cross-Polarization Effects and Validation

The first lumped element equivalent circuit models of SRR-loaded CPWs and CSRR-loaded microstrip lines were reported in [7] and [9], respectively, and these models were later revised and improved in [15] and [16]. Actually, in [15] and [16], the considered structures are CPWs loaded with SRRs and shunt strips, and microstrip lines loaded with CSRRs and capacitive gaps, respectively. The main improvement in [15] and [16] is relative to the fact that by adding shunt strips (in SRR-loaded CPWs) and series gaps (in CSRR-loaded microstrip lines), the transmission zero related to the presence of the resonator (SRR or CSRR) is displaced, and this fact was not predicted by the models reported in [7] and [9]. In this letter, the presence of series gaps or shunt strips is not considered, and therefore the new models must be compared to those reported in [7] and [9], which are depicted in Fig. 1 for better comprehension and completeness (the topologies are also included). For the circuits of Fig. 1, L and C model, respectively, the per-section line inductance and capacitance. The SRRs and the CSRR are described by the resonant tanks $L_{\rm s}-C_{\rm s}$ and $L_{\rm c}-C_{\rm c}$, respectively. The magnetic coupling between the line and the SRRs is modeled by the mutual inductance M, whereas C accounted for the electric

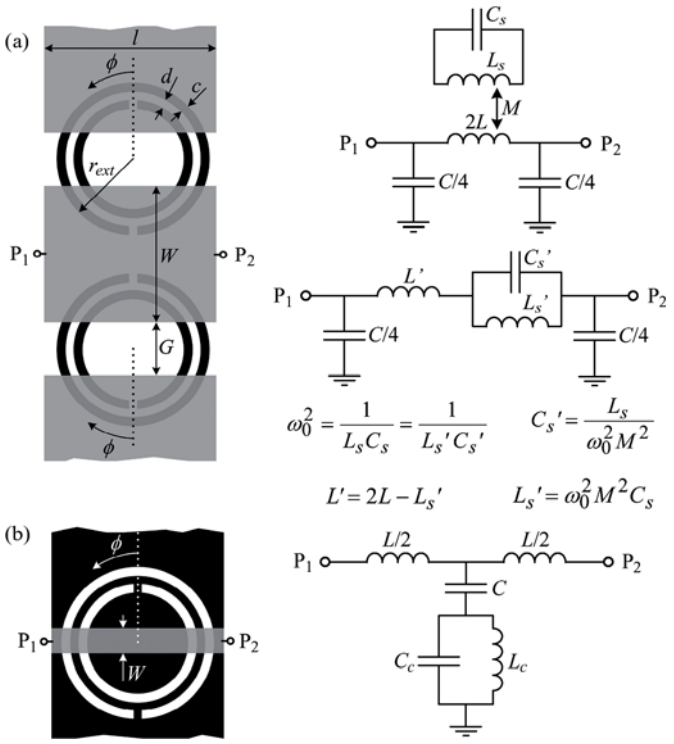

Fig. 1. Unit-cell topology and equivalent circuit model of (a) a CPW loaded with SRRs and (b) a microstrip line loaded with CSRRs. The upper metal level is depicted in gray, whereas the lower one is depicted in black. In (a), the magnetic wall concept is used, and the transformed circuit model is also shown. The rotation angle that defines the slits orientation is $\phi = 0°$. Notice that the rotation in (a) is that in which the slot mode cannot be excited.

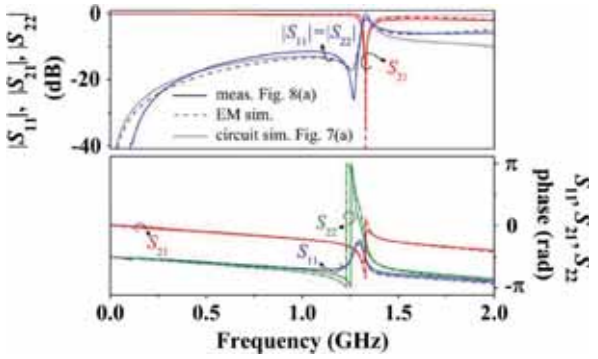

Fig. 2. Frequency response of the considered SRR-loaded CPW structure. The substrate is the *Rogers RO3010* with dielectric constant $\varepsilon_r = 11.2$ and thickness $h = 1.27$ mm. Dimensions are $W = 10.4$ mm, $G = 1.6$ mm, $l = 10.4$ mm, $r_{ext} = 5$ mm, and $c = d = 0.2$ mm. The rotation angle is $\phi = 90°$.

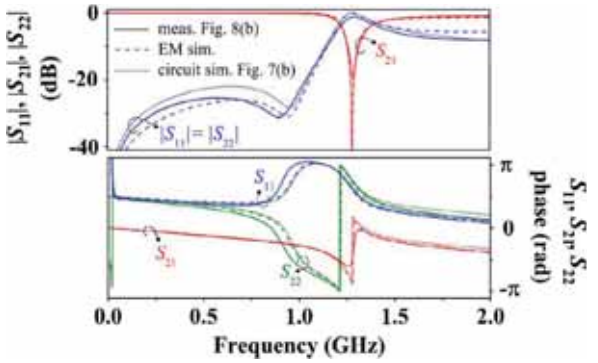

Fig. 3. Frequency response of the considered CSRR-loaded microstrip structure. The substrate is the *Rogers RO3010* with $\varepsilon_r = 11.2$ and $h = 1.27$ mm. Dimensions are $W = 1.15$ mm, $l = 10.4$ mm, $r_{ext} = 5$ mm, and $c = d = 0.2$ mm. The rotation angle is $\phi = 90°$.

coupling between the line and the CSRR. In both circuit models, losses are neglected.

It has been demonstrated through parameter extraction [17], [18] that the models depicted in Fig. 1 describe the frequency response of the corresponding structures to a very good approximation. However, if the symmetry of the structures (with regard to the input and output ports) is truncated by rotating the SRRs or CSRRs, the models as well as the parameter extraction procedures may fail. Indeed, for the particular case of a $\phi = 90°$ rotation (i.e., the slits oriented in parallel to the line axis), the asymmetry leads to substantially different phase of the reflection coefficients S_{11} and S_{22} (even though $|S_{11}| = |S_{22}|$ and the transmission coefficients satisfy $S_{12} = S_{21}$, as results from unitarity and reciprocity). Fig. 2 depicts the simulated frequency response (performed by the full-wave electromagnetic solver *Agilent Momentum*) of the indicated SRR-loaded structure for $\phi = 90°$, where it can be appreciated that the phase of S_{11} and S_{22} are significantly different. Obviously, this behavior cannot be obtained by the symmetric two-port network in Fig. 1(a). The same phenomenology applies to a CSRR-loaded microstrip line (see Fig. 3).

The previous results suggest that by rotating the SRRs/CSRRs, these particles are not only driven by the axial magnetic/electric field generated by the host line. This explains the disagreement between the predictions of the models of Fig. 1, inferred from parameter extraction (not shown), and the frequency responses of the structures shown in Figs. 2 and 3. In the models of Fig. 1, cross-polarization effects are not considered. However, it is well known that SRRs/CSRRs can actually be excited by an axial time-varying magnetic/electric field or by means of an electric/magnetic field applied to the orthogonal direction with regard to their symmetry plane [see Fig. 4(a)] [3], [9], [19], [20]. If the SRRs/CSRRs are oriented as shown in Fig. 1 (i.e., the slits are aligned orthogonally to the line axis), they cannot be excited through electric/magnetic coupling. However, if the particles are rotated, a nonnegligible component of the electric/magnetic field orthogonal to the symmetry plane of the SRRs/CSRRs appears, and both magnetic and electric coupling must be considered. Obviously, the

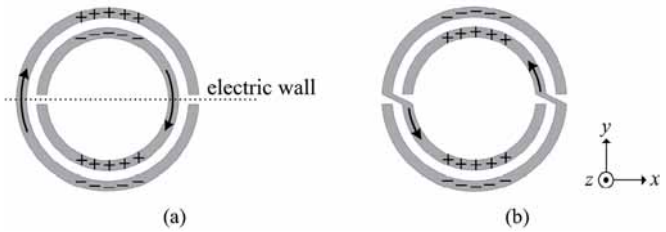

Fig. 4. Sketch of currents and charge distribution at the first resonance of (a) an SRR and (b) an NB-SRR. At the symmetry plane of the SRR, there is an electric wall. For the NB-SRR, there is not that electric dipole in the y-direction; hence, the NB-SRR cannot be excited by a time-varying electric field applied to this direction. From the Babinet principle, it follows that the NB-CSRR cannot be driven by a magnetic field applied to the y-direction [8].

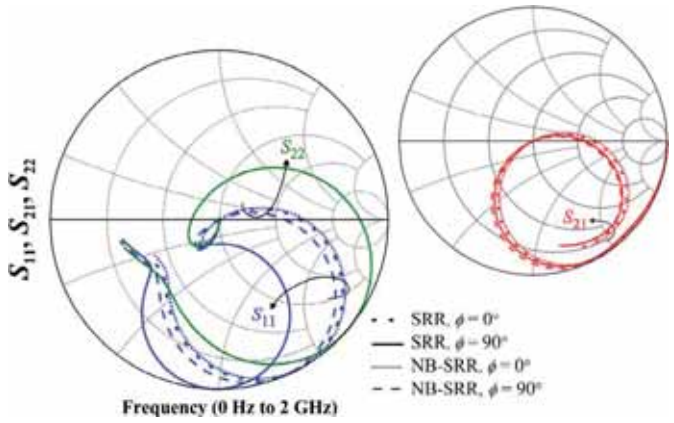

Fig. 5. Frequency response in Smith Chart of a CPW loaded with a pair of SRRs or NB-SRRs for two different rotation angles. The considered substrate and dimensions are those of Fig. 2.

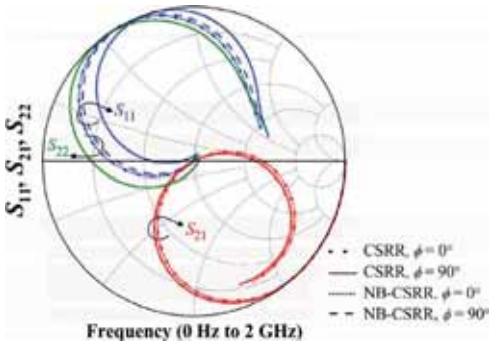

Fig. 6. Frequency response in Smith Chart of a microstrip line loaded with a CSRR or a NB-CSRR for two different rotation angles. The considered substrate and dimensions are those of Fig. 3.

optimum case to favor cross polarization is a $\phi = 90°$ rotation (i.e., the slits are oriented in parallel to the line axis).

To gain insight on the effects of SRR or CSRR rotation on the frequency response of the considered structures, let us consider the nonbianisotropic SRR (NB-SRR) [21] and the nonbianisotropic CSRR (NB-CSRR). These particles do not exhibit cross polarization since they have inversion symmetry with regard to their center, and this prevents the appearance of the electric and magnetic dipole for the SRR and CSRR, respectively, in the plane of the particles [Fig. 4(b)]. According to it, we do expect that CPW and microstrip lines loaded with NB-SRRs and NB-CSRRs, respectively, are insensitive to particle rotation. This has been verified from electromagnetic simulation by considering two different rotation angles (Figs. 5 and 6). As can be seen, the frequency response does not change appreciably by rotating the NB-SRRs and NB-CSRRs. Moreover, the responses of the SRR- and CSRR-loaded lines for $\phi = 0°$ present the same pattern (unlike for $\phi = 90°$) as those of the lines loaded with NB-SRRs and NB-CSRRs.

The previous results support the hypothesis that the dependence of the electromagnetic behavior of the SRR- and CSRR-loaded lines on particle orientation is related to cross-polarization effects. Therefore, in order to accurately describe the lines with arbitrarily oriented SRRs or CSRRs, it is necessary to include both electric and magnetic coupling in the models.

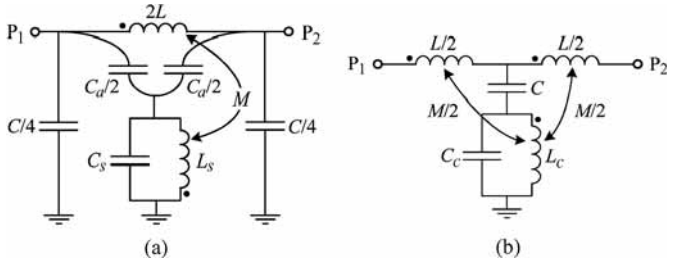

Fig. 7. Proposed equivalent circuit model (unit cell) of (a) a CPW loaded with arbitrarily oriented SRRs and (b) a microstrip line loaded with arbitrarily oriented CSRRs. The magnetic wall concept is applied in (a).

The proposed circuit model for SRR-loaded CPWs is shown in Fig. 7(a). The circuit parameters are those in reference to Fig. 1(a), plus the coupling capacitance, $C_{\rm a}$, that takes into account the electric coupling between the line and the SRRs (it is assumed that $C_{\rm a}$ depends on ϕ, being $C_{\rm a} = 0$ if $\phi = 0°$). Notice that the asymmetry in the circuit model (necessary to explain that $S_{11} \neq S_{22}$) comes from the magnetic coupling (the dot convention for the mutual inductance is used, where the currents entering dot-marked terminals produce additive magnetic fluxes), although this is not manifested if electric coupling is not present.

We have extracted the parameters of the circuit model corresponding to the SRR-loaded line of Fig. 2. To this end, we have first considered the SRRs oriented as depicted in Fig. 1(a). By these means, the circuit parameters according to the procedure explained in [17] have been inferred ($L' = 2.5$ nH, $C = 6$ pF, $L'_{\rm s} = 0.4$ nH, $C'_{\rm s} = 38.8$ pF, and $L = 1.45$ nH). Then, $L_{\rm s} - C_{\rm s}$, M, and $C_{\rm a}$ are adjusted by curve fitting the circuit simulation to the electromagnetic response, such that the resulting $L_{\rm s} - C_{\rm s}$ values are similar to the analytical SRR parameters given by [3], [19] ($L_{\rm s} = 27.8$ nH and $C_{\rm s} = 0.6$ pF). The resulting circuit parameters are: $L = 1.5$ nH, $C = 6.1$ pF, $L_{\rm s} = 28.2$ nH, $C_{\rm s} = 0.43$ pF, $M = 2.7$ nH, and $C_{\rm a} = 0.08$ pF. The agreement between the circuit and the electromagnetic simulation is good (see Fig. 2).

Fig. 7(b) depicts the equivalent circuit model of CSRR-loaded microstrip lines that includes electric and magnetic coupling. The circuit parameters are the same as in Fig. 1(b), plus the mutual inductance M that depends on ϕ ($M = 0$ if $\phi = 0°$), which accounts for the magnetic coupling between the line and the CSRR. We have extracted the parameters of the circuit model corresponding to the CSRR-loaded line of Fig. 3. Similar to the SRR-loaded CPW, we have first extracted the parameters (all except M) for $\phi = 0°$ according to the method reported in [18] ($L = 7.87$ nH, $C = 1.62$ pF, $L_{\rm c} = 2.94$ nH, and $C_{\rm c} = 3.9$ pF). Finally, M has been obtained by curve fitting, where a slight optimization of the other parameters has been required. The resulting circuit elements are $L = 7$ nH, $C = 1.7$ pF, $L_{\rm c} = 2.74$ nH, $C_{\rm c} = 3.95$ pF, and $M = 0.27$ nH. As Fig. 3 reveals, the circuit simulation accurately describes the electromagnetic simulation.

We have fabricated and measured the SRR- and CSRR-loaded lines of Figs. 2 and 3. The photographs are shown in Fig. 8, whereas the measured responses are depicted in

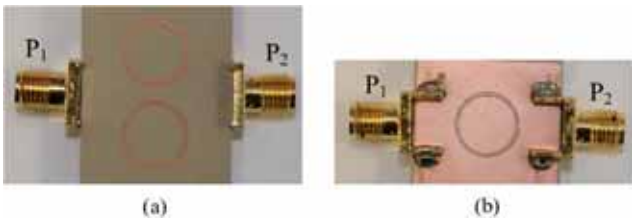

Fig. 8. Bottom-side photograph of the fabricated (a) SRR-loaded CPW of Fig. 2 and (b) CSRR-loaded microstrip line of Fig. 3.

Figs. 2 and 3. The simulations are in good agreement with the measurements (phase reference planes were calibrated).

III. Conclusion

To conclude, we have investigated the effects of rotating SRRs and CSRRs in the frequency response of SRR-loaded CPWs and CSRR-loaded microstrip lines. The stopband behavior in the vicinity of particle resonance is present in all the cases. However, it is demonstrated that to accurately describe the behavior of the considered structures with arbitrary SRR or CSRR orientation, it is necessary to account for both electric and magnetic coupling between the host line and the resonators. Unless the ring slits are aligned in the orthogonal direction to the line axis, magneto-electric coupling must be considered. Such mixed coupling changes essentially the phase response of the reflection coefficients. The analysis of NB-SRR- and NB-CSRR-loaded lines, where cross-polarization effects are not present, has confirmed the need to account for both coupling mechanisms in SRR- and CSRR-loaded lines. Thus, we have proposed circuit models for transmission lines loaded with arbitrarily oriented SRRs or CSRRs, where simultaneous mixed coupling is considered. It has been pointed out that magnetic coupling provides the necessary asymmetry in the circuit models to explain the lack of symmetry in the layouts and frequency responses. The good agreement of the circuit simulations with full-wave electromagnetic simulations and measurements is indicative of the validity of the new proposed circuit models.

References

[1] G. V. Eleftheriades and K. G. Balmain, *Negative Refraction Metamaterials: Fundamental Principles and Applications*. Hoboken, NJ, USA: Wiley, 2005.

[2] C. Caloz and T. Itoh, *Electromagnetic Metamaterials: Transmission Line Theory and Microwave Applications*. Hoboken, NJ, USA: Wiley, 2006.

[3] R. Marqués, F. Martín, and M. Sorolla, *Metamaterials With Negative Parameters: Theory, Design and Microwave Applications*. Hoboken, NJ, USA: Wiley, 2007.

[4] A. K. Iyer and G. V. Eleftheriades, "Negative refractive index metamaterials supporting 2-D waves," in *Proc. IEEE-MTT Int. Microw. Symp.*, Seattle, WA, USA, Jun. 2002, vol. 2, pp. 412–415.

[5] A. A. Oliner, "A periodic-structure negative-refractive-index medium without resonant elements," in *Proc. IEEE-AP-S USNC/URSI Nat. Radio Sci. Meeting*, San Antonio, TX, USA, Jun. 2002, p. 41.

[6] C. Caloz and T. Itoh, "Application of the transmission line theory of left-handed (LH) materials to the realization of a microstrip LH transmission line," in *Proc. IEEE-AP-S USNC/URSI Nat. Radio Sci. Meeting*, San Antonio, TX, USA, Jun. 2002, vol. 2, pp. 412–415.

[7] F. Martín, F. Falcone, J. Bonache, R. Marqués, and M. Sorolla, "Split ring resonator based left handed coplanar waveguide," *Appl. Phys. Lett.*, vol. 83, pp. 4652–4654, Dec. 2003.

[8] F. Falcone, T. Lopetegi, J. D. Baena, R. Marqués, F. Martín, and M. Sorolla, "Effective negative- ε stop-band microstrip lines based on complementary split ring resonators," *IEEE Microw. Wireless Compon. Lett.*, vol. 14, no. 6, pp. 280–282, Jun. 2004.

[9] J. D. Baena, J. Bonache, F. Martín, R. Marqués, F. Falcone, T. Lopetegi, M. A. G. Laso, J. García, I. Gil, M. Flores-Portillo, and M. Sorolla, "Equivalent circuit models for split ring resonators and complementary split rings resonators coupled to planar transmission lines," *IEEE Trans. Microw. Theory Tech.*, vol. 53, no. 4, pp. 1451–1461, Apr. 2005.

[10] J. García-García, F. Martín, F. Falcone, J. Bonache, I. Gil, T. Lopetegi, M. A. G. Laso, M. Sorolla, and R. Marqués, "Spurious passband suppression in microstrip coupled line band pass filters by means of split ring resonators," *IEEE Microw. Wireless Compon. Lett.*, vol. 14, no. 9, pp. 416–418, Sep. 2004.

[11] J. García-García, J. Bonache, I. Gil, F. Martín, R. Marqués, F. Falcone, T. Lopetegi, M. A. G. Laso, and M. Sorolla, "Comparison of electromagnetic bandgap and split rings resonator microstrip lines as stop band structures," *Microw. Opt. Technol. Lett.*, vol. 44, pp. 376–379, Feb. 2005.

[12] J. Naqui, A. Fernández-Prieto, M. Durán-Sindreu, F. Mesa, J. Martel, F. Medina, and F. Martín, "Common mode suppression in microstrip differential lines by means of complementary split ring resonators: Theory and applications," *IEEE Trans. Microw. Theory Tech.*, vol. 60, no. 10, pp. 3023–3034, Oct. 2012.

[13] J. Naqui, M. Durán-Sindreu, and F. Martín, "Alignment and position sensors based on split ring resonators," *Sensors 2012*, vol. 12, pp. 11790–11797, Aug. 2012.

[14] J. Naqui, M. Durán-Sindreu, and F. Martín, "On the symmetry properties of coplanar waveguides loaded with symmetric resonators: Analysis and potential applications," in *IEEE MTT-S Int. Microw. Symp. Dig.*, Montreal, QC, Canada, Jun. 2012, pp. 1–3.

[15] F. Aznar, J. Bonache, and F. Martín, "An improved circuit model for left handed lines loaded with split ring resonators," *Appl. Phys. Lett.*, vol. 92, p. 043512, Feb. 2008.

[16] J. Bonache, M. Gil, O. García-Abad, and F. Martín, "Parametric analysis of microstrip lines loaded with complementary split ring resonators," *Microw. Opt. Technol. Lett.*, vol. 50, pp. 2093–2096, Aug. 2008.

[17] F. Aznar, M. Gil, J. Bonache, L. Jelinek, J. D. Baena, R. Marqués, and F. Martín, "Characterization of miniaturized metamaterial resonators coupled to planar transmission lines through parameter extraction," *J. Appl. Phys.*, vol. 104, p. 114501, Dec. 2008.

[18] J. Bonache, M. Gil, I. Gil, J. Garcia-García, and F. Martín, "On the electrical characteristics of complementary metamaterial resonators," *IEEE Microw. Wireless Compon. Lett.*, vol. 16, no. 10, pp. 543–545, Oct. 2006.

[19] R. Marqués, F. Medina, and R. Rafii-El-Idrissi, "Role of bianisotropy in negative permeability and left-handed metamaterials," *Phys. Rev. B*, vol. 65, p. 144440, 2002.

[20] P. Gay-Balmaz and O. J. F. Martin, "Electromagnetic resonances in individual and coupled split-ring resonators," *J. Appl. Phys.*, vol. 92, pp. 2929–2936, Sep. 2002.

[21] R. Marqués, J. D. Baena, J. Martel, F. Medina, F. Falcone, M. Sorolla, and F. Martin, "Novel small resonant electromagnetic particles for metamaterial and filter design," in *Proc. ICEAA*, Turin, Italy, 2003, pp. 439–442.

Article APA12

Selective mode suppression in coplanar waveguides using metamaterial resonators

J. Naqui, M. Durán-Sindreu, and F. Martín

Appl Phys A
DOI 10.1007/s00339-012-7384-6

Applied Physics A
Materials Science & Processing

Selective mode suppression in coplanar waveguides using metamaterial resonators

Jordi Naqui · Miguel Durán-Sindreu · Ferran Martín

Received: 25 February 2012 / Accepted: 10 October 2012

Abstract In this paper, it is shown that split-ring resonators (SRRs) and complementary split-ring resonators (CSRRs) can be used to selectively suppress the odd (slot) mode or the even (fundamental) mode, respectively, in coplanar waveguides. To this end, it is necessary to symmetrically etch the SRRs and the CSRRs in the line. An interpretation of this behavior is reported. The paper is also supported by experimental results, and some applications are highlighted.

1 Introduction

Coplanar waveguides (CPWs) loaded with pairs of split-ring resonators (SRRs) (see Fig. 1a) have been proposed as a means to achieve one-dimensional planar negative-permeability structures [1]. As consequence of the negative effective permeability, these structures inhibit the fundamental (even) mode of the CPW in the vicinity of the resonance frequency of the SRRs. Alternatively, the stop-band behavior of these structures can be interpreted as due to the inductive coupling between the CPW and the pairs of SRRs at resonance. The circuit model (unit cell) of CPW transmission lines loaded with pairs of SRRs was first introduced in [1] and later revised in [2]. In [1], the magnetic wall concept was used, taking benefit of the symmetry of the structure and the even nature of the fundamental mode of the CPW. In [2], the unit cell was modeled by considering both SRRs (i.e. the magnetic wall concept was not used). Indeed, the main relevant improvement of the model reported in [2], as compared to the model reported in [1], is the position of the inductance modeling the shunt strips of CPWs loaded with the pairs of SRRs and shunt-connected strips (i.e. left-handed lines). However, this aspect is not fundamental for this paper since we are not considering left-handed lines, that is, the CPW lines are only loaded with SRRs.

The lines considered in this paper are CPWs loaded with single SRRs symmetrically etched in the back substrate side. As will be shown, these lines are transparent to signal propagation for the fundamental (even) CPW mode, whereas they inhibit the odd (slot) mode in the vicinity of SRR resonance. For completeness, we will also analyze CPWs loaded with complementary split-ring resonators (CSRRs) [3] symmetrically etched in the central strip. As will be shown, these CSRR-loaded CPW lines are transparent for the slot mode and opaque for the fundamental mode in the vicinity of CSRR resonance. The circuit model of a CPW loaded with symmetrically etched SRRs/CSRRs is provided in this paper, and used to analyze the behavior of the line. The paper is supported by experimental results and, finally, some potential applications are highlighted.

2 Selective mode suppression in SRR- and CSRR-loaded CPW transmission lines

The first CPW transmission lines under study are loaded with single and symmetrically etched SRRs, as depicted in Fig. 1b. For the fundamental CPW mode, there is a magnetic wall at the symmetry plane of the structure, and the SRRs cannot be excited at their first resonance since they exhibit an electric wall at their symmetry plane at this resonance [4]. The magnetic field lines generated by the currents flowing on the CPW structure are contra-directional in the slot regions. Since the SRRs are symmetrically etched

J. Naqui · M. Durán-Sindreu · F. Martín (✉)
GEMMA/CIMITEC, Departament d'Enginyeria Electrònica, Universitat Autònoma de Barcelona, 08193 Bellaterra (Barcelona), Spain
e-mail: Ferran.Martin@uab.es

Published online: 01 November 2012

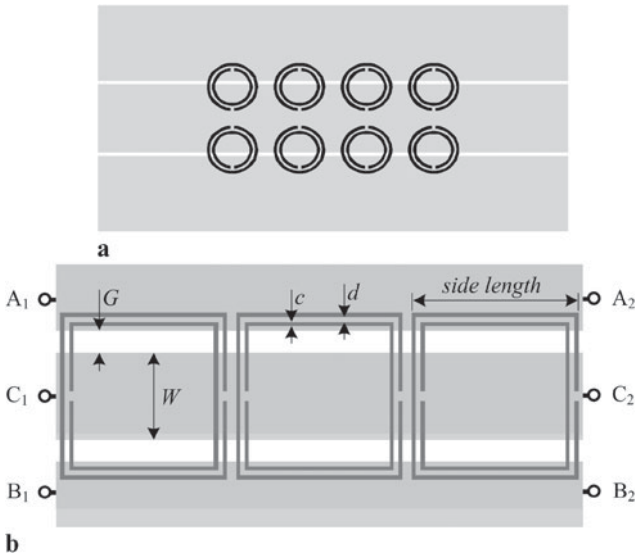

Fig. 1 CPWs loaded with symmetrically etched SRRs; CPW loaded with pairs of SRRs (**a**) [1] and CPW loaded with single SRRs (**b**). The upper metal is depicted in *light gray*. The SRRs are etched in the back substrate side. The relevant dimensions are indicated

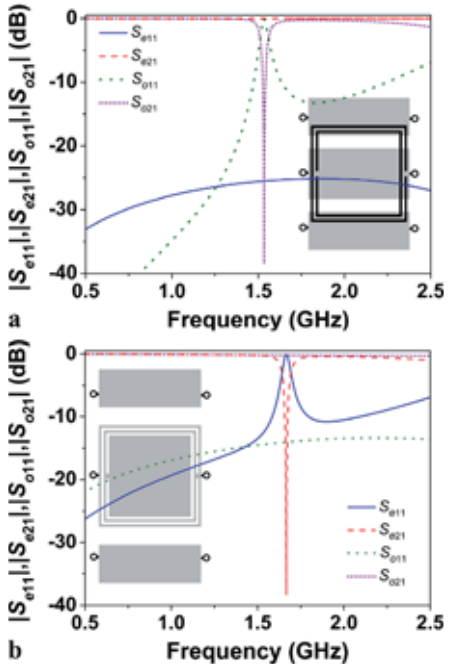

Fig. 2 Frequency response for CPW (e) and slot (o) modes of the indicated CPW loaded with (**a**) SRR and (**b**) CSRR. The substrate is Rogers RO3010 with thickness $h = 1.27$ mm and dielectric constant $\varepsilon_r = 10.2$. The dimensions are: for the SRR and CSRR, $c = d = 0.2$ mm and side length $= 7.6$ mm; for the CPW lines, $W = 4$ mm (**a**), $W = 8$ mm (**b**), $G = 1$ mm (**a**), and $G = 1.4$ mm (**b**). The characteristic impedance of the CPW mode (even mode) is 50 Ω. The even and odd modes are fed by, respectively, a 50 Ω coplanar port and a 100 Ω differential port

in the back substrate side, the axial components of the magnetic field lines within the SRR region exactly cancel, there is not a net axial magnetic field in that region, and the SRRs cannot be magnetically driven (the symmetry also precludes that the particles can be excited by means of the electric field present between the central strip and the ground planes). Thus, the structure is transparent for the fundamental CPW mode. However, there is a net axial magnetic field within the SRR region for the slot (odd) mode, the particle is excited at its first resonance, and, as a result, the injected power is expected to return to the source at that frequency.

Let us now consider that the CPW is loaded with a square-shaped CSRR symmetrically etched in the central strip, as the inset of Fig. 2b illustrates. In this case, the magnetic wall of the CPW structure (fundamental mode) is perfectly aligned with the magnetic wall of the particle at its resonance frequency [5], and the signal is inhibited in the vicinity of CSRR resonance. Conversely, for the slot mode, there is not a net axial electric field in the inner metallic region of the CSRR, the resonator cannot be excited, and the line is transparent for this mode (symmetry also cancels the particle activation through the magnetic field induced in the line).

To demonstrate the previous statements, we have simulated (by means of the commercial software Agilent Momentum) the transmission and reflection coefficients of a CPW loaded with a single square-shaped SRR for the even and odd modes (see Fig. 2a). As can be seen, the structure is transparent to the fundamental (even) mode, but a notch is clearly visible at SRR resonance for the slot mode. For the CPW loaded with a CSRR (Fig. 2b), the fundamental mode is inhibited in the vicinity of CSRR resonance, whereas the slot mode is transmitted between the input and output ports.

The main conclusions of this section are: (i) a CPW loaded with a symmetric SRR exhibits for the odd mode an identical behavior to that of a CPW loaded with pairs of SRRs for the fundamental mode, that is, a notch in the transmission coefficient; however, the line is transparent to the fundamental mode; (ii) a CPW loaded with a CSRR in the central strip inhibits the fundamental mode in the vicinity of particle resonance (similar to microstrip lines with CSRRs etched in the ground plane), but it is transparent to the odd mode.

3 Circuit model of a CPW loaded with symmetric SRRs

The lumped element equivalent circuit model of the structure of Fig. 1b (unit cell) is depicted in Fig. 3a. The coupling between adjacent resonators is considered to be negligible. The metallic terminals at ports 1 and 2 (shown in Fig. 1b) are also indicated for a better comprehension. C models the slot capacitance of the CPW line, L_e is the inductance of the line for the fundamental mode, L_o is the inductance of the line for the odd mode, the SRR is modeled as a resonant

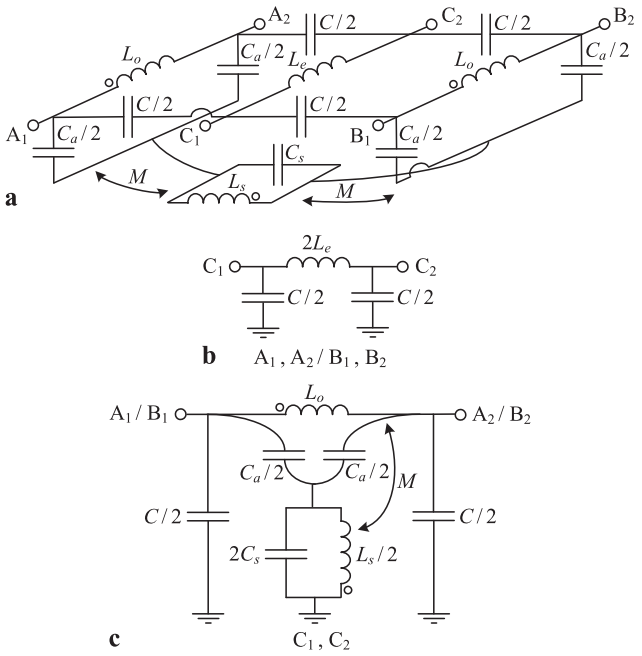

Fig. 3 Equivalent circuit model (unit cell) of a CPW loaded with symmetrically etched SRRs (**a**); equivalent circuit model for the even mode (**b**); equivalent circuit model for the odd mode (**c**)

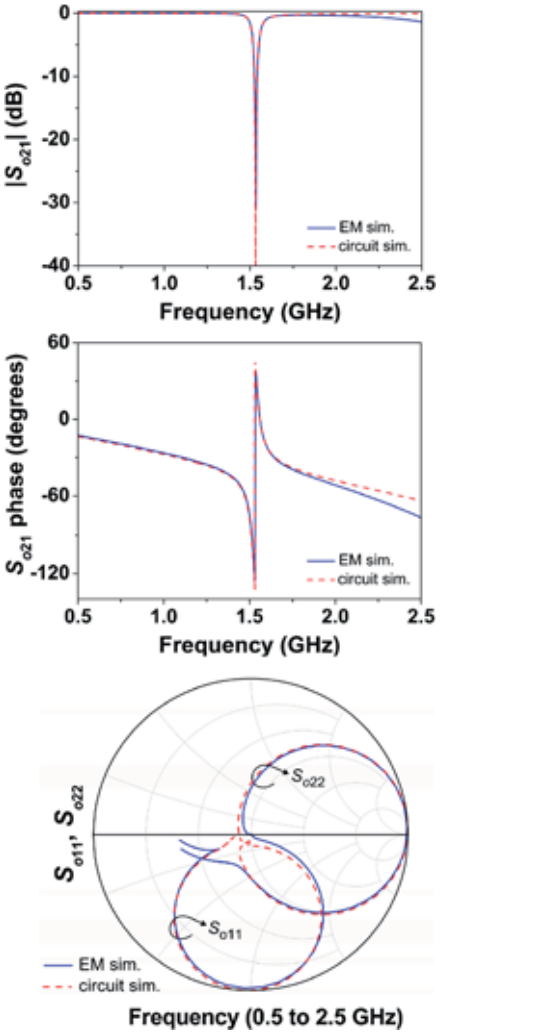

Fig. 4 Comparison of the electromagnetic and circuit simulations of the structure of Fig. 2a for the odd mode. The element values (referred to the circuit of Fig. 3c) are: $C = 1.38$ pF, $L_o = 2.96$ nH, $L_s = 3.66$ nH, $C_s = 2.73$ pF, $M = 0.66$ nH, and $C_a = 0.4$ pF

tank (L_s–C_s), M is the mutual inductance between the SRR and each half of the CPW transmission line, and, finally, C_a accounts for the electric coupling between the line and the SRRs. The electric coupling between the CPW transmission line and the SRR has been neglected so far. However, contrary to previous reported structures (for instance, that shown in Fig. 1a), in the structure of Fig. 1b, the slits of the SRR are aligned with the line axis. It is well known that SRRs exhibit cross polarization, that is, they can be excited by means of an axial magnetic field, but they can also be driven by means of an electric field with a non-negligible component in the plane of the particle and orthogonal to the plane containing the slits. Since for the odd mode of a CPW, there is a net electric field across the slots of the CPW transmission line, the electric coupling cannot be a priori neglected.

For the fundamental (even) mode, the terminals A_1, A_2, B_1, and B_2 are grounded, a magnetic wall arises in the symmetry plane, the SRR is opened, and the equivalent circuit model is simply that of a conventional transmission line (Fig. 3b). For the odd mode, the feeding signal is applied between the terminals A_1 and B_1 (i.e. ports 1 and 2 are differential ports). Thus, the symmetry plane exhibits a virtual ground, and the equivalent circuit model that results after applying the electric wall concept is identical to that of a CPW loaded with a pair of SRRs [1], namely a transmission line inductively coupled to a SRR, but including electric coupling as well (Fig. 3c).

From the electromagnetic simulation of the structure of Fig. 2a corresponding to the odd mode, we can extract the parameters of the model of Fig. 3c, according to the procedure described in [6]. Actually, the procedure described in [6] does not account for electric coupling. The circuit simulation obtained from the extracted parameters does not accurately fit the full-wave simulations of Fig. 2a for the odd mode. This means that electric coupling must be considered for an accurate description of the structure. Therefore, we have inferred the new circuit values (including C_a) by curve fitting. The comparison between the circuit and electromagnetic simulations is shown in Fig. 4, where the element values are indicated (see figure caption). As can be appreciated, good agreement is obtained by including electric coupling in the circuit simulation.

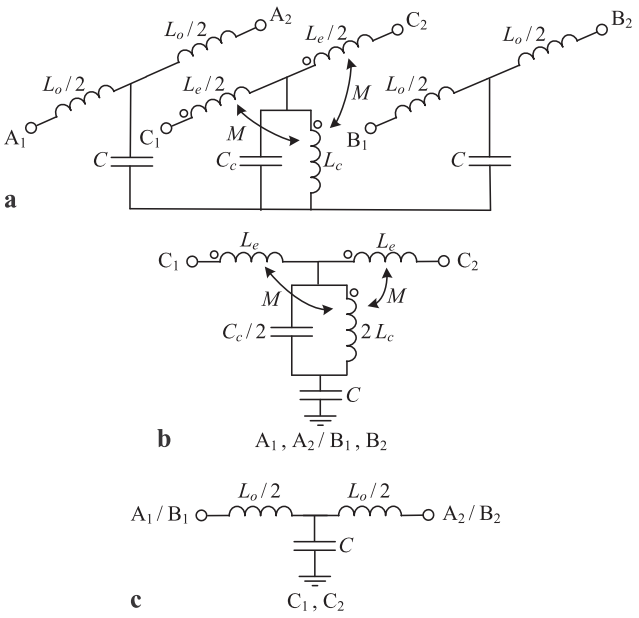

Fig. 5 Equivalent circuit model (unit cell) of a CPW loaded with symmetrically etched CSRRs (**a**); equivalent circuit model for the even mode (**b**); equivalent circuit model for the odd mode (**c**)

4 Circuit model of a CPW loaded with symmetric CSRRs

The lumped element equivalent circuit model of the CPW loaded with CSRRs in the central strip (Fig. 2b) is shown in Fig. 5 (inter-resonator coupling has not been considered). The capacitance C models the slot capacitance of the CPW line, L_e is the inductance of the line for the fundamental mode, L_o is the inductance of the line for the odd mode, the CSRR is modeled as a resonant tank (L_c–C_c), and, finally, M accounts for the magnetic coupling between the line and the CSRR. The magnetic coupling between the CPW transmission line and the CSRR has been neglected so far. However, contrary to previous reported structures, in the structure of Fig. 2b, the slits of the CSRR are aligned with the line axis. Under these conditions, cross-polarization effects are present and, hence, inductive coupling must also be included for accurate modeling.

Following a procedure similar to that explained in the previous section, we have extracted the parameters for the even mode corresponding to the electromagnetic simulation of the structure shown in Fig. 2b [7]. The comparison between the electromagnetic and circuit simulations is depicted in Fig. 6 (the element values are indicated in the caption), where it can be appreciated that the circuit and electromagnetic simulations are in good accordance.

5 Experimental validation

In order to experimentally validate the selective mode suppression in CPWs, we have designed some structures. One of them consists of a CPW loaded with a SRR in its back substrate side and with a CSRR in the central strip (Fig. 7a), while another structure is the same structure without the SRR. We have fed the CPWs by means of a slot line to generate the odd mode, and it is clear from Fig. 7b that the presence of the SRR inhibits this mode at SRR resonance (while this mode is not affected by the CSRR). On the other hand, we have designed two additional structures without the CPW to slot line transition: one of them with a SRR and a CSRR of identical dimensions to those of Fig. 7a (Fig. 8a); in the other one, the CSRR has been removed. We have obtained the transmission coefficient (Fig. 8b) which corresponds to the fundamental mode. In this case, the situation is reversed, that is, the notch is caused by the CSRR and the line is transparent at the resonance frequency of the SRR.

Notice that in Fig. 7b the response exhibits certain insertion losses due to the impedance mismatch on the coaxial (50 Ω impedance) to slot line (it has been found that it exhibits about 100 Ω impedance) transition. Nevertheless, this is irrelevant for the purpose of this work, since the main aim is to demonstrate the selective mode suppression of both CPW even and odd modes by using either SRRs or CSRRs.

6 Potential applications

CPW structures loaded with single SRRs or CSRRs may find applications in several fields. For example, CPW transmission lines with symmetrically loaded SRRs inhibit the slot mode, keeping the fundamental mode unaltered. Thus, a set of SRRs properly designed can be useful in certain CPW applications where the slot mode typically appears and must be suppressed. Another potential application of SRR-loaded lines concerns the implementation of novel sensors and detectors based on the loss of symmetry of the reported structures [8]. The lack of symmetry can be caused by many different reasons, such as a displacement or rotation, the presence of particles, inhomogeneities in the surrounding medium, etc., and sensing/detection can be simply carried out by measuring the transmission coefficient (many other sensors based on the variation of the resonance frequency of split rings have been reported [9–16]).

Concerning CSRR-loaded CPWs, the presence of these particles causes notches in the transmission coefficient for the fundamental mode, and this can be useful for the rejection of interfering signals in communication systems. As long as the CSRRs are etched in the central strip, this undesired signal suppression can be achieved without the penalty of increasing device area and cost.

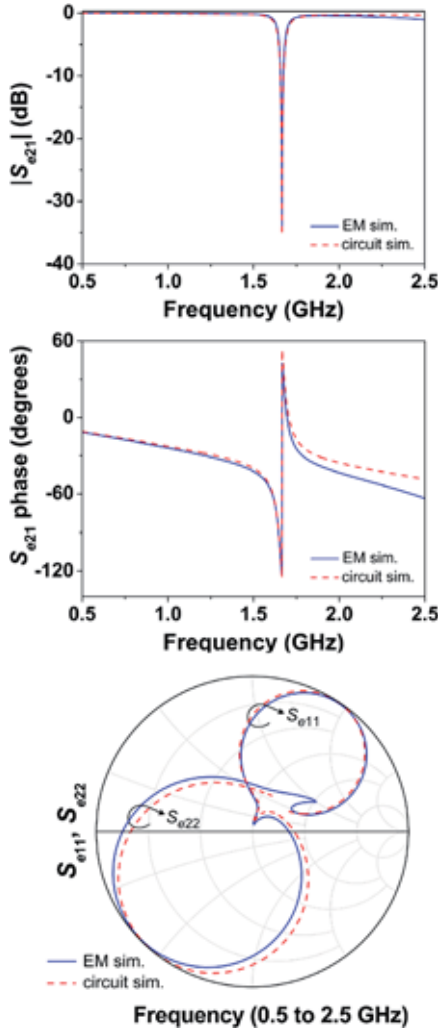

Fig. 6 Comparison of the electromagnetic and circuit simulations of the structure of Fig. 2b for the even mode. The element values (referred to the circuit of Fig. 5b) are: $C = 0.75$ pF, $L_e = 2.13$ nH, $L_c = 0.49$ nH, $C_c = 17.3$ pF, and $M = 0.2$ nH

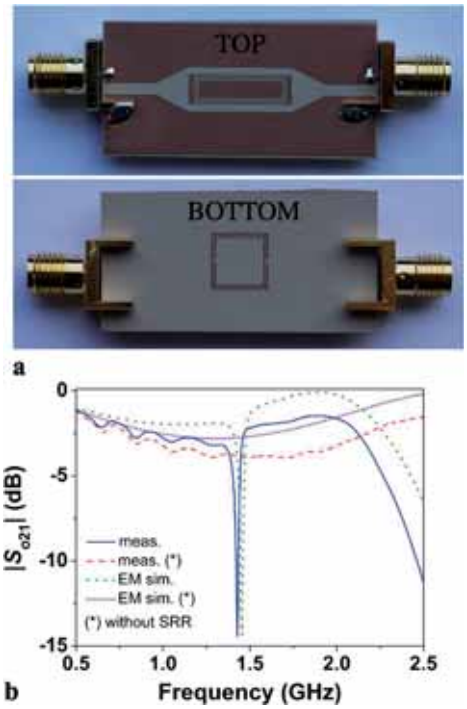

Fig. 7 CPW loaded with a SRR and a CSRR and fed through a slot line to generate the slot mode (**a**) and the frequency response (**b**). The substrate is Rogers RO3010 with $h = 1.27$ mm, $\varepsilon_r = 11.2$, and loss tangent $\tan\delta = 0.0023$. The dimensions are: for the SRR, $c = d = 0.2$ mm and side length = 7.6 mm; for the CSRR, $c = d = 0.2$ mm, longitudinal side length = 12.6 mm, and transverse side length = 3.6 mm; for the CPW, $W = 4$ mm and $G = 1$ mm; for the slot line, the slot width is 1.5 mm

In this paper, the potentiality of the reported structures is illustrated by means of a proof-of-concept demonstrator of a radio-frequency bar code [17]. The idea is to etch SRRs with different dimensions (i.e. providing different resonance frequencies) in the back substrate side of a CPW transmission line. If the SRRs are aligned with the symmetry plane of the CPW structures, the line is transparent. However, we can codify the line by laterally displacing the SRRs, since this produces a transmission zero in the transmission coefficient at the corresponding frequency, and this can be easily monitored. This frequency-domain codification is similar to that reported in [18], but in our case it is not necessary to remove the SRR to set a logic '1'; it suffices by aligning it with the line; hence, our approach opens the possibility to implement reconfigurable radio-frequency bar codes. A three-bit bar code with the sequence '010', that is, with two SRRs laterally shifted and with one SRR centered, is depicted in Fig. 9a, whereas Fig. 9b shows the simulated and measured frequency responses. For comparison, the frequency response corresponding to the code '101' is also depicted. With the purpose to prevent the presence of the odd mode, the ground planes are connected through back side strips and vias. With these results, the radio-frequency bar code proof-of-concept based on CPW structures loaded with SRRs is validated.

7 Conclusions

In conclusion, the selective suppression of either the fundamental (even) or the slot (odd) mode in CPW structures by using complementary split-ring resonators (CSRRs) and split-ring resonators (SRRs), respectively, has been demonstrated. In order to preserve the integrity of the mode for which the line is transparent, it is necessary to etch the particles symmetrically in the line. We have provided the circuit models of SRR and CSRR symmetrically loaded CPW transmission lines, including those for even and odd mode excitations, and it has been demonstrated through parameter extraction that these models describe the structures to a good approximation. It has been necessary to include both

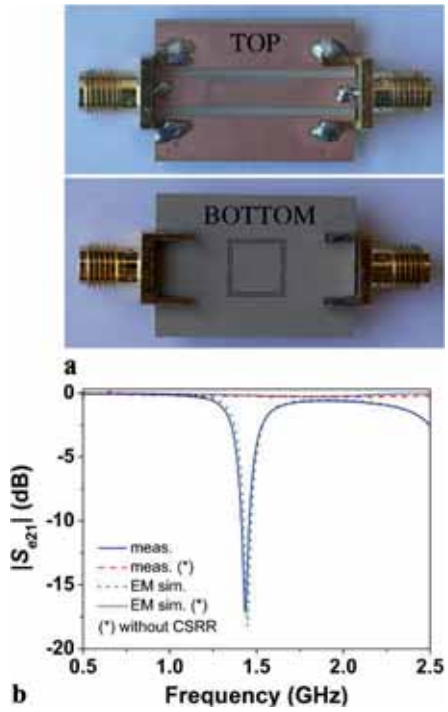

Fig. 8 CPW loaded with a SRR and a CSRR and excited through the fundamental (even) mode (**a**) and the frequency response (**b**). The substrate and dimensions are those indicated in the caption of Fig. 7

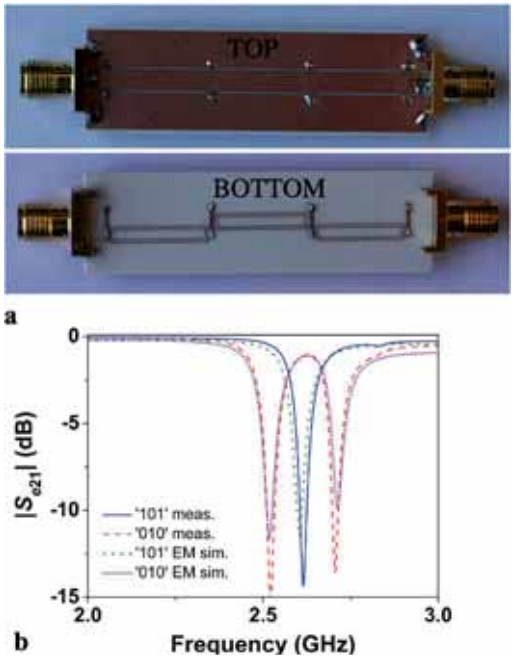

Fig. 9 CPW loaded with three SRRs resonating at 2.39 GHz, 2.48 GHz, and 2.57 GHz and codified with the code '010' (**a**) and the frequency response (**b**). The frequency response corresponding to the code '101' is also depicted. The substrate is Rogers RO4003C with $h = 0.8128$ mm, $\varepsilon_r = 3.1$, and $\tan\delta = 0.0021$. The dimensions are: for the SRRs, $c = d = 0.2$ mm, transverse side length $= 2.47$ mm, and longitudinal side length $= 14.3$ mm, 13.75 mm, and 13.25 mm; for the CPW, $W = 3.3$ mm and $G = 0.2$ mm

magnetic and electric coupling between the line and the resonators for an accurate modeling. The need for this twofold coupling has been justified as due to the alignment of the resonator cuts with the CPW line axis. The selective mode suppression has been experimentally validated and potential applications of these structures have been highlighted, with special emphasis to radio-frequency bar codes. A proof-of-concept demonstrator of a CPW transmission line with a three-bit spectral signature has been provided. Work is in progress to implement practical bar codes with a higher number of bits, and to develop new sensors based on the symmetry properties of CPW transmission lines.

Acknowledgements This work has been supported by MICIIN-Spain (projects TEC2010-17512 and CSD2008-00066) and by AGAUR-Generalitat de Catalunya, through project 2009SGR-421.

References

1. F. Martín, F. Falcone, J. Bonache, R. Marqués, M. Sorolla, Appl. Phys. Lett. **83**, 4652 (2003)
2. F. Aznar, J. Bonache, F. Martín, Appl. Phys. Lett. **92**, 043512 (2008)
3. F. Falcone, T. Lopetegi, J.D. Baena, R. Marqués, F. Martín, M. Sorolla, IEEE Microw. Wirel. Compon. Lett. **14**, 280 (2004)
4. R. Marqués, F. Medina, R. Rafii-El-Idrissi, Phys. Rev. B **65**, 144441 (2002)
5. J.D. Baena, J. Bonache, F. Martín, R. Marqués, F. Falcone, T. Lopetegi, M.A.G. Laso, J. García, I. Gil, M. Flores-Portillo, M. Sorolla, IEEE Trans. Microw. Theory Tech. **53**, 1451 (2005)
6. F. Aznar, M. Gil, J. Bonache, J.D. Baena, L. Jelinek, R. Marqués, F. Martín, J. Appl. Phys. **104**, 114501 (2008)
7. J. Bonache, M. Gil, I. Gil, J. Garcia-García, F. Martín, IEEE Microw. Wirel. Compon. Lett. **16**, 543 (2006)
8. J. Naqui, M. Durán-Sindreu, F. Martín, Sensors **11**, 7545 (2011)
9. X.-J. He, Y. Wang, J.-M. Wang, T.-L. Gui, Microsyst. Technol. **16**, 1735 (2010)
10. E. Cubukcu, S. Zhang, Y.-S. Park, G. Bartal, X. Zhang, Appl. Phys. Lett. **95**, 043113 (2009)
11. T. Driscoll, G.O. Andreev, D.N. Basov, S. Palit, S.Y. Cho, N.M. Jokerst, D.R. Smith, Appl. Phys. Lett. **91**, 062511 (2007)
12. R. Melik, E. Unal, N.K. Perkgoz, C. Puttlitz, H.V. Demir, Appl. Phys. Lett. **95**, 011106 (2009)
13. R.A. Yogi, R.S. Parolia, R.N. Karekar, R.C. Aiyer, Microw. Meas. Sci. Technol. **13**, 1558 (2002)
14. P.K. Pattnaik, B. Vijayaaditja, T. Srinivas, A. Selvarajan, in *Proc. Int. Conf. MEMS, NANO and Smart Systems (ICMENS'05)*, (2005)
15. X. Liu, C. Xue, S. Yan, J. Xiong, W. Zhang, in *Proc. 4th IEEE Int. Conf. Nano/Micro Engineered and Molecular Systems*, Shenzhen, China, 5–8 January (2009), pp. 1000–1003
16. C. Mandel, B. Kubina, M. Schüßler, R. Jakoby, in *Eur. Microwave Conf. Dig*, October (2011), pp. 79–82
17. S. Preradovic, N.C. Karmakar, IEEE Microw. Mag. **11**, 87 (2010)
18. S. Preradovic, I. Balbin, N.C. Karmakar, G.F. Swiegers, IEEE Trans. Microw. Theory Tech. **57**, 1411 (2009)

Article APA13

Selective mode suppression in microstrip differential lines by means of electric-LC (ELC) and magnetic-LC (MLC) resonators

J. Naqui, M. Durán-Sindreu, F. Martín

Appl Phys A
DOI 10.1007/s00339-013-8031-6

Applied Physics A
Materials Science & Processing

Selective mode suppression in microstrip differential lines by means of electric-LC (ELC) and magnetic-LC (MLC) resonators

J. Naqui · M. Durán-Sindreu · F. Martín

Received: 2 October 2013 / Accepted: 2 October 2013

Abstract In this paper, it is demonstrated that the so-called electric-LC (ELC) resonators, and their dual counterparts, the magnetic-LC (MLC) resonators, are useful for the selective suppression of either the differential or the common mode in microstrip differential lines. The key point to mode suppression is the alignment of the resonator with the electric (differential mode) or magnetic (common mode) wall of the line. It is shown that by simply rotating the resonators 90° we can selectively choose the suppressed mode in the vicinity of the resonator's fundamental resonance frequency. The theory is validated through full-wave electromagnetic simulation, the lumped element equivalent circuit models of the proposed structures and experimental data.

1 Introduction

Split-ring resonators (SRRs) [1] and their complementary counterparts (CSRRs) [2] (Fig. 1) have been extensively used for the implementation of metamaterials and many devices based on them [3]. One of the applications of these metamaterial resonators is the selective mode suppression in multimode transmission lines. Specifically, SRRs etched in the back substrate side of a CPW with their symmetry plane (xz plane) aligned with the symmetry plane of the line, are useful to suppress the parasitic slot mode of the line at their fundamental resonance, whereas they are transparent for the fundamental CPW (common) mode [4] [Fig. 2(a)]. On the other hand, CSRRs have been applied to suppress the common mode in microstrip differential lines and balanced circuits [5]. In these applications, the CSRRs must be etched in the ground plane with their symmetry plane aligned with the symmetry plane of the differential line [Fig. 2(b)].

The key aspect to suppress either the differential or the common mode, keeping the other mode unaltered (or almost unaltered), is the perfect alignment of electric or magnetic walls between the line and the resonator. Thus, for the CPW loaded with symmetrically etched SRRs, the electric wall of the SRR at their symmetry plane is responsible for the slot mode suppression, since the CPW exhibits an electric wall at the symmetry plane for this mode. For a microstrip differential line, the symmetry plane is a magnetic wall for the common mode. Therefore, by symmetrically etching a CSRR in the ground plane, where the symmetry plane is also a magnetic wall, the common mode is suppressed in the vicinity of the fundamental CSRR resonance, whereas the differential mode is kept unaltered.

SRRs/CSRRs exhibit bianisotropy [3, 6, 7], which means that they can be excited by means of a uniform axial time-varying magnetic/electric field, and/or through an electric/magnetic field orthogonally applied to the symmetry plane of the particle. When these particles (SRRs or CSRRs) are loading elements of a transmission line, it is clear that the driving fields generated by the line are not uniform. Nevertheless, it has been demonstrated that both CPW and microstrip lines loaded with symmetrically etched SRRs and CSRRs, respectively, exhibit mixed coupling between the line and the resonators for those line modes that are suppressed [8].

In this paper, alternative resonators are considered, namely, the so-called electric-LC resonator, ELC [9], and its complementary particle, the magnetic-LC resonator, MLC (see Fig. 3). Such resonators are bisymmetric, one of the

J. Naqui · M. Durán-Sindreu · F. Martín ( )
GEMMA/CIMITEC, Departament d'Enginyeria Electrònica, Universitat Autònoma de Barcelona, 08193 Bellaterra, Barcelona, Spain
e-mail: Ferran.Martin@uab.cat

Published online: 16 October 2013

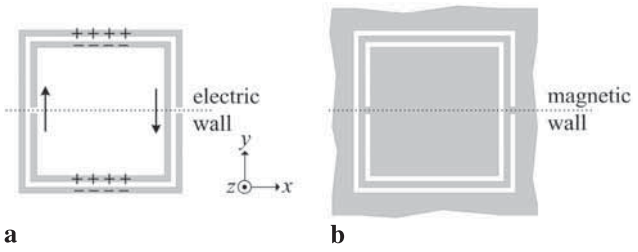

Fig. 1 Typical topology of an SRR (**a**) and a CSRR (**b**). A sketch of the currents and the distribution of charges for the SRR at the fundamental resonance is also indicated. Note that the symmetry plane is an electric wall. From the Babinet principle, it follows that the CSRR exhibits a magnetic wall at the symmetry plane

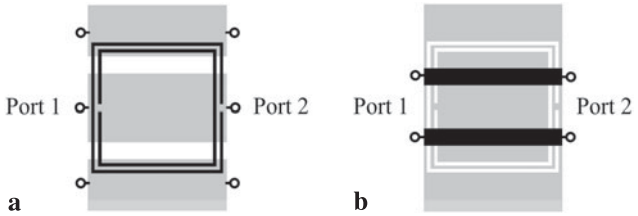

Fig. 2 CPW loaded with a symmetrically etched SRR (**a**) and microstrip differential line loaded with a symmetrically etched CSRR (**b**)

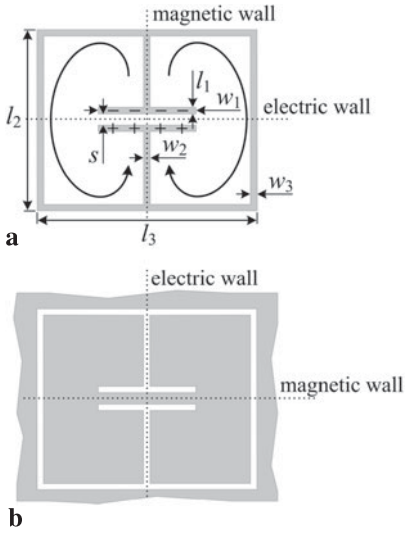

Fig. 3 Typical topology of an ELC (**a**) and an MLC (**b**) resonator. The nature of the symmetry planes at the fundamental resonance is indicated, as well as a sketch of the currents and the distribution of charges for the ELC

symmetry planes being a magnetic wall and the other one being an electric wall at the fundamental resonance. Moreover, the resonators are non-bianisotropic because of the inversion symmetry with regard to its center. The selective mode suppression with ELC and MLC resonators in microstrip differential lines is discussed on the basis of symmetry properties. The theory is validated through electromagnetic simulation, circuit simulation of the lumped element equivalent circuit models, and experiment.

2 ELC and MLC resonators

The ELC resonator was proposed by Schurig et al. for the implementation of resonant-type negative permittivity metamaterials, as an alternative to the well-known wire media, described by the Drude model [9]. The ELC resonator consists of two closed inductive loops connected to a common capacitor. At the fundamental resonance, the instantaneous current is clockwise in one loop and counterclockwise in the other loop [see Fig. 3(a)], thus giving rise to a net displacement current in the central capacitor. Therefore, at the fundamental resonance, the magnetic moment associated with currents in both loops cancels out and the particle cannot be excited by a uniform time-varying magnetic field applied in the axial direction (this is the main driven mechanism in SRRs). However, there is still an electric dipole moment associated with the capacitor. Thus, the ELC resonator can be electrically driven (or coupled) by means of an electric field applied in the particle plane in the direction orthogonal to the electric wall. Note that due to charge and current symmetry, the vertical symmetry plane in Fig. 3(a) is a magnetic wall for the fundamental resonance.

For the MLC, we can invoke the Babinet principle and conclude that this particle also exhibits electric and magnetic walls, rotated 90° as compared to those of the ELC. In other words, the particle cannot be excited by means of a uniform axial time-varying electric field (as a CSRR is driven), but it can be driven through a magnetic field orthogonally applied to the magnetic wall.

3 Microstrip differential lines loaded with ELCs and MLCs

As it was discussed before [5], if a symmetric transmission line is loaded with a symmetric resonator with both symmetry planes aligned, and the symmetry planes are of the same nature (electric or magnetic walls), signal propagation in the vicinity of the fundamental resonance is inhibited (i.e., a transmission zero appears). However, the line is transparent if such symmetry planes are distinct. In particular, if we consider a microstrip differential line loaded with an ELC or an MLC, there are 4 cases of interest for selective mode suppression, depicted in Figs. 4 and 5. In Figs. 4(a) and (b), the differential line is loaded with an ELC etched on the upper side of the substrate, with a relative orientation of 90° between the loading elements. According to these orientations, it is expected that the structure of Fig. 4(a) is transparent for the differential mode and produces a notch for the common mode, contrarily to Fig. 4(b).

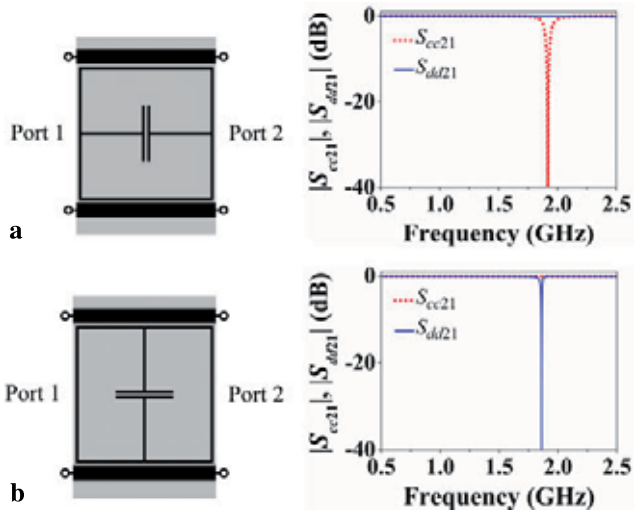

Fig. 4 Microstrip differential line loaded with an ELC with the magnetic (**a**) and electric (**b**) wall aligned with the symmetry plane of the line. The substrate is *Rogers RO3010* with thickness $h = 1.27$ mm and dielectric constant $\varepsilon_r = 10.2$. The line dimensions are: line width $W = 1.1$ mm and line separation $S = 10.4$ mm, which corresponds to a 50 Ω even mode (common mode related) and odd mode (differential mode related) characteristic impedance. The ELC dimensions are: $w_1 = 4$ mm, $w_2 = w_3 = l_1 = s = 0.2$ mm, $l_2 = l_3 = 10$ mm

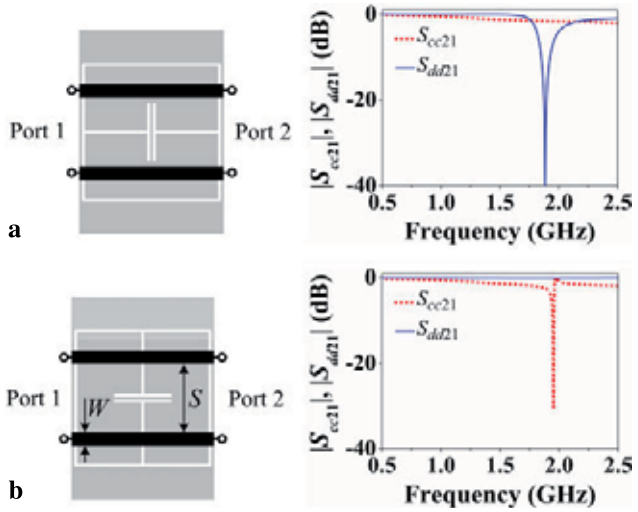

Fig. 5 Microstrip differential line loaded with an MLC with the electric (**a**) and magnetic (**b**) wall aligned with the line. The substrate is *Rogers RO3010* with thickness $h = 1.27$ mm and dielectric constant $\varepsilon_r = 10.2$. The line dimensions are: $W = 1$ mm and $S = 5$ mm, corresponding to a 50 Ω even mode and odd mode characteristic impedance without the MLC etching. The MLC dimensions are: $w_1 = 4$ mm, $w_2 = w_3 = l_1 = s = 0.2$ mm, and $l_2 = l_3 = 10$ mm

In Figs. 5(a) and (b), the differential line is loaded with an MLC resonator etched in the ground plane. In this case the situation is reversed since the electric and magnetic walls of ELCs and MLCs are interchanged. The reflection and the transmission coefficients for the differential (S_{dd11} and S_{dd21}) and common (S_{cc11} and S_{cc21}) modes of the structures of Figs. 4 and 5 have been inferred by means of the *Agilent Momentum* commercial software. The transmission coefficient results (also depicted in Figs. 4 and 5) validate the selective mode suppression achievable in these differential lines by merely rotating the resonators 90°.

It is important to emphasize that the driving fields of the particles are not uniform. Indeed, in the configuration of Fig. 4(a), the ELC cannot be excited by the electric field generated by the differential line in the common mode. However, for this mode, the magnetic fields generated by the differential line have contra-directional axial components with regard to the midplane, sufficient to excite the particle. Therefore, the ELC resonator is excited by means of the magnetic field generated by the line under common mode operation. Similarly, in the configuration of Fig. 5(a), the MLC is excited under differential mode operation which, because of the electric field generated by the pair of lines, is able to induce an electric dipole moment and a net current flow in the ground plane, across the symmetry plane of the differential line (or across the electric wall of the MLC). Thus, the terminology of these particles does not obey the nature of the driving fields in the considered configurations (the reason is that the fields are not uniform). However, the original nomenclature, given by Schurig et al. [9] to the resonator of Fig. 3(a), i.e. ELC, is preserved. For coherence, the resonator of Fig. 3(b) is called MLC particle by the authors.

4 Lumped element equivalent circuit models

Let us now consider the lumped element equivalent circuit models of the structures of Figs. 4 and 5. In Fig. 4(a), the ELC can only be excited by the magnetic field generated by the line (common mode), but not by the electric field, due to the particle orientation. Similarly, for the MLC of Fig. 5(a), excitation under differential mode operation is only possible through the electric field generated by the line. In Figs. 4(b) and 5(b), particle excitation under differential and common mode, respectively, is more complex, since both electric and magnetic coupling between the line and the resonator must be considered. Let us thus start with the lumped element equivalent circuit models of the structures of Figs. 4(a) and 5(a), where mixed coupling is not present.

The model of the ELC-loaded differential line of Fig. 4(a) is depicted in Fig. 6(a). The electric and magnetic coupling between the pair of lines has been neglected due to the significant separation between the individual lines (necessary to accommodate the ELC). The per-section inductance and capacitance of the individual lines are modeled by L and C, respectively. The ELC resonator is modeled by the inductances L_e and the capacitance C_e, and the magnetic coupling between the lines and the resonator is accounted for through the mutual inductances M. The equivalent circuit models for

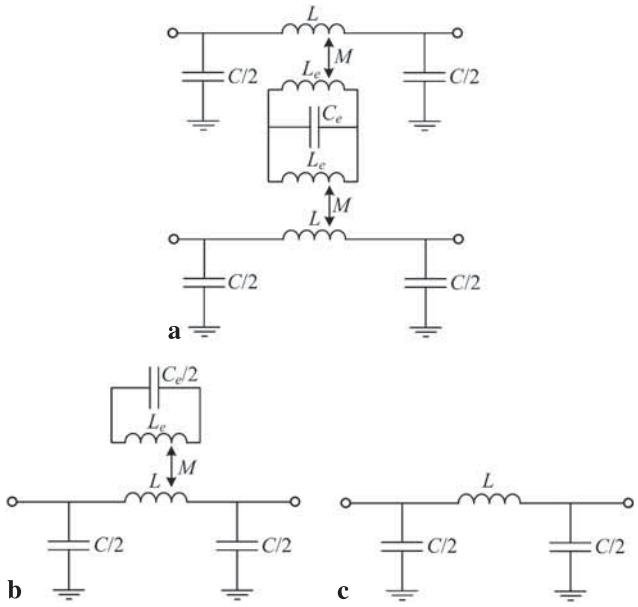

Fig. 6 (**a**) Lumped element equivalent circuit model of the ELC-loaded differential line of Fig. 4(a); (**b**) circuit model for the even mode; (**c**) circuit model for the odd mode.

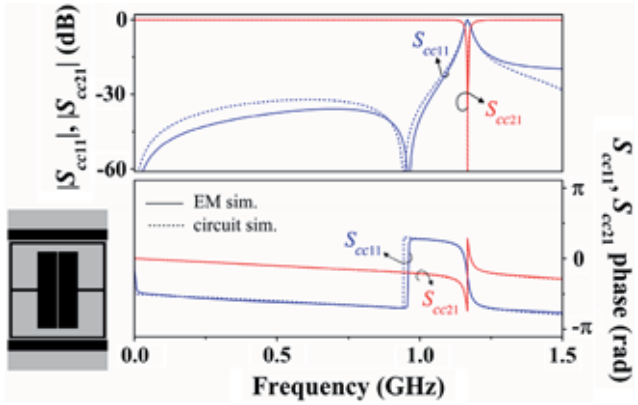

Fig. 7 Frequency response (common mode) for the structure of Fig. 4(a) with $l_1 = 2$ mm and $w_1 = 8$ mm and for its circuit model of Fig. 6(b). The circuit parameters are: $L = 4.57$ nH, $C = 2.2$ pF, $L_e = 4.57$ nH, $C_e = 8.14$ pF, and $M = 1$ nH

even and odd mode (common and differential mode related, respectively) excitation are depicted in Figs. 6(b) and (c). For the common mode, the symmetry plane is an open circuit, and the model is identical to that of an SRR-loaded line, giving a notch in the transmission coefficient at resonance [10, 11]. For the differential mode, the symmetry plane is a short circuit and the ELC no longer plays an active role. Therefore, the line is transparent for this mode. For the ELC-loaded line of Fig. 7, we have extracted the circuit parameters from the electromagnetic simulation of the frequency response for the common mode following the procedure explained in [12]. The agreement between circuit and electromagnetic simulations is remarkable. Note that the topology

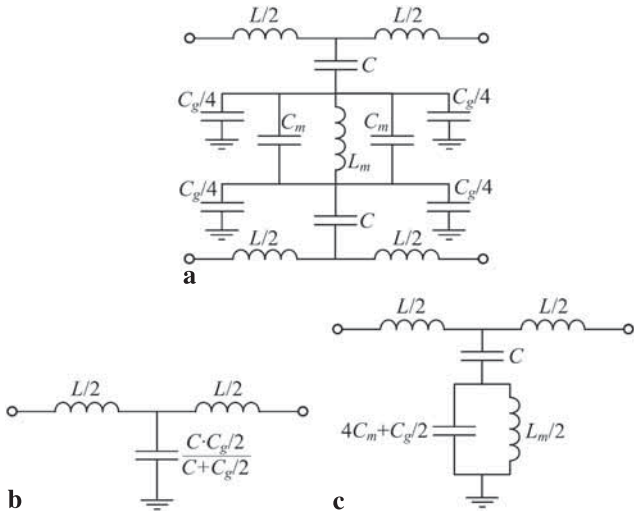

Fig. 8 (**a**) Lumped element equivalent circuit model of the MLC-loaded differential line of Fig. 5(a); (**b**) circuit model for the even mode; (**c**) circuit model for the odd mode

of the ELC of Fig. 7 has been modified as compared with that of Fig. 4 in order to reduce the electrical size of the particle at resonance (under these conditions the lumped element circuit model is valid in a wider frequency range).

The model of the MLC-loaded differential line of Fig. 5(a) is depicted in Fig. 8(a). The per-section line inductance and capacitance are modeled, respectively, by L and C (again, the coupling between the line pair is not significant). However, note that actually L is the line inductance with the presence of the MLC and C acts as the coupling capacitance between the lines and the MLC. The resonator is modeled by the inductance L_m and the capacitances C_m. Finally, the particle is capacitively connected to the ground plane through the slot ring capacitance modeled by C_g. The equivalent common and differential mode models are depicted in Figs. 8(b) and (c), respectively. For the common mode, the resonator is opened, and the resulting model is that of a transmission line with modified shunt capacitance. Thus, some attenuation can occur as can be seen in Fig. 5(a), as a consequence of the MLC etching (i.e., a defected ground structure) that disturbs the return current flowing on the ground plane modifying the line parameters [5]. On the other hand, for the differential mode, there is a short circuit in the symmetry plane, and the circuit model is identical to that of a CSRR-loaded microstrip line, providing a notch in the transmission coefficient for such mode at resonance. We have considered the MLC-loaded line of Fig. 9, and we have extracted the circuit parameters for the differential mode from the electromagnetic simulation of the frequency response for this mode as reported in [13]. The agreement between circuit and electromagnetic simulations is also good.

Let us now focus on the lumped element equivalent circuit models that result by rotating the ELC and the MLC

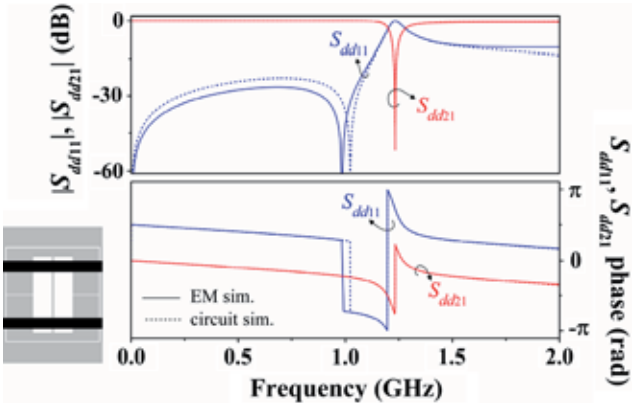

Fig. 9 Frequency response (differential mode) for the structure of Fig. 5(a) with $l_1 = 2$ mm and $w_1 = 8$ mm and for its circuit model of Fig. 8(c). The circuit parameters are: $L = 6.07$ nH, $C = 1.53$ pF, $4C_m + C_g/2 = 7.47$ pF, and $L_m = 3.71$ nH

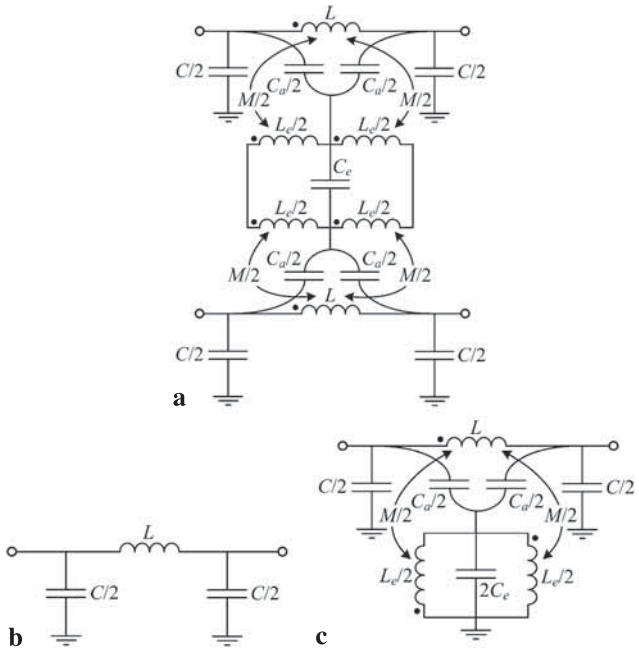

Fig. 10 (**a**) Lumped element equivalent circuit model of the ELC-loaded differential line of Fig. 4(b); (**b**) circuit model for the even mode; (**c**) circuit model for the odd mode

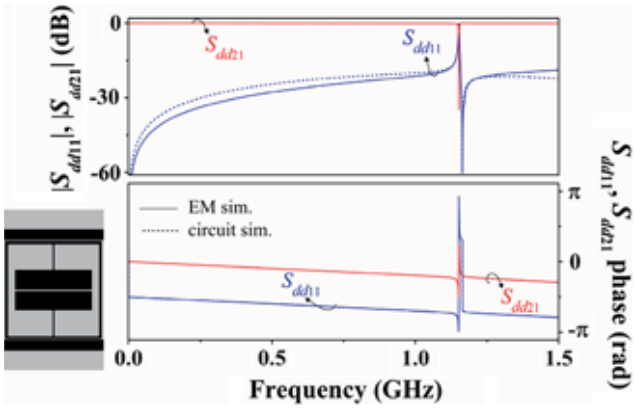

Fig. 11 Frequency response (differential mode) for the structure shown in Fig. 4(b) with $l_1 = 2$ mm and $w_1 = 8$ mm and for its circuit model in Fig. 10(c). The circuit parameters are: $L = 4.09$ nH, $C = 1.88$ pF, $L_e = 4.62$ nH, $C_e = 8.04$ pF, $M = 1.12$ nH, and $C_a = 0.44$ pF

90°, that is, the models describing the structures of Figs. 4(b) and 5(b), where both electric and magnetic coupling must be considered. For the structure of Fig. 4(b), the circuit model is that depicted in Fig. 10(a). In this circuit, the magnetic coupling's sign is provided by the dot convention to avoid any ambiguity. The resonator has been rotated, and the coupling capacitances, C_a, have been added to account for electric coupling. Indeed, since the symmetry plane in the configuration of the structure of Fig. 4(b) is an electric wall for the differential mode, electric coupling is the main driving mechanism of the ELC for this mode (the magnetic coupling is not able to induce resonant currents by itself). The circuit models for the common and differential modes are depicted in Figs. 10(b) and (c), respectively, where it is clear that the common mode is not able to excite the particle and the structure is transparent for this mode. Conversely, the differential mode produces a notch in the transmission coefficient, as the equivalent circuit model of such a mode confirms. In order to match the frequency response for the circuit model (differential mode) to that inferred from the electromagnetic simulation, we have considered the structure of Fig. 11 and we have tuned the coupling capacitance, readjusting slightly the rest of parameters corresponding to Fig. 7 (the geometries of the differential line and the ELC are identical). As can be seen, the agreement is reasonably good.

The MLC-loaded differential line of Fig. 5(b) is modeled by the circuit of Fig. 12(a). This is obtained by rotating the particle and splitting the coupling capacitances. Moreover, magnetic coupling has been introduced and is accounted for by the mutual inductances M. The equivalent circuit models for the common and differential modes, which are shown respectively in Figs. 12(b) and (c), indicate that the structure is transparent for the differential mode, whereas a notch appears for the common mode. For the latter mode, the magnetic coupling to the strip connecting the two inner halves of the MLC is absolutely necessary to excite the particle. Otherwise, resonance could not be driven exclusively through the electric coupling. Note also that, by applying the magnetic wall concept, the resulting mutual inductance in Fig. 12(b) is twice that considered in Fig. 12(a). Conversely, an electric wall in Fig. 10(a) does not scale the mutual inductance, as can be appreciated in Fig. 10(c). Again, the electromagnetic simulation for the common mode is compared to the circuit simulation for such a mode (Fig. 13), and the agreement is also good, thus confirming the validity of the proposed model.

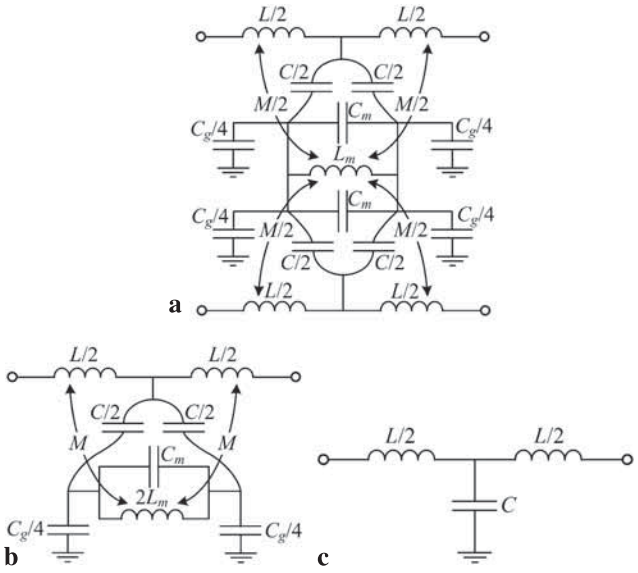

Fig. 12 (**a**) Lumped element equivalent circuit model of the MLC-loaded differential line of Fig. 5(b); (**b**) circuit model for the even mode; (**c**) circuit model for the odd mode

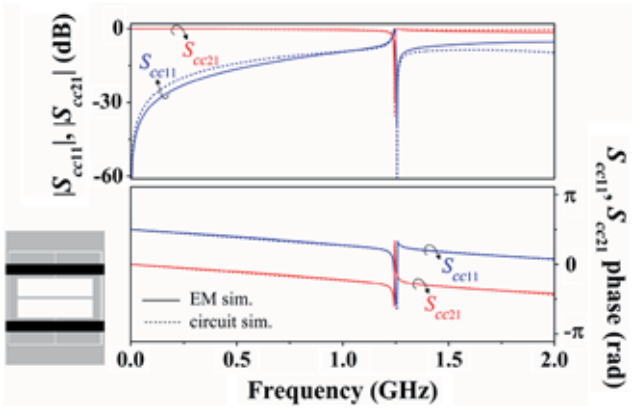

Fig. 13 Frequency response (common mode) for the structure shown in Fig. 5(b) with $l_1 = 2$ mm and $w_1 = 8$ mm and for its circuit model in Fig. 12(b). The circuit parameters are: $L = 9.3$ nH, $C = 1.53$ pF, $L_m = 3.64$ nH, and $C_m = 0.93$ pF, $C_g = 7.5$ pF, and $M = 0.5$ nH

Finally, it is worth to highlight that all the proposed structures are symmetric with regard to the ports (i.e., $S_{cc11} = S_{cc22}$ and $S_{dd11} = S_{dd22}$), and their corresponding circuits as well.

5 Applications

The proposed structures can be useful for common mode suppression in differential lines and balanced circuits [5], for differential notch/stopband filters, or for the implementation of sensors based on symmetry properties [14]. Specifically, with a circular structure based on the configurations of Fig. 4, it is possible to implement a rotation sensor in microstrip technology similar to that based on the CPW structure reported in [14]. On the other hand, as compared with the structures used in [5], based on CSRRs, the structure of Fig. 4(a) is able to suppress the common mode keeping the ground plane unaltered. However, this solution seems to be not so suitable for common mode suppression because of its inherent narrow-band rejection. On the contrary, a narrow balanced stopband filter with low insertion loss in the transmission bands can be useful in order to suppress undesired differential signals. To this end, we have designed an order-3 balanced stopband filter based on the structure of Fig. 5(a). The filter is composed of three cascaded MLCs with slightly different longitudinal dimensions to widen the stopband. A photograph of the fabricated filter and the frequency response are shown in Fig. 14. The measured response exhibits a rejection of more than 20 dB for differential signals over a fractional bandwidth of 14.3 % centered at 1.3 GHz.

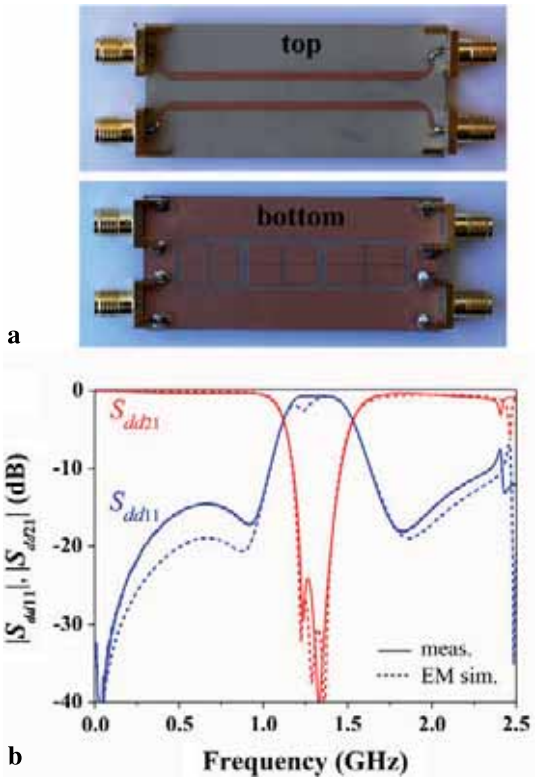

Fig. 14 (**a**) Photograph and (**b**) differential mode frequency response for the designed differential stopband filter. The substrate is Rogers *RO3010* with $h = 1.27$ mm, $\varepsilon_r = 10.2$, and loss tangent $\tan(\delta) = 0.0023$. Line dimensions are: $W = 1.6$ mm and $S = 5$ mm (not corresponding to a 50-Ω odd mode impedance), designed to mitigate the passband insertion loss due to the presence of the resonators. MLC dimensions are: $w_1 = 8$ mm, $w_2 = l_1 = s = 0.2$ mm, $w_3 = 0.8$ mm, $l_2 = [13.2, 15.1, 17.6]$ mm, and $l_3 = 10$ mm. The inter-resonator distance is 0.2 mm

6 Conclusions

In conclusion, it has been demonstrated that the differential and common modes in microstrip differential lines can be selectively suppressed by loading the lines with either ELC or MLC bisymmetric resonators. Key to this selective mode suppression at the fundamental resonance frequency of the particles is the presence of a magnetic and an electric wall, orthogonally oriented, in these resonators. Hence, it is possible to either suppress the common or the differential mode by simply rotating the considered particle (ELC or MLC) 90°. We have proposed lumped element circuit models for microstrip differential lines loaded with both resonators for the two considered orientations, and the agreement between the frequency responses inferred from the circuit and electromagnetic simulations is good. Finally, potential applications have been highlighted, and a differential stopband filter has been presented.

Acknowledgements This work has been supported by MICIIN-Spain (projects TEC2010-17512, CSD2008-00066, and TEC2011-13615-E) and by AGAUR-*Generalitat de Catalunya*, through project 2009SGR-421. Jordi Naqui feels also indebted to MECD (Spain) for supporting his work through the FPU grant AP2010-0431.

References

1. J.B. Pendry, Magnetism from conductors and enhanced nonlinear phenomena. IEEE Trans. Microw. Theory Tech. **47**, 2075–2084 (1999)
2. F. Falcone, T. Lopetegi, J.D. Baena, R. Marqués, F. Martín, M. Sorolla, Effective negative-ε stop-band microstrip lines based on complementary split ring resonators. IEEE Microw. Wirel. Compon. Lett. **14**, 280–282 (2004)
3. R. Marqués, F. Martín, M. Sorolla, *Metamaterials with Negative Parameters: Theory, Design and Microwave Applications* (Wiley, New York, 2008)
4. J. Naqui, M. Durán-Sindreu, F. Martín, Selective mode suppression in coplanar waveguides using metamaterial resonators. Appl. Phys. A, Mater. Sci. Process. **109**, 1053–1058 (2012)
5. J. Naqui, A. Fernández-Prieto, M. Durán-Sindreu, F. Mesa, J. Martel, F. Medina, F. Martín, Common mode suppression in microstrip differential lines by means of complementary split ring resonators: theory and applications. IEEE Trans. Microw. Theory Tech. **60**, 3023–3034 (2012)
6. R. Marques, F. Medina, R. Rafii-El-Idrissi, Role of bi-anisotropy in negative permeability and left handed metamaterials. Phys. Rev. B **65**, 144441 (2002)
7. R. Marqués, F. Mesa, J. Martel, F. Medina, Comparative analysis of edge and broadside couple split ring resonators for metamaterial design. Theory and experiment. IEEE Trans. Antennas Propag. **51**, 2572–2582 (2003)
8. J. Naqui, M. Durán-Sindreu, F. Martín, Modeling split ring resonator (SRR) and complementary split ring resonator (CSRR) loaded transmission lines exhibiting cross polarization effects. IEEE Antennas Wirel. Propag. Lett. **12**, 178–181 (2013)
9. D. Schurig, J.J. Mock, D.R. Smith, Electric-field-coupled resonators for negative permittivity metamaterials. Appl. Phys. Lett. **88**, 041109 (2006)
10. F. Martín, F. Falcone, J. Bonache, R. Marqués, M. Sorolla, Split ring resonator based left handed coplanar waveguide. Appl. Phys. Lett. **83**, 4652–4654 (2003)
11. F. Aznar, J. Bonache, F. Martín, Improved circuit model for left handed lines loaded with split ring resonators. Appl. Phys. Lett. **92**, 043512 (2008)
12. F. Aznar, M. Gil, J. Bonache, L. Jelinek, J.D. Baena, R. Marqués, F. Martín, Characterization of miniaturized metamaterial resonators coupled to planar transmission lines through parameter extraction. J. Appl. Phys. **104**, 114501 (2008)
13. J. Bonache, M. Gil, I. Gil, J. Garcia-García, F. Martín, On the electrical characteristics of complementary metamaterial resonators. IEEE Microw. Wirel. Compon. Lett. **16**, 543–545 (2006)
14. J. Naqui, M. Durán-Sindreu, F. Martín, Transmission lines loaded with bisymmetric resonators and applications, in *IEEE MTT-S Int. Microwave Symp.*, Seattle USA, June 2013

Conference article IMS11*

Split Rings-Based Differential Transmission Lines with Common-Mode Suppression

J. Naqui, A. Fernández-Prieto, M. Durán-Sindreu, J. Selga, F. Medina, F. Mesa, and F. Martín

*Conference article included in this thesis for completeness but that cannot be oficially part of the compendium of articles of the Ph.D thesis.

Split Rings-Based Differential Transmission Lines with Common-Mode Suppression

[1]Jordi Naqui, [2]Armando Fernández-Prieto, [1]Miguel Durán-Sindreu, [1]Jordi Selga, [2]Francisco Medina, [2]Francisco Mesa, and [1]Ferran Martín

[1]GEMMA/CIMITEC, Departament d'Enginyeria Electrònica. Universitat Autònoma de Barcelona. 08193 BELLATERRA (Barcelona), Spain. E-mail: Ferran.Martin@uab.es

[2]Departamento de Electrónica y Electromagnetismo, Universidad de Sevilla. Avenida Reina Mercedes s/n, 41012 Sevilla, Spain. E-mail: Medina@us.es

***Abstract* — A novel microstrip differential transmission line with common-mode noise suppression is proposed and experimentally validated. It is implemented by periodically etching complementary split ring resonators (CSRRs) in the ground plane. For the differential signals, the symmetry of the structure efficiently cancels the electric field components axial to the CSRRs, and these particles have no effect on signal transmission. However, the CSRRs are activated under common mode excitation, with the result of a stop-band behavior. For the designed and fabricated prototype device, over 20 dB suppression of common-mode noise is achieved over a frequency range from 1.18 GHz to 1.74 GHz.**

***Index Terms* — Differential transmission lines, metamaterials, complementary split ring resonators (CSRRs).**

I. Introduction

High immunity to noise, low crosstalk and low electromagnetic interference are key issues of differential signals that make them very interesting for high-speed digital circuits. However, the presence of common-mode noise in differential lines is unavoidable in practical circuits. This unwanted noise is mainly caused by amplitude unbalance or time skew of the differential signals and must be reduced as much as possible to avoid common-mode radiation or EMI. Therefore, the design of differential lines able to suppress the common-mode noise while keeping the integrity of the differential signals is of great importance.

For GHz differential signals, compact common mode filters based on multilayer LTCC [1] or negative permittivity [2] structures have been reported. These structures are compact and provide efficient common-mode rejection over wide frequency bands, but are technologically complex. There have been also several approaches for the design of common-mode suppressed differential lines based on defected ground structures. In [3], dumbbell shaped periodic patterns etched in the ground plane, underneath the differential lines, were used to suppress the even mode by opening the return current path through the ground plane. This has small effect on the differential signals (odd mode) since relatively small current density returns through the ground plane for such signals. In [4], the authors achieve a wide stop-band for the common-mode by using U-shaped and H-shaped coupled resonators symmetrically etched in the ground plane.

In the present work, another approach for the design of differential lines with common-mode suppression is investigated. It is also based on defect ground structures, but using complementary split ring resonators (CSRRs). As will be later shown, by symmetrically etching the CSRRs in the ground plane, efficient common-mode suppression over a wide band can be achieved. As compared to other approaches, the proposed common-mode suppression strategy is technologically simple (only two metal levels are used), the resulting common-mode filters are electrically small, provide wide and high-rejection stop-bands, and their design is simple.

II. CSRR-based differential lines: principle for common-mode suppression and modeling

The CSRRs were first introduced in [5], where it was demonstrated that these particles are useful for the design of negative permittivity structures in microstrip technology. Etched in the ground plane of a microstrip line, underneath the conductor strip, CSRRs efficiently suppress signal transmission in the vicinity of their resonance frequency. This result can be interpreted as due to the negative effective permittivity of the line, but it can also be explained in terms of circuit theory, as a result of the capacitive coupling between the line and the CSRR. The topology and circuit model of a microstrip line loaded with a CSRRs are depicted in Fig 1(a). As reported in [6], L models the inductance of the line, C accounts for the electric coupling between the line and the resonator, and the CSRR is modeled by the parallel resonant tank, L_c-C_c. The unit cell structure of the proposed differential line is depicted in Fig. 1(b). It consists on a pair of coupled lines with a CSRR etched in the ground plane. The circuit model of this structure is also depicted in Fig. 1(b), where C_m and L_m model the mutual capacitance and inductance between the coupled lines.

The circuit model of Fig. 1(b) explains that the differential signals are insensitive to the presence of the CSRRs, while

978-1-61284-757-3/11/$26.00 C2011 IEEE

these resonators prevent the transmission of the common-mode at certain frequencies. The equivalent circuit model of the structure of Fig. 1(b) under common mode excitation is depicted in Fig. 2(a), whereas for the odd mode is depicted in Fig. 2(b). For the odd mode, the resonator is short circuited to ground, and the resulting model is that of a conventional transmission line. For the even mode, we obtain the same circuit as that of a CSRR-loaded line (Fig. 1a), but with modified parameters. Thus, we do expect a similar stop band behavior for the common-mode.

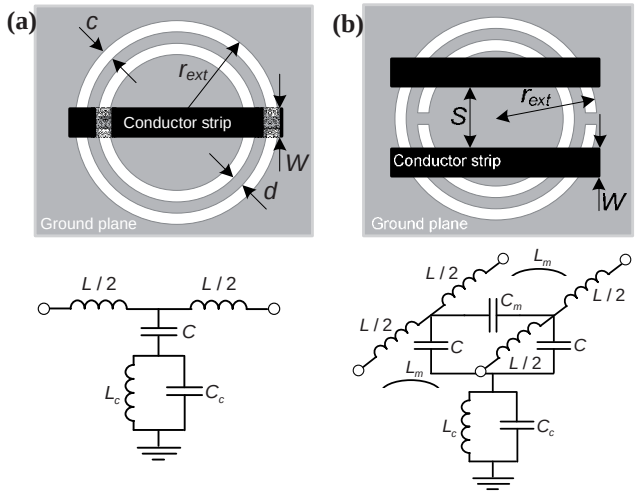

Fig. 1. Topology and circuit model (elemental cell) of a microstrip line (a) and differential line (b) loaded with a CSRR.

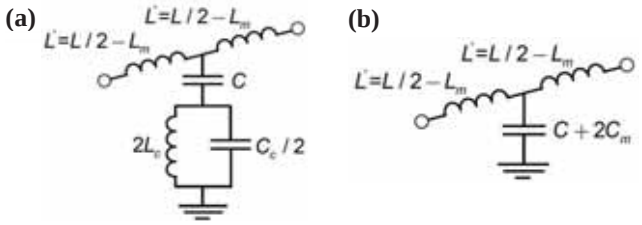

Fig. 2. Circuit models for the even mode (a) and odd mode (b).

In terms of field distributions, it is well known that the CSRR (first resonance) can be excited by means of a time varying axial electric field [5]. For the common mode, there is a strong density of electric field lines in the same direction below both lines. This causes CSRR excitation and hence a stop band. For the odd mode, the electric field distribution depends on the level of coupling between both lines. In tightly coupled lines, the electric field lines are mainly concentrated in the (necessarily narrow) gap region between the lines. In weakly coupled lines, the electric field intensity is higher below the lines (similar to the even mode). However, the direction of the electric field lines is opposite in both strips of the differential line. If the structure is symmetric, (i.e., the gaps of the CSRRs are aligned with the symmetry plane of the differential lines), the opposite electric field vectors in both lines exactly cancel and the CSRR is not activated.

To verify the integrity of the differential signals in these CSRR-loaded lines, we have designed a differential line with weakly coupled lines (the layout is depicted in Fig. 3). The width and distance between the lines necessary to obtain a 50Ω odd mode impedance has been determined by means of the transmission line calculator incorporated in the *Agilent ADS* commercial software (a *Rogers RO3010* microwave substrate with dielectric constant ε_r = 10.2 and thickness h=1.27mm has been considered). To analyze the effects of the asymmetry in the circuit, we have also simulated the structure that results by rotating the CSRR 90º. The simulated differential and common-mode insertion losses for both structures are depicted in Fig. 3 (these simulations have been obtained by means of the *Agilent Momentum* commercial software). For the even mode the results are comparable (in the region of interest) and a notch appears at the frequency where the shunt impedance (Fig. 2a) vanishes:

$$f_z = \frac{1}{2\pi\sqrt{2L_c(C_c/2+C)}} \quad (1)$$

However, for the odd mode, whereas the insertion loss is less than 0.1dB (in the considered frequency range) for the symmetric structure, a notch appears in the structure with the rotated CSRR. Thus, these results validate the common-mode suppression principle and point out the need to symmetrically etch the CSRRs in the differential line in order to preserve the differential signal integrity over a wide band.

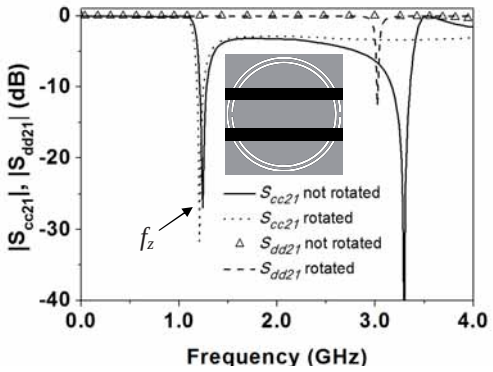

Fig. 3. Simulated common-mode $|S_{cc21}|$ and differential $|S_{dd21}|$ insertion loss for the structure of the inset, with and without 90º rotated CSRR. Dimensions are c=0.2mm, d=0.2mm, r_{ext}=5mm, W=1mm, S=2.5mm.

III. Design of CSRR-based differential lines

To efficiently suppress the common-mode noise it is necessary to achieve wide stop bands for the even mode. To this end, the strategy is to widen the stop band of the individual resonators, to couple them as much as possible, to etch CSRRs with slightly modified dimensions in order to obtain different transmission zero frequencies within the

978-1-61284-757-3/11/$26.00 C2011 IEEE

desired stop band, or a combination of all these effects. To widen the rejection bandwidth of an individual CSRR (which is relevant to achieve wide stop bands), it is necessary to increase the coupling capacitance, C, and to reduce the inductance, L_c, and capacitance, C_c, of the CSRR as much as possible. According to it, weakly coupled lines will be considered, since the width of the lines necessary to achieve an odd mode impedance of 50Ω is wider, and this enhances the coupling capacitance of the even mode. To reduce the inductance and capacitance of the CSRR, preserving the coupling level, it is necessary to increase the rings width, c, and separation, d. Obviously, this results in a larger CSRR size (for a given transmission zero frequency), but the achievable bandwidth is also larger.

In the present paper, the bandwidth is enhanced by tightly coupling identical CSRRs. We have considered two different structures: in one of them, the rings of the CSRRs are wide and appreciably separated; in the other one, the rings are narrow and tiny spaced. In both cases, in order to enhance the inter-CSRR's coupling, we have considered square-shaped rings.

In the first design, the purpose has been to reduce the size of the structure as much as possible. For this reason, we have considered a CSRR unit cell with narrow and tiny spaced rings (c=0.2mm and d=0.2mm). These values are close to the limit of the available technology. With these values, the model of the CSRR reported in [6], and the per-unit length capacitance of the coupled lines (common mode), we have estimated the side of the CSRR in order to obtain a transmission zero frequency at f_z=1.4GHz (obviously, optimization has been required since the model reported in [6] is valid under conditions not exactly fulfilled in the structure). The simulation of the common mode insertion loss is depicted in Fig. 4. The circuit simulation of the structure with the parameters extracted according to the procedure reported in [7] is also depicted in Fig. 4. There is good agreement between the circuit and electromagnetic simulation. In order to enhance the rejection bandwidth, we have implemented an order-3 structure with tightly coupled CSRRs. The bandwidth is closely related to the level of inter-resonator's coupling. Therefore, we have separated the CSRR 0.15mm in order to enhance the bandwidth as much as possible. The simulation of the resulting structure is shown in Fig. 5, where for comparison purposes we have also included the circuit simulation. The simulated circuit is that resulting by cascading the elemental cells, but with the addition of coupling capacitances between adjacent resonators. The coupling capacitance has been considered to be an adjustable parameter, and we have found that the capacitance that provides a better fit is C_{Coup}=0.11pF. The dimensions of the structure are 23mm×7.6mm, that is 0.28λ×0.09λ (where λ is the guided wavelength at the central frequency). The device is thus very small, although bandwidth has not been optimized in this structure. It is clear that the differential signal is not altered by the presence of the CSRRs (see also Fig. 5).

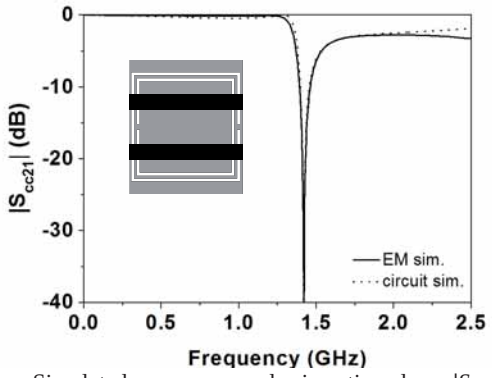

Fig. 4. Simulated common-mode insertion loss $|S_{cc21}|$ for the structure shown in the inset. CSRR dimensions are: c=0.2mm, d=0.2mm, W=1mm, S=2.5mm, and side length 7.6mm. Extracted parameters are L'=4.93nH, C=1.06pF, C_c=2.68pF and L_c=3.36nH.

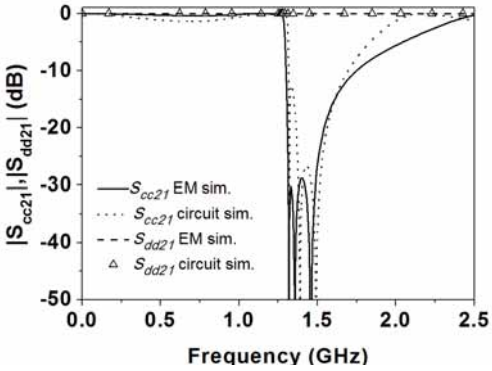

Fig. 5. Simulated common-mode and differential-mode insertion loss $|S_{cc21}|$ and $|S_{dd21}|$ for the order-3 structure that results by cascading 3 unit cells like the one shown in Fig. 4.

To enhance the bandwidth, we have considered CSRRs with wider rings and inter-ring's space. The target is to achieve at least 20dB common-mode rejection in the frequency range between 1.2GHz and 1.8GHz. The model of the CSRR is not so simple in this case because the particle cannot be considered to be electrically small; therefore we have directly made the optimization at the layout level. It has been found that three square shaped CSRRs separated 0.2mm, with a side length of 10.8mm and c=1.2mm and d=0.8mm, suffice to achieve the target specifications. The structure has been fabricated by means of a *LPKF H100* drilling machine. Access lines have been added in order to solder the connectors. The photograph of the whole structure is depicted in Fig. 6. Fig. 7 shows the simulated differential and common-mode insertion loss of the structure, as well as the measured even and odd mode frequency response. The dimensions of the active region of the structure are 32.8mm×10.8mm, that is 0.43λ×0.14λ. It is remarkable that the measured insertion loss for the differential signal is smaller than 0.5 dB in the considered range, being the loss tangent of the substrate 0.0023.

978-1-61284-757-3/11/$26.00 C2011 IEEE

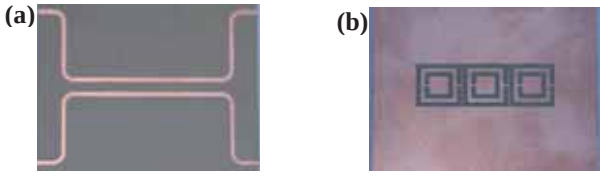

Fig. 6. Photograph of the (a) top view and (b) bottom view of the differential line with wide band common-mode rejection.

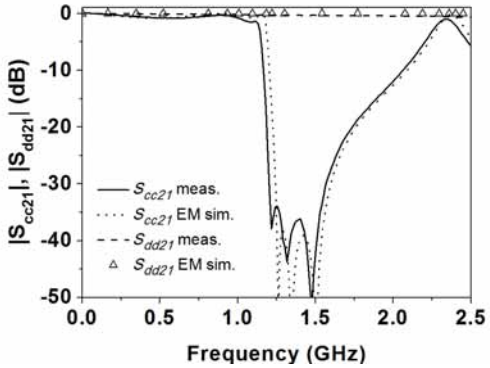

Fig. 7. Common-mode and differential-mode insertion loss $|S_{cc21}|$ and $|S_{dd21}|$ for the structure of Fig. 6.

Our fabricated wide band structure (Fig. 6) is compared with other structures reported in the references (see table I). The combination of size, bandwidth and stop-band rejection is competitive. The structure in [2] exhibits small dimensions and relatively wide bandwidth, but it needs three metal levels. In summary, we have presented an alternative and promising approach for the design of differential lines with common-mode suppression.

TABLE I: COMPARISON OF SEVERAL DIFFERENTIAL LINES

Ref	*length* [λ]	*Width* [λ]	*Surface* [λ^2]	*FBW* [%]	
				–10 dB	–30 dB
[2]	0.26	0.16	0.04	60	24
[3]	0.76	0.47	0.36	53	40
[4]	0.44	0.44	0.19	87	----
This	**0.43**	**0.14**	**0.06**	**54**	**24**

IV. CONCLUSIONS

We have demonstrated that CSRRs are useful particles for the suppression of the even mode in microstrip differential lines. The circuit models of the structure for both the differential and common modes have been reported and validated. The fabricated prototype device exhibits a rejection bandwidth for the common mode that extends from 1.18 GHz up to 1.74 GHz with more than 20 dB rejection. The measured insertion loss for the differential mode is better than 0.5 dB from DC up to at least 2.5 GHz. Therefore, the presence of the CSRRs has little influence on the differential signals. Since the CSRRs are compact resonators, the required space of the differential line to achieve efficient common-mode suppression is small. Therefore, the proposed approach is of interest for application in structures based on differential lines. The immediate future work by the authors will be the combination of CSRRs and other electrically small resonators for the design of differential line band pass filters with common-mode suppression.

ACKNOWLEDGEMENT

This work has been supported by MICIIN-Spain (contract TEC2010-17512 METATRANSFER), *Generalitat de Catalunya* (project 2009SGR-421) and MICIIN-Spain (project CONSOLIDER EMET CSD2008-00066).

REFERENCES

[1] B.C. Tseng, L.K. Wu, "Design of miniaturized common-mode filter by multilayer low-temperature co-fired ceramic", *IEEE Trans. Electromagn. Compat.*, vol. 46, no.4, pp. 571-579, Nov. 2004.

[2] C-H. Tsai, T-L. Wu, "A broadband and miniaturized common-mode filter for gigahertz differential signals based on negative-permittivity metamaterials", *IEEE Trans. Microw. Theory Techn.*, vol. 58, no.1, pp. 195-202, Jan. 2010.

[3] W.T. Liu, C-H. Tsai, T-W. Han, T-L. Wu, "An embedded common-mode suppression filter for GHz differential signals using periodic defected ground plane", *IEEE Microw. Wireless Comp. Lett.*, vol. 18, no. 4, pp. 248-250, April 2008.

[4] S-J. Wu, C-H. Tsai, T-L. Wu, T. Itoh, "A novel wideband common-mode suppression filter for gigahertz differential signals using coupled patterned ground structure", *IEEE Trans. Microw. Theory Techn.*, vol. 57, no.4, pp. 848-855, April 2009.

[5] F. Falcone, T. Lopetegi, J.D. Baena, R. Marqués, F. Martín and M. Sorolla, "Effective negative-ε stop-band microstrip lines based on complementary split ring resonators", *IEEE Microwave and Wireless Components Letters*, vol. 14, pp. 280-282, June 2004.

[6] J.D. Baena, J. Bonache, F. Martín, R. Marqués, F. Falcone, T. Lopetegi, M.A.G. Laso, J. García, I Gil, M. Flores-Portillo and M. Sorolla, "Equivalent circuit models for split ring resonators and complementary split rings resonators coupled to planar transmission lines", *IEEE Transactions on Microwave Theory and Techniques*, vol. 53, pp. 1451-1461, April 2005.

[7] J. Bonache, M. Gil, I. Gil, J. Garcia-García and F. Martín, "On the electrical characteristics of complementary metamaterial resonators", *IEEE Microwave and Wireless Components Letters*, vol. 16, pp. 543.545, October 2006.

Article TMTT12

Common Mode Suppression in Microstrip Differential Lines by Means of Complementary Split Ring Resonators: Theory and Applications

J. Naqui, A. Fernández-Prieto, M. Durán-Sindreu, F. Mesa, J. Martel, F. Medina, and F. Martín

Common-Mode Suppression in Microstrip Differential Lines by Means of Complementary Split Ring Resonators: Theory and Applications

Jordi Naqui, *Student Member, IEEE*, Armando Fernández-Prieto, *Student Member, IEEE*, Miguel Durán-Sindreu, *Member, IEEE*, Francisco Mesa, *Senior Member, IEEE*, Jesús Martel, *Member, IEEE*, Francisco Medina, *Fellow, IEEE*, and Ferran Martín, *Fellow, IEEE*

***Abstract*—This paper is focused on the application of complementary split-ring resonators (CSRRs) to the suppression of the common (even) mode in microstrip differential transmission lines. By periodically and symmetrically etching CSRRs in the ground plane of microstrip differential lines, the common mode can be efficiently suppressed over a wide band whereas the differential signals are not affected. Throughout the paper, we present and discuss the principle for the selective common-mode suppression, the circuit model of the structure (including the models under even- and odd-mode excitation), the strategies for bandwidth enhancement of the rejected common mode, and a methodology for common-mode filter design. On the basis of the dispersion relation for the common mode, it is shown that the maximum achievable rejection bandwidth can be estimated. Finally, theory is validated by designing and measuring a differential line and a balanced bandpass filter with common-mode suppression, where double-slit CSRRs (DS-CSRRs) are used in order to enhance the common-mode rejection bandwidth. Due to the presence of DS-CSRRs, the balanced filter exhibits more than 40 dB of common-mode rejection within a 34% bandwidth around the filter pass band.**

***Index Terms*—Complementary split-ring resonator (CSRR), differential transmission lines, metamaterial-inspired lines, split-ring resonator (SRR).**

I. Introduction

In a recent work presented by the authors [1], it was demonstrated that complementary split-ring resonators (CSRRs) [2] are useful for the suppression of the even (common) mode in microstrip differential lines. The suppression of the even mode is of interest in high-speed digital circuits based on differential signals in order to reduce common-mode radiation and electromagnetic interference (EMI). Prior to our work [1], several approaches were reported to efficiently suppress the even mode while keeping the integrity of the differential signals in differential transmission lines. The common-mode filters based on low-temperature cofired ceramic (LTCC) technology reported in [3] or the negative permeability structures of [4] are compact and provide efficient common-mode rejection over wide frequency bands, but they are technologically complex. Common-mode filters based on defected ground structures were also reported. In [5], dumbbell-shaped periodic patterns etched in the ground plane, underneath the differential lines, were used to suppress the even mode by opening the return current path through the ground plane. This has a small effect on the differential signals (odd mode), since relatively small current density returns through the ground plane for such signals. In [6], a wide stopband for the common mode was achieved by using U-shaped and H-shaped coupled resonators symmetrically etched in the ground plane. A comparison of the previous approaches, including our CSRR-based common-mode filters, was reported in [1], and it was found that the combination of size, bandwidth, and stopband rejection achievable by means of CSRR-loaded differential lines is very competitive.

As reported in [1], tightly coupled CSRRs are necessary [7] to enhance the rejection bandwidth of the common mode. To gain insight on this, the dispersion relation of the equivalent circuit model for the common mode, including inter-resonator coupling, will be obtained. Due to the electric coupling between adjacent CSRRs, the equivalent circuit model of the unit cell for the common mode consists of a four-port network. By applying Floquet's analysis to the circuit, the dispersion relation will be inferred, and it will be demonstrated that bandwidth enhancement is due to the destructive interference of complex modes (see, for instance, [8] and references therein).

It was also shown in [1] that, to enhance the rejection bandwidth of an individual resonator (common mode), it is necessary to increase the coupling capacitance between the pair of lines and the CSRR and to decrease the inductance and capacitance of the CSRR. This was achieved in [1] by increasing the rings width and separation. Alternatively, it will be shown in this paper that bandwidth enhancement can be obtained by replacing the CSRRs with double-slit CSRRs (DS-CSRRs) [9]. The advantage of using DS-CSRRs is that the bandwidth can be enhanced while preserving the description of the particle

Manuscript received March 05, 2012; revised June 25, 2012; accepted June 27, 2012. Date of publication August 28, 2012; date of current version September 27, 2012. This work was supported in part by MICIIN-Spain under Contract TEC2010-17512, Contract TEC2010-16948, and Contract TEC2011-13615-E, Generalitat de Catalunya under Project 2009SGR-421 and VALTEC08-1-0009, and by MICIIN-Spain Project CONSOLIDER EMET CSD2008-00066. The work of J. Naqui was supported by MICIIN-Spain through FPU Grant AP2010-0431.

J. Naqui, M. Durán-Sindreu, and F. Martín are with GEMMA/CIMITEC, Departament d'Enginyeria Electrònica, Universitat Autònoma de Barcelona, 08193 Bellaterra, Spain (e-mail: Ferran.Martin@uab.es).

A. Fernández-Prieto, F. Mesa, J. Martel, and F. Medina are with Grupo de Microondas, Universidad de Sevilla, 41012 Sevilla, Spain (e-mail: Medina@us.es).

Color versions of one or more of the figures in this paper are available online at http://ieeexplore.ieee.org.

Digital Object Identifier 10.1109/TMTT.2012.2209675

through an *LC* resonant tank. The validity of the circuit model is important for synthesis purposes. This means that broadband common-mode filters based on largely separated and wide slot rings can be implemented (as was demonstrated in [1]), but not following a systematic approach, which is one of the main motivations of the present work.

This paper is organized as follows. The principle for selective common-mode suppression in microstrip differential lines loaded with CSRRs is presented in Section II. The equivalent circuit model of the structure, as well as the models that result from even- and odd-mode excitation, are presented and used to validate the principle for common-mode suppression. As long as the proposed common-mode filters can be considered as truncated periodic structures, the knowledge of the dispersion relation of these CSRR-loaded differential lines is a powerful tool to estimating the maximum achievable common mode rejection bandwidth. Thus, Section III is devoted to infer the dispersion relation for the common-mode signals by considering inter-resonator coupling in the common-mode equivalent circuit model. Section IV discusses the effects of inter-resonator coupling and number of resonators on bandwidth enhancement and compares the common-mode filtering capabilities of CSRRs and DS-CSRRs. A methodology to designing CSRR or DS-CSRR common-mode filters and to estimating the achievable common-mode rejection bandwidth is presented in Section V. Section VI is focused on the characterization of two devices designed to demonstrate the selective mode suppression in DS-CSRR-based differential lines, and the enhanced rejection of the common mode in balanced filters loaded with DS-CSRRs. A comparison to other common mode filters is given in Section VII. Finally, the main conclusions are highlighted in Section VIII.

II. Selective Common-Mode Suppression in Differential Lines by Means of CSRRs: Principle and Modeling

SRRs and CSRRs magnetically and electrically coupled, respectively, to transmission lines have been used for the implementation of stopband filters in microstrip and coplanar waveguide (CPW) technology [10]–[13]. In the vicinity of their resonance frequency, an array of electrically small SRRs/CSRRs excited with the magnetic/electric field in the axial direction (i.e., normal to the SRR or CSRR plane) behaves as an effective medium with negative permeability/permittivity [14]–[16]. Under these polarization conditions such media are opaque and signal propagation is inhibited around resonance. The stopband characteristics of transmission lines periodically loaded with SRRs or CSRRs have been interpreted as due to the negative effective permeability or permittivity of these one-dimensional (1-D) effective structures [2], [15]. However, the stopband behavior of these artificial lines can also be explained from circuit theory, since the SRRs and CSRRs (coupled to the lines) introduce transmission zeros.

Let us now discuss how CSRRs can be used to selectively suppress the even mode in microstrip differential transmission lines. As reported in [1], the strategy to suppress the common mode in microstrip differential lines, while keeping the fundamental (odd) mode unaffected, is to symmetrically etch an array

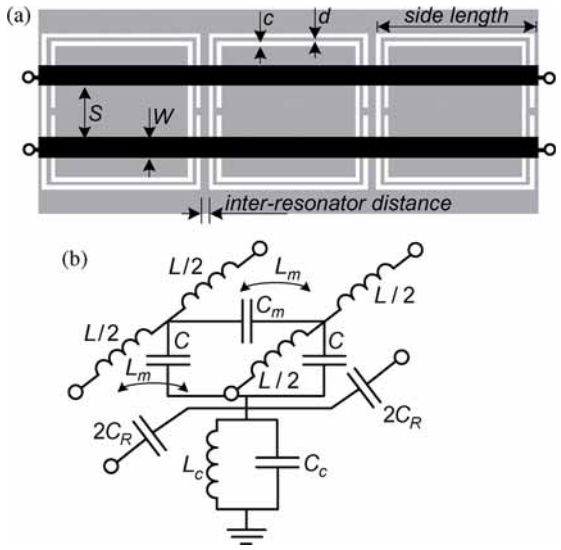

Fig. 1. (a) Typical topology of a microstrip differential transmission line with square-shaped CSRRs symmetrically etched in the ground plane to suppress the even mode. (b) Equivalent circuit model of the unit cell, including inter-resonator coupling. The ground plane is depicted in gray. The relevant dimensions are indicated.

of CSRRs in the ground plane, as shown in Fig. 1(a). The circuit model of the unit cell of this structure (including the electric coupling between adjacent resonators by means of a capacitor) is depicted in Fig. 1(b). As reported in [1], L models the inductance of the lines, C accounts for the electric coupling between the lines and the resonator, the CSRR is modeled by the parallel resonant tank, $L_c - C_c$, and C_m and L_m model the mutual capacitance and inductance between the coupled lines, respectively. Finally, C_R models the electric coupling between adjacent resonators. In the model reported in [1], such inter-resonator coupling was neglected. However, our intention is to study the effects of such coupling on the rejection bandwidth for the common mode. Therefore, the introduction of C_R in the model is necessary, and the result is a six-port network.

In view of Fig. 1(b), the differential signals are insensitive to the presence of the CSRRs, but these resonators prevent the transmission of the common mode at certain frequencies. The equivalent circuit models (unit cell) of the structure of Fig. 1(a) under even and odd mode excitation are depicted in Fig. 2(a) and (b), respectively. For the odd mode, the resonator is short-circuited to ground, and the resulting model is that of a conventional transmission line. For the even mode, we obtain the circuit of a conventional CSRR-loaded line [17], but with modified parameters and inter-resonator coupling (hence a four-port network). Thus, we do expect a stopband behavior for the common mode, enhanced by the presence of coupling between adjacent CSRRs (as will be shown later).

In terms of field distributions, it is well known that the CSRR (first resonance) can be excited by means of a time-varying axial electric field [2]. For the common mode, there is a strong density of electric field lines in the same direction below both lines. This causes CSRR excitation and hence a stopband. For the odd mode, the axial components of the electric field distribution exactly cancel if the structure is symmetric, (i.e., the gaps of the

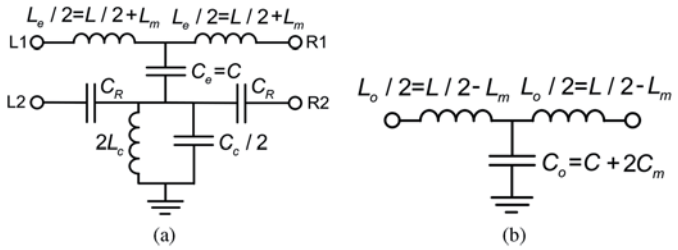

Fig. 2. Circuit model (unit cell) of the differential line loaded with CSRRs for (a) the even and (b) odd modes.

CSRR are aligned with the symmetry plane of the differential line), and the CSRR is not activated.

III. Common-Mode Dispersion Relation

Here, we infer the dispersion relation for the common mode of a differential line periodically loaded with CSRRs. Let us consider an infinite structure formed by cascading the four-port blocks that describe the unit cell of a microstrip differential line loaded with CSRRs for the common mode [Fig. 2(a)]. Let V_{L1}, V_{L2}, I_{L1}, and I_{L2} be the voltages and currents at the ports (1 and 2) of the left-hand-side (subscript L) of the unit cell, and V_{R1}, V_{R2}, I_{R1}, and I_{R2} the variables at the right-hand-side ports. From multiconductor line theory [18], [19], it follows that the variables at both sides of the unit block are related by

$$\begin{pmatrix} \boldsymbol{V_L} \\ \boldsymbol{I_L} \end{pmatrix} = \begin{pmatrix} \boldsymbol{A} & \boldsymbol{B} \\ \boldsymbol{C} & \boldsymbol{D} \end{pmatrix} \begin{pmatrix} \boldsymbol{V_R} \\ \boldsymbol{I_R} \end{pmatrix} \tag{1}$$

where $\boldsymbol{A}, \boldsymbol{B}, \boldsymbol{C}$ and $\boldsymbol{D}$ are 2×2 matrices while $\boldsymbol{V_L}, \boldsymbol{I_L}, \boldsymbol{V_R}$ and $\boldsymbol{I_R}$ are column vectors composed of the pair of port variables. As it follows from Bloch mode theory, the dispersion relation is obtained from the eigenmodes of the above system, which are inferred by forcing a given phase shift along the unit block, and setting the determinant of the resulting 4×4 matrix to be null:

$$\det \begin{pmatrix} \boldsymbol{A} - e^{\gamma l} \cdot \boldsymbol{I} & \boldsymbol{B} \\ \boldsymbol{C} & \boldsymbol{D} - e^{\gamma l} \cdot \boldsymbol{I} \end{pmatrix} = 0 \tag{2}$$

where $\boldsymbol{I}$ is the identity matrix, the phase-shift factor $e^{\gamma l}$ is the eigenvalue, γ is the complex propagation constant, and l is the unit cell length. For reciprocal, lossless, and symmetric networks, the eigenvalue solution can be simplified to the solution of the following equation [20], [21]:

$$\det \left(\boldsymbol{A} - \cosh(\gamma l) \cdot \boldsymbol{I} \right) = 0. \tag{3}$$

The $\boldsymbol{A}$ matrix elements for the network of Fig. 2(a) can easily be calculated as

$$\boldsymbol{A} = \begin{pmatrix} A_{11} & A_{12} \\ A_{21} & A_{22} \end{pmatrix} \tag{4}$$

with

$$A_{11} = 1 - L_e C_e \omega^2 / 2 \tag{5a}$$

$$A_{12} = \frac{L_e C_e \omega^2}{2} \tag{5b}$$

$$A_{21} = -\frac{C_e}{C_R} \tag{5c}$$

$$A_{22} = 1 + \frac{C_e}{C_R} + \frac{C_c}{2C_R} \left(1 - \frac{1}{L_c C_c \omega^2} \right) \tag{5d}$$

where ω is the angular frequency. By introducing (4) into (3) and solving the determinant, we can obtain γl. In this four-port network, there are two solutions (denoted later by a and b) for γl:

$$\cosh(\gamma l) = \frac{1}{2} \left(A_{11} + A_{22} \pm \sqrt{(A_{11} - A_{22})^2 + 4 A_{12} A_{21}} \right). \tag{6}$$

The dispersion relation (6) will be used in Sections IV and V, respectively, to study the effects of inter-resonator coupling on bandwidth enhancement and to predict the maximum achievable bandwidth of periodic CSRR-loaded differential lines.

IV. Broadening the Common-Mode Rejection Bandwidth

As pointed out in [1], there are three main strategies to enhance the rejection bandwidth in CSRR-based structures: 1) to tune the resonance frequency of several resonators in order to cover a wide band [10]; 2) to couple the resonators; and 3) to enhance the bandwidth of the individual resonators (and, obviously, a combination of the previous approaches). The multiple tuned resonators approach is efficient, but many particles are needed to cover a wide band if narrowband resonators are used. In the following subsections, the other two strategies for common-mode rejection enhancement in microstrip differential lines are discussed.

A. Inter-Resonator Coupling

The analysis of the dispersion relation is a convenient mean to gain insight on the rejection bandwidth for the common mode and, specifically, to analyze the effects of inter-resonator coupling on bandwidth enhancement. We have obtained the two modal propagation constants by considering the following element values: $L_e = 6.3$ nH, $C_e = 1.1$ pF, $L_c = 2.1$ nH, $C_c = 3.2$ pF, and $C_R = 0.1$ pF (i.e., those extracted from an electrically small CSRR-based structure considered in Section V). The results, shown in Fig. 3, indicate that, for each mode, there are regions where γl is purely real (evanescent mode), purely imaginary (propagating mode), or complex (complex mode). If complex modes are present, these modes must appear as conjugate pairs [8], and this is exactly the case in the region comprised between 1.42 GHz and 1.61 GHz, that is $\alpha_a = \alpha_b$ and $\beta_a = -\beta_b$, where $\gamma = \alpha + \mathrm{j}\beta$. The forbidden band includes the region where complex modes are present (these modes do not carry net power [8], [22]–[24]), plus an additional region where $\beta_a = \beta_b = 0$, $\alpha_a \neq 0$, and $\alpha_b \neq 0$ (between 1.61 GHz

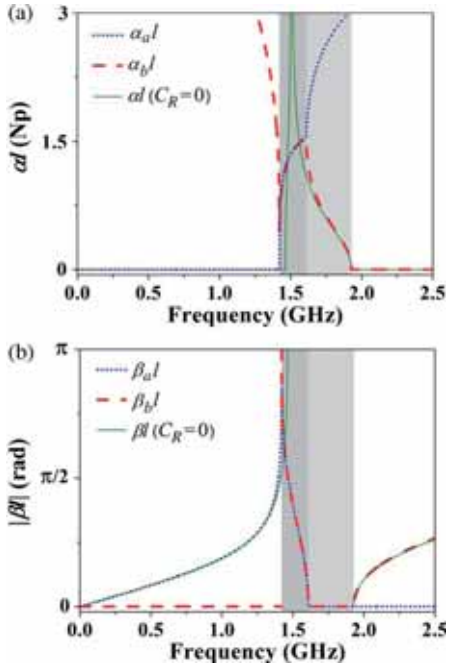

Fig. 3. (a) Attenuation constant and (b) magnitude of the phase constant of γl corresponding to the two modes of the network of Fig. 2(a). If inter-resonator coupling is cancelled ($C_R = 0$), the two modes degenerate in a single mode, also depicted. The evanescent and complex mode regions are highlighted in light and dark gray, respectively.

and 1.93 GHz) in which the modes are evanescent. As pointed out in [24], the pair of complex modes also inhibits signal propagation since such modes co-exist and have contra directional phase. The forward complex mode is related to microstrip wave propagation, whereas the backward complex mode resembles electroinductive waves [25] (the dispersion behavior is similar to that found in a shielded Sievenpiper structure [24]). The presence of coupling results in a wider stop band, as compared to the structure without electric coupling between adjacent resonators. This has been corroborated from the dispersion relation that results by forcing $C_R = 0$ (also depicted in Fig. 3). However, by magnifying inter-resonator coupling (large value of C_R), the forbidden band does not substantially increase as compared with the case with $C_R = 0.1$ pF. Thus, inter-resonator coupling helps to broaden the stopband of the common mode in CSRR-loaded differential lines, but the sensitivity in bandwidth based on CSRR-to-CSRR coupling is limited, which makes apparent the convenience of implementing the common-mode rejection filters with broadband resonators.

The dispersion relation of common-mode filters described by a similar circuit to that of Fig. 2(a) is reported in [4], where the four-port Z-matrix of the circuit model and periodic boundary conditions related with the Bloch–Floquet theorem are used. Our reported approach is based on the transmission $ABCD$ matrix and multiconductor transmission line theory, and the complex modes are pointed out as the cause of rejection bandwidth enhancement for the common mode.

B. Wideband Resonators: DS-CSRRs

As was illustrated in Section IV-A, inter-resonator coupling enhances bandwidth but, in practice, such effect is limited.

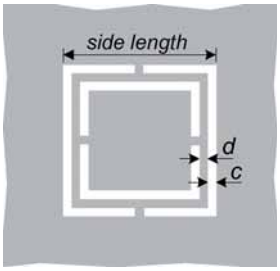

Fig. 4. Topology of a square-shaped DS-CSRR.

Therefore, it is important to increase the bandwidth of the individual resonators as much as possible. Here, we consider an alternative to that reported in [1] to obtaining wideband resonators.

In order to obtain a wide stopband response with a single CSRR coupled to a transmission line, it is necessary to increase the coupling capacitance between the line and the resonator and to reduce the CSRR inductance and capacitance. In [1], this was achieved by increasing the rings width and inter-rings space, with the result of a structure with tiny coupled slot rings. Under these circumstances, the CSRR is properly described by an *LC* resonant tank capacitively coupled through the main line in a very narrow region in the vicinity of the transmission zero (nevertheless, it was demonstrated in [1] that, for CSRRs with narrow and closely spaced rings, the equivalent circuit of Fig. 2(a) is valid within a wide band).

As an alternative to obtain wideband resonators, the DS-CSRR can be considered [9] (see Fig. 4). Like the CSRR, the DS-CSRR is topologically symmetric, which makes it appropriate for the selective common-mode suppression. In comparison to a CSRR with the same dimensions and etched in the same substrate, the DS-CSRR has almost the same capacitance, but four times smaller inductance [9]. Hence, the DS-CSRR resonance frequency and electrical size are twice those of the CSRR. Since for a given (required) transmission zero, the DS-CSRR is larger than the CSRR, the coupling capacitance can also be larger, and, by virtue of a smaller inductance (as compared to that of a CSRR), we can obtain a wider bandwidth. Notice that since the DS-CSRR is electrically larger than the CSRR, it is expected that the circuit model of Fig. 2(a) provides an accurate description for the common mode over a wider band for the CSRR-loaded lines. This means that any prediction on common-mode rejection bandwidth based on the circuit model (Section V) is expected to be more accurate for CSRR-loaded lines. Nevertheless, it will be shown that approximate estimations can also be made by considering DS-CSRRs. Obviously, DS-CSRRs with wide and distant slot rings can also be considered to further enhancing the common-mode rejection bandwidth, but in this case the circuit model cannot be used for predicting the stopband (the same occurs with CSRRs with wide and distant slot rings). Indeed, the accuracy of the model depends not only on the electrical size of the particles, but also on the slot width and the inter-slot distance. The electrical size is intimately related to the coupling (and hence to the separation d) between the inner and outer slot rings. In practice, the minimum printable slot and strip width

(in conventional PCB technology) is limited to 100 or 150 μm, and this dictates the frequency limits where the circuit model of Fig. 2(a) provides an accurate description of the structure.

To compare the effects of both particles on common-mode rejection bandwidth and to study the effects of increasing their number (filter order), we have designed several CSRR- and DS-CSRR-loaded differential lines. For a proper comparison, we have set c and d to the same value for both particles, specifically to our minimum nominal value that guarantees acceptable tolerance deviations in the actual values of the fabricated prototypes ($c = d = 200$ μm). In addition, the side length of the particles has been adjusted in order to obtain the required filter central frequency f_0. By means of the *Agilent Momentum* full-wave electromagnetic solver, we have computed the fractional rejection bandwidth for the common mode, $\mathrm{FBW} = \mathrm{BW}/f_0 = |f_1 - f_2|/(f_1 \cdot f_2)^{1/2}$, where the upper and lower frequency limits of the stopband f_1 and f_2 have been considered to be those frequencies where the common-mode rejection level is 20 dB (losses have been excluded in these simulations). The results for different orders and central filter frequencies are shown in Fig. 5(a). As expected, the common-mode rejection bandwidth is wider for DS-CSRR-loaded differential lines. Despite the fact that, for a given central frequency an individual DS-CSRR is larger than a CSRR, if we compare CSRR- and DS-CSRR-loaded lines with the same area [see Fig. 5(b)], we see that the rejection bandwidth is wider for the latter. With these results, it can be concluded that DS-CSRRs exhibit a good balance between common-mode filter size and achievable bandwidth.

The results of Fig. 5 also show that the electrical size of the structures increases as the central frequency increases. That occurs because, in shifting the central frequency up, the particle dimensions have not been scaled down, that is, resonator side length has been decreased, but c and d have been kept constant (as well as the substrate height). It is also worth mentioning that the common-mode rejection bandwidth decreases as the central frequency increases. This aspect is attributed to a drastic decrease in the coupling capacitance between the differential line and the resonators due to the fact that the substrate thickness is not scaled down.

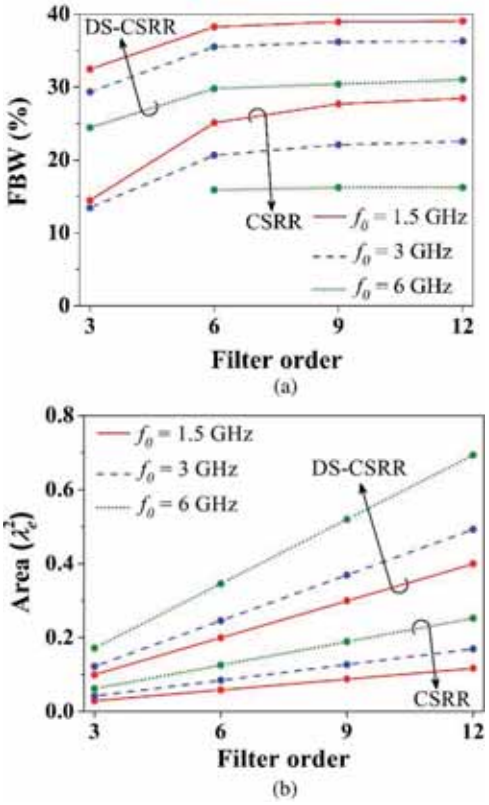

Fig. 5. (a) Fractional rejection bandwidth (FBW) at -20 dB for the common mode given by electromagnetic simulation and (b) area as a function of the even mode guided wavelength γ_e of CSRR- and DS-CSRR-loaded differential lines. Dimensions are: for the CSRRs and DS-CSRRs, $c = d = 0.2$ mm, and inter-resonator distance $= 0.2$ mm; for the CSRRs, side length $= 7.3$ mm ($f_0 = 1.5$ GHz), 4.3 mm ($f_0 = 3$ GHz), and 2.6 mm ($f_0 = 6$ GHz); for the DS-CSRRs, side length $= 3.8$ mm ($f_0 = 1.5$ GHz), 7.5 mm ($f_0 = 3$ GHz), and 4.3 mm ($f_0 = 6$ GHz); for the differential line, $2W + S = side\ length - 2(2c - d) + 0.4$ mm exhibiting a 50-Ω characteristic impedance (odd mode). The considered substrate is the *Rogers RO3010* with thickness $h = 1.27$ mm, and dielectric constant $\varepsilon_r = 10.2$.

V. Common-Mode Filter Design

A. Filter Design

The aim of this section is to provide a methodology for the design of microstrip differential lines with common-mode suppression and to predict the achievable rejection bandwidth on the basis of the common-mode equivalent circuit model and dispersion relation. For the reasons explained before, relative to the validity of the model of Fig. 2(a) and fabrication tolerances, we will consider $c = d = 200$ μm (notice that this reduces the degrees of freedom and eases the common-mode filter design). We use square-shaped resonators (rather than circular) to enhance the electric coupling between the differential line and the resonators and between adjacent resonators as well. To further enhance inter-resonator coupling, the separation between adjacent resonators is also set to 200 μm. The differential line is designed to exhibit an odd-mode characteristic impedance of 50 Ω. In order to achieve a strong electric coupling between the pair of lines and the resonator, the lines must be fitted inside the CSRR (or DS-CSRR) region and must be as wide as possible and, hence, as uncoupled as possible (line dimensions can easily be inferred from a transmission line calculator). The side length of the resonator is determined from the model of the CSRR reported in [17] (which gives L_c and C_c) and the per-unit length capacitance of the coupled lines for the even mode (which gives C_e). The transmission zero frequency, given by

$$f_z = \frac{1}{2\pi\sqrt{2L_c(C_e + C_c/2)}} \tag{7}$$

is adjusted to the required central filter frequency, and this provides the CSRR side length (for a DS-CSRR the side length can also be determined by taking into account that the inductance is four times smaller than the inductance of the CSRR). Obviously, optimization of the resonator side length in order to fit the required transmission zero is necessary (notice that the transmission zero frequency provides a reasonable estimate of the central filter frequency).

TABLE I
EXTRACTED PARAMETERS AND MAXIMUM FRACTIONAL BANDWIDTH INFERRED FROM THE CIRCUIT MODEL

f_0 (GHz)	L_e (nH)	C_e (pF)	L_c (nH)	C_c (pF)	C_R (pF)	*FBW* (%)
CSRR-loaded differential lines						
1.5	6.3	1.1	2.1	3.2	0.1	30.7
3	4.2	0.5	1.0	2.0	0.06	26.4
6	3.0	0.2	0.4	1.4	0.08	20.7
DS-CSRR-loaded differential lines						
1.5	15.9	1.6	1.0	8.6	0.64	32.6
3	9.0	0.8	0.45	4.8	0.18	29.4
6	6.9	0.3	0.15	3.6	0.1	23.6

With the previous procedure, the common-mode filter dimensions are perfectly determined. To predict the maximum achievable bandwidth, i.e., the bandwidth obtained by considering an infinite number of cells, the dispersion relation is used. However, since optimization at the layout level is required, it is necessary to extract the parameters of the circuit model following the procedure reported in [26], where the element values are obtained from certain mapping conditions such as the transmission zero frequency and the intercept of the reflection coefficient (S_{11}) with the unit resistance circle. Thus, L_e, C_e, L_c, and C_c are first extracted by considering a single cell structure, and then C_R is adjusted to fit the electromagnetic simulation of an order-2 common-mode filter. Once the circuit parameters are known, (6) can be evaluated, and the common-mode stopband can be determined.

Following the previous approach, we have obtained the maximum achievable rejection bandwidth for different CSRR and DS-CSRR common-mode filters. To compare with full-wave electromagnetic simulations, we have considered those central frequencies and that substrate of Fig. 5. The extracted circuit parameters and estimated fractional bandwidths are shown in Table I. By comparing the maximum fractional bandwidths predicted by the reported approach with the saturation values of Fig. 5(a), we can conclude that the reported approach is more accurate for CSRR-loaded lines, as expected. Fig. 6 compares the circuit and electromagnetic simulation (common mode) of the order-1, -2, and -3 CSRR-based common-mode filters designed to exhibit a central frequency (actually the transmission zero for the single-stage structure) of 1.5 GHz. Note that, in the circuit simulation, the inter-resonator capacitance at input and output ports have been left opened since the CSRRs of the input and output cells are not externally fed, resulting in a two-port circuit. There is good agreement between the circuit and electromagnetic simulation.

As can be seen in Fig. 5(a), six resonators are sufficient to nearly achieve the maximum rejection bandwidth. Obviously, filter size can be reduced by decreasing the number of resonators but at the expense of a reduced common mode rejection bandwidth. Thus, following a systematic approach based on the circuit model of the common mode, we can infer whether a specified rejection bandwidth and central frequency can be roughly fulfilled or not. If the required bandwidth is wider, we are forced to consider resonators with wider slots (c) and inter-slot distance (d), or, alternatively, multiple tuned resonators. In this case, however, filter design and maximum bandwidth estimation

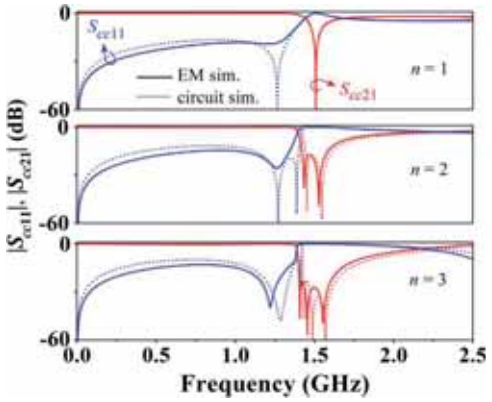

Fig. 6. Common-mode return loss $|S_{cc11}|$ and insertion loss $|S_{cc21}|$ given by the electromagnetic and circuit simulation for the order-1, -2, and -3 common-mode filters (1.5 GHz central frequency) based on CSRRs. Dimensions and substrate are indicated in the caption of Fig. 5. Circuit parameters are given in Table I.

are not so straightforward. Notice that the reported approach allows us to infer the maximum achievable rejection bandwidth, rather than setting the common mode rejection bandwidth to a given value.

B. Discussion on the Rejection Bandwidth Definition

Finally, it is important to discuss if the meaning of the maximum fractional bandwidth inferred from the dispersion relation actually corresponds to the -20 dB bandwidth of a structure with a large number of cells. Indeed, the dispersion relation provides the frequency regions where signal propagation is allowed or forbidden for an infinite number of cells. For a finite number of cells, the most relevant effects that may occur are impedance mismatch in the allowed bands or small rejection within the forbidden bands. Therefore, an analysis to determine the rejection level that properly defines the forbidden band is very convenient.

It is well known that the transmission coefficient in two-port periodic structures exhibits ripple in the allowed bands. Such ripple is caused by impedance mismatch, and maximum transmission is produced at those frequencies where either the Bloch impedance is matched to the impedance of the ports (impedance matching) or the electrical length is a multiple of π (phase matching). Between adjacent transmission peaks, the transmission coefficient is a minimum at those frequencies where the phase is an odd multiple of $\pi/2$. The transmission coefficient at these frequencies of minimum transmission can easily be obtained according to [27]

$$f_{\text{env}}(\omega) = 10\log\left\{1 - \left|\frac{Z_B^2(\omega) - Z_o^2}{Z_B^2(\omega) + Z_o^2}\right|^2\right\}. \tag{8}$$

Indeed, the previous function gives the envelope of the transmission coefficient in the allowed bands. Expression (8) corresponds to a two-port structure, where $Z_B(\omega)$ is the Bloch impedance and Z_o the reference impedance of the ports $(Z_o = 50\ \Omega)$. However, the structure under analysis is described by a circuit model with two input and two output ports [Fig. 2(a)]. In a two-port structure, the Bloch impedance is obtained by the ratio between the eigenvector variables (voltage and current). For the circuit of Fig. 2(a), the pair of eigenvectors

($[V_{1a}, V_{2a}, I_{1a}, I_{2a}]$ and $[V_{1b}, V_{2b}, I_{1b}, I_{2b}]$) can be obtained by using (1) and (6), and we can infer from them the characteristic impedance matrix as follows [18]:

$$\boldsymbol{Z_c} = \boldsymbol{V_{ab}} \cdot \boldsymbol{I_{ab}^{-1}} \tag{9}$$

where $\boldsymbol{V_{ab}}$ and $\boldsymbol{I_{ab}}$ are 2×2 matrices formed by column vectors composed of the eigenvector voltages and currents

$$\boldsymbol{V}_{ab} = \begin{pmatrix} V_{1a} & V_{1b} \\ V_{2a} & V_{2b} \end{pmatrix} \tag{10a}$$

$$\boldsymbol{I_{ab}} = \begin{pmatrix} I_{1a} & I_{1b} \\ I_{2a} & I_{2b} \end{pmatrix}. \tag{10b}$$

The diagonal elements of $\boldsymbol{Z_c}$ (Z_{11} and Z_{22}) are simply the ratios between the voltage and current in the corresponding port when the other port is left open, whereas the anti-diagonal elements determine the effects of the current injected in one port on the voltage in the other port when it is open. Notice that Z_{11} and Z_{22} are not the ratios of the voltage and current at ports 1 and 2 for each eigenvector. Let us denote such voltage-to-current ratios for port 1 as Z_{B1a} and Z_{B1b}, where a and b discriminate each mode. If we now compare Z_{11} with Z_{B1a} and Z_{B1b} (Fig. 7), it can be appreciated that $Z_{11} \approx Z_{B1a}$ to the left of the forbidden band, whereas $Z_{11} \approx Z_{B1b}$ to the right of that band. This means that, in the allowed bands, the propagation in an infinite structure resulting by cascading the networks of Fig. 2(a) with port L2 of the first cell left opened, can be described as if it was a two-port network that supports the eigenvector composed of the variables referred to port 1 (mode a and b to the left and right of the stopband, respectively) and Bloch impedance given by Z_{11}. This approximation is valid as long as mode mixing is negligible, as occurs in the whole allowed frequency region except in a narrow band to the left of the stopband, where modes a and b coexist (this leads to a complex value of Z_{11} in that region).

From previous statements, it follows that the envelope function of the transmission coefficient of any finite structure with ports L2 and R2 of the first and last cell, respectively, left open (actual conditions), can be approximated by means of (8), considering $Z_B = Z_{11}$. The envelope function in the allowed bands inferred through (8) with Z_{11} of Fig. 7 is compared with the response of a 12-cell structure in Fig. 8. It is confirmed that we can use (8) to obtain the envelope function to a very good approximation.

With regard to the maximum bandwidth, it coincides with the region delimited by those frequencies where the envelope function exhibits a vertical slope. This vertical slope is clearly achieved at a rejection level of 20 dB. Hence, this is a good rejection level to define the common-mode rejection bandwidth. We would like to emphasize that the proposed procedure to infer the envelope function is approximate. However, (8) provides very good results because the coupling capacitance between resonators, C_R, is necessarily small in the considered structures. If this condition is not fulfilled, mode mixing is more pronounced, and the envelope function that results when the ports L2 and R2 of the input and output cell, respectively, are opened, cannot be inferred following this simple procedure.

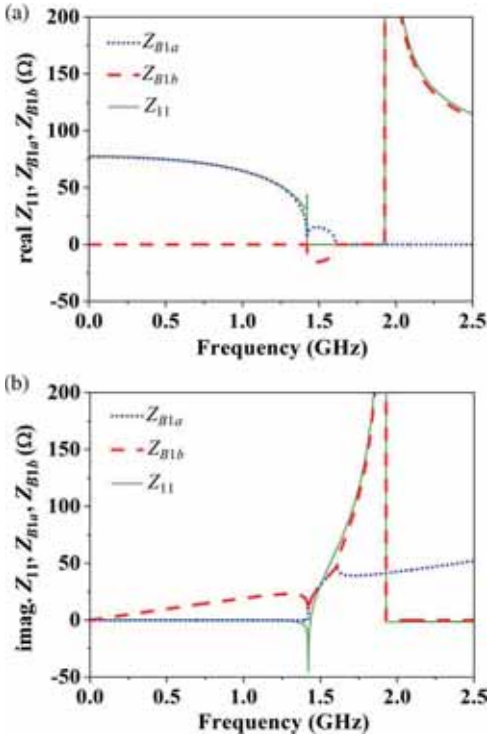

Fig. 7. (a) Real and (b) imaginary parts of Z_{11}, Z_{B1a}, and Z_{B1b}. The considered circuit parameters [refer to Fig. 2(a)] are those corresponding to the CSRR common-mode filter with 1.5-GHz central frequency (i.e., those indicated in the first row of Table I).

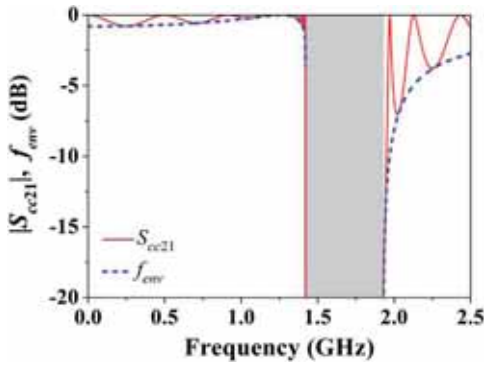

Fig. 8. Frequency response of the 12-cell structure resulting by cascading the four-port networks of Fig. 2(a) with L2 and R2 ports of stages 1 and 12, respectively, left opened, and envelope function in the allowed bands. The forbidden band is depicted in gray.

VI. Experimental Validation and Applications

Two application examples of the considered structures are presented in this section: 1) a DS-CSRR-loaded differential line with common-mode suppression and 2) a differential (balanced) bandpass filter with common-mode rejection enhanced by the presence of DS-CSRRs.

A. Differential Line With Common-Mode Rejection

Here, the common-mode suppression in microstrip differential lines loaded with DS-CSRRs is experimentally validated. We have designed a common-mode filter similar to that reported in [1], but in this case by using DS-CSRRs with tightly coupled slot rings. The target is to implement a common-mode

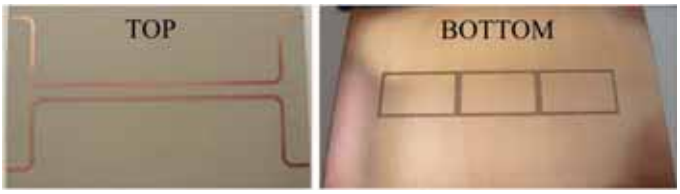

Fig. 9. Photograph of the designed differential line with common-mode suppression based on DS-CSRRs. Dimensions are: for the DS-CSRRs, $c = d =$ 0.2 mm, longitudinal side length $=$ 17.6 mm, and transverse side length $=$ 10.8 mm; inter-resonator distance $=$ 0.2 mm; for the differential line, $W =$ 1 mm, and $S =$ 2.5mm. The considered substrate is the *Rogers RO3010* with thickness $h =$ 1.27 mm, dielectric constant $\varepsilon_r = 10.2$, and loss tangent $\tan\delta = 0.0023$.

filter roughly centered at 1.35 GHz and exhibiting at least 35% fractional bandwidth (at 20-dB rejection level). According to the previous methodology, these specifications cannot be fulfilled by using CSRRs with $c = d =$ 200 μm. However, it is possible to achieve these filter requirements by means of DS-CSRRs. Indeed, the estimated maximum bandwidth for a common-mode filter centered at 1.35 GHz has been found to be 37.3%, but we do expect a larger value since the model tends to slightly underestimate the maximum achievable bandwidth for DS-CSRR-loaded lines [this can be appreciated by comparing Table I and Fig. 5(a)]. Moreover, for comparison purposes, a rectangular-shaped DS-CSRR has been considered with its transverse side length identical to that of the CSRR reported in [1]. This favors the electric coupling between the pair of lines and the DS-CSRRs and, hence, the common-mode stopband expansion (the reason is that the DS-CSRR longitudinal side is longer than the transverse one, and this increases the coupling capacitance C_e as compared with that of a square-shaped DS-CSRR with identical transmission zero frequency). The longitudinal side length is thus the single design parameter, and this has been determined following the same approach applied to square-shaped particles (the geometrical parameters of the structure are given in the caption of Fig. 9).

The photograph and frequency response of the device, an order-3 common-mode filter, are depicted in Figs. 9 and 10, respectively (this filter order has been found to be sufficient to satisfy the bandwidth requirements). As can be seen, the differential signal is almost unaltered whilst the common mode is rejected within a fractional bandwidth (41%) comparable to that achieved in [1] by using CSRRs with wide and widely spaced rings. The DS-CSRR-based structure is a bit larger than that reported in [1], but the design has been done following the systematic procedure explained in the previous section.

Fig. 11 shows the measured differential eye diagrams with the excitation of 0.2-V amplitude in 2.5 Gb/s for the differential line of Fig. 9 with and without DS-CSRRs. The eye diagram quality in terms of eye height, eye width, jitter, and eye opening factor is compared for these two structures (see Table II). According to these results, the presence of the DS-CSRRs does not significantly degrade the differential mode. The peak-to-peak jitter varies notably, but it is still within very acceptable limits for the DS-CSRR-based structure. Moreover, the eye opening factor, which measures the ratio of eye height and eye amplitude, is identical.

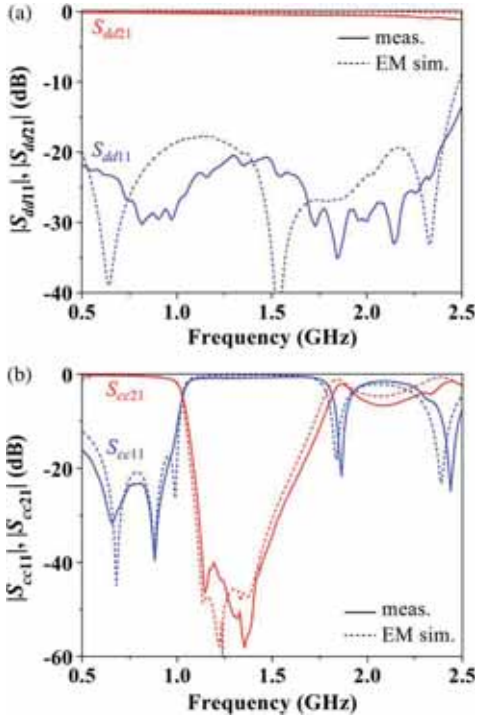

Fig. 10. (a) Differential-mode return loss $|S_{dd11}|$ and insertion loss $|S_{dd21}|$ and (b) common-mode return loss $|S_{cc11}|$ and insertion loss $|S_{cc21}|$ for the structure of Fig. 9.

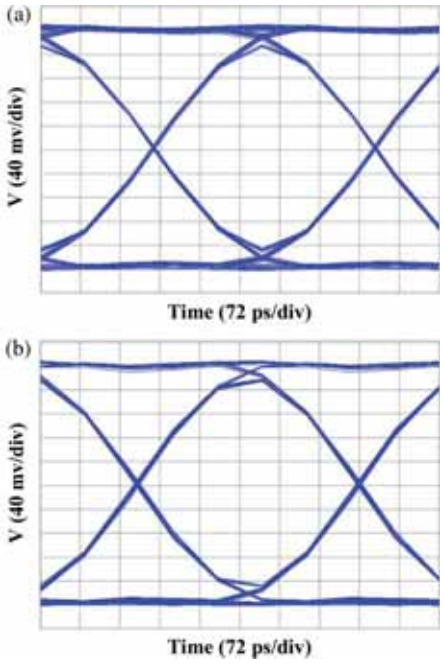

Fig. 11. Measured differential eye diagrams for the differential line of Fig. 9 (a) with and (b) without DS-CSRRs. The eye diagram in (a) reveals that the common-mode rejection does not degrade the differential signals.

B. Differential Bandpass Filter With Common-Mode Rejection

Differential bandpass filters with common-mode rejection have been reported in the literature [28]–[32]. Here, we report a balanced filter consisting of a pair of coupled stepped-impedance resonators (SIRs) fed by a differential line,

TABLE II
MEASURED EYE PARAMETERS

	With DS-CSRRs	*Without DS-CSRRs*
Eye height	278 mV	281 mV
Eye width	371 ps	383 ps
Jitter (PP)	29.3 ps	16.9 ps
Eye opening factor	0.76	0.76

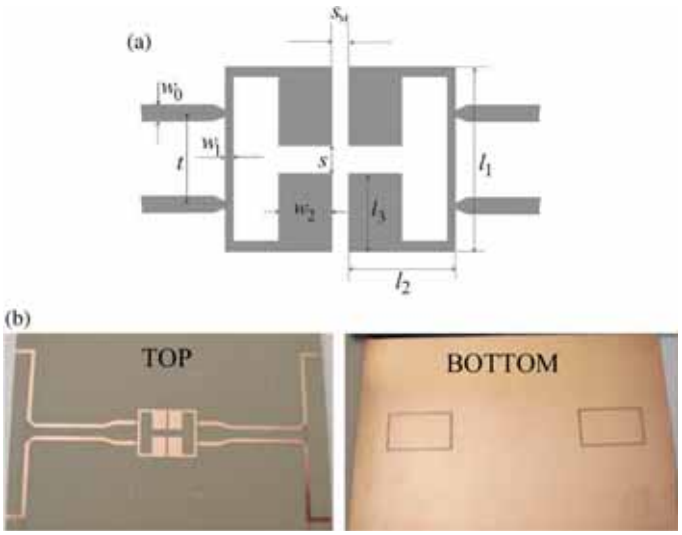

Fig. 12. (a) Layout and (b) photograph of the designed differential bandpass filter with improved common-mode rejection. Dimensions are: for the DS-CSRRs, $c = d =$ 0.2 mm, longitudinal side length $=$ 17.6 mm, and transverse side length $=$ 10.8 mm; for the differential line, $W =$ 1 mm, and $S =$ 2.5 mm; for the differential filter, $S_M =$ 0.5 mm, $s =$ 2 mm, $w_0 =$ 1.2 mm, $w_1 =$ 0.7 mm, $w_2 =$ 3.7 mm, $l_1 =$ 12.8 mm, $l_2 =$ 7.5 mm, $l_3 =$ 5.4mm, and $t =$ 5.5 mm. The considered substrate is the *Rogers RO3010* with thickness $h =$ 1.27 mm, dielectric constant $\varepsilon_r = 10.2$, and loss tangent $\tan\delta = 0.0023$.

as shown in the layout of Fig. 12(a) (other balanced filters based on SIRs have been reported in [33] and [34]). The filter by itself rejects the common mode due to the symmetry of the structure, since the symmetry plane of the resonator exhibits an electric wall at the first SIR resonance. Therefore, such resonators cannot be excited by means of common-mode signals, and the even mode is reflected back to the source due to the presence of the slots between the pair of SIRs. However, the rejection level of the common mode in the region of interest is very limited since it depends on the distance between resonators, and such inter-resonator distance is dictated by filter specifications. Next, we show that the common mode can be further rejected by introducing (cascading) DS-CSRRs.

The proposed differential filter is a second-order Chebyshev bandpass filter with a central frequency of 1.37 GHz, a fractional bandwidth of 10%, and 0.1-dB ripple. The considered substrate is the *Rogers RO3010* with thickness $h =$ 1.27 mm, and dielectric constant $\varepsilon_r = 10.2$. With these specifications and substrate, the layout of the filter is that depicted in Fig. 12(a) (the design of the filter has been done following the procedure described in [35]).

The frequency response of the filter (differential mode, S_{dd21} and S_{dd11}) is shown in Fig. 13. The common-mode insertion loss (S_{cc21}), also depicted in the figure, exhibits a rejection

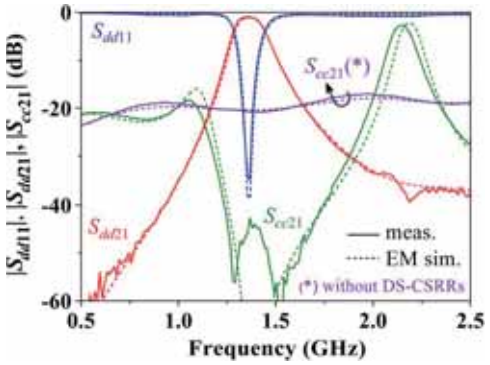

Fig. 13. Simulated and measured differential-mode return loss $|S_{dd11}|$ and insertion loss $|S_{dd21}|$, and common-mode insertion loss $|S_{cc21}|$ for the structure of Fig. 12(b) with and without the presence of the DS-CSRRs.

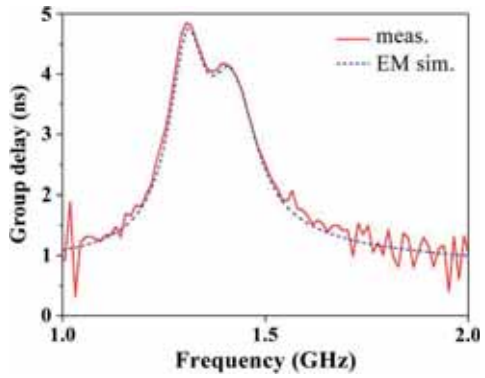

Fig. 14. Group delay for the differential filter of Fig. 12(b).

level of about 20 dB in the passband region. In order to enhance the common-mode rejection, we have cascaded two identical DS-CSRRs as shown in Fig. 12(b). Such DS-CSRRs have been designed to generate a stopband for the common mode in the passband region of the differential filter and are identical to those of Fig. 9. The presence of the DS-CSRRs does not affect the filter response (odd mode). However, by merely introducing two DS-CSRRs, the common mode rejection is roughly increased up to 50 dB in the region of interest (see Fig. 13). To completely characterize the differential filter, the group delay for the differential mode is shown in Fig. 14. These results point out that DS-CSRRs provide an efficient path to enhance the common mode noise rejection in balanced filters.

VII. COMPARISON WITH OTHER COMMON-MODE FILTERS

The fabricated differential line with common mode suppression of Fig. 9 is compared with that presented in [1] and with other reported differential lines in Table III. The physical dimensions given in the table correspond to the active area (defected ground area in the defected ground structures), and the guided wavelength γ_e is the one corresponding to the even mode. As compared with other approaches, our CSRR and DS-CSRR based differential lines exhibit a competitive combination of size, bandwidth and rejection level. The filter reported in [4] is very competitive in terms of size and bandwidth, but the maximum rejection level is moderate. Moreover, such a common-mode filter is based on a multilayer structure, and this has extra cost and complexity. The filters reported in [5] and [6]

TABLE III
COMPARISON OF SEVERAL DIFFERENTIAL LINES WITH COMMON-MODE SUPPRESSION

Ref.	*Length* (λ_e)	*Width* (λ_e)	*Area* (λ_e^2)	*FBW* (%) -10 dB	-20 dB	-40 dB
[4]	0.26	0.16	0.04	60	32	-
[5]	0.76	0.47	0.36	70	53	-
[6]	0.44	0.44	0.19	87	-	-
[1]	0.43	0.14	0.06	54	37	14
This work	0.64	0.13	0.08	51	41	23

have larger dimensions than our CSRR- and DS-CSRR-based filters do. The filter reported in [6] exhibits a huge stopband considering a -10-dB bandwidth, but, again, the maximum rejection level is poor as compared with that of our proposed filters.

In summary, the proposed common-mode suppression strategy is technologically simple and low cost (only two metal levels are used), and the resulting common-mode rejection filters are compact and provide wide and high-rejection stopbands, with a simple and systematic design procedure.

VIII. CONCLUSION

It has been demonstrated that CSRRs and DS-CSRRs are useful to selectively suppress the even (common) mode in microstrip differential lines. The lumped element equivalent circuit model (unit cell) of a differential line loaded with an array of symmetrically etched CSRRs (or DS-CSRRs) has been reported. From symmetry properties and the magnetic and electric wall concepts, the circuit models under even- and odd-mode excitation have also been obtained. Such models have been used to support the conclusions relative to the selective mode suppression (i.e., the suppression of the even mode maintaining the integrity of the differential signals) inferred from symmetry analysis and field distributions.

Since the common-mode rejection bandwidth is a key parameter to common mode filters design, the main strategies for bandwidth enhancement have been considered. Concerning inter-resonator coupling, it has been justified from Bloch mode theory that bandwidth enhancement in common mode filters with tightly coupled resonators is related to the presence of complex waves. Although inter-resonator coupling can enhance the bandwidth, this effect is limited by technological restrictions and, therefore, the use of intrinsically wideband resonators is essential to achieve competitive common mode rejection bands. For this reason, DS-CSRRs have been considered in this work.

A simple methodology for common-mode filter design (valid for CSRR and DS-CSRR) has been proposed, and several periodic common-mode filters with different central frequency and order have been designed and compared. Clearly, DS-CSRRs are more efficient in terms of rejection bandwidth, though the prediction of the maximum achievable bandwidth is more accurate for CSRR-loaded lines. It has also been found that the common-mode rejection bandwidth roughly saturates for order-6 filters.

The theory has been validated against measurements through the fabrication of a DS-CSRR-loaded differential transmission line and a balanced bandpass filter with common-mode suppression. In the DS-CSRR-loaded line, a measured common-mode rejection level better than 20 dB within a 41% fractional bandwidth has been obtained (whilst preserving the integrity of the differential signal). The reported differential bandpass filter exhibits a measured common-mode rejection better than 40 dB in a 34% bandwidth (including the differential passband region) thanks to the presence of the DS-CSRRs, which do not affect the differential filter performance.

REFERENCES

[1] J. Naqui, A. Fernández-Prieto, M. Durán-Sindreu, J. Selga, F. Medina, F. Mesa, and F. Martín, "Split rings-based differential transmission lines with common-mode suppression," in *IEEE MTT-S Int. Microw. Symp. Dig.*, Baltimore, MD, Jun. 2011.

[2] F. Falcone, T. Lopetegi, J. D. Baena, R. Marqués, F. Martín, and M. Sorolla, "Effective negative- ε stop-band microstrip lines based on complementary split ring resonators," *IEEE Microw. Wireless Compon. Lett.*, vol. 14, no. 6, pp. 280–282, Jun. 2004.

[3] B. C. Tseng and L. K. Wu, "Design of miniaturized common-mode filter by multilayer low-temperature co-fired ceramic," *IEEE Trans. Electromagn. Compat.*, vol. 46, no. 4, pp. 571–579, Nov. 2004.

[4] C.-H. Tsai and T.-L. Wu, "A broadband and miniaturized common-mode filter for gigahertz differential signals based on negative-permittivity metamaterials," *IEEE Trans. Microw. Theory Tech.*, vol. 58, no. 1, pp. 195–202, Jan. 2010.

[5] W. T. Liu, C.-H. Tsai, T.-W. Han, and T.-L. Wu, "An embedded common-mode suppression filter for GHz differential signals using periodic defected ground plane," *IEEE Microw. Wireless Compon. Lett.*, vol. 18, no. 4, pp. 248–250, Apr. 2008.

[6] S.-J. Wu, C.-H. Tsai, T.-L. Wu, and T. Itoh, "A novel wideband common-mode suppression filter for gigahertz differential signals using coupled patterned ground structure," *IEEE Trans. Microw. Theory Techn.*, vol. 57, no. 4, pp. 848–855, Apr. 2009.

[7] G. V. Eleftheriades, "Analysis of bandwidth and loss in negative-refractive-index transmission-line (NRI-TL) media using coupled resonators," *IEEE Microw. Wireless Compon. Lett.*, vol. 17, no. 6, pp. 412–414, Jun. 2007.

[8] F. A. Fernández, Y. Lu, J. B. Davies, and S. Zhu, "Finite element analysis of complex modes in inhomogeneous waveguides," *IEEE Trans. Magn.*, vol. 29, pp. 1601–1604, Mar. 1993.

[9] R. Marqués, J. D. Baena, J. Martel, F. Medina, F. Falcone, M. Sorolla, and F. Martín, "Novel small resonant electromagnetic particles for metamaterial and filter design," in *Proc. Int. Conf. Electromagn. Adv. Applications*, Torino, Italy, Sep. 8–12, 2003, pp. 439–443.

[10] F. Martín, F. Falcone, J. Bonache, T. Lopetegi, R. Marqués, and M. Sorolla, "Miniaturized CPW stop band filters based on multiple tuned split ring resonators," *IEEE Microw. Wireless Compon. Lett.*, vol. 13, no. 12, pp. 511–513, Dec. 2003.

[11] J. García-García, J. Bonache, F. Falcone, J. D. Baena, F. Martín, I. Gil, T. Lopetegi, M. A. G. Laso, A. Marcotegui, R. Marqués, and M. Sorolla, "Stepped-impedance low pass filters with spurious passband suppression," *Electron. Lett.*, vol. 40, pp. 881–883, Jul. 2004.

[12] J. García-García, F. Martín, F. Falcone, J. Bonache, I. Gil, T. Lopetegi, M. A. G. Laso, M. Sorolla, and R. Marqués, "Spurious passband suppression in microstrip coupled line bandpass filters by means of split ring resonators," *IEEE Microw. Wireless Compon. Lett.*, vol. 14, no. 9, pp. 416–418, Sep. 2004.

[13] J. García-García, F. Martín, F. Falcone, J. Bonache, J. D. Baena, I. Gil, E. Amat, T. Lopetegi, M. A. G. Laso, J. A. Marcotegui, M. Sorolla, and R. Marqués, "Microwave filters with improved stop band based on sub-wavelength resonators," *IEEE Trans. Microw. Theory Tech.*, vol. 53, no. 6, pp. 1997–2006, Jun. 2005.

[14] D. R. Smith, W. J. Padilla, D. C. Vier, S. C. Nemat-Nasser, and S. Schultz, "Composite medium with simultaneously negative permeability and permittivity," *Phys. Rev. Lett.*, vol. 84, pp. 4184–4187, May 2000.

[15] F. Martín, F. Falcone, J. Bonache, R. Marqués, and M. Sorolla, "Split ring resonator based left handed coplanar waveguide," *Appl. Phys. Lett.*, vol. 83, pp. 4652–4654, Dec. 2003.
[16] F. Falcone, T. Lopetegi, M. A. G. Laso, J. D. Baena, J. Bonache, R. Marqués, F. Martín, and M. Sorolla, "Babinet principle applied to the design of metasurfaces and metamaterials," *Phys. Rev. Lett.*, vol. 93, p. 197401, Nov. 2004.
[17] J. D. Baena, J. Bonache, F. Martín, R. Marqués, F. Falcone, T. Lopetegi, M. A. G. Laso, J. García, I. Gil, and M. Sorolla, "Equivalent circuit models for split ring resonators and complementary split rings resonators coupled to planar transmission lines," *IEEE Trans. Microw. Theory Tech.*, vol. 53, no. 4, pp. 1451–1461, Apr. 2005.
[18] R. Mongia, I. Bahl, and P. Barthia, "Multiconductor transmission lines," in *RF and Microwave Coupled Line Circuits*. Norwood, MA: Artech House, 1999.
[19] S. Gupta, A. Parsa, E. Perret, R. V. Snyder, R. J. Wenzel, and C. Caloz, "Group-delay engineered noncommensurate transmission line all-pass network for analog signal processing," *IEEE Trans. Microw. Theory Tech.*, vol. 58, no. 9, pp. 2392–2407, Sep. 2010.
[20] J. Shekel, "Matrix analysis of multi-terminal transducers," *Proc. IRE*, vol. 42, no. 5, pp. 840–847, May 1954.
[21] R. Islam, M. Zedler, and G. V. Eleftheriades, "Modal analysis and wave propagation in finite 2-D transmission-line metamaterials," *IEEE Trans. Antennas Propag.*, vol. 59, no. 5, pp. 1562–1570, May 2011.
[22] U. Crombach, "Complex waves on shielded lossless rectangular dielectric image guide," *Electron. Lett.*, vol. 19, pp. 557–558, Jul. 1983.
[23] M. Mrozowski and J. Mazur, "Matrix theory approach to complex waves," *IEEE Trans. Microw. Theory Tech.*, vol. 40, no. 4, pp. 781–785, Apr. 1992.
[24] F. Elek and G. V. Eleftheriades, "Dispersion analysis of the shielded Sievenpiper structure using multiconductor transmission line theory," *IEEE Microw. Wireless Compon. Lett.*, vol. 14, no. 9, pp. 434–436, Sep. 2004.
[25] M. Beruete, F. Falcone, M. J. Freire, R. Marqués, and J. D. Baena, "Electroinductive waves in chains of complementary metamaterial elements," *Appl. Phys. Lett.*, vol. 88, no. 8, Feb. 2006, Art. ID 083503.
[26] J. Bonache, M. Gil, I. Gil, J. Garcia-García, and F. Martín, "On the electrical characteristics of complementary metamaterial resonators," *IEEE Microw. Wireless Compon. Lett.*, vol. 16, no. 10, pp. 543–545, Oct. 2006.
[27] M. Gil, J. Bonache, I. Gil, J. García-García, and F. Martín, "On the transmission properties of left handed microstrip lines implemented by complementary split rings resonators," *Int. J. Numer. Model.: Electron. Netw., Devices Fields*, vol. 19, pp. 87–103, Mar. 2006.
[28] C. H. Wu, C. H. Wang, and C. H. Chen, "Novel balanced coupled-line bandpass filters with common-mode noise suppression," *IEEE Trans. Microw. Theory Tech.*, vol. 55, no. 2, pp. 287–295, Feb. 2007.
[29] B. L. Teck and Z. Lei, "A differential-mode wideband bandpass filter on microstrip line for UWB applications," *IEEE Microw. Wireless Compon. Lett.*, vol. 19, no. 10, pp. 632–634, Oct. 2009.
[30] J. Shi and Q. Xue, "Novel balanced dual-band bandpass filter using coupled stepped-impedance resonators," *IEEE Microw. Wireless Compon. Lett.*, vol. 20, no. 1, pp. 19–21, Jan. 2010.
[31] J. Shi and Q. Xue, "Dual-band and wide-stopband single-band balanced bandpass filters with high selectivity and common-mode suppression," *IEEE Trans. Microw. Theory Tech.*, vol. 58, no. 8, pp. 2204–2212, Aug. 2010.
[32] J. Shin and Q. Xue, "Balanced bandpass filters using center-loaded half-wavelength resonators," *IEEE Trans. Microw. Theory Tech.*, vol. 58, no. 4, pp. 970–977, Apr. 2010.
[33] C.-H. Wu, C.-H. Wang, and C. H. Chen, "Stopband-extended balanced bandpass filter using coupled stepped-impedance resonators," *IEEE Microw. Wireless Compon. Lett.*, vol. 17, no. 7, pp. 507–509, Jul. 2007.
[34] C.-H. Lee, C.-I. G. Hsu, and C.-C. Hsu, "Balanced dual-band BPF with stub-loaded SIRs for common-mode suppression," *IEEE Microw. Wireless Compon. Lett.*, vol. 20, no. 2, pp. 70–73, Feb. 2010.
[35] J.-S. Hong and M. J. Lancaster, "Lowpass and Bandpass Filters and Coupled Resonator Circuits," in *Microstrip Filters for RF/Microwave Applications*. New York: Wiley, 2001.

Jordi Naqui (S'11) was born in Granollers, Spain, in 1984. He received the Telecommunication Technical Engineering diploma and Telecommunication Engineering degree from the Universitat Autònoma de Barcelona, Belleterra, Spain, in 2006 and 2010, respectively, where he is currently working toward the Ph.D. degree.

His research subjects are related to innovative passive microwave devices based on metamaterial concepts.

Armando Fernández-Prieto (S'11) was born in Ceuta, Spain, in 1981. He received the Licenciado degree in physics from the Universidad de Sevilla, Seville, Spain, in 2006, where he is currently working toward the Ph.D. degree in electronics and electromagnetism.

His research focuses on printed passive microwave filters, couplers, and metamaterials.

Miguel Durán-Sindreu (S'09–M'11) was born in Barcelona, Spain, in 1985. He received the Telecommunications Engineering diploma, Telecommunications Engineering degree, and Ph.D. degree from the Universitat Autònoma de Barcelona, Belleterra, Spain, in 2007, 2008 and 2011, respectively.

His research interests are microwave filters, metamaterials, and multiband components.

Francisco Mesa (M'93–SM'01) was born in Cádiz, Spain, in April 1965. He received the Licenciado and Ph.D. degrees from the University of Seville, Seville, Spain, in 1989 and 1991, respectively, both in physics.

He is currently a Professor with the Department of Applied Physic 1, University of Seville, Seville, Spain. His research interests focus on electromagnetic propagation/radiation in planar structures.

Jesús Martel (M'08) was born in Seville, Spain, in 1966. He received the Licenciado and Ph.D. degrees from the University of Seville, Seville, Spain, in 1989 and 1996, respectively, both in physics.

Since 1992, he has been with the Department of Applied Physics II, University of Seville, Seville, Spain, where, in 2000, he became an Associate Professor. His current research interests are focused on the numerical analysis of planar transmission lines, the modeling of planar microstrip discontinuities, the design of passive microwave circuits, microwave measurements, and artificial media.

Francisco Medina (M'90–SM'01–F'10) was born in Cádiz, Spain, in November 1960. He received the Licenciado and Ph.D. degrees from the University of Seville, Seville, Spain, in 1983 and 1987 respectively, both in physics.

From 1986 to 1987, he spent the academic year with the Laboratoire de Microondes de l'ENSEEIHT, Toulouse, France, as the recipient of a Spanish Ministry of Science and Education Research Scholarship. From 1985 to 1989, he was an Assistant Professor with the Department of Electronics and Electromagnetism, University of Seville, Seville, Spain, where, since 1990, he has been an Associate Professor of electromagnetism. Since July 2009, he has been a Full Professor of electromagnetism and Head of the Microwaves Group. His research interests include analytical and numerical methods for guiding, resonant, and radiating structures, passive planar circuits, periodic structures, and the influence of anisotropic materials (including microwave ferrites) on such systems. He is also interested in artificial media modeling and extraordinary transmission phenomena. He is on the Editorial Board of the *International Journal of RF and Microwave Computer-Aided Engineering.*

Dr. Medina is a Fellow of the Massachusetts Institute of Technology (MIT) Electromagnetics Academy. He is a reviewer of the IEEE TRANSACTIONS ON MICROWAVE THEORY AND TECHNIQUES and of many other journals. He has been a member of the Technical Programme Committees (TPC) of several international and local conferences and has organized a few conferences and workshops.

Ferran Martín (M'04–SM'08–F'12) was born in Barakaldo Spain, in 1965. He received the B.S. degree in physics and Ph.D. degree from the Universitat Autònoma de Barcelona, Belleterra, Spain, in 1988 and 1992, respectively.

From 1994 to 2006, he was an Associate Professor in electronics with the Departament d'Enginyeria Electrònica, Universitat Autònoma de Barcelona (UAB), Belleterra, Spain, and since 2007 he has been a Full Professor of electronics. In recent years, he has been involved in different research activities including modelling and simulation of electron devices for high-frequency applications, millimeter-wave and terahertz generation systems, and the application of electromagnetic bandgaps to microwave and millimeter-wave circuits. He is now very active in the field of metamaterials and their application to the miniaturization and optimization of microwave circuits and antennas. He is the head of the Microwave and Millimeter Wave Engineering Group (GEMMA Group) at UAB, and director of CIMITEC, a research Center on Metamaterials supported by TECNIO (Generalitat de Catalunya). He has authored and co-authored over 350 technical conference, letter and journal papers and he is coauthor of the monograph on metamaterials, entitled *Metamaterials with Negative Parameters: Theory, Design and Microwave Applications* (Wiley, 2008). He has filed several patents on metamaterials and has headed several Development Contracts.

Dr. Martín received the 2006 Duran Farell Prize for Technological Research, he holds the Parc de Recerca UAB—Santander Technology Transfer Chair, and he was the recipient of an ICREA ACADEMIA Award. He has organized several international events related to metamaterials, including Workshops at the IEEE Microwave Theory and Techniques Society (IEEE MTT-S) International Microwave Symposium (years 2005 and 2007) and European Microwave Conference (2009). He has acted as a guest editor for three Special Issues on metamaterials in three international journals.

Article S11

Novel Sensors Based on the Symmetry Properties of Split Ring Resonators (SRRs)

J. Naqui, M. Durán-Sindreu and F. Martín

Sensors **2011**, *11*, 7545-7553; doi:10.3390/s110807545

OPEN ACCESS

sensors

ISSN 1424-8220

www.mdpi.com/journal/sensors

Article

Novel Sensors Based on the Symmetry Properties of Split Ring Resonators (SRRs)

Jordi Naqui *, Miguel Durán-Sindreu and Ferran Martín

CIMITEC, Departament d'Enginyeria Electrònica, Universitat Autònoma de Barcelona, Bellaterra, Barcelona 08193, Spain; E-Mails: miguel.duransindreu@uab.cat (M.D.-S.); ferran.martin@uab.cat (F.M.)

* Author to whom correspondence should be addressed; E-Mail: Jordi.Naqui@uab.cat; Tel.: +34-93-581-35-21; Fax: +34-93-581-26-00.

Received: 1 June 2011; in revised form: 21 July 2011 / Accepted: 22 July 2011 / Published: 29 July 2011

Abstract: The symmetry properties of split ring resonators (SRRs) are exploited for the implementation of novel sensing devices. The proposed structure consists of a coplanar waveguide (CPW) loaded with movable SRRs on the back substrate side. It is shown that if the SRRs are placed with the slits aligned with the symmetry plane of the CPW, the structure is transparent to signal propagation. However, if the symmetry is broken, a net axial magnetic field can be induced in the inner region of the SRRs, and signal propagation is inhibited at resonance. The proposed structures can be useful as alignment sensors, position sensors and angle sensors. This novel sensing principle is validated through experiment.

Keywords: split ring resonators; metamaterials; coplanar waveguide; position sensors; angle sensors

1. Introduction

Split ring resonators (SRRs) consist of a pair of concentric metallic rings, etched on a dielectric substrate, with slits etched on opposite sides (see Figure 1). SRRs can be electrically small if the rings are tightly coupled [1]. These resonators have been used for the synthesis of left handed [2] and negative refractive index media [3], where the necessary value of the negative effective permeability is

due to the presence of the SRRs (if an array of electrically small SRRs is excited by means of an axial time varying magnetic field, the structure behaves as an effective medium with negative effective permeability in a narrow band above SRR resonance). SRRs have also been coupled to planar transmission lines, for the synthesis of transmission line metamaterials. Specifically, it was demonstrated in [4] that a coplanar waveguide (CPW) loaded with pairs of SRRs in the back substrate side inhibits signal propagation in the vicinity of SRR resonance, and this was interpreted as due to the negative effective permeability of the structure. Indeed, if a CPW is loaded with a single pair of SRRs, the transmission coefficient exhibits a transmission zero, indicative of the resonance frequency of the SRRs. Such resonance frequency is given by the inductance and capacitance of the SRR, where a quasi-static model can be applied if the particle is electrically small [5]. Thus, for electrically small circular SRRs, the inductance is calculated from the inductance of a single ring with average radius, and the capacitance is given by the series connection of the distributed capacitance of the upper and lower halves of the SRR [5]. Actually, the SRR exhibits many resonance frequencies [6], but the frequency of interest for the implementation of effective media is the first one, because the particle can only be considered to be electrically small at this resonance.

Figure 1. Typical topology and relevant dimensions of (**a**) a circular and (**b**) a rectangular SRR.

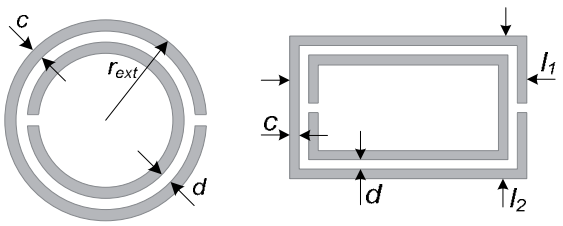

(**a**) (**b**)

Different kind of sensors based on SRRs have been proposed, such as thin-film sensors [7], particle detectors [8,9], stress sensors [10], moisture sensors [11], pressure sensors [12], or displacement sensors [13], among others. In most of these applications, the variation of the resonance frequency or the quality factor of the particles, caused by changes in the variable to be sensed, has been the considered sensing strategy. In this paper, a different approach for the implementation of sensors based on SRRs is proposed, *i.e.*, to exploit the symmetry properties of SRRs coupled to CPWs. The detection principle is based on the loss of symmetry caused, for instance, by a displacement or a rotation.

In Section 2, the theory behind the proposed detection principle is explained in detail; in Section 3, the principle is validated through electromagnetic simulation; the sensitivity of a prototype device is evaluated through simulation and experiment in Section 4 to demonstrate the proof-of-concept; finally, the main conclusions of the work are highlighted in Section 5.

2. The Sensing Principle

As reported in [4], a CPW structure loaded with pairs of SRRs inhibits signal propagation in the vicinity of SRR resonance. In the reported prototypes, the pairs of SRRs are etched on the back substrate side, with the center of the SRRs underneath the slots. Under these conditions, the magnetic field in the inner region of each SRRs is contradirectional, but the SRRs can be excited at resonance.

Let us consider, instead, that only one SRR is etched in the back substrate side of a CPW structure, and that the slit of each ring is perfectly aligned with the symmetry plane of the CPW structure [see Figure 2(a)]. Under these conditions, it is clear that the axial components of the magnetic field in the inner region of the SRR must cancel, and the SRR cannot be excited at resonance. However, if the symmetry is broken, a net magnetic field in the inner region of the SRR is expected and the rings will be excited at resonance. This situation can be simply monitored by measuring the transmission coefficient. A transmission zero at SRR resonance is expected, with the magnitude of such transmission zero being dependent on the deviation from symmetry (the considered sensitivity in this work is thus given by the derivative of the notch magnitude with the variable to be sensed, that is, lateral displacement or rotation).

Figure 2. CPW loaded with a circular shaped SRR; (**a**) symmetrically placed; (**b**) displaced 0.5 mm; and (**c**) rotated 10°. Dimensions are: L = 10.4 mm, W = 1.67 mm, G = 0.2 mm, $c = d$ = 0.2 mm and r_{ext} = 5 mm.

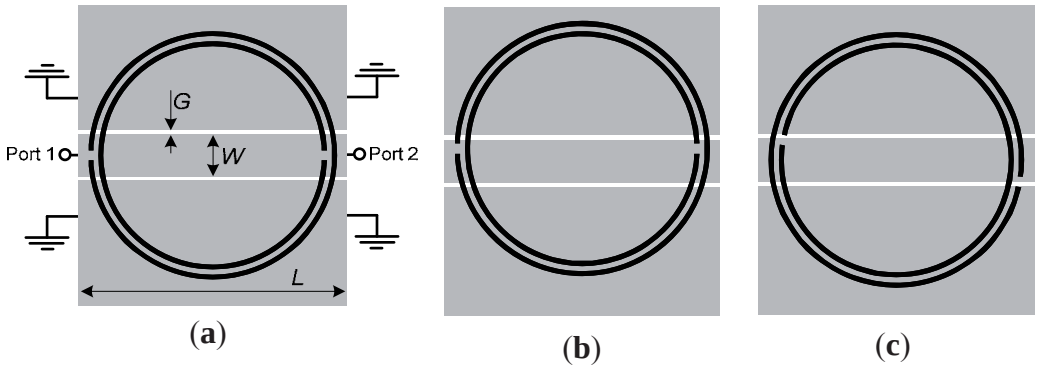

(**a**) (**b**) (**c**)

Alternatively, the fact that the SRR is not excited if the slits are perfectly aligned with the symmetry plane of the CPW can be explained since the symmetry plane of the SRR is an electric wall at resonance [5], *i.e.*, the distribution of charges is anti-symmetric with respect to that plane. However, the symmetry plane of a CPW structure is a magnetic wall for the fundamental (even) mode. Thus, the SRR cannot be excited if both symmetry planes (that of the CPW and that of the SRR) coincide.

3. Validation

In order to validate the previous principle, we have considered a CPW loaded with a circular SRR (Figure 2) in three configurations: (a) symmetrically etched; (b) displaced 0.5 mm; and (c) rotated 10°. Although the lack of symmetry can be produced by many different causes, in this work we have considered the following two possibilities: a lateral displacement and a rotation of the SRR. The resonance frequency of the SRR has been estimated by means of the model reported in [5] (f_0 = 1.94 GHz), by considering the Rogers RO3010 substrate with dielectric constant ε_r = 10.2, thickness h = 127 μm, and loss tangent tanδ = 0.0023. In these structures, we have obtained the transmission coefficient (S_{21}) by means of a full wave electromagnetic simulator (Agilent Momentum). The results, shown in Figure 3, reveal that if the SRR is symmetrically etched, the structure is transparent at SRR resonance. However, if the symmetry is altered by simply displacing or rotating the SRR, a notch appears in the transmission coefficient at the resonance frequency of the SRR. It is worth

to mention that actually, in the current validation, there are two notches which are the corresponding ones to the inner and outer ring. It has been observed that they are very close because the rings have nearly the same length and are loosely coupled due to the thin substrate thickness (a short distance between the SRR and the top layer, with respect to the gap between rings, favors the coupling between the top layer and the SRR at the expense of the inter-coupling between rings). Notice that the substrate thickness (127 μm) is thinner than the inter-ring separation (200 μm), a value close to the fabrication limit. If the two rings forming the SRRs are loosely coupled, the SRR cannot be considered to be electrically small. Hence, the first resonance frequency is no longer quasi-static, but the symmetry properties and sensing principle described in the previous section are exactly the same. Thus, it is clear that we are able to detect the lack of symmetry in CPWs loaded with a single SRR. The effects of substrate thickness on inter-rings coupling are analyzed later, on the basis of the structures considered to validate the sensing principle.

Figure 3. Simulated transmission coefficients of the structures of Figure 2.

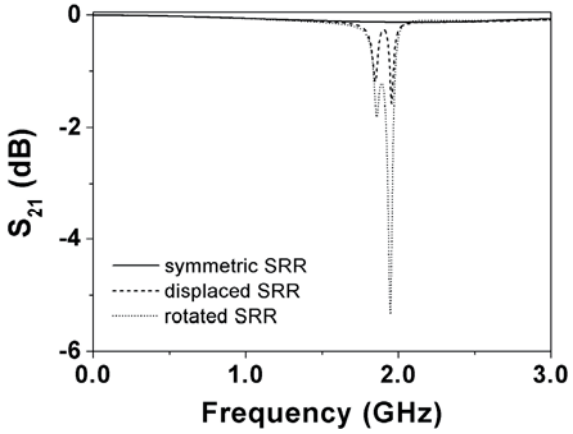

It is important to obtain a high sensitivity of the notch magnitude with the variable that destroys the symmetry of the structure. Obviously the sensitivity is expected to be dependent on the SRR and CPW geometry, but we do also expect the influence of substrate thickness. In structures with thick substrates, the magnetic field lines generated by current flow in the CPW scarcely penetrate the SRR region and hence we do not expect a high sensitivity under these conditions. Therefore, CPW structures with thin substrates are preferred for the design of sensors. Among the commercially available low-loss microwave substrates of our laboratory, we have thus chosen the Rogers RO3010 with thickness h = 127 μm.

With regards to the geometry, by decreasing the overall dimensions of the CPW and SRR, the sensitivity for a linear displacement can be enhanced. The reason is that if we scale down the structure and a particular displacement, the frequency response experiences a shift upwards roughly maintaining the same notch magnitude (such notch magnitudes being identical if losses are neglected). Nevertheless, the limits are dictated by the available fabrication technology (a photo mask/etching process with a minimum strip and slot width of 200 μm in our case). The critical aspect to enhance sensitivity is to choose the appropriate shape factor for the SRR. Namely, if we choose a circular SRR with an internal diameter much larger than the distance between the CPW slots (as in Figure 2), the magnetic field lines within the SRR region do not exactly cancel if symmetry is broken, but the effects of asymmetry

are not significant. Conversely, if the SRR does not extend beyond the slots of the CPW, the effects of the asymmetry on the frequency response of the structure (notch magnitude) are more pronounced. Indeed, the magnitude of the notch increases by etching the SRR just below the central strip of the CPW. To validate the previous comments we have considered three different SRR-loaded CPW structures. One of them is that depicted in Figure 2(a); the others are those depicted in Figure 4. In all these structures, the symmetry has been broken by applying a lateral displacement and by applying a rotation to the SRR of 0.5 mm and 10°, respectively. The simulated transmission coefficients obtained after applying the previous translation and rotation operations to the SRR are depicted in Figure 3 and in Figure 5. According to these figures, the structure of Figure 4(a) provides the deepest notch for the displacement, whereas the structure of Figure 4(b) seems to be the best choice for detecting rotation. It is also remarkable that although for the square-shaped SRR the rings are uncoupled (as for the circular and rectangular shaped SRRs), the notches are substantially distant because the lengths of the inner and outer ring are very different.

Figure 4. (**a**) CPW loaded with a square shaped SRR; and (**b**) CPW loaded with a rectangular shaped SRR. Dimensions are: L_1 = 2.07 mm (**a**), L_1 = 12.4 mm (**b**), W = 1.67 mm, G = 0.2 mm, c = d = 0.2 mm, l_1 = 1.67 mm (**a**), l_1 = 12 mm (**b**) and l_2 = 1.67 mm.

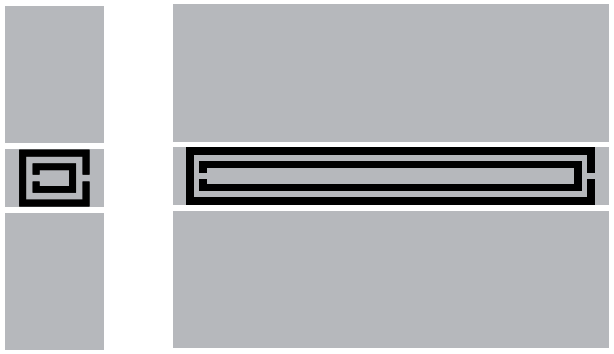

(**a**) (**b**)

Figure 5. Simulated transmission coefficients of the structures of Figure 4 and those obtained by displacing 0.5 mm and rotating 10° the SRR; (**a**) Figure 4(a) and (**b**) Figure 4(b).

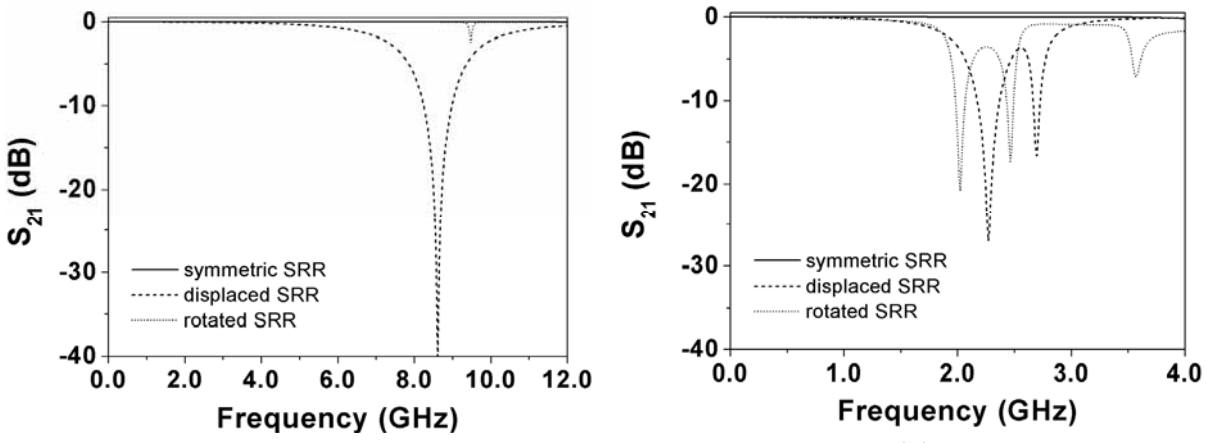

(**a**) (**b**)

To gain more insight on the effects of the substrate thickness on inter-resonator's coupling, the frequency response of the CPW with the individual rings of Figure 4(b) laterally displaced 0.5 mm has been simulated. The results are compared with the frequency response of the SRR-loaded CPW in Figure 6(a). Clearly, the rings are uncoupled. However, if substrate thickness is increased to 635 μm [Figure 6(b)], the first two resonances of the SRR experience a frequency shift caused by an evident inter-rings coupling. However, the depth of the notches decreases; thus thin substrates are preferred, even though this can result in a negligible inter-rings coupling.

Figure 6. Simulated transmission coefficients of the structure of Figure 4(b) by laterally displacing 0.5 mm the SRR, and by considering only the inner or the outer ring (also displaced); **(a)** h = 127 μm and **(b)** h = 635 μm.

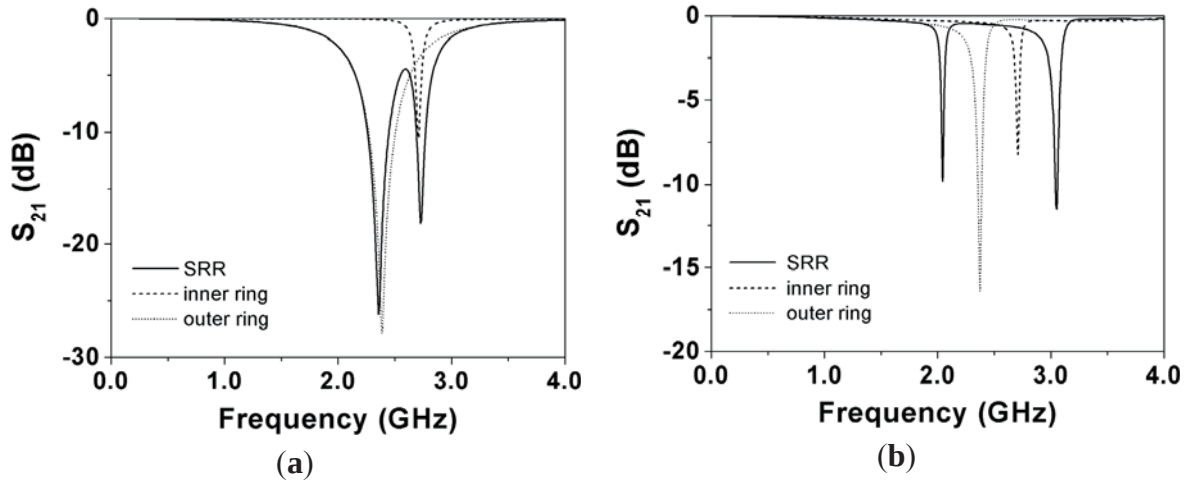

4. Experimental Results

The purpose of this section is to analyze the sensitivity of the proposed sensing devices by means of full wave electromagnetic simulation and experiment. To this end, rather than fabricating a sensing device with movable SRRs, which is technologically more complex, we will study the effects of displacing or rotating the SRRs by fabricating several devices with different displacements and rotations (the key point of this paper is to validate the proof-of-concept for this novel sensing principle).

The base structure (*i.e.*, the symmetric structure) is depicted in Figure 7. In such structure, the slot and central strip widths of the CPW are G = 0.2 mm and W = 1.67 mm, respectively (corresponding to a 50 Ω line in the Rogers RO3010 substrate indicated before). The width, c, of the metal strips of the SRR as well as their separation, d, are $c = d$ = 0.2 mm; finally, the length and width of the SRR is l_1 = 12 mm and l_2 = 1.67 mm, respectively. These dimensions have been optimized to enhance the sensitivity, taking into account the minimum strip and slot width of the available technology and the effects of losses. From this structure, we have fabricated some additional CPWs with different displaced and rotated SRRs. For these structures, we have obtained the magnitude of the insertion loss at the first and second resonance; the results are depicted in Figure 8. There is a reasonable agreement between the electromagnetic simulations and the measurements. The sensitivity S ($\Delta S_{21}/\Delta x$ and $\Delta S_{21}/\Delta \varphi$, where x and φ denote displacement and rotation, respectively), simply inferred from the discrete derivative of the insertion loss magnitude (after applying a smoothing algorithm), is also

depicted in the figure. The results are reasonable for the first resonance, taking into account the dimensions of the considered SRR and CPW. For the second resonance, the sensitivity is not as good as the one corresponding to the first resonance, the reason being that the ring producing the second resonance is smaller and further displacement is required to notice the effects of asymmetry (*i.e.*, the inner ring needs more lateral displacement to reach the slot area of the CPW).

To end this section, the notch magnitude (first resonance) obtained by electromagnetic simulation of the structure of Figure 7 that results from lateral displacement of the SRR is compared (Figure 9) to that of an identical structure but with all dimensions scaled down by a factor of two and four (dielectric and ohmic losses are included in the simulations). As can be seen, sensitivity is enhanced by scaling dimensions down, the improvement being nearly proportional to the scaling factor. However, as the scaling factor increases losses play an increasingly significant role and, for a too large scaling factor, sensitivity might be lower than expected. From the results of this section, it can be inferred that the sensing principle is validated.

Figure 7. Photograph of the fabricated base structure; (**a**) top view of the CPW; and (**b**) SRR etched in the back substrate side.

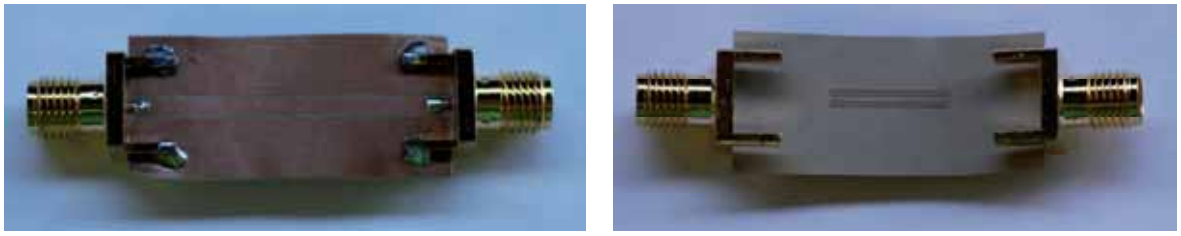

(**a**) (**b**)

Figure 8. (**a**) Insertion loss at first resonance and (**b**) sensitivity of the insertion loss magnitude for the prototype device shown in Figure 7, resulting by laterally displacing and by rotating the SRR. In (**c**) and (**d**), the results for the second resonance are depicted. The measured frequency responses, necessary to obtain the magnitude of the first and second notch, have been obtained by means of the Agilent E8364B vector network analyzer.

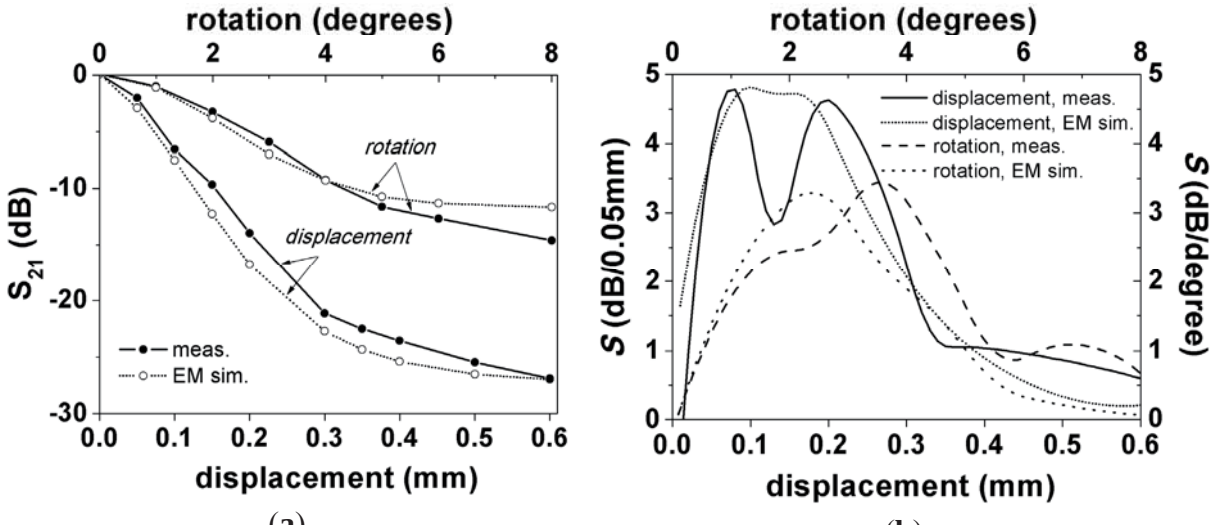

(**a**) (**b**)

Figure 8. *Cont.*

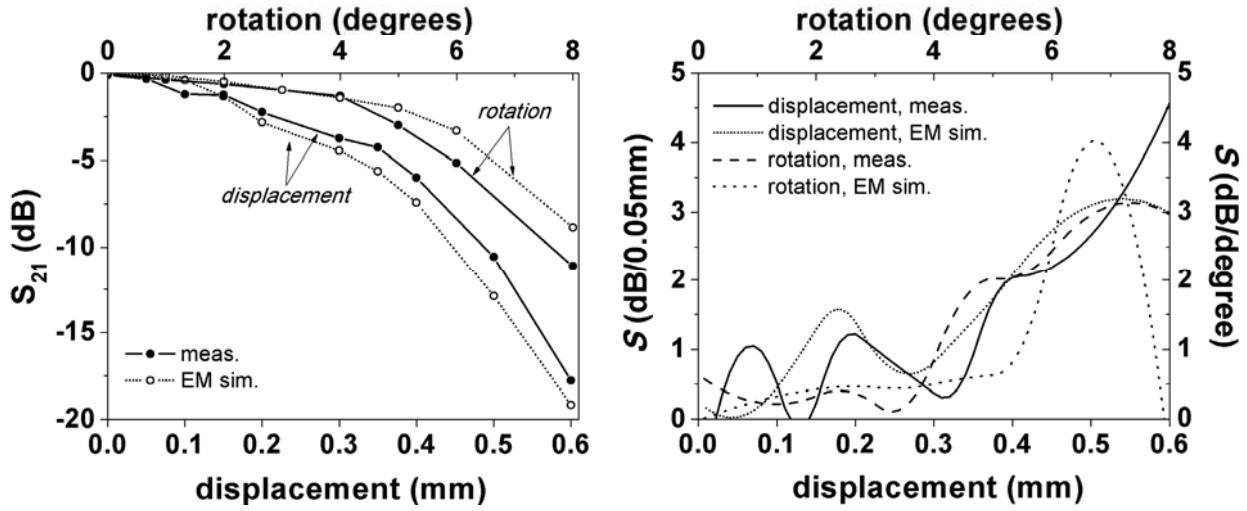

(**c**) (**d**)

Figure 9. Comparison between the notch depth given by electromagnetic simulation for the structure of Figure 7 and for the same structure with all dimensions scaled down.

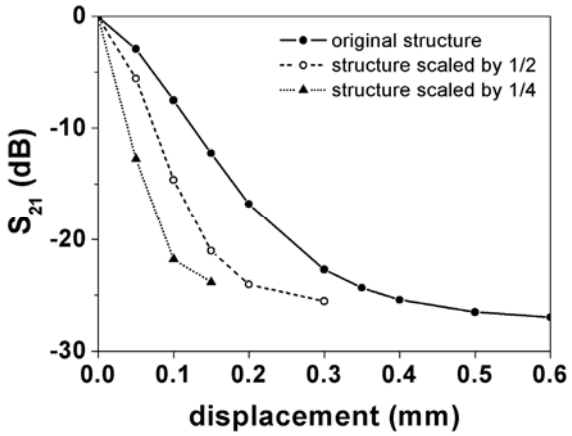

4. Conclusions

In conclusion, a new sensing principle for the detection of displacement and rotation, based on the loss of symmetry in SRR-loaded CPW structures, has been validated through theory and experiment. It has been shown that thin substrates and square/rectangular shaped SRR are necessary to enhance the sensitivity of the structures. A set of structures with different laterally shifted and rotated SRRs have been fabricated to validate the sensing principle. The resulting sensitivity of these structures exhibits a maximum measured value of roughly 95 dB/mm and 3.4 dB/degree for the displacement and angle sensor (first resonance), respectively.

Acknowledgements

This work has been supported by MICIIN-Spain (contract TEC2010-17512 METATRANSFER), Generalitat de Catalunya (project 2009SGR-421) and MICIIN-Spain (project CONSOLIDER EMET CSD2008-00066).

References

1. Pendry, J.B.; Holden, A.J.; Robbins, D.J.; Stewart, W.J. Magnetism from conductors and enhanced nonlinear phenomena. *IEEE Trans. Microwave Theory Tech.* **1999**, *47*, 2075-2084.
2. Smith, D.R.; Padilla, W.J.; Vier, D.C.; Nemat-Nasser, S.C.; Schultz, S. Composite medium with simultaneously negative permeability and permittivity. *Phys. Rev. Lett.* **2000**, *84*, 4184-4187.
3 Shelby, R.A.; Smith, D.R.; Schultz, S. Experimental verification of a negative index of refraction. *Science* **2001**, *292*, 77-79.
4. Martín, F.; Falcone, F.; Bonache, J.; Marqués, R.; Sorolla, M. A new split ring resonator based left handed coplanar waveguide. *Appl. Phys. Lett.* **2003**, *83*, 4652-4654.
5. Marqués, R.; Medina, F.; Rafii-El-Idrissi, R. Role of bianisotropy in negative permeability and left handed metamaterials. *Phys. Rev. B* **2002**, *65*, 1-6.
6. García-García, J.; Martín, F.; Baena, J.D.; Marques, R.; Jelinek, L. On the resonances and polarizabilities of split rings resonators. *J. Appl. Phys.* **2005**, *98*, 1-9.
7. He, X.-J.; Wang, Y.; Wang, J.-M.; Gui, T.-L. Thin film sensor based tip-shaped splits ring resonator metamaterial for microwave application. *Microsyst. Technol.* **2010**, *16*, 1735-1739.
8. Cubukcu, E.; Zhang, S.; Park, Y.-S.; Bartal, G.; Zhang, X. Split ring resonator sensors for infrared detection of single molecular monolayers. *Appl. Phys. Lett.* **2009**, *95*, 1-3.
9. Driscoll, T.; Andreev, G.O.; Basov, D.N.; Palit, S.; Cho, S.Y.; Jokerst, N.M.; Smith, D.R. Tuned permeability in terahertz split ring resonators for devices and sensors. *Appl. Phys. Lett.* **2007**, *91*, 1-3.
10. Melik, R.; Unal, E.; Perkgoz, N.K.; Puttlitz, C.; Demir, H.V. Metamaterial-based wireless strain sensors. *Appl. Phys. Lett.* **2009**, *95*, 1-3.
11. Yogi, R.A.; Parolia, R.S.; Karekar, R.N.; Aiyer, R.C. Microwave Microstrip ring resonator as a paper moisture sensor: Study with different grammage. *Meas. Sci. Technol.* **2002**, *13*, 1558-1562.
12. Pattnaik, P.K.; Vijayaaditja, B.; Srinivas, T.; Selvarajan, A. Optical MEMS Pressure Sensor Using Ring Resonator on a Circular Diaphragm. In *Proceedings of the 2005 International Conference on MEMS, NANO, and Smart Systems (ICMENS 2005)*, Banff, AB, Canada, 24–27 July 2005; pp. 277-280.
13. Liu, X.; Xue, C.Y.; Yan, S.B.; Xiong, J.J.; Zhang, W.D. Integrated High Sensitivity Displacement Sensor Based on Micro Ring Resonator. In *Proceedings of the 2009 4th IEEE International Conference on Nano/Micro Engineered and Molecular Systems*, Shenzhen, China, 5–8 January 2009; pp. 1000-1003.

Article S12

Alignment and Position Sensors Based on Split Ring Resonators

J. Naqui, M. Durán-Sindreu, and F. Martín

Sensors **2012**, *12*, 11790-11797; doi:10.3390/s120911790

OPEN ACCESS

sensors

ISSN 1424-8220

www.mdpi.com/journal/sensors

Article

Alignment and Position Sensors Based on Split Ring Resonators

Jordi Naqui *, Miguel Durán-Sindreu and Ferran Martín

CIMITEC, Departament d'Enginyeria Electrònica, Universitat Autònoma de Barcelona, 08193 Bellaterra (Barcelona), Spain; E-Mails: miguel.duransindreu@uab.cat (M.D.-S.); ferran.martin@uab.cat (F.M.)

* Author to whom correspondence should be addressed; E-Mail: Jordi.Naqui@uab.cat; Tel.: +34-93-581-3521; Fax: +34-93-581-2600.

Received: 10 July 2012; in revised form: 16 August 2012 / Accepted: 20 August 2012 / Published: 29 August 2012

Abstract: In this paper compact alignment and position sensors based on coplanar waveguide (CPW) transmission lines loaded with split ring resonators (SRRs) are proposed. The structure consists of a folded CPW loaded with two SRRs tuned at different frequencies to detect both the lack of alignment and the two-dimensional linear displacement magnitude. Two additional resonators (also tuned at different frequencies) are used to detect the displacement direction. The working principle for this type of sensor is explained in detail, and a prototype device to illustrate the potential of the approach has been designed and fabricated.

Keywords: split ring resonators; coplanar waveguide; alignment sensors; position sensors

1. Introduction

This paper is a continuation of a previous paper published by the authors [1], where, for the first time, the symmetry properties of split ring resonators (SRRs) were considered to detect displacement (many other works where SRRs are used for sensing purposes have been reported in the literature [2–8]). In [1], we reported a displacement sensor, able to detect angular or one-dimensional linear displacement. The structure, shown in Figure 1 for completeness, is a coplanar waveguide (CPW) loaded with a single SRR etched in the back side of the substrate. If the SRR is symmetrically etched as in Figure 1, the particle (SRR) cannot be excited and signal transmission between the input and the output port is allowed. However, if the symmetry is broken, for instance by either a rotation or a lateral linear

displacement (*i.e.*, along the *y*-axis), the SRR is excited, and a notch arises in the transmission coefficient at SRR resonance which depends on the displacement. The resulting sensitivity (45 dB/mm in average value for linear displacement) and its linearity are reasonable, relative to the considered CPW and SRR dimensions (in the millimeter-scale). The sensitivity was defined as the variation of the notch magnitude of the transmission coefficient with the variable to be sensed, that is, the displacement. However, the structure of Figure 1 is not able to detect a relative displacement between the SRR and the CPW in the axial direction of the CPW (*i.e.*, the *x*-axis). Moreover, it is not possible to distinguish between lateral displacements in the two possible directions (*i.e.*, ±*y*). In this paper, we provide a solution to these two issues. In Section 2, the proposed sensing device is presented, and the working principle is explained in detail. The design strategy, the fabricated prototype device, and the characterization of this prototype are reported in Section 3. Finally the main conclusions of the paper are highlighted in Section 4.

Figure 1. Typical topology of an angular or linear displacement sensor consisting of a CPW transmission line loaded with an SRR (in black) etched in the back side of the substrate. A rectangular shaped SRR is etched just below the central strip of the CPW to improve the sensitivity performance.

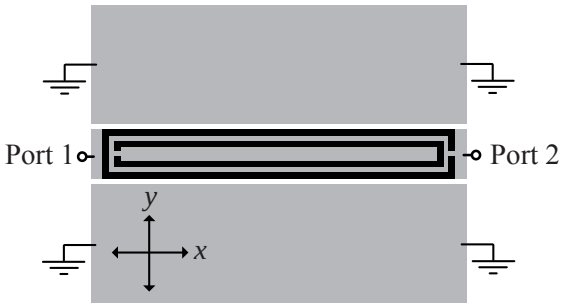

2. The Proposed Sensor and Principle of Operation

It is well known that an SRR can be excited by means of an axial time varying magnetic field [9]. Nevertheless, an SRR exhibits cross polarization, that is, it can also be driven by means of an electric field confined in or parallel to the plane of the particle and orthogonal to the plane containing the slits. In [10,11], it was demonstrated that by loading a CPW transmission line with pairs of SRRs, that is, with the centers of the SRRs aligned with the slots of the CPW structure, these particles are excited and a stop band in the transmission coefficient arises. The excitation of the resonators comes from the coupling of the rings with the magnetic and electric field generated by the currents flowing on the CPW. However, if single SRRs (rather than pairs) are symmetrically etched in the back side of the line (as Figure 1 illustrates), the magnetic and electric field components inside the SRR exactly cancel, and the particle is not driven at the fundamental resonance. This situation does not hold if the symmetry is broken, and therefore, a possible lack of alignment or relative lateral displacement between the line and the SRR can be detected and measured, respectively, as was shown in [1]. Provided the symmetry plane of the SRR does not extend beyond the CPW slots, the larger the lateral shift, the deeper the notch in the transmission coefficient. Therefore, the lateral displacement range will be limited to the distance between the two slots of the considered CPW.

In order to extend the sensing capability to two dimensions for alignment and linear displacement, one possible strategy is to introduce a right angle bend in the CPW transmission line, and to etch an SRR in each CPW section. Obviously, these SRRs must be tuned at different frequencies in order to discriminate between displacement in the *x*- or *y*-axis. However, by these means it is not possible to distinguish between up or down and right or left shift in the *y* and *x* orientation, respectively. Our proposal to detect the displacement direction consists of introducing two additional resonators, one in the *x*-oriented CPW section and the other one in the *y*-oriented section, both etched also in the back side of the substrate, but situated beneath one of the CPW ground planes, near a CPW slot. If the displacement direction drives such additional resonators towards the slot of the CPW, this will be detected by a notch at the resonance frequency of these resonators. Conversely, by shifting the SRRs in the opposite direction such notch will not appear. Since it is necessary that the four required SRRs are tuned at different frequencies, the resonators dimensions must be different. Notice that these two additional resonators are introduced to simply detect the displacement direction (they do not provide information on the displacement magnitude). Therefore, we can call these SRRs as direction sensing resonators, to differentiate them from the displacement sensing resonators, those which measure the linear displacement magnitude.

The layout of the designed sensor is depicted in Figure 2. The considered substrate is the *Rogers RO3010* with dielectric constant ε_r = 10.2, thickness h = 127 μm, and loss tangent tanδ = 0.0023. As discussed in [1], narrow substrates are necessary to boost the sensitivity. For these very narrow substrates, the coupling between the inner and the outer ring of the SRR (Figure 1) is negligible. In the present work single ring SRRs are considered, whose second resonance frequency is located beyond the one of SRRs with two rings [12], and this is important to avoid interference between the transmission notches of different resonators. The vias and backside strips are used to connect the ground plane regions and thus prevent the appearance of the CPW parasitic slot mode.

Figure 2. Layout of the proposed sensing device for the aligned position (*i.e.*, the CPW and the displacement sensing SRRs are aligned). The CPW strip and slot widths are W = 1.67 mm and G = 0.2 mm, respectively, the vias have a 0.2 mm radius, and the narrow strips between vias have a width of 0.2 mm. The dimensions of the SRRs are: l_1 (SRR$_{\Delta x}$) = 9.95 mm, l_1 (SRR$_{\pm x}$) = 7.05 mm, l_1 (SRR$_{\Delta y}$) = 13.4 mm, l_1 (SRR$_{\pm y}$) = 7.8 mm, l_2 = 1.67 mm, and c = 0.2 mm.

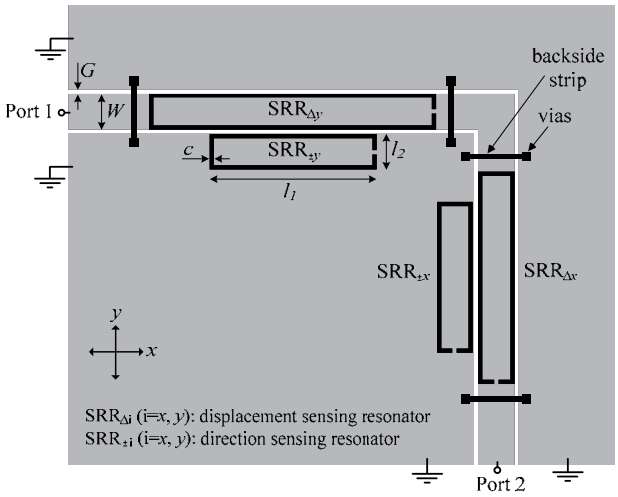

For a better comprehension of the principle of operation of the proposed sensor, let us consider the four different displacements indicated in Figure 3 from the aligned structure, that is, right, left, up, and down displacements. The resonance frequencies of the four SRRs are denoted as $f_{\Delta y}$, $f_{\Delta x}$, $f_{\pm y}$, and $f_{\pm x}$ (see Figure 2). It can be seen that displacements in the $\pm x$- and $\pm y$-direction can be detected (by means of the resonators $SRR_{\pm x}$ and $SRR_{\pm y}$) and measured (by the resonators $SRR_{\Delta x}$ and $SRR_{\Delta y}$). Any other linear displacement is a combination of the previous ones, and hence it can also be detected and measured. As an illustration, Figure 4 shows the obtained transmission coefficient for $\Delta x = 0.3$ mm and $\Delta y = 0.25$ mm.

Figure 3. Scheme indicating the primitive shifting operations and the resulting transmission coefficient S_{21}. A notch is indicative of an SRR excitation. A linear displacement in the x- and y-orientation is indicated as Δx and Δy, respectively, relative to the aligned position (*i.e.*, $\Delta x = \Delta y = 0$).

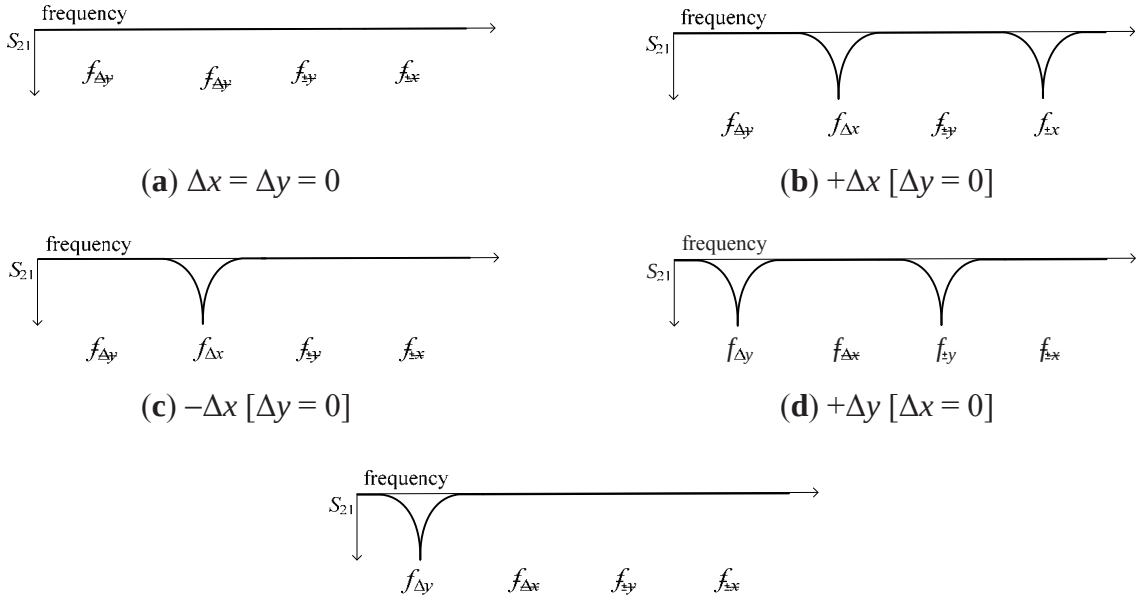

(**a**) $\Delta x = \Delta y = 0$

(**b**) $+\Delta x$ [$\Delta y = 0$]

(**c**) $-\Delta x$ [$\Delta y = 0$]

(**d**) $+\Delta y$ [$\Delta x = 0$]

(**e**) $-\Delta y$ [$\Delta x = 0$]

Figure 4. Transmission coefficient S_{21} of the sensor for $\Delta x = 0.3$ mm and $\Delta y = 0.25$ mm.

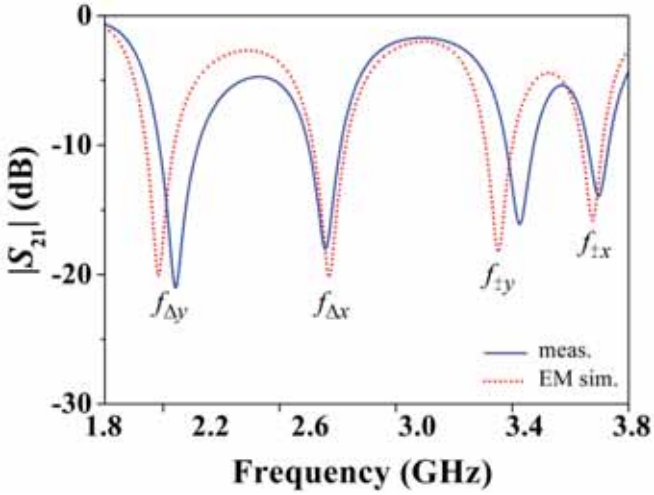

3. Results

The proposed sensing structure is validated by considering several proof-of-concept prototypes with different displacements, by measuring the frequency responses and by representing the notch magnitude of the different involved resonance frequencies (Figure 5 shows a photograph of the device for the case $\Delta x = \Delta y = 0$). Obviously, in a real sensor, the SRRs must be etched on a different substrate in order to achieve relative motion between the sensing SRRs and the bended CPW transmission line, but this complicates the measurement (from the mechanical viewpoint) and, for this reason, by the moment, we have proceeded in this way. In order to validate the proposed approach, we have considered positive and negative displacement in the *x*-direction (horizontal shift), as well as in the $x = y$-direction (diagonal shift). This is representative of the potentiality and validity of the proposal.

Figure 5. Photograph of the proposed device for the aligned position; (**a**) top and (**b**) bottom face.

(**a**) (**b**)

Figure 6 depicts the dependence of the notch magnitude (simulated and measured) with displacement in the $\pm x$-direction. The measurements have been inferred by means of the *Agilent* E8364B vector network analyzer, whereas the simulations have been carried out by means of the *Agilent Momentum* commercial software. As expected, for positive displacements, the $SRR_{\pm x}$ is activated as is manifested by a clear increase in the notch at $f_{\pm x}$, whereas the specified −3 dB threshold level is not exceeded for negative displacements (indicating that the shift is in the negative direction). The dependence of the notch magnitude for $f_{\Delta x}$ is similar and roughly linear in both directions, with a measured value of approximately −20 dB for $\Delta x = \pm 0.3$ mm, which is indicative of a significant sensitivity of roughly 65 dB/mm (average value). On the other hand, the notch corresponding to $f_{\Delta y}$ is approximately 0 dB, which indicates that the structure is aligned with the *y*-axis (for $\Delta x = 0.3$ mm the notch is slightly above −3 dB because for this sample the *y*-axis position sensing resonators are somewhat misaligned due to fabrication tolerances and under-etching).

Figure 6. Notch magnitude of the transmission coefficient S_{21} at the indicated frequencies for *x*-oriented displacement; results for (**a**) *x*- and (**b**) *y*-axis position sensing.

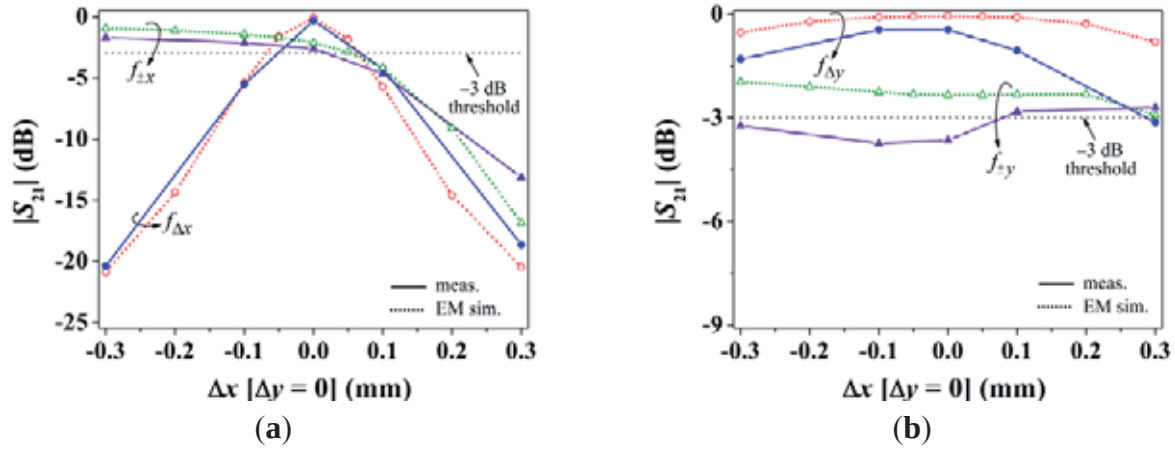

(**a**) (**b**)

The results of the relative displacement in the diagonal orientation ($\Delta x = \Delta y$) are depicted in Figure 7. Similar conclusions to those pointed out for *x*-motion can be inferred to the light of this figure. Nevertheless, it is worth mentioning that the notch magnitude associated to a displacement sensing resonator depends not only on the displacement, but also on inter-notch interference and resonator dimensions. This causes that, for the same displacement, the notch magnitude of the *y*-axis displacement sensing resonator produces a deeper notch than that of the *x*-axis. With these results, the proposed alignment and two-dimensional linear displacement sensing structure is validated.

Figure 7. Notch magnitude of the transmission coefficient S_{21} at the indicated frequencies for $x = y$-oriented displacement; results for (**a**) *x*- and (**b**) *y*-axis position sensing.

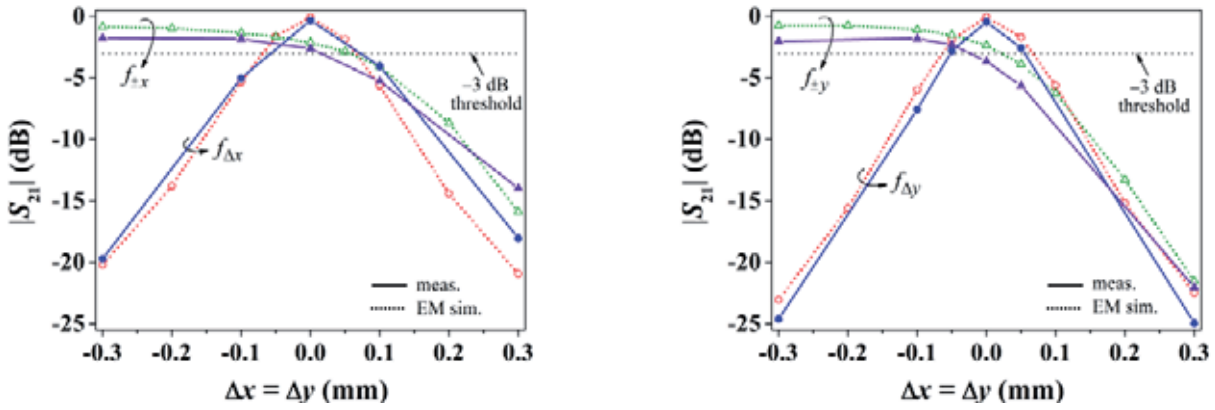

(**a**) (**b**)

Another two-dimensional displacement sensor based on split ring-loaded lines was reported in [13]. The operation principle of that approach is founded on the shift of the resonance frequency by using triangular complementary split rings in Microstrip technology. Since external (ambient) conditions may affect the resonator resonance frequency but not the transparency of the lines with perfectly aligned resonators, the proposed sensor of this work is more robust and specially suited for alignment purposes.

4. Conclusions

In conclusion, an alignment and a two-dimensional linear displacement sensor device based on the symmetry properties of SRRs has been proposed and validated. The sensing mechanism is based on the electromagnetic coupling between a CPW transmission line and an array of SRRs. The device is able to detect the lack of alignment and the relative linear displacement between two surfaces, one containing the SRRs tuned at different frequencies, the other one including the CPW used to identify the displacement magnitude and direction (by measuring the transmission coefficient). The position sensor characterization has revealed that two-dimensional linear displacement with reasonable sensitivity and linearity can be measured. This represents a significant progress as compared to the former approach reported in [1].

Acknowledgments

This work has been supported by MICIIN-Spain (projects TEC2010-17512 METATRANSFER, CONSOLIDER EMET CSD2008-00066, and EXPLORA TEC2011-13615-E), and by Generalitat de Catalunya (project 2009SGR-421).

References

1. Naqui, J.; Durán-Sindreu, M.; Martín, F. Novel sensors based on the symmetry properties of Split Ring Resonators (SRRs). *Sensors* **2011**, *11*, 7545–7553.
2. He, X.-J.; Wang, Y.; Wang, J.-M.; Gui, T.-L. Thin film sensor based tip-shaped splits ring resonator metamaterial for microwave application. *Microsyst. Technol.* **2010**, *16*, 1735–1739.
3. Cubukcu, E.; Zhang, S.; Park, Y.-S.; Bartal, G.; Zhang, X. Split ring resonator sensors for infrared detection of single molecular monolayers. *Appl. Phys. Lett.* **2009**, *95*, 043113:1–043113:3.
4. Driscoll, T.; Andreev, G.O.; Basov, D.N.; Palit, S.; Cho, S.Y.; Jokerst, N.M.; Smith, D.R. Tuned permeability in terahertz split ring resonators for devices and sensors. *Appl. Phys. Lett.* **2007**, *91*, 062511:1–062511:3.
5. Melik, R.; Unal, E.; Perkgoz, N.K.; Puttlitz, C.; Demir, H.V. Metamaterial-based wireless strain sensors. *Appl. Phys. Lett.* **2009**, *95*, 011106:1–011106:3.
6. Yogi, R.A.; Parolia, R.S.; Karekar, R.N.; Aiyer, R.C. Microwave Microstrip ring resonator as a paper moisture sensor: Study with different grammage. *Meas. Sci. Technol.* **2002**, *13*, 1558–1562.
7. Pattnaik, P.K.; Vijayaaditja, B.; Srinivas, T.; Selvarajan, A. Optical MEMS Pressure Sensor Using Ring Resonator on a Circular Diaphragm. In *Proceedings of the 2005 International Conference on MEMS, NANO and Smart Systems (ICMENS'05)*, Banff, AB, Canada, 24–27 July 2005; pp. 277–280.
8. Liu, X.; Xue, C.; Yan, S.; Xiong, J.; Zhang, W. Integrated High Sensitivity Displacement Sensor Based on Micro Ring Resonator. In *Proceedings of the 2009 4th IEEE International Conference Nano/Micro Engineered and Molecular Systems*, Shenzhen, China, 5–8 January 2009; pp. 1000–1003.
9. Pendry, J.B.; Holden, A.J.; Robbins, D.J.; Stewart, W.J. Magnetism from conductors and enhanced nonlinear phenomena. *IEEE Trans. Microw. Theory Tech.* **1999**, *47*, 2075–2084.

10. Martín, F.; Falcone, F.; Bonache, J.; Marqués, R.; Sorolla, M. A new split ring resonator based left handed coplanar waveguide. *Appl. Phys. Lett.* **2003**, *83*, 4652–4654.
11. Falcone, F.; Martin, F.; Bonache, J.; Marqués, R.; Sorolla, M. Coplanar waveguide structures loaded with split ring resonators. *Microw. Opt. Technol. Lett.* **2004**, *40*, 3–6.
12. García-García, J.; Martín, F.; Baena, J.D.; Marques, R.; Jelinek, L. On the resonances and polarizabilities of split rings resonators. *J. Appl. Phys.* **2005**, *98*, 033103:1–033103:9.
13. Mandel, C.; Kubina, B.; Schüßler, M.; Jakoby, R. Passive Chipless Wireless Sensor for Two-Dimensional Displacement Measurement. In *Proceedings of the 41st European Microwave Conference*, Manchester, UK, 10–13 October 2011; pp. 79–82.

Conference article IMS12*

On the Symmetry Properties of Coplanar Waveguides Loaded with Symmetric Resonators: Analysis and Potential Applications

J. Naqui, M. Durán-Sindreu, and F. Martín

*Conference article included in this thesis for completeness but that cannot be oficially part of the compendium of articles of the Ph.D thesis.

On the Symmetry Properties of Coplanar Waveguides Loaded with Symmetric Resonators: Analysis and Potential Applications

Jordi Naqui, Miguel Durán-Sindreu, and Ferran Martín

GEMMA/CIMITEC, Departament d'Enginyeria Electrònica. Universitat Autònoma de Barcelona. 08193 BELLATERRA (Barcelona), Spain. E-mail: Ferran.Martin@uab.es

***Abstract* — This paper is focused on the analysis of coplanar waveguides (CPW) loaded with symmetric resonators (such as split ring resonators and stepped impedance resonators) whose symmetry plane behaves as an electric wall at the fundamental resonance frequency. If these resonators are symmetrically etched in the back substrate side of the CPW, the resonators are not excited, and signal propagation along the CPW is allowed. Conversely, if the symmetry is truncated, the magnetic wall of the CPW (fundamental mode) is not aligned with the electric wall of the resonator, and signal propagation is inhibited in the vicinity of the first resonance frequency. These structures can be of interest for the design of novel sensors or radiofrequency (RF) bar codes, based on the deviation from symmetry. The principle of operation of such structures is illustrated and experimentally validated by proof-of-concept devices.**

***Index Terms* — Coplanar waveguide (CPW), split ring resonator (SRR), stepped impedance resonator (SIR), microwave sensors, radiofrequency bar codes.**

I. Introduction

Coplanar waveguides (CPW) periodic-loaded with pairs of split ring resonators (SRRs) were reported in 2003 as one-dimensional (1D) effective media exhibiting negative effective permeability in the vicinity of SRR resonance [1]. These structures are transparent to signal propagation except in a narrow region where the effective permeability is either negative (above SRR first resonance) or highly positive (just below SRR resonance). Alternatively, the stop band behavior of SRR-loaded CPWs can be simply interpreted as a result of magnetic coupling between the line and the pairs of SRRs. In the vicinity of resonance, the SRRs are excited through the axial magnetic field generated by the line, and the injected power is reflected back to the source.

In the present paper, novel applications of CPWs loaded with symmetric resonators, such as the SRR or the folded stepped impedance resonator (SIR), are investigated. The symmetry of the structure is the key aspect to explain the principle of operation. By symmetrically etching the resonators in the line (back substrate side), the line is transparent. However, if the symmetry is broken, the resonators are excited, and this can be detected through a notch in the transmission coefficient. Therefore, CPWs loaded with such kind of symmetric resonators can be useful for the design of novel devices based on the truncation of symmetry. This includes sensors and detectors (such as alignment, position, or angle sensors), or radiofrequency (RF) bar codes.

II. CPWs loaded with symmetric resonators: SRRs and folded SIRs

Figure 1 shows the typical topologies of an SRR [2] and a folded SIR [3], including the distribution of charges at their first resonance. Many other electrically small planar resonators have been reported in the literature (spiral resonators [4], non-bianisotropic SRRs [5], etc.), but such resonators are discarded since they do not exhibit an electric wall at their first resonance, as is required for the purpose of the present work. By loading a CPW transmission line with SRRs or folded SIRs symmetrically etched in the back substrate side (Fig. 2), these particles cannot be excited at their first resonance given that the magnetic wall of the CPW structure (fundamental mode) is aligned with the symmetry

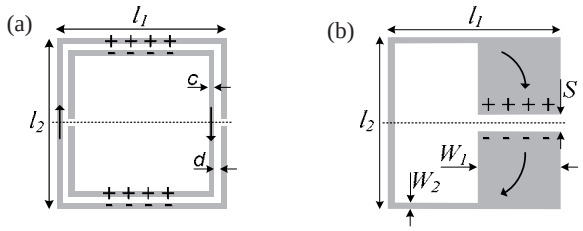

Fig. 1. Typical topologies of a square shaped SRR (a) and folded SIR (b), including the distribution of charges at the first resonance (the symmetry plane, indicated in dotted line, is an electric wall).

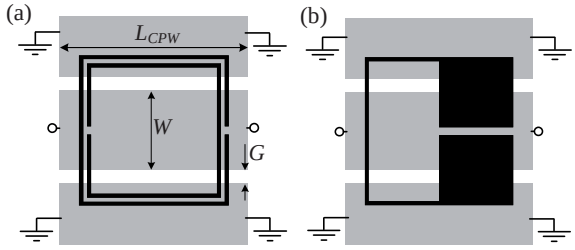

Fig. 2. CPW loaded with a symmetrically etched SRR (a) and folded SIR (b). The substrate is the *Rogers RO3010* with dielectric constant ε_r=10.2, thickness h=0.635 mm, and tanδ=0.0023. CPW dimensions are: L_{CPW}=9.6 mm, W=4 mm, and G=0.7 mm; SRR dimensions are: l_1=l_2=7.6 mm and c=d=0.2 mm; SIR dimensions are: l_1=l_2=7.6 mm, W_1=3.8 mm, W_2=0.2 mm, and S=0.4 mm. The metallization in the back substrate side is indicated in black.

978-1-4673-1088-8/12/$31.00 ©2012 IEEE

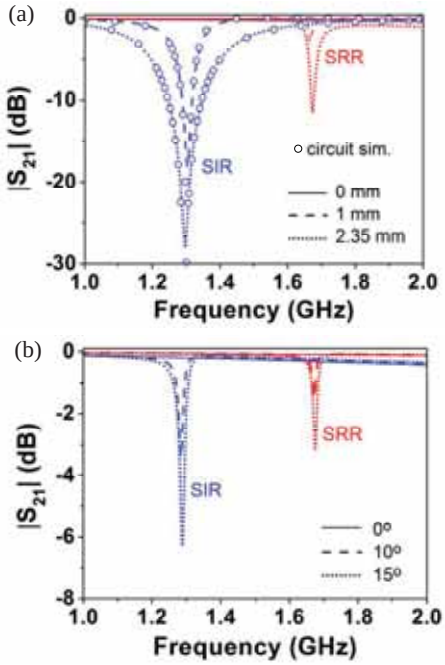

Fig. 3. Simulated transmission coefficients of the structures shown in Fig. 2 and those corresponding to the same structures with the resonators laterally displaced (a) or rotated (b). Circuit parameters are: L=2.4 nH, C=0.97 pF, L_s=13.8 nH, C_s=0 pF; for 1 mm, C_{sc1}=0.57 pF, C_{sc2}=1.8 pF, C_{sg1}=1.6 pF, and C_{sg2}=0.4 pF; for 2.35 mm, C_{sc1}=0 pF, C_{sc2}=2.2 pF, C_{sg1}=2.2 pF, and C_{sg2}=0 pF.

plane of the particles. However, if the symmetry is truncated, for instance by rotating or laterally displacing the resonator, a notch in the transmission coefficient is expected. This effect is illustrated in Fig. 3, where the simulated transmission coefficient of the structures depicted in Fig. 2, and those resulting after different displacements and rotations are represented (the simulations have been obtained by means of the *Agilent Momentum* commercial software). The results show that by using a folded SIR deeper notches are obtained. Moreover, the folded SIR is electrically smaller, as compared to the SRR. Therefore, the focus will be on the folded SIR, rather than on the SRR.

The equivalent circuit model of the structure of Fig. 2(b) is depicted in Fig. 4. The CPW and the SIR are coupled mainly electrically, being such coupling represented by the capacitances C_{sci} and C_{sgi} (i=1, 2). Such capacitances depend on the relative position between the SIR and the CPW. Thus, any symmetry truncation can be modeled by adjusting these capacitances. If the structure is symmetric (i.e., $C_{sc1} = C_{sc2}$ and $C_{sg1} = C_{sg2}$), the resonator L_s-C_s is opened because of the magnetic wall at the symmetry plane, and the resulting model is that of a conventional transmission line. By contrast, if the symmetry is broken, the capacitances are unbalanced and a transmission zero appears. In the simplest case in which C_{sc1}=C_{sg2}=0 (or C_{sc2}=C_{sg1}=0), the model is equivalent to that of a transmission line loaded with a grounded series resonator (the capacitance C_s can be neglected). We have extracted the model parameters for the two cases indicated in Fig. 3(a). In both cases, the circuit simulations are in good agreement with the electromagnetic simulations.

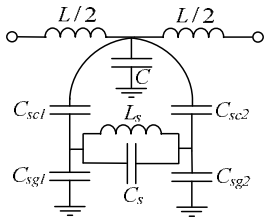

Fig. 4. Equivalent circuit model of the CPW loaded with a folded SIR. L is the line section inductance, C is the line section capacitance, the resonant tank L_s-C_s models the SIR inductance-capacitance, C_{sci} is the capacitance between the central strip and the upper or lower half (i indicating the half) of the SIR patch below it, and C_{sgi} are the capacitances between the SIR halves and ground.

III. Application to Sensors and RF Bar Codes

CPWs loaded with movable resonators can be used as displacement or angle sensors. In order to achieve a high sensitivity of the notch magnitude with lateral displacement or rotation, it is necessary to use very narrow substrates and resonators whose transverse dimension (l_2) does not excessively extend beyond the slot regions of the CPW structure. For narrow-substrate CPWs loaded with SRRs, the metal region of the CPW limits the coupling between the two split rings forming the SRR, and the first resonance frequency is identical to the one obtained with the larger isolated split ring. Hence, for narrow substrates, the SIR provides a fundamental resonance frequency far below the one achievable with SRRs (SIR-loaded CPWs are thus electrically smaller). As a proof-of-concept demonstrator, we have designed a symmetric base structure (Fig. 5) and additional structures with the SIR laterally displaced by steps of 0.1 mm and rotated by steps of 1°. The simulated and measured (by means of the *Agilent E8364B* vector network analyzer) notch magnitudes are depicted in Fig. 6, where it is clear that the sensing principle is validated. As compared to other displacement or alignment sensors based on split ring loaded lines [6] (where the operation principle is based on the shift of the resonance frequency), **the proposed sensors are more robust and specially suited for alignment purposes**. The reason is that **external (ambient) conditions may affect the resonator frequency, but not the transparency of the lines with perfectly aligned resonators**.

The second potential application is in the field of RF bar codes [7]. These devices can be implemented by creating defects in slow wave structures and by obtaining the reflected response to feeding pulses. Alternatively to this time domain approach, it is possible to implement RF finger prints by means of resonators with different resonance frequencies. By this means, we can set a binary code, where each bit value (logic '1' or '0') is controlled by the presence or absence of

978-1-4673-1088-8/12/$31.00 ©2012 IEEE

the resonator corresponding to that bit [7]. However, by using symmetric resonators, it is not necessary to remove the resonator to set any bit value to '0'; it suffices to align it with the CPW. **The main advantage of the proposed approach** is that **the binary values can be simply modified by displacing or rotating the resonators, or by any other means of truncating the symmetry of the bit cells**. Therefore, this strategy opens the possibility to implement **reconfigurable RF bar codes** in a simple fashion. We have designed a 3-bit RF bar code consisting of a CPW loaded with 3 different folded SIRs to demonstrate the proof-of-concept. Fig. 7 shows a photograph of the structure with the code '111'. In order to prevent the presence of the slot mode, the ground planes are connected through backside strips and vias. In view of the transmission coefficients of this structure and those corresponding to other bit configurations (Fig. 8), the principle is validated. Although somehow degraded, the bar code functionality (not shown) is still preserved if the backside strip and vias are removed. Nevertheless, since the parasitic slot mode is intimately related to asymmetry in CPWs, work is in progress towards the design of via-less RF bar codes in microstrip technology based on same principle.

Fig. 5. Fabricated symmetric base CPW loaded with a folded SIR to validate the sensing principle. The substrate is the *Rogers RO3010* with ε_r=10.2, h=0.127 mm, and tanδ=0.0023. CPW dimensions are: L_{CPW}=20 mm, W=1.66 mm, and G=0.2 mm; SIR dimensions are: W_1=9 mm, W_2=0.2 mm, S=0.2 mm, l_1=12 mm, and l_2=2 mm.

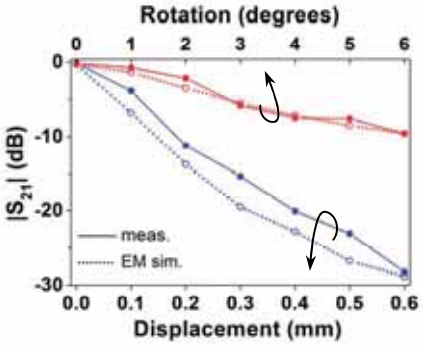

Fig. 6. Simulated and measured notch magnitude for the structure of Fig. 5 with the SIR laterally displaced and rotated from its centre.

V. Conclusion

In summary, it has been shown that CPW transmission lines loaded with symmetrically etched resonators (such as SRRs or folded SIRs) do not inhibit signal propagation as a result of the perfect alignment between the magnetic wall of the CPW fundamental mode and the electric wall that the resonators exhibit at resonance. However, by properly setting the resonator geometry and substrate, it is possible to detect the lack of symmetry with significant sensitivity by simply measuring the transmission coefficient. This principle can be applied to the implementation of displacement or angle sensors, or to the design of reconfigurable RF bar codes.

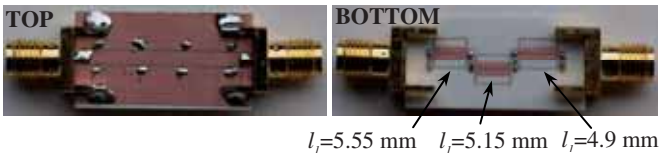

Fig. 7. Fabricated CPW with 3 folded SIRs corresponding to the binary code '111' of the designed 3-bit RF bar code. The substrate is the *Rogers RO4003C* with ε_r=3.55, h=0.8128 mm, and tanδ=0.0021. CPW dimensions are: L_{CPW}=23.9 mm, W=2.16 mm, and G=0.15 mm; SIR dimensions are: W_1=0.825 mm, W_2=0.15 mm, S=0.15 mm, l_2=4.47 mm, and l_1 is shown in the photograph.

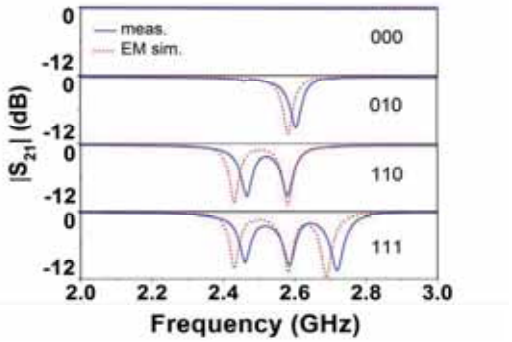

Fig. 8. Simulated and measured transmission coefficient of the structure of Fig. 7 and those corresponding to the indicated codes.

Acknowledgement

To Spain MICIIN (TEC2011-13615-E and CSD2008-00066).

References

[1] F. Martín, F. Falcone, J. Bonache, R. Marqués and M. Sorolla, "Split ring resonator based left handed coplanar waveguide", *Appl. Phys. Lett.*, vol. 83, pp. 4652-4654, December 2003.

[2] J.B. Pendry, A.J. Holden, D.J. Robbins and W.J. Stewart, "Magnetism from conductors and enhanced nonlinear phenomena", *IEEE Trans. Microw. Theory Tech.*, vol. 47, pp. 2075-2084, Nov. 1999.

[3] D. Packiaraj, M. Ramesh, and A. T. Kalghatgi, "Design of a tri-section folded SIR filter", *IEEE Microw. Wireless Comp. Lett.*, vol. 16, pp. 317-319, May 2006.

[4] F. Bilotti, A. Toscano, and L. Vegni, "Design of Spiral and Multiple Split-Ring Resonators for the Realization of Miniaturized Metamaterial Samples," *IEEE Trans. Ant. Prop.*, vol. 55, pp. 2258-2267, Aug. 2007.

[5] R. Marqués, F. Medina and R. Rafii-El-Idrissi, "Role of bianisotropy in negative permeability and left handed metamaterials", *Phys. Rev. B*, vol. 65, pp. 144441 (1-6) (2002).

[6] C. Mandel, B. Kubina, M. Schüßler, and R. Jakoby "Passive chipless wireless sensor for two-dimensional displacement measurement", *41st Europ. Microw. Conf.*, pp. 79-82, Oct. 2011.

[7] S. Preradovic and N. Chandra-Karmakar, "Chipless RFID: bar code of the future", *IEEE Microw. Mag.*, vol. 11, pp. 87-98, Dec. 2010.

Conference article IMS13*

Transmission Lines Loaded with Bisymmetric Resonators and Applications

J. Naqui, M. Durán-Sindreu, F. Martín

*Conference article included in this thesis for completeness but that cannot be oficially part of the compendium of articles of the Ph.D thesis.

Transmission Lines Loaded with Bisymmetric Resonators and Applications

Jordi Naqui, Miguel Durán-Sindreu, and Ferran Martín

GEMMA/CIMITEC, Departament d'Enginyeria Electrònica. Universitat Autònoma de Barcelona. 08193 BELLATERRA (Barcelona), Spain. E-mail: Ferran.Martin@uab.es

Abstract — This paper studies the symmetry properties of transmission lines loaded with electrically small bisymmetric resonators, that is, resonators that exhibit two orthogonal symmetry planes. The considered resonators are the so-called electric-LC (ELC) resonator, and its complementary counterpart, the magnetic-LC resonator (MLC). Both resonators exhibit orthogonal electric and magnetic walls at the fundamental resonance. Hence, the orientation of the symmetry planes relative to the line axis determines the transmission/reflection characteristics of the loaded-lines. It is demonstrated that through a proper design, the considered ELC-loaded lines can be useful as rotation or angular velocity sensors.

Index Terms — Coplanar waveguide, microstrip, electric-LC (ELC) resonator, complementary structures.

I. Introduction

Transmission lines loaded with electrically small resonators have been used for the design of planar filters, antennas, and many other microwave devices based on the metamaterial transmission line concept [1-3]. There is a wide variety of electrically small planar resonators. Their classification can be done according to various criteria, but we will consider some planar loop- or ring-based resonators classified according to the nature of coupling (electric, magnetic or mixed) with an external uniform field at their fundamental resonance.

Capacitively-loaded loops, split ring resonators (SRRs) [4], and folded stepped impedance resonators (SIRs) [5] (Fig. 1), among others, can be driven by means of an axial time-varying magnetic field, or by a time-varying electric field applied in the direction orthogonal to the symmetry plane (electric wall). There are several strategies to prevent particle excitation through a uniform electric field. Specifically, through the topologies shown in Fig. 2, the *y*-oriented electric dipole moment (present in the resonators of Fig. 1) disappears. Hence the non-bianisotropic SRR (NB-SRR) [6] and the broadside-coupled SRR (BC-SRR) [7] are magnetically driven resonators. Conversely, to implement an electrically coupled resonator, a possible strategy is to combine (merge) two capacitively-loaded loops (or folded SIRs), as depicted in Fig. 3. At the fundamental resonance, a magnetic wall appears in the new symmetry plane orthogonal to the electric wall, and the particle can no longer be excited by means of a uniform axial magnetic field. Following [8], the resonators depicted in Fig. 3 are called electric-LC (ELC) resonators in this paper, thus emphasizing that the fundamental mode couples strongly to a uniform electric field, whereas it cannot be excited by a uniform magnetic field.

By applying the Babinet principle to these particles, the role of the electric and magnetic fields (and hence the electric and magnetic walls) are interchanged, although the fundamental resonance frequency is roughly the same [9,10]. Fig. 4 depicts the complementary counterparts of the ELC resonators shown in Fig. 3. Since the fundamental resonance of these particles is excited by a uniform magnetic field, the term given to them is magnetic-LC (MLC) resonators.

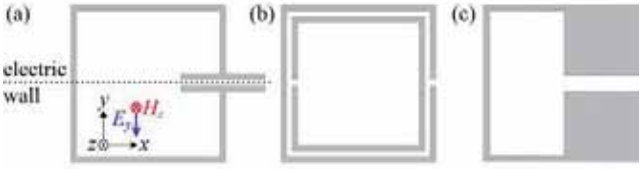

Fig. 1. Electric and magnetic resonators. (a) Capacitively-loaded loop, (b) SRR, and (c) folded SIR.

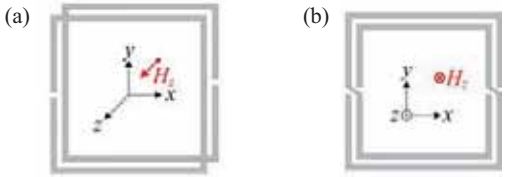

Fig. 2. Magnetic resonators. (a) BC-SRR and (b) NB-SRR.

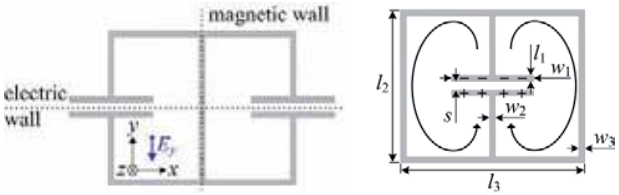

Fig. 3. Electric-LC (ELC) resonators based on paired capacitively-loaded loops.

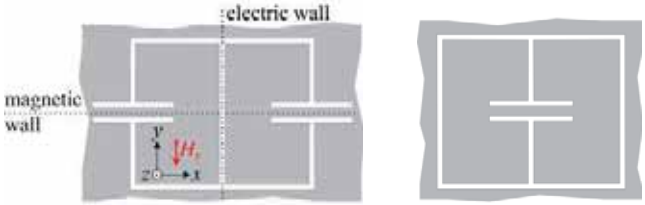

Fig. 4. Complementary counterparts of the resonators depicted in Fig. 3 (i.e., magnetic-LC –MLC– resonators).

978-1-4673-2141-9/13/$31.00 ©2013 IEEE

II. Transmission lines loaded with ELCs and MLCs

The symmetry planes, electric and magnetic walls, and the charge and current distributions for the ELC resonators at the fundamental resonance frequency are sketched in Fig. 3. As mentioned before, ELCs cannot be excited by means of a uniform axial magnetic field. However, the fields generated by a transmission line are not uniform. Therefore, the analysis of an ELC-loaded line must be done according to the alignment between the symmetry plane of the line and the symmetry planes of the particle [11].

Specifically, for an ELC-loaded coplanar waveguide (CPW) transmission line as the one depicted in Fig. 5(a), given that the electric wall of the particle is perfectly aligned with the symmetry plane of the line (magnetic wall), we do expect signal transmission in the vicinity of the fundamental resonance. Conversely, if both magnetic walls are aligned [as in Fig. 5(b)], a notch in the transmission coefficient at the first ELC resonance is expected due to particle excitation. Notice that, since the magnetic field lines generated by the line at both sides are contra-directional, aligning the magnetic walls is a sufficient condition to magnetically drive the ELC resonator. Figure 6 shows the frequency responses (lossless electromagnetic simulations) of the considered ELC-loaded CPW for different resonator orientations. The results confirm the above predictions and points out that the notch in the transmission coefficient is maximum for perfectly aligned magnetic walls (i.e. $\phi = 90°$).

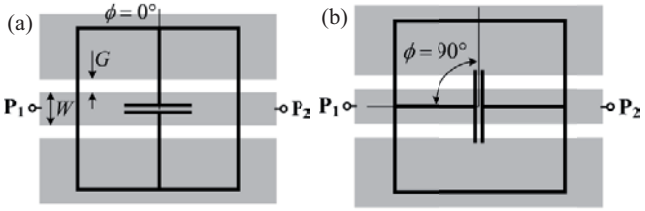

Fig. 5. CPW loaded with an ELC resonator etched in the back substrate side; (a) electric wall and (b) magnetic wall of the ELC aligned with the line axis. The alignment between the CPW and the resonator is defined by the rotation angle $0° \le \phi \le 90°$. CPW dimensions are: $W = 0.78$ mm and $G = 2$ mm, corresponding to a 50 Ω line. ELC dimensions are: $w_1 = 4$ mm, $w_2 = w_3 = l_1 = s = 0.2$ mm, and $l_2 = l_3 = 10$ mm. The substrate is the *Rogers RO3010* with thickness $h = 1.27$ mm and dielectric constant $\varepsilon_r = 11.2$.

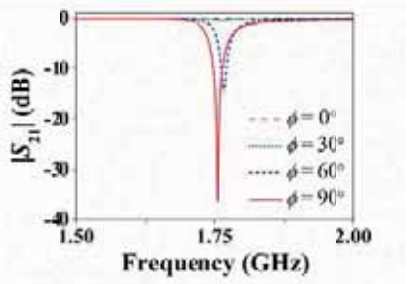

Fig. 6. Transmission coefficient S_{21} of the structure of Fig. 5 with different resonator rotation angles. The angles 0° and 90° correspond to the extreme cases of orthogonally oriented magnetic walls and perfectly aligned magnetic walls, respectively.

Similar results (not shown) are obtained by considering a microstrip line loaded with a MLC resonator etched in the ground plane. However, the maximum notch at the fundamental resonance, that appears when both magnetic walls are aligned, corresponds to the MLC particle rotated 90° with regard to the ELC loading a CPW (i.e., $\phi = 0°$).

III. Application to rotation and angular velocity sensors using ELC-loaded CPWs

We have optimized the topology of a CPW loaded with an ELC in order to obtain a linear dependence of the logarithmic notch magnitude with the rotation angle, and we have concluded that a circular ELC loading a non-uniform CPW (also circularly shaped) is the optimum solution. The photograph of the fabricated structure (for a rotation angle of 30°) is shown in Fig. 7. The dependence of the notch magnitude with the rotation angle is depicted in Fig. 9. Good linearity is obtained, with an average measured sensitivity of roughly −0.18 dB/°, and the agreement between measurement and electromagnetic simulation is good. Notice that in this first proof-of-concept, we have fabricated various structures with different ELC orientations.

In a practical rotation sensor, the resonator must be etched on a different (movable) substrate, but similar results are expected. This has been corroborated through electromagnetic simulation and measurement, by considering an additional suspended dielectric slab on top of the CPW, with the resonator etched in its back substrate side (Fig. 8), and similar results (also shown in Fig. 9) are obtained (although the resonance frequency of the ELC and the magnitude of the notch have experienced an increase).

The implementation of an angular velocity sensor can be done in time domain by cascading a circulator at the output port of the line (to avoid unwanted reflections) followed by an envelope detector. By feeding the line with a harmonic signal tuned at the fundamental resonator frequency, the time distance between consecutive transmission peaks at the detector output corresponds to half a period; hence, the

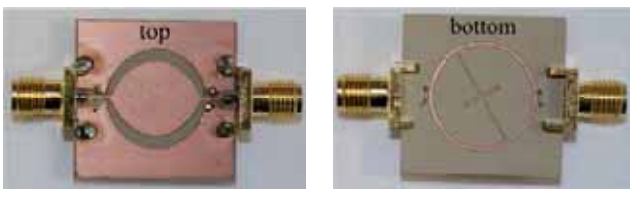

Fig. 7. Photograph of the fabricated ELC-loaded CPW (for a specific rotation angle of 30°). The considered substrate is the *Rogers RO3010* with thickness $h = 1.27$ mm, dielectric constant $\varepsilon_r = 11.2$, and loss tangent $\tan\delta = 0.0023$. Dimensions are: for the CPW, W and G are tapered such that the characteristic impedance is 50 Ω; for the ELC resonator: diameter = 16.6 mm, $w_1 = 6$ mm, $w_2 = l_1 = s = 0.2$ mm, and $w_3 = 0.5$ mm. Vias and backside strips are used to eliminate the slot mode. The notch frequency is $f_0 \approx 1.21$ GHz.

978-1-4673-2141-9/13/$31.00 ©2013 IEEE

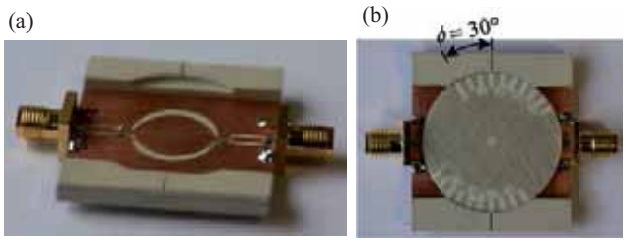

Fig. 8. Rotation sensor with the resonator etched on a suspended movable substrate, separated 1.27 mm from the CPW metal layer. (a) CPW structure; (b) whole sensor with the suspended movable substrate with a graded angular grid for angle identification (in the photograph, $\phi = 30°$). The movable substrate is *Rogers RO4003C* with h = 0.8128 mm, $\varepsilon_r = 3.55$ and $\tan\delta = 0.0021$. Dimensions are identical to those of Fig. 7. The notch frequency is $f_0 \approx 2.29$ GHz.

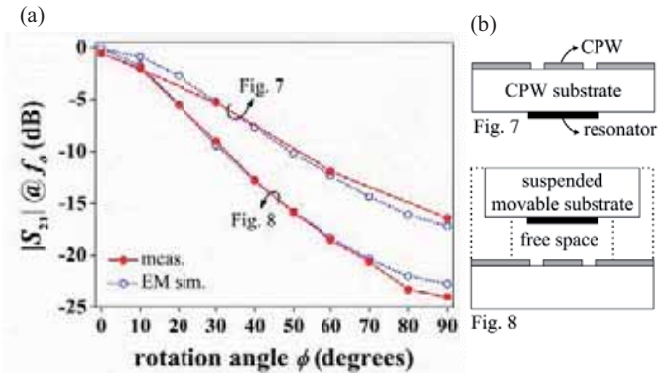

Fig. 9. Dependence of the notch magnitude with the rotation angle (a) and layer cross-section (b) for the structures of Figs. 7 and 8.

angular velocity can be easily measured. Work is in progress to implement the experimental set-up, which also includes positioners and an engine for rotation.

To end this section, we would like to highlight that the use of the considered circularly-shaped bisymmetric resonators (ELC and MLC) represents a clear advantage over those resonators of Figs. 1 and 2 for angular displacement and rotation speed measurements, since higher linearity and wider dynamic range can be achieved.

IV. Conclusion

In summary, we have analyzed the transmission properties of transmission lines loaded with electrically small resonators exhibiting two symmetry planes, one acting as a magnetic wall, and the other as an electric wall at the fundamental resonance frequency. It has been demonstrated that the relative orientation of such planes with regard to the symmetry plane of the line determines the notch magnitude of the transmission coefficient at the resonance frequency, the line being transparent when the electric wall of the resonator is aligned with the symmetry plane of the line (which is a magnetic wall for CPWs and microstrip lines). Finally, it has been demonstrated that ELC-loaded CPWs can be useful for the implementation of rotation sensors. The proof-of concept has been reported by considering a non-uniform CPW transmission line loaded with circular ELCs etched on a suspended movable substrate. Since the structure exhibits a strong (maximum) notched response or total transmission by rotating the resonators 90°, the possibility to implement an angular velocity sensor in time-domain has been discussed as well. Application to radio-frequency bar codes is also under investigation.

Acknowledgement

This work has been supported by MICIIN/MINECO-Spain (projects TEC2010-17512, CSD2008-00066 and TEC2011-13615-E), and by AGAUR-Generalitat de Catalunya, through project 2009SGR-421. Jordi Naqui is also in debt to MINECO (Spain) for supporting his work through the FPU grant AP2010-0431.

References

[1] G.V. Eleftheriades and K.G. Balmain Editors, *Negative-Refraction Metamaterials: Fundamental Principles and Applications*, John Wiley & Sons Inc., New York, 2005.

[2] C. Caloz and T. Itoh, *Electromagnetic Metamaterials: Transmission Line Theory and Microwave Applications*, John Wiley & Sons, Inc., New York, 2006.

[3] R. Marqués, F. Martin and M. Sorolla, *Metamaterials with Negative Parameters: Theory, Design and Microwave Applications*, John Wiley& Sons Inc., New York, 2007.

[4] J.B. Pendry, A.J. Holden, D.J. Robbins and W.J. Stewart, "Magnetism from conductors and enhanced nonlinear phenomena", *IEEE Transactions Microwave Theory Techn.*, vol. 47 pp. 2075-2084, Nov. 1999.

[5] M. Makimoto and S. Yamashita, "Band pass filters using parallel coupled stripline stepped impedance resonators," *IEEE Trans. Microw. Theory Tech.*, vol. MTT-28, no. 12, pp. 1413–1417, Dec. 1980.

[6] R. Marqués, J. D. Baena, J. Martel, F. Medina, F. Falcone, M. Sorolla, and F. Martin, "Novel small resonant electromagnetic particles for metamaterial and filter design," *Proc. ICEAA'03*, pp. 439–442, Torino, Italy, 2003.

[7] R. Marqués, F. Medina and R. Rafii-El-Idrissi "Role of bi-anisotropy in negative permeability and left handed metamaterials." *Phys. Rev. B*, vol. 65, paper 144441, 2002.

[8] D. Schurig, J. J. Mock, and D. R. Smith "Electric-field-coupled resonators for negative permittivity metamaterials." *Appl. Phys. Lett.*, vol. 88, paper 041109, 2006.

[9] F. Falcone, T. Lopetegi, J.D. Baena, R. Marqués, F. Martín and M. Sorolla, "Effective negative-ε stop-band microstrip lines based on complementary split ring resonators", *IEEE Microwave and Wireless Components Letters*, vol. 14, pp. 280-282, June 2004.

[10] F. Falcone, T. Lopetegi, M.A.G. Laso, J.D. Baena, J. Bonache, R. Marqués, F. Martín, M. Sorolla, "Babinet principle applied to the design of metasurfaces and metamaterials", *Phys. Rev. Lett.*, vol. 93, paper 197401, November 2004.

[11] J. Naqui, M. Durán-Sindreu, F. Martín, "On the symmetry properties of coplanar waveguides loaded with symmetric resonators: analysis and potential applications", *IEEE MTT-S Int. Microwave Symp.*, June 2012, Montreal (Canada).

978-1-4673-2141-9/13/$31.00 ©2013 IEEE

Article TMTT13

Transmission Lines Loaded with Bisymmetric Resonators and Their Application to Angular Displacement and Velocity Sensors

J. Naqui, and F. Martín

Transmission Lines Loaded With Bisymmetric Resonators and Their Application to Angular Displacement and Velocity Sensors

Jordi Naqui, *Student Member, IEEE*, and Ferran Martín, *Fellow, IEEE*

***Abstract*—This paper is focused on the analysis of coplanar waveguides (CPWs) loaded with circularly shaped electric-LC (ELC) resonators, the latter consisting of two coplanar loops connected in parallel through a common gap. Specifically, the resonator axis is aligned with the CPW axis, and a dynamic loading with ELC rotation is considered. Since the ELC resonator is bisymmetric, i.e., it exhibits two orthogonal symmetry planes, the angular orientation range is limited to 90°. It is shown that the transmission and reflection coefficients of the structure depend on the angular orientation of the ELC. In particular, the loaded CPW behaves as a transmission line-type (i.e., all-pass) structure for a certain ELC orientation (0°) since the resonator is not excited. However, by rotating the ELC, magnetic coupling to the line arises, and a notch in the transmission coefficient (with orientation dependent depth and bandwidth) appears. This feature is exploited to implement angular displacement sensors by measuring the notch depth in the transmission coefficient. To gain more insight on sensor design, the lumped element equivalent-circuit model for ELC-loaded CPWs with arbitrary ELC orientation is proposed and validated. Based on this approach, a prototype displacement sensor is designed and characterized. It is shown that by introducing additional elements (a circulator and an envelope detector), novel and high precision angular velocity sensors can also be implemented. An angular velocity sensor is thus proposed, characterized, and satisfactorily validated. The proposed solution for angular sensing is robust against environmental variations since it is based on the geometrical alignment/misalignment between the symmetry planes of the coupled elements.**

***Index Terms*—Bisymmetric resonator, coplanar waveguide (CPW), electrically small resonators, microwave sensors.**

I. Introduction

MICROWAVE-BASED devices for sensing applications are attracting growing interest because they feature properties (related, e.g., to cross-sensitivity, miniaturization, or cost) that cannot be provided by sensors working at lower frequencies or based on other sensing principles [1]. Microwave sensors are based on electromagnetic sensing principles, namely, a physical variable is measured from the variations of the characteristics of an RF/microwave signal.

Resonator-based microwave sensors are common devices where sensing is typically achieved through the variations experienced by the resonance frequency, phase, and/or quality factor of the resonant structures. In particular, split ring resonators (SRRs) [2], and other related particles, have been exhaustively used for sensing purposes due to their small electrical size and high-Q factor at the fundamental resonance. Different kind of sensors based on SRRs have been proposed, such as thin-film sensors [3], particle detectors [4], [5], stress sensors [6], moisture sensors [7], pressure sensors [8], displacement sensors [9], [10], or sensors for organic tissue analysis [11].

Recently, the authors have introduced a novel RF/microwave sensor concept based on symmetry properties of transmission lines loaded with resonant structures [12], [13]. The key idea behind this novel approach is simple: wave propagation is related to the relative orientation between the line and the resonant element. Typically, if the loaded line is symmetric (symmetry planes of line and resonator aligned), the structure is transparent to signal transmission. Contrarily, transmission is inhibited at the resonance frequency if the structure is non-symmetric. Following this principle, by breaking the symmetry through a linear or an angular displacement, proof-of-concepts of alignment, displacement, and position sensors have been reported in the last years [13]–[18]. One key advantage of these sensors is their robustness against changes in ambient conditions since the symmetry/asymmetry is not affected by environmental variations. In [18], the authors investigated coplanar waveguides (CPWs) loaded with bisymmetric electric-LC (ELC) resonators. A proof-of-concept of an angular displacement sensor was reported. It was shown that the notch magnitude varies by rotating the ELC, and the potential of these sensors for measuring angular velocities was highlighted. Since the basic idea behind many velocity or acceleration sensors is a measurement of the displacement of an object with respect to some reference object, displacement sensors are integral parts in many of them [19].

The aim of this paper is to extend the research work initiated in [18] to the analysis of CPWs loaded with ELC resonators, and their application to angular displacement and velocity sensors. In this paper, an equivalent circuit model that describes the electromagnetic behavior of the structure is proposed and validated. It is shown that the sensing principle of the angular displacement sensor is based on the electromagnetic induction since the

Manuscript received July 05, 2013; revised September 18, 2013; accepted September 30, 2013. Date of publication October 24, 2013; date of current version December 02, 2013. This work was supported by MICIIN-Spain under Contract TEC2010-17512, Contract EMET CSD2008-00066, and Contract TEC2011-13615-E, and by the Generalitat de Catalunya under Project 2009SGR-421. The work of J. Naqui was supported by MECD-Spain under FPU Grant AP2010-0431. This paper is an expanded paper from the IEEE MTT-S International Microwave Symposium, Seattle, WA, USA, June 2–7, 2013.

The authors are with GEMMA/CIMITEC, Departament d'Enginyeria Electrònica, Universitat Autònoma de Barcelona, 08193 Bellaterra, Spain (e-mail: Ferran.Martin@uab.es).

Color versions of one or more of the figures in this paper are available online at http://ieeexplore.ieee.org.

Digital Object Identifier 10.1109/TMTT.2013.2285356

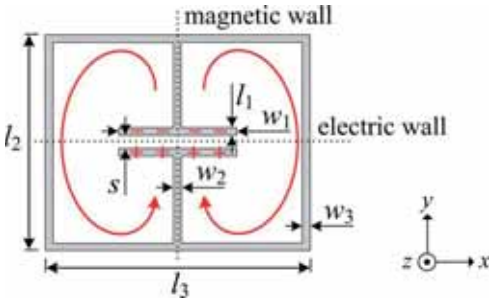

Fig. 1. Bisymmetric ELC resonator. The electric and magnetic walls at the fundamental resonance, as well as a sketch of the distribution of charges and currents, are indicated.

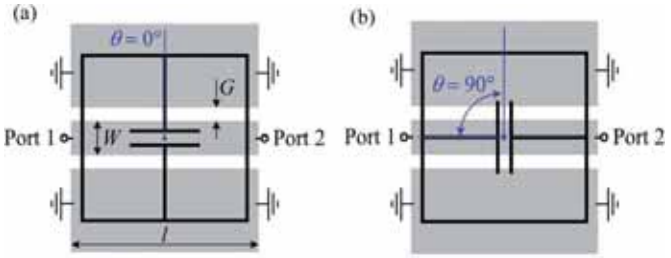

Fig. 2. CPW (in gray) symmetrically loaded with an ELC resonator (in black) etched in the back side of the substrate. The orientation between the CPW and the resonator is determined by the rotation angle θ; the line axis is perfectly aligned: (a) with the resonator electric wall for $\theta = 0°$ and (b) with the resonator magnetic wall for $\theta = 90°$.

magnetic coupling between the CPW and the resonator is sensitive to the displacement. It should be noted that electromagnetic induction is also the basis for the operation of commercial position and displacement sensors implemented by linear variable differential transformer (LVDT) or rotary variable differential transformer (RVDT) [19], [20]. Concerning applications, we go beyond the proof-of concept reported in [18] (where the resonator was attached to a movable suspended substrate), and we propose an angular displacement sensor, characterized through a specific experimental setup. Basically, the resonant element is attached to a cylinder, which is rotated by a step motor. Afterwards, it is also demonstrated that the angular velocity of a rotating object can be measured in a simple manner by using the displacement sensor as a building block.

This paper is organized as follows. In Section II, the electromagnetic behavior of CPWs loaded with ELC resonators is exhaustively investigated by the proposed equivalent circuit model. Section III is devoted to the application of the considered structures to angular displacement and velocity sensors, discussing the performance of the proposed sensors. Finally, the main conclusions are highlighted in Section IV.

II. CPWs Loaded With ELC Resonators

In this section, the wave propagation in CPWs coupled to ELC resonators is analyzed for different angular orientations of the ELC. An equivalent circuit model is proposed and validated through a simple method to extract the lumped element values. The effect of losses on the notch that appears in the transmission coefficient is also evaluated through the circuit model including losses.

A. Effects of Angular Orientation of the ELC

As explained in [18], the so-called ELC resonator [21] consists of two loops connected to a common capacitive gap (see Fig. 1). The particle is bisymmetric, exhibiting orthogonal electric and magnetic walls at the fundamental resonance. The charge and current distributions at that frequency (depicted in Fig. 1) reveal that there is an electric dipole moment in the plane of the particle (y oriented). However, the clockwise and counterclockwise current loops prevent the presence of an axial magnetic dipole moment (z oriented). Hence, the resonator can be electrically excited by a uniform time-varying electric field orthogonal to the electric wall, but not by a uniform time-varying axial magnetic field. However, the particle can be magnetically driven by a nonuniform magnetic field if the magnetic field lines in the individual loops are in opposite directions. Indeed, this is the coupling mechanism in the considered CPWs loaded with ELC resonators, where the electromagnetic field generated by the line is not uniform.

In [18], a CPW was loaded with an ELC resonator whose geometrical center was aligned with the line axis. Since an ELC resonator exhibits two symmetry planes, the resonator can symmetrically load a CPW by aligning the line axis with either the electric or the magnetic wall of the resonator, as depicted, respectively, in Fig. 2(a) and (b). For the fundamental CPW mode (i.e., the even mode), the symmetry plane along the line axis behaves as a virtual magnetic wall. Hence, an ELC resonator cannot be excited if its electric wall is aligned with the line axis. In this situation, perfect cancellation of the axial magnetic field lines through the individual loops occurs (i.e., there is not a net magnetic flux in each ELC loop). Conversely, the resonator is magnetically driven if its magnetic wall is aligned with the line axis. In this case, there is a net magnetic flux axially penetrating each loop, and it has opposite directions with regard to the magnetic wall.

In addition to these two symmetric loading orientations, intermediate (and thus, asymmetric) orientations were also considered, where neither the electric, nor the magnetic wall of the resonator was aligned with the line axis. With the aim of identifying an arbitrary orientation between the CPW and the resonator, a rotation angle, θ (with $0° \leq \theta \leq 90°$ due to the bisymmetry), was defined as illustrated in Fig. 2. For intermediate orientations, there are both inward and outward axial magnetic field components in each of the loops canceling each other. Therefore, in the lower limit, when the electric wall of the resonator is aligned with the line (i.e., $\theta = 0°$), there is a total cancellation. As the resonator is rotated, the cancellation gradually decreases until it finally vanishes when the magnetic wall of the ELC resonator is lined up with the line axis (i.e., $\theta = 90°$). Notice that regardless of the rotation angle, the net magnetic flux passing the individual loops is always in opposite directions to each other. This is necessary to magnetically drive the particle. As a result, the net magnetic flux through the loops of the resonator is dependent on the rotation angle, and this can be detected through inspection of the transmission/reflection coefficient.

It was demonstrated in [18] by electromagnetic simulation and measurement that the transmission coefficient of the structure depends on the resonator orientation. The results confirmed

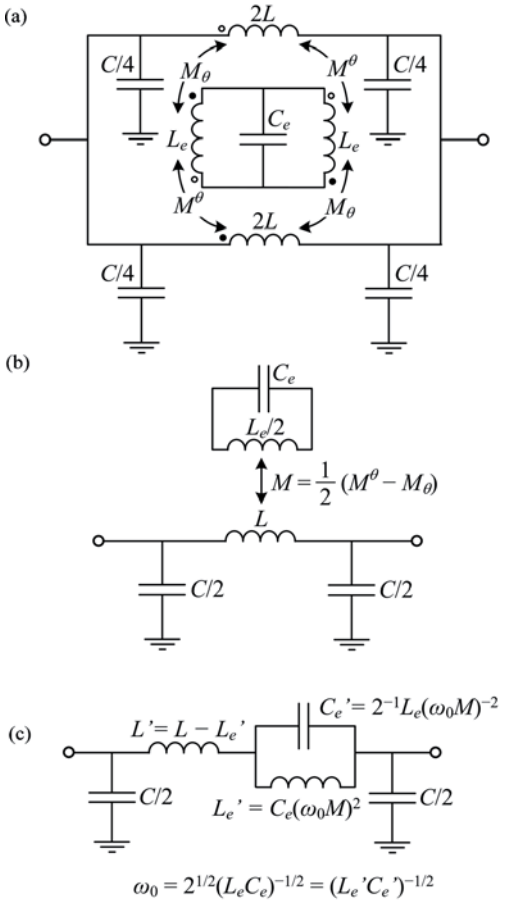

Fig. 3. (a) Lossless equivalent circuit model of a CPW loaded with an ELC resonator such as those shown in Fig. 2, including the different magnetic coupling mechanisms, accounted for through the mutual inductances M_θ and M^θ. (b) Simplified circuit model. (c) Transformed simplified circuit model.

that, for symmetric loadings, if the alignment is between walls of different nature (electric and magnetic), the structure is transparent to signal transmission. By contrast, if the alignment is between walls of the same kind (in our case, magnetic), a wide and deep notch appears in the transmission coefficient. Furthermore, for asymmetric orientations, a notch, whose bandwidth and depth is a function of the angle θ, also arises; the higher the angle, the stronger the notch.

B. Equivalent Circuit Model and Circuit Parameter Extraction Procedure

In this paper, the electromagnetic behavior of a CPW transmission line loaded with an ELC resonator is also explained using the circuit theory. The proposed equivalent circuit model is depicted in Fig. 3(a). This circuit is valid as long as the cell length l is electrically small (losses are not considered at the moment). The ELC resonator is represented by the inductances L_e and the capacitance C_e, modeling the inductive loops and the capacitive gap, respectively. The CPW is modeled by its inductance and capacitance, L and C, respectively, and it is divided into two identical halves for convenience. Finally, each half is magnetically coupled to each loop through the mutual inductances M_θ and M^θ, both being dependent on θ (different dots are used to distinguish the magnetic coupling sign associated to

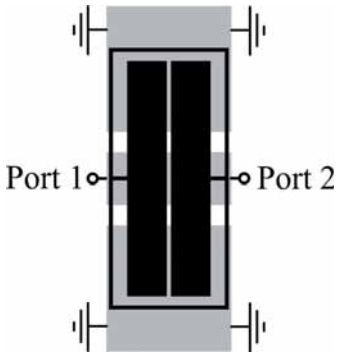

Fig. 4. Layout of an electrically small unit cell composed of a CPW loaded with an ELC resonator oriented such that $\theta = 90^\circ$. The considered substrate is Rogers RO3010 with thickness $h = 1.27$ mm and dielectric constant $\varepsilon_r = 11.2$. Line dimensions are $l = 4.8$ mm, $W = 2$ mm, and $G = 0.78$ mm, corresponding to a 50-Ω transmission line. Resonator dimensions are $w_1 = 9$ mm, $w_2 = w_3 = s = 0.15$ mm, $l_1 = 1.5$ mm, $l_2 = 4.6$ mm, and $l_3 = 10$ mm.

each of the halves). Therefore, the frequency response of the circuit of Fig. 3(a) directly depends on the angle θ. When $\theta = 0^\circ$, due to symmetry, $M_\theta = M^\theta \neq 0$, which means that the currents flowing on the CPW induce a pair of equal and antiphase voltages in the loops; no net voltage is induced in the resonator due to an absolute cancellation. In other words, there is not a net magnetic coupling, the resonator cannot be magnetically driven, and the resulting model is that of a conventional transmission line. On the other hand, as θ increases, the magnetic coupling is complementarily distributed; M^θ increases at the expense of a decrease in M_θ. Hence, for $\theta > 0^\circ$, a net induced voltage arises and the line is indeed capable of magnetically exciting the resonator. The larger the angle, the higher the induced voltage. Thus, at the upper limit, $\theta = 90^\circ$, M^θ is maximum while M_θ completely vanishes; the magnetic coupling cancellation disappears and the resonator is expected to be tightly coupled to the line.

Briefly, the behavior of the circuit of Fig. 3(a) is consistent with the results obtained in [18]. Moreover, the physical understanding of magnetic coupling cancellation relative to the resonator orientation is well illustrated by this model. Nevertheless, such a circuit is somewhat complex and has too many parameters for both parameter extraction and design purposes. An equivalent and simplified circuit model is the one depicted in Fig. 3(b), where an effective mutual inductance M is defined. Such a model is equivalent to that of an SRR magnetically coupled to a CPW transmission line, which can be transformed to the circuit model of Fig. 3(c) [22]. From the latter model, it can be concluded that there is not only a transmission zero at f_0 as long as M is different than zero, but also the rejection bandwidth broadens with M (the reason is that the susceptance slope of the parallel resonator decreases as the ratio L_e'/C_e' increases). Furthermore, the lumped element values of that circuit can be easily extracted from the method reported in [22].

In order to validate the circuits of Fig. 3, a sub-wavelength dimension of the unit cell is required. To this end, let us consider a unit cell with a short length l, a large capacitor w_1-l_1, and narrow inductive strips w_2 and w_3 with $\theta = 90^\circ$ (see Fig. 4). The resulting reflection and transmission coefficients inferred from the

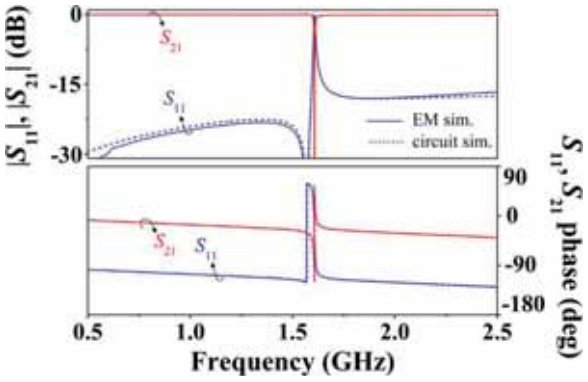

Fig. 5. Magnitude and phase of the reflection (S_{11}) and transmission (S_{21}) coefficients obtained from the lossless electromagnetic simulation for the structure of Fig. 4 and from the circuit simulation of the models of Fig. 3. The lumped element values are $C = 1.09$ pF, $L = 1.67$ nH, $C_e = 1.61$ pF, $L_e = 12.2$ nH, and $M = 0.50$ nH.

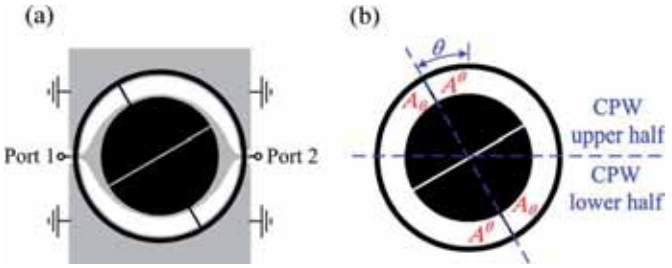

Fig. 6. (a) Layout of the circular-shaped structure reported in [18] with a circular and larger resonator capacitor. (b) Illustration of the areas A_θ and A^θ (for a specific angle of 30°). The considered substrate is Rogers RO3010 with $h = 1.27$ mm and $\varepsilon_r = 11.2$. The dimensions are: for the line, W and G are tapered such that the characteristic impedance is 50 Ω; for the ELC resonator: mean radius $r_0 = 8.05$ mm, capacitor outer radius $r_1 = 5.6$ mm, $w_2 = s = 0.2$ mm, and $w_3 = 0.5$ mm.

lossless electromagnetic simulation (using Agilent Momentum commercial software) are plotted in Fig. 5. Afterwards, from the electromagnetic simulation, the elements of the circuit of Fig. 3(c) are extracted following the procedure detailed in [22]. The parameters of the circuit of Fig. 3(b) are then obtained by estimating L_e as that inductance seen from the end terminals of the isolated loops (i.e., neither considering the resonator capacitor, nor the metallic planes of the CPW). Since the input impedance of an electrically small loop is primarily inductive [23], the equivalent input inductance was extracted from the electromagnetic simulation of the isolated loops.

The previous technique to estimate the inductance of the resonator can be performed regardless of the loop shape. Indeed, the technique seems to give very close values to the inductance given by the analytical expressions reported in [24] and [25] for circular SRRs. SRRs are electrically small resonators that consist of two coupled concentric split rings with cuts in opposite sides and separated by a tiny distance, whose inductance is approximated by the inductance of a single ring with the same average radius and ring width (this is plausible because in a quasi-static analysis the total current on both rings of the SRR is constant). For instance, for a loop with mean radius $r_0 = 8.05$ mm and ring width $c = 0.5$ mm, the extracted equivalent input inductance of a single ring was 42.5 nH, while the analytically estimated inductance was 44.03 nH.

In reference to the circuit of Fig. 3(b), all the extracted lumped element values are indicated in the caption of Fig. 5. For comparison purposes, the results of the circuit simulation are also shown in that figure. As can be seen, the circuit simulation is able to accurately fit the electromagnetic simulation in a wide frequency range around the notch frequency.

Notice that the structure depicted in Fig. 4 was optimized to be electrically small in the longitudinal direction for a particular case (i.e., $\theta = 90°$). This validates the circuit model for a given ELC orientation. Unfortunately, for a dynamic orientation, the electrical size l of the considered unit cell increases if the resonator is rotated (from 90° to 0°). For this reason, to deal with different orientations, we will consider a circular-shaped structure (see Fig. 6). By this means, the cell length l is independent on the orientation, and the mutual inductance as a function of the orientation can be easily obtained. The considered unit cell is the same as that reported in [18], but with a large (and circular) capacitor in order to reduce the electrical size at resonance. The results of the electromagnetic simulation for different resonator orientations are plotted in Fig. 7. Indeed, the transmission zero frequency (notch position) has been decreased from 1.21 GHz [18] to 0.80 GHz by increasing the capacitor. Thereby, the structure is electrically smaller, and the circuit model is more accurate in a wider frequency range (as compared to the structure of [18]). However, the circular shape has the disadvantage of increasing the effective electrical length (since the path for wave propagation between the input and output ports increases).

Therefore, the frequency region where the model accurately predicts the frequency response is not as wide as in the case of the structure of Fig. 4. Following the same procedure as in the preceding parameter extraction, the extracted parameters for the circular structure (under different orientations) are listed in Table I. Notice that with the exception of the mutual inductance, all the circuit parameters are roughly invariant with the rotation angle. The reflection and transmission coefficients inferred from the circuit simulation with the extracted parameters are also depicted in Fig. 7. Good agreement between the circuit and the electromagnetic simulations in the vicinity of the transmission zero frequency (i.e., the region of interest) results, thus validating the proposed circuits with arbitrary ELC orientation.

It is worth mentioning that L_e was assumed to be the inductance of the isolated resonator, i.e., the self-inductance. Thus, the effect of the CPW on that inductance value is accounted for by the mutual inductance M. According to the circuit model, regardless of the value of M, the notch frequency f_0 is invariant with the ELC orientation. Indeed, in the structure of Fig. 6, the notch frequency is roughly constant with the angle (the maximum frequency deviation is 0.48%) and this is because the parameters L_e and C_e are nearly invariant with the angular orientation. Nevertheless, it should be clarified that, in the proposed circuit model, C_e is the effective capacitance of the resonator with the presence of the CPW. Therefore, electric interaction between the resonator and the CPW may actually exist and change the effective capacitances of them.

Finally, to gain more insight into the effective mutual inductance, Fig. 8 shows the extracted value of M (as well as M_θ and M^θ) for the structure of Fig. 6 as a function of the rotation

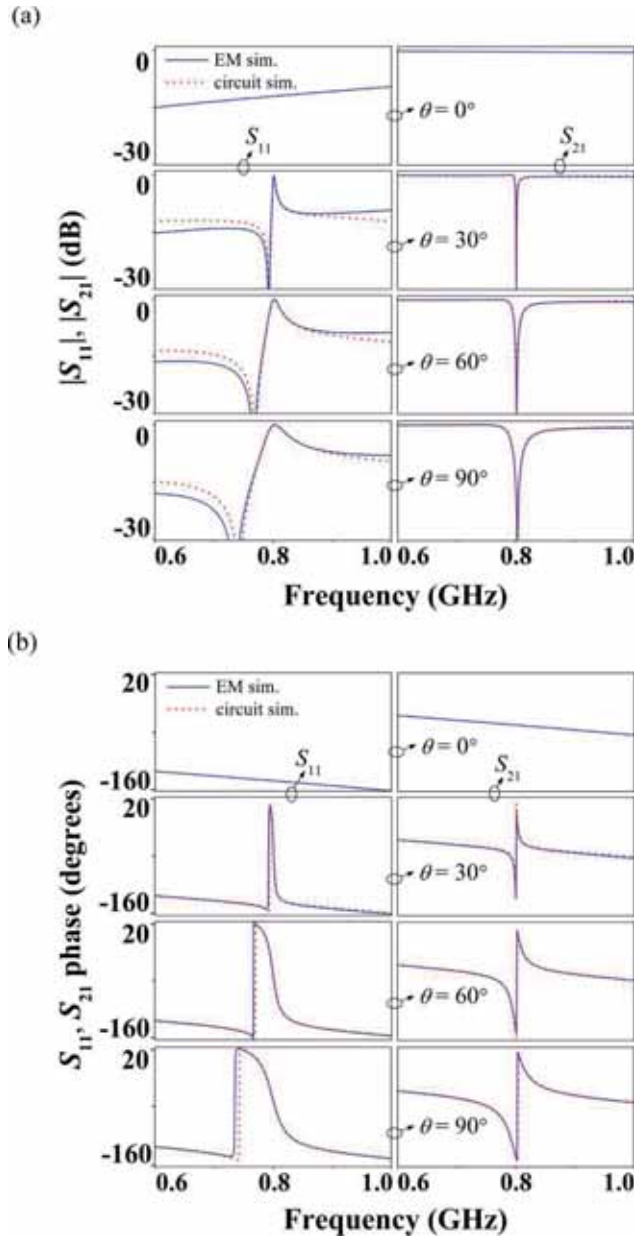

Fig. 7. (a) Magnitude and (b) phase of the reflection and transmission coefficients given by the lossless electromagnetic simulation for the structure of Fig. 6 and by the circuit simulation for the models of Fig. 3. The circuit parameters are those given in Table I.

TABLE I
EXTRACTED LUMPED ELEMENT VALUES OF THE CIRCUIT OF FIG. 3(B) FOR THE STRUCTURE OF FIG. 6

θ (degrees)	C (pF)	L (nH)	C_e (pH)	L_e (nH)	M (nH)
30	5.86	5.95	3.09	25.6	0.94
60	5.73	6.22	3.09	25.6	1.91
90	5.59	6.40	3.07	25.6	2.72

angle. Notice that for $\theta = 0°$, it was assumed that $M = 0$ because the lack of a notch does not allow the circuit parameters to be extracted from the procedure reported in [22]. In a similar fashion, for small angles ($\theta = 10°$), the parameters cannot be accurately extracted on account of the small mutual inductance.

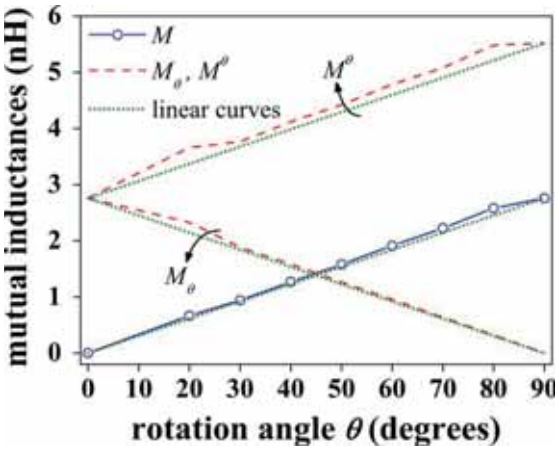

Fig. 8. Estimated mutual inductances of the models of Fig. 3 for the structure of Fig. 6 versus the rotation angle. The ideal linear curves are also shown for comparison purposes.

Nonetheless, the most meaningful result is that M varies continuously and quasi-linearly (the ideal curve is also plotted) as a consequence of the circular shape of the line and ELC. This phenomenology can be explained from the definition of the mutual inductance between two circuits

$$M_{ij} = \frac{\Phi_{ij}}{I_j} \tag{1}$$

where Φ_{ij} is the magnetic flux through circuit i generated by a current I_j flowing on a circuit j. The magnetic flux through any surface S can be computed as the integral surface

$$\Phi_{ij} = \int_S B_n \cdot ds \tag{2}$$

where B_n is the normal component to S of the magnetic flux density generated on the circuit j. If B_n is assumed to be uniform over the entire surface, then (2) yields

$$\Phi_{ij} = B_n A_S \tag{3}$$

the magnetic flux being proportional to the area A_S of the surface over which the flux is being quantified. In our case, we are interested in the magnetic flux generated by the CPW linking either loop of the resonator. According to the considered circular resonator (Fig. 6), the area of each loop is $A_l = \pi[(r_0 - w_3/2)^2 - r_1^2]/2$. If A_s is chosen to be that portion of the loop area that lies beneath half of the CPW (as illustrated in Fig. 6), the resulting complementary areas are then

$$A_\theta = A_l\left(\frac{1}{2} - \frac{\theta}{\pi}\right) = A_l - A^\theta \tag{4}$$

$$A^\theta = A_l\left(\frac{1}{2} + \frac{\theta}{\pi}\right) = A_l - A_\theta \tag{5}$$

which are linearly dependent on the angle θ. Regarding the magnetic flux density generated by a CPW, it is not spatially uniform. However, for an electrically small and uniform (i.e., the per-unit length inductance is uniform) CPW transmission line section, like the one shown in Fig. 4, it seems reasonable to assume the magnetic flux density to be longitudinally uniform

(i.e., the per-unit length magnetic flux density is uniform). Analogously, for a small circular-shaped CPW as the considered one, the magnetic flux density can be assumed to be radially uniform with θ (although in a nonuniform CPW, the per-unit length inductance is not strictly uniform, this approximation is reasonable). Therefore, assuming a uniform B_n over the areas (4) and (5) along θ, the mutual inductance (1) can be written as

$$M_\theta = \frac{B_n}{I_{2L}} A_l \left(\frac{1}{2} - \frac{\theta}{\pi}\right) \tag{6}$$

$$M^\theta = \frac{B_n}{I_{2L}} A_l \left(\frac{1}{2} + \frac{\theta}{\pi}\right) \tag{7}$$

where I_{2L} is the current through one of the halves of the CPW. With regard to the effective mutual inductance, since the effective area is found to be

$$A = A^\theta - A_\theta = A_l \left(\frac{2\theta}{\pi}\right) \tag{8}$$

and the current flowing on the circuit in this case is

$$I_L = 2I_{2L} \tag{9}$$

the resulting effective mutual inductance is

$$M = \frac{B_n}{I_L} A_l \left(\frac{2\theta}{\pi}\right) = \frac{1}{2}(M^\theta - M_\theta). \tag{10}$$

Equation (10) indicates that, in a first-order approximation, for a circularly shaped ELC-loaded CPW, the net mutual inductance modeling the magnetic coupling between the line and the resonator depends linearly on the loading angle θ. The key is the linear dependence of the net magnetic flux penetrating the loops. Notice that the assumed uniform B_n in (6), (7), and (10) will depend on the spatial location of the resonator so that it decreases with the physical distance (given by the substrate thickness h) between the coupled elements. In the limiting case, $\theta = \pi/2$ and $h \to 0$, (10) can be expressed as $M = Lf$ [26], where f is the fraction of the loops that lies beneath the slots. Since in our geometry $f \approx 1$, in this hypothetic case, the magnetic flux linkage would be maximum, i.e., $M \approx L$.

C. Effects of Losses on the Notch Magnitude

The notch magnitude in the transmission coefficient of a lossless notch filter, such as those shown in Fig. 3, is infinite (i.e., $S_{21} = 0$). However, in real circuits, losses always prevent the attenuation from going to infinity. In addition, losses round off the stopband characteristic [27], thus enhancing the rejection bandwidth around the notch frequency. There exist different loss mechanisms in both CPWs and planar resonators. The most relevant are ohmic or conductor losses, dielectric losses in the substrate, and radiation losses (our metallization layers are copper with conductivity $\sigma = 5.8 \cdot 10^7$ S/m and thickness $t = 35$ μm, and the loss tangent in Rogers RO3010 is $\tan\delta = 0.0023$). As in the majority of practical transmission lines, losses in the considered CPWs are negligible. Conversely, losses in planar resonant elements may be critical, and hence, dominate the power loss.

Accordingly, losses in an ELC-loaded CPW can be modeled to a good approximation by a series resistance R_s representing the losses in the resonator, as illustrated in Fig. 9(a). This is equivalent to introduce a parallel resistance R' in the transformed model, as depicted in Fig. 9(b) [25]. In the absence of losses, R_s vanishes while R' is infinite. It is also important to emphasize that the equivalent resistance R' indicates that minimum losses in the equivalent circuit model are achieved by maximizing M, and obviously, by minimizing R_s. On one hand, M is proportional to the area of the loops A_l according to (10), and it is also influenced by the distance between the coupled elements. On the other hand, in general, the larger the resonator, the higher the radiation losses, but the smaller the conductor losses (there is a tradeoff) [28]. Since commonly the radiation efficiency of a small loop antenna is small [23], the conductor loss of the ELC resonator is likely to be larger than the radiation loss. To sum up, what is to be expected is that the notch depth at a given frequency increases with the electrical size of the resonator and with the proximity between the line and the resonator.

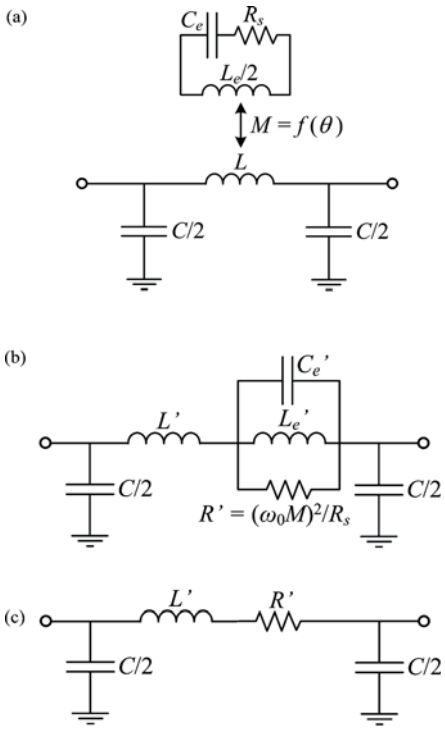

Fig. 9. (a) Equivalent circuit model of a CPW loaded with an ELC resonator, including losses in the resonator. (b) Transformed circuit model. (c) Transformed circuit model at the notch frequency.

The series resistance R_s of the structure of Fig. 6 has been extracted by curve fitting the lossy circuit simulation to the lossy electromagnetic simulation. The equivalent parallel resistance R' is then estimated from the transformation equation given in Fig. 9(b) by using the extracted mutual inductance of Fig. 8. The resulting extracted resistances are shown in Fig. 10. As can be seen, R_s is roughly constant while R' grows strongly with the rotation angle due to its quadratic dependence on M that also increases with the angle. Fig. 11 shows the transmission coefficient of the lossy electromagnetic and circuit simulations. As expected, the higher the parallel resistance R', the deeper the notch magnitude. This is intimately related to the

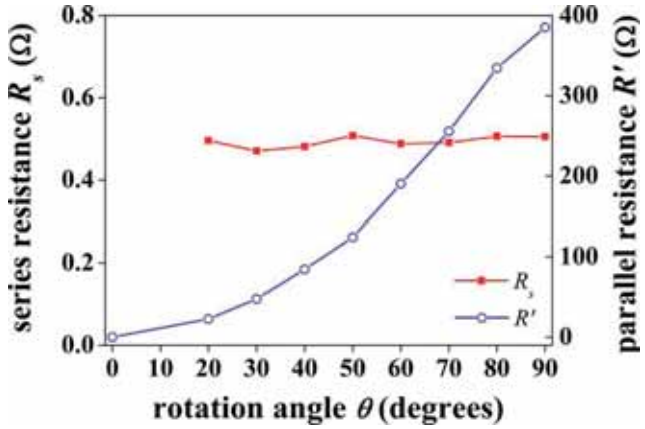

Fig. 10. Extracted series and parallel resistance of the circuit models of Fig. 9 for the structure of Fig. 6 versus the rotation angle.

fact that an increase in M simultaneously broadens the stopband bandwidth (because L'_e/C'_e increases). Therefore, the higher the M, the higher the stopband attenuation (depth and bandwidth). The previous results are in accordance with the estimated maximum stopband attenuation in bandstop filters designed from the low-pass prototypes since the attenuation increases with the stopband bandwidth and the Q factor of the resonators [27].

The notch magnitudes observed in the transmission coefficients shown in Fig. 11 were recorded, and the results are plotted in Fig. 12. It is seen that the magnitude of the notch in the logarithmic scale is almost linearly dependent with the rotation angle (i.e., the sensitivity is nearly constant). Indeed, from 10° to 80°, the linearity is quite good (for comparison purposes, the ideal linear curve is also shown). To gain insight on the linearity, let us now focus on the circuit model at the notch frequency. At that frequency, the resonator $L'_eC'_e$ opens and the resulting equivalent circuit is that of a conventional transmission line with R' in the series branch, as depicted in Fig. 9(c). The series inductance is $L' \approx L$ since L'_e is typically negligible as compared with L. Given that the line parameters L and C are roughly constant with the rotation, the sensitivity is then an exclusive function of R', which depends on θ through M. By the calculation of the transmission $(ABCD)$ matrix of that circuit model, the analytical transmission coefficient is found to be [29]

$$S_{21} = \frac{2}{(Z_L + R')(3Y_C + 1/Z_0) + 3} \tag{11}$$

where Z_L is the impedance of the line inductance, Y_c is the admittance of the line capacitance, and Z_0 is the port impedance. It has been verified that the analytical solution of (11) coincides with the value obtained through circuit simulation. Despite the fact that the sensitivity of the notch magnitude (in logarithmic scale) with θ may be obtained in closed form, the resulting expression is cumbersome. Nevertheless, in the light of numerical solutions (Fig. 12) and experimental data ([18] and Section III), the sensitivity is approximately constant.

To end this section, it is of paramount importance to highlight that besides the desired CPW mode, CPW transmission lines can support another parasitic mode, namely, the slot mode. In symmetric CPW structures, the propagation of the CPW and slot modes (also known as even and odd modes, respectively) is

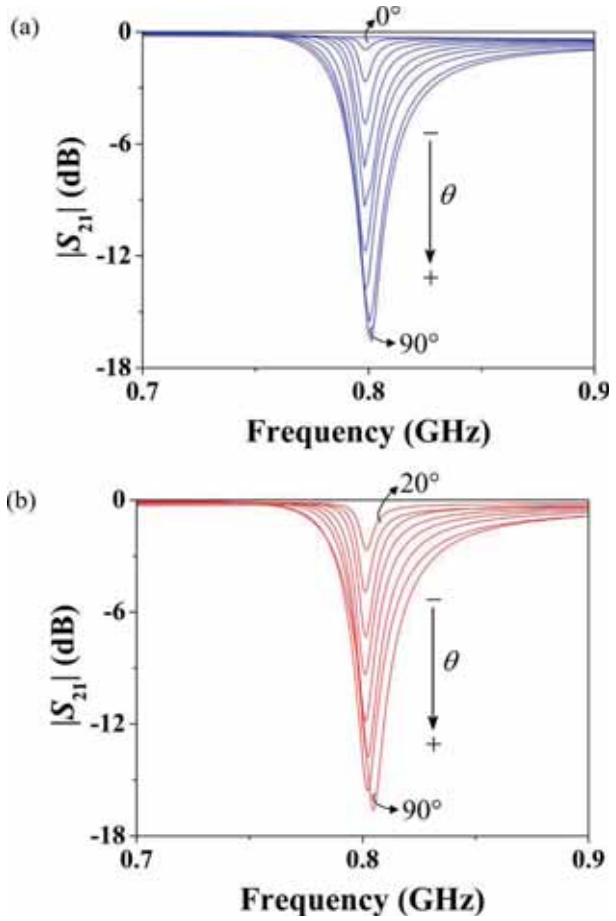

Fig. 11. (a) Lossy electromagnetic simulation of the structure shown in Fig. 6. (b) Its corresponding lossy circuit simulation of the equivalent models in Fig. 9. The notch depth and the rejection bandwidth increases with the rotation angle θ from 0° to 90°, incremented in steps of 10° (once again, the circuit simulation for 0° and 10° is not performed). The circuit parameters for some of the orientations are given in Table I with $R_s \approx 0.49\ \Omega$.

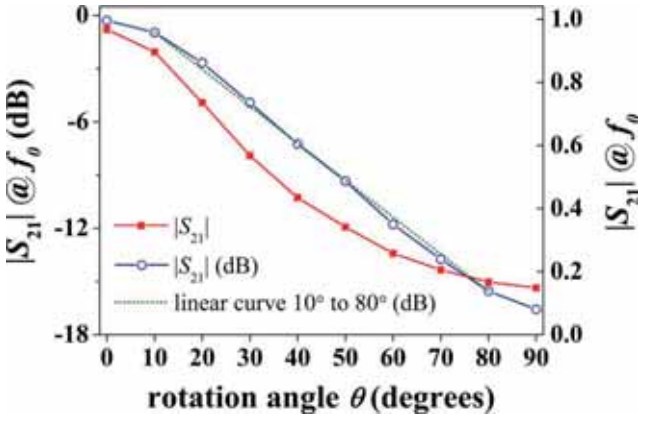

Fig. 12. Notch magnitude at the notch frequency f_0 extracted from the lossy simulations of Fig. 11. Good linearity is obtained in logarithmic scale.

independent, and power conversion from one mode to another does not arise. Therefore, an even mode excitation cannot generate an odd mode signal along the structure, and vice versa. However, in asymmetric CPW structures, the modes are coupled to each other and energy is continuously exchanged between the coupled modes [30]. Hence, from an even mode source, the

parasitic slot mode may be excited by coupling power from the desired CPW mode. A common procedure to suppress the slot mode generation in CPWs consists of introducing air bridges to electrically short circuit the ground planes in a transversal plane. In this work, for nonsymmetric resonator loadings ($0^\circ < \theta < 90^\circ$), mode conversion may exist and should be suppressed to avoid power loss in the CPW mode of interest. Thus far, air bridges were not used and mode conversion was neglected because the CPWs were electrically small. However, in larger structures, air bridges may be mandatory. For example, let us consider that we cascade 10-mm line sections at the ports of the structure shown in Fig. 6, and that the input port is driven by an even mode excitation, the other one being terminated with a 100-Ω differential load connecting the ground planes (the CPW central strip is left opened). The simulated mode conversion by the transmission coefficient is -4.3 dB, which is significantly reduced to -17.0 dB using air bridges at both sides of the resonator. In printed circuit board (PCB) technology, via-holes across the substrate and strips etched on the back substrate side are used, as will be shown in Section III.

III. Application to Angular Sensors

A sensor is a device that measures a physical quantity and converts it into a signal that can be read by an observer or by an instrument. This section is thus devoted to the application of the considered ELC-loaded CPWs to angular sensors involving the measurement of spatial rotations. As shown in Section II, the electromagnetic properties of the ELC resonator make it an interesting particle to detect angular variations within the range of 0°–90° from an electrical parameter. First of all, design considerations of the angular displacement sensor proposed in [18] are discussed, and a more realistic prototype is presented. A novel angular velocity sensor based on a displacement sensor is then proposed for the first time. The description of sensor parameters can be found in many literature sources [19], [20].

A. Angular Displacement Sensor

In Section II, it was demonstrated that the transmission/reflection coefficient of the considered loaded line depends on the angular orientation of the ELC, $0^\circ \leq \theta \leq 90^\circ$. Hence, one expects to be able to sense the physical angular displacement or position by looking at some electrical variable (amplitude, phase, or frequency), allowing us the implementation of an angular displacement sensor. In a sensor, the relationship between an input physical variable and an output electrical variable is given by the so-called transfer function. Obviously, the input dynamic range, i.e., the maximum angle that can be measured, is limited to 90°. Regarding the electrical variable, the sensitivity (i.e., the slope of the transfer function) should be, in general, as high and as constant as possible. To increase the sensitivity, the output dynamic range should be widened, while linearity is indicative of the deviation of the transfer function from an ideal straight line (a linear transfer function is characterized by a constant sensitivity).

The notch amplitude was chosen as the electrical variable to measure the angular displacement. Note that other electrical variables could have been also used, but the characterization with the amplitude allows us the implementation of the angular velocity sensor that is presented in Section III-B. Therefore, although in most practical circuits and applications losses are undesirable, we take advantage of them to use the notch magnitude as a sensing electrical variable (in the absence of losses, the notch magnitude would be always infinite). This functionality was exploited in [18] to implement a rotation sensor whose layout is that shown in Fig. 13. The sensing element is a CPW transmission line specifically designed to enhance the electromagnetic coupling with the ELC resonator.

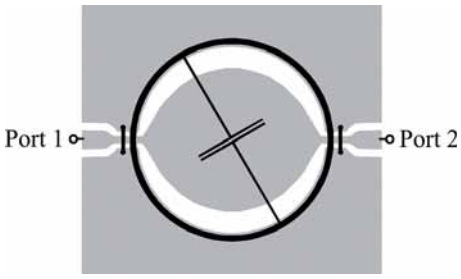

Fig. 13. Layout of the angular displacement sensor presented in [18] for an angle of $\theta = 30^\circ$. The dimensions are those given in the caption of Fig. 6 with the exception of $l_1 = 0.2$ mm and $w_1 = 6$ mm. Vias and backside strips at each side of the resonator are used to suppress the parasitic slot mode since access lines to solder the connectors have been added.

As seen in Section II-C, the sensitivity k of the variation of the notch amplitude with the rotation angle

$$k = \frac{\Delta 20 \log_{10} |S_{21}|}{\Delta \theta} \ (\mathrm{dB}/^\circ) \tag{12}$$

is relatively high and quasi-constant. In order to maximize the output dynamic range, the notch for 90° should be increased. As detailed in Section II-C, the smaller the R_s and the higher the M values, the deeper the notch. On one hand, R_s decreases and M increases with the electrical size of the particle. For that reason, the ELC capacitor was kept small. On the other hand, the smaller the distance between the CPW and the resonator, the higher the M. However, for very tiny distances, the increase in the dynamic range may be at the expense of some insertion loss for 0°, caused by a strong influence of the resonator to the line parameters, L and C (this produces line mismatching). The distance was set to 1.27 mm, providing good balance between the insertion loss at 0° and the dynamic range. In order to improve the linearity, both the CPW and the resonator were designed circularly shaped (this particularity was discussed in Section II-C). Since access lines were added to solder the connectors, vias and backside strips to connect the ground planes were introduced at each side of the resonator in order to cancel the propagation of the parasitic slot mode that arises for nonsymmetric orientations (i.e., $0^\circ < \theta < 90^\circ$).

Firstly, in [18], the ELC resonator was etched on the back side of the substrate, and some samples for different orientations were fabricated and measured. As expected, the angular displacement could be sensed as a function of the notch magnitude. However, with displacement sensing purposes, the resonator must be attached to another substrate (or object) in order to allow a relative motion between the resonator and the CPW. Thus, in [18], the CPW and the resonator were etched on different substrates in parallel planes with an air layer in between.

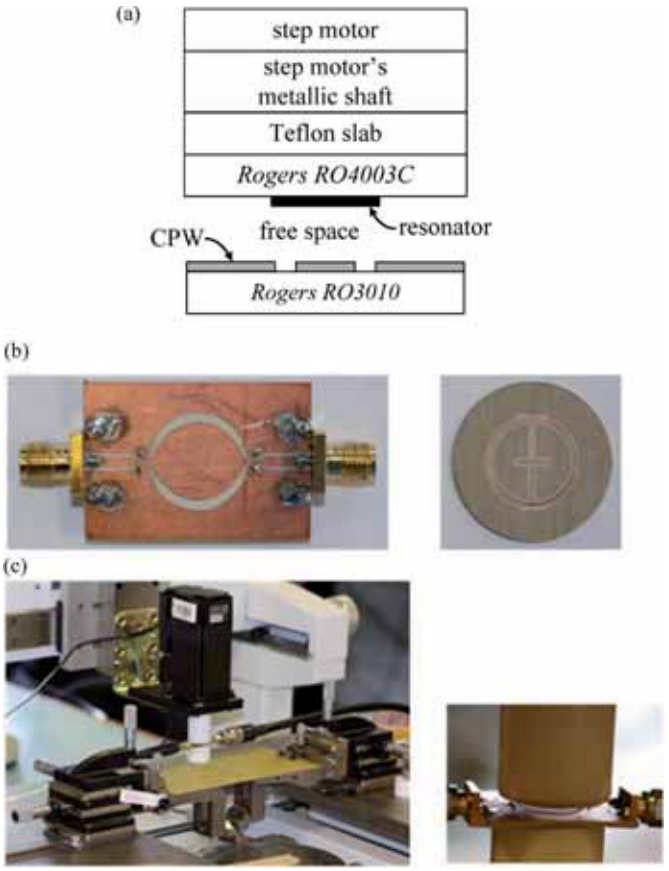

Fig. 14. Setup for the angular displacement measurement. (a) Layer cross section, (b) photograph of the fabricated CPW and ELC resonator, and (c) photographs of the experimental setup with positioners and a step motor STM 23Q-3AN. The parameters of the substrates are: Rogers RO3010, $\varepsilon_r = 11.2, h = 1.27$ mm, and $\tan\delta = 0.0023$; Rogers RO4003C, $\varepsilon_r = 3.55$, $h = 0.8128$ mm, and $\tan\delta = 0.0021$; Teflon, $\varepsilon_r = 2.08, h = 3.5$ mm, and $\tan\delta = 0.0004$; in-between air layer, $h = 1.27$ mm, $\varepsilon_r = 1$, and $\tan\delta = 0$.

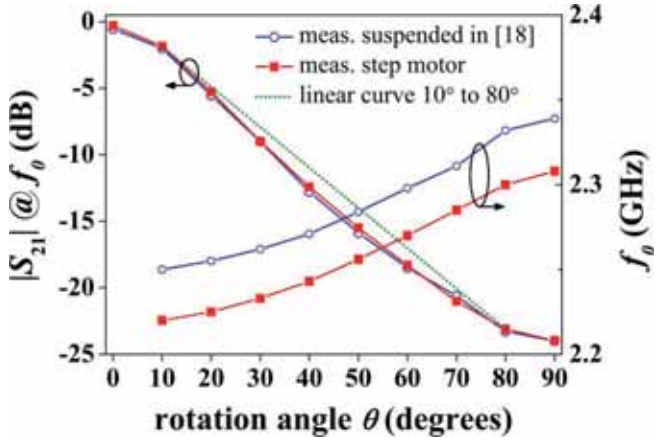

Fig. 15. Transfer function of the measured notch magnitude at the notch frequency in the transmission coefficient versus the rotation angle. The experimental setup of Fig. 14 was used.

TABLE II
PERFORMANCE OF THE ANGULAR DISPLACEMENT SENSOR OF FIG. 14

input	physical spatial variable	θ (°)
	dynamic range	$0° \le \theta \le 90°$
output	electrical variable	$\lvert S_{21}\rvert$ @ f_0 (dB)
	dynamic range	23.7 dB
input-output	average sensitivity	0.26 dB/°
	average linearity	1.21 dB (5.1%)

The resonator substrate was suspended (by a suspending substrate attached to the top of the CPW substrate), and it was manually moved so that the angular orientation was inferred by the use of a graded angular grid. This experimental setup offered robustness and reliability to the measurement, and the approach was validated successfully since the sensor operated as expected. Nonetheless, that sensor was simply a proof-of-concept device.

The results obtained in [18] encouraged the authors to go beyond the proof-of-concept in the present work. In this section, the sensor is tested using a realistic experimental setup, which is shown in Fig. 14. The resonator substrate, rather than being a suspended substrate, is attached to the metallic shaft of a step motor by means of a Teflon cylindrical slab. The latter is used to avoid close proximity between the resonator and the metallic shaft. Otherwise, the electrical performance of the sensor may change. Given that a step motor divides a full rotation into discrete and equal steps, the angular position can be accurately controlled by holding the position at one of these steps. The step motor STM 23Q-3AN, configured with a step resolution of 36 000 steps/revolution, was used (it can be easily controlled through software from a host computer).

After a 3-D spatial calibration between the CPW and the resonator by means of positioners, the measured notch magnitude and frequency as a function of the rotation is plotted in Fig. 15. The results are very similar to those with the suspended substrate in [18], which were also in good agreement with the lossy electromagnetic simulation. In comparison to [18], the notch frequency has experienced a slight decrease of 30 MHz due to the Teflon slab, while the change in the notch depth is negligible. These results seem to indicate that the notch magnitude exhibits not only quite robustness, but also less sensitivity than frequency-based sensors to variations or tolerances on the substrate properties.

The sensor parameters are summarized in Table II. It should be noted that a high output dynamic range was achieved while preserving a low insertion loss for small angles (0.29 dB for 0°), although the measured linearity was not as good as that of the structure shown in Fig. 6. As compared to the case where the resonator was attached to the back side of the substrate ($f_0 \approx 1.21$ GHz) [18], the notch position has been substantially shifted upwards, and the reason for such a phenomenon are the parameters of the resonator substrate. The thinner the substrate and the lower the dielectric constant, the higher the resonance frequency, the wider the bandwidth, and the deeper the notch. Thus, the resonator substrate was chosen to be relatively thin and with low dielectric constant to enhance the notch depth. It is also worth to mention that the notch frequency is shifted from 2.22 GHz (10°) to 2.308 GHz (90°), and thus frequency could be even used as a sensing variable. This frequency deviation may be due to the fact that resonator parameters are angle dependent (the structure cannot be considered electrically small at

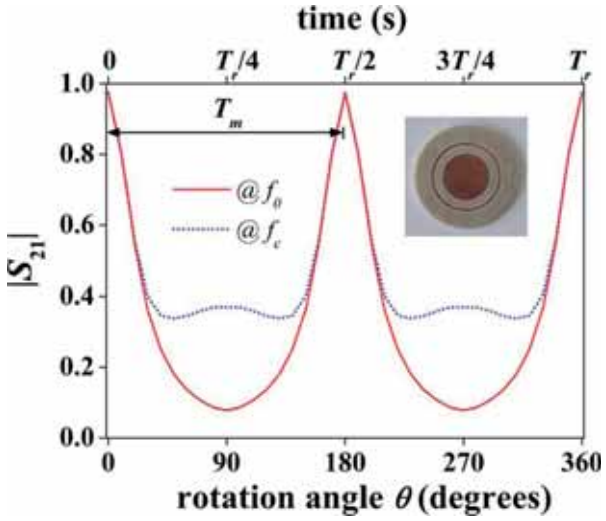

Fig. 16. Magnitude of the measured transmission coefficient in linear scale as a function of the angular position (or time if the resonator is rotating at a particular angular velocity) at the notch frequency f_0 and at the carrier frequency $f_c = 1.515$ GHz for the displacement sensor of Fig. 14 with the ELC resonator of Fig. 6 shown in the inset.

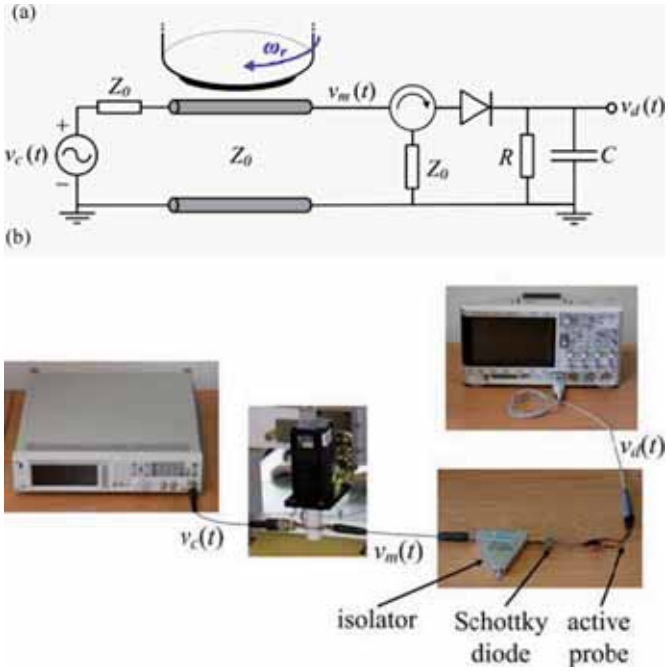

Fig. 17. Setup for the angular velocity measurement. (a) Schematic and (b) photographs of the experimental implementation. The transfer function of the loaded CPW is that shown in Fig. 16. The source impedance, the CPW characteristic impedance, and the circulator impedance is $Z_0 = 50\ \Omega$.

these frequencies). Therefore, the multi-layer substrate plays an active role to the sensor performance and its choice will depend on the specifications that are required to be optimized.

B. Angular Velocity Sensor

An angular displacement sensor as the one presented in Section III-A can also be used for measuring angular velocities (speed or rate of motion). The angular velocity ω_r is the change of the angular position θ with time t and can be found from the time period of rotation T_r as follows:

$$\omega_r = \frac{\Delta\theta}{\Delta t} = \frac{2\pi}{T_r}\ (\text{rad/s}). \tag{13}$$

Since the angular position varies with time, the notch magnitude in the transmission coefficient varies as well. As a result, the transfer function of the notch magnitude can be expressed not only with the angular position, but also with time. Fig. 16 shows the typical transfer function (in linear scale for convenience) at the notch frequency for a full rotation. Due to the displacement sensor symmetry, the transfer function is periodic varying between a maximum and a minimum. Thus, the period of the transfer function is 180° in angular position and $T_m = T_r/2$ in time. The principle to measure the angular velocity is based on detecting the time period T_m of the transfer function.

The schematic of the complete angular velocity sensor system is shown in Fig. 17(a). The resonator is assumed to be attached to an object with a particular angular velocity ω_r, the variable to be measured. The sensor system resembles an amplitude modulation (AM) system, in which a carrier signal at a frequency f_c is amplitude modulated by an information signal at $f_m \ll f_c$ that is subsequently recovered through the envelope of the modulated signal. Analogously, in the sensor system, a harmonic signal $v_c(t)$ tuned at the notch frequency of the angular displacement sensor is injected to the CPW. Since the attenuation varies with time according to the transmission coefficient, the signal $v_m(t)$ at the output port of the CPW is periodically modulated in amplitude with a time period T_m. Therefore, the angular displacement sensor with a time-varying resonator orientation acts as an amplitude modulator. To demodulate the signal, the classical envelope detector circuit composed of a diode and a capacitor–resistor (*RC*) filter is used. Given that the input impedance of the circuit is not matched to 50 Ω, a circulator with one of the ports terminated with a matched load (i.e., an isolator) is used to absorb reflections from the detector circuit, thus avoiding reflections back to the displacement sensor. At the output of the detector, the time distance between two consecutive transmission peaks in the amplitude of the demodulated (i.e., the envelope) signal $v_d(t)$ corresponds to the period T_m. Afterwards, the angular velocity can be easily extracted from $\omega_r = \pi/T_m$.

The experimental setup is illustrated in Fig. 17(b). As in Section III-A, the notch frequency of the considered displacement sensor varies slightly with the angle. Thus, a signal generator Agilent N5182A MXG injects a harmonic signal to the CPW at a carrier frequency of $f_c = 1.515$ GHz, corresponding to the notch frequency for an angle of 10°. The magnitude of the transmission coefficient at this frequency is shown in Fig. 16. The dynamic range of attenuation at this frequency is poorer than the one at the (variable) notch frequency, but this is not crucial in this application. Indeed, we used the electrically smaller resonator of Fig. 6 instead of the one shown in Fig. 13. The important aspect is to obtain a transfer function with a well-defined period.

The step motor offers smooth step motion and is configured with a uniform angular velocity of $\omega_r = 2\pi f_r$, for $f_r = 1$ Hz and 50 Hz (60 and 3000 rpm, respectively, the latter being the maximum angular velocity of the motor). A broadband (1–2 GHz) coaxial circulator ATM ATc1-2 with a matched load is used as an isolator. Concerning the envelope detector circuit,

the surface mount microwave Schottky detector diode Avago Technologies HSMS-2860 is utilized. The detector works on a charging–discharging scheme [31]. Assuming an ideal diode, in the positive half-cycle of the modulated signal, the diode is forward biased and the capacitor C charges rapidly to the peak value of the modulated signal with a time constant

$$\tau_c = Z_0 C \ll T_c \tag{14}$$

where $T_c = 1/f_c$ is the period of the carrier signal. When the input signal falls below the peak value, the diode becomes reverse biased, and the capacitor discharges slowly through the load resistor R until the next positive half-cycle, with a time constant, τ_d, satisfying

$$T_c \ll \tau_d = RC \ll T_m. \tag{15}$$

At the detector output, the envelope signal in the time domain is visualized by the oscilloscope Agilent 3054A. Ideally, the input impedance of an oscilloscope should be infinite. However, in practice, loading effects arise (the input impedance is finite and complex with resistive and capacitive components in parallel). Thus, for low loading effect, high resistance and low capacitance is required. For the available oscilloscope, the input impedance is 1 MΩ in parallel with 14 pF. Regardless of the value of C, the input capacitance of the oscilloscope is not small enough, and condition (15) cannot be satisfied. Nevertheless, notice that the input impedance of the oscilloscope is indeed an *RC* filter as that of the detector circuit. Therefore, we may take advantage of the loading effect to inherently implement the filter with the measurement. However, as mentioned before, the input capacitance is not small enough. For this reason, we used the single-ended active probe Agilent N2795A, achieving an effective input impedance of 1 MΩ in parallel with 1 pF. Therefore, conditions (14) and (15) are properly satisfied as follows:

$$\begin{aligned} T_c/\tau_c &= 13.2 \gg 1 \\ T_m/\tau_d &= 5 \cdot 10^5 (f_r = 1) \gg 1 \\ T_m/\tau_d &= 1 \cdot 10^4 (f_r = 50) \gg 1 \\ \tau_d/T_c &= 1.52 \cdot 10^3 \gg 1. \end{aligned} \tag{16}$$

The measured envelope signals are shown in Fig. 18. Notice that the waveform of the amplitude peaks is directly related to that of the transmission peaks in the transfer function (ideally they should be identical). The measured time periods between consecutive peaks have been $T_m(\text{meas.}) = 501$ ms ($f_r = 1$ Hz) and 10.05 ms ($f_r = 50$ Hz). The measured linear velocities have then been $f_r(\text{meas.}) = 0.998$ Hz and 49.751 Hz, values very close to the velocities specified in the step motor, thus validating the proposed sensor. To enhance precision, the measure could be done between very distant nonconsecutive peaks, although the rotation velocity should be constant.

It is important to remark that the sensor is able to measure the speed (i.e., the magnitude) of the angular motion, but not the direction. As long as the carrier frequency is much higher than the linear frequency of rotation, the measurable range of velocities is theoretically unlimited. It should be also pointed out that the broadband coaxial circulator could be replaced by a narrowband surface mount circulator operating at the carrier frequency. Alternatively, the circulator and the detector could be replaced by a post-processing stage, able to provide not only the angular velocity, but also angular acceleration (if it is present) and position.

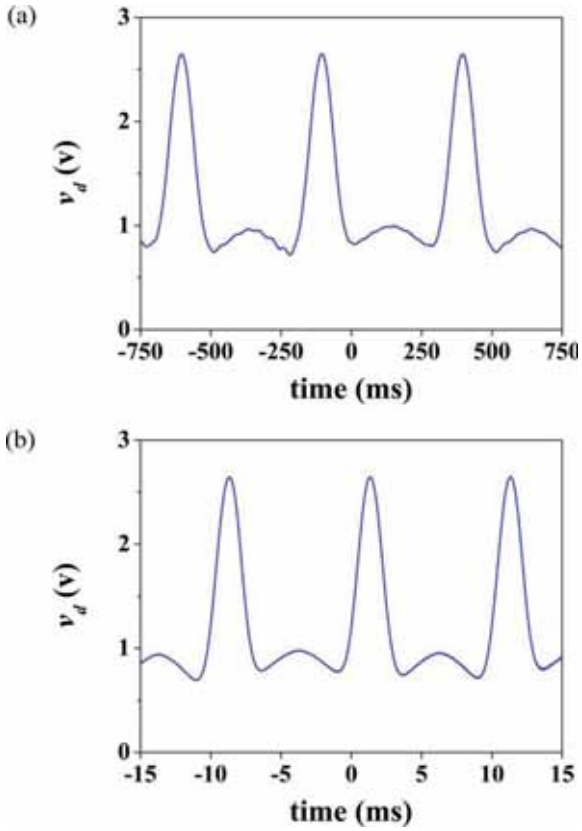

Fig. 18. Measured envelope signal using the experimental setup of Fig. 17. (a) $f_r = 1$ Hz and (b) $f_r = 50$ Hz.

C. Performance of Angular Sensors Based on Symmetry Properties

Many and very different technologies for the implementation of angular displacement and velocity sensors are commercially available [19], [20], each of them presenting its advantages and disadvantages. A comparative analysis in terms of performance, size, and cost between the proposed sensors and commercial sensors would be very long and is far beyond the scope of this paper. Therefore, this section tries to highlight the performance and capabilities of the presented sensors.

Ideal sensors are designed to be linear or linear to some simple mathematical function of the measurement (e.g., logarithmic or exponential) [19], [20]. However, to some extent, the sensor may be sensitive to other properties, being the cross-sensitivity to ambient perturbations a key issue. For instance, in laser interferometer displacement sensors, environmental parameters that influence the speed of light will affect and degrade the precision of the measurement [20]; in optical fiber displacement sensors sensitive to ambient fluctuations in temperature and pressure, techniques that compensate for changes in the output signal due to the undesired perturbations must be provided [20]; finally, microwave sensors based on

the frequency shift of resonant elements [10] can be altered by drifts caused by environmental changes.

The proposed angular displacement sensors produce amplitude outputs in logarithmic scale (as usual to quantify attenuation). The sensitivity is reasonably constant, and linearization could be improved, if necessary, by post processing [19]. The sensing notch magnitude seems to exhibit better cross-sensitivity than other variables (e.g., frequency) to variations on the substrate that may be due to fabrication tolerances or ambient conditions. However, the disadvantage of sensing the amplitude is its susceptibility to electromagnetic interference or noise that may seriously affect the performance of the sensors. Nevertheless, in case that some interfering signals were present and degrade the sensor performance, the frequency of operation could be easily shifted by changing the substrate or tailoring resonator dimensions. Another way of reducing unwanted interference may consider the appropriate shielding of the sensor. Alternatively, in an electromagnetic noisy environment, the inspection of the phase or frequency may be considered.

The principle of operation of the proposed sensors relies on the alignment of geometrical symmetry planes. Therefore, the sensors are inherently robust against ambient conditions because the alignment cannot be altered, and especially suitable for alignment purposes. Thus, the angular velocity measurement can be regarded as an application of an angular alignment measurement since the working principle relies on a periodic angular position. This means that a perfect alignment between the CPW and the resonator (i.e., a perfect spatial calibration) is not absolutely required, and as a consequence, the sensor may be insensitive to small mechanical vibrations. In case of nonperfect alignment, the transfer function simply would have a period of 360° instead of 180° (the velocity would be measured between nonconsecutive peaks). Another implication is that any structure capable of producing a periodically time-varying transmission coefficient with angular motion may be used. However, the advantage of our solution is that since the angular velocity sensor uses an angular displacement sensor as a building block, an all-in-one sensor able to measure (unidirectional) displacement, velocity and even acceleration and position may be possible through a suitable calibration and post-processing stage.

The presented sensors are only driven with an harmonic signal, and some factors should be considered about the optimal choice of its operating frequency. A great advantage of higher frequencies is the higher degree of device miniaturization. Ideally, if the loaded CPW structure was scaled down, the frequency response would experience an upwards shift. However, the frequency response would be altered by losses, which cannot be disregarded and increase with frequency. As a result, the notch depth in the transmission coefficient would be expected to be attenuated with an increase in frequency. Furthermore, more sophisticated external circuitry to the loaded line is required as frequency increases since the nonideal behavior of components arises when frequency is increased. Another important factor in determining the operation frequency may be the effectiveness of the shield, as long as the sensor is shielded.

The proposed approach for sensing purposes consists of a sensitive element, which is merely a resonator-loaded transmission line in printed technology, plus external circuitry. Although in this paper the external circuitry has been implemented by multifunctional, but heavy and expensive equipment (e.g., a vector network analyzer or a signal generator), the circuitry may be implemented through or in part replaced with low-cost electronic systems and circuits. For example, as mentioned in Section III-B, the angular velocity can be determined by cascading a post-processing unit to the output port of the CPW, avoiding the use of the circulator, detector, and oscilloscope. Therefore, the proposed approach is a good solution for relatively small-size and low-cost systems [obviously, small size is not featured as compared to sensors on the microscale or nanoscale, such as microelectromechanical systems (MEMS)].

Finally, although the proposed sensing elements (i.e., the ELC-loaded CPWs) are wire-connected to the source and reading (processing) devices, by simply adding cross-polarized antennas to the input and output ports of the CPW transmission line, a wireless link between the sensing element and the source and processing stages is also possible [10].

IV. Conclusion

In this work, which is an extension of [18], a CPW loaded with an ELC resonator has been analyzed in terms of the angular orientation of the resonant element. The analysis has been done on the basis of symmetry properties. It has been shown that at the fundamental resonance of the ELC, which is a bisymmetric resonator, an electric wall and a magnetic wall in the orthogonal symmetry planes arise. If the ELC electric wall is aligned with the symmetry plane of the line (a magnetic wall for the fundamental CPW mode), the loaded line is transparent. Conversely, for the other loading orientations, the particle is excited and a transmission zero in the transmission coefficient appears. The optimum orientation for the strongest attenuation (maximum notch depth and bandwidth) is the one corresponding to perfect alignment between the ELC magnetic wall and the symmetry plane of the line. Therefore, by spatially rotating the resonator the frequency response switches from an all-pass to a stopband behavior, the latter being dependent on the angular orientation.

An equivalent circuit model, valid for any arbitrary loading angle and very useful for design purposes, has been proposed. The circuit model shows that both the magnitude and the phase of the transmission/reflection coefficient are modulated by the mutual inductance accounting for the magnetic coupling between the CPW and the ELC. Hence, the angular orientation can be inferred by inspection of the mutual inductance, thus being the electromagnetic induction, the physical principle of sensing. However, instead of looking at the mutual inductance, we have focused our attention on the notch magnitude in the transmission coefficient since it can be directly obtained by measuring signal amplitudes. The resulting sensitivity of the notch magnitude with the angle is reasonably high and constant, provided the structure is circularly shaped. Thus, the transfer function of the notch magnitude with the rotation angle has been exploited for the implementation of angular displacement and velocity sensors.

An experimental setup for the characterization of the proposed sensors has been proposed. It includes a step motor, with

the associated software and control unit, which allows us to accurately control the angular rotation and velocity of the loading element. With this experimental setup, the angular displacement sensor reported in our prior work [18] has been characterized in a more realistic environment. For the angular velocity sensor, a circulator and an envelope detector, plus a signal source (providing a carried signal) and an oscilloscope, have been added in order to extract the envelope of the modulated signal (caused by rotation). The angular velocity can be simply inferred from the period of the envelope signal, recorded by the oscilloscope. This novel angular velocity sensor, properly characterized through two different rotation speed measurements, is able to measure an ultra-wide range of angular velocities with high precision.

The proposed sensors are simple (from the design viewpoint), compact in size and low cost (provided the external circuitry is implemented by electronic systems and circuits), robust against environmental variations and fabrication tolerances, and highly integrable. Moreover, wireless connectivity of the sensing element with the microwave source and processing stage is also possible. Future work is focused on sensing other physical variables, and on the implementation of the sensing element in microstrip technology.

REFERENCES

[1] M. Schueler, C. Mandel, M. Puentes, and R. Jakoby, "Metamaterial inspired microwave sensors," *IEEE Microw. Mag.*, vol. 13, no. 2, pp. 57–68, Mar. 2012.

[2] J. B. Pendry, A. J. Holden, D. J. Robbins, and W. J. Stewart, "Magnetism from conductors and enhanced nonlinear phenomena," *IEEE Trans. Microw. Theory Techn.*, vol. 47, no. 11, pp. 2075–2084, Nov. 1999.

[3] X.-J. He, Y. Wang, J.-M. Wang, and T.-L. Gui, "Thin film sensor based tip-shaped splits ring resonator metamaterial for microwave application," *Microsyst. Technol.*, vol. 16, pp. 1735–1739, 2010.

[4] E. Cubukcu, S. Zhang, Y.-S. Park, G. Bartal, and X. Zhang, "Split ring resonator sensors for infrared detection of single molecular monolayers," *Appl. Phys. Lett.*, vol. 95, pp. 043113-1–043113-3, 2009.

[5] T. Driscoll, G. O. Andreev, D. N. Basov, S. Palit, S. Y. Cho, N. M. Jokerst, and D. R. Smith, "Tuned permeability in terahertz split ring resonators for devices and sensors," *Appl. Phys. Lett.*, vol. 91, pp. 062511-1–062511-3, 2007.

[6] R. Melik, E. Unal, N. K. Perkgoz, C. Puttlitz, and H. V. Demir, "Metamaterial-based wireless strain sensors," *Appl. Phys. Lett.*, vol. 95, pp. 011106-1–011106-3, 2009.

[7] R. A. Yogi, R. S. Parolia, R. N. Karekar, and R. C. Aiyer, "Microwave Microstrip ring resonator as a paper moisture sensor: Study with different grammage," *Meas. Sci. Technol.*, vol. 13, pp. 1558–1562, 2002.

[8] P. K. Pattnaik, B. Vijayaaditja, T. Srinivas, and A. Selvarajan, "Optical MEMS pressure sensor using ring resonator on a circular diaphragm," in *Proc. Int. MEMS, NANO, Smart Syst. Conf.*, 2005, pp. 277–288.

[9] X. Liu, C. Xue, S. Yan, J. Xiong, and W. Zhang, "Integrated high sensitivity displacement sensor based on micro ring resonator," in *Proc. 4th IEEE Int. Nano/Micro Engineered and Molecular Syst. Conf.*, Shenzhen, China, Jan. 5–8, 2009, pp. 1000–1003.

[10] C. Mandel, B. Kubina, M. Schüßler, and R. Jakoby, "Passive chipless wireless sensor for two-dimensional displacement measurement," in *41st Eur. Microw. Conf.*, Manchester, U.K., Oct. 2011, pp. 79–82.

[11] M. Puentes, M. Maasch, M. Schüßler, and R. Jakoby, "Frequency multiplexed 2-dimensional sensor array based on split-ring resonators for organic tissue analysis," *IEEE Trans. Microw. Theory Techn.*, vol. 60, no. 6, pp. 1720–1727, Jun. 2012.

[12] J. Naqui, A. Fernández-Prieto, M. Durán-Sindreu, F. Mesa, J. Martel, F. Medina, and F. Martín, "Common mode suppression in microstrip differential lines by means of complementary split ring resonators: Theory and applications," *IEEE Trans. Microw. Theory Techn.*, vol. 60, no. 10, pp. 3023–3034, Oct. 2012.

[13] J. Naqui, M. Durán-Sindreu, and F. Martín, "Novel sensors based on the symmetry properties of split ring resonators (SRRs)," *Sensors*, vol. 11, pp. 7545–7553, Jul. 2011.

[14] J. Naqui, M. Durán-Sindreu, and F. Martín, "Alignment and position sensors based on split ring resonators," *Sensors (Special Issue)*, vol. 12, pp. 11790–11797, Aug. 2012.

[15] A. Horestani, C. Fumeaux, S. Al-Sarawi, and D. Abbott, "Displacement sensor based on diamond-shaped tapered split ring resonator," *IEEE Sens. J.*, vol. 13, no. 4, pp. 1153–1160, Apr. 2013.

[16] A. Horestani, D. Abbott, and C. Fumeaux, "Rotation sensor based on horn-shaped split ring resonator," *IEEE Sens. J.*, vol. 13, no. 8, pp. 3014–3015, May 2013.

[17] J. Naqui, M. Durán-Sindreu, and F. Martín, "On the symmetry properties of coplanar waveguides loaded with symmetric resonators: Analysis and potential applications," in *IEEE MTT-S Int. Microw. Symp. Dig.*, Montreal, QC, Canada, Jun. 2012.

[18] J. Naqui, M. Durán-Sindreu, and F. Martín, "Transmission lines loaded with bisymmetric resonators and applications," in *IEEE MTT-S Int. Microw. Symp. Dig.*, Seattle, WA, USA, Jun. 2013.

[19] J. Fraden, "Position, displacement, and level, and velocity and acceleration," in *Handbook of Modern Sensors: Physics, Design, and Applications*, 3rd ed. New York, NY, USA: Springer, 2004.

[20] J. G. Webster, "Displacement measurement, linear and angular," in *The Measurement Instrumentation and Sensors Handbook*. Boca Raton, FL, USA: CRC, 1999.

[21] D. Schurig, J. J. Mock, and D. R. Smith, "Electric-field-coupled resonators for negative permittivity metamaterials," *Appl. Phys. Lett.*, vol. 88, 2006, Art. ID 041109.

[22] F. Aznar, M. Gil, J. Bonache, L. Jelinek, J. D. Baena, R. Marqués, and F. Martín, "Characterization of miniaturized metamaterial resonators coupled to planar transmission lines through parameter extraction," *J. Appl. Phys.*, vol. 104, Dec. 2008, Art. ID 114501.

[23] C. Balanis, "Loop antennas," in *Antenna Theory: Analysis and Design*, 2nd ed. New York, NY, USA: Wiley, 1997.

[24] R. Marqués, F. Medina, and R. Rafii-El-Idrissi, "Role of bianisotropy in negative permeability and left-handed metamaterials," *Phys. Rev. B, Condens. Matter*, vol. 65, 2002, Art. ID 144440.

[25] R. Marqués, F. Martín, and M. Sorolla, *Metamaterials With Negative Parameters: Theory, Design and Microwave Applications*. Hoboken, NJ, USA: Wiley, 2008.

[26] F. Martín, F. Falcone, J. Bonache, R. Marqués, and M. Sorolla, "Split ring resonator based left handed coplanar waveguide," *Appl. Phys. Lett.*, vol. 83, pp. 4652–4654, Dec. 2003.

[27] J.-S. Hong and M. J. Lancaster, "Basics concepts and theory of filters," in *Microstrip Filters for RF/Microwave Applications*. New York, NY, USA: Wiley, 2001.

[28] J.-S. Hong and M. J. Lancaster, "Compact filters and filter miniaturization," in *Microstrip Filters for RF/Microwave Applications*. New York, NY, USA: Wiley, 2001.

[29] D. M. Pozar, "Microwave network analysis," in *Microwave Engineering*, 3rd ed. New York, NY, USA: Wiley, 2005.

[30] R. Mongia, I. Bahl, and P. Barthia, "Broadband forward-wave directional couplers," in *RF and Microwave Coupled Line Circuits*. Norwood, MA, USA: Artech House, 1999.

[31] S. Haykin, "Continuous-wave modulation," in *Communication Systems*, 4th ed. New York, NY, USA: Wiley, 2001.

Jordi Naqui (S'11) was born in Granollers, Spain, in 1984. He received the Telecommunication Technical Engineering diploma (with a specialty in electronics), Telecommunication Engineering degree, Micro and Nanoelectronics Engineering Master degree from the Universitat Autònoma de Barcelona (UAB), Bellaterra, Spain, in 2006, 2010, and 2011, respectively, and is currently working toward the Ph.D. degree in subjects related to innovative passive microwave devices based on metamaterial concepts at UAB.

Ferran Martín (M'04–SM'08–F'12) was born in Barakaldo (Vizcaya), Spain, in 1965. He received the B.S. degree in physics Ph.D. degree from the Universitat Autònoma de Barcelona (UAB), Bellaterra, Spain, in 1988 and 1992, respectively.

From 1994 to 2006, he was an Associate Professor of electronics with the Departament d'Enginyeria Electrònica, UAB, and since 2007, he has been a Full Professor of electronics. In recent years, he has been involved in different research activities including modeling and simulation of electron devices for high-frequency applications, millimeter-wave, and terahretz generation systems, and the application of electromagnetic bandgaps to microwave and millimeter-wave circuits. He is currently very active in the field of metamaterials and their application to the miniaturization and optimization of microwave circuits and antennas. He is the Head of the Microwave and Millimeter Wave Engineering Group (GEMMA Group), UAB, and Director of CIMITEC, a research Center on Metamaterials supported by TECNIO (Generalitat de Catalunya), UAB. He has been a Guest Editor for three special issues on metamaterials in three international journals. He has authored or coauthored over 400 technical conference, letter, and journal papers. He coauthored a monograph on metamaterials, entitled *Metamaterials with Negative Parameters: Theory, Design and Microwave Applications* (Wiley, 2008). He has filed several patents on metamaterials and has headed several development contracts.

Dr. Martín has organized several international events related to metamaterials, including workshops at the IEEE Microwave Theory and Techniques Society (IEEE MTT-S) International Microwave Symposium (IMS) (2005 and 2007) and the European Microwave Conference (2009). Among his distinctions. He was the recipient of the 2006 Duran Farell Prize for Technological Research. He holds the Parc de Recerca UAB—Santander Technology Transfer Chair, and was the recipient of an ICREA ACADEMIA Award.

Article SJ13

Angular Displacement and Velocity Sensors Based on Electric-LC (ELC) Loaded Microstrip Lines

J. Naqui and F. Martín

Angular Displacement and Velocity Sensors Based on Electric-LC (ELC) Loaded Microstrip Lines

Jordi Naqui, *Student Member, IEEE*, and Ferran Martín, *Fellow, IEEE*

***Abstract*— Planar microwave angular displacement and angular velocity sensors implemented in microstrip technology are proposed. The transducer element is a circularly shaped divider/combiner, whereas the sensing element is an electric-LC resonator, attached to the rotating object and magnetically coupled to the circular (active) region of the transducer. The angular variables are measured by inspection of the transmission characteristics, which are modulated by the magnetic coupling between the resonator and the divider/combiner. The degree of coupling is hence sensitive to the angular position of the resonator. As compared with coplanar waveguide angular displacement and velocity sensors, the proposed microstrip sensors do not require air bridges, and the ground plane provides backside isolation.**

***Index Terms*— Angular sensors, microstrip technology, microwave sensors, rotation speed sensors.**

I. Introduction

MICROWAVE sensors based on split rings that deal with the measurement of spatial variables (e.g., alignment or displacement) are increasingly popular [1]–[7]. These sensors usually consist of a transmission line coupled to a resonator, and the relative motion between these two elements is measured through the transmission characteristics of an RF/microwave signal. The sensing principle in [2]–[7] relies on symmetry properties; typically, in transmission lines symmetrically loaded with resonators, line-to-resonator coupling is prevented, and the lines exhibit total transmission. However, by breaking the symmetry through the effects of a spatial variable (e.g., a rotation), a transmission zero emerges, and the spatial variable can thus be inferred.

This paper proposes angular displacement and velocity sensors consisting of a microstrip line loaded with an electric-LC (ELC) resonator [8], based on the aforementioned symmetry properties. The proposed implementation is an alternative to the coplanar waveguide (CPW) microwave sensors reported in [7], and particularly suited in systems that require backside isolation. A discussion on the performance of the considered symmetry-based approach can be found in [7].

Manuscript received October 18, 2013; revised December 11, 2013; accepted December 16, 2013. Date of publication December 20, 2013; date of current version February 12, 2014. This work was supported in part by the projects TEC2010-17512, EMET CSD2008-00066, TEC2011-13615-E, 2009SGR-421 and in part by the FPU under Grant AP2010-0431. The associate editor coordinating the review of this paper and approving it for publication was Dr. Francis P. Hindle.

The authors are with the Departament d'Enginyeria Electrònica, GEMMA/CIMITEC, Universitat Autònoma de Barcelona, Bellaterra 08193, Spain (e-mail: jordi.naqui@uab.cat; ferran.martin@uab.es).

Color versions of one or more of the figures in this letter are available online at http://ieeexplore.ieee.org.

Digital Object Identifier 10.1109/JSEN.2013.2295518

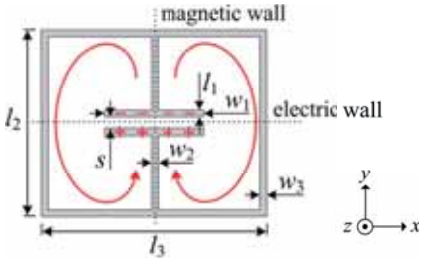

Fig. 1. Typical topology of an ELC resonator. A sketch of the current and charge pattern at the fundamental resonance is indicated.

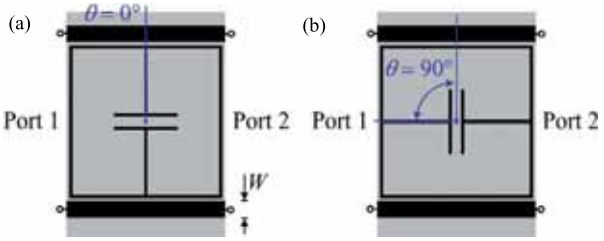

Fig. 2. Parallel microstrip lines loaded with an ELC resonator for the two extreme cases of angular orientation; (a) $\theta = 0°$ and (b) $\theta = 90°$.

II. Principle of Operation

An ELC resonator is composed of two connected metallic loops with a common gap (Fig. 1). The resonator is bisymmetric, and exhibits electric and magnetic walls in orthogonal planes at the fundamental resonance. Fig. 2 illustrates an ELC resonator symmetrically etched between a pair of parallel microstrip lines. Let us consider that the line pair is fed by a common-mode signal, so that the symmetry plane (i.e., the midplane) behaves as a magnetic wall. As proven in [9], the line is transparent to signal transmission if the ELC electric wall is aligned with the symmetry plane of the lines [Fig. 2(a)]. Contrarily, a transmission zero arises if the alignment is with the ELC magnetic wall [Fig. 2(b)]. In the former situation, the fundamental ELC resonance cannot be excited. However, the resonator is strongly coupled (magnetically) to the lines if the magnetic walls are aligned. Such behavior, explained through equivalent circuit models in [9], suggests that rotations with a 90° dynamic range can be measured from the common-mode transmission coefficient.

III. Angular Displacement and Velocity Sensors

An angular displacement sensor inspired on the ELC-loaded parallel microstrip line pair operating in common-mode was designed (Fig. 3). However, rather than using a common-mode source, a T-junction power divider cascaded to another

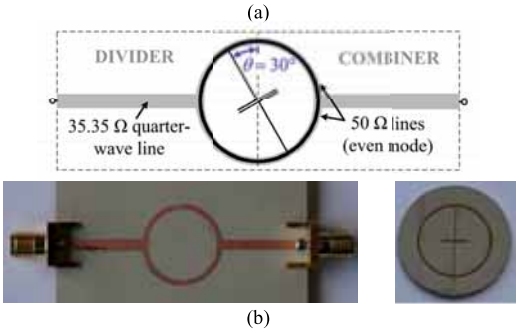

Fig. 3. Angular displacement sensor. (a) Layout, and (b) photograph. The substrates are *Rogers RO3010* with dielectric constant $\varepsilon_r = 11.2$, thickness $h = 1.27$ mm (microstrip line) and $h = 0.635$ mm (resonator), and loss tangent $\tan\delta = 0.0023$. The line widths W are 2.06 mm and 1.04 mm. ELC mean radius $r_0 = 8.05$ mm, $w_1 = 6$ mm, $w_2 = l_1 = s = 0.2$ mm, and $w_3 = 0.5$ mm.

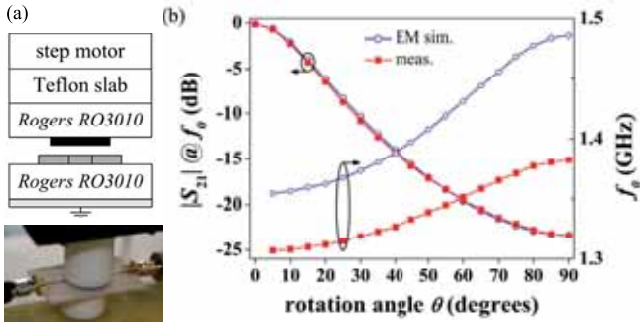

Fig. 4. (a) Experimental set-up, and (b) notch magnitude and frequency versus the angular displacement. The frequency shift is attributed to substrate and fabrication tolerances (f_0 is very sensitive to the resonator parameters).

one acting as a combiner was used. Thus, by feeding the structure with a single-ended signal, the divider acts as a single-ended to common-mode signal transition. Conversely, the combiner converts the common-mode signal into a single-ended signal. The circularly-shaped lines exhibit 50 Ω even-mode characteristic impedance. The combiner/divider is implemented with 35.35 Ω impedance inverters (quarter wavelength lines at 1.45 GHz) to achieve matching to 50 Ω reference ports. The circular 50 Ω line pair (which is the active part of the transducer and hence responsible for resonator coupling) must be arranged face-to-face with the ELC external ring in order to enhance electromagnetic coupling. Furthermore, the line pair as well as the resonator was circularly-shaped to enhance linearity.

Undesired common-to-differential mode conversion may arise for asymmetric loadings (i.e., $0° < \theta < 90°$). Mode conversion in [7] was cancelled by air bridges cascaded at both sides of the ELC. In the present implementation, the divider/combiner indeed suppresses the differential mode. However, if the circularly-shaped lines are electrically long, mode mixing is generated along them. In order to reduce electrically the size of these lines at resonance, the electrical size of the resonator was decreased by using a high dielectric constant substrate ($\varepsilon_r = 11.2$). The displacement measurement was performed following the procedure in [7] [see Fig. 4(a)].

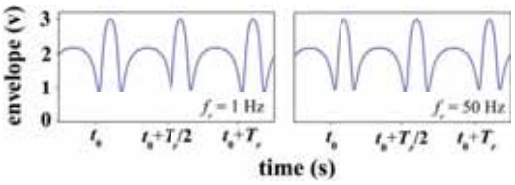

Fig. 5. Angular velocity measurements for an arbitrary initial time t_0.

The ELC substrate was attached to a step motor through a Teflon slab with 3.5 mm thickness and dielectric constant $\varepsilon_r = 2.08$. The air gap between the ELC and the microstrip lines was set to 0.254 mm. As shown in Fig. 4(b), the rotation angle can be sensed from the notch magnitude and frequency, being the dependence reasonably linear.

Let us now consider that the ELC is continuously rotating. To obtain the angular velocity, ω_r, the set-up reported in [7] was used. Specifically, a harmonic signal tuned at the notch frequency corresponding to $\theta = 10°$ ($f_0 = 1.308$ GHz) was injected to the input port, whereas an isolator plus an envelope detector were cascaded to the output port. The step motor was configured with $f_r = 1$ Hz and 50 Hz ($\omega_r = 2\pi f_r$). The envelope signals (which are dependent on the transmission coefficient) were captured by an oscilloscope (Fig. 5), and the velocities were derived from the time difference between consecutive transmission peaks $T_m = T_r/2 = 1/2 f_r$. The measured velocities ($f_r = 0.998$ Hz and 50.251 Hz) validate the approach.

In summary, a novel microstrip sensor to measure angular displacements and velocities has been proposed. Rotation speeds as high as required can be measured, and precision can be improved by averaging the time between peaks.

REFERENCES

[1] C. Mandel, B. Kubina, M. Schüßler, and R. Jakoby, "Passive chipless wireless sensor for two dimensional displacement measurement," in *Proc. 41st Eur. Microw. Conf.*, Manchester, U.K., Oct. 2011, pp. 79–82.

[2] J. Naqui, M. Durán-Sindreu, and F. Martín, "Alignment and position sensors based on split ring resonators," *Sensors*, vol. 12, pp. 11790–11797, Aug. 2012.

[3] J. Naqui, M. Durán-Sindreu, and F. Martín, "On the symmetry properties of coplanar waveguides loaded with symmetric resonators: Analysis and potential applications," in *Proc. IEEE MTT-S Int. Microw. Symp.*, Montreal, QC, Canada, Jun. 2012, pp. 1–3.

[4] A. Horestani, C. Fumeaux, S. Al-Sarawi, and D. Abbott, "Displacement sensor based on diamond-shaped tapered split ring resonator," *IEEE Sensors J.*, vol. 13, no. 4, pp. 1153–1160, Apr. 2013.

[5] A. Horestani, D. Abbott, and C. Fumeaux, "Rotation sensor based on horn-shaped split ring resonator," *IEEE Sensors J.*, vol. 13, no. 8, pp. 3014–3015, Aug. 2013.

[6] J. Naqui, M. Durán-Sindreu, and F. Martín, "Transmission lines loaded with bisymmetric resonators and applications," in *Proc. IEEE MTT-S Int. Microw. Symp.*, Seattle, WA, USA, Jun. 2013, pp. 1–3.

[7] J. Naqui and F. Martín, "Transmission lines loaded with bisymmetric resonators and their application to angular displacement and velocity sensors," *IEEE Trans. Microw. Theory Tech.*, vol. 61, no. 12, pp. 4700–4713, Dec. 2013.

[8] D. Schurig, J. J. Mock, and D. R. Smith, "Electric-field-coupled resonators for negative permittivity metamaterials," *Appl. Phys. Lett.*, vol. 88, no. 4, pp. 041109-1–041109-3, 2006.

[9] J. Naqui, M. Durán-Sindreu, and F. Martín, "Selective mode suppression in microstrip differential lines by means of electric-LC (ELC) and magnetic-LC (MLC) resonators," *Appl. Phys. A*, Oct. 2013.

Article IJAP13

Differential and Single-Ended Microstrip Lines loaded with Slotted Magnetic-LC Resonators

J. Naqui, M. Durán-Sindreu, and F. Martín

Hindawi Publishing Corporation
International Journal of Antennas and Propagation
Volume 2013, Article ID 640514, 8 pages
http://dx.doi.org/10.1155/2013/640514

Research Article

Differential and Single-Ended Microstrip Lines Loaded with Slotted Magnetic-LC Resonators

J. Naqui, M. Durán-Sindreu, and F. Martín

GEMMA/CIMITEC, Departament d'Enginyeria Electrònica, Universitat Autònoma de Barcelona, Bellaterra, 08193 Barcelona, Spain

Correspondence should be addressed to F. Martín; ferran.martin@uab.es

Received 28 February 2013; Revised 25 April 2013; Accepted 20 May 2013

Academic Editor: Sha Luo

This paper is focused on magnetic-LC (MLC) resonators, namely, slotted resonators that can be considered the complementary counterparts of the so-called electric-LC (ELC) resonators. Both resonators exhibit two symmetry planes (i.e., they are bisymmetric), one of them being an electric wall and the other a magnetic wall at the fundamental resonance. Therefore, compared to other electrically small resonators such as folded stepped impedance resonators (SIRs), split ring resonators (SRRs), and their complementary counterparts, MLC and ELC resonators exhibit a very rich phenomenology. In this paper, single-ended microstrip lines and differential microstrip lines loaded with MLC resonators are studied, and potential applications are highlighted.

1. Introduction

Split-ring resonators (SRRs) [1, 2] and their complementary counterparts (CSRRs) [3] (Figure 1) have been extensively used for the implementation of metamaterials and many devices based on them [4]. SRRs can be excited by means of a uniform axial (z direction) time-varying magnetic field and/or by an electric field applied in the plane of the particle (y direction); that is, the particle exhibits bianisotropy [5]. The distribution of charges at the fundamental resonance (see Figure 1(a)) reveals that the symmetry plane of the SRR is an electric wall at that frequency. From duality considerations, it follows that the CSRR can be excited through an axial electric field and/or a magnetic field applied in the y direction, whose symmetry plane behaves as a virtual magnetic wall at the fundamental resonance [6]. Capacitively loaded (C loaded) loops and folded stepped impedance resonators (SIRs), and their complementary counterparts (Figure 2), exhibit a similar phenomenology when they are illuminated with properly polarized radiation to drive the particles.

As long as SRRs, C-loaded loops, folded SIRs, and their dual particles are electrically small, they can be used for the implementation of effective media metamaterials. Specifically, SRRs, C-loaded loops, and folded SIRs are useful for the implementation of negative permeability media following the Lorentz model [1, 7], whereas CSRRs, complementary C-loaded loops, and complementary SIRs can be used as building blocks for the implementation of negative permittivity artificial media [3, 8]. However, resonant-type negative permittivity media can also be achieved by means of metallic particles, as it was pointed out by Schurig and co workers [9]. The particle reported in [9] and depicted in Figure 3 was called electric-LC (ELC) resonator. It was argued that such particle cannot be excited by means of a uniform axial magnetic field since the currents in both loops are opposite at the fundamental resonance; namely, the instantaneous current is clockwise in one of the loops and counterclockwise in the other one. This means that, at the fundamental resonance, the ELC does not exhibit a net magnetic dipole moment in the axial direction, and for such reason it cannot be driven by means of a uniform axial time-varying magnetic field. However, an electric dipole moment appears in the orthogonal direction to the electric wall (indicated in Figure 3), which means that the ELC can be excited through a uniform time-varying electric field applied to that direction. This is the reason that explains the terminology used to designate this particle, which prevents bianisotropy. Notice also that there is another symmetry plane in the particle that acts as a magnetic

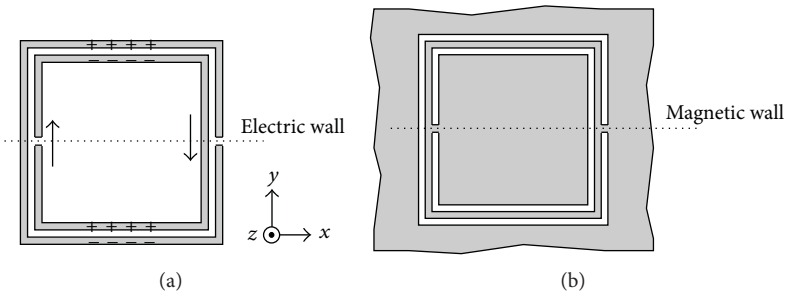

Figure 1: Typical topology of an SRR (a) and a CSRR (b). A sketch of the currents and the distribution of charges for the SRR at the fundamental resonance is also indicated (notice that the symmetry plane is an electric wall). From Babinet's principle, it follows that the CSRR exhibits a magnetic wall at the symmetry plane.

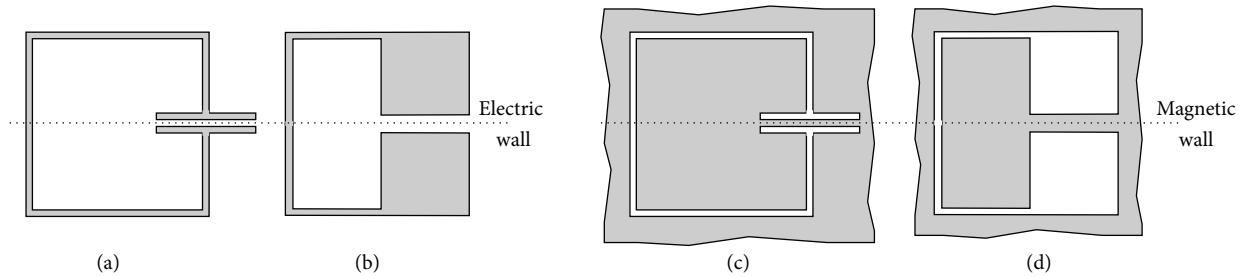

Figure 2: Typical topology of a capacitively loaded loop (a), a folded SIR (b), a complementary capacitively loaded loop (c), and a complementary folded SIR (d).

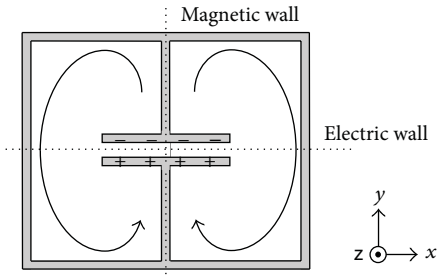

Figure 3: Typical topology of an ELC resonator, indicating the electric and magnetic walls and a sketch of the currents and the charge distribution at the fundamental resonance.

wall at the fundamental resonance by virtue of the symmetry in the currents and charges with regard to that plane.

The previous electrically small resonators, including the ELC, can also be used as loading resonant elements in planar transmission lines, where the fields are no longer uniform. In particular, for the ELC, if the driving fields are not uniform, it is also possible to magnetically drive the particle. This can be achieved, for instance, by forcing opposite magnetic flux lines in the loops of the ELC. According to this, the ELC can be a very interesting and useful particle as a loading element in planar transmission lines. However, the main focus in this paper is the study of the dual particle of the ELC, that is, the magnetic-LC (MLC) resonator. This is a slot resonator that can be etched in the ground plane of a single-ended microstrip or a differential microstrip line. The analysis of this particle as well as the potential applications in microstrip configuration, is the main objective of the present work.

2. Magnetic-LC (MLC) Resonators

A typical topology of a square-shaped MLC resonator is depicted in Figure 4(a). It is the negative image of the ELC. Hence, by applying the Babinet's principle, it follows that the MLC can be excited by means of a time-varying magnetic field applied in the plane of the particle (y direction), but not by a uniform electric field normal to the particle plane (which is the usual driving mechanism in CSRRs [3] and in the complementary structures of Figure 2).

Like the ELC, the MLC exhibits two symmetry planes, one being a magnetic wall and the other an electric wall at the fundamental resonance. However, notice that the magnetic and electric walls are rotated 90° compared to those of the ELC. If the aspect ratio of the slot widths w_1/w_2 is high enough, a quasistatic approximation can be made, and the particle can be described by means of a lumped element-equivalent circuit model, depicted in Figure 4(b). The inductance L_m accounts for the inductive path connecting the two inner metallic regions of the particle. This inductance is parallel connected to the capacitances designated as C_m that model the slots present between both inner halves of the MLC. Finally, the edge capacitance of the external square-shaped slot ring is called C_g, and it can be divided into the capacitances of the two MLC halves, as depicted in Figure 4(b).

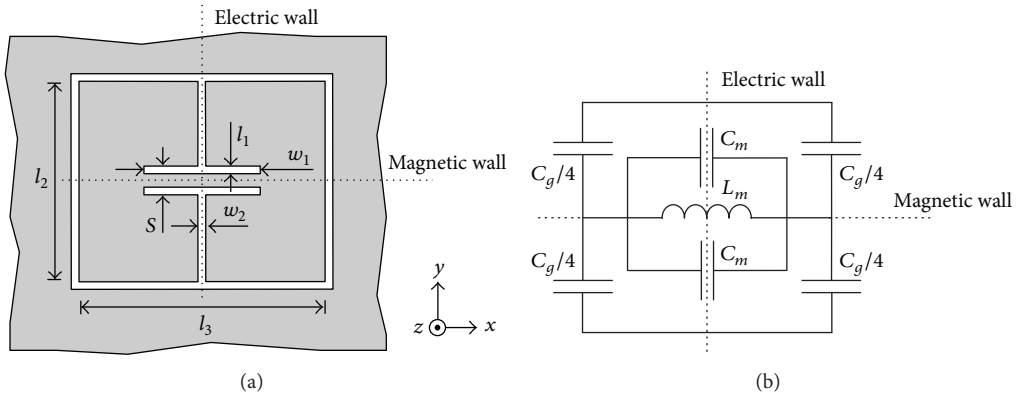

FIGURE 4: Typical topology of an MLC (a) and its equivalent circuit model (b). The relevant dimensions and the electric and magnetic walls are indicated.

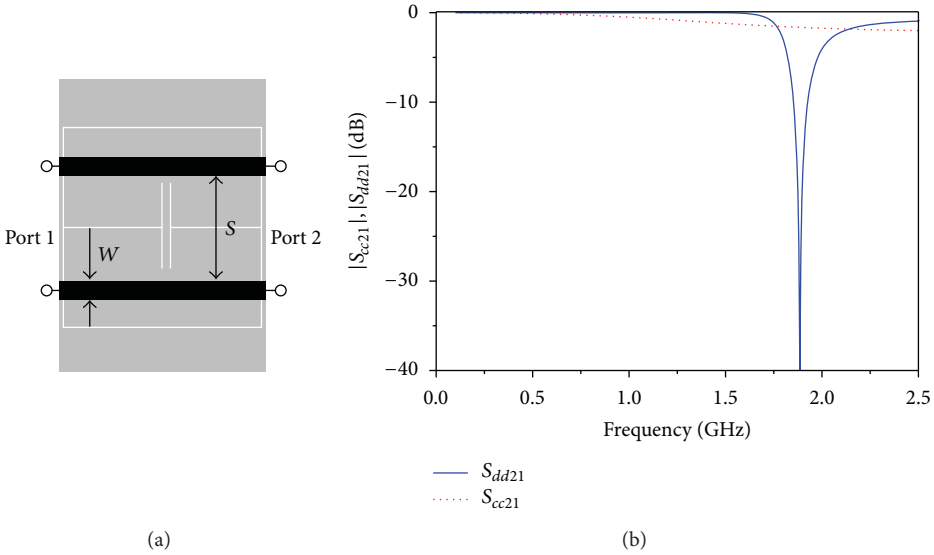

FIGURE 5: Differential microstrip line loaded with an MLC with the electric wall aligned with the line (a) and frequency response (transmission coefficient) for the common (S_{cc21}) and differential (S_{dd21}) modes (b). The substrate is *Rogers RO3010* with thickness $h = 1.27$ mm and dielectric constant $\varepsilon_r = 11.2$. The line dimensions are $W = 1$ mm and $S = 5$ mm, corresponding to a 50 Ω odd-mode impedance without the presence of the MLC. The MLC dimensions are $w_1 = 4$ mm, $w_2 = l_1 = s = 0.2$ mm, and $l_2 = l_3 = 10$ mm.

Compared to the other complementary structures shown in Figures 1 and 2, which exhibit a magnetic wall at its unique symmetry plane, the MLC exhibits not only a magnetic wall, but also an electric wall, and this additional wall can be useful in certain applications, as it is discussed in the next sections.

3. Single-Ended Microstrip and Differential Microstrip Lines Loaded with MLCs

The unusual electric wall that the MLC exhibits at resonance (in comparison to other slotted resonators) opens new research lines. Let us now consider the MLC loading both single-ended microstrip and differential microstrip transmission lines by assuming that the electric wall of the MLC is aligned with the symmetry plane of the lines.

3.1. Differential Microstrip Lines Loaded with MLCs. Figure 5(a) depicts a differential microstrip line loaded with an MLC with the electric wall aligned with the symmetry plane of the line. For the common mode, the symmetry plane of the line is a magnetic wall. Therefore, MLC excitation is not expected for this mode. Conversely, for the differential mode, there is an electric wall at the symmetry plane, and the MLC can be driven. The vertical components of the electric field generated by each individual line under differential mode operation are contra directional (i.e., upwards in one line and downwards in the other line of the pair). Therefore, as long as each inner half of the MLC is below each line of the differential pair, the particle can be excited by the non uniform electric field generated under differential mode excitation. This behavior has been verified through the electromagnetic

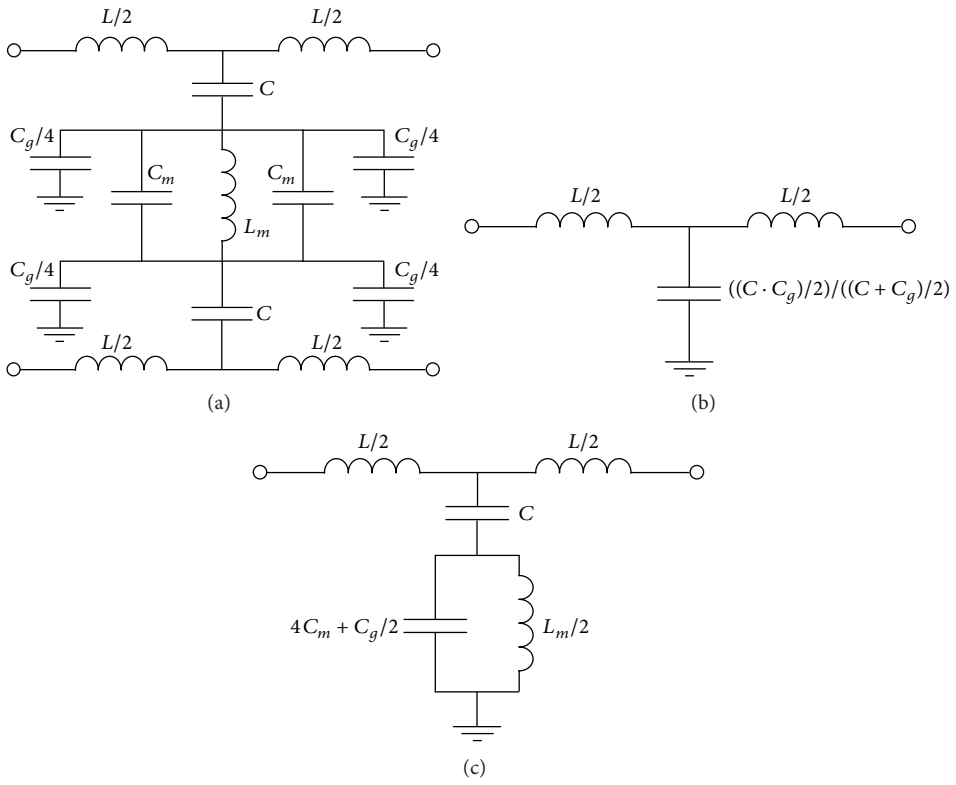

Figure 6: (a) Lumped element-equivalent circuit model of a differential microstrip line loaded with an MLC with the electric wall aligned with the line; (b) circuit model for the even mode, where the symmetry plane is an open circuit; (c) circuit model for the odd mode, the symmetry plane being a short circuit.

simulation of the structure depicted in Figure 5(a) by means of the *Agilent Momentum* commercial software for both the common and the differential mode (see Figure 5(b)). As expected, the differential line is roughly transparent for the common mode, but it exhibits a notch in the transmission coefficient for the differential mode.

The circuit model of the structure of Figure 5(a) is depicted in Figure 6, where the equivalent circuits for the odd (or differential) and even (or common) modes are also included. The model includes the elements describing the MLC, plus the line inductance L and capacitance C. Actually, the former is the line inductance with the presence of the MLC and the later accounts for the electric coupling between the line and the MLC. As it can be appreciated, for the common mode there is no transmission zero even though the shunt capacitance is modified. On the contrary, for the differential mode, the resulting model is the same as that for a CSRR-loaded microstrip line which exhibits a transmission notch [10]. In order to validate the model for the differential mode, we have considered the structure depicted in Figure 7(a) which is electrically smaller at resonance than that in Figure 5(a) mainly by virtue of the higher aspect ratio w_1/w_2 (by enlarging the capacitor length l_1 also achieves an electrical size reduction). Under these conditions, it is expected that the model is valid in a wider frequency range. We have performed the full-wave electromagnetic simulation of the structure for the differential mode, and we have extracted the elements of that model by means of a procedure reported elsewhere [10]. Qualitatively, that technique is based on measurable characteristics of the transmission and reflection coefficients provided by the electromagnetic simulation. Briefly, the lumped elements are obtained by means of the following conditions: (i) the transmission zero frequency corresponds to the frequency that the shunt impedance nulls, (ii) the frequency for which the shunt admittance vanishes is the resonant frequency of the parallel tank, (iii) the frequency whose phase of the transmission coefficient is $\pi/2$ is where the series and the shunt impedances are conjugate, and (iv) the intersection between the reflection coefficient and the unit normalized resistance circle gives the series impedance. The electromagnetic simulation and the circuit simulation of the equivalent circuit model using the extracted parameters are depicted in Figure 7(b). As can be seen the agreement is good, hence validating the proposed model of the MLC-loaded differential microstrip line.

3.2. Single-Ended Microstrip Lines Loaded with MLCs. Let us now consider the MLC loading a single-ended microstrip transmission line, as depicted in Figure 8. Since the symmetry plane is a magnetic wall, the MLC cannot be excited. The proposed circuit model is depicted in Figure 9(a), which is similar to that reported in [11] for folded SIR-loaded coplanar waveguides. After applying the magnetic wall concept, this circuit model can be simplified as Figure 9(b) illustrates;

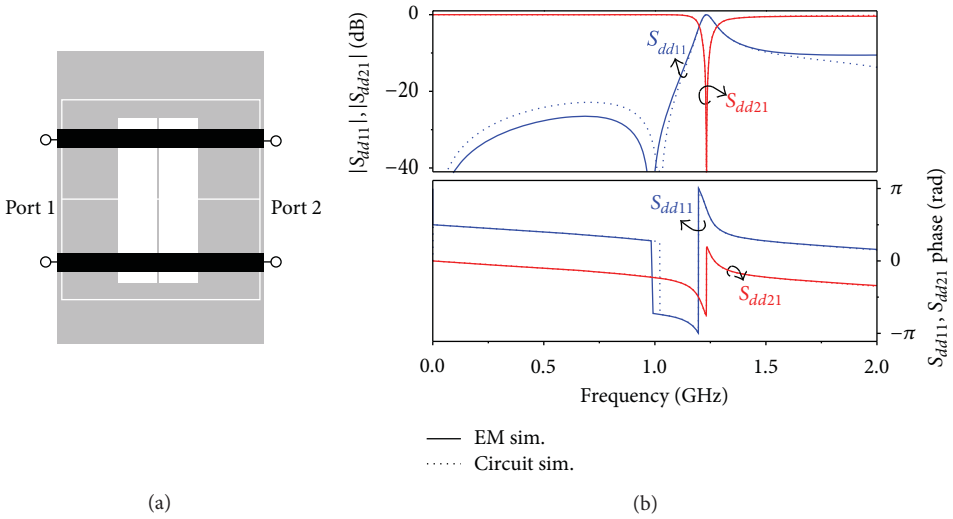

Figure 7: Layout (a) and differential mode frequency response (b) for a differential microstrip line loaded with an MLC with the electric wall aligned with the line and for its circuit model of Figure 6. The dimensions and the substrate are the same as those given in the caption of Figure 5, except for $l_1 = 2$ mm and $w_1 = 8$ mm. The circuit parameters are $L = 6.07$ nH, $C = 1.53$ pF, $4C_m + C_g/2 = 7.47$ pF (where for dimensions $C_g \approx 14C_m$), and $L_m = 3.71$ nH.

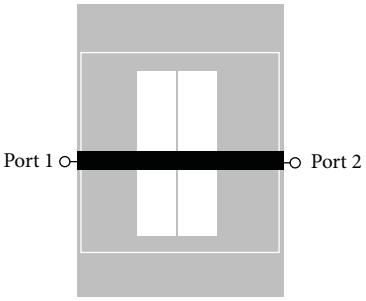

Figure 8: Microstrip line loaded with an MLC with the electric wall aligned with the line. The dimensions and the substrate are the same as those considered in Figure 7.

that is, it is a transmission line model with modified shunt capacitance. However, a notch in the transmission coefficient is not expected according to this model.

The interest in these single-ended microstrip transmission lines loaded with MLCs may be the truncation of symmetry, for instance, by means of a lateral displacement of the particle. In this case, the symmetry planes are no longer aligned, and the particle can be excited by the electric field generated by the line. The effect of this symmetry truncation by laterally shifting the MLC can be taken into account in the model of Figure 9(a) by simply considering the coupling capacitances (i.e., C_1 and C_2) as variable capacitances. From the circuit model viewpoint, these asymmetric values of the coupling capacitances allow current flowing through the MLC inductance and capacitance, and hence the particle is electrically driven by the line. As reported in [11], such kind of circuit can be useful for the implementation of displacement sensors or radio frequency (RF) barcodes.

We have simulated the structure of Figure 8 by considering two different lateral displacements (0.5 and 2 mm) of the MLC. The results are depicted in Figure 10. In order to extract the lumped element values of its circuit model, as a starting point we consider the values given in the caption of Figure 7 since the same dimensions and substrate are considered. Afterwards, we have adjusted the variable coupling capacitances by curve fitting the electromagnetic simulation, which depend on the amount of displacement. The other elements of the circuit left nearly unaltered (a slight optimization may be required), except for the line inductance which is also modified by the position of the slotted resonator. The circuit simulations, also depicted in Figure 10, are in good agreement with the electromagnetic simulations. Therefore, the proposed model is validated, and it is demonstrated that the lateral shift of the MLC can be basically taken into account by modifying the coupling capacitances and the line inductance.

4. Potential Applications

Etched in the ground plane of differential microstrip lines, MLC resonators can be used for the implementation of balanced notch filters and stop-band filters. This functionality is clear to the light of the results depicted in Figure 7, where a notch for the differential mode appears in the vicinity of the fundamental resonance of the MLC. The rejection band can be widened by etching further MLC resonators with slightly different resonance frequency (as reported in [12] for the design of SRR-based CPW stopband filters) or with identical resonance frequency but separated by a small distance in order to enhance interresonator's coupling (as discussed in [13] in reference to common mode suppression in differential lines by means of CSRRs).

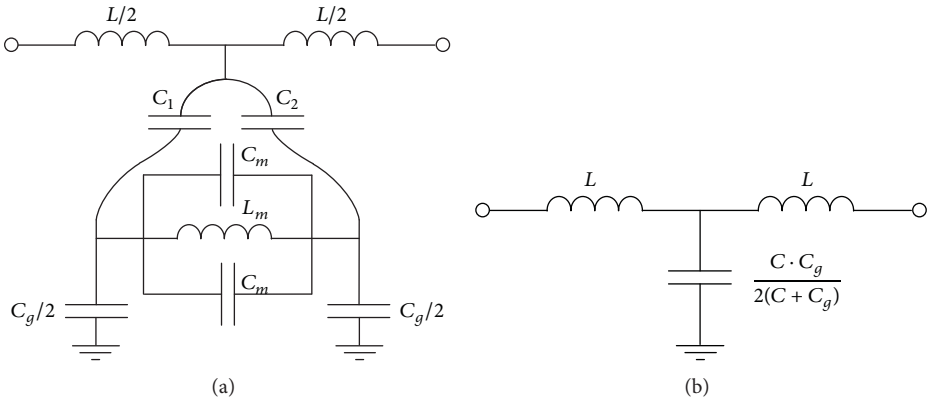

FIGURE 9: (a) Lumped element-equivalent circuit model of a microstrip line loaded with an MLC whose electric wall is aligned with or laterally displaced with regard to the line; (b) circuit model after applying the magnetic wall concept under the assumption of alignment, that is, $C_1 = C_2 = C/2$.

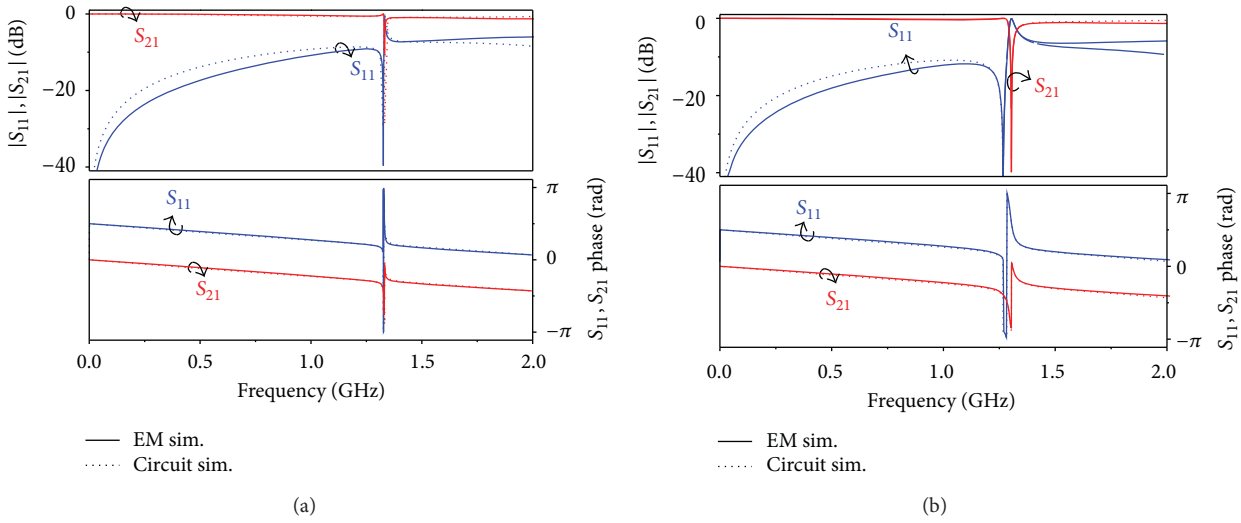

FIGURE 10: Frequency response for the structure of Figure 8 that results by laterally shifting the MLC 0.5 mm (a) and 2 mm (b) and for its circuit model of Figure 9. The circuit parameters are $L_m = 3.71$ nH and $C_g = 9.5$ pF; for 0.5 mm, $L = 9.48$ nH, $C_1 = 0.89$ pF, $C_2 = 0.36$ pF, and $C_m = 0.59$ pF; for 2 mm, $L = 8.94$ nH, $C_1 = 1.36$ pF, $C_2 = 0.083$ pF, and $C_m = 0.66$ pF.

With regard to microstrip lines loaded with MLCs, we can take benefit of the effects of a lateral shift (or another means of symmetry truncation) in the transmission coefficient. Namely, the line is transparent if the electric wall of the MLC is perfectly aligned with the symmetry plane of the line. However, a notch appears when the MLC is shifted in the transverse direction, and the bandwidth and magnitude of the notch increase with the displacement (see Figure 10). Similarly, a notch is expected if the MLC is not displaced, but it is nonsymmetrically loaded with a certain dielectric load. Thus, the structure can be used for sensing purposes [14–17]. Furthermore, microstrip lines loaded with multiple MLCs can be used as RF bar codes, where each bit is associated to a certain resonator (and its resonance frequency), and the logic states "1" or "0" are simply set by etching the MLCs symmetrically or laterally shifted or by other means of truncating the symmetry (RF bar codes not based on such a symmetry approach were reported in [18]). As an example, Figure 11(a) shows a photograph of a 3-bit bar code with the central MLC aligned with the line and the external ones laterally displaced (corresponding to the code "101"). The frequency response is depicted in Figure 11(b) and exhibits a transmission zero at the frequencies of the external resonators, in coherence with the considered codification. The resonators were designed to achieve relatively narrow notches, thus diminishing interference between adjacent notches (this is a key issue to bits embedding and the related spectral band efficiency). Even though the notch level (intimately related to the bandwidth) is not very deep, this is not a critical drawback in binary bar codes. It is also interesting to mention that compared to CPW-based RF-bar codes, implemented by means of folded SIRs or SRRs (they also exhibit an electric wall at their symmetry plane) [11], the proposed bar code is more simple since no parasitic modes

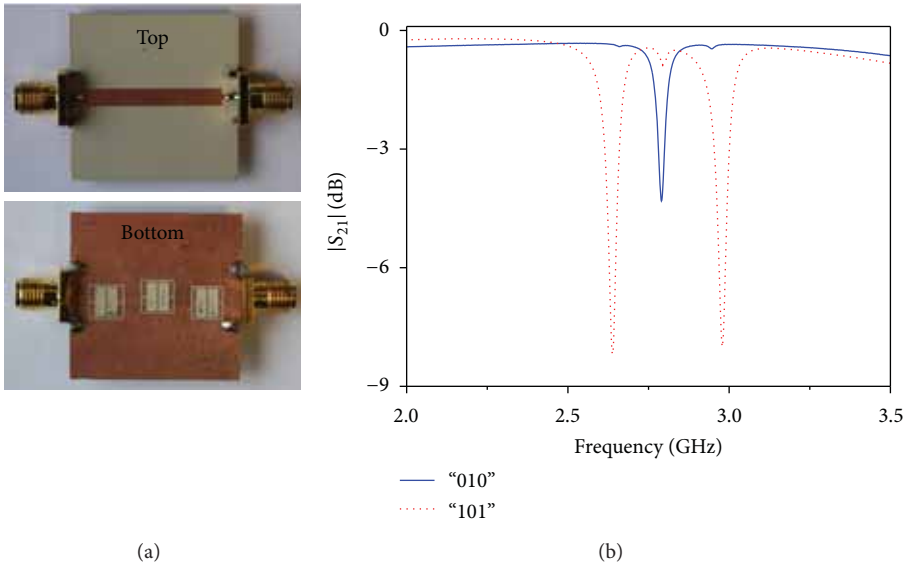

FIGURE 11: Photograph of a 3-bit RF bar code (codified as "101") (a) and measured frequency response (b). For completeness, the measurement for the code "010" is also shown. The substrate is *Rogers RO3010* with thickness $h = 1.27$ mm, dielectric constant $\varepsilon_r = 11.2$, and loss tangent $\tan\delta = 0.0023$. The line width is designed to minimize the insertion loss with the presence of the MLCs symmetrically etched, that is, $W = 3.13$ mm. The MLC dimensions are $w_1 = 5.2$ mm, $w_2 = s = 0.2$ mm, $l_1 = 1.9$ mm, $l_2(2.6\,\text{GHz}) = 6.32$ mm, $l_2(2.8\,\text{GHz}) = 6$ mm, $l_2(3\,\text{GHz}) = 5.72$ mm, and $l_3 = 6$ mm. The distance between adjacent resonators is set to that for which interresonator coupling can be neglected, that is, 3 mm. The lateral displacement to set the logic state "1" is 1 mm.

are generated by displacing the MLCs (in contrast, air bridges were necessary in the CPW bar codes reported in [11]). Alternatively, codification can be achieved by symmetrically etching the MLCs and truncating symmetry in the required resonator by adding adhesives with metallic or dielectric loads.

5. Conclusions

In conclusion, it has been shown that the MLC is a slot resonator that exhibits two symmetry planes, one being a magnetic wall and the other one an electric wall at the fundamental resonance. Given that other related slot resonators do not exhibit any electric wall, this paper focuses on such wall, which brings a wider variety of applications. If the driving fields of the particle are uniform, the MLC cannot be excited by an electric field orthogonal to the particle plane, but by means of a magnetic field in the plane of the particle. However, it has been shown that, in single-ended microstrip lines and differential microstrip lines, where the fields are no longer uniform, the MLC can be electrically excited. Equivalent circuit models of both differential and single-ended microstrip lines loaded with MLCs with the electric wall aligned with the symmetry plane of the lines have been reported and validated. Finally, some applications have been highlighted, including balanced notch filters, as well as sensors and bar codes based on the truncation of symmetry.

Acknowledgments

This work has been supported by MINECO, Spain (Projects TEC2010-17512, CSD2008-00066, and TEC2011-13615-E) and by AGAUR-*Generalitat de Catalunya*, through Project 2009SGR-421. Jordi Naqui is also in debt to MINECO Spain for supporting his work through the FPU Grant AP2010-0431.

References

[1] J. B. Pendry, A. J. Holden, D. J. Robbins, and W. J. Stewart, "Magnetism from conductors and enhanced nonlinear phenomena," *IEEE Transactions on Microwave Theory and Techniques*, vol. 47, no. 11, pp. 2075–2084, 1999.

[2] F. Martín, J. Bonache, F. Falcone, M. Sorolla, and R. Marqués, "Split ring resonator-based left-handed coplanar waveguide," *Applied Physics Letters*, vol. 83, no. 22, pp. 4652–4654, 2003.

[3] F. Falcone, T. Lopetegi, J. D. Baena, R. Marqués, F. Martín, and M. Sorolla, "Effective negative-ε stopband microstrip lines based on complementary split ring resonators," *IEEE Microwave and Wireless Components Letters*, vol. 14, no. 6, pp. 280–282, 2004.

[4] R. Marqués, F. Martín, and M. Sorolla, *Metamaterials with Negative Parameters: Theory, Design and Microwave Applications*, John Wiley & Sons, New York, NY, USA, 2008.

[5] R. Marques, F. Medina, and R. Rafii-El-Idrissi, "Role of bi-anisotropy in negative permeability and left handed metamaterials," *Physical Review B*, vol. 65, paper 144441, 2002.

[6] J. D. Baena, J. Bonache, F. Martín et al., "Equivalent-circuit models for split-ring resonators and complementary split-ring resonators coupled to planar transmission lines," *IEEE Transactions on Microwave Theory and Techniques*, vol. 53, no. 4, pp. 1451–1460, 2005.

[7] D. R. Smith, W. J. Padilla, D. C. Vier, S. C. Nemat-Nasser, and S. Schultz, "Composite medium with simultaneously negative

permeability and permittivity," *Physical Review Letters*, vol. 84, no. 18, pp. 4184–4187, 2000.

[8] F. Falcone, T. Lopetegi, M. A. G. Laso et al., "Babinet principle applied to the design of metasurfaces and metamaterials," *Physical Review Letters*, vol. 93, no. 19, Article ID 197401, 2004.

[9] D. Schurig, J. J. Mock, and D. R. Smith, "Electric-field-coupled resonators for negative permittivity metamaterials," *Applied Physics Letters*, vol. 88, no. 4, Article ID 041109, pp. 1–3, 2006.

[10] J. Bonache, M. Gil, I. Gil, J. Garcia-García, and F. Martín, "On the electrical characteristics of complementary metamaterial resonators," *IEEE Microwave and Wireless Components Letters*, vol. 16, pp. 543–545, 2006.

[11] J. Naqui, M. Durán-Sindreu, and F. Martín, "On the symmetry properties of coplanar waveguides loaded with symmetric resonators: analysis and potential applications," in *Proceedings of IEEE MTT-S International Microwave Symposium*, Montreal, Canada, June 2012.

[12] F. Martín, F. Falcone, J. Bonache, R. Marqués, and M. Sorolla, "Miniaturized coplanar waveguide stop band filters based on multiple tuned split ring resonators," *IEEE Microwave and Wireless Components Letters*, vol. 13, no. 12, pp. 511–513, 2003.

[13] J. Naqui, A. Fernández-Prieto, M. Durán-Sindreu et al., "Common mode suppression in microstrip differential lines by means of complementary split ring resonators: theory and applications," *IEEE Transactions on Microwave Theory and Techniques*, vol. 60, pp. 3023–3034, 2012.

[14] C. Mandel, B. Kubina, M. Schusler, and R. Jakoby, "Passive chipless wireless sensor for two-dimensional displacement measurement," in *Proceedings of the 14th European Microwave Conference (EuMC '11)*, pp. 79–82, October 2011.

[15] J. Naqui, M. Durán-Sindreu, and F. Martín, "Alignment and position sensors based on split ring resonators," *Sensors*, vol. 12, pp. 11790–11797, 2012.

[16] M. Puentes, M. Maasch, M. Schubler, and R. Jakoby, "Frequency multiplexed 2-dimensional sensor array based on split-ring resonators for organic tissue analysis," *IEEE Transactions on Microwave Theory and Techniques*, vol. 60, no. 6, pp. 1720–1727, 2012.

[17] A. Karami Horestani, C. Fumeaux, S. F. Al-Sarawi, and D. Abbott, "Displacement sensor based on diamond-shaped tapered split ring resonator," *IEEE Sensors Journal*, vol. 13, no. 4, pp. 1153–1160, 2013.

[18] S. Preradovic and N. C. Karmakar, "Chipless RFID: bar code of the future," *IEEE Microwave Magazine*, vol. 11, no. 7, pp. 87–97, 2010.

Article IJAP14

Mechanically Reconfigurable Microstrip Lines Loaded with Stepped Impedance Resonators and Potential Applications

J. Naqui and F. Martín

Hindawi Publishing Corporation
International Journal of Antennas and Propagation
Volume 2014, Article ID 346838, 8 pages
http://dx.doi.org/10.1155/2014/346838

Research Article

Mechanically Reconfigurable Microstrip Lines Loaded with Stepped Impedance Resonators and Potential Applications

J. Naqui and F. Martín

GEMMA/CIMITEC, Departament d'Enginyeria Electrònica, Universitat Autònoma de Barcelona, 08193 Bellaterra, Spain

Correspondence should be addressed to F. Martín; ferran.martin@uab.es

Received 15 January 2014; Accepted 16 January 2014; Published 20 February 2014

Academic Editor: Giacomo Oliveri

This paper is focused on exploring the possibilities and potential applications of microstrip transmission lines loaded with stepped impedance resonators (SIRs) etched on top of the signal strip, in a separated substrate. It is shown that if the symmetry plane of the line (a magnetic wall) is perfectly aligned with the electric wall of the SIR at the fundamental resonance, the line is transparent. However, if symmetry is somehow ruptured, a notch in the transmission coefficient appears. The notch frequency and depth can thus be mechanically controlled, and this property can be of interest for the implementation of sensors and barcodes, as it is discussed.

1. Introduction

The topic of metamaterials has experienced an exponential growth in the field of science and technology since 2000, when the first metamaterial structure (a one-dimensional left-handed medium) was reported [1]. In particular, metamaterial transmission lines (first reported in [2–4]) have attracted the attention of RF/microwave engineers, since such artificial lines exhibit further controllability than ordinary lines, and they can be used as building blocks for the implementation of microwave devices with small size and/or high performance and with novel functionalities as well [5–7].

There are nowadays many different approaches and types of metamaterial transmission lines. Among them, the so-called resonant type approach has been revealed to be very useful for the implementation of microwave components (including filters, dividers, and leaky wave antennas) [7]. Resonant type metamaterial transmission lines are implemented by loading a host line with electrically small resonant elements, typically, although not exclusively, split ring resonators (SRRs) [8, 9] and complementary split ring resonators (CSRRs) [10]. By loading a host line with a coupled (electrically, magnetically, or both) resonator, a notch in the transmission coefficient (at the fundamental frequency) appears, and such notch widens if the line is loaded with several resonators. The stopband characteristic exhibited in a transmission line loaded with an array of electrically small resonators has been interpreted as due to the negative effective permeability (SRRs) or permittivity (CSRRs) of the lines [9–11].

However, it is not necessary to invoke metamaterials theory to interpret and understand the stopband functionality of SRR or CSRR loaded lines. In most applications, the lines are loaded with a single resonator stage because this reduces size or suffices to achieve the required functionality. Indeed the modeling through equivalent circuits of transmission lines loaded with electrically small resonators, such as those aforementioned, has been a subject of an intensive study in the last years [11–16]. Certainly, transmission lines loaded with a single or with few resonators cannot be considered to be effective media metamaterials. However, in certain applications, the controllability of the dispersion and characteristic impedance of the loaded lines are fundamental to achieve the required functionality, and for this reason such lines are typically referred to as metamaterial transmission lines [17]. In other applications, the key point is to achieve stopband functionality. In these cases, as long as the considered resonators are electrically small and potentially useful

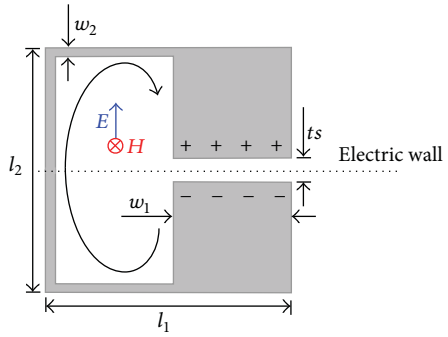

Figure 1: Typical topology of a folded SIR and relevant dimensions. The resonator can be excited by a time varying electric or magnetic field oriented in the indicated directions. The distribution of current and charges is also sketched.

for the implementation of effective media metamaterials, the lines are usually designated as transmission lines with metamaterial loading. The structures considered in this work belong to this category: microstrip lines loaded with stepped impedance resonators (SIRs). We have considered both folded SIRs and conventional SIRs coupled to the lines and separated from the signal strip of the line by means of a dielectric slab. It will be seen that the response of the SIR loaded lines can be tailored through mechanical actuation and potential applications of this effect are discussed.

2. Microstrip Lines Loaded with Stepped Impedance Resonators (SIRs)

Stepped impedance resonators are common planar resonators in microwave engineering [18]. Essentially SIRs are metallic open-ended strip resonators where the width of the strip is varied abruptly. In a trisection SIR, it is well known that by narrowing the central section and widening the external ones, the resonator can be made electrically small as compared to a uniform half wavelength resonator [18]. Additional miniaturization can be achieved by folding the SIR, as Figure 1 illustrates. It is important to mention, for the purposes of this paper, that the SIR exhibits an electric wall at the indicated (symmetry) plane (see Figure 1) at the fundamental resonance. Hence, the resonator exhibits an electric dipole perpendicular to the symmetry plane, and it can be excited through an electric field oriented in that direction. Moreover, in a folded SIR, as the one depicted in Figure 1, the current loop induces a magnetic dipole moment and therefore the resonator can also be magnetically driven (this is not the case in unfolded SIRs).

According to the previous statements, in a transmission line loaded with a folded SIR, the line-to-resonator coupling may be electric, magnetic, or mixed, whereas in a transmission line loaded with an unfolded SIR the magnetic coupling is prevented. For instance, it was demonstrated in [19] that in coplanar waveguide (CPW) transmission lines loaded with folded SIRs on the back side of the substrate (with meaningful line-to-resonator capacitances and thin substrates), the dominant line-to-resonator coupling mechanism is electric.

Regardless of the coupling mechanism, if both the resonator and the line are symmetric, there is a necessary condition for particle excitation: either the symmetry planes of the line and resonator are not aligned, or, if they are aligned, they must be of the same electromagnetic nature (either an electric wall or a magnetic wall). In other words, if the symmetry planes of the line and resonator are aligned and they are of distinct electromagnetic nature, then electromagnetic coupling capable of exciting the resonator does not arise. The result is a transmission coefficient for the loaded line close to 1 even at the fundamental resonance of the considered particle. This operating principle is universal, being independent of the line type, the resonator, and the resonator-to-line coupling mechanism [19, 20].

To gain more insight into this feature, let us consider a symmetric structure consisting of a microstrip line loaded with a folded SIR on top of the signal strip, with aligned symmetry planes. As mentioned above, the particle cannot be excited at the fundamental resonance, by neither the magnetic field nor the electric field generated by the line. Due to symmetry, the magnetic field components at both sides of the symmetry plane of the particle are perfectly cancelled, and the magnetic field is not able to induce circulating currents in the SIR. Analogously, for electric field excitation, a net component of the electric field orthogonal to the symmetry plane is required, and this is impossible due to the symmetry of the line and to the fact that the symmetry plane of the line is a magnetic wall. However, if the symmetry is broken, the perfect cancellation of fields vanishes, the particle is excited, and the incident power is partially reflected at the fundamental resonance, thus providing a notch in the transmission coefficient at that frequency.

3. Mechanical Reconfigurability of the SIR Loaded Microstrip Lines and Possible Applications

In order to symmetrically load a microstrip line with an SIR, three metal levels are required. A possible multilayer structure is the one depicted in Figure 2, with top and bottom substrates. To mechanically rupture the symmetry of the structure and thus achieve a notch in the transmission coefficient, there are several possibilities. For instance, the SIR and the line can be etched on different (movable) substrates with a relative motion. Thus, by laterally displacing the top substrate, symmetry is broken. Another interesting approach to rupture symmetry is by implementing the SIRs with deflectable cantilever type (movable) arms through microelectromechanical systems (MEMS) (similar to the reconfigurable SRR loaded lines reported in [21]). Any physical variable able to deflect the suspended parts of the SIR can potentially be detected/sensed through its effect on the transmission coefficient of the loaded line. Of course the MEMS-based SIRs can be actuated electronically, with the potential to implement reconfigurable notch filters. However, it is also possible to break symmetry through the effects of an external

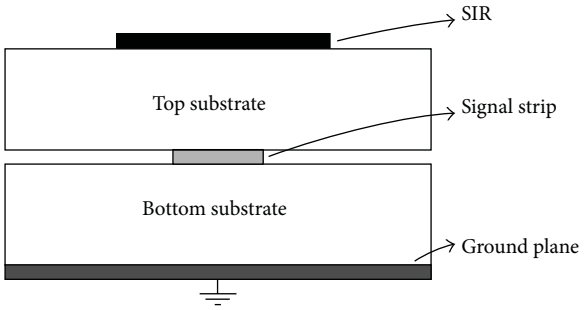

Figure 2: Cross-sectional view of a microstrip line loaded with an SIR, etched on top of it.

force, pressure, torque, and so forth. Alternatively, the effects of these variables can also be potentially sensed/detected by using malleable/flexible substrates, rather than deflectable SIRs. This eases the fabrication process and reduces costs. Finally, dielectric loading may be another strategy to rupture symmetry. The idea behind this approach is to add a material or substance on top of the SIR or in specific test regions of the structure (for instance, by creating symmetric holes inside the top substrate). As long as the material or substance exhibits a symmetric distribution of the dielectric permittivity, the line is transparent to signal propagation. However, if the dielectric loading is not symmetric, this can be detected by the appearance of a notch in the transmission coefficient. One possibility that this approach opens concerns the detection of defects or imperfections in certain substances by comparison to a reference or standard. This approach may be useful for analysis of substances, including organic tissues and microfluidics. Sensors for analysis of organic tissues and dielectric monitoring of microfluidic channels based on the frequency or quality-factor variation of resonant elements have recently been proposed (see, e.g., [22–24]).

4. Illustrative Preliminary Examples

In this section, two application examples of SIR loaded microstrip lines are reported. Firstly, the symmetry properties of such loaded lines are exploited as an encoding mechanism to implement an RF (radiofrequency) barcode. Secondly, the symmetry rupture is used as a sensing mechanism to design an alignment/displacement sensor.

4.1. RF Barcode. A multiresonator-based chipless radiofrequency identification (RFID) tag is an RF barcode where the information is stored in the so-called spectral signature of the tag. Such spectral signature is obtained by loading a transmission line with several resonators, each resonating at a different frequency [25]. Each resonator corresponds to a bit, and the logic "1" or "0" is chosen by the presence or absence of the notch at the resonance frequency (i.e., the encoding is in amplitude). By coupling the resonator to the line, the notch appears, giving the logic level "1." On the contrary, the notch can be prevented (logic level "0") by removing or short-circuiting the resonator (this shifts the resonance frequency outside the region of interest) [25]. An alternative to these conventional approaches is to align the symmetry planes of the line and resonator. Thus, by using a microstrip line loaded with folded SIRs, if the resonator symmetry plane is aligned with that of the line, the resonator is not coupled to the line and the notch at the fundamental resonance does not arise. Conversely, the logic "1" can be achieved, for instance, by laterally displacing the resonator. Under these conditions, the magnetic wall of the line and the electric wall of the resonator are not aligned, and the resonator is excited. Interestingly, as long as the SIRs can be laterally shifted independently, a reconfigurable barcode is potentially possible. Figure 3(a) depicts the top view of a microstrip line loaded with three folded SIRs, each designed to resonate at a different frequency. Notice that in this configuration the central SIR is aligned with the line, whereas the SIRs of the extremes are nonaligned. Therefore the line is encoded with the code "101." Figure 3(b) depicts the simulated frequency response (i.e., the spectral signature) of this structure and also the one corresponding to the complementary code, that is, "010," where the aligned SIRs are those of the extremes.

In the proposed barcode, the ground plane is kept unaltered, this being an advantage as compared to other proposals [26]. An important aspect to highlight is that the design of the line and SIRs does not require special attention, since the main purpose is to achieve narrow notches. This allows accommodating the maximum number of resonators (resonance frequencies) in a predefined frequency spectrum, thus embedding as many bits as possible. Narrow notches typically arise if the coupling between the line and the resonator is weak, as shown in the structure of Figure 3 (the reason is that the dominant electric coupling is poor because of the extremely narrow line). Conversely, in the next example, the aim is to obtain a high sensitivity of the notch magnitude (depth) with the lateral displacement, and this requires a specific design.

4.2. Alignment/Position Sensor. Let us now consider the application of SIR loaded microstrip lines to detect lack of lateral alignment or to measure lateral shift between two surfaces with relative motion to each other (other proposals can be found in [27, 28]). In this case, a figure of merit is the sensitivity of the notch magnitude and/or frequency with the lateral displacement. For the implementation of these sensors, it is critical to adequately choose the topology of

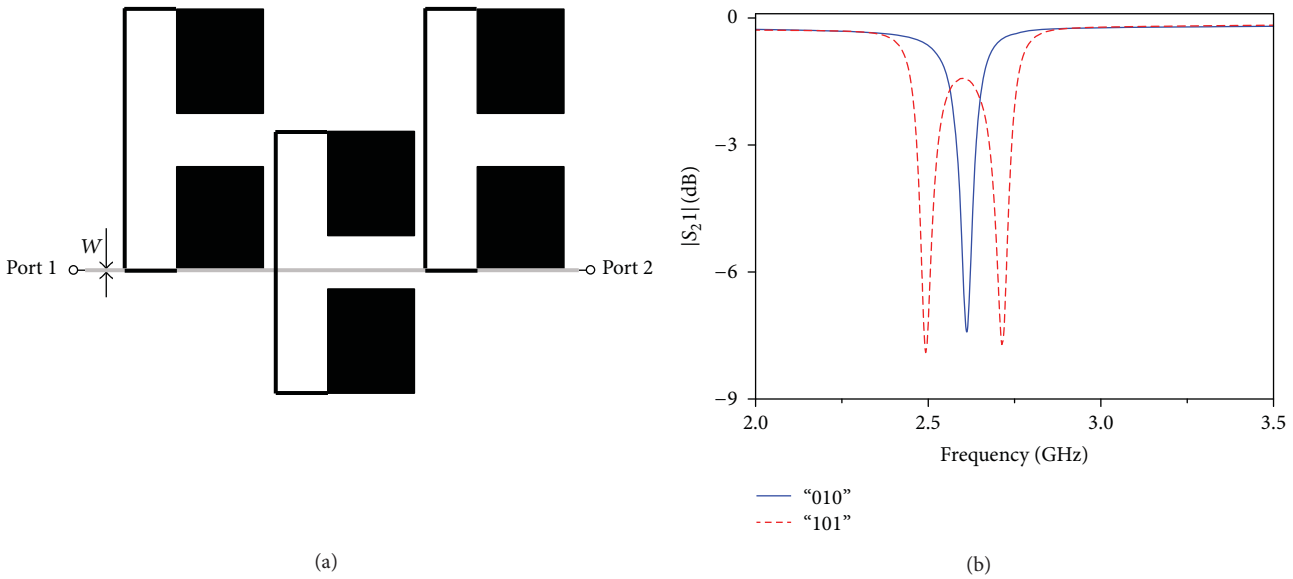

FIGURE 3: Microstrip line loaded with folded SIRs for the code "101" (a) and lossy electromagnetic simulation of the transmission coefficient corresponding to the indicated codes (b). The top and bottom substrates are *Rogers RO3010* with thickness $h = 0.254$ mm, dielectric constant $\varepsilon_r = 11.2$, and loss tangent $\tan\delta = 0.0023$. The dimensions are line width $W = 0.2$ mm, corresponding to a characteristic impedance close to 50 Ω; for the folded SIRs, w_1 (2.5 GHz) = 2 mm, w_1 (2.6 GHz) = 1.8 mm, w_1 (2.7 GHz) = 1.64 mm, $w_2 = 0.2$ mm, $s = 1.2$ mm, l_1 (2.5 GHz) = 3.26 mm, l_1 (2.6 GHz) = 3.06 mm, l_1 (2.7 GHz) = 2.9 mm, and $l_2 = 6$ mm.

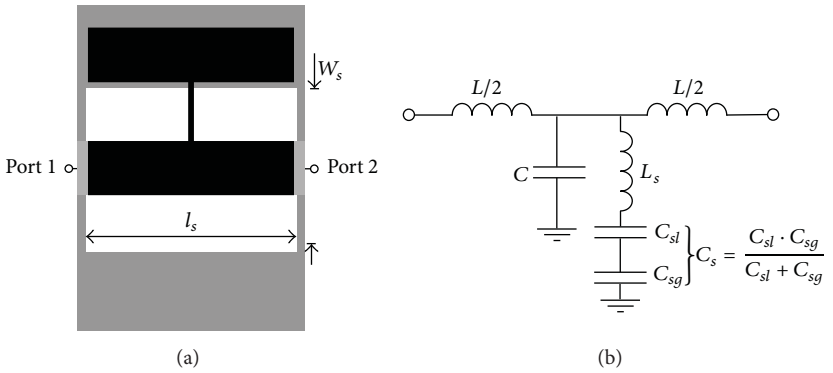

FIGURE 4: Proof of concept demonstrator of an SIR loaded microstrip line useful as alignment/position sensor for a displacement corresponding to the strongest notch (a) and lumped element equivalent circuit model (b). The microstrip line dimensions are $W = 2$ mm, $W_s = 5.8$ mm, and $l_s = 7.8$ mm; the lengths of the SIR sections are 2 mm, and the widths are $w_1 = 7.6$ mm and $w_2 = 0.2$ mm. The top and bottom substrates are *Rogers RO3010* with $h = 0.254$ mm, $\varepsilon_r = 11.2$, and $\tan\delta = 0.0023$. The inductance and capacitance of the line section are L and C, the inductance of the SIR is L_s, the SIR-to-line capacitance is C_{sl}, and the SIR-to-ground capacitance is C_{sg}.

both the SIR and the line. In order to boost the electric coupling between the line and the SIR, it is important to enhance the patch capacitance of the SIR to the line (as well as to the ground), and for this reason the line width must be widened. Since this reduces the line characteristic impedance, in order to match the ports to 50 Ω, a window in the ground plane below the position of the signal strip can be etched. This enhances the line inductance and drops the line capacitance simultaneously, compensating the reduction of the characteristic impedance. Moreover, since the electric coupling is generally stronger than magnetic coupling in SIRs, we have opted to use an unfolded configuration. Specifically, we have designed the proof of concept prototype shown in Figure 4(a), corresponding to the lateral shift providing the widest and deepest notch. To enhance the electric coupling for nonsymmetric loadings, the width of the line has been chosen to be identical to the length of the wide strip sections of the SIR. We have thus etched a slot in the ground plane (see the dimensions in Figure 4) to achieve good matching to 50 Ω in the symmetrically loaded line.

A lumped element equivalent circuit model of the structure of Figure 4(a) is proposed and depicted in Figure 4(b). According to this simple model, it is clear that to strengthen the notch it is necessary to increase the ratio between the resulting patch capacitance, C_s (given by the capacitance between the SIR and line, C_{sl}, and by that between the

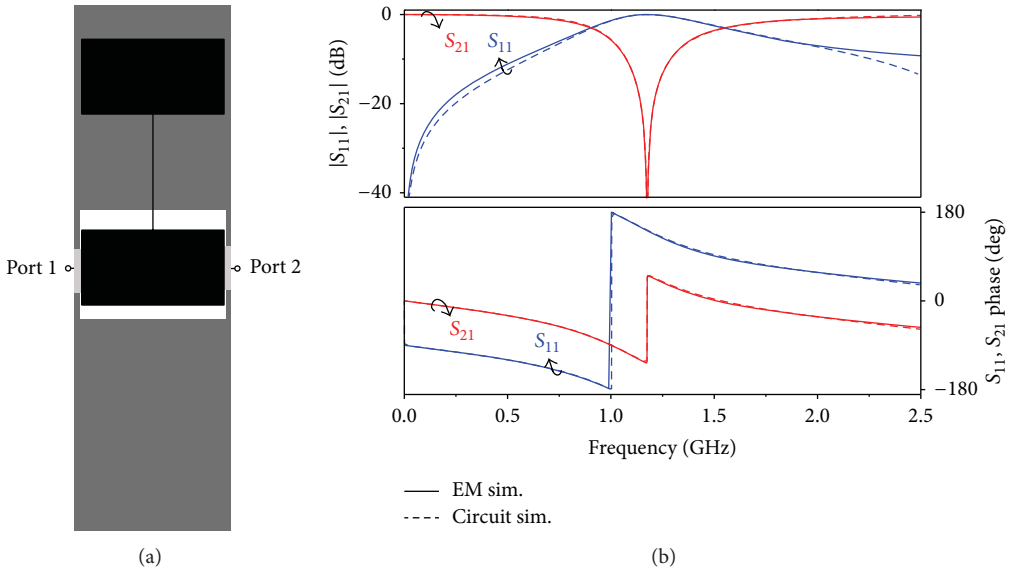

FIGURE 5: Topology of an electrically small SIR loaded microstrip line (a) and transmission/reflection coefficients from the lossless electromagnetic and circuit simulations (b). The structure is the same as that of Figure 4(a) with the exception of the SIR length, with the lengths of the wide and narrow sections being, respectively, 4 mm and 6 mm. The lumped element values are $L = 4.43$ nH, $C = 1.58$ pF, $L_s = 6.90$, and $C_s = 2.66$ pF.

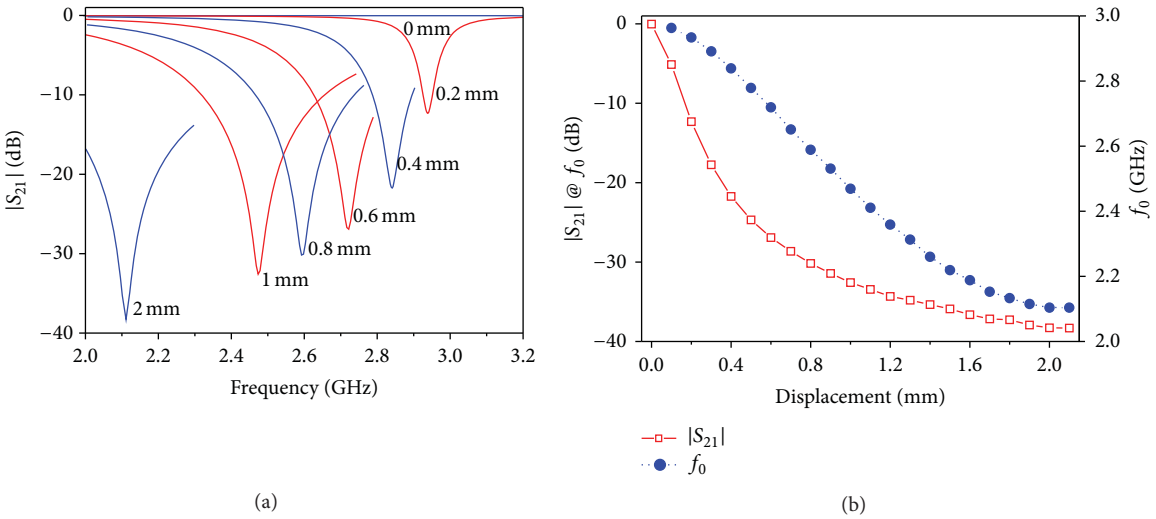

FIGURE 6: Transmission coefficient (a) and dependence of the notch magnitude and frequency (b) with lateral displacement corresponding to the structure of Figure 4, inferred from the lossy electromagnetic simulation. The displacement for maximum notch magnitude, that is, the dynamic range, is 2 mm.

SIR and ground, C_{sg}), and the SIR inductance, L_s. Hence, the equivalent circuit confirms that the electric coupling should be enhanced as much as possible, and for this reason the step in width in the considered SIR is substantially extreme. With a view to validate the circuit model, we have increased the inductance L_s and the capacitance C_s by lengthening, respectively, the narrow and the wide SIR sections, as shown in Figure 5(a). By this means the unit cell length is shortened at the resonance frequency and the circuit model is expected to predict the frequency response of the structure more accurately (note that this is at the expense of sensitivity due to the increase in the transversal dimension). The circuit parameters have been extracted in an analogous manner as in the procedure reported in [29]. In particular, such systematic method is based on a mapping from the electromagnetic simulation to the circuit response as follows: (i) the impedance of the series resonator L_s-C_s nulls at the notch frequency, (ii) when the series and shunt impedances are conjugate the transmission coefficient phase is −90°, and (iii) the intersection between the reflection coefficient and the unit normalized resistance circle provides the resonance frequency of the parallel resonator C-L_s-C_s and also (iv) the

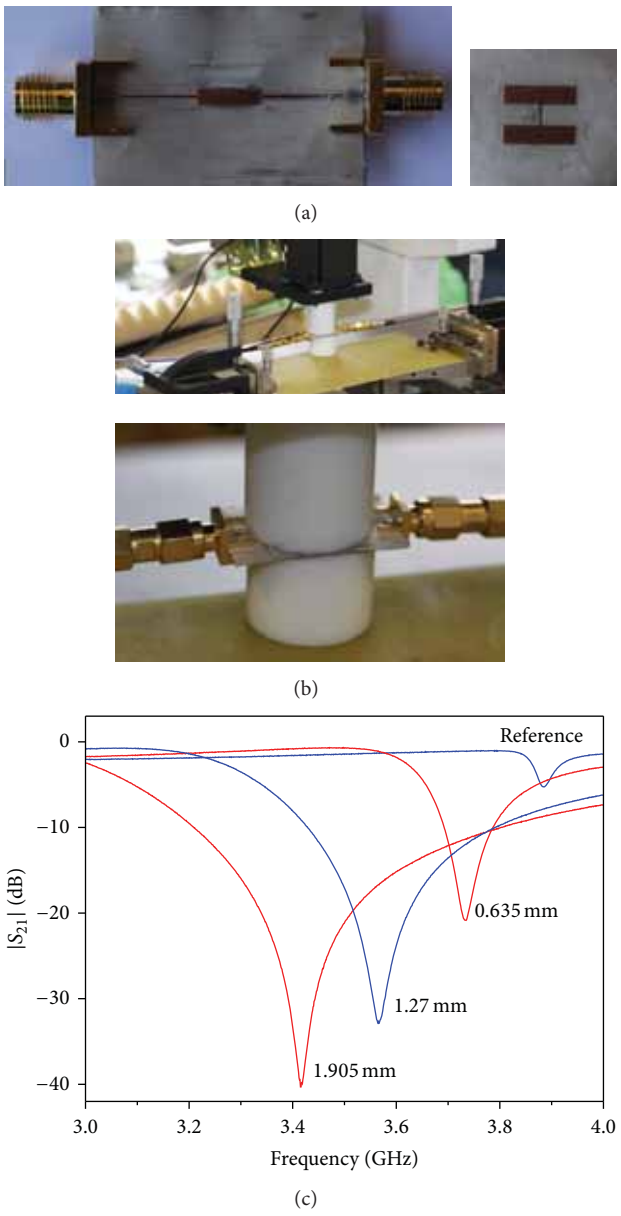

FIGURE 7: Photograph of the fabricated SIR loaded microstrip line of Figure 4 on separate substrates, where matched input/output lines of $W = 0.2$ mm have been added to solder the connectors (a). Photograph of the experimental setup with the substrates attached to Teflon slabs (a material with a low dielectric constant, $\varepsilon_r = 2.08$) and with manual positioners labeled in inches (b). Measured transmission coefficient for some lateral displacements of the SIR (c).

series inductance L. As can be appreciated in Figure 5(b), the circuit simulation fits the lossless electromagnetic simulation in a very good approximation.

Figure 6(a) plots the transmission coefficient inferred from the lossy electromagnetic simulation of the proof of concept structure shown in Figure 6(a) for different lateral displacements. The notch magnitude and frequency versus the displacement were recorded and are indicated in Figure 6(b). As can be observed, both electrical variables are quite sensitive to the displacement, indicative of a significant increase in the capacitive line-to-SIR-to-ground coupling with the displacement. Note that the sensitivity is particularly very high in magnitude for small displacements, and hence the sensor is very suitable for alignment purposes. Specifically, the average sensitivity in frequency is 42.95 MHz/100 μm in the full dynamic range, while in magnitude is −5.42 dB/100 μm in the range up to 400 μm.

The previous proof of concept demonstrator was fabricated and measured in an experimental setup that enables 3D calibrations through manual positioners (see Figure 7). Thus, the measurement of the transmission coefficient was carried out for different displacements, manually performed. Note that it was not possible to perfectly align the SIR with the line due to the fact that the sensor features a very high sensitivity for small shifts (for this reason a measured sample close to the symmetric structure was labeled as the reference one). Furthermore, the measured notch frequencies were relatively much higher than those obtained by electromagnetic simulations, and this is primarily attributed to a drop of the capacitance C_s caused by a thin air layer between the top and bottom substrates (indeed further simulations have suggested that an in-between air layer of 75 μm shifts the notch frequency upwards up to the measured results). Nevertheless, the proof of concept is experimentally validated. In the near future, we plan to characterize the structure by considering a specific distance between the line and the SIR (using a setup similar to that reported in [30]). It is also worth to bear in mind the acquisition of a more sophisticated experimental setup to perform 3D calibrations with higher accuracy.

To end this section, we would like to mention that the notch magnitude and spectral position are also sensitive to the force applied on top of the SIR substrate. This opens the possibility to implement force or pressure sensors based on the reported approach.

5. Conclusions

In conclusion, it has been shown that the SIRs are useful resonant particles as loading elements in microstrip lines aimed to act as microwave sensors or RF barcodes based on symmetry rupture. Specifically, for sensing purposes, SIRs provide high sensitivity due to the strong electric coupling between the line and the resonator. This is an advantage over other proposed sensors based on symmetry properties (e.g., displacement sensors that use split ring resonators). Moreover, these SIR loaded lines can also be potentially useful for other types of sensors, such as pressure sensors, or sensors for dielectric characterization, where the high sensitivity of SIR loaded lines can represent an advantage over other exiting approaches. Work is in progress in this regard. Concerning barcodes, a proof of concept has been developed. Although the number of bits achievable with the reported approach is limited (unless the spectral bandwidth is very high), tags based on the reported approach can be of interest in systems that do not require to store too much information and do not need a high level of security. Moreover, these

tags can be programmable (symmetry can be achieved by adding metallic strips to the SIRs) and can be implemented in flexible substrates by means of printed techniques (including low cost paper substrates). Thus, the potential can be very high (they can be useful, e.g., for document identification, product identification, electoral processes with small voting members, etc.). In summary, several applications of SIR loaded lines have been discussed, and a proof of concept (experimentally validated) of an alignment/position sensor has been provided.

Conflict of Interests

The authors declare that there is no conflict of interests regarding the publication of this paper.

Acknowledgments

This work has been supported by MINECO (Spain) (Projects TEC2010-17512, CSD2008-00066, and TEC2011-13615-E) and by AGAUR (Generalitat de Catalunya), through Project 2009SGR-421. Jordi Naqui is also in debt to MECD (Spain) for supporting his work through the FPU Grant AP2010-0431.

References

[1] D. R. Smith, W. J. Padilla, D. C. Vier, S. C. Nemat-Nasser, and S. Schultz, "Composite medium with simultaneously negative permeability and permittivity," *Physical Review Letters*, vol. 84, no. 18, pp. 4184–4187, 2000.

[2] A. K. Iyer and G. V. Eleftheriades, "Negative refractive index metamaterials supporting 2-D waves," in *Proceedings of the IEEE MSS-S International Microwave Symposium Digest*, pp. 412–415, Seattle, Wash, USA, June 2002.

[3] A. A. Oliner, "A periodic-structure negative-refractive-index medium without resonant elements," in *Proceedings of the IEEE AP-S International Symposium and USNC/URSI National Radio Science Meeting*, San Antonio, Tex, USA, June 2002.

[4] C. Caloz and T. Itoh, "Application of the transmission line theory of left-handed (LH) materials to the realization of a microstrip 'LH line'," in *Proceedings of the IEEE Antennas and Propagation Society International Symposium*, vol. 2, pp. 412–415, San Antonio, Tex, USA, June 2002.

[5] G. V. Eleftheriades and K. G. Balmain, *Negative Refraction Metamaterials: Fundamental Principles and Applications*, John Wiley and Sons, New Jersey, NJ, USA, 2005.

[6] C. Caloz and T. Itoh, *Electromagnetic Metamaterials: Transmission Line Theory and Microwave Applications*, John Wiley and Sons, 2006.

[7] R. Marqués, F. Martín, and M. Sorolla, *Metamaterials with Negative Parameters: Theory, Design and Microwave Applications*, John Wiley and Sons, 2008.

[8] J. B. Pendry, A. J. Holden, D. J. Robbins, and W. J. Stewart, "Magnetism from conductors and enhanced nonlinear phenomena," *IEEE Transactions on Microwave Theory and Techniques*, vol. 47, no. 11, pp. 2075–2084, 1999.

[9] F. Martín, J. Bonache, F. Falcone, M. Sorolla, and R. Marqués, "Split ring resonator-based left-handed coplanar waveguide," *Applied Physics Letters*, vol. 83, no. 22, pp. 4652–4654, 2003.

[10] F. Falcone, T. Lopetegi, J. D. Baena, R. Marqués, F. Martín, and M. Sorolla, "Effective negative-ε stopband microstrip lines based on complementary split ring resonators," *IEEE Microwave and Wireless Components Letters*, vol. 14, no. 6, pp. 280–282, 2004.

[11] J. D. Baena, J. Bonache, F. Martín et al., "Equivalent-circuit models for split-ring resonators and complementary split-ring resonators coupled to planar transmission lines," *IEEE Transactions on Microwave Theory and Techniques*, vol. 53, no. 4, pp. 1451–1460, 2005.

[12] L. J. Roglá, J. Carbonell, and V. E. Boria, "Study of equivalent circuits for open-ring and split-ring resonators in coplanar waveguide technology," *IET Microwaves, Antennas and Propagation*, vol. 1, no. 1, pp. 170–176, 2007.

[13] F. Aznar, J. Bonache, and F. Martín, "Improved circuit model for left-handed lines loaded with split ring resonators," *Applied Physics Letters*, vol. 92, no. 4, Article ID 043512, 2008.

[14] J. Bonache, M. Gil, O. García-Abad, and F. Martín, "Parametric analysis of microstrip lines loaded with complementary split ring resonators," *Microwave and Optical Technology Letters*, vol. 50, no. 8, pp. 2093–2096, 2008.

[15] J. Naqui, M. Durán-Sindreu, A. Fernández-Prieto, F. Mesa, F. Medina, and F. Martín, "Multimode propagation and complex waves in CSRR-based transmission line metamaterials," *IEEE Antennas and Wireless Propagation Letters*, vol. 11, pp. 1024–1027, 2012.

[16] J. Naqui, M. Durán-Sindreu, and F. Martín, "Modeling split ring resonator (SRR) and complementary split ring resonator (CSRR) loaded transmission lines exhibiting cross polarization effects," *IEEE Antennas and Wireless Propagation Letters*, vol. 12, pp. 178–181, 2013.

[17] M. Durán-Sindreu, A. Vélez, G. Sisó et al., "Recent advances in metamaterial transmission lines based on split rings," *Proceedings of the IEEE*, vol. 99, pp. 1701–1710, 2011.

[18] M. Makimoto and S. Yamashita, "Compact bandpass filters using stepped impedance resonators," *Proceedings of the IEEE*, vol. 67, no. 1, pp. 16–19, 1977.

[19] J. Naqui, M. Durán-Sindreu, and F. Martín, "On the symmetry properties of coplanar waveguides loaded with symmetric resonators: analysis and potential applications," in *Proceedings of the IEEE MTT-S International Microwave Symposium digest*, Montreal, Canada, June 2012.

[20] J. Naqui, A. Fernández-Prieto, M. Durán-Sindreu et al., "Common mode suppression in microstrip differential lines by means of complementary split ring resonators: theory and applications," *IEEE Transactions on Microwave Theory and Techniques*, vol. 60, pp. 3023–3034, 2012.

[21] D. Bouyge, D. Mardivirin, J. Bonache et al., "Split ring resonators (SRRs) based on micro-electro-mechanical deflectable cantilever-type rings: application to tunable stopband filters," *IEEE Microwave and Wireless Components Letters*, vol. 21, no. 5, pp. 243–245, 2011.

[22] M. Puentes, C. Weiss, M. Schüssler, and R. Jakoby, "Sensor array based on split ring resonators for analysis of organic tissues," in *Proceedings of the IEEE MTT-S International Microwave Symposium Digest*, Baltimore, Md, USA, June 2011.

[23] M. Schüßeler, C. Mandel, M. Puentes, and R. Jakoby, "Metamaterial inspired microwave sensors," *IEEE Microwave Magazine*, vol. 13, no. 2, pp. 57–68, 2012.

[24] T. Chretiennot, D. Dubuc, and K. Grenier, "Optimized electromagnetic interaction microwave resonator/microfluidic channel for enhanced liquid bio-sensor," in *Proceedings of the European Microwave Conference*, Nuremberg, Germany, October 2013.

[25] S. Preradovic and N. C. Karmakar, "Chipless RFID: bar code of the future," *IEEE Microwave Magazine*, vol. 11, no. 7, pp. 87–97, 2010.

[26] J. Naqui, M. Durán-Sindreu, and F. Martín, "Differential and single-ended microstrip lines loaded with slotted magnetic-LC resonators," *International Journal of Antennas and Propagation*, vol. 2013, Article ID 640514, 8 pages, 2013.

[27] C. Mandel, B. Kubina, M. Schüssler, and R. Jakoby, "Passive chipless wireless sensor for two-dimensional displacement measurement," in *Proceedings of the 41st European Microwave Conference*, pp. 79–82, Manchester, UK, October 2011.

[28] A. Horestani, C. Fumeaux, S. Al-Sarawi, and D. Abbott, "Displacement sensor based on diamond-shaped tapered split ring resonator," *IEEE Sensors Journal*, vol. 13, no. 4, pp. 1153–1160, 2013.

[29] J. Bonache, M. Gil, I. Gil, J. Garcia-García, and F. Martín, "On the electrical characteristics of complementary metamaterial resonators," *IEEE Microwave and Wireless Components Letters*, vol. 16, pp. 543–545, 2006.

[30] J. Naqui and F. Martín, "Transmission lines loaded with bisymmetric resonators and their application to angular displacement and velocity sensors," *IEEE Transactions on Microwave Theory and Techniques*, vol. 61, no. 12, pp. 4700–4713, 2013.

Conference article IMS14*

Transmission lines loaded with pairs of magnetically coupled stepped impedance resonators (SIRs): modeling and application to microwave sensors

J. Naqui, C. Damm, A. Wiens, R. Jakoby, L. Su, and F. Martín

*Conference article included in this thesis for completeness but that cannot be oficially part of the compendium of articles of the Ph.D thesis.

Transmission Lines Loaded with Pairs of Magnetically Coupled Stepped Impedance Resonators (SIRs): Modeling and Application to Microwave Sensors

[1]Jordi Naqui, [2]Christian Damm, [2]Alex Wiens, [2]Rolf Jakoby, [1]Lijuan Su, and [1]Ferran Martín.

[1]GEMMA/CIMITEC, Departament d'Enginyeria Electrònica. Universitat Autònoma de Barcelona. 08193 BELLATERRA (Barcelona), Spain. E-mail: Ferran.Martin@uab.es

[2]Institute for Microwave Engineering and Photonics. Technische Universitaet Darmstadt (Merckstrasse 25) (64283 Darmstadt, Germany)

Abstract — This paper is focused on the analysis and modeling of transmission lines loaded with pairs of shunt-connected stepped impedance resonators (SIRs), and their application to differential sensors for dielectric characterization, and for diagnosis and quality control of material samples by comparison to a reference. It is demonstrated that by placing the SIR junctions in the same position of the line, the SIRs are magnetically coupled. Such coupling has significant influence on the sensitivity of the sensor, determined by the split in frequency caused by an asymmetric dielectric loading of the SIRs. The circuit model of the structure, including magnetic coupling between SIRs, is proposed and validated through electromagnetic simulations and measurements. Finally, the principle of sensing is experimentally validated by a proof-of-concept demonstrator.

Index Terms — Circuit modeling, stepped impedance resonator (SIR), microstrip technology, microwave sensor.

I. Introduction

Stepped impedance resonators (SIRs) were initially proposed as high-Q resonators useful for the design of compact bandpass filters [1]. For decades, SIRs have been implemented in many different topologies and have found many applications in microwave engineering, mainly, although not exclusively, in the field of planar filters [2]. Particularly, this work focuses on transmission lines loaded with pairs of shunt-connected SIRs.

By using pairs of magnetically coupled SIRs, this paper investigates the potentiality of these resonant elements for the design of differential microwave sensors for dielectric characterization of materials. An interesting application is the detection of defects or anomalies in material samples by comparison to a reference. Specifically, this approach can be useful for the analysis of organic tissues and microfluidics, as an alternative to recent proposals for medical diagnosis of malignant tissues [3] and for bio-sensing [4], among others.

The target is to make real-time differential measurements that deliver the difference in dielectric constant between a reference and a material under test (MUT). Differential measurements offer major robustness against variable environmental conditions, since the dielectric constant depends on temperature, moisture, and test frequency as well [5]. Interestingly, the sensor relies on symmetry properties, rather than on differential signals.

II. Topologies and Equivalent Circuit Models

Fig. 1(a) shows a microstrip line loaded with a single shunt-connected SIR, composed of a narrow strip section cascaded to an open-ended wide strip section. If the impedance contrast is high (so that the SIR can be considered to be a semi-lumped resonator), and the microstrip line is electrically small, the SIR-loaded line can be modeled by the equivalent circuit depicted in Fig. 1(b). The inductance and capacitance of the line section are L and C, respectively, whereas the SIR inductance and capacitance, L_s and C_s, are primarily determined by the dimensions of the narrow and wide strips, respectively [6]. Losses are not considered in the model.

According to this circuit model, a transmission zero arises at the resonance frequency of the shunt-connected series resonator, i.e., $\omega_0 = (L_sC_s)^{-1/2}$. Therefore, any variation in C_s caused by a certain perturbation or abnormality can be easily inferred through the change in ω_0. In order to compare two capacitive perturbations, one way to proceed is to separately measure the resonance frequencies (from now on denoted by the subscript $i = 0$ in case that such frequencies are identical and by $i = 1, 2$ when they are different to each other) caused by each perturbation. Therefore, frequency sensitivity can be defined as the variation in the difference between the resonance frequencies (f_1 and f_2) due to the difference in the capacitive perturbations, i.e.

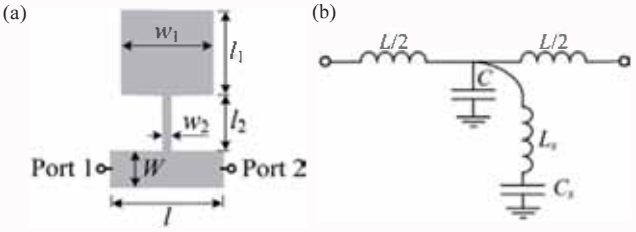

Fig. 1. (a) SIR-loaded microstrip line and (b) circuit model.

978-1-4799-3869-8/14/$31.00 ®2014 IEEE

$$S = \frac{\Delta(f_2 - f_1)}{\Delta(C_{s2} - C_{s1})} \text{ (Hz/F)}. \quad (1)$$

However, we are interested in performing a single real-time differential measurement (hence avoiding a two-step process). To this end, a pair of identical SIRs is required, and thus we consider a microstrip line loaded with a pair of symmetric parallel-connected SIRs, as shown in Fig. 2(a). The proposed lumped element equivalent circuit model is depicted in Fig. 2(b). Magnetic coupling between the SIRs is present, and it is accounted for by the mutual inductance M. Such coupling is negative because the currents in the mirrored SIRs flow in opposite directions. By using the equivalent T-circuit model of a two-port network consisting of a pair of coupled inductors [7], the circuit model shown in Fig. 2(c) is obtained. If the capacitive perturbations are identical ($\pm\Delta C_{s1} = \pm\Delta C_{s2}$), there is a magnetic wall along the line axis, and the resulting circuit is the one depicted in Fig. 2(d) which exhibits a single transmission zero at $\omega_0 = [(L_s - |M|)(C_s \pm \Delta C_s)]^{-1/2}$ (the negative inter-resonator coupling shifts the resonance frequency upwards). Contrarily, if the symmetry in the shunt branch is altered by means of unbalanced perturbations ($\pm\Delta C_{s1} \neq \pm\Delta C_{s2}$), two split resonance frequencies arise (an additional lower resonance frequency appears). The resonant condition occurs at the frequencies where the shunt branch impedance becomes zero. This leads to the resonance frequencies of a circuit network of two magnetically coupled resonators given by [7]

$$\omega_{1,2} = \sqrt{\frac{L_s(C_{s1} + C_{s2}) \pm \sqrt{[L_s(C_{s1} - C_{s2})]^2 + 4C_{s1}C_{s2}M^2}}{2C_{s1}C_{s2}(L_s^2 - M^2)}}. \quad (2)$$

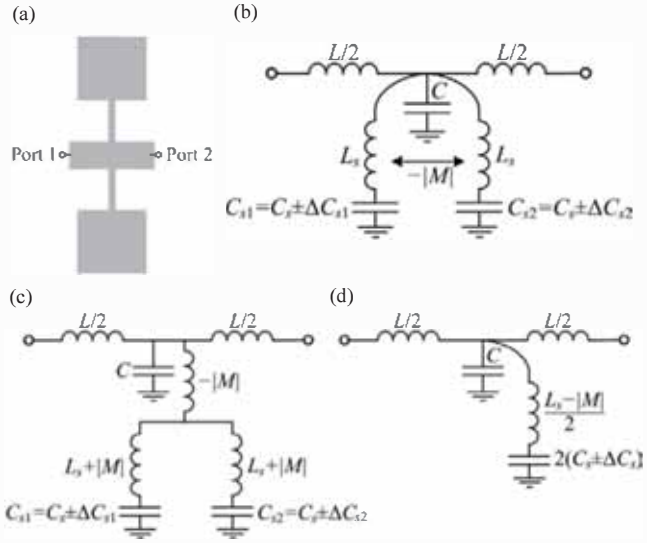

Fig. 2. (a) Microstrip line loaded with a pair of shunt-connected symmetric SIRs; (b) equivalent circuit model with capacitive perturbations; (c) transformed equivalent circuit model; (d) transformed equivalent circuit model with symmetric perturbations.

Hence, no difference exists between the perturbations if a single transmission zero is monitored. By contrast, the appearance of two transmission zeros in the frequency response indicates that non-symmetric capacitive variations are introduced.

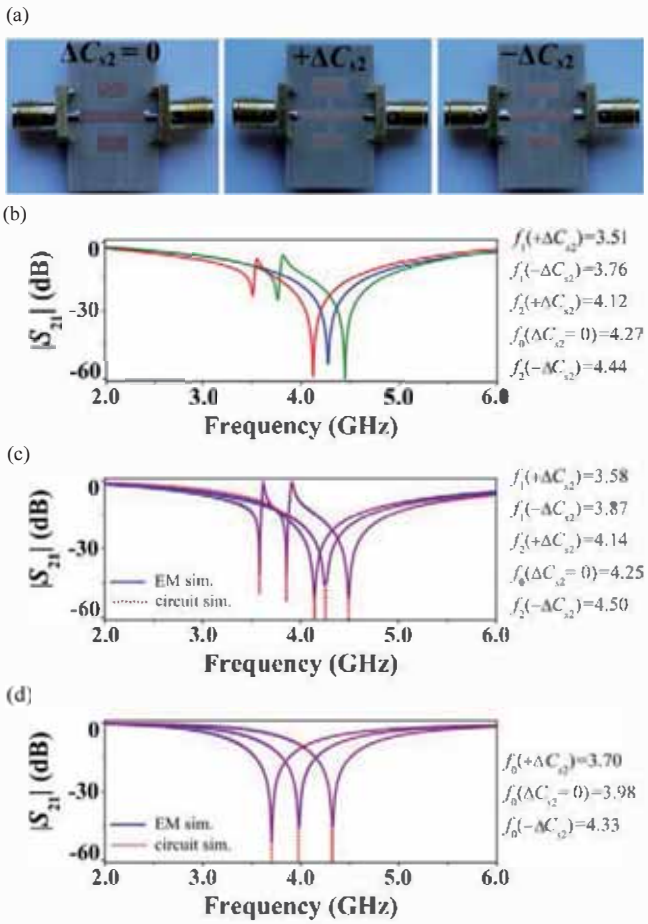

Fig. 3. (a) Photograph of the fabricated SIR-loaded transmission lines; (b) measured transmission coefficient; (c) transmission coefficient of the lossless electromagnetic and circuit simulations; (d) transmission coefficient with a single SIR [not fabricated, but used in the extraction procedure of the circuit elements]. The dimensions are $W = 1.83$ mm, $l = 15.9$ mm, $l_1 = l_2 = 2.6$ mm, $\Delta l_1 = \pm 0.5$ mm, $w_1 = 5.5$ mm, $w_2 = 250$ µm. The substrate is *Rogers RO4003C* with considered dielectric constant $\varepsilon_r = 3.1$, thickness $h = 812.8$ µm, and loss tangent $\tan\delta = 0.0021$. The circuit values are $L = 1.80$ nH, $C = 0.57$ pF, $L_s = 2.46$ nH, $C_s = 0.65$ pF, $\Delta C_{s2} = 0.15C_s = \pm 0.10$ pF, and $|M| = 0.31$ nH ($k_m = -0.13$).

In order to validate the models of Figs. 1 and 2 we have designed three structures consisting of a microstrip line loaded with: a symmetric pair of SIRs, an asymmetric pair by increasing l_1 in one of the SIRs ($+\Delta C_{s2}$), and another asymmetric pair by decreasing l_1 ($-\Delta C_{s2}$). These structures have been fabricated and measured, as shown in Fig. 3(a) and (b), respectively. The lumped element values have been extracted as follows: (*i*) the parameters in Fig. 1(b) have been

978-1-4799-3869-8/14/$31.00 ©2014 IEEE

extracted using a single SIR without any perturbation. The extraction procedure reported in [8] adapted to the considered circuit, which is based on the scattering parameters inferred from the electromagnetic simulation, has been used; (*ii*) each perturbation is extracted using $\pm\Delta C_{s2} = L_s^{-1}\omega_0^{-2} - C_s$ from the electromagnetic simulation employing a single perturbed SIR; (*iii*) M has been obtained by curve fitting the circuit simulation of the model in Fig. 2(b) to the electromagnetic simulation of the line loaded with symmetric SIRs [alternatively, (2) can also be used]. The extracted values are indicated in the caption of Fig. 3. As can be observed in Figs. 3(c) and (d) for parallel and single SIRs, respectively, the agreement between the circuit and electromagnetic simulations in the magnitude of the transmission coefficient is excellent. Although it is not shown, this also applies to the phase of S_{21}, and to the magnitude and phase of S_{11}, thus validating the circuit model. There is also good agreement between simulations and measurements, in spite that a slight discrepancy is present attributed to fabrication tolerances and some uncertainty in the dielectric constant.

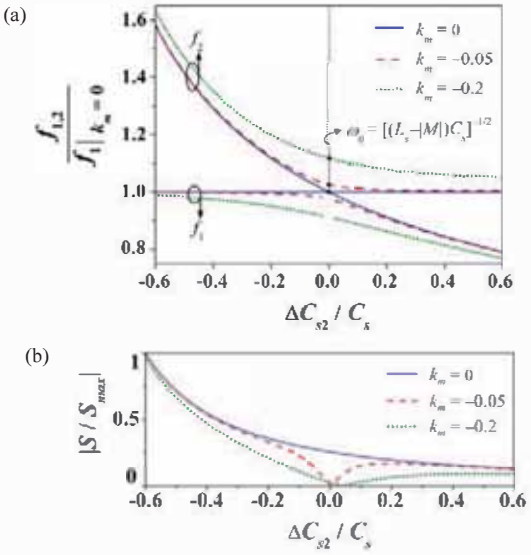

Fig. 4. Normalized (a) resonance frequencies and (b) sensitivity magnitude in symmetric parallel-connected pair of SIRs loaded with the capacitive perturbations $\Delta C_{s1} = 0$ and $-0.6 \le \Delta C_{s2} / C_s \le 0.6$ for different k_m; the resonance frequencies are normalized to the constant frequency of the non-perturbed uncoupled SIR, f_1 with $k_m = 0$; sensitivity is normalized to its maximum value S_{max}.

III. SENSITIVITY ANALYSIS

To gain insight on sensitivity, the resonance frequencies of the circuit depicted in Fig. 2(c) are plotted in Fig. 4(a). Unbalanced perturbations have been introduced by a capacitive variation in one of the SIRs ($\Delta C_{s1} = 0$, $\Delta C_{s2} \neq 0$), and different coupling coefficients $k_m = -|M|/L_s$ are considered. Although the case with $k_m = 0$ cannot be implemented with a pair of shunt-connected SIRs sharing the same junction plane to the line, this situation illustrates the case where uncoupled SIRs are used (by loading a line with a single SIR or with uncoupled cascaded SIRs). As can be seen in Fig. 4(a), when $k_m \neq 0$, the lower frequency f_1 is more sensitive to $+\Delta C_{s2}$ than f_2, and complementarily the upper frequency f_2 is more sensitive to $-\Delta C_{s2}$. These curves tend to follow the resonance frequency of the perturbed uncoupled SIR (f_2 for $k_m = 0$). As k_m increases, the frequency splitting $|f_2 - f_1|$ strengthens and degrades sensitivity. Indeed, the maximum sensitivity corresponds to the case of uncoupled SIRs. Specially, a significant drop in the sensitivity occurs for small perturbations. These effects are clearly depicted in the resulting sensitivity, shown in Fig. 4(b). Nevertheless, the frequency splitting phenomenon can be interesting as a differential comparator between two capacitively-perturbed SIRs in order to detect defects by comparison to a reference.

IV. EXPERIMENTAL VALIDATION OF THE SENSING PRINCIPLE

A proof-of-concept demonstrator based on a symmetric pair of SIRs on conductor-backed coplanar waveguide (CB-CPW) technology has been fabricated. The structure has been measured through on-wafer microwave probes without any dielectric load, and with a piece of glass ($\varepsilon_r = 4.6$) on top of one of the SIRs (see Fig. 5). The appearance of a lower transmission zero in the latter case caused by the symmetry perturbation validates experimentally the sensing principle.

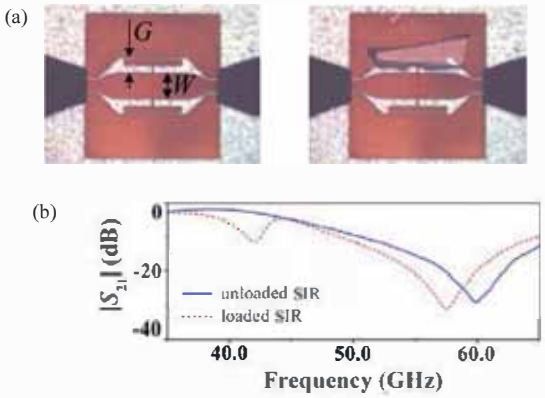

Fig. 5. (a) Photograph of the proof-of-concept demonstrator without (left) and with (right) a piece of glass on top; (b) measured transmission coefficient. The dimensions are: $W = 350$ µm, $G = 210$ µm, $l_1 = 90$ µm, $l_2 = 100$ µm, $w_1 = 800$ µm, $w_2 = 20$ µm. The substrate parameters are $\varepsilon_r = 4.6$, $h = 200$ µm, and $\tan\delta = 0.0021$.

V. CONCLUSION

This work has explored the potential of transmission lines loaded with pairs of magnetically-coupled SIRs for the development of differential microwave sensors and comparators for dielectric characterization and diagnosis of material samples. The sensing principle to detect the difference between two capacitive perturbations by inspection of the transmission zero frequencies has been experimentally demonstrated. Beyond these preliminary results, work is in

978-1-4799-3869-8/14/$31.00 ®2014 IEEE

progress to develop and characterize functional devices. Since the proposed structures are simple and fully planar, small and low-cost sensors and comparators are envisaged.

ACKNOWLEDGEMENT

This work was supported by MICIIN-Spain under Contract TEC2010-17512, Contract EMET CSD2008-00066, and Contract TEC2011-13615-E, and by the Generalitat de Catalunya under Project 2009SGR-421. The work of J. Naqui was supported by MECD-Spain under FPU Grant AP2010-0431. F. Martin is in debt to Institució Catalana de Recerca i Estudis Avançats (ICREA) for being awarded with an ICREA Academia distinction (call 2008). The authors would like to thank Karin Boye for her great help during the fabrication process.

REFERENCES

[1] M. Makimoto and S. Yamashita, "Compact bandpass filters using stepped impedance resonators," *Proc. IEEE*, vol. 67 (1), pp. 16-19, Jan 1979.

[2] J. Shi, and Q. Xue, "Novel balanced dual-band bandpass filter using coupled stepped-impedance resonators," *IEEE Microw. Wireless Compon. Lett.*, vol. 20, pp. 19-21, Jan. 2010.

[3] M. Puentes, C. Weiß, M. Schüßler, and R. Jakoby, "Sensor array based on split ring resonators for analysis of organic tissues," *Proc. IEEE MTT-S Int. Microw. Symp. Digest*, Baltimore, USA, Jun. 2011.

[4] T. Chretiennot, D. Dubuc and K. Grenier, "Optimized electromagnetic interaction microwave resonator/microfluidic channel for enhanced liquid bio-sensor," *Proc. European Microw. Conf.,* Nuremberg, Germany, Oct. 2013.

[5] J. Fraden, "Physical Principles of Sensing," in *Handbook of Modern Sensors: Physics, Design, and Applications*, 3th Ed., USA, Springer, 2004.

[6] J. Naqui, M. Durán-Sindreu, J. Bonache and F. Martín, "Implementation of shunt connected series resonators through stepped-impedance shunt stubs: analysis and limitations," *IET Microw. Antennas Propag*., vol. 5, no. 11, pp.1336-1342, Aug. 2011.

[7] J.-S. Hong and M. J. Lancaster, "General theory of couplings," in *Microstrip Filters for RF/Microwave Applications*. New York, NY, USA: Wiley, 2001.

[8] J. Bonache, M. Gil, I. Gil, J. Garcia-García and F. Martín, "On the electrical characteristics of complementary metamaterial resonators," *IEEE Microw. Wireless Compon. Lett.,* vol. 16, pp. 543.545, Oct. 2006.

978-1-4799-3869-8/14/$31.00 ©2014 IEEE

Publications by the Author

Journal Publications

J1: A. K. Horestani, J. Naqui, Z. Shaterian, D. Abbott, C. Fumeaux, and F. Martín, "Two-dimensional alignment and displacement sensor based on movable broadside-coupled split ring resonators," *Sensor Actuat. A Phys.*, vol. 210, no. 0, pp. 18–24, Apr. 2014.

J2: J. Naqui, A. Fernández-Prieto, F. Mesa, F. Medina, and F. Martín, "Effects of inter-resonator coupling in split ring resonator loaded metamaterial transmission lines," *J. App. Phys.*, vol. 115, no. 194903, May 2014.

J3: A. K. Horestani, J. Naqui, D. Abbott, C. Fumeaux, and F. Martín, "Two-dimensional displacement and alignment sensor based on reflection coefficients of open microstrip lines loaded with split ring resonators," *IET Electron. Lett.*, vol. 50, no. 8, pp. 620–622, Apr. 2014.

J4: P. Vélez, M. Durán-Sindreu, J. Naqui, J. Bonache, and F. Martín, "Common-mode suppressed differential bandpass filter based on open complementary split ring resonators fabricated in microstrip technology without ground plane etching," *Microw. Opt. Technol. Lett.*, vol. 56, no. 4, pp. 910–916, Apr. 2014. Published online in Feb. 2014.

J5: J. Naqui and F. Martín, "Mechanically reconfigurable microstrip lines loaded with stepped impedance resonators and potential applications," *Int. J. Antennas Propag.*, vol. 2014, Article ID 346838, 8 pages, Feb. 2014. Invited.

J6: A. K. Horestani, M. Durán-Sindreu, J. Naqui, C. Fumeaux, F. Martín, "S-Shaped complementary split ring resonators and their application to compact differential bandpass filters with common-mode suppression," *IEEE Microw. Wireless Compon. Lett.*, vol. 24, no. 3, pp. 149–151, Mar. 2014. Published online in Jan. 2014.

J7: J. Naqui and F. Martín, "Angular displacement and velocity sensors based on Electric-LC (ELC) loaded microstrip lines," *IEEE Sens. J.*, vol. 14, no. 4, pp. 939–940, Apr. 2014. Published online in Dec. 2013.

J8: J. Naqui, and F. Martín, "Transmission lines loaded with bisymmetric resonators and their application to angular displacement and velocity sensors," *IEEE Trans. Microw. Theory Techn.*, vol. 61, no. 12, pp. 4700–4713, Dec. 2013. Published online in Oct. 2013.

J9: J. Naqui, M. Durán-Sindreu, F. Martín, "Selective mode suppression in microstrip differential lines by means of electric-LC (ELC) and magnetic-LC (MLC) resonators," *Appl. Phys. A: Mater. Sci. Process.*, vol. 115, no. 2, pp. 637–643, May 2014. Published online in Oct. 2013.

J10: A. Fernández-Prieto, J. Martel, F. Medina, F. Mesa, S. Qian, J.-S. Hong, J. Naqui, and F. Martín, "Dual-band differential filter using broadband common-mode rejection artificial transmission line," *Progress In Electromagnetics Research*, vol. 139, pp. 779–797, 2013.

J11: J. Naqui, M. Durán-Sindreu, and F. Martín, "Differential and single-ended microstrip lines loaded with slotted magnetic-LC resonators," *Int. J. Antennas Propag.*, vol. 2013, Article ID 640514, 8 pages, May 2013. Invited.

J12: J. Naqui, M. Durán-Sindreu, and F. Martín, "Modeling split ring resonator (SRR) and complementary split ring resonator (CSRR) loaded transmission lines exhibiting cross polarization effects," *IEEE Antenn. Wireless Propag. Lett.*, vol. 12, pp. 178–181, Feb. 2013.

J13: P. Vélez, J. Naqui, A. Fernández-Prieto, M. Durán-Sindreu, J. Bonache, J. Martel, F. Medina, and F. Martín, "Differential bandpass filter with common-mode suppression based on open split ring resonators and open complementary split ring resonators," *IEEE Microw. Wireless Compon. Lett.*, vol. 23, no. 1, pp. 22–24, Jan. 2013.

J14: P. Vélez, J. Naqui, M. Durán-Sindreu, J. Bonache, and F. Martín, "Broadband microstrip bandpass filter based on open complementary split ring resonators," *Int. J. Antennas Propag.*, vol. 2012, Article ID 174023, 6 pages, Oct. 2012.

J15: J. Naqui, M. Durán-Sindreu, and F. Martín, "Selective mode suppression in coplanar waveguides using metamaterial resonators," *Appl. Phys. A: Mater. Sci. Process.*, vol. 109, no. 4, pp. 1053–1058, Dec. 2012. Published online in Nov. 2012.

J16: J. Naqui, A. Fernández-Prieto, M. Durán-Sindreu, F. Mesa, J. Martel, F. Medina, and F. Martín, "Common mode suppression in microstrip differential lines by means of complementary split ring resonators: theory and applications," *IEEE Trans. Microw. Theory Techn.*, vol. 60, no. 10, pp. 3023–3034, Oct. 2012. Published online in Aug. 2012.

J17: J. Naqui, M. Durán-Sindreu, A. Fernández-Prieto, F. Mesa, F. Medina, and F. Martín, "Multimode propagation and complex waves in CSRR-based transmission line metamaterials," *IEEE Antenn. Wireless Propag. Lett.*, vol. 11, pp. 1024–1027, Aug. 2012.

J18: J. Naqui, M. Durán-Sindreu, and F. Martín, "Alignment and position sensors based on split ring resonators," *Sensors: Special Issue Ultra-Small Sensor Systems and Components*, vol. 12, no. 9, pp. 11790–11797, Aug. 2012. Invited.

J19: M. Durán-Sindreu, J. Naqui, F. Paredes, J. Bonache and F. Martín, "Electrically small resonators for planar metamaterial, microwave circuit and antenna design: a comparative analysis," *Appl. Sci. 2012*, vol. 2, no. 2, pp. 375–395, Apr. 2012.

J20: M. Durán-Sindreu, J. Naqui, J. Bonache, and F. Martín, "Split rings for metamaterial and microwave circuit design: a review of recent developments," *Int. J. RF Microw. C. E.*, vol. 22, no. 4, pp. 439–458, Jul. 2012. Invited.

J21: J. Naqui, M. Durán-Sindreu and F. Martín, "Novel sensors based on the symmetry properties of split ring resonators (SRRs)," *Sensors: Special Issue Metamaterials for Sensing*, vol. 11, no. 8, pp. 7545–7553, Jul. 2011.

J22: J. Naqui, M. Durán-Sindreu, J. Bonache and F. Martín, "Implementation of shunt connected series resonators through stepped-impedance shunt stubs: analysis and limitations," *IET Microw. Antennas Propag.*, vol. 5, no. 11, pp. 1336–1342, Aug. 2011.

Conference Contributions

C1: P. Vélez, J. Naqui, G. Zamora, J. Bonache, F. Martín, "Applications of electromagnetic band gaps (EBGs) in microstrip and balanced microstrip lines," *International Conf. on Electromagnetics in Advanced Applications* (*ICEAA*14), Palm Beach, Aruba, Aug. 2014. Invited.

C2: L. Su, J. Naqui, J. Mata, F. Martín, "Recent Advances in Modeling Metamaterial Transmission Lines Based on Pairs of Split Ring Resonators (SRRs): Coupling between the SRRs Forming the Pair," *Metamaterials 2013*, Copenhagen, Denmark, Aug. 2014. Invited.

C3: J. Naqui, L. Su, J. Mata, and F. Martín, "Analysis of transmission lines loaded with pairs of coupled resonant elements and application to sensors," *Moscow Int. Symp. Magn.* (*MISM*-2014), Moscow, Russia, Jun. 2014. Invited

C4: J. Naqui, C. Damm, A. Wiens, R. Jakoby, L. Su, and F. Martín, "Transmission lines loaded with pairs of magnetically coupled stepped impedance resonators (SIRs): modeling and application to microwave sensors," *IEEE MTT-S Int. Microw. Symp.*, Tampa, FL, USA, Jun. 2014.

C5: J. Selga, J. Naqui, M. Durán-Sindreu, F. Martín, A. Rodríguez and V. E. Boria, "Application of aggressive space mapping (ASM) to the synthesis of stepped impedance resonators (SIRs)," *Europ. Microw. Conf. (EuMC)*, Nurember, Germany, Oct. 2013.

C6: J. Naqui, M. Durán-Sindreu, and F. Martín, "Strategies for the implementation of sensors and RF barcodes based on transmission lines loaded with symmetric resonators," *21st Int. Conf. on App. Electromagnetics and Communications* (*ICEcom 2013*), Dubrovnik, Croatia, Oct. 2013. Invited.

C7: J. Naqui, M. Durán-Sindreu, F. Martín, A. Fernández-Prieto, F. Mesa, and F. Medina, "Complex modes in periodic transmission lines based on split rings," *International Conference on Electromagnetics in Advanced Applications* (*ICEAA13*), Torino, Italy, Sept. 2013. Invited.

C8: J. Naqui, M. Durán-Sindreu, F. Martín, "Transmission lines loaded with bisymmetric resonators and applications," *IEEE MTT-S Int. Microw. Symp.*, Seattle, WA, USA, Jun. 2013.

C9: P. Vélez, J. Naqui, M. Durán-Sindreu, A. Fernández-Prieto, J. Bonache, J. Martel, F. Medina, F. Martín, "Differential bandpass filters with common-mode suppression based on stepped impedance resonators (SIRs)," *IEEE MTT-S Int. Microw. Symp.*, Seattle, WA, USA., Jun. 2013.

C10: J. Naqui, M. Durán-Sindreu, and F. Martín, "Selective mode suppression in microstrip differential lines by means of electric-LC

(ELC) and magnetic-LC (MLC) resonators," *META 2013: 4th Int. Conf. on Metamaterials, Photonic Crystals and Plasmonics*, Sharjah, UAE, Mar. 2013. Invited.

C11: J. Naqui, M. Durán-Sindreu, and F. Martín, "Transmission lines loaded with folded stepped impedance resonators (SIRs): modeling and applications," *Metamaterials 2012: the 6th Int. Cong. on Advanced Electromagnetic Materials in Microwaves and Optics*, St. Petersburg, Russia, Sept. 2012. Invited.

C12: J. Naqui, M. Durán-Sindreu, and F. Martín, "On the symmetry properties of coplanar waveguides loaded with symmetric resonators: analysis and potential applications," *IEEE MTT-S Int. Microw. Symp.*, Montreal, Canada, Jun. 2012.

C13: J. Naqui, M. Durán-Sindreu, and F. Martín, "Selective mode suppression in coplanar waveguides using metamaterial resonators," *META 2012: 3rd Int. Conf. on Metamaterials, Photonic Crystals and Plasmonics*, Paris, France, Apr. 2012. Invited.

C14: J. Naqui, M. Durán-Sindreu, A. Fernández-Prieto, F. Mesa, F. Medina, and F. Martín, "Differential transmission lines loaded with split ring resonators (SRRs) and complementary split ring resonators (CSRRs)," *Metamaterials 2011: the 5th Int. Cong. on Advanced Electromagnetic Materials in Microwaves and Optics*, Barcelona, Spain, Oct. 2011. Invited.

C15: J. Naqui, A. Fernández-Prieto, M. Durán-Sindreu, J. Selga, F. Medina, F. Mesa, and F. Martín, "Split rings-based differential transmission lines with common-mode suppression," *IEEE MTT-S Int. Microw. Symp.*, Baltimore, MD, USA, Jun. 2011.

C16: J. Naqui, M. Durán-Sindreu, J. Bonache and F. Martín, "Stepped impedance shunt stubs (SISS): analysis and potential applications in planar metamaterials," *4th Young Scientist Meeting on Metamaterials* (*YSMM11*), Valencia, Spain, Feb. 2011.

Book Chapters

B1: M. Durán-Sindreu, J. Naqui, J. Selga, P. Vélez, J. Bonache, F. Martín, "Composite right/left handed transmission line metamaterials," *Wiley Encyclopedia of Electrical and Electronics Engineering*, John Wiley & Sons, Apr. 2013.

B2: F. Martín, J. Bonache, M. Durán-Sindreu, J. Naqui, F. Paredes, G. Zamora, "Artificial transmission lines," *Wiley Encyclopedia of Electrical and Electronics Engineering*, John Wiley & Sons, Jul. 2012.

Workshop Contributions

W1: J. Naqui, J. Bonache and F. Martín, "Revisiting equivalent circuit models for emerging technologies: from microwaves to THz,"in "Equivalent circuit models for metamaterial-inspired planar circuits based on split rings and related resonators," *IEEE MTT-S Int. Microw. Symp.*, Tampa, FL, USA, Jun. 2014.

W2: J. Naqui, M. Durán-Sindreu and F. Martín, "On the symmetry properties of transmission lines loaded with metamaterial resonators: theory and applications,"in "Microwave Metamaterial Concepts, Circuits and Applications," *European Microw. Week*, Nurember, Germany, Oct. 2013.

W3: F. Martín, J. Naqui, P. Vélez, M. Durán-Sindreu and J. Bonache, "Split ring resonator (SRR) and stepped impedance resonator (SIR) based metamaterial transmsision lines: application to microwave components and novel sensing strategies,"in "Metamaterials in communications and sensing: reality or fiction?," *IEEE Radio Wireless Week*, Austin, TX, USA, Jan. 2013.

Acronyms

AM (amplitude modulation)

ASM (aggressive space mapping)

BW (backward wave)

CB-CPW (conductor backed coplanar waveguide)

CMRR (common-mode rejection ratio)

CPS (coplanar strips)

CRLH (composite right/left-handed)

CSRR (complementary split-ring resonator)

CSSRR (complementary split squared ring resonator)

CPW (coplanar waveguide)

DGS (defected ground structure)

DMLIN (differential microstrip line)

DPS (double positive)

DNG (double negative)

DS-CSRR (double-slit complementary split-ring resonator)

DS-SRR (double-slit split-ring resonator)

EIW (electroinductive wave)

EMI (electromagnetic interference)

ENG (epsilon negative)

ELC (electric inductive-capacitive)

FBW (fractional bandwidth)

FW (forward wave)

IC (integrated circuit)

LH (left-handed)

LTTC (low temperature co-fired ceramic)

MLC (magnetic inductive-capacitive)

MLIN (microstrip line)

MIW (magnetoinductive wave)

NB-CSRR (non-bianisotropic complementary split-ring resonator)

NB-SRR (non-bianisotropic split-ring resonator)

MNG (mu negative)

NRI (negative-refractive index)

OSRR (open split-ring resonator)

OCSRR (open complementary split-ring resonator)

PCB (printed circuit board)

PGS (patterned ground structure)

PLH (purely left-handed)

PRH (purely right-handed)

RH (right-handed)

RF (radio frequency)

RFID (radio-frequency identification)

SIR (stepped-impedance resonator)

SISS (stepped-impedance shunt-stub)

SNG (single negative)

SRR (split-ring resonator)

SSRR (split squared ring resonator)

TEM (transverse electromagnetic)

TL (transmission line)

VNA (vector network analyzer)

1D (one-dimensional)

2D (two-dimensional)

3D (three-dimensional)